Alexander Busch

On particle transport and turbulence in wellbore flows of non-Newtonian fluids

Findings from a cuttings transport process analysis by means of computational fluid dynamics, rheometry, and dimensional analysis

Thesis for the degree of Philosophiae doctor

Trondheim, April 2020

Norwegian University of Science and Technology
Faculty of Engineering
Department of Energy and Process Engineering

NTNU – Trondheim
Norwegian University of
Science and Technology

NTNU

Norwegian University of Science and Technology

Thesis for the degree of Philosophiae doctor

Faculty of Engineering
Department of Energy and Process Engineering

ISBN 978-82-326-4543-5 (printed version)
ISBN 978-82-326-4542-8 (electronic version)
ISSN 1503-8181

Doctoral theses at NTNU, 2020:95

Printed by Skipnes Kommunikasjon AS

Abstract

Cuttings transport modeling was analyzed with a major focus on three-dimensional (3D) Computational Fluid Dynamics (CFD) approaches including rheometry and to a lesser extent on one-dimensional modeling and dimensional analysis.

As a first step, the relevant parameter space was analyzed and field values typical for the Norwegian Continental Shelf were established. Dimensional Analysis was applied to further understand the parameter space and to establish a process description based on a polynomial.

For the fluid phase (i.e., the drilling fluid or a drilling fluid model system), the classical General Newtonian Fluid (GNF) concept was investigated by means of rheometry and the example of polymeric solutions (Polyanionic Cellulose (PAC) dissolved in distilled water) typically used in experimental cuttings transport studies. It is shown that the GNF assumption only holds if the fluid is at steady-state with respect to its microstructure and that such a steady-state may be hard to achieve in experimental works because of the long rheological timescales of the fluid.

Concerning the solid phase (i.e., the cuttings), the performance of the typical modeling concept utilized in cuttings transport research, namely the Kinetic Theory of Granular Flow (KTGF) in combination with a frictional viscosity model accounting for dense granular regions, was evaluated by means of CFD simulations of the cliff collapse problem. Several fluids (air, water, two PAC solutions) and spatial scales (cliff height and particle diameter), among other parameters such as the cliff's aspect ratio and initial solid volume fraction were investigated. While the typical sloped deposits were obtained in most cases shortly after the collapse these were found to be unstable: The top layer of the sediment bed continues flowing after the collapse which eventually leads to an entirely flat deposit. This is attributed to the utilized modeling approach which is not capable of

handling the top sediment bed layer successfully.

As an alternative, a modeling approach prominent in the field of environmental sediment transport modeling was tested. The dense region is dynamically excluded from the computational domain, and the Exner equation is used to describe the evolution of the sediment bed. Problems such as proper closures for the bed load transport models as well as contact problems were encountered, disqualifying this approach for use of cuttings transport simulations within the scope of this project.

The relevance and magnitude of turbulence and dunes in wellbore flows were estimated and several pipe and annular single-phase RANS simulations were compared with DNS data (generated in the AdWell project) for Newtonian and shear-thinning fluids. While wellbore flows are laminar to transitional (mostly depending on the fluids' viscosity), none of the turbulence models investigated appears to be universally applicable. However, this part is still in progress and only preliminary conclusions are presented.

A subproblem of cuttings transport, a particle subjected to a cross-flow of a mildly viscoelastic, shear-thinning fluid, was investigated by means of CFD. The particle is treated in a Lagrangian manner and the particle-induced shear is accounted for in the computation of the fluids viscosity as seen by the particle. Several cases were investigated and the model was validated with results from the literature. Discrepancies are found close to the lower channel wall were the particles in the experiments are advected much farther than in the simulations.

Finally, drill pipe rotation in combination with orbital drill pipe motion was investigated. Specifically, the effect of forward, i.e., synchronous, and backward, i.e., asynchronous, whirl (SW and AW, respectively) on cuttings transport was evaluated and compared with classical concentric and eccentric arrangements. AW and, more dramatically, SW improve cuttings transport, albeit depending on other system parameters such as the fluid's rheological parameters and the drill pipe's rotational rate. However, for the parameter space investigated, best transport of cuttings was obtained in a positively eccentric drill pipe system because the main flow occurs at the top of the bed and consequently high shear stresses acting on the bed.

This thesis highlights current shortcomings and potential for improvement of CFD cuttings transport simulation. Further work is required on all individual topics to achieve better quantitative results and to integrate subscale models into a model on the annular scale. The findings presented here will hopefully contribute to a more comprehensive understanding of cuttings transport and support further development of CFD models applicable to the annular scale and more coarse, real-time models applicable to the entire wellbore.

Knowledge is fundamental to all human achievements and progress.

Neil Armstrong (1971 CE)

Preface

This thesis is submitted as partial fulfillment of the requirements for the degree of Philosophiae Doctor (PhD) at the Norwegian University of Science and Technology (NTNU) in Trondheim, Norway.

The research results presented in this thesis were generated in the period December 2014 to December 2018 at the Fluid Mechanics Group (today the Thermo Fluids Research Group at the Department of Energy and Process Engineering (EPT) at NTNU. The PhD project was a subproject (PhD2 "Turbulence structure and particle transport in particle loaded non-Newtonian fluids") of the Advanced Wellbore Transport Modelling (AdWell) research project. The AdWell project was initiated by a research consortium consisting of NTNU, the International Research Institute of Stavanger (IRIS)[1], SINTEF Materials and Chemistry[2], the University of Stavanger (UiS), STATOIL[3], and GDF Suez E&P[4]) [1] in 2013. It was mainly funded by the Research Council of Norway (RCN) (project number 228391) under the *Large-scale Programme for Petroleum Research* (PETROMAKS2) as part of the Norwegian Oil and Gas in the 21st century (OG21) strategy [2].The major objective was to enhance the understanding of the complex physics of cuttings transport by means of (partly intertwined) numerical and experimental investigations in order to gain knowledge to build improved real-time (RT) models relevant for the (Norwegian) drilling industry [3].

Concurrent activities in the AdWell project included the experimental and numerical modeling of drill string vibrations (PhD1), experimental cuttings transport investigations (PhD3) [4], and supporting activities such as Direct Numerical Simulations (DNS) as well as modeling framework definitions [5, 6].

---

[1] Today: Norwegian Research Centre (NORCE)

[2] Today: SINTEF Industry

[3] Today: Equinor

[4] Today: Neptune Energy

The explicit concept of the AdWell project was to link experimental and numerical approaches to investigate cuttings transport and generate a better physical understanding of the involved physical processes and effects. Hence, PhD2 and PhD3 had a close collaboration and worked jointly on some topics.

While the majority of the work presented in this thesis was conducted at EPT at NTNU, Trondheim, some initial work was conducted at the Flow Technology research group at SINTEF Industry, Trondheim. Rheometric data was generated in the laboratories of SINTEF Petroleum AS, Bergen, the Department of Geoscience and Petroleum at NTNU, and by UiS personnel at the Department of Energy and Petroleum Engineering at UiS, Stavanger.

This thesis is based on collaborative work done by research colleagues (both from within and outside the AdWell project) and myself. Thus, it is a summary I have written on the individual research I have done in collaboration with many other researchers. Therefore, work done individually is referred to as "we" instead of "I" in the main part of the thesis because without the dedication and contribution of the entire team, the individual research summarized and presented in this thesis would not have been possible. In addition, "we" is used to include the reader in the introduction.

Nine months of the four years of this PhD project were dedicated to teaching duties in the NTNU master courses System Simulation, Multiphase Transport, and Modelling of Multiphase Flow. Teaching duties included tutoring students, developing new course material such as lecture notes and exercises, and substitute lecturing. In addition, three months were dedicated to board membership in the Interest Organization for PhDs, Post-Docs, and Temporary Scientific Employees at NTNU (DION), kindly supported by NTNU. Besides concrete support of the PhD, Post-Doc, and temporary scientific employee community at NTNU in the form of supporting case handling, four DION projects addressing various issues relevant to the community were conducted [**XVIII**–**XXI**].

Personally, with this PhD thesis, I am closing an educational gap, namely the physics and simulation of multiphase flow systems. I started out as a diving instructor, where I experienced respiratory flows and the drag of underwater currents exerted on divers first-hand and also got interested in decompression physics, i.e., gas saturation processes in the human body, which are multiphase by nature. Later, I moved on towards design engineering of respiratory systems for diving and respiratory protection and developing of 1D system simulation models for diving rebreathers.

Now, through the work summarized in this thesis, I have further advanced in terms of three-dimensional mathematical and physical modeling of multiphase flow systems. I hope to have contributed to the scientific knowledge of cuttings transport with this thesis. Professionally, I have in the meantime moved on to 3D and 1D modeling of expansions valves and refrigerant flows—yet another exciting multiphase flow technology.

Alexander Busch
Lübeck/Trondheim, March 2020

> *One, remember to look up at the stars and not down at your feet. Two, never give up work. Work gives you meaning and purpose and life is empty without it. Three, if you are lucky enough to find love, remember it is there and don't throw it away.*
>
> Stephen Hawking (2010 CE)

Acknowledgments

My sincerest thanks go to my first supervisor Professor Stein Tore Johansen, for warmheartedly showing us around in Trondheim in May 2014 and convincing us to move to Norway for three and a half years. Moreover, thank you very much for allowing and encouraging me to pursue my own ideas, while ensuring that each of these were developed further in a scientific and physically sound manner, for your helpful advice, support, and always positive attitude. In addition, I am particularly thankful for your patience during the first years of my PhD when I had a lot to learn and absorb. Thank you to my second supervisor Ernst Arne Meese (deceased) for teaching me some basic math concepts and the introduction to Maple and for your straightforward guidance whenever I stopped by your office to discuss an issue. And thank you to my third supervisor Professor Rune W. Time for all the good discussions and beneficial experimental input to our modeling efforts.

I am grateful to the entire AdWell team for your continuous support of my work in the form of technical advice and thought-provoking discussions. Especially, I would like to thank my experimental counterpart Milad Khatibi for a great collaboration, for all the challenging and yet fruitful discussions, and your valuable input to our modeling work. Thank you to the industry representatives, Aminul Islam and Dwayne Werner Martins, for providing guidance on drilling, hole cleaning and cuttings transport, and your support in developing our research project. And thank you to Fionn P. Iversen for fabulously orchestrating the project team and for your helpful feedback and challenging ideas.

I further thank all my co-authors whom I have collaborated with and who have been a vital part of my work. Each and everyone of you helped to contribute to this work and I am very grateful for that. A special thank you to Velaug Myrseth Oltedal for your superb introduction to the field of experimental rheology and to Paal Skjetne for the theoretical part.

Thank you to all the Flow Technology Research Group people at SINTEF Industry (formerly known as SINTEF Materials and Chemistry), namely Are Simonsen, Balram Palwani, Jan Erik Olsen, Jan Henrik Cloete, John Morud, Paal Skjetne, Schalk Cloete, Sigrid K. Dahl, and Sverre Gullikstad Johnsen, who, besides having been very helpful discussing different matters of my research, helped me getting started with ANSYS Fluent, helped me dealing with the peculiarities of Fluent, and supported me in dealing with Fluent UDF programming.

Thank you to all my peers and colleagues from EPT and other places at NTNU, who have contributed immensely to my personal and professional time at NTNU. Especially, thank you Andrey Chesnokov for many good shared hours, some mathematical concepts, and properly introducing me to LaTeX. Thank you Benjamin Werner for all the pleasant lunch meetings, the shared stories, and burgers'n'beers. The latter also applies to Marin Prebeg, and furthermore, thank you for collectively suffering but successfully making it through the *Modeling of Multiphase Flows* course and the granted LaTeX support. And thank you, Son Tung Dang, for many helpful discussions and pleasant lunch periods.

Thank you to the funding organizations that supported my doctoral work: RCN, NTNU, SINTEF, UiS, Equinor, Neptune Energy, and NORCE.

Thank you to the High Performance Computing group at NTNU, and to the staff at EDRMedeso and UNINETT Sigma2 AS for all the great support throughout the years.

Thank you to Ole Jørgen Nydal and Reidar Kristofferson for letting me join your courses as a teaching assistant and granting me the freedom to pursue my own ideas and concepts.

Thank you to my fellow board members in DION from 2015 to 2018, especially my project team members and report co-authors, for the great collaboration and working together to make NTNU a better place for all PhD students, post-docs, and temporary employees. In particular, thank you to Mathias Hauan Arbo for many fascinating discussions outside the box and burgers'n'beers and Kam Sripada for the very same. Moreover, a big thank you to Kam Sripada for making an English thesis out of my German English thesis!

Thank you to all my friends and family for your support and being there. Especially, Herr Dipl.-Ing. A. Schubert, MBA a.k.a. Sport-und-Technik Adi for many shared burgers'n'beers and many more to come, Bastian a.k.a. Stierhoden for celebrating some (and hopefully saving some more) R'n'R together, Daniel the Wild a.k.a. Deichy for simply being the Wild, Florian for fundamental contributions to astronomy and always making me laugh.

Vaness, Joshi, Lukas, Mum & Dad—thank you for your unconditional love, your continuous support, and everything else!

Finally, thank you in advance to the members of my PhD defense committee for the time and effort you have set aside to read (Sincere apologies for long sentences and any incorrect/missing commas) and evaluate my thesis.

Alexander Busch
Lübeck/Trondheim, March 2020

Just 'cos you got the power, That don't mean you got the right.

Burston, Campbell, Taylor, and Kilmister (1987 CE)

Ethical considerations

Many valid reasons against petroleum production and research exist. For instance, climate change caused by carbon dioxide emissions, general environmental impact of oil drilling exploration and production processes and particular incidents such as the Exxon Valdez and the Deepwater Horizons oil spills, plastics pollution of oceans and accumulation of microplastics in animals and humans, the support of non-democratic regimes, just to name a few, are all legitimate and important reasons to not back the oil industry in general.

On the other hand, our world runs on fossil fuels and plastics, despite the increasing efforts to develop alternatives. Our cars, ships, and airplanes require fuel. Most everyday items such as computers and smartphones, clothing and shoes, as well as medicines require petroleum. While alternatives to both fossil fuels and plastics are becoming more and more mature and prominent, the change towards an oil-free world requires time and further efforts.

Norway is an interesting example for that change. On one hand, Norway benefits tremendously from its petroleum income. The oil and gas industry accounts for almost a fifth of the gross domestic product, and a fifth to a third of state revenues [7, 8] (e.g. 264.1 billion NOK in 2018 and 285.8 billion NOK in 2019 [8]) originate from the petroleum sector. On the other hand, Norway invests heavily in future non-fossil technology, both directly by means of research funding, legislation, and subsidies, as well as indirectly by means of investments via its oil fund.

In 2014, the Norwegian National Committee for Research Ethics in Science and Technology (NENT) was challenged by the University of Bergen to evaluate the ethics of petroleum research. NENT concluded that petroleum research is in accordance with its Guidelines for Research Ethics in Science and Technology [9] and justifiable as long as it does not hinder restructuring attempts and transition efforts targeted towards petroleum alternatives such as renewable forms of energy [10]. This is reflected by RCN research funding. For instance, wind power, hydro power, and carbon dioxide storage research have seen more and more funding over recent years. Since 2014, the RCN has allocated more than twice as much funding to renewable forms of energy and climate-related research (e.g. wind power, hydro power, and carbon dioxide storage) than to petroleum research [11].

Beyond research, Norway leads the way when it comes to the shift away from the negative impacts of oil. For instance, Norway introduced a carbon dioxide tax as early as 1991 [8]. It has one of the most sophisticated deposit return schemes for plastic bottles and cans with a recycling rate of 97 % [12]. Moreover, Norway leads the change towards electric auto-mobility on a per capita basis [13, 14], generates most of its power supplies by means of hydropower [15], and is aiming for fossil free public transport by 2025.

In addition, NENT acknowledged that petroleum research remains relevant in the transition process [10]. As only 45 % of the estimated total recoverable resources on the NCS have been produced so far [8, 16], Norway will most likely further rely and thrive on its petroleum industry despite its general shift towards renewables for its own power supply and means of transportation. However, some of these recoverable oil resources are located in very sensitive arctic environments such as the Lofoten and Vesterålen archipelagos. Oil exploration in these areas has been heavily debated for years in Norway [17]. However, these regions are to remain off-limits to oil firms until the next election for parliament in 2021 [18], and very recently a majority in parliament against oil exploration in these areas was established [19].

The Norwegian Government Pension Fund Global (GPFG), also known as the oil fund, to some extent ensures a redistribution of oil revenues to renewables. The GPFG was established in 1990 and has been fed with the yearly revenues of Norwegian oil production since 1996 [7], accumulating 8256 billion NOK at the end of 2018 [20] and on average holding 1.4 % of all of the world's stock exchange listed companies. This is because the Norwegian state formally owns not only all oil found on the NCS and generates corresponding income from taxes and license fees [16], it also holds 67 % of the shares in Equinor (formerly known as STATOIL), Norway's largest oil company [8, 17]. The GPFG has comparatively strict ethical standards when it comes to its investment policies and excludes companies that violate human rights, use child labor, manufacture nuclear weapons or cluster munitions, or base their operations on coal [21, 22]. Furthermore, the GPFG regularly evaluates its investments regarding exclusion policies and increasingly invests in green bonds while divesting from companies that are considered to impose substantial costs and risks on society as a whole [20]. Very recently, the GPFG announced plans to dump all its investments which are purely based on oil and gas exploration [23]. Moreover, the GPFG aims to vote at all general meetings of the companies it invests in [20] and actively engages in dialogues with its companies covering topics such as deforestation and marine pollution from agriculture [20].

This research project aims to contribute to the increase of drilling efficiency by means of knowledge building. It is largely funded by the RCN with a minor contribution from industry, and all its research results are publicly available. In general terms, an increase in efficiency will directly contribute to an increase in profit and thereby allow for other expenditures. The majority of the income from the revenues of Equinor, taxes on petroleum production, and profits from direct investments of the Norwegian state on petroleum fields are funneled to the oil fund [8]. Therefore, paradoxically, a part of petroleum revenues are in fact reallocated to the investigation and development of an oil-free future.

On a final note, the problem of solids transport in liquids occurs in many other industries such as mining, waste management, civil engineering as well as in environmental flows. The findings of this oil-funded research project may help to advance research in other relevant fields.

Alexander Busch
Lübeck/Trondheim, March 2020

Nomenclature

Abbreviations

1D	One-dimensional.
3D	Three-dimensional.
3ITT	Three-Interval-Thixotropy-Test.
AdWell	Advanced Wellbore Transport Modelling.
AS	Amplitude Sweeps.
AW	Asynchronous Whirl.
BC	Boundary Condition.
BHA	Bottom Hole Assembly.
CFD	Computational Fluid Dynamics.
CMC	Carboxy Methyl Cellulose.
CTR	Cuttings Transport Ratio.
DA	Dimensional Analysis.
DDPM	Dense Discrete Phase Model.
DEM	Discrete Element Method.
DNS	Direct Numerical Simulation.
DoE	Design of Experiments.
DPM	Discrete Phase Model.

Nomenclature

DR	Drag Reduction.
EPT	Department of Energy and Process Engineering.
FC	Flow Curve.
FNSD	First Normal Stress Difference.
FS	Frequency Sweeps.
GNF	Generalized Newtonian Fluid.
GPFG	Government Pension Fund Global.
KCl	Potassium Chloride.
KTGF	Kinetic Theory of Granular Flows.
LAOS	Large Amplitude Oscillatory Shear.
LES	Large Eddy Simulation.
MR	Metzner and Reed [24].
MWD	Measurement While Drilling.
NCS	Norwegian Continental Shelf.
NORCE	Norwegian Research Centre.
NPD	Norwegian Petroleum Directorate.
NSD	Normal stress difference.
NTNU	Norwegian University of Science and Technology.
OBM	Oil-Based Muds.
OG21	*Oil and Gas in the 21st century* national strategy initiative.
PAC	Polyanionic Cellulose.
PETROMAKS2	Large-scale Programme for Petroleum Research.
PhD	Philosophiae doctor.
PIV	Particle Image Velocimetry.

PL	Power Law, equivalent to the Ostwald/deWaele [25–27] material function.
PTV	Particle Tracking Velocimetry.
PV	Plastic viscosity.
RANS	Reynolds-Averaged Navier-Stokes.
RCN	Research Council of Norway.
ROP	Rate of Penetration.
RSA	Response Surface Analysis.
RSM	Reynolds Stress Model.
RT	Real-Time.
SM	Soil Mechanics.
SST	Shear Stress Transport.
SW	Synchronous Whirl.
TFM	Two Fluid Model.
UDF	User-Defined Function
UiS	University of Stavanger.
VOF	Volume of Fluid.
WBM	Water-Based Muds.
WOB	Weight On Bit.
YP	Yield Point.
YPL	Yield Power Law, equivalent to the Herschel-Bulkley [28] material function.

Greek symbols

α	Volume fraction.
$\dot{\gamma}$	Shear rate (Magnitude of the rate of deformation tensor).

Nomenclature

ϵ	Dissipation rate.
η	Shear viscosity.
$\mathit{\Gamma}$	Deposition and entrainment rates.
κ	Bulk viscosity.
λ	Cross/Carreau timescale.
μ	Newtonian shear viscosity.
ω	Specific dissipation rate, Angular velocity.
ϕ	Angle of internal friction.
$\mathit{\Pi}$	Dimensionaless quantity/group.
ρ	Density.
σ	Yield stress.
τ	Relaxation time.
$\mathit{\Theta}$	Granular temperature.

Indices

0	Zero, Low shear.
$3ITT$	Three Intervall Thixotropy Test.
∞	Infinity, High shear.
$\mathit{\Theta}_s$	Granular.
a	Annulus.
b	Cuttings bed.
Ca	Carreau [29].
CFD	Computational Fluid Dynamics solver.
Cr	Cross [30].
D	Drag.

d	Damping.
f	Fluid (if used as first index), Frictional (if used as second index, e.g. $_{s,f}$), Final.
FC	Flow Curve.
h	Hydraulic, Homogenous.
h,s	Solid particles in homogenous suspension.
i	Inner, Free index.
j	Joint, Free index.
l	Limiting.
Max	Maxwell.
MR	Metzner and Reed (1955) [24].
o	Outer.
p,set	Terminal settling (velocity) of a particle.
PL	Power Law.
PV	Plastic viscosity.
r	Relative.
RS	Recoverable shear.
s	Solid.
s,f	Solid, Frictional regime.
$s,k/c$	Solid, Kinetic/Collisional.
s,mpd	Maximum packing density of solid phase.
St	Stokes.
t	Turbulent.
w	Whirl.

Nomenclature

x	Extra.
YP	Yield point.
YPL	Yield Power Law.

Latin symbols

$\mathbf{D}$	Rate of deformation tensor (symmetric part of the velocity gradient).
$\mathbf{f}$	Particle force.
$\mathbf{g}$	Gravity.
$\mathbf{T}$	Stress tensor $\mathbf{T}_i = -p_i\mathbf{I} + {}^{x}\mathbf{T}_i$.
$\mathbf{u}$	Instantanious or volume and ensemble averaged velocity.
A	Area, Amplitude.
b	Blending function.
c	Coefficient.
d	Diameter.
De	Deborah number.
E	Dimensional eccentricity.
e	Coefficient of restitution.
f	Functional.
g	Radial distribution function.
h	Height.
K	Interphase momentum exchange coefficient, Consistency index.
k	Conductivity, Turbulent kinetic energy.
L	Length scale.
P	Production.
p	Particles, Pressure.

Pr	Turbulent Prandtl number.
Re	Reynolds number.
t	Time.
U	Bulk velocity/Superficial velocity.
V	Volume.
v	Velocity magnitude.
w	Width.
Wi	Weissenbergh number.
x	Spatial x-coordinate.
Y	Radial distribution function.
y	Spatial y-coordinate.
z	Spatial z-coordinate.

Contents

The one who does the work does the learning.

Terry Doyle (2011 CE)

1

Introduction

1.1. Cuttings transport in petroleum drilling

When drilling a hole in a wall by means of a home-use drilling machine, solid particles, so-called cuttings, are generated by the sharp blades at the tip of the drill bit and subsequently transported out of the hole by the helical motion of the drill bit geometry due to its rotation.

In petroleum drilling, a mechanical drill bit mostly driven by a rotating drill string cuts the formation into solid particles. However, when comparing petroleum drilling to the home-use drilling machine example, transport of the cuttings out of the well is achieved in a very different manner. Figure 1.1 depicts a conceptual sketch of a wellbore system. The scale of the entire wellbore is very much larger ($\mathcal{O}\left(L\right) = 10^3 - 10^4$ m) than the hole in the wall and the wellbore may feature a trajectory quite different from a simple hole. Therefore, cuttings cannot be transported mechanically out of the hole by means of a rotating spiral.

Instead, transport of the solid particles out of the wellbore is principally achieved by pumping a drilling fluid, also termed drilling mud in the industry, into the well through the drill string which continuously flushes and cools the drill bit and picks up the cuttings. The drilling fluid is pumped down either through the drill string consisting of mechanically connected drill pipe elements or coiled tubing. At the bit, the drilling

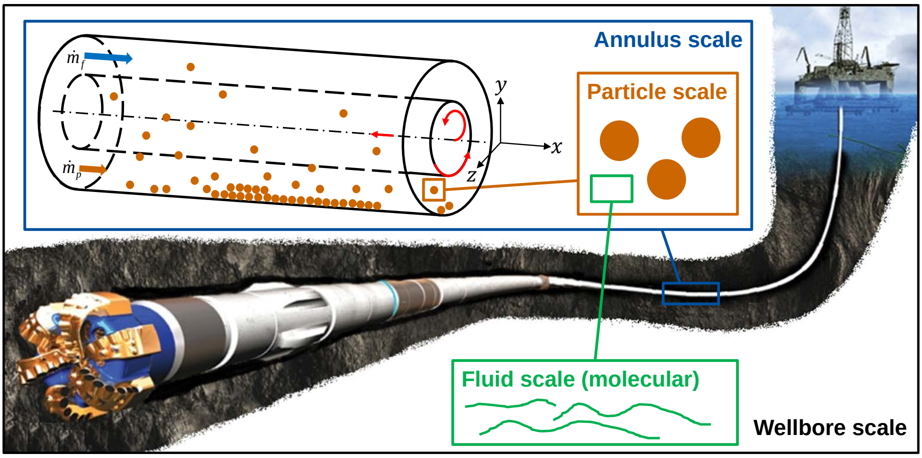

Figure 1.1.: Conceptual sketch of the drilling process with its different spatial scales. Picture adapted from [31]

fluid runs through a set of nozzles and flushes as well as cools the cutting blades. The return path of the now solids-carrying drilling fluid is the annulus, i.e., the annular gap between the drill pipe and the outer wall, as conceptually displayed in the zoom of a wellbore element entitled *annulus scale* in figure 1.1. The scale of the annular domain in cuttings transport studies is in the order of the length of one drill pipe element ($\mathcal{O}(L) \approx 10^1$ m)[1]. The solids are flushed and transported through the annulus back to the surface where they are separated from the drilling fluid. Eventually, the drilling fluid is then recirculated into the well.

Locally, the drill string's position relative to the annulus may be concentric as shown in figure 1.1. However, due to the three-dimensional (3D) wellbore trajectory, the mass and compliance of the drill string subjected to gravity and the axial force generated during drilling, the drill string is typically off-centric [32, 33]. Using a coordinate system as depicted in figure 1.1, one may locally distinguish between vertical and horizontal eccentricity. Depending on the type of drilling, the drill string may or may not be rotating. In conventional drilling, the drill bit is driven by the rotating drill string, which itself is driven by a motor at the top. In

---

[1] On this level, an alternative length scale is the hydraulic diameter $d_h = d_o - d_i$, where d_i and d_o are the inner and outer annular diameter, respectively. The magnitude of d_h on the *annulus scale* is ($\mathcal{O}(d_h) \approx 10^{-1}$ m.

coiled tubing operations, the drill bit is typically driven by a downhole mud motor and the tubing does not rotate. In the presence of rotation, the aforementioned eccentricities may not be constant and the drill string may feature additional lateral motion [34–36], such as forward or backward whirling or more chaotic lateral oscillating motions [37–39]. The reasons for these motions are many: the compliance of the segmented drill string system, the damping due to viscous and coulomb forces, and the 3D trajectory of the wellbore are major factors. Lateral drill string motion is known to positively influence cuttings transport [32, 40] but may also cause mechanical damage to the drill pipe collars [41].

The outer wall may be the borehole wall or steel casing. Following specific intervals, steel casing is cemented into the borehole in order to mechanically stabilize the wellbore and prevent influx of formation fluid or loss of drilling fluid into the formation [42–44]. As the wellbore's depth and distance increases, smaller and smaller casings are used and hence the wellbore's outer diameter decreases with depth and distance.

On the *particle scale*, the transported solids vary significantly in size and shape. They may be as large as 40 mm and as small as 0.001 mm [45] and typically all sizes can be found in the well. However, the size distribution is not constant because the rotating and whirling drill pipe as well as the mechanical interaction of the cuttings themselves lead to abrasive wear and shift the distribution towards smaller sizes [43]. The longer the solids are transported the more abrasive wear occurs, which may eventually alter the rheological properties of the drilling fluid [43, 46]. While typically assumed to be spherical, cuttings may come in any shape [45]. Because their preferred settling orientation is the one that offers the greatest possible resistance [47], the drag may be about three times higher [48] in the case of non-spherical particles. In addition, non-spherical particles will not roll as easily as spherical ones and hence cuttings transport will be negatively affected [49, 50].

Drilling fluids are highly engineered systems consisting of many components and additives because they, in addition to cuttings transport, serve other purposes such as cooling the bit, stabilizing the wellbore, and avoiding fluid loss into the formation [42–44]. The *drilling fluid scale* depicted in figure 1.1 constitutes another relevant scale of the cuttings transport problem because the rheological properties of the drilling fluid are defined by its constituents and molecular structure on a length scale $\mathcal{O}(L) < 10^{-6}$ m. Depending on the primary liquid, one may divide drilling fluid systems into Water-Based Muds (WBM) and Oil-Based Muds (OBM) [42, 44]. For

WBM, further additives may include Bentonite, Potassium Chloride (KCl), and modified natural polymers such as Carboxy Methyl Cellulose (CMC) or Polyanionic Cellulose (PAC) [42, 44]. The role of polymers is to viscosify the drilling fluid system and provide shear-thinning properties, which, in conjunction with a potential yield stress, may improve the cuttings carrying capacity of the drilling fluid. In addition, polymers may cause viscoelastic and thixotropic behavior [51, 52], where the stress acting on a drilling fluid element is then additionally a function of strain or the time derivative of stress, and the state of the fluids microstructure [53].

In general, the shallower sections of a well are drilled vertically, and the deeper sections of a well may deviate into more inclined and even horizontal directions [31]. While for angles smaller than 30°from vertical, the rate of cuttings accumulation in the wellbore changes little [54, 55], for larger inclinations particles may settle and a cuttings bed may form on the low side of the annulus. Intermediate inclinations are challenging to drill because cuttings avalanches may occur.

To ensure continuous operation, adequate transport of all cuttings out of the well, also referred to as hole cleaning, is critical. Inadequate cuttings transport leads to insufficient hole cleaning with potentially severe consequences such as damaged or lost equipment, and broken formation, which then cause well downtime and increased costs. For instance, as much as 70 % of downtime may be due to stuck pipe [56] and poor hole cleaning is the cause of a third of stuck pipe related issues [57].

The quality of solids transport throughout the wellbore back to the surface depends on many parameters, which are sometimes related [**IX**, 58–60]. The cuttings have to be transported by the drilling fluid over very long distances and against gravity. Many of the previously mentioned parameters are not constant along the wellbore path (e.g. eccentricity and rheological properties), which is why the probability that a concrete part of the well (i.e., a wellbore element such as the annular domain depicted in figure 1.1) is sufficiently clean also varies along the wellbore path. For cuttings transport modeling, it is therefore crucial to identify the critical part of the wellbore where cuttings are not adequately transported and accumulate instead. In other words, in order to make a statement about hole cleaning, the definition of which is a sufficiently clean wellbore to ensure continuous operations, one needs to quantitatively investigate cuttings transport in individual parts and then aggregate this information to a global scale.

In recent years, downhole sensors and measurement devices located at the Bottom Hole Assembly (BHA)[2] have become standard to allow for Measurement While Drilling (MWD) [31] in order to precisely track the 3D trajectory of the hole as it is drilled and provide other operationally-relevant downhole information such as rotational speed, vibration, temperature as well as torque and weight on bit (WOB). This information may be used by RT models to predict the state of the entire wellbore [43].

For more details on drilling as well as cuttings transport and hole cleaning, the reader is referred to [31, 61–63] and the cuttings transport review papers cited in section 1.4.

1.2. Modeling approaches

Historically, cuttings transport modeling considered a small part of the wellbore only. Moreover, only one-dimensional (1D) modeling was performed [e.g. 64–66], where the 3D annular domain depicted in figure 1.1 is simplified by appropriately averaging over the cross-sectional area [67] and hence only the x-direction is considered. With recent developments in computational power, cuttings transport modeling has diversified as depicted in figure 1.2.

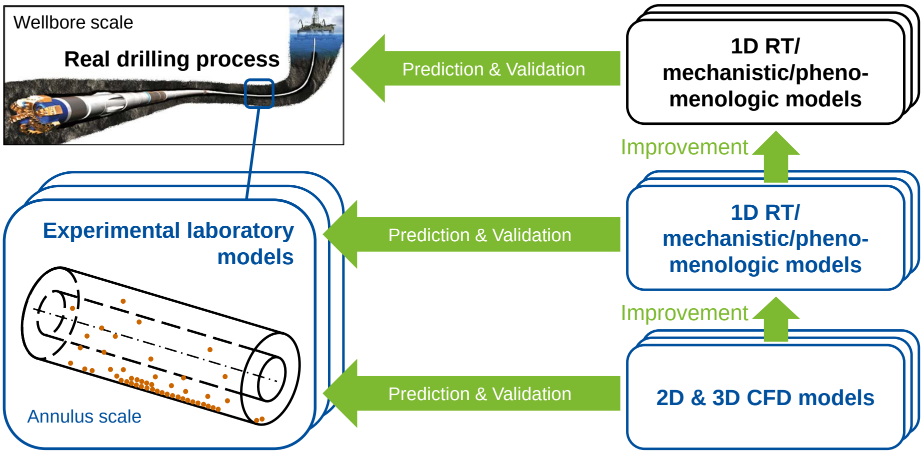

*Figure 1.2.: Conceptual cuttings transport modeling architecture, adapted from [**I**, **X**].*

---

[2] As displayed in figure 1.1, the BHA is the lowest part of the drill string, extending from the drill bit to the first drill pipe element. It may incorporate drill collars, stabilizers, a steerable rotary, reamers, the drill bit as well as sensors and measurement devices.

The purpose of numerical models is to predict the process of interest, here the cuttings transport process. In order to do so, numerical models must be validated against real-life data, which may be laboratory or field data. However, one or multiple modeling errors may be present. For instance, simplifications such as neglected parameters or usage of drilling fluid model systems such as polymeric solutions represent approximations and may render the results invalid. Consequently, benchmarking numerically obtained results with field data is often not straightforward, and data obtained in laboratory experiments is used instead for model validation. Note that when using laboratory models such as flow loops, one still models the full scale cuttings transport process as it occurs in the field, and care must be taken to properly translate the field problem to the lab scale.

Numerical and empirical models may directly utilize laboratory data, for instance in the form of rheological closures or laboratory-generated look-up tables. Computationally cheap and thus fast—potentially real-time (RT)—computing approaches are used to simulate wellbore elements or even the wellbore in its entirety [5, 43, 68]. However, most of these models are 1D, and either empirical [e.g. 69] or mechanistic [e.g. 70–72]. The latter often rely on empirical closures or closure laws derived from more sophisticated modeling approaches such as 3D Computational Fluid Dynamics (CFD)[3] or experimental laboratory models which enable a much more detailed analysis of the physical problem.

Experimental laboratory-based work typically involves a flow loop, where drilling fluid (model) systems are circulated and the transport of solids may be studied in detail (in a pipe or annular test section, which may even be inclined, and in the case of an annular geometry, the inner pipe may be rotating). Technical developments in Particle Image Velocimetry (PIV) and Particle Tracking Velocimetry (PTV) have led to increasingly more experimental studies using translucent fluids and providing insight information of the complex fluid-solid interactions [e.g. 4]. Techniques such as Response Surface Analysis (RSA) and Design of Experiments (DoE), for instance based on multidimensional fit functions derived by means of Dimensional Analysis (DA), may be used to establish a process relationship in the form of an empirical correlation.

Numerical 3D modeling of fluid flows, i.e., CFD, requires an adequate

---

[3] Strictly speaking, CFD also encompasses 1D and 2D models which are respectively applied on a 1D or 2D computational grid. However, it has been become customary to associate the term CFD with 3D CFD.

computational treatment of the two phases. Various multiphase modeling techniques exist, the most realistic ones are based on Eulerian-Lagrangian concepts, where the fluid as the first phase is treated as a continuum and the dispersed solid particles are followed individually in a Lagrangian manner and are subject to Newton's second law of motion [73, 74]. One may categorize the different methods based on the volume fraction of the dispersed phase and the computational coupling between the phases. One-way coupling, where the momentum exchange from the fluid to the solid phase is considered unilateral, and two-way coupling (bilateral momentum exchange) are valid for dilute flows where no interactions between the particles are relevant. The Discrete Phase Model (DPM) is an example, which we used in paper [**II**] to study trajectories of a single particle. In case of denser systems, particle interactions need to be considered (four-way coupling) and this field is known as the Discrete Element Method (DEM). However, for larger systems this modeling approach leads to severe computational expenses.

An alternative is to treat the particles as a second continuum and apply a Eulerian-Eulerian frame of reference. In this study, the Eulerian-Eulerian Two Fluid Model (TFM) has been mostly used and a detailed description is given in section 1.3. For the sake of completeness, other modeling approaches include the Volume of Fluid (VOF) method, which is suited for clearly separated phases sharing a large interface. A single set of momentum equations is solved and the volume fraction of each of the phases is tracked throughout the computational domain. The mixture model is a simplified version of the TFM, where a momentum transport equation is solved for the mixture instead for each of the phases.

The phenomenon of turbulence—chaotic motions of fluid elements due to flow instabilities—may be dealt with in different ways, mainly depending on the available computational power and the desired accuracy of the result [75, 76]:

- Direct Numerical Simulation (DNS) resolves turbulent eddies on all length and timescales down to the Kolmogorov length and timescale, which is the smallest relevant length and timescale in turbulent flows, where energy dissipation takes place [77].

- Large Eddy Simulations (LES) resolve turbulence on length and timescales larger than the computational grid size and time step. Hence, large eddies are resolved, but turbulence is modeled on subgrid scales.

- Reynolds-Averaged Navier-Stokes (RANS) approaches model the effect of turbulence on all length and timescales. The governing equations of fluid flow, classically the Navier-Stokes equations, are for instance ensemble-averaged and the resulting turbulent quantities in the transport equations are modeled. The respective turbulence model is to be chosen with regards to the physics of the problem.

The RANS concept is mostly being used for CFD cuttings transport modeling purposes because it requires the least computational effort. It is further detailed in section 1.3.5 and is investigated in chapter 5 with a focus on cuttings transport modeling.

1.3. Continuum description of dense two-phase flow

This section briefly presents the physical model mostly utilized in this PhD project and its mathematical representation. First, the TFM is introduced. Subsequently, the relevant closure laws for the particle forces, fluid and solid rheological properties and fluid turbulence are provided.

1.3.1. The Two Fluid Model framework

In the TFM framework, both the first and second phase are assumed to behave as interpenetrating continua in an Eulerian frame of reference [78–81]. We consider the fluid (index f) and solid (index s) phases to be isothermal (and later also incompressible). For an arbitrary volume element V_i, the phase volume fractions α_i must therefore sum to one.

$$V_i = \int_V \alpha_i dV \wedge \sum_i \alpha_i = 1 \wedge i \in \{f, s\} \tag{1.1}$$

and the conservation of mass is given by

$$\frac{\partial \left(\alpha_i \rho_i\right)}{\partial t} + \nabla \cdot \left(\alpha_i \rho_i \mathbf{u}_i\right) = 0, \tag{1.2}$$

where ρ_i and $\mathbf{u}_i$ denote the phasic intrinsic volume averages of density and velocity, respectively.

Both phases obey a generic Cauchy momentum transport equation of the form

$$\frac{\partial\left(\alpha_i\rho_i\mathbf{u}_i\right)}{\partial t}+\nabla\cdot\left(\alpha_i\rho_i\mathbf{u}_i\mathbf{u}_i\right)=\nabla\cdot\left(\alpha_i\mathbf{T}_i\right)+\alpha_i\rho_i\mathbf{g}+\frac{1}{V}\int_S\left(\mathbf{T}_f\cdot\mathbf{n}\right)dS, \tag{1.3}$$

where $\mathbf{T_i}$ is the phasic stress tensor and $\mathbf{g}$ is gravity. The last term $\frac{1}{V}\int_S\left(\mathbf{T}_f\cdot\mathbf{n}\right)dS$, with S being the total fluid-particle interface area in the control volume and $\mathbf{n}$ being the interface normal vector, is representing the interfacial momentum transfer of one phase to the other (here expressed as the sum of all fluid forces).

Developing this term further [e.g. 82, 83] and manipulating equation 1.3 for $i\in\{f,s\}$ yields phase-specific momentum equations, which for the fluid and solid phase respectively read

$$\begin{aligned}\frac{\partial\left(\alpha_f\rho_f\mathbf{u}_f\right)}{\partial t}&+\nabla\cdot\left(\alpha_f\rho_f\mathbf{u}_f\mathbf{u}_f\right)\\&=-\alpha_f\nabla p_f+\nabla\cdot\left(\alpha_f{}^{\mathbf{x}}\mathbf{T}_f\right)+\alpha_f\rho_f\mathbf{g}+\frac{1}{V}\sum_{p\in V}\mathbf{f}_j-{}^{\mathbf{x}}\mathbf{T}_f\cdot\nabla\alpha_f\end{aligned} \tag{1.4a}$$

$$\begin{aligned}\frac{\partial\left(\alpha_s\rho_s\mathbf{u}_s\right)}{\partial t}&+\nabla\cdot\left(\alpha_s\rho_s\mathbf{u}_s\mathbf{u}_s\right)=\\&-\alpha_s\nabla p_f-\nabla p_s+\nabla\cdot{}^{\mathbf{x}}\mathbf{T}_s+\alpha_s\rho_s\mathbf{g}-\frac{1}{V}\sum_{p\in V}\mathbf{f}_j+\alpha_s\nabla\cdot{}^{\mathbf{x}}\mathbf{T}_f,\end{aligned} \tag{1.4b}$$

where ${}^{\mathbf{x}}\mathbf{T_i}$ is the phasic extra stress tensor[4] and $\pm\frac{1}{V}\sum_{p\in V}\mathbf{f}_j$ represents the interfacial momentum transfer of one phase to the other, where the sum of the individual forces $\mathbf{f}_j$ acting on particles is taken over all particles p in the control volume V.

Note that the terms $-{}^{\mathbf{x}}\mathbf{T}_f\cdot\nabla\alpha_f$ and $+\alpha_s\nabla\cdot{}^{\mathbf{x}}\mathbf{T}_f$ in equation 1.4 are often neglected and thus typically not implemented in commercial CFD codes [82] and are also not considered by ANSYS Fluent R17.2 [86, 87], the code utilized in this PhD project. These terms may, however, play important

---

[4] The extra stress tensor ${}^{\mathbf{x}}\mathbf{T}$ [84] contains both shear and bulk viscous stresses and is thus also referred to as the *viscous stress tensor* [e.g. 85]. However, we use the term *extra stress tensor* because when modeling turbulence it also includes the turbulent stresses in the then ensemble-averaged transport equations, see section 1.3.5, and, more generally, it may also incorporate elastic stresses. Note that the solid volume fraction α_s does not show up in the solid stress term $\nabla\cdot{}^{\mathbf{x}}\mathbf{T}_s$ in equation 1.4b because it is contained in the respective solid material functions, see section 1.3.4.

roles in regions with large solid volume fraction gradients (equation 1.4a), e.g. at a solid bed surface, and regions where the viscous stress gradient is significant (equation 1.4b), e.g. the acceleration of particles away from the center towards the walls in laminar particle-loaded pipe flow.

The extra stress tensor ${}^{\mathrm{x}}\mathbf{T}_i$ contains a constitutive equation and material functions for the rheological properties of the phases and has the general form of a compressible Generalized Newtonian Fluid (GNF)

$$ {}^{\mathrm{x}}\mathbf{T}_i = 2\eta_i \mathbf{D}_i + \left(\left(\kappa_i - \frac{2}{3}\eta_i \right) \nabla \cdot \mathbf{u}_i \right) \mathbf{I}, \tag{1.5} $$

where $\mathbf{D}$ is the symmetric part of the fluid or solid velocity gradient (also known as the rate of deformation tensor, or alternatively the rate of strain tensor)

$$ \mathbf{D} = \frac{1}{2} \left(\nabla \mathbf{u}_i + (\nabla \mathbf{u}_i)^T \right) \tag{1.6} $$

and η_i and κ_i are phase-dependent material functions for the shear and bulk viscosities, respectively. Rheological closures for the fluid phase are provided in section 1.3.3.

We do not solve equations 1.2 and 1.4 to the smallest length scales of the flow. Thus, the phenomenon of turbulence must be modeled [75, 76]. Performing Reynolds averaging [88] of the instantaneous balance equations for mass and momentum, i.e., splitting variables into a mean (indicated with overbar) and fluctuating (indicated with prime) part, a so-called Reynolds stress term $\nabla \cdot \left(-\rho_i \overline{\mathbf{u}_i' \mathbf{u}_i'} \right)$ arises in the now ensemble-averaged momentum conservation equations originating from the advective term in the instantaneous equations. The Reynolds stress tensor ${}^{\mathrm{x}}\mathbf{T}_{i,t} = -\rho_i \overline{\mathbf{u}_i' \mathbf{u}_i'}$, also known as turbulent stress tensor, is usually assumed symmetric and may be modeled by applying the Boussinesque hypothesis [89], also known as the diffusion gradient or eddy-viscosity hypothesis, to relate the Reynolds stresses to the mean deformation rate tensor by means of the turbulent viscosity in the form of

$$ {}^{\mathrm{x}}\mathbf{T}_{i,t} = -2\eta_{i,t} \mathbf{D}_i. \tag{1.7} $$

The turbulent stresses are added to the (now-ensemble averaged) extra stress tensor ${}^{\mathrm{x}}\mathbf{T}_i$ such that the total extra stress tensor to be considered in the (now-ensemble averaged) momentum equation 1.4 is the sum of equation 1.5 and equation 1.7. Closures for the turbulent viscosity $\eta_{i,t}$ are provided in section 1.3.5.

1.3.2. Particle force models

The interphase momentum exchange term $\pm\frac{1}{V}\sum_{p\in V}\mathbf{f}_j$ generally includes a multitude of forces acting on the particles in a control volume, most notably the drag force. Other forces may include the lift forces due to shear [90, 91] and rotation [92, 93], the virtual mass force representing the required acceleration of fluid mass displaced by the accelerating particle and the Basset/history force accounting for the build-up of a boundary layer on the particle surface. For the sake of conciseness, we here only consider the drag force $\mathbf{f}_D$. The role of other particle forces is to some extent investigated in section 6.1.

Defining the relative velocity as $\mathbf{u}_r = \mathbf{u}_s - \mathbf{u}_f$, the drag force term in equation 1.4 may be modeled as

$$\frac{1}{V}\sum_{p\in V}\mathbf{f}_D = K\mathbf{u}_r, \tag{1.8}$$

where the interphase momentum exchange coefficient K is generically expressed as

$$K = \frac{\alpha_s\rho_s f}{\tau_{St}}, \tag{1.9}$$

with the Stokes relaxation time τ_{St} written as

$$\tau_{St} = \frac{\rho_s d_s^2}{18\eta_f}, \tag{1.10}$$

where d_s is the nominal diameter of a solid particle[5].

We here assume spherical and mono-sized particles, a typical simplification made in cuttings transport modeling. Particles in a well come in different shapes and sizes [45] and also change size and shape along the wellbore path due to frictional processes between particles and the wall and in between particles leading to abrasive wear. The transport of spherical solids along the bed may be handled with the consideration of the median particle size d_{50} [94]. In the TFM framework, additional solid phases may be added to account for different particle sizes. Particle shape, however, may be accounted for by means of sphericity-dependent correction factors in a later step.

---

[5] Please note, that we may use d_s and d_p interchangeably. However, in principle we refer to index p by focusing on one single particle and to s by focusing on multiple particles constituting the solid phase as a continuum.

The functional f in equation 1.10 includes a specific drag function $c_D\left(Re_p\right)$ and depends on the particular drag model utilized [e.g. 95]. It is generally a function of the particle Reynolds number Re_p defined as

$$Re_p = \frac{\rho_f d_p \left\|\mathbf{u}_r\right\|}{\eta_f}. \tag{1.11}$$

However, to account for the large variety in solid volume fraction α_s, i.e., the number of particles, in the control volume, we use the formulation of Gidaspow [96], which is a combination of the Wen and Yu model [97] and the Ergun equation [98]. Here, the interphase momentum exchange coefficient K is given as

$$\alpha_s \leq 0.2: \quad K = c_D \frac{3\alpha_s \rho_f \left\|\mathbf{u}_r\right\|}{4{\alpha_f}^{0.65} d_s} \tag{1.12a}$$

$$\alpha_s > 0.2: \quad K = 150\frac{{\alpha_s}^2 \eta_f}{\alpha_f {d_s}^2} + 1.75\frac{\alpha_s \rho_f \left\|\mathbf{u}_r\right\|}{d_s} \tag{1.12b}$$

and the coefficient of drag c_D is defined as

$$c_D = \frac{24}{\alpha_f \mathrm{Re}_p}\left(1 + 0.15\left(\alpha_f \mathrm{Re}_p\right)^{0.687}\right). \tag{1.13}$$

1.3.3. Rheological models of the fluid

Drilling fluids cover a large variety of viscosity ranges and are typically shear-thinning. Often, they feature a yield stress, i.e., flow occurs only if a certain stress level is exceeded.

We are here concerned with either Newtonian fluids, where the viscosity η_f in equation 1.5 is constant (e.g. $\eta_f = 0.001$ Pa·s for water) or more complex GNF, where the viscosity η_f in the GNF constitutive equation 1.5 is a function of the shear rate $\dot{\gamma}$ defined as the magnitude of the rate of deformation tensor

$$\dot{\gamma}_i = \sqrt{2\mathbf{D}_i : \mathbf{D}_i}. \tag{1.14}$$

In any case, the fluid is assumed incompressible and thus the bulk viscosity κ_f in the GNF constitutive equation 1.5 becomes zero. Moreover, by manipulating the continuity equation and applying the definition of the material derivative it can be shown that the divergence of the velocity field becomes zero in case of incompressible fluids (and hence flows), i.e., $\nabla \cdot \mathbf{u}_i = 0$.

The particular material function to be employed for the description of η_f depends on the shape of the so-called Flow Curve (FC)—a plot of steady-state shear stress vs. shear rate obtained by means of viscometry—as well as the shear rate range relevant to the particular problem. Figure 1.3 depicts the performance of different material functions currently in use when fitted to example Fann viscometric data [44] based on current petroleum industry guidelines [99].

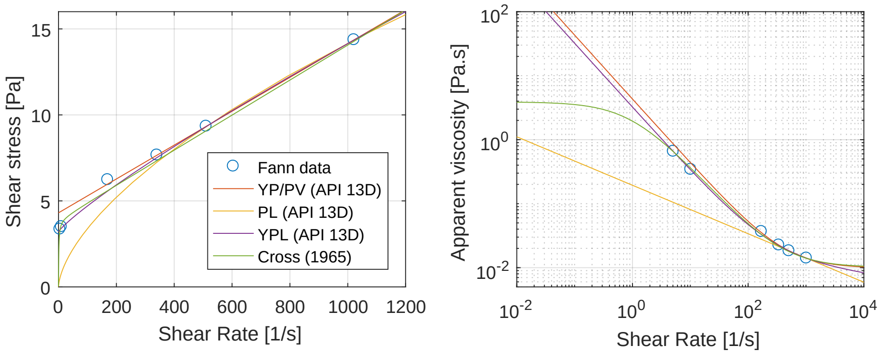

Figure 1.3.: Example of the predictive capability of different fluid material functions as currently in use in the petroleum industry [99] and related academic fields. The exemplified Fann viscosity data was taken from [44].

Illustrated is the Bingham [100] model, also known as Yield Point (YP)/ Plastic Viscosity (PV) model, where the viscosity is given as

$$\eta_f = \sigma_{YP}\dot{\gamma}^{-1} + \mu_{PV} \tag{1.15}$$

and which has been used in many different applications in the oil and gas industry over the last several decades [101]. In equation 1.15, σ_{YP} is the yield stress and μ_{PV} is the plastic viscosity[6]. The Ostwald/deWaele [25–27] model, also known as the Power Law (PL) model, is given by

$$\eta_f = K_{PL}\dot{\gamma}^{n_{PL}-1}, \tag{1.16}$$

and the Herschel-Bulkley [28] model, also known as Yield Power Law (YPL) model, reads

$$\eta_f = \sigma_{YP}\dot{\gamma}^{-1} + K_{YPL}\dot{\gamma}^{n_{YPL}-1}. \tag{1.17}$$

---

[6] Note that σ_{YP} and μ_{PV} differ from PV and YP as defined in [99]: $\sigma_{YP} = 0.511PV$ and $\mu_{PV} = 0.001PV$. See the memo [**XI**] for details.

In equations 1.16 and 1.17 K and n are the PL and YPL consistency index and exponent, respectively. The YPL represents the current industry standard [99] because it combines the YP-PV and the PL model and is a more representative description for many drilling fluid systems over the entire range of relevant shear rates [102], as may be verified from figure 1.3. However, when it comes to large shear rate ranges comprising both the very low ($\dot{\gamma} < 0.1s$) and high ($\dot{\gamma} > 1000s$) shear rate ranges, many materials are best-represented by four-parameter-models such as the Cross [30] model[7]

$$\eta_f = \frac{\mu_0 - \mu_\infty}{1 + (\lambda_{Cr}\dot{\gamma})^{1-n_{Cr}}} + \mu_\infty. \tag{1.18}$$

In equation 1.18, λ_{Cr} is the Cross timescale, n_{Cr} is the Cross exponent, and μ_0 and μ_∞ are the low-shear and high-shear viscosity plateaus, respectively.

When the YPL model is used based on current industry standards [99] it is prone to extrapolation error. Current industry guidelines [99] base the application of the YPL on only four viscometric data points. Moreover, in case of vanishing yield stress or non-shear-thinning behavior, the resulting PL and YP/PV are only based on two data points. As shown in figure 1.3, these material functions may produce wrong stress predictions in the case of particle settling (low shear rate range) or turbulent flow (high shear rate range), simply because of data extrapolation error.

Drilling fluid model systems such as CMC and PAC solutions often do not fit the YPL model family in terms of their typical flow curve and may be more accurately described with the Cross [30] material function, or alternatively with the Carreau [29] family of models.

In case of viscoelasticity and thixotropy, the GNF constitutive equation 1.5 has to be respectively extended by the addition of a term accounting for elasticity and an additional transported scalar structure quantity characterizing the structural break-down and build-up of viscosity. The stress is then made up of two components [53]:

- A viscous stress component dependent on viscosity, which is a function of the shear rate but, when it comes to thixotropy, also of the history of shear in the form of the scalar structure quantity describing the state of the microstructure.

---

[7] While there exist many more GNF material functions based on four (or more) model coefficients such as the Carreau family of models [29, 103], these do not add more value in terms of the shape of the flow curve.

- An elastic stress component, which—depending on the applied modeling approach—is a function of the strain (Bingham-based approach) or of the time derivative of the stress (Maxwell-based approach). However, the Maxwell approach is physically more sound because it reduces correctly to inelastic models in the limit of zero elasticity [53]. In case of additional thixotropy, the material parameters are also functions of the scalar structure quantity.

A variety of models capable of describing elasto-viscoplastic thixotropic [e.g. 104–108], elasto-viscoplastic [109] or thixotropic behavior exist [110–114]. Recently the important role of the yield stress as a tensorial quantity has been pointed out [115]: Not only shear stresses but also so-far underconsidered normal stresses, or more precisely normal stress differences (NSD), do contribute to the yield stress magnitude at the yield point.

However, all these models require sufficient rheometric data to fit model coefficients. Moreover, none of these models have so far seen implementation in commercially available CFD codes such as ANSYS Fluent. Such efforts are beyond the scope of this thesis. We will nevertheless investigate the possible error that is introduced by a GNF treatment of viscoelastic-thixotropic fluids in chapter 3.

1.3.4. Rheological models of the solid

In the context of the TFM, the solid phase is considered a second continuum interpenetrating the first, fluid phase. Hence, the GNF constitutive equation 1.5 is also used for the second phase, albeit with an entirely different set of closures.

To describe the loose or collisional/kinetic regime, where the solid volume fraction $\alpha_s < \alpha_{s,f} = 0.50$ and solid particles interact with each other in terms of collisions characterized by their kinetic energy, we apply the Kinetic Theory of Granular Flows (KTGF) developed by Savage et al. [116–119]. Additional closures from soil mechanics (SM) are employed to handle the dense or frictional regime, where the solid volume fraction $\alpha_s > \alpha_{s,f} = 0.50$ and solid particles interact with each other in terms of sliding and rolling frictional contacts[8].

Assuming additivity [118], the entire solid stress tensor, namely equation 1.5 and the isotropic pressure, is split into two parts $\mathbf{T}_s = \mathbf{T}_{s,c/k} + \mathbf{T}_{s,f}$

---

[8] Note that the numerical value of $\alpha_{s,f}$ is a model tuning parameter. 0.5 is an often used value in KTGF-SM closures.

and reads

$$\mathbf{T}_s = \sum_{j \in \{k/c,f\}} \left[\left(-p_{s,j} + \left(\kappa_{s,j} - \frac{2}{3}\eta_{s,j} \right) \nabla \cdot \mathbf{u}_s \right) \mathbf{I} + 2\eta_{s,j}\mathbf{D}_s \right]. \tag{1.19}$$

The stencil is still that of a GNF, although normal and shear stresses are now made up of two contributions each. However, the set of closures utilized is entirely different:

- The kinetic/collisional pressure [117]

$$p_{s,k/c} = \alpha_s \rho_s \Theta_s + 2{\alpha_s}^2 \rho_s \Theta_s \left(1 + e_{ss}\right) g_{0,ss}. \tag{1.20}$$

- The collisional shear viscosity [117]

$$\eta_{s,c} = \frac{4}{5}{\alpha_s}^2 \rho_s d_s g_{0,ss} \left(1 + e_{ss}\right) \left(\frac{\Theta_s}{\pi} \right)^{\frac{1}{2}}. \tag{1.21}$$

- The kinetic shear viscosity [96]

$$\eta_{s,k} = \frac{10 \rho_s d_s \sqrt{\Theta_s \pi}}{96 \left(1 + e_{ss}\right) g_{0,ss}} \left(1 + \frac{4}{5}\alpha_s \left(1 + e_{ss}\right) g_{0,ss} \right)^{\frac{1}{2}}. \tag{1.22}$$

- The kinetic/collisional bulk viscosity [117]

$$\kappa_{s,c/k} = \frac{4}{3}{\alpha_s}^2 \rho_s d_s g_{0,ss} \left(1 + e_{ss}\right) \left(\frac{\Theta_s}{\pi} \right)^{\frac{1}{2}}. \tag{1.23}$$

- The frictional pressure [120]

$$p_{s,f} = 0.05 \frac{\left(\alpha_s - \alpha_{s,f}\right)^2}{\left(\alpha_{s,mpd} - \alpha_s\right)^5}. \tag{1.24}$$

- The frictional shear viscosity [121]

$$\eta_{s,f} = \frac{p_s \sin \phi_s}{\sqrt{2} \left\| \mathbf{D}_s \right\|}, \tag{1.25}$$

  where the solid pressure p_s is based on the sum of its kinetic/collisional and frictional components according to equation 1.19.

The closure laws characterizing the kinetic/collisonal regime, namely equations 1.20 to 1.23, are functions of the granular temperature Θ_s, which is a measure of the velocity fluctuations in a fluidized granular system due to individual particle collisions [122] and is proportional to the kinetic energy of the random motion of the particles [123]:

$$\Theta_s = \frac{1}{3}\left\langle u'_{s,i} u'_{s,i} \right\rangle . \tag{1.26}$$

Here, $u'_{s,i}$ is the i-th fluctuating component of the solids velocity in the Cartesian coordinate system and the brackets represent an ensemble average of the fluctuating velocities of all particles within a finite volume [123]. The granular temperature Θ_s is a transported property and obeys the following transport equation [123]:

$$\frac{3}{2}\left[\frac{\partial}{\partial t}\left(\alpha_s \rho_s \Theta_s\right) + \nabla \cdot \left(\alpha_s \rho_s \mathbf{u}_s \Theta_s\right)\right] = \\ {}^{\mathbf{x}}\mathbf{T}_s : \nabla \mathbf{u}_s + \nabla \cdot \left(k_{\Theta_s} \nabla \Theta_s\right) - D_{\Theta_s} + K_{fs}, \tag{1.27}$$

where k_{Θ_s} is the granular conductivity [e.g. 124]. The two final terms in equation 1.27 are the collisional dissipation of energy [117] and the interphase exchange between the particle fluctuations and the liquid phase [96]. Equation 1.27 is a partial differential equation, but can be simplified to an algebraic equation by neglecting the convection and diffusion terms—an often used assumption in dense, slow moving fluidized beds, where the local generation and dissipation of granular temperature far outweigh the transport by convection and diffusion.

In equations 1.20 to 1.23, d_s is the diameter of a solid particle, $e_{ss} = 0.9$ is the coefficient of restitution for particle collisions and

$$g_{0,ss} = \left[1 - \left(\frac{\alpha_s}{\alpha_{s,mpd}}\right)^{\frac{1}{3}}\right]^{-1} \tag{1.28}$$

is the radial distribution function accounting for the probability of particle collisions, where $\alpha_{s,mpd} = 0.63$ is the maximum packing density, and which has been used frequently in the history of granular flows [e.g. 117, 125–127] in the form presented in equation 1.28.

The closure laws characterizing the frictional regime, namely equations 1.24 and 1.25, are only active for $\alpha_s > \alpha_{s,f} = 0.50$ and effectively solidify the solid phase for $\alpha_s \rightarrow \alpha_{s,mpd}$ because of the diverging solid frictional pressure. This process is self-enforcing because of the shear rate $\dot{\gamma}_s$ in the denominator of equation 1.25: For vanishing shear rates in the frictional regime, a Bingham-type [100] flow behavior is obtained due to the yield feature inherent in equation 1.25. The maximum packing density $\alpha_{s,mpd} = 0.63$ and the angle of internal friction ϕ are also model constants. While the former may be derived analytically for close-packings of spheres, the latter is a physical quantity characterizing failure of soils due to shear stress and may be related to the angle of repose [128].

1.3.5. Turbulence models

The Reynolds-Averaging process and the Boussinesque hypothesis leads to the turbulent viscosity η_t in the transport equations, as described in section 1.3.1 and formulated in equation 1.7 which has to be modeled by a suitable RANS closure.

Concerning the fluid phase, here we mainly use the Shear Stress Transport (SST) $k - \omega$ model [129, 130], because of its suitability for swirling flows and the possibility to either integrate it to the laminar sublayer or apply wall functions. It is designed to blend the standard $k - \omega$ model, which is robust and accurate in the near-wall region, with a $k - \epsilon$ model [131] converted into a $k - \omega$ formulation, which is robust and accurate in the free stream, by means of blending functions b_1 and b_2. The turbulent viscosity $\eta_{f,t}$ becomes a function of the two transported quantities turbulent kinetic energy k and specific dissipation rate[9] ω and is then defined as

$$\eta_{f,t} = f_l f_d \frac{\rho_f k}{\omega}, \tag{1.29}$$

where f_d is a damping function for low Reynolds-number corrections and $l = f(b_2)$ is a limiter coefficient ensuring that overprediction of the turbulent viscosity is avoided and therefore enabling the SST k-ω model to better predict the onset and amount of flow separation from smooth surfaces [129, 130].

The two transport equations for the turbulent kinetic energy k and the

---

[9] ω can also be thought of as the ratio of the rate of dissipation of turbulence ϵ to turbulent kinetic energy k. The inverse of ω is the timescale on which dissipation of turbulence energy occurs [132].

specific dissipation ω are

$$\frac{\partial}{\partial t}\left(\alpha_f \rho_f k\right) + \nabla \cdot \left(\alpha_f \rho_f \mathbf{u}_f k\right) \\ = \nabla \cdot \left[\alpha_f \left(\eta_f + \frac{\eta_{f,t}}{Pr_k}\right) \nabla k\right] + \alpha_f G_k - \alpha_f Y_k + \alpha_f \rho_f \mathit{\Pi}_{k,f}, \quad 1.30$$

and

$$\frac{\partial}{\partial t}\left(\alpha_f \rho_f \omega\right) + \nabla \cdot \left(\alpha_f \rho_f \mathbf{u}_f \omega\right) \\ = \nabla \cdot \left[\alpha_f \left(\eta_f + \frac{\eta_{f,t}}{Pr_\omega}\right) \nabla \omega\right] + \alpha_f G_\omega - \alpha_f Y_\omega + \alpha_f D_\omega + \alpha_f \rho_f \mathit{\Pi}_{\omega,f}, \quad 1.31$$

where $Pr_i = f(b_1)$ are the respective turbulent Prandtl numbers, G_i are respective production terms, Y_i are respective dissipation terms and D_ω is a cross diffusion term, which arises in equation 1.31 as a consequence of the blending of the k-ω model and the standard k-ϵ model [131] (converted to a k-ω formulation). The last terms account for influences of the particles on the fluid, i.e., turbulence interaction.

The turbulence quantities of the solid phase are obtained from the fluid phase by applying the Tchen theory of dispersion of discrete particles by homogeneous turbulence [133, 134], as given by Simonin and Viollet [135]. Here, the fluctuating quantities of the solid phase are related to the mean characteristics of the primary phase and particle relaxation time τ_{sf}^F (equation 1.10 with corrections for high Re drag and, if applicable, virtual mass) and eddy-particle interaction time τ_{sf}^t (based on the energetic turbulent eddy time scale $(3C_\eta k_f)/(2\epsilon)$, where the constant C_η = 0.09, and crossing-trajectory effect [136]). The turbulent viscosity for the granular phase is approximated as

$$\eta_{s,t} = \rho_s \left(\frac{1}{3} f_1 \tau_{sf}^t + \frac{2}{3} f_2 \tau_{sf}^F\right), \quad 1.32$$

where f_1 and f_2 are functions of $\tau_{sf}^t / \tau_{sf}^F$ as well as the turbulent kinetic energy of the fluid phase k_f. For further details see [87]. Alternatives to the SST k-ω model include the aforementioned k-ϵ model and its derivatives as well as the Reynolds Stress Model (RSM). In a RSM, the Boussinesq hypothesis is avoided and, assuming symmetry of the Reynolds stress tensor $-\rho_i \overline{\mathbf{u}_i' \mathbf{u}_i'}$, six transport equations are solved for the individual Reynolds stresses and one for the dissipation rate. For further details as well as all relevant closures of the SST k-ω model utilized, the reader is referred to the works of Menter [129, 130] and Simonin and Viollet [135] as well as the Fluent theory manual [87].

Note that the k-ω and k-ϵ turbulence model families do not account for any non-Newtonian effects. The Reynolds-averaging is performed assuming a Newtonian, i.e., constant and thus non-fluctuating viscosity, hence no interaction between the closures presented in section 1.3.3 and section 1.3.5. This is the formulation typically used in cuttings transport CFD studies [e.g. 137–139]. However, turbulence is affected by the non-Newtonian rheological properties of the fluid [e.g. 140–144] and possibly vice-versa [145]. This issue is further investigated and discussed in chapter 5.

1.4. CFD cuttings transport modeling—State of the art

We here briefly cover recent 3D CFD cuttings transport studies[10] regarding their models used and findings. For a more comprehensive picture covering the many (interdependent) effects of the most relevant parameters as well as mechanistic or phenomenological 1D models, and experimental studies, the reader is referred to review papers [58, 59, 154–162].

The role of CFD has only been focused on recently in review papers [154, 157, 158]. However, the focus here was on the results of the simulations [157, 158] or on providing a general picture [154] and not on the CFD setup and models utilized.

CFD (and also experimental) studies of wellbore flows can be categorized based on physical complexity as depicted in the left-hand side of figure 1.4.

Physical complexity is here defined as the number of physical complexities and their inter-dependencies. The advantage of this model categorization concept is the direct linkage to the mass and momentum conservation equations and the phasic stress tensors. For instance, in case of ①, the

---

[10] As pointed out by Meese and Simonsen [6], CFD has also been used in other physically very similar fields where a dispersed solid phase is transported in a liquid, for instance slurry transport [e.g. 146–148], fluidized beds [e.g. 82, 149, 150], or environmental transport of solids in rivers [e.g. 151–153]. However, the computational domain is different (annulus vs. pipe/channel/open conduits), and the effects of inclination are only partly reflected (fluidized beds are equivalent to vertical annuli, while slurry transport and environmental transport of solids are equivalent to horizontal annuli). Nevertheless, on the *particle scale*, many similarities are found and thus works from these fields may also be very beneficial to advancements of wellbore flow models.

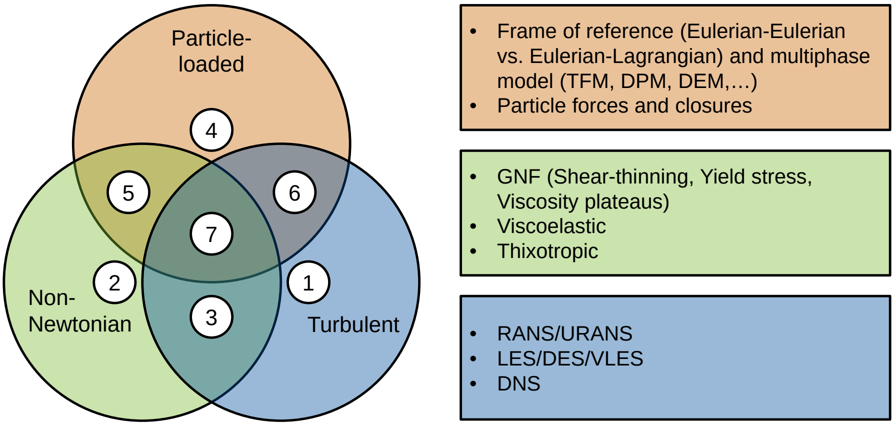

Figure 1.4.: Categorization of CFD studies based on physical complexity and other physic-specific attributes. Not depicted is case ⓪, which is simply the single-phase laminar flow of a Newtonian fluid.

transport equations 1.2 and 1.4a and the extra stress tensor as the sum of equation 1.5 and equation 1.7 in conjunction with $\eta_f = const.$ and, assuming a RANS approach, a turbulence model describe the fluid system ($i = f$). In case of ②, the transport equations 1.2 and 1.4 and the stress tensor as given by equation 1.5 in conjunction with a material function $\eta_f(\dot{\gamma})$, describe the fluid system ($i = f$), at least as long as a GNF framework is valid. In case of ④, the transport equations 1.2 and 1.4 and the stress tensor as given by equation 1.5 in conjunction with $\eta_f = const.$, describe the fluid-solid system ($i = f, s$). For the highest physical complexity, i.e., ⑦, the transport equations 1.2 and 1.4 and the extra stress tensor as the sum of equation 1.5 and equation 1.7 in conjunction with a turbulence model and with a material function $\eta_f(\dot{\gamma})$, describe the fluid-solid system ($i = f, s$).

The right-hand side of figure 1.4 exemplifies additional classification categories for each physical field, some of which may include subcategories. For instance, the RANS framework requires employment of a specific turbulence model. Other relevant parameters affecting the quality of cuttings transport are an equally valid choice for the categorization. For example, the inclination of the annulus may be used because only in non-vertical situations a cuttings bed may form. Such information is important as it might affect the choice of the multiphase mode utilized.

In the most complex case a wellbore flow is a non-Newtonian fluid transporting solids under turbulent flow conditions as indicated by ⑦ in figure 1.4. However, to simplify the problem, many studies have either focused on Newtonian fluids, i.e., ①, ④, and ⑥, or on the laminar flow regime, i.e., ②, ④, and ⑤. We here only focus on the multiphase studies, i.e., ④–⑦, and not on the pure hydrodynamic studies, i.e., ①–③:

④ Only three studies appear to have focused on the cuttings transport in laminar flows of Newtonian fluids [163–165]. All have used the Eulerian-Eulerian TFM of ANSYS Fluent and considered a multitude of particle forces and found the drillpipe rotation rate to be a major factor.

⑤ Cuttings transport in laminar flows of non-Newtonian fluids has been investigated much more often [49, 50, 166–181]. The fluid rheological properties are always handled with a GNF framework and either the PL or the YPL are used as material functions. The Eulerian-Eulerian TFM of ANSYS Fluent or CFX has been used equally often [168, 169, 172, 175–177, 179] as an Eulerian-Lagrangian concept [49, 50, 173, 174, 178, 180, 181], and a mixture model was used in four studies [166, 167, 170, 171].

⑥ Cuttings transport in turbulent flows of Newtonian fluids has been investigated equally well [182–192]. All studies used the TFM framework of Fluent with the exception of Sun et al. [184] who applied a DEM concept and Osgouei et al. [190], who used CFX instead. In all studies the k-ϵ or k-ω model (or some variant) were applied, with the notable exception of Dykes [185] who used an RSM.

⑦ Cuttings transport in turbulent flows of non-Newtonian fluids has been investigated increasingly often in recent years [137–139, 193–201]. Most studies used the TFM framework of Fluent in conjunction with the KTGF, only some studies employed Eulerian-Lagrangian concepts [195, 199, 200]. Lucas [198] used OpenFOAM with a VOF concept. In all studies, the k-ϵ or k-ω model (or some variant) were applied, with the notable exception of Heydari et al. [193] who applied an RSM. As mentioned in section 1.3.5, no interactions between the turbulent stress tensor ${}^{\mathrm{x}}\mathbf{T}_{f,t}$ and the extra stress tensor ${}^{\mathrm{x}}\mathbf{T}_{f}$ are considered in these studies.

Xiaofeng et al. [157] conclude that most CFD work done has made use of "as-is" commercial software and respective models without further detailed mechanistic modeling of the associated physics. Based on the studies published since the publication of Xiaofeng et al. [157], this conclusion still holds.

1.5. Motivation

Despite RT hole cleaning analysis in the form of MWD down hole sensors and monitoring devices being on the rise [e.g. 68, 202], the major part of the wellbore from the surface to the BHA remains a black box [46]. Thus, sophisticated and validated models are required for interpretation and prediction of the wellbore state.

Industrial simulators for cuttings transport [e.g 203–205] are generally based on simplified 1D models in order to generate predictions in RT. However, lack of accuracy (when compared with experimental data and other models) and lack of understanding of the complex, combined physics (e.g. the effect of mud properties and cuttings concentration on drill string dynamics and turbulent flow of non-Newtonian fluids) remain major issues [160–162]. In fact, there is no "generalized systematic" [59] and "comprehensive and proven" [154] model available for hole cleaning and cuttings transport. Technology in the form of "Realistic RT integrated drilling simulation models" [206] to provide RT information on conditions downhole is required to avoid drilling issues, which may be as high as 35 % of well costs [206].

CFD has proven to be a very beneficial support tool in order to elaborate on RT model accuracy, both qualitatively and quantitatively. To further improve 1D models, CFD work should focus on local fluid velocity profiles, characteristic turbulence parameters such as Reynolds stresses and turbulent intensity, shear stresses, solid entrainment rates, and the pipe rotation effect on the solids transport [154].

1.6. Goals and thesis outline

The primary aim of the AdWell project is to enhance the current understanding of the physics involved in the complex transport phenomena during cuttings transport as well as related hydrodynamics. The goal of this PhD project is to advance existing models and create new in-depth knowledge of flow details and general process understanding. Results are expected to support the improved mathematical modeling on a 1D RT level.

In particular, our goals are:

- Analyze the cuttings transport process and perform a DA.
- Investigate the impact of the non-Newtonian drilling fluid on the solid transport mechanisms and advance current models.
- Investigate the validity of granular flow models to describe the cuttings transport process and develop alternatives.
- Investigate the role of turbulence and the validity of turbulent flow models to describe the non-Newtonian hydrodynamics.
- Investigate the effect of drill pipe rotation on cuttings transport by accounting for lateral whirl pipe motion.

The thesis is structured accordingly and each individual chapter contains a summary of the main findings, which may be composed of one or more research papers given in appendix A. As visualized in figure 1.5, the main body of the thesis is structured as follows:

- In chapter 2, we analyze a generic cuttings transport process with regards to parameters and variables on the two hierarchical levels *wellbore scale* and *annulus scale* (see figure 1.1) as well as respective numerical validity ranges for the Norwegian Continental Shelf (NCS) [**I**, **X**]. In addition, this work identifies several research topics and builds the basis for all further work. We explore the scaling of parameter sets from one setup to the other, e.g. transferring field values to laboratory values, and develop a comprehensive cuttings transport scaling approach accounting for GNF fluids [**III**]. Finally, we briefly exemplify a 1D cuttings transport model, which, as a sample representation of RT models, imposes requirements for our level of modeling and highlights certain relevant aspects of cuttings transport physics [**XII**].
- In chapter 3, we focus on the *fluid scale* and study the GNF assumption typically employed in cuttings transport studies for the example

of aqueous PAC solutions[11] and develop an understanding of the limitations and errors of the GNF framework [**IV**]. The results provide the rheological basis in terms of fluid closures for the following chapters. For a subset of the established parameter sets [**I**, **X**], we deepen our understanding of modeling errors introduced by the GNF framework with the application of Pipkin spaces [**XIV**].

- Chapter 4 is dedicated to the modeling approach of the solid phase and in particular its dense regions where particle contacts occur frequently. By means of the cliff collapse problem[12], we evaluate the TFM performance with KTGF and SM closures as described in section 1.3, hereafter simply referred to as TFM-KTGF-SM, for different fluids and spatial scales [**IX**, **V**]. In addition, we explore an alternative modeling approach from environmental sediment modeling, where the cuttings bed is dynamically excluded from the computational domain by means of mesh deformation [**VI**].

- In chapter 5, we again exploit the established parameter sets [**I**, **X**] to estimate the turbulence level prevailing in wellbore flows [**XIII**] by means of the bulk-velocity-based Reynolds number. We subsequently study the performance of several turbulence models for the transitional flow regime and benchmark the CFD results with DNS data [**VII**].

- In chapter 6, we study two different flow problems relevant for cuttings transport:
  - Focusing on the *particle scale* (see figure 1.1) first, we study the trajectory of an individual particle subjected to a channel flow of a shear-thinning fluid in section 6.1. Based on initial research [**XV**, 207], we develop and evaluate a new modeling

---

[11] PAC solutions are water-based drilling fluid model systems often used in cuttings transport studies due to their shear-thinning behavior and translucency. Four concentrations (1 g/L, 2 g/L, 3 g/L, 4 g/L of PAC granules in distilled water) were used in the experimental campaign of the AdWell project [4] and are hereafter respectively referred to as PAC1, PAC2, PAC3, PAC4. A comparison of the individual PAC solutions with the drilling fluids used on the NCS is provided in the report [**XIII**].

[12] The cliff collapse problem is the granular flow analog to the dam-break scenario in fluid mechanics and constitutes a collapse of a column of granular media under the pure influence of gravity. This may be considered a simplified test case for cuttings transport models because it represents an extreme case of what might happen in an inclined wellbore element in the sudden absence of flow.

  approach where the effect of the particle on the magnitude of the shear rate, as seen by the particle, is considered [**II**, **XVI**].
  - Secondly, in section 6.2, we focus on 3D wellbore flows, i.e., the *annulus scale* depicted in figure 1.1, and investigate the effect of pipe rotation and eccentricity. Moreover, we account for the lateral motion of the drill string by implementing specific orbital motion patterns to accordingly deform the computational grid throughout CFD simulations. We show that this approach is both a viable option and a necessity in order to simulate wellbore flows more accurately [**VIII**].

- Finally, chapter 8 closes with conclusions and recommendations for further research directions.

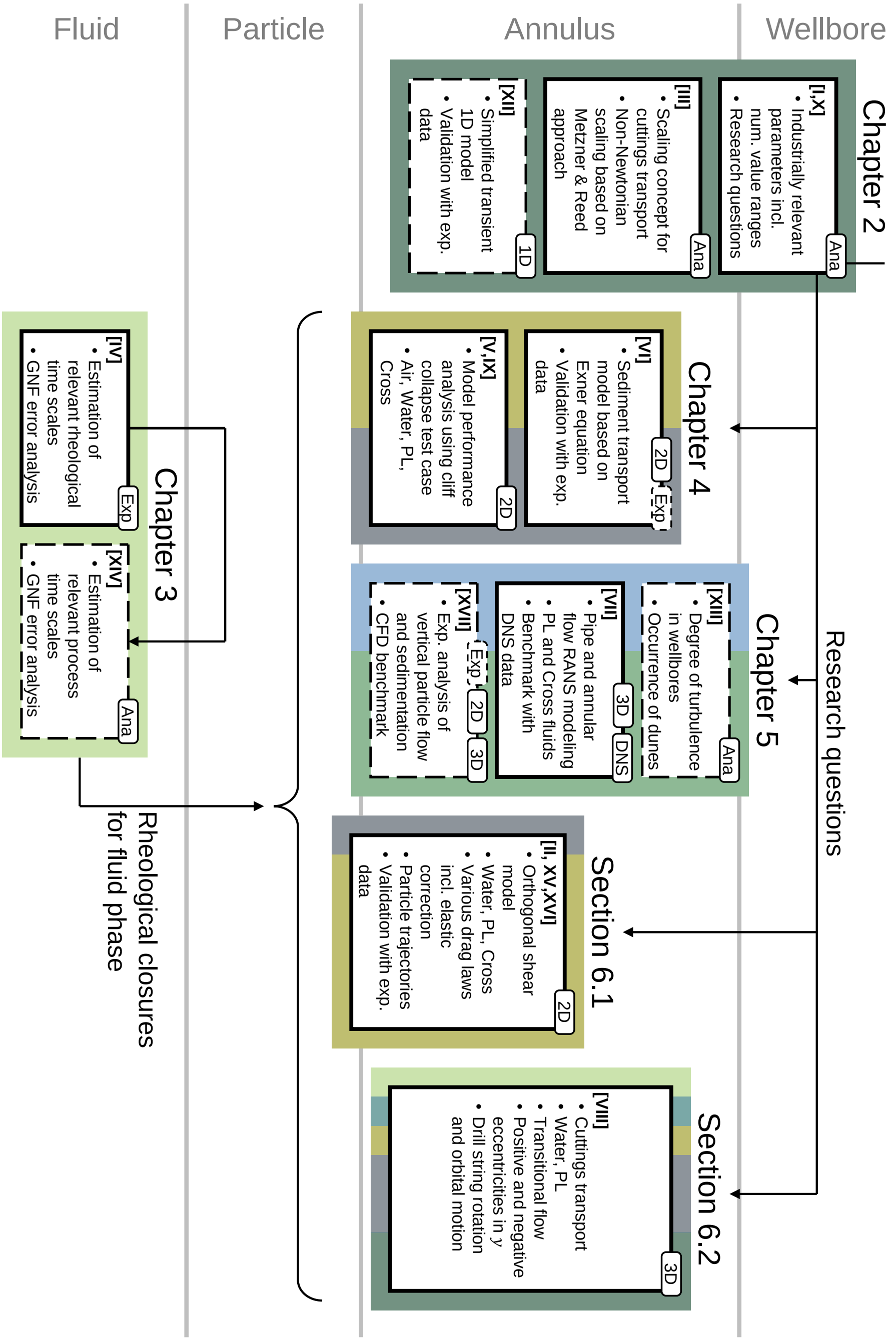

Figure 1.5.: Structure of the individual research topics and corresponding papers. The colors refer to the physical complexity levels as provided in figure 1.4, the tags provide the method utilized as conceptually displayed in figure 1.2, and the vertical axis represents the four scales depicted in figure 1.1. Solid lines characterize the publications constituting the main body of this thesis, as provided in appendix A.1. Dashed lines represent additional contributions, as provided in appendix A.2.

]

All models are wrong, but some are useful.

George Box (1978 CE)

2

Relevant parameters, dimensional analysis and scaling

In order to model any process, a detailed understanding of the relevant parameters and variables is required. Moreover, an understanding of the ultimate goal of the modeling process has to be developed. In this section, we present the relevant parameter space of cuttings transport, elaborate on scaling of the process and understand the requirements of coarser models imposed on CFD modeling based on the research works [**IX**, **X**, **III**, **XII**].

2.1. Relevant parameters

In [**IX**, **X**], a generic cuttings transport process for the case of directional drilling is analyzed regarding the industrially-relevant parameter space, with a particular focus on drilling on the NCS.

A distinction is made between the *wellbore scale* displayed in figure 1.1 and the scale of an annular element of the wellbore at some arbitrary depth down hole, termed *annulus scale*[1]. The latter constitutes the computational domain of interest primarily relevant for this study, see also figure 1.1. In order to derive the relevant parameters for the *annulus scale* from the *wellbore scale*, a detailed analysis of both scales is required first.

---

[1] This scale is termed *wellbore subsection* in [**IX**, **X**]. However, in the petroleum industry, *section* refers to particular sections, e.g. the 8.5 inch section used in the CFD study [**VIII**]. Thus, the term *annulus scale* is used.

While in many cases the two hierarchy levels feature the same parameters and variables, a few notable exceptions exist. For instance, the Rate of Penetration (ROP)[2] is a parameter on the *wellbore scale*. However, it does not necessarily appear as a relevant parameter on the *annulus scale*[3]. Instead, a more meaningful parameter on the *annulus scale* is the cuttings volumetric flow rate or mass flow rate which is related to the ROP through mass conservation[4]. Another effect of the ROP is the associated drill string x-velocity which manifests itself as a non-zero velocity on the inner wall. While this may be simply considered a kinematic boundary condition (BC) on the *annulus scale*, it is typically neglected in 3D CFD cuttings transport studies because it is one to two orders of magnitudes smaller than the mean axial flow velocity.

In a second step, the established parameter spaces, both on the *wellbore scale* and *annulus scale*, were numerically parameterized based on a database dump of aggregated NCS wellbore statistics obtained from the Norwegian Petroleum Directorate (NPD) . By means of adequate filtering[5], numerical validity ranges were generated for each *wellbore scale* and *annulus scale* parameter.

2.2. Dimensional analysis and scaling

In a subsequent study [**III**], a cuttings transport scaling framework accounting for GNF behavior is proposed based on the established parameter sets of the first part [**IX**, **X**]. Based on the concept of Metzner and Reed (MR) [24], a DA of a cuttings transport process, as described in paper [**I**], is performed for a PL fluid behavior, i.e., equation 1.16. In a second step, the more generic YPL, i.e., equation 1.17, is introduced via the local PL approximation of MR. In essence, the cuttings bed area fraction $\alpha_b = A_b/A_a$, where A is the respective cross-sectional area, as a characteristic variable for the quality of cuttings transport is a function of 12 dimensionless groups Π_i, including the MR Reynolds number and corresponding versions of other

---

[2] The Rate of Penetration is the speed at which the drill bit is advanced through the formation during drilling ahead.

[3] Note that in [**IX**, **X**] the ROP is erroneously attributed to the *annulus scale* instead of the *wellbore scale*.

[4] Note that eq. (1) in [**IX**, **X**] provides L/s. Hence, the conversion factor needs to be multiplied by 60 s/min in order to yield the stated volumetric flow rate in L/min.

[5] The AdWell projects focus was a drilling-ahead operation of directionally drilling the 8.5 inch section of an arbitrary formation with WBM.

classical dimensionless quantities, e.g. the Shields number, the (macroscopic) Stokes number, the Archimedes number, the Taylor number, and the Froude number. The Π-space is completed by the dimensionless eccentricities in y and z, the PL exponent n, the Cuttings Transport Ratio (CTR), and the aforementioned α_b as the dependent variable. In addition, the Π-space is supplemented with dimensionless quantities on the microscopic, i.e., the *particle scale*. The established Π-space is provided in two variants for annular flow and pipe flow because experimental studies from outside the drilling community often apply a pipe geometry.

The obtained set of dimensionless numbers can be used to fit large, comprehensive sets of experimental data to higher-order polynomials to obtain an empirical steady-state 1D model for cuttings transport. The applied dimensional parameter space predetermines model validity and the chosen form of the polynomial fit function highly determines model accuracy. The experimental data must obey all parameters in the applied parameter space. Moreover, no other relevant parameters are to distort the picture. For instance, while viscoelasticity and thixotropy of the fluid as well as free lateral movement of the drill string are certainly relevant in a wellbore, they must not occur here because they were neglected in the first place.

2.3. A simple example for wellbore flow models

Many mechanistic 1D models addressing wellbore cuttings transport are based on the two-layer (flowing suspension + fixed bed) slurry transport pipe flow model of Doron et al. [208], which was extended to a three-layer model (flowing suspension + sliding bed + fixed bed) by Doron and Barnea [209] and finally incorporated inclination [210]. Various 1D transient models have been subsequently proposed in the literature (see paper [**I**] for a brief summary). However, these models are relatively complex and require a multitude of closure laws.

As an alternative, we derived a simple, phenomenological, 1D transient model framework [**XII**], which may be fed with available steady-state experimental or field data based on simple closures or more sophisticated closures. Simple closures may be needed for real-time applications of the results, e.g. monitoring and advisory systems, or when a large number of simulations is needed to figure out the optimal operational parameters. In paper [**XII**], the simple closure concept is exemplified with the experimental data of Sanchez [40]. Alternatively, sophisticated closures for solid deposition and entrainment rates as well as a slip formulation may be used, all of which may be derived from more complicated models. In the paper [**XII**], a sophisticated closure approach is based on the mathematical model formulation of Charru et al. [211].

Starting from a three-layer concept and conservation equations for mass and momentum, we obtain a simple set of two or three (depending on the number of layers considered) hyperbolic equations characterizing the accumulation of solids in a domain by exploiting several equilibrium assumptions. For instance, for a two-layer concept, two transport equations for solid volume fraction (equivalent to solid mass) for a homogeneously moving mixture (index h, equation 27 in [**XII**]) and a stationary bed (index b, equation 28 in paper [**XII**]) are sufficient to capture the dynamics of the system. The volume fraction of the bed is related to the solid volume fraction in the bed (equation 29 in paper [**XII**]) and the sum of all solid volume fractions has to equal 1 (equation 30 in paper [**XII**]). The slip velocity of particles in suspension, $v_{h,s}$, is modeled as the vector-sum of the liquid velocity and the solids settling velocity and for the erosion-deposition model $\Gamma_s^{b,h}$ the model formulation of Charru et al. [211] is employed.

Model validation was performed by investigating several experimental results obtained by Sanchez [40] with the tuned model variant. While the general picture—both qualitatively and quantitatively—was fairly well replicated, specific points in time were not so well predicted by the model. A more powerful model with enhanced prediction capabilities may be obtained by directly specifying closure relations instead of performing model tuning. However, this requires all relevant data and information to be disclosed in experimental works [**IX**, **X**].

The mountains flow before the Lord.
Prophetess Deborah (1200 BCE)

3

Rheological properties and description of drilling fluid model systems

Throughout the course of this PhD project, the drilling fluid behavior in modeling works was modeled as a GNF and considered to behave purely shear-thinning without any yield stress property, i.e., described by the material functions equation 1.18 or equation 1.16. However, drilling fluid systems are known to posses thixotropic and viscoelastic properties [51, 52, 212, 213], which manifest themselves as thixotropic loops in FCs [e.g. 214–216]. For the PAC fluids used in the experimental campaign of the AdWell project [4], we studied in depth the rheological properties in order to assess the associated GNF model error [**IV**], that is the prediction error when GNF behavior is assumed.

3.1. The fluid picture

We performed a comprehensive rheological characterization of PAC solutions (with PAC granule concentrations of 2 g/L and 4 g/L and distilled water being the solvent) to understand the change of viscosity with time due to fluid microstructure build-up and break-down processes in case of shearing. The campaign included FC measurements to obtain the steady-state shear viscosity material function, Amplitude Sweeps (AS) and Frequency Sweeps (FS) to characterize the (linear) viscoelastic properties and Three-Interval-Thixotropy-Tests (3ITT). NSDs were also analyzed although not directly measured due to laboratory constraints. Instead, these were estimated based on the empirical correlation of Laun [217], based on FS data.

Viscoelastic and thixotropic timescales were associated with the obtained rheometric data and we showed that PAC solutions indeed act linearly viscoelastic on short timescales ($\mathcal{O}\left(\tau\right) \approx 10^{-4}...10^{0}$ s)[1] and feature viscosity changes due to thixotropic microstructure changes on longer timescales ($\mathcal{O}\left(\tau\right) \approx 10^{0}...10^{3}$ s).

The time constant of GNF material functions such as Cross, Carreau, and PL in a timescale formulation provides a ball-park figure of the classic viscoelastic timescale τ_{RS}, which is a "Recoverable Shear"-based relaxation time and is thus constructed from the GNF PL coefficients and coefficients of a PL fit of the First Normal Stress Difference (FNSD).

In contrast, the thixotropic timescales determined experimentally by means of 3ITT were not based on any particular model. Instead, we applied the timescale definition of a saturation function. Normalizing the 3ITT data with the respective FC viscosity provides a direct estimate of the error between a GNF model and the true in-situ apparent viscosity, as depicted in figure 3.1.

Ideal GNF behavior corresponds to the horizontal line $\eta_f/\eta_{FC} = 1.0$, i.e., the fluid's viscosity reacts instantly to any change in stress. Hence, purely viscous interpretation of data and corresponding constitutive equations/-material functions may increase uncertainty by an order of ≈ 75 to 90% in extreme cases, but more commonly ≈ 10 to 20 %. However, this depends on the magnitude of transient flow changes, e.g. shear rate steps and the time of observation.

When performing FC measurements, sufficiently long measurement point durations, i.e., the time it takes to obtain a single FC data point, have to be used such that the actual measurement occurs when the fluid sample has reached a steady-state with regards to its microstructure.

PAC solutions at steady-state are rheologically best-described with a material function featuring both a low-shear and high-shear viscosity plateau such as the Cross [30] or Carreau [29] models. While the PL

---

[1] Because several fields of research use the greek letter τ for different purposes, we here define the following in line with the official symbols and nomenclature of The Society of Rheology [218]: Stress is represented by the small greek letter σ and timescales are represented by the small greek letter τ, with the exception of the Cross [30] and Carreau [29] model coefficients, λ_{Cr} and λ_{Ca}, respectively, which have units of time.

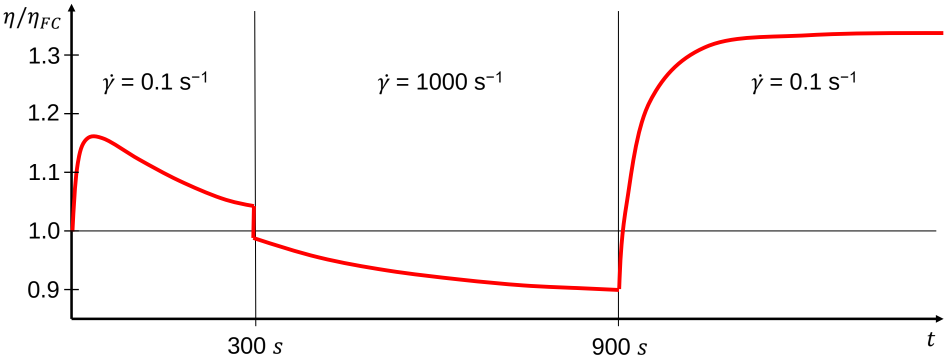

*Figure 3.1.: Qualitative result of a typical 3ITT as disseminated in paper [**IV**], where the fluids instantaneous viscosity η_f normalized with the respective FC steady-state viscosity is displayed over time. The first intervals purpose is to erase any existing fluid history and establish a reference level, which for the depicted case has not been established because the interval is insufficiently long. Running the rheometer with a very high shear rate over a certain period of time in the second interval breaks the fluids microstructure. The fluids microstructural response to a sudden cessation of flow is obtained in the third interval (which must be very much longer if a complete restructuring, i.e,* $\eta\left(t \rightarrow 0\right)/\eta_{FC} = 0$*, is to be observed).*

may be adequate for an intermediate shear rate range it fails to account for the Newtonian viscosity limit at low shear rates as well as for the high viscosity plateau at high shear rates where the viscosity approaches that of the solvent, i.e water. Therefore, material functions accounting for viscosity-plateaus are required if these shear rate ranges are relevant for the particular problem investigated, e.g. the low-shear rate range ($\dot{\gamma} < 1s^{-1}$) for a particle settling in a quiescent fluid.

3.2. The process picture

In a subsequent study [**XIV**], we related the rheological timescales of the fluid established in the previous section 3.1 to kinematic timescales characterizing a cuttings transport process in a Deborah number [219] sense to further understand the impact of viscoelastic and thixotropic fluid behavior on experimental results.

For both the *particle scale* and the *annulus scale*[2], Deborah [219] and

---

[2] Unfortunately, this scale is inconsistently termed *main flow scale* and *fluid scale* in paper [**XIV**]. However, due to the ambiguity of the terms "main flow" as well as "fluid" and for consistency purposes, the term *annulus scale* is used.

Weissenberg [220] numbers were established and visualized in so-called Pipkin spaces [221].

Historically, the Deborah number represents the ratio of a fluidic timescale characterizing the material response to changes in stress to the timescale of observation[3] and serves as an indicator for viscoelastic behavior [219].

$$De = \frac{\tau}{T_{obs}} \tag{3.1}$$

Our interpretation is a bit wider: The Deborah number serves as an indicator for GNF behavior and may take either a viscoelastic timescale or a thixotropic timescale in the nominator and a timescale characterizing the process in the denominator. The latter is generally built from the ratio of a process-characteristic length scale and a process-characteristic velocity, e.g. L/U_f and $d_p/v_{p,set}$, where $v_{p,set}$ is the terminal settling velocity of a particle. Note that the process-characteristic length scale L is defined along the direction of the flow. Therefore, the Deborah number De accounts for the degree of transient nature of the flow and becomes zero for (Lagrangian rather than Eulerian) steady flows [222, 223].

In contrast, the Weissenbergh number Wi represents the degree of nonlinear behavior of the material as it contains the inverse of the shear rate, i.e., the inverse of either equation 1.14 or equation 6.1, in the denominator. This corresponds to a process timescale definition, where the process-characteristic length scale L is defined normal to the principal flow direction, i.e., d_h for the annular case. However, the particle time scale $d_p/v_{p,set}$ results in $De = Wi$ for the particle scale. Thus, for a settling particle, a better choice for the characteristic distance a particle settles may be d_h, instead.

The basis for the fluid description in both the Deborah and Weisenbergh numbers are the fluidic, or rheological, timescales as described in the previous section 3.1 and therefore represent the rheological behavior of PAC solutions, specifically. The process timescales are built from the numerical parameter ranges established in the parameter analysis ([**I**, **X**], see section 2.1). Here, several cases are defined somewhat arbitrarily (Table 1 in [**XIV**]) to cover the numerical parameter ranges established in [**I**, **X**].

---

[3] The *timescale of observation* may simply be interpreted as the total time one observes the flow as paraphrased by the verse "The mountains flowed before the Lord" [219]. However, rheologists have come to use timescales relevant for the particular process, for instance constructed from a characteristic length scale (in the direction of the flow) over a characteristic velocity.

Unfortunately, for the fluids and cases considered, no unequivocal result is obtained by computing respective ranges of the Deborah number, the Weissenberg number, and the Reynolds number.

However, in general, the orders of magnitudes of De, Wi, and Re as well as their definitions indicate that for the GNF model to hold on the *annular scale*:

- sufficient development lengths L must be incorporated in an experimental setup,
- a steady-state of the entire process has to be ensured,
- and a steady-state of the flow at the point of observation is required.

For the GNF to be valid on the *particle scale*, the following points should be considered:

- Particles should be sufficiently small, such that induced settling velocities are small. Otherwise, viscoelastic corrections to the drag coefficient [224] may have to be considered.
- Rheological relaxation times must be sufficiently short. The combination of higher PAC concentrations and multi-particle systems of larger particles must be taken with care, because the settling of particles following in the wake of a particle will be affected by the altered microstructure of the fluid [225, 226]. Even for single particles care must be taken in case of high fluid relaxation times because this may significantly increase the particle drag [225] due to an inhomogeneous viscosity field around the particle.

No generally valid conclusion may be drawn from the analysis. Instead, the stencil presented in [**XIV**] has to be used on an individual basis in order to asses the validity of the GNF assumption for a particular experimental or numerical campaign. If the GNF formulation is to be used for experimental data analysis and concurrent numerical modeling, careful design of flow loops and test setups is required to minimize the effect of transient viscosity changes and viscoelastic stresses.

$\pi\alpha\nu\tau\alpha$ $\rho\varepsilon\iota$—Everything flows.
Simplicius (490–560 CE)

4

Modeling of dense granular flows

In this chapter, we first investigate the application of the TFM-KTGF-SM model to a simple test case, namely the cliff collapse problem, which may also be considered a subproblem of wellbore flows. In a second step, we consider the so-called Exner [227] equation as a model alternative to the TFM-KTGF-SM approach.

4.1. The cliff collapse problem as a simple test case for wellbore flow models

The Two Fluid Model (TFM), in combination with the Kinetic Theory of Granular Flows (KTGF) and additional closures from soil mechanics (SM) as described in section 1.3 is used in the majority of CFD cuttings transport studies, see section 1.4. Here, the TFM-KTGF transport equations for mass, momentum, and granular temperature as well as turbulence quantities are solved in the entirety of the computational domain. Dense regions, where particles are in frequent contact with each other and frictional contact dominates, are rheologically handled with the SM viscosity material function equation 1.25: Small shear rates and large solid pressures lead to a large solid viscosity which effectively leads to cessation of flow.

However, the model is usually not validated in a proper manner. Validation with real field data is challenging due to the difference in scales and the many unknown parameters, hence experimental data from laboratory studies may be used instead. But validation is often conducted inadequately: Some studies perform validation with single-phase experimental data only and others benchmark their results with other simulation results only (both may be due to absence of adequate experimental data), and yet others use debatable quantities such as the CTR [176, 177][1].

Therefore, we decided to evaluate the TFM-KTGF-SM approach as described in section 1.3 with a much simpler test case: the sudden collapse of a cliff of granular media [**IX**, **V**], as depicted in figure 4.1. As the cliff starts to disintegrate under the influence of gravity at $t = 0$ s, the cliff collapse problem may be considered the granular media equivalent to the single-phase fluid mechanics dam-break scenario.

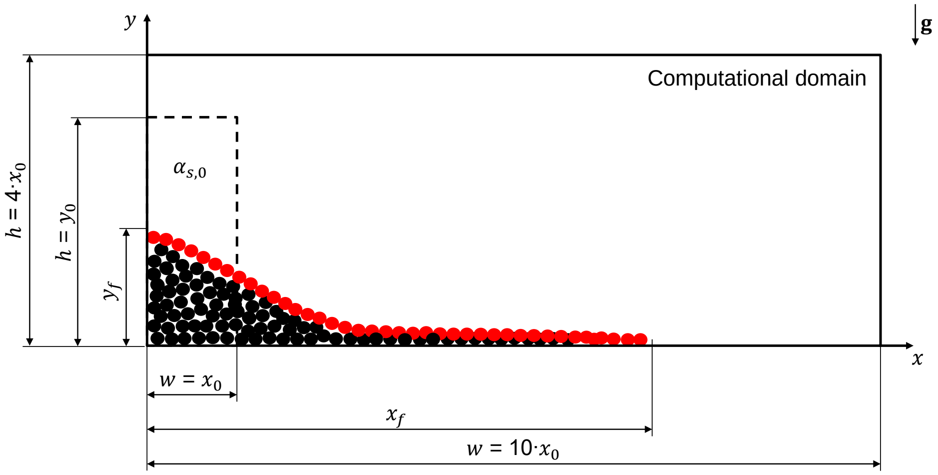

*Figure 4.1.: Qualitative result of a typical cliff collapse as disseminated in papers [**IX**, **V**]. The spheres conceptually indicate a typical shape of a fully collapsed cliff, and the red spheres represent its top-layer. The dashed line denotes the IC.*

In terms of the parameter space investigated, we have studied the influence of the cliff aspect ratio $a = y_0/x_0$, the scale of the initial cliff, the scale of the particle size, four different interstitial fluids (air, water, PAC solutions), and the role of the ICs such as solid volume fraction α_s and solid pressure p_s fields. The latter was evaluated by two different strategies: (1) Let solids settle to establish a compacted granular bed in dynamic equilibrium prior to allow the cliff to collapse, or (2) simply patch the solid volume fraction α_s into the computational domain at $t = 0$ s.

---

[1] If the solution is steady-state, the CTR is predetermined by the BCs (the inlet phase velocity and the solid volume fraction α_s), unless a pressure gradient in combination with periodic BCs is specified, see paper [**VIII**].

However, validation with experimentally obtained scaling laws from the literature [228, 229] was not comprehensively successful because the top-layer of the deposit depicted in red in figure 4.1 does not stop flowing, albeit with a very small velocity. While most of the simulations produced a quasi-final deposit featuring an angle similar to the angle of repose at a presumed steady-state, the flowing layer results in a scale-dependent disintegration of the cliff over longer periods of time which ultimately results in a flat bed. We suspect this phenomenon, hereafter termed *top-bed velocity defect*, to be a consequence of the numerical solution strategy of ANSYS Fluent which may result in some solid flux imbalance at top-bed regions where the gradient of the solids kinetic/collisional pressure $p_{s,k/c}$ is high.

Comprehensive model tuning is required to yield a better physical representation of the IC, for instance by adjusting the angle of internal friction ϕ, the solid volume fraction threshold for the frictional regime $\alpha_{s,f}$, and the maximum packing density $\alpha_{s,mpd}$.

In addition, alternative closures for both solid frictional pressure $p_{s,f}$ and solid frictional viscosity $\eta_{s,f}$ may help to better reproduce the experimental data. On the other hand, experimental spread and missing experimental data for the shear-thinning fluids require more comprehensive experimental data for validation purposes.

If the model in its current form is used for transport modeling of cuttings in wellbore flows, the aforementioned *top-bed velocity defect* will likely lead to an unknown overestimation of transported cuttings. When it comes to the modeling of dune migration, the *top-bed velocity defect* will likely cause disintegration of the dune over longer periods of time.

4.2. The Exner equation - An alternative modeling approach for wellbore flows

In the TFM-KTGF-SM approach, the entire domain of interest is discretized. However, in most cases, solid mass transport only occurs in regions on top of the cuttings bed[2]. At the top of the bed, dunes may start to form [66,

---

[2] We here primarily consider horizontal flows, where the majority of the cuttings bed is static due to internal frictional forces. However, for intermediate inclinations, a cuttings bed may start to slide in its entirety as gravitational forces start to overcome frictional forces. Furthermore, avalanches may occur.

155, **XIII**] depending on several quantities[3].

As a computationally cheaper alternative to the TFM-KTGF-SM approach and in order to further investigate the role of dunes, we evaluated an alternative modeling approach commonly used in environmental solid transport modeling (e.g. the transport of sediments in rivers or deserts) [e.g. 151–153], where the dense region is dynamically excluded from the computational domain and the evolution of the cuttings bed is described with the Exner [227] equation [**VI**].

The sediment bed (defined by grid cells where the solid volume fraction exceeds e.g. 0.6) is excluded from the computational domain on a per time step and per grid cell basis, as conceptually depicted in figure 4.2: The evolution of the sediment bed is described by mass conservation in the form of the Exner [227] equation. The computational grid is then dynamically updated by mesh deformation techniques to account for the changing sediment bed height in time and space. Consequently, the frictional closures, i.e., equations 1.24 and 1.25 are not required and the solid stress tensor, namely equation 1.19 only contains the kinetic and collisional contributions.

For a 2D channel, we implemented the Exner [227] equation in the form of an additional scalar transport equation for the bed height in a Fluent User-Defined Function (UDF), where the resulting changes in the sediment bed height are used to reposition the nodes at the lower channel wall and the mesh is subsequently deformed using Fluent's dynamic meshing capabilities [**VI**]. Consequently, the mesh is morphed throughout the simulation on a per grid cell and per time step basis in order to represent the morphodynamical changes of the solids bed. The convective fluxes in the scalar transport equation are modeled with closures relating these fluxes to the mixture/fluid/solid velocity and/or bed shear stress.

The model accounts for local bed slope, hindered settling, and non-Newtonian, shear-thinning viscosity of the fluid phase as well as turbulence.

Model validation with channel flow data obtained at the UiS laboratories showed that extensive tuning of the models convective flux, and deposition

---

[3] In the appended report [**IV**], we map the industrially relevant cuttings transport parameter space, in the form of the bulk flow quantities established in paper [**I**], to the flow pattern map of Ouriemi et al. [230, 231]. While generally dependent on bed height and superficial Reynolds number, as well as particle diameter and Archimedes number, the low viscous fluids tend to generate larger vortex dunes and sinuous dunes whereas the more viscous fluids result in smaller dunes.

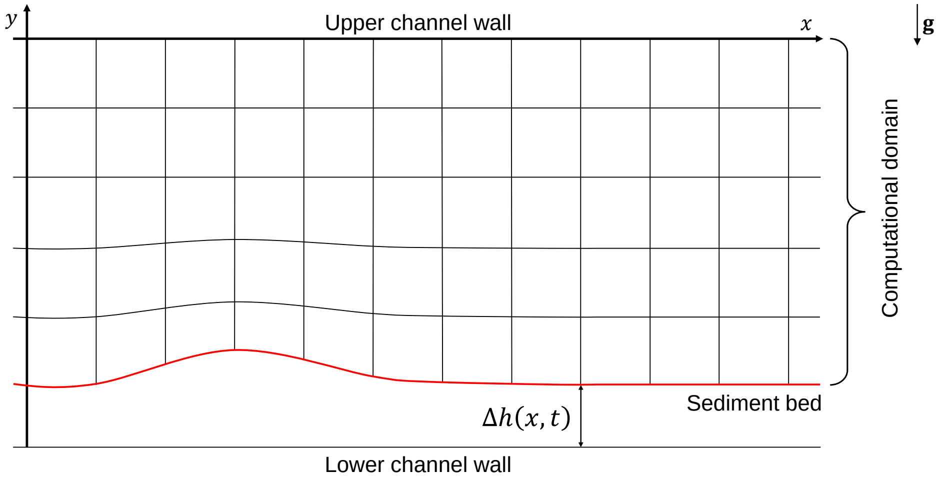

Figure 4.2.: Conceptual sketch of the Exner equation concept and the modeling approach utilized in paper [VI]. The red line represents the top of the sediment bed and the lower part of the computational domain. The y-position of the lower channel boundary is updated on a per grid cell and per time step basis and the mesh is deformed accordingly.

and entertainment rate closures as well as the (unknown) in-situ solid volume fraction at the inlet is required. Moreover, for the PAC solutions investigated, the effect of the non-constant fluid viscosity η_f needs to be introduced to the Newtonian closures utilized.

The model does correctly predict bed deformation as a consequence of non-equilibrium BC. However, most probably due to the utilized RANS framework, the model is not capable of predicting flow-induced dunes. Regardless of Re and the IC, the steady-state is always a entirely flat sediment bed, i.e., $\Delta h \left(x, t \rightarrow \infty\right) = const.$, as visualized by the red line in figure 4.2. A RANS approach does by definition not account for locally varying turbulence and therefore an instability causing perturbation of the sediment bed does not occur. A simplified LES approach, e.g. the VLES [232, 233] concept, may lead to a model capable of describing flow-induced dynamic bed shapes such as traveling dunes.

Because of the many open issues (VLES turbulence model integration, non-Newtonian viscosity formulation of closures, tuning of model parameters, extension to 3D) and the fact that, in case of annular flow, mesh deformation will be very complex to handle when the sediment bed establishes contact with the drill string, we decided to not further elaborate on this modeling technique.

I have never really understood turbulence. However, when my second son started to walk and the kids interacted in terms of motion I got an idea of it.

Note to myself (2016 CE)

5

Modeling of turbulence

It is known that interaction between the rheological properties of the fluid and the turbulence of the flow exist. Therefore, we have estimated the magnitude of turbulence in wellbore flows and subsequently evaluated the performance of several turbulence models used often in cuttings transport modeling.

5.1. The degree of turbulence in wellbore flows

A simple Reynolds number-based estimate [**XIII**] was performed on the numerical parameter space established in paper [**I**]. We applied the Reynolds number concept of Metzner and Reed [24] as well as the Bingham Reynolds number of Wilson and Thomas [234] to compute ballpark figures for several specific cases [**XIII**] representing the industrially-relevant parameter space of [**I**].

In general, drill pipe flows are fully turbulent for water and transitional for drilling fluids, regardless of the Reynolds number concept used. However, annular flows are at best transitional and mostly laminar, depending on the YP/PV combination (approximately $YP \geq 10$ Pa, $PV \geq 0.015$ mPa·s [**XIII**]). The order of magnitude of the estimated Reynolds numbers is not heavily affected by the presence of a cuttings bed with a relative height of $\frac{1}{3}$ of the hydraulic diameter. Simple rotation does not really affect the pure flow dynamics in the deeper, smaller wellbore sections either. Here, here the axial flow velocity is so large that the additional rotational velocity accounted for by a simple vector magnitude concept does not contribute significantly[1].

In a well, drill pipe agitation as well as strong local accumulation of cuttings along with the flow disturbances induced by drill collars will certainly increase the turbulence level. The presence of particles will either dampen or contribute to turbulence, depending on particle shape, density ratio, and loading [235–237].

In any case, considering the magnitude of the Reynolds number as estimated in [**I**], the turbulence level is most likely still transitional, which is the most challenging regime for turbulence models. In fact, transitional flow may be problematic as it is rarely well-captured by standard turbulence models.

5.2. Evaluation of industrially-relevant turbulence models

In all cuttings transport studies mentioned in section 1.4, no interaction between turbulence and the non-Newtonian rheological properties of the fluid is assumed. However, turbulence is for instance influenced by properties such as the yield stress [238, 239] or the shear-thinning behavior [e.g. 140, 142, 144]. Polymer loading may lead to the phenomenon of *Drag Reduction* (DR) [240, 241]. Consequently, a proper Reynolds-Averaging accounting for the viscosity as a fluctuating quantity is required [242, 243] and the viscoelastic drag reduction effects should be taken into consideration [244].

Furthermore, when making use of a wall function in order to reduce computational effort by not resolving the near wall layer, non-Newtonian wall functions [245–247] should be applied.

However, neither the non-Newtonian k-ϵ turbulence models [242, 243], nor the non-Newtonian wall functions [245–247] have yet found their way into commercially available CFD codes.

Based on the findings of a first study [**XVII**] and the outcomes of our estimates as summarized in section 5.1, we have investigated the performance of the SST k-ω model presented in section 1.3.5 as well as the low-Reynolds number k-ϵ model of Lam-Bremhorst [248] in conjunction with its non-Newtonian modification [249] for several pipe and annular

---

[1] Future work may distinguish more properly between the axial velocity and the rotational velocity. As our DA shows [**III**], the former leads to the Reynolds number and the latter to the Taylor number.

flow cases using the PL and Cross material functions. The results have been compared with corresponding DNS data for Newtonian, PL, and Cross fluids. The DNS data was generated by SINTEF Industry under the work package four in the AdWell project.

At the time of writing, only preliminary results are available. Further work is required to comprehensively evaluate the relevant parameter space, in particular with regards to different PL and Cross fluids, in order to understand the magnitude of the error when applying Newtonian turbulence models. In the following, some preliminary findings are summarized:

- Most industrially available models overestimate the friction factor. While some models such as the SST k-ω do correctly collapse to the laminar friction factor for low Reynolds numbers, this is not necessarily the case for all models investigated.
- While being considered the industrial workhorse of turbulence modeling, the SST k-ω model in general overpredicts turbulence, in particular when rotation is present.
- For a Newtonian fluid, the Lam-Bremhorst [248] variant of the Standard k-ϵ model performs better than the SST k-ω model for $Re_{MR} < 10000$.
- However, for a shear-thinning fluid, the Lam-Bremhorst [248] variant of the Standard k-ϵ model underpredicts the mass flow rate for a given pressure drop. In case of a PL material function, the modified k-ϵ of Lam-Bremhorst by Marin [249] appears to work well. While it has been considered unsuitable by some researchers, it does fit our DNS data and friction factor correlations [250, 251] best. A possible explanation is that the experimental data used by those researchers actually may have featured viscoelastic and thixotropic behavior which then distorts the results (see chapter 3).

Stir it up, come on, baby! Come on and
stir it up, yeah!
Bob Marley (1978 CE)

6

Wellbore flow problems

6.1. Trajectory of a single particle in orthogonal shear flow

Earlier work in the project [**VI**, **XV**, **XVII**] indicated that evaluation of the shear rate given in equation 1.14 is not entirely accurate for non-neutrally buoyant particles in a flowing shear-thinning fluid because equation 1.14 does not account for the contribution from the relative velocity of the particle. Therefore, following up on the work of our experimental colleagues [207], we amended the computation scheme of Fluent's DPM in order to account for the particle contribution based on the vector magnitude concept of Novotny [252], as described in publications [**I**, **XVI**].

In the laboratory experiments of Khatibi [207], single particles (d_p = 1.2, 2, 3 mm) are injected into a 2D channel flow of water or PAC2 or PAC4. It then settles due to gravity through the cross-flow to the bottom of the channel while at the same time it is advected downstream by the cross-flow, as conceptually depicted in figure 6.1. We performed DPM simulations in order to numerically compute the experimentally observed particle trajectories.

In order to compute a physically more correct (shear-rate dependent) viscosity as seen by the particle, we employed the vector magnitude concept of Novotny [252] to calculate the shear rate. The total shear rate as seen by

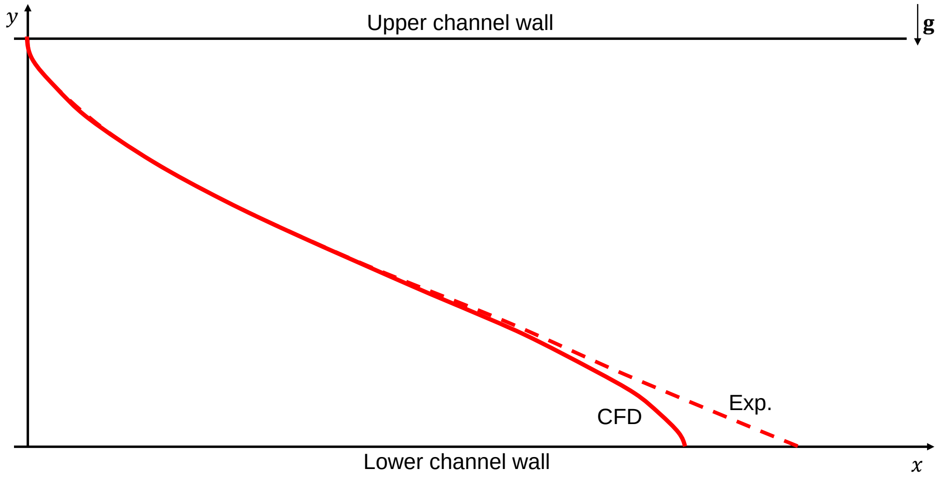

*Figure 6.1.: Conceptual sketch of the 2D channel flow experiments performed by [207] and numerically replicated in the paper [**I**]. The red curves represent observed particle trajectories. A single particle is injected at the top and settles under the sole influence of gravity through the cross flow.*

the particle is then given by

$$\dot{\gamma}_f = \sqrt{\dot{\gamma}_{f,CFD}^2 + \left(\frac{\|\mathbf{v}_r\|}{d_p}\right)^2}, \tag{6.1}$$

where $\dot{\gamma}_{f,CFD}$ is the shear rate as computed by the CFD solver based on the solved velocity field of the primary phase.

We implemented this concept in a UDF, where based on equation 6.1 viscosity is determined using the Cross material function equation 1.18. Then the particle Reynolds number, i.e., equation 1.11, and a corresponding coefficient of drag are computed. The coefficient of drag is then supplied to the solver. Several drag laws [95, 224, 253, 254] were investigated: If the shear rate is computed as given in equation 6.1, the Newtonian Schiller and Naumann [95] drag law provides sufficient results.

While the new model produces the small particle trajectories comparatively well, the large particle trajectories are not matching in the lower part of the channel, in particular for the PAC fluids. This is illustrated in figure 6.1, where the dashed line represents a typical J-shaped trajectory obtained in the experiments, and the S-shaped trajectory exemplifies a typical CFD result.

The mismatch in trajectories is due to the x-velocity component. Plotting the particle's x-velocity component $\Delta x/\Delta t$ normalized with the local fluid velocity $u_x(y)$ over the channels y-coordinate shows, that for the Newtonian, i.e., H2O cases, the particle has sufficient inertia and momentum to yield faster x-velocity (by a factor of 1...3 compared to the local fluid velocity) close to the lower wall of the channel. Given the higher viscosity, one would expect less for the PAC cases.

However, for the PAC cases, and in particular for the cases of $d_p = 2$ mm where the trajectories do not coincide close to the lower channel wall, particles are advected much faster than the fluid (Factor 2...6). For the same cases, focusing on the upper channel half, the particles relax to the fluid velocity comparatively fast.

While we discuss several possible causes in paper [**II**], it remains unclear what exactly causes this discrepancy.

The viscoelasticity of the PAC solutions (see chapter 3 and papers [**IV**, **XIV**]) does not explain the mismatch. The drag law of Acharya [224, 254] provides a simple drag coefficient correction for viscoelastic effects (drag enhancement or drag reduction) based on a characteristic fluid timescale. Here, the Carreau model [29] coefficient λ has been used. While this improves the match for one PAC case, the match gets worse for the other PAC cases.

For high fluid relaxation times, the particle drag may be significantly increased because of a localization of the flow around the particle surface caused by an in-homogeneous viscosity field [225]. This topic needs further investigation because such effets are not captured by the DPM model utilized in our simulations as the flow around the particle is not resolved.

Other forces than drag may be considered but are not affecting the trajectories significantly, in particular for the PAC cases, where the drag force is by far dominating due to its dependency on viscosity. In the paper [**I**], we have evaluated the effect of other particle forces, namely the virtual mass force [81, 255] representing the required acceleration of fluid mass displaced by the accelerating particle as well as Saffman [81, 90, 91, 256] and Magnus [81, 93] lift forces, on the computed trajectories for the case of water. While the acceleration phase of the particle after the injection point is affected by the additional particle forces, the overall trajectories do not change much. This is especially so for the PAC cases. Here, only the drag force scales linearly with viscosity (see either equations 1.8 to 1.10 or equations 1.8 and 1.11 to 1.13), whereas the other forces are independent of viscosity with the exception of the Saffman lift force, which depends on the square root of viscosity [81, 90, 91, 256].

6.2. The effect of drill pipe rotation and lateral motion on cuttings transport

Drill pipe rotation is considered a relevant factor when it comes to the efficiency of cuttings transport and hole cleaning [59, 60, 157, 158]. However, in many cuttings transport studies, the term "rotation" is in fact often used as a moniker for the combination of plain drill pipe rotation around its own axis and a more complex lateral motion, as many laboratory setups [e.g. 4, 40, 257–261] feature an unconstrained drill string. The lateral motion, which encompasses specific patterns such as forward or backward whirl, is generally thought to assist the transport of cuttings due to increased bed agitation [40, 161, 262]. Generally, accounting for and thus purposely replicating drill string lateral motion in laboratory cuttings transport studies is reasonable because it reflects the conditions in the field [32, 33]. In wellbores, the drill string is subject to various forces [34, 36, 38, 263] resulting in a variety of motion patterns [39].

However, the lateral motion of the drill string is not very often explicitly addressed in experimental work and even less in CFD studies, where *rotation* is typically interpreted and applied as *plain rotation around the drill string's own axis* as depicted on the left-hand side of figure 6.2, with the notable exceptions of the work of Demiralp [195] concerning cuttings transport and several other studies focusing on single-phase pressure loss [41, 264–267].

Therefore, because the experimental setup of the AdWell project [4, 207, 257] featured an unconstrained drill string, we investigated the role of combined plain rotation around the drill string's own axis and its whirling motion on cuttings transport [**VIII**], as depicted on the right-hand side of figure 6.2.

Based on the physical model presented in section 1.3, we have investigated the role of whirling drill string motion on cuttings transport for water and PAC1 by exploiting the dynamic meshing capabilities of ANSYS Fluent R17.2.

Synchronous Whirl (SW) and Asynchronous Whirl (AW), as displayed on the right-hand side of figure 6.2, are two extreme cases of lateral, or more specifically, orbital drill string motion. In case of AW, the drill string collars

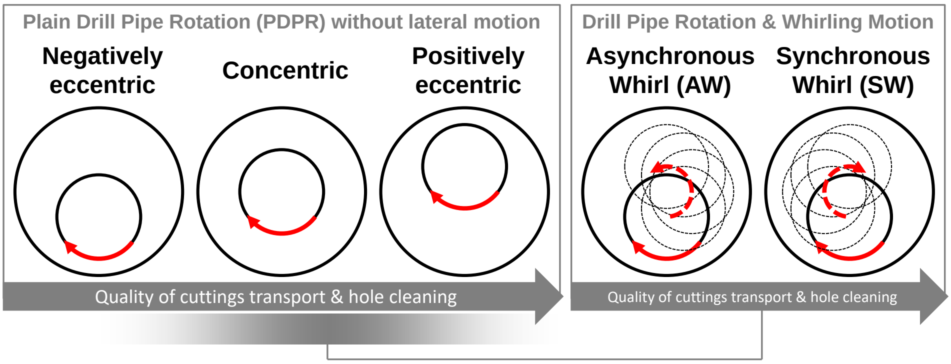

Figure 6.2.: Conceptual sketch of the various rotation patterns found in drilling. Picture adapted from [VIII]. Depending on particular case parameters, the cuttings transport performance of AW and SW falls somewhere in the shaded area.

are in frictional and slip-free contact with the outer wall of the annulus and feature a pure rolling motion on the outer annular wall where the whirling motion is in opposite direction to the drill pipe rotation. Thus, for a given drill pipe angular velocity ω_p, the angular velocity of the whirling motion $\omega_w = -d_j/d_o\omega_p$ is purely defined by the ratio of the drill pipe joint and annulus outer diameter, d_j and d_o, respectively. In contrast, SW is defined by total slip between drill pipe joints and annulus wall and the whirling motion is in the same direction as the pipe rotation with an identical speed. Consequently, the drill pipe is always facing the same side to the annular wall, i.e., there is continous frictional contact, which may cause severe wear [41].

The reason for specifically investigating SW and AW is that these motion patterns are relatively simple and hence straightforward to describe by analytical oscillatory equations of motion for the y- and z-coordinates of the center of the drill string, namely

$$y_w = \left(E_y + A_y\right) - A_y \cos\left(\omega_y t\right) \tag{6.2a}$$

$$z_w = E_z + A_z \sin\left(\omega_z t\right), \tag{6.2b}$$

where E_i with $i \in \{y, z\}$ is the dimensional eccentricity, A_i is the whirl amplitude based on a negative eccentric initial position, and ω_i are the respective angular velocities. For AW and SW, $\omega_y = \omega_z$, $E_y = E_z$, and $A_y = A_z$.

The time derivatives of equation 6.2 were implemented in an UDF, which provides the velocities of the center of gravity of the orbital motion of the drill pipe to the solver. Nodes are displaced accordingly and the spring-based smoothing method, were the cell edges are treated as elastic springs, is used to update the mesh every time step[1].

The simulations were done with periodical BCs, i.e., an infinitesimally long annulus was assumed. Single-phase simulations were based on the specification of a flow rate while in the case of multi-phase simulations a pressure gradient $\Delta p/\Delta x$ in combination with a certain mass of solids, i.e., solid volume fraction α_s, in the computational domain was applied[2].

We first semi-validated the model with unsatisfactory success using single-phase flow cases generated in the AdWell project [4, 257, 258]. In addition, the numerical results were compared to friction factor correlations [250, 251] corrected for eccentricity [268, 269]. While the non-rotating CFD cases fit the friction factor correlations, this is not so when comparing our CFD results to the results of Khatibi et al. [4, 257, 258]: The motion patterns in the experiments of Khatibi et al. [4, 257, 258] were neither AW nor SW but rather dependent on the fluid's superficial velocity, the fluid's viscosity, and the rotation rate of the drill string. In the experiments, the drill string was totally free to move in the annulus (besides one end which was constrained concentrically by the motor) and hence dynamically interacted with the flow. Therefore, the aforementioned assumptions, namely $\omega_y = \omega_z$, $E_y = E_z$, and $A_y = A_z$, are not valid and the individual quantities had to be estimated based on visual observations.

In a second step, we investigated several cuttings transport, i.e., multi-phase flow, cases: The two previously mentioned AW and SW cases, and three base cases (negative eccentric, concentric, and positive eccentric), as summarized in figure 6.2, were investigated for benchmark purposes.

Whirling motion helps tremendously to disperse cuttings into main regions of the flow and hence improves the quality of cuttings transport and hole cleaning. For a given pressure gradient, the quality of cuttings transport was evaluated by means of the CTR as well as the achievable

---

[1] See https://youtu.be/vV-0C9GXkWM for a visualization of the spring-based smoothing dynamic meshing method of Fluent and the mesh deformation of the employed annular domain, specifically.

[2] For periodical BCs applied to multiphase flows, a specification of individual phase velocities is not possible in Ansys Fluent. Instead, the specification of a mixture pressure gradient along with a solid volume fraction is required and velocity fields are obtained as solutions which if integrated over the cross-sectional area result in bulk velocities for both the fluid and the solid phases.

ROP. SW outperforms by far AW because of the cumulative tangential and radial velocities. The effect is much more prominent for water than for the more viscous, shear-thinning PAC1 fluid because in the absence of rotation and whirling motion, PAC1 already has comparatively good cuttings transport performance when compared to water.

In the case of the PAC1 solution, the positive eccentric annulus provides even better cuttings transport capability compared to AW and SW, when comparing equivalent pressure gradients. Because of the higher viscosity level, the whirling motion reduces the axial throughput, which despite the increased bed agitation results in worse performance compared to the positive eccentric case, where the main flow occurs on top of the cuttings bed with high shear stresses acting on the bed. Hence, transport of cuttings primarily occurs in a rolling and sliding manner at the top of the sediment bed.

In summary, for the investigated parameter ranges, the best transport of solids is achieved when the annular configuration is positively eccentric, followed by a concentric arrangement. As visualized in figure 6.2, AW and SW generally fall in between the two, depending on the type of fluid and the means of evaluation (CTR vs ROP).

Since lateral drill string motion has such a strong effect, the cuttings transport research community should distinguish between plain drill pipe rotation around its own axis and rotation involving different types of whirling motion or more complex lateral motion patterns. Experimentalists are advised to carefully design their laboratory setups such that occurring whirling motion can be quantified, both in terms of kinematic parameters such as angular velocities and amplitudes of the whirling motion (see equation 6.2), and wellbore system parameters such as string compliance, mass, and bearings leading to the whirling motions.

More research is required to explore the entire industry-relevant design space, both experimentally and numerically. We have only investigated the role of eccentricity and pressure gradient $\Delta p/\Delta x$ for a fixed solid loading, i.e., solid volume fraction α_s, and low viscous fluids in one particular horizontal annulus. Other geometries, both in terms of the *annulus scale* and *particle scale* as well as inclined sections, need to be investigated. Furthermore, more viscous and different degrees of shear-thinning fluids as well as different yield stress magnitudes have to be considered. Finally, laminar flow in the form of lower pressure gradients (and the previously mentioned higher viscosity levels) and a variety of solid loadings have to be studied. Experimental data fullfilling the above mentioned requirement concerning quantitative description of the whirling motion, and which is ideally obtained with translucent fluids, is required to perform model tuning and validation.

It can scarcely be denied that the supreme goal of all theory is to make the irreducible basic elements as simple and as few as possible without having to surrender the adequate representation of a single datum of experience.

Albert Einstein (1933 CE)

7

Discussion

7.1. The role of the parameter space and dimensionless scaling

On the *annulus scale*, both the dimensional parameter space [IX, X] and the Π-space established by means of DA [III] need to be enlarged in order to address neglected but nevertheless relevant wellbore flow phenomena, for example:

- Thixotropy and viscoelasticity.
- Lateral drill string motion.
- Solid phase quantities such as the angle of internal friction and potentially particle size distribution and sphericity factors.
- Local temperature and pressure.

Thixotropy, viscoelasticity, and lateral drill string motion manifest themselves as transient effects. Hence, time as an additional relevant physical quantity must be considered in the DA in order to incorporate these cases. By doing so, one would also automatically address the cases where the BC and IC state a transient problem in non-equilibrium, for instance a build-up of a cuttings bed over time or, conversely, an erosion process of an existing cuttings bed.

Thixotropy and viscoelasticity could be added in a generic, i.e., model-unspecific manner due to the huge variety of existing models. For instance, a timescale as measured in the 3ITT (see chapter 3 and paper [**IV**]) could be considered to describe a fluid's microstructural break-up and break-down behavior. In a similar manner, an elastic timescale could be defined e.g. based on creep tests. Such a description has the benefit of naturally incorporating an information about the relative GNF stress offset. This topic will be discussed further in section 7.2.

Lateral drill string motion, which has a large impact on the quality of cuttings transport [**VIII**] as described in section 6.2, could be added in two different ways:

1. A full mechanistic approach where mechanical properties such as drill string compliance are considered and the drill string deformation and kinematics are obtained from a respective model. This would allow for preserving wellbore physics by appropriate scaling from field to laboratory setups.

2. A simple kinematic approach where a particular motion is prescribed and the kinematic parameters such as the amplitudes in y and z (see figure 1.1 and figure 6.2) are easy to measure in laboratory studies.

While the former is best in terms of replicating wellbore conditions the latter is more suitable for CFD studies [**VIII**]. Hence, further work is required to establish particular parameter sets for different motion patterns, i.e., 2) by means of 1).

The simple characterization of the solid phase by a (mean) particle diameter and its density is insufficient and the angle of internal friction should be added as a minimum. While the steady-state rheological description of the fluid is characterized well with the GNF and a specific material function, this is not so for the solid phase. As apparent from chapter 4, quantities such as the angle of internal friction (or alternatively, because of measurement limitations, the angle of repose [128, 270]), the coefficient of restitution, and the maximum packing density also affect the rheological description of the solids and a correct quantification of these parameters appears very important to achieve a good match of CFD model results and experiments [**V**].

In general, local fluid temperature should be considered as it heavily affects the viscosity of the drilling fluid [271–273]. However, when it comes to modeling, in-situ fluid temperature becomes only relevant if experimental or CFD studies are used for prediction of in-situ downhole field conditions. Here, the fluid temperature in the annulus varies heavily depending on the position measured and the hours of drilling conducted [271]. Local formation temperature can be estimated based on the geothermal gradient. Local formation temperature can be estimated based on the geothermal gradient. The appropriate local fluid temperature (as the inlet BC in a CFD model) should be calculated with thermodynamic wellbore system models. That is because the wellbore is essentially a counter-current heat exchanger: surface-conditioned fluid flows downwards through the drill pipe, while fluid heated by bits and high formation temperature is convected upwards by the annular fluid flow.

In addition, dependencies between individual parameters should be investigated more closely. For instance, in hindsight our analysis should have also focused on the specific combinations of YP and PV. In [**IX**, **X**], YP and PV were considered as entirely independent parameters. However, plotting YP vs. PV, i.e., Fig. 9 vs. Fig. 8 in [**IX**, **X**], shows that there exists a relation between YP and PV.

In a similar manner, the model proposed in [**XII**] needs to be further elaborated. While tuning the model to the experimental results of Sanchez [40] yielded satisfactory results, this is not expected for the application of the more sophisticated model variant based on the closures of Charru et al. [211]. For instance, plain drill string rotation is simply accounted for by the corresponding circumferential velocity, whereas in the experimental campaign of Sanchez [40], the drill string was allowed to move freely and the resulting lateral motion was thought to have a major influence on the results [40].

Finally, the proposed scaling method needs to be further developed in order to use it to account for turbulent wellbore flows. The MR concept used here is based on the relation of wall shear stress to bulk velocity, i.e., $\tau_w = f(U)$, where the latter is a function of the laminar velocity profile, i.e., $U = f(u(x,y))$. A viable alternative is to base the wall shear stress on the pressure gradient, i.e., $\tau_w = \frac{d_h \Delta p}{4 \Delta x}$, see [**III**, **VII**].

7.2. The limitations of the GNF framework and the determination of viscosity

In [**IV**, **XIV**], we show that the laboratory liquids used in our experimental campaign possess more complex non-Newtonian behavior such as thixotropy as well as linear viscoelasticity and NSDs. Depending on the particular flow problem, the application of a GNF framework may thus lead to erroneous results when comparing CFD with experimental data.

Some of the established timescales do not provide information on the error magnitude of the GNF formulation directly. Therefore, timescale definitions such as the utilized saturation function timescale τ_{3ITT} are preferred. The timescale definitions used to characterize viscoelastic behavior were all model dependent. For instance, the coefficient λ appearing in the PL (in its timescale formulation) or the Cross material function were used. These, as well as τ_{RS} (the NSD PL-based timescale definition) or the Maxwell-model based τ_{Max}, are all based on model constants. For these timescale definitions, corresponding stress (or viscosity as in the 3ITT) information is required to properly quantify the GNF error for a particular flow case. On the other hand, the timescale definition applied to characterize thixotropy, namely τ_{3ITT}, is based on a model-independent saturation function as the analytical solution to a first-order Ordinary Differential Equation. Because the latter is model-independent, it is much more generic and universal. Moreover, by definition, it contains information on the relative stress magnitude as the timescale is defined as the time it takes to relax to approximately 66 % of the final dynamic equilibrium value.

Direct measurement of NSDs will help to better understand the relevance of NSDs for the fluids studied in this project. NSDs are important when particles settle in such fluids (see section 6.1 and paper [**II**]) and also in entrance and exit flows. Viscoelastic extensions of ANSYS Fluent's GNF realm have been developed in the last years to account for elastic stresses, e.g. implementations of the classical Upper-Convected Maxwell and Oldroyd-B models [274, 275], and may possibly be used for further model development. The effect of shear-thinning is relevant for wellbore flows and may be accounted for by the Yeleswarapu [276] model (as implemented by [277]) or the Finitely Extensive Nonlinear Elastic-Peterlin (FENE-P) model (as implemented by [278] and for which also a k-ϵ turbulence model exists [279]) to handle the phenomena of turbulent drag reduction.

Large Amplitude Oscillatory Shear (LAOS) [280, 281] tests are required to better understand the viscoelastic properties of the PAC solutions. The definitions of the linear viscoelastic moduli G' and G'' are based on sinusoidal stress response, which is not correct for larger deformations [281].

The presence of smaller particles will also have an effect on the rheology of the fluid. While this is not so relevant for e.g. the CFD studies conducted in this PhD project [**IX**, **II**, **V**, **VI**, **XVI**, **VIII**] as well as in the concurrent experiments [4] because the particle diameter was sufficiently large, the very small particle sizes occurring in wellbore flows are known to affect the rheology of the drilling fluid [46, 282].

Even though we have performed our rheometric analysis [**IV**] with drilling fluid model systems rather than real drilling fluids as used in the field, the results are applicable to the modeling of real systems. However, the order of magnitude may be different. In fact, an evaluation of the thixotropic-viscoelastic degree of a particular fluid of interest is required for every sample.

In essence, more rheometric data and a quantitative evaluation are required to further understand the effect and limitations of the GNF approach. Mainly because real drilling fluids exhibit comparable GNF behavior (see figures 4-7 in [**XIII**] for a comparison), partly caused by the very same natural polymers we have used. However, we have only investigated a small part of the design space for the specific example of PAC solutions. More data is necessary to cover the entire design space in terms of amplitude, frequencies, and shear rate steps as well as other fluid systems.

More generally, additional rheometric data is required to capture the effect of temperature on viscosity for the particular fluid used in an experimental campaign in order to allow modeling of field situations, for instance following the CFD modeling approach of Schwalbert [283].

In addition, the practical implications of potential GNF errors need to be investigated. For instance, the conclusion of our paper [**XIV**] is that in some cases the use of a GNF model is not accurate. However, we generally do not know the quantitative effect of a specific GNF error on integral solutions of a particular (wellbore) flow problem. For instance, what is the error on volumetric flow rates or mixture pressure drop when conveying particles? Specific cases have to be studied, both with a simple GNF approach and more complex thixotropic-viscoleastic concepts, and compared with each other to properly asses GNF model error quantitatively.

In hindsight, the approach presented in paper [**XIV**] should have distinguished more clearly between non-particle loaded and particle loaded flows. The analysis conducted on the *annulus scale* implicitly assumed the absence of particles. Clearly, the presence of sufficiently small particles affects the rheometric properties. Larger particles, or more precisely the presence of a bed, will affect the timescale definitions.

Finally, as in the previous section, the effect of turbulence needs to be understood, in particular on the *annulus scale*. Rheometric flows are laminar by definition. Wellbore flows may be turbulent or at least transitional [**XIII**]. Therefore, thixotropic and viscoelastic effects may become less relevant for larger Reynolds numbers, where turbulent eddies and inertial instabilities may prevail.

7.3. The capabilities of the TFM-KTGF-SM approach

The TFM-KTGF-SM approach has hitherto been used in many cuttings transport studies (see section 1.4). Yet the results of papers [**IX**, **V**, **VIII**] indicate that the TFM-KTGF-SM approach (both the implementation in Fluent and the general concept) may not be the optimal choice for cuttings transport modeling.

Most importantly, the *top-bed velocity defect* identified in [**IX**, **V**] needs to be understood and an adequate mitigation of the error needs to be implemented in order to rectify the associated quantitative error on solids transport.

Secondly, the viscosity correction as applied in paper [**II**, **XVI**] needs to be introduced into the TFM. Generally, the viscosity of the first phase is not affected by the second phase. However, the particles exert shear and thereby have an effect on the total shear rate and thus viscosity.

In addition, the TFM was originally developed for solid-gas flows and according to some researchers solid-liquid flows are out of the scope of validity of the model. However, there does not appear to be any relevant literature addressing these concerns.

A known failure of the TFM is its inability to accurately reproduce a jet of solids directed at a wall or two crossing jets. Using the TFM, particles are trapped in wall-adjacent cells or lead to a single jet directed downwards, respectively, as there is just one averaged velocity for the solid phase in a cell [284]. A DEM approach will correctly lead to two crossing streams with some colliding and randomly dispersed particles [284]. The moment quadrature method is known to cure the TFM inabilities [284, 285] but has not yet found its way into Fluent.

Polysized systems may be modeled more straightforwardly with a DPM/DEM concept. While in the Eulerian-Eulerian realm every particle size has to be represented as an additional phase, in an Eulerian-Lagrangian world the solids are tracked individually and may thus simply be described by a specified particle size distribution.

A potential alternative, combining the strengths of both worlds, is the Dense Discrete Phase Model (DDPM) available in Fluent [86, 87]. Here, the first phase is modeled as a continuum and the second phase is treated in a Lagrangian manner with the specialty that particle effects such as collisions are modeled by means of the KTGF. Particle size distributions can be easily accounted for with a conventional DPM/DEM approach, and the DDPM is also capable of correctly solving the crossing jet problem [286].

Regardless of the modeling approach utilized, a scale issue is prevalent in wellbore flows. The size of particles in cuttings transport may be up to several millimeters large [**I**, **X**]. For small particles ($\mathcal{O}\left(d_p\right) < 10^{-4}$ m), an individual particle is much smaller than a typical computational cell and the continuum assumption inherent in the TFM holds. However, for larger particle sizes ($\mathcal{O}\left(d_p\right) > 10^{-4}$ m), the particles size approaches or even exceeds the usual computational grid size. DPM and DEM methods just as well require the particle size to be much smaller than the grid size. In recent versions, Fluent has the option to perform a node-based averaging of DPM source terms such that the solid's effect on the fluid is distributed to neighboring cells. Nevertheless, a critical assessment seems required to further understand the potential errors.

7.4. The state of turbulence modeling

At the time of writing, we have not yet finished our CFD-DNS benchmark activities. However, we may tentatively conclude that if the standard turbulence models available in commercial codes are utilized without further elaboration such as model tuning, no quantitative modeling of wellbore flows appears possible. We offer the following reasons for this:

- The inter-dependencies with non-Newtonian fluid behavior, e.g. shear-thinning and the phenomena of drag reduction due to extensional viscosities, as shown in [**VII**].

- The application of Newtonian wall functions, where the wall proximity is described by wall functions based on a constant viscosity, as mentioned in [**VI**, **XVII**].

- The assumption of an isotropic turbulent stress tensor and the consequently bad modeling of rotational flows, as indicated in [**VII**].

- The transitional flow regime, which is the predominant case for most industrially relevant flows [**XIII**] and is not predicted well by any model investigated [**VII**].

The first can be handled by adopting turbulence models accounting for fluid viscosity being a fluctuating quantity [242, 279, 287]. If based on a viscoelastic fluid description, elastic-inertial effects such as DR may also be handled. Alternatively, DR may be accounted for by simpler models [e.g. 288]. In any case, to further develop fast-computing models, wall functions accounting for a non-constant viscosity [245–247] should be further developed and implemented in in (commercial) codes followed by subsequent validation and model benchmark activities.

Improving modeling of rotational flows (e.g. drill string rotation and whirl) may require more complex models such as RSM or LES. Further activities should include the quantitative benchmarking of two-equation models, RSM, LES, and DNS for the industrially-relevant dimensional design space as given in [**I**]. This should also include the computationally cheap VLES [232, 233] approach to handle large scale turbulence, which may be beneficial to better modeling of turbulence. In addition, it allows for large scale eddies and hence may perturb sediment beds and cause dune formation (see chapter 4). Moreover, VLES seems to handle rotating/swirling flows surprisingly well [233].

Model calibration may be required to fine-tune any approach to the transitional flow regime. Alternatively, transitional turbulence models available in ANSYS Fluent may be employed. These include the k-kl-ω-transition model based on the laminar kinetic energy as an additional scalar quantity to predict boundary layer development and transition [289] or the Intermittency Transition Model, where an additional transport equation for the intermittency is solved [290]. However, while the latter may also handle crossflows it is based on proprietary formulation of the source terms [87]. Furthermore, the aforementioned non-Newtonian inter-dependencies and the effect of flow rotation would also need consideration.

From a pragmatic modeling point of view [**XV**, 291], it is not obvious which of the aforementioned steps is the most relevant one to pursue first because it is not clear to what extent each of the aforementioned model deficiencies affects the overall picture. Quantifying the error is not possible straightforwardly and also depends on what integral quantity is to be considered most important. For instance, capturing near wall effects, i.e., wall functions, seems most important if one aims for a correct pressure estimate and is needed to avoid resolution of the near wall layer.

Finally, note that the above mentioned reasons and the potential approaches presented here already apply to single-phase cases, i.e., either ① or ③ as categorized in figure 1.4 in section 1.4. In the case of multiphase flows of non-Newtonian fluids, i.e., ⑦ in figure 1.4, momentum exchange mechanisms need to be considered adequately, such as the effect of the second phase on the first phase. Hence, for multiphase systems comprising non-Newtonian fluids, a critical review of the Tchen theory of dispersion of discrete particles by homogeneous turbulence [133–135] may be required in addition to the aforementioned steps.

7.5. Implications for three-dimensional wellbore flow modelling

The findings of this project have implications for the wellbore flow problems presented in chapter 6. We here focus on the drill pipe rotation flow problem presented in section 6.2 because it represents an actual wellbore flow, whereas the particle trajectory flow case presented in section 6.1 only represents a subset of the full problem. Moreover, most of the potential particle trajectory flow model issues have been discussed in section 6.2 and section 7.2.

More sophisticated turbulence models may be required. There are missing links between classical RANS turbulence models and rheological models. In addition, as discussed in section 7.4, the SST k-ω model utilized did not perform well in case of the rotational flow problem investigated in manuscript [**VII**]. In the case of the laterally moving drill string problem [**VIII**], we nevertheless used the SST k-ω model because it correctly collapses to a laminar solution in case of low Reynolds numbers and allows for a certain flexibility when it comes to the $y+$ values of the wall-adjacent cells, which due to the mesh deformation are not constant. Therefore, the boundary layer should be excluded from the scope of the dynamic grid adaption. Generally, a VLES or RSM modeling approach as mentioned in section 7.4 may be a better choice.

A DEM approach may provide better results when it comes to quantification of solid transport. The TFM-KTGF-SM approach has been used primarily because the first version of the model was not based on periodic BC and thus the computational domain was considerably larger. However, with periodic BC in place, the number of particles in the system becomes, depending on the particle size, considerably smaller such that DEM may become a viable option.

The parameter range investigated here represents only a small part of the industrially relevant range and needs to be enlarged. More viscous fluids and more laminar regime data needs to be gathered. Other particle sizes, densities and particle loadings need to be investigated as well as intermediate inclinations.

Experimental data is required for validation purposes. We could not find experimental data sets that contained all the required information needed to replicate the respective drill string motion.

Assuming an extensive and comprehensive experimental data set allowing for quantitative model validation is available, several other elements of the model need to be improved prior to future validation attempts:

- As discussed in section 7.3,
  - the local viscosity concept for particles developed in [**II**] needs implementation.
  - the *top-bed velocity defect* identified in [**IX**, **V**] needs rectification.
- Depending on the particular model fluid system used in an experimental campaign as well as the flow regime and the corresponding relevance of viscosity-related or instability-related effects,
  - a more suitable viscosity material function covering the entire shear rate range of interest is to be used, as discussed in section 3.1.
  - a more complex rheological description appears required to account for viscoelastic and thixotropic effects, as discussed in section 7.2.

Regarding the local viscosity concept: This most likely would not have a major effect in a non-moving drill pipe situation at steady-state because typically most of the solid transport takes place as *bed load*, i.e., in a sliding and rolling manner on top of the cuttings bed. However, in case of a laterally moving drill pipe, the periodic agitation and re-suspension leads to a significant part of the solids being transported in a dispersed manner and thus the correct estimate of the surrounding fluid viscosity is of utmost importance.

In contrast, the *top-bed velocity defect* is most likely of minor importance as the solids velocity at the top of a potential sediment bed is more determined by fluid drag caused by the heavy drill pipe motion and the axial flow, rather than relative weight.

Regardless of the physical modeling approach utilized, the dynamic meshing concept needs further attention. The dynamic mesh moving feature of Fluent R17.2 led to severe mesh deformation with flow time. Depending on the orbital frequency, the mesh had to be replaced after several seconds of flow time in order to avoid mesh deformation errors. One workaround in serial computations is to replace the entire mesh after several seconds of flow time and interpolate all fields from the old to the new mesh. However, this has not worked in parallel on our Linux cluster. The dynamic meshing feature of Fluent R17.2 is not meant to be applied in the case of large rotational mesh deformations [86]. A sliding mesh approach as utilized by Bicalho et al. [265, 266] may be a viable alternative.

7.6. Commercial CFD codes vs. Open Source Alternatives

A simple answer to the question "What CFD code should be used for this problem?" is often not straightforward and depends on many parameters. For several reasons, the commercial code Fluent has been used in this research project. However, all codes both define and limit the modeling approaches for a particular problem. Hence, for future prospects, a reassessment of available codes and their capabilities is recommended.

While many commercial codes are pretty comprehensive in terms of their capabilities, outside the commercial realm a variety of dedicated codes exist, either open-source or in-house. For instance, Semtex is a dedicated DNS code for turbulent flows based on spectral elements [292], which has been used by SINTEF to investigate turbulent flows (see manuscript [**VII**]). MFIX is a dedicated multiphase flow code and offers many of the physical models available in Fluent [124, 293].

Fluent is a stable and reliable code that allows for ease of use and features a broad variety of model implementations from the fields ①, ②, and ④ in figure 1.4. However, interdependent phenomena, i.e., ③ as well as ⑤–⑦, are not well represented. The UDS, UDF, and dynamic mesh capabilities have been successfully used to some extent in this project and in principle allow for further implementation of more complex models, for instance the aforementioned viscoelastic constitutive equations. However, we have also encountered many obstacles, e.g. the velocity effect [**IX**, V] discussed in chapter 4 or the mesh degradation issue described in the previous section. Moreover, due to the proprietary nature, relevant information is not fully disclosed in the manuals [86, 87], for example the exact implementation of pressure-velocity coupling in multiphase flows is implemented. In addition, some of the definitions and equations in the documentation are incorrect, or inconsistent or simply not provided. For example, the Malin [249] modification of the Lam-Bremhorst [248] turbulence model is available in the text user interface, but no information is provided in the manuals. If customized via UDF programming, the frictional pressure needs to be returned to the solver directly, while the frictional viscosity needs to be returned divided by the solid volume fraction. Several available computational routines are not disclosed in the UDF manual, e.g. macros for the wall shear stress or the different frictional pressure models.

Documentation of Fluent is extensive and, despite the issues mentioned above, comparatively good. However, debugging and implementing new features becomes complicated because the actual code is proprietary and hence undisclosed.

Besides the aforementioned MFIX code, other potential alternatives include OpenFOAM, which has seen many contributions in the area of DEM multiphase models recently [e.g. 294, 295], or the SIMCOFLOW [296–298] framework for complex 3D multiphase and multi physics flows.

However, a critical review is necessary in terms of code features and extension capabilities. Any potential alternative should be evaluated based on relevant requirements, for instance, the dynamic meshing feature of Fluent is, despite the mesh degradation issues, a perfectly-suited tool to simulate orbital drill string motion. Any code substitute needs to either feature similar means of mesh deformation or allow for implementation of these.

Obtaining a PhD is about figuring out what you don't know.

Unknown

8

Conclusions and Outlook

8.1. Conclusions

We investigated the cuttings transport process in its entirety and specific aspects such as the role of drill pipe rotation and eccentricity. Our major contributions are presented in chapter 2 to chapter 6 and can be summarized as follows:

- Prior to any experimental or numerical campaign, an unequivocal definition of the process to be investigated along with its inputs and outputs is required. We provide such an analysis for drilling on the NCS, along with relevant numerical value ranges for each input parameter. We emphasize the need for completeness by the example of drill pipe rotation. For a field scenario as well as many experimental setups, drill pipe rotation has to be broken down into the plain rotational rate and other parameters describing any existing lateral drill pipe motion.

- By means of Dimensional Analysis, we established a scaling concept for the cuttings transport process accounting for shear-thinning fluid and yield behavior based on a set of dimensionless numbers (Π-space). Using a polynomial fit function on the established Π-space and accompanying comprehensive experimental data, a steady-state cuttings transport model may be built by means of RSA/DoE regression methods.

- For the lab fluids used in our research project, we showed that these do feature viscoelastic and thixotropic properties and that the GNF constitutive equation typically used in cuttings transport studies does not hold under all circumstances. A critical assessment based on fluid and process timescales is required for a particular experimental or numerical setup in order to justify a GNF approach.

- We evaluated the TFM-KTGF-SM approach often used in cuttings transport CFD studies by means of the cliff collapse problem and showed that, while generally and qualitatively providing physically sound results, the model was unable to describe the top interface of a sediment bed correctly. This may result in an error when it comes to quantitative solid transport investigations.

- We investigated an alternative modeling approach used in research of environmental flows, where the dense sediment bed is dynamically excluded from the computational domain and the evolution of the sediment bed is tracked via the Exner equation. While this may be a potential alternative, we found that major model tuning is required to quantitatively predict solids transport. Furthermore, the efforts required to extend the approach to 3D and account for possible contact problems (e.g. collision of the sediment bed and the drill pipe) were out of the scope of this PhD project.

- Wellbore flows may become transitional based on a simple Reynolds number estimate. Considering geometrical obstructions such as drill collars as well as laterally moving and rotation drill strings and a cuttings bed, wellbore flows should be considered intermittent if not transitional. In a second step, we investigated the performance of several commercially available turbulence models and compared these with DNS results. While this work is ongoing, a preliminary conclusion is that none of the turbulence models typically employed in cuttings transport studies was able to describe the entire range of relevant Reynolds numbers and at the same time provide quantitatively correct results for PL and Cross fluids.

- We numerically replicated a UiS experimental campaign, namely the settling of an individual particle in a channel flow of a non-Newtonian (shear-thinning and mildly viscoelastic/thixotropic) fluid. Our results showed that the current state of the art of Lagrangian particle tracking by means of a Discrete Phase Model cannot predict the exact particle trajectories found in the experiments. Even though we have improved the numerical evaluation of the viscosity as seen by the particle by accounting for the particle-induced shear, the numerical and analytical solution is an S-shaped trajectory, while the experimental trajectories feature a J-shape.

- By means of dynamic meshing, we accounted for the lateral motion of drill pipes. Specifically, we investigated the influence of whirling motion on cuttings transport and showed that whirling motion significantly changes the picture as it contributes tremendously to hole cleaning. Thus, it is essential to strictly distinguish between plain drill pipe rotation and the additional effect of whirling motion in case the drill string may move freely in the well or test section of a flow loop.

8.2. Future outlook

Cuttings transport modeling has been a major research field for several decades, yet many aspects remain unclear. At the same time, new research as well as technological and procedural advancements have increased the number of research questions to be investigated. The very same holds for this PhD project. Therefore, we provide a brief overview of potential future research prospects:

- The developed scaling concept requires further elaboration with respect to:
  - Treatment of the viscosity as it is predominantly based on the PL. YPL and YP/PV models can be inferred via the MR local PL assumption. However, the equations become cumbersome and a more holistic approach may be required.
  - Consideration of further relevant process parameters. The obtained Π-space should be adequately extended to cover additional effects such as thixotropy, viscoelasticity, particle size distributions and non-spherical shapes, temperature, and drill pipe lateral motion.
  - The correct basis for scaling the viscosity. Currently, because of the MR method employed, the scaling concept is based on *a priori*

known quantities such as bulk velocity and geometry. However, the wall shear stress and the wall viscosity are directly linked to the pressure gradient $\Delta p/\Delta x$ rather than the bulk velocity of the fluid phase or the mixture. Further work is required to formulate a $\Delta p/\Delta x$-based formulation of the established Π-space.

- More comprehensive rheometric data is required to adequately assess the limitations of a GNF modeling approach. In addition, a holistic benchmark of drilling fluid model systems and actual drilling fluids is required to understand the error introduced by simplifying drilling fluid systems with polymeric solutions.

- To yield models with better quantitative performance, more sophisticated models and closures should be developed on several levels:
  - Turbulence models could be improved regarding their interactions with the rheological models applied, their ability to handle swirling/rotational cases, and their stability throughout the entire industrially-relevant Reynolds number range.
  - Computationally simple rheological models should be implemented into CFD solvers accounting for more complex rheological effects such as viscoelasticity, NSDs, and drag reduction as well as thixotropy.
  - Drag laws as well as models for other particle forces may be improved by accounting for a non-constant fluid viscosity as well as particle clusters.
  - All of the above need calibration and tuning on simplified yet physically-related subproblems such as the cliff collapse problem or even simpler particle settling experiments.

- The particle trajectory flow problem needs further concurrent modeling and experimental work to overcome the trajectory discrepancy in the lower wall region. In addition, turbulent flows and settling of more than one particle should be investigated to extend the current model to cover these effects.

- Further research is required concerning lateral drill string motion, both with numerical and concurrent experimental efforts:

- A better-suited turbulence model, validated with single-phase and simpler multiphase flows, should be identified and implemented.
- The correct description of viscosity accounting for the particle-induced shear should be implemented into the model.
- The multiphase approach should be critically reassessed. Benchmarking with a DEM and a DPDM approach is recommended. If the TFM-KTGF-SM approach remains a viable option, the reason for the *top-bed velocity defect* is to be identified or, at a minimum, quantified.
- The industrially-relevant parameter space should be explored more comprehensively. The effect of more viscous fluids and more laminar flows, other particle properties and loadings, as well as inclinations, have to be investigated.
- The current model needs to be improved in terms of the dynamic meshing concept utilized. Sliding meshes or other mesh deformation alternatives may be considered and special attention is required for parallelization.

On a final note, we emphasize that future research projects should be based on tightly coupled experimental-numerical simultaneous activities in order to optimize outcome and impact. For validation and further development of numerical models, high-quality experimental data is required. Moreover, the BC in experiments should correspond to the BC of numerical models. In addition, locations and specifications of sensors in the experiments must be precisely aligned with the numerical model setup.

Bibliography

[1] Sigbjørn Nygård. *Consortium Agreement between IRIS, SINTEF, UiS, NTNU and Industry Participants Regarding the Project AdWell – "Advanced Wellbore Transport Modelling"*. Stavanger: International Research Institute of Stavanger AS, Sept. 16, 2013.

[2] The Research Council of Norway. *Oil and Gas for the 21st Century - OG21*. Strategy Document. Oslo: The Research Council of Norway, 2010. URL: www.og21.no.

[3] Ernst A. Meese. *Advanced Wellbore Transport Modelling - Project Description for Knowledge-Building Project for Industry*. 2013.

[4] Milad Khatibi. "Investigation on Cuttings Transportation in Non-Newtonian Turbulent Well Flow". PhD thesis. Stavanger: University of Stavanger, 2017. URL: https://www.researchgate.net/publication/323812976_Investigation_on_Cuttings_Transportation_in_non-Newtonian_Turbulent_Well_Flow_Advanced_Wellbore_Transport_Modeling.

[5] Liv A. Carlsen, Fionn Iversen, Steinar Kragset, Jafar Mahmoudi, Johnny Petersen, Hardy Siahaan, and Tore Flåtten. *Guidelines and Concepts for Real-Time Models*. Project report. Bergen: AdWell project, Jan. 13, 2016. URL: http://www.ad-well.no/research-/guidelines.

[6] Ernst A. Meese and Are Simonsen. *AdWell Milestone E2 - Guidelines and Concepts for CFD Modelling*. Project report. Trondheim: AdWell project, Mar. 23, 2015. URL: http://www.ad-well.no/research-/guidelines.

[7] W. Gibbs. *North Sea Saga: The Oil Age in Norway*. Horn Forlag AS, 2007. URL: https://books.google.de/books?id=iR52twAACAAJ.

[8] Ministry of Petroleum and Energy and the Norwegian Petroleum Directorate. *The Government's Revenues*. 2019. URL: https://www.norskpetroleum.no/en/economy/governments-revenues/ (visited on 03/17/2019).

[9] NENT. *Guidelines for Research Ethics in Science and Technology*. The National Committee for Research Ethics in Science and Technology (NENT), 2008. URL: https://www.etikkom.no/globalassets/documents/english-publications/guidelines-for-research-ethics-in-science-and-technology-2008.pdf (visited on 03/10/2019).

[10] NENT. *Regarding the Assessment of Research Ethics in Petroleum Research*. The National Committee for Research Ethics in Science and Technology (NENT), 2014. URL: http://www.etikkom.no/en/news/news-archive/2015/nents-assessment-of-research-ethics-in-petroleum-research/regarding-the-assessment-of-research-ethics-in-petroleum-research/ (visited on 03/10/2019).

[11] Norges forskningsråd. *Årsrapport 2017*. Lysaker: Norges forskningsråd, 2018. URL: www.forskningsradet.no/publikasjoner.

[12] Matthew Taylor. "Can Norway Help Us Solve the Plastic Crisis, One Bottle at a Time?" In: *The Guardian. Environment* (July 12, 2018). URL: https://www.theguardian.com/environment/2018/jul/12/can-norway-help-us-solve-the-plastic-crisis-one-bottle-at-a-time (visited on 03/17/2019).

[13] Camilla Knudsen and Alister Doyle. "Norway's Electric Cars Zip to New Record: Almost a Third of All Sales". In: *Reuters* (Jan. 2, 2019). URL: https://www.reuters.com/article/us-norway-autos-idUSKCN1OW0YP (visited on 03/10/2019).

[14] Norsk elbilforening. *Nordic EV Barometer 2018*. 2019. URL: https://elbil.no/elbilstatistikk/nordic-ev-barometer/ (visited on 03/10/2019).

[15] Ministry of Petroleum and Energy. *Electricity Production*. 2019. URL: https://energifaktanorge.no/en/norsk-energiforsyning/kraftproduksjon/ (visited on 03/10/2019).

[16] Ministry of Petroleum and Energy. *Norway's Oil History in 5 Minutes*. Oct. 9, 2013. URL: https://www.regjeringen.no/en/topics/energy/oil-and-gas/norways-oil-history-in-5-minutes/id440538/ (visited on 03/10/2019).

[17] Indra Overland. “Norway: Public Debate and the Management of Petroleum Resources and Revenues”. In: *Public Brainpower*. Ed. by Indra Overland. Cham: Springer International Publishing, 2018, pp. 217–245. DOI: 10.1007/978-3-319-60627-9_13.

[18] Joachim Dagenborg. “Norway’s Lofoten Region to Remain off-Limits to Oil Firms: Government”. In: *Reuters* (Jan. 14, 2018). URL: https://www.reuters.com/article/us-norway-government-oil-idUSKBN1F30QT (visited on 05/30/2019).

[19] Harry Cockburn. “Norway Refuses to Drill for Billions of Barrels of Oil in Arctic, Leaving ‘Whole Industry Surprised and Disappointed’”. In: *The Independent* (Apr. 9, 2019). URL: https://www.independent.co.uk/environment/norway-oil-drilling-arctic-ban-labor-party-unions-a8861171.html (visited on 05/30/2019).

[20] Government Pension Fund Global. *Annual Report*. Oslo: Government Pension Fund Global, 2019. URL: https://www.nbim.no/contentassets/02bfbbef416f4014b043e74b8405fa97/annual-report-2018-government-pension-fund-global.pdf (visited on 03/10/2019).

[21] Etikkradet. *Guidelines for Observation and Exclusion of Companies from the Government Pension Fund Global*. Oslo: Council on Ethics for the Government Pension Fund Global, 2017. URL: www.etikkradet.no.

[22] Government Pension Fund Global. *Responsible Investment*. Oslo: Norges Bank Investment Management, 2019. URL: https://www.nbim.no/contentassets/e1632963319146bbb040024114ca65af/responsible-investment_2018.pdf (visited on 03/10/2019).

[23] Rob Davies. “Norway’s $1tn Wealth Fund to Divest from Oil and Gas Exploration”. In: *The Guardian. World news* (Mar. 8, 2019). URL: https://www.theguardian.com/world/2019/mar/08/norways-1tn-wealth-fund-to-divest-from-oil-and-gas-exploration (visited on 05/30/2019).

[24] A. B. Metzner and J. C. Reed. “Flow of Non-Newtonian Fluids-Correlation of the Laminar, Transition, and Turbulent-Flow Regions”. In: *AIChE Journal* 1.4 (Dec. 1955), pp. 434–440. DOI: 10.1002/aic.690010409.

[25] Wolfgang Ostwald. "Über Die Geschwindigkeitsfunktion Der Viskosität Disperser Systeme". In: *Colloid & Polymer Science* 36.2 (1925), pp. 99–117. URL: http://www.springerlink.com/index/KV8036R785W57318.pdf (visited on 06/13/2016).

[26] Wolfgang Ostwald. "Über Die Rechnerische Darstellung Des Strukturgebietes Der Viskosität". In: *Colloid & Polymer Science* 47.2 (1929), pp. 176–187. URL: http://www.springerlink.com/index/wm40406803q35n69.pdf (visited on 06/13/2016).

[27] Armand De Waele. "Viscometry and Plastometry". In: *Oil Color Chem Assoc J* 6 (1923), pp. 33–88.

[28] Winslow H. Herschel and Ronald Bulkley. "Konsistenzmessungen von Gummi-Benzollösungen". In: *Kolloid-Zeitschrift* 39.4 (1926), pp 291–300. DOI: 10.1007/BF01432034.

[29] Pierre Jean Carreau. "Rheological Equations from Molecular Network Theories". PhD thesis. Madison: University of Wisconsin, 1968. URL: https://search.library.wisc.edu/catalog/999638316602121.

[30] Malcolm M. Cross. "Rheology of Non-Newtonian Fluids: A New Flow Equation for Pseudoplastic Systems". In: *Journal of Colloid Science* 20.5 (1965), pp. 417–437. DOI: 10.1016/0095-8522(65)90022-X.

[31] Tianshou Ma, Ping Chen, and Jian Zhao. "Overview on Vertical and Directional Drilling Technologies for the Exploration and Exploitation of Deep Petroleum Resources". In: *Geomechanics and Geophysics for Geo-Energy and Geo-Resources* 2.4 (Dec. 2016), pp. 365–395. DOI: 10.1007/s40948-016-0038-y.

[32] Arild Saasen. "Annular Frictional Pressure Losses During Drilling - Predicting the Effect of Drillstring Rotation". In: *Journal of Energy Resources Technology* 136.3 (Mar. 4, 2014), p. 034501. DOI: 10.1115/1.4026205.

[33] Ramadan Mohammed Ahmed, Majed Sadeg Enfis, Hamza Miftah El Kheir, Morten Laget, and Arild Saasen. "The Effect of Drillstring Rotation on Equivalent Circulation Density: Modeling and Analysis of Field Measurements". In: *SPE Annual Technical Conference and Exhibition*. SPE Annual Technical Conference and Exhibition. Florence, Italy: Society of Petroleum Engineers, 2010. DOI: 10.2118/135587-MS.

[34] Wensheng Xiao, Yang Zhang, and Yifang Zhong. “Annulus Whirling Motion Analysis of the Rotary Drill String by the Action of Hydrodynamic Pressure and Friction Force”. In: *Volume 5: 19th Biennial Conference on Mechanical Vibration and Noise, Parts A, B, and C*. ASME 2003 International Design Engineering Technical Conferences and Computers and Information in Engineering Conference. Vol. 2003. Chicago, Illinois, USA: ASME, 2003, pp. 1003–1010. DOI: 10.1115/DETC2003/VIB-48423.

[35] Oney Erge, Mehmet E. Ozbayoglu, Stefan Z. Miska, Mengjiao Yu, Nicholas Takach, Arild Saasen, and Roland May. “Effect of Drillstring Deflection and Rotary Speed on Annular Frictional Pressure Losses”. In: *Journal of Energy Resources Technology* 136.4 (Dec. 1, 2014), p. 042909. DOI: 10.1115/1.4027565.

[36] Oney Erge, Evren Mehmet Ozbayoglu, Stefan Miska, Mengjiao Yu, Nicholas Takach, Arild Saasen, and Roland May. “The Effects of Drillstring-Eccentricity, -Rotation, and -Buckling Configurations on Annular Frictional Pressure Losses While Circulating Yield-Power-Law Fluids”. In: *SPE Drilling & Completion* 30.03 (Sept. 1, 2015), pp. 257–271. DOI: 10.2118/167950-PA.

[37] Rong-Juin Shyu. “Bending Vibration of Rotating Drill Strings”. PhD thesis. Massachusetts Institute of Technology (MIT), 1989. URL: https://dspace.mit.edu/bitstream/handle/1721.1/14205/22248770-MIT.pdf?sequence=2.

[38] R. I. Leine, D. H. van Campen, and W. J. G. Keultjes. “Stick-Slip Whirl Interaction in Drillstring Dynamics”. In: *Journal of Vibration and Acoustics* 124.2 (2002), p. 209. DOI: 10.1115/1.1452745.

[39] Guohua Gao. “Dynamic Buckling and Snaking Motion of Rotating Drilling Pipe in a Horizontal Well”. In: *SPE Journal* (2010), p. 11.

[40] R. Alfredo Sanchez, J.J. Azar, A.A. Bassal, and A.L. Martins. “Effect of Drillpipe Rotation on Hole Cleaning During Directional-Well Drilling”. In: *SPE Journal* 4.2 (June 1, 1999). DOI: 10.2118/56406-PA.

[41] E. Cayeux, H. J. Skadsem, L. A. Carlsen, L. M. Stokland, and S. Cruikshank. “Analysis of Asymmetric Tool-Joint Wear While Drilling Long Horizontal Sections”. In: *SPE Norway One Day*

Seminar. SPE Norway One Day Seminar. Bergen, Norway: Society of Petroleum Engineers, 2018. DOI: 10.2118/191339-MS.

[42] Ryen Caenn and George V Chillingar. "Drilling Fluids: State of the Art". In: *Journal of Petroleum Science and Engineering* (1996). DOI: 10.1016/0920-4105(95)00051-8.

[43] F.P. Iversen, E. Cayeux, E. W. Dvergsnes, J.E. Gravdal, E. H. Vefring, B. Mykletun, A. Torsvoll, S. Omdal, and A. Merlo. "Monitoring and Control of Drilling Utilizing Continuously Updated Process Models". In: *SPE-99207-MS*. SPE: Society of Petroleum Engineers, Jan. 1, 2006. DOI: 10.2118/99207-MS.

[44] Ryen Caenn, H. C. H. Darley, and George R. Gray. *Composition and Properties of Drilling and Completion Fluids*. 6th ed. Waltham: Gulf Professional Publishing, 2011. URL: https://www.elsevier.com/books/composition-and-properties-of-drilling-and-completion-fluids/caenn/978-0-12-383858-2.

[45] Arild Saasen, Bjørn Dahl, and Kjell Jødestøl. "Particle Size Distribution of Top-Hole Drill Cuttings from Norwegian Sea Area Offshore Wells". In: *Particulate Science and Technology* 31.1 (Jan. 2013), pp. 85–91. DOI: 10.1080/02726351.2011.648824.

[46] Fionn Petter Iversen and Aminul Islam. *Hole Cleaning / Cuttings Transport Workshop Meeting Summary*. Stavanger: Equinor, Sept. 18, 2018.

[47] James M. Peden and Yuejin Luo. "Settling Velocity of Variously Shaped Particles. in Drilling and Fracturing Fluids". In: *SPE Drilling Engineering* 2.04 (1987). DOI: 10.2118/16243-PA.

[48] Ajaz Rashid and Zeiad A Razzaq Aswad. "The Combined Effect of Irregular Shape Particles and Fluid Rheology on Settling Velocity Measurement". In: 10th International Conference on Heat Transfer, Fluid Mechanics and Thermodynamics (HEFAT2014). Orlando, FL, June 14, 2014. URL: https://repository.up.ac.za/bitstream/handle/2263/44660/Aswad_Combined_2014.pdf.

[49] Siamak Akhshik, Mehdi Behzad, and Majid Rajabi. "On the Particle–Particle Contact Effects on the Hole Cleaning Process via a CFD–DEM Model". In: *Particulate Science and Technology* 34.6 (Nov. 2016), pp. 736–743. DOI: 10.1080/02726351.2015.1116475.

[50] Siamak Akhshik, Mehdi Behzad, and Majid Rajabi. "CFD-DEM Simulation of the Hole Cleaning Process in a Deviated Well Drilling: The Effects of Particle Shape". In: *Particuology* 25 (Apr. 2016), pp. 72–82. DOI: 10.1016/j.partic.2015.02.008.

[51] Velaug Myrseth Oltedal, Benjamin Werner, Bjørnar Lund, Arild Saasen, and Jan David Ytrehus. "Rheological Properties of Oil Based Drilling Fluids and Base Oils". In: *Proceedings of the ASME 2015 34th International Conference on Ocean, Offshore and Arctic Engineering OMAE2015*. ASME 2015 34th International Conference on Ocean, Offshore and Arctic Engineering. St. John's, Newfoundland: American Society of Mechanical Engineers, 2015. URL: https://www.researchgate.net/profile/Velaug_Myrseth/publication/301418917_Rheological_Properties_of_Oil_Based_Drilling_Fluids_and_Base_Oils/links/58d99cdea6fdccca1c4c0064/Rheological-Properties-of-Oil-Based-Drilling-Fluids-and-Base-Oils.pdf.

[52] Ahmadi Tehrani. "Thixotropy in Water-Based Drilling Fluids". In: *Annual Transactions of the Nordic Rheology Society* 16 (2008). URL: http://nordicrheologysociety.org/Content/Transactions/2008/Posters/Tehrani.pdf.

[53] Paulo R. de Souza Mendes and Roney L. Thompson. "A Critical Overview of Elasto-Viscoplastic Thixotropic Modeling". In: *Journal of Non-Newtonian Fluid Mechanics* 187-188 (Nov. 2012), pp. 8–15. DOI: 10.1016/j.jnnfm.2012.08.006.

[54] Peter H. Tomren. "The Transport of Drilled Cuttings in an Inclined Eccentric Annulus". Master thesis. Tulsa, OK: University of Tulsa, 1979. URL: http://library.utulsa.edu//record=b1539944.

[55] A. W. Iyoho. "Drilled-Cuttings Transport by Non-Newtonian Drilling Fluids through Inclined, Eccentric Annuli". PhD. Tulsa, OK: University of Tulsa, 1980. URL: http://library.utulsa.edu//record=b1054710.

[56] Gary W. Massie, . Castle-Smith, J.W. Lee, and M.S. Ramsey. "Amocos Training Initiative Reduces Wellsite Drilling Problems". In: *Petroleum Engineer International* 67.3 (1995). URL: https://www.osti.gov/biblio/39900.

[57] C. J. Hopkins and R. A. Leicksenring. “Reducing the Risk of Stuck Pipe in the Netherlands”. In: SPE/IADC Drilling Conference. Amsterdam: Society of Petroleum Engineers, Feb. 28, 1995. DOI: 10.2118/29422-MS.

[58] Titus Ntow Ofei, S. Irawan, and W. Pao. “Drilling Parameter Effects on Cuttings Transport in Horizontal Wellbores: A Review”. In: *ICIPEG 2014*. Ed. by Mariyamni Awang, Berihun Mamo Negash, Nur Asyraf Md Akhir, and Luluan Almanna Lubis. Singapore: Springer Singapore, 2015, pp. 199–207. DOI: 10.1007/978-981-287-368-2_18.

[59] Tahmineh Nazari, Geir Hareland, and Jamal Joseph Azar. “Review of Cuttings Transport in Directional Well Drilling: Systematic Approach”. In: SPE Western Regional Meeting. Anaheim, CA: Society of Petroleum Engineers, May 27, 2010. DOI: 10.2118/132372-MS.

[60] Rishi B. Adari, Stefan Miska, Ergun Kuru, Peter Bern, and Arild Saasen. “Selecting Drilling Fluid Properties and Flow Rates for Effective Hole Cleaning in High-Angle and Horizontal Wells”. In: *SPE Annual Technical Conference and Exhibition*. SPE Annual Technical Conference and Exhibition. Dallas: Society of Petroleum Engineers, Oct. 1, 2000. DOI: /10.2118/63050-MS.

[61] Robert F. Mitchell and Stefan Z. Miska. *Fundamentals of Drilling Engineering*. Vol. 12. SPE Textbook Series. Richardson, TX: Society of Petroleum Engineers, 2011. URL: https://store.spe.org/Fundamentals-of-Drilling-Engineering-P468.aspx.

[62] James P. Brill and Hemant Kumar Mukherjee. *Multiphase Flow in Wells*. Vol. 17. Society of Petroleum Engineers, 1999. URL: https://store.spe.org/Multiphase-Flow-in-Wells-P39.aspx.

[63] A.T. Bourgoyne, K.K. Millheim, M.E. Chevenert, and F.S. Young Jr. *Applied Drilling Engineering*. 2nd ed. Vol. 2. SPE Textbook Series. Richardson, TX: Society of Petroleum Engineers, 1991. URL: https://store.spe.org/Applied-Drilling-Engineering-P10.aspx.

[64] Yuejin Luo. “Non-Newtonian Annular Flow and Cuttings Transport through Drilling Annuli at Various Angles”. PhD thesis. Edinburgh: Heriot-Watt University, 1988. URL: http://www.ros.hw.ac.uk/handle/10399/1477.

[65] Alain A. Gavignet and Ian J. Sobey. “Model Aids Cuttings Transport Prediction”. In: *Journal of Petroleum Technology* 41.09 (1989), pp. 916–921. DOI: 10.2118/15417-PA.

[66] A. W. Iyoho and H. Takahashi. *Modeling Unstable Cuttings Transport in Horizontal, Eccentric Wellbores*. 1993. URL: https://www.onepetro.org/general/SPE-27416-MS.

[67] D. A. Drew. “Mathematical Modeling of Two-Phase Flow”. In: *Annual Review of Fluid Mechanics* 15.1 (1983), pp. 261–291. DOI: 10.1146/annurev.fl.15.010183.001401.

[68] Fred Florence and Fionn Petter Iversen. “Real-Time Models for Drilling Process Automation: Equations and Applications”. In: IADC/SPE Drilling Conference and Exhibition. New Orleans, LA: Society of Petroleum Engineers, Jan. 1, 2010. DOI: 10.2118/128958-MS.

[69] Yuejin Luo, P. A. Bern, and B. D. Chambers. “Flow-Rate Predictions for Cleaning Deviated Wells”. In: SPE/IADC Drilling Conference. New Orleans, LA: Society of Petroleum Engineers, Feb. 18, 1992. DOI: 10.2118/23884-MS.

[70] R. K. Clark and K. L. Bickham. “A Mechanistic Model for Cuttings Transport”. In: SPE Annual Technical Conference and Exhibition. New Orleans, LA: Society of Petroleum Engineers, 1994. DOI: 10.2118/28306-MS.

[71] Shigemi Naganawa and Tsuyoshi Nomura. “Simulating Transient Behavior of Cuttings Transport over Whole Trajectory of Extended Reach Well”. In: IADC/SPE Asia Pacific Drilling Technology Conference and Exhibition. Bangkok: Society of Petroleum Engineers, Nov. 13, 2006. DOI: 10.2118/103923-MS.

[72] F. Zhang, A. Filippov, X. Jia, J. Lu, V. Khoriakov, et al. “Transient Solid-Liquid Two-Phase Flow Modelling and Its Application in Real-Time Drilling Simulations”. In: Banff: BHR Group, June 8, 2016. URL: https://www.onepetro.org/conference-paper/BHR-2016-017.

[73] Yu Guo and Jennifer Sinclair Curtis. “Discrete Element Method Simulations for Complex Granular Flows”. In: *Annual Review of Fluid Mechanics* 47.1 (Jan. 3, 2015), pp. 21–46. DOI: 10.1146/annurev-fluid-010814-014644.

[74] Shankar Subramaniam. “Lagrangian–Eulerian Methods for Multiphase Flows”. In: *Progress in Energy and Combustion Science* 39.2-3 (Apr. 2013), pp. 215–245. DOI: 10.1016/j.pecs.2012.10.003.

[75] L. M. Portela and R. V. A. Oliemans. “Possibilities and Limitations of Computer Simulations of Industrial Turbulent Dispersed Multiphase Flows”. In: *Flow, Turbulence and Combustion* 77.1-4 (Oct. 12, 2006), pp. 381–403. DOI: 10.1007/s10494-006-9051-5.

[76] S. Balachandar and John K. Eaton. “Turbulent Dispersed Multiphase Flow”. In: *Annual Review of Fluid Mechanics* 42.1 (Jan. 2010), pp. 111–133. DOI: 10.1146/annurev.fluid.010908.165243.

[77] A. N. Kolmogorov. “A Refinement of Previous Hypotheses Concerning the Local Structure of Turbulence in a Viscous Incompressible Fluid at High Reynolds Number”. In: *Journal of Fluid Mechanics* 13.01 (May 1962), p. 82. DOI: 10.1017/S0022112062000518.

[78] C. T. Crowe, T. R. Troutt, and J. N. Chung. “Numerical Models for Two-Phase Turbulent Flows”. In: *Annual Review of Fluid Mechanics* 28.1 (1996), pp. 11–43. DOI: 10.1146/annurev.fl.28.010196.000303.

[79] Donald A. Drew and Stephen L. Passman. *Theory of Multicomponent Fluids*. New York: Springer, 1999. URL: https://link.springer.com/book/10.1007%2Fb97678.

[80] Andrea Prosperetti and Gretar Tryggvason. *Computational Methods for Multiphase Flow*. Leiden: Cambridge University Press, 2007. URL: https://doi.org/10.1017/CBO9780511607486.

[81] C. T. Crowe, J. D. Schwarzkopf, M. Sommerfeld, and Y. Tsuji. *Multiphase Flows with Droplets and Particles*. Boca Raton: CRC Press Taylor & Francis Group, 2012. URL: https://doi.org/10.1201/b11103.

[82] Harald Laux. “Modeling of Dilute and Dense Dispersed Fluid-Particle Two-Phase Flow”. PhD dissertation. Trondheim: Norwegian University of Science and Technology, Norway, 1998.

[83] A. Prosperetti and A.V. Jones. “Pressure Forces in Disperse Two-Phase Flow”. In: *International Journal of Multiphase Flow* 10.4 (Aug. 1984), pp. 425–440. DOI: 10.1016/0301-9322(84)90054-5.

[84] Fridtjov Irgens. *Rheology and Non-Newtonian Fluids*. Cham: Springer International Publishing, 2014. URL: https://doi.org/10.1007/978-3-319-01053-3.

[85] Frank M. White. *Fluid Mechanics*. 4th ed. Mcgraw-Hill Series in Mechanical Engineering. New York, NY: McGraw-Hill, 1999. 862 pp. URL: http://hdl.handle.net/123456789/10466.

[86] ANSYS, Inc. *ANSYS Fluent User Guide R17.2*. Canonsburg, PA: ANSYS, Inc., 2016.

[87] ANSYS, Inc. *ANSYS Fluent Theory Guide R17.2*. Canonsburg, PA: ANSYS, Inc., 2016.

[88] Osborne Reynolds. "On the Dynamical Theory of Incompressible Viscous Fluids and the Determination of the Criterion". In: *Philosophical Transactions of the Royal Society of London* 186 (1895), pp. 123–164. URL: https://www.jstor.org/stable/90643.

[89] J. Boussinesque. "Essai Sur La Theories Des Eaux Courantes". In: *Memoires presentes par divers savants a l'Academie des Sciences de l'Institut de France* XXIII.2 (1877). URL: https://www.irphe.fr/~clanet/otherpaperfile/articles/Boussinesq/N0003328_PDF_1_770.pdf.

[90] P. G. T. Saffman. "The Lift on a Small Sphere in a Slow Shear Flow". In: *Journal of fluid mechanics* 22.02 (1965), pp. 385–400. DOI: 10.1017/S0022112065000824.

[91] P. G. T. Saffman. "Corrigendum to "The Lift on a Small Sphere in a Slow Shear Flow"". In: *Journal of fluid mechanics* 31 (1968), p. 624. DOI: 10.1017/S0022112068999990.

[92] G. Magnus. "Über die Abweichung der Geschosse, und: Über eine auffallende Erscheinung bei rotierenden Körpern". In: *Annalen der Physik und Chemie* 164.1 (1853), pp. 1–29. DOI: 10.1002/andp.18531640102.

[93] S. I. Rubinow and Joseph B. Keller. "The Transverse Force on a Spinning Sphere Moving in a Viscous Fluid". In: *Journal of Fluid Mechanics* 11.03 (1961), pp. 447–459. DOI: 10.1017/S0022112061000640.

[94] Ahmed Ramadan. "Solids Bed Removal in Deviated Boreholes". PhD. Trondheim: University of Science and Technology (NTNU), 2001.

[95] L. Schiller and A. Naumann. "Über Die Grundlegenden Berechnungen Bei Der Schwerkraftaufbereitung". In: *Zeitschrift des Vereins Deutscher Ingenieure* 77.12 (1933), pp. 318–320.

[96] Dimitri Gidaspow, R. Bezburuah, and J. Ding. "Hydrodynamics of Circulating Fluidized Beds: Kinetic Theory Approach". In: *Fluidization VII, Proceedings of the 7th Engineering Foundation Conference on Fluidization*. 7th International Conference on Fluidization. Gold Coast, May 3, 1992. URL: https://www.osti.gov/servlets/purl/5896246.

[97] C. Y. Wen and Y. H. Yu. "Mechanics of Fluidization". In: Chem. Eng. Prog., Symp. Ser. Vol. 62. 1966, pp. 100–111.

[98] Sabri Ergun. "Fluid Flow through Packed Columns". In: *Chem. Eng. Prog.* 48 (1952), pp. 89–94.

[99] API RP 13D. *Rheology and Hydraulics of Oil-Well Drilling Fluids*. Washington, D. C.: American Petroleum Institute (API), 2010. URL: https://www.api.org/standards/.

[100] Eugene Cook Bingham. *Fluidity and Plasticity*. Vol. 2. McGraw-Hill Book Company, Inc., 1922.

[101] Ian A. Frigaard, Kristofer G. Paso, and Paulo R. de Souza Mendes. "Bingham's Model in the Oil and Gas Industry". In: *Rheologica Acta* 56.3 (Mar. 2017), pp. 259–282. DOI: 10.1007/s00397-017-0999-y.

[102] Terry Hemphill, Wellington Campos, and Ali Pilehvari. "Yield Power Law Model More Accurately Predicts Mud Rheology". In: *Oil & Gas Journal* 91 (1993). URL: http://www.ogj.com/articles/print/volume-91/issue-34/in-this-issue/drilling/yield-power-law-model-more-accurately-predicts-mud-rheology.html.

[103] Kenji Yasuda. "Investigation of the Analogies between Viscometric and Linear Viscoelastic Properties of Polystyrene Fluids". PhD. Cambridge: Massachusetts Institute of Technology. Dept. of Chemical Engineering., 1979. URL: https://dspace.mit.edu/handle/1721.1/16043.

[104] Ashutosh Mujumdar, Antony N. Beris, and Arthur B. Metzner. "Transient Phenomena in Thixotropic Systems". In: *A Collection of Papers Dedicated to Professor ANDREAS ACRIVOS on the Occasion of his Retirement from the Benjamin Levich Institute for Physiochemical Hydrodynamics and the City College of the CUNY* 102.2 (Feb. 15, 2002), pp. 157–178. DOI: 10.1016/S0377-0257(01)00176-8.

[105] Paulo R. de Souza Mendes and Roney L. Thompson. “A Unified Approach to Model Elasto-Viscoplastic Thixotropic Yield-Stress Materials and Apparent Yield-Stress Fluids”. In: *Rheologica Acta* 52.7 (July 2013), pp. 673–694. DOI: 10.1007/s00397-013-0699-1.

[106] J. Esteban López-Aguilar, Michael F. Webster, Hamid Reza Tamaddon-Jahromi, and Octavio Manero. “Numerical Modelling of Thixotropic and Viscoelastoplastic Materials in Complex Flows”. In: *Rheologica Acta* 54.4 (Apr. 2015), pp. 307–325. DOI: 10.1007/s00397-014-0810-2.

[107] Paulo R. de Souza Mendes, Behbood Abedi, and Roney L. Thompson. “Constructing a Thixotropy Model from Rheological Experiments”. In: *Journal of Non-Newtonian Fluid Mechanics* (Aug. 2018). DOI: 10.1016/j.jnnfm.2018.08.003.

[108] Christopher J. Dimitriou and Gareth H. McKinley. “A Canonical Framework for Modeling Elasto-Viscoplasticity in Complex Fluids”. In: *Journal of Non-Newtonian Fluid Mechanics* (Oct. 2018). DOI: 10.1016/j.jnnfm.2018.10.004.

[109] Pierre Saramito. “A New Elastoviscoplastic Model Based on the Herschel–Bulkley Viscoplastic Model”. In: *Visco-plastic fluids: From theory to application* 158.1–3 (May 2009), pp. 154–161. DOI: 10.1016/j.jnnfm.2008.12.001.

[110] B. Herzhaft, A. Ragouillaux, and P. Coussot. “How To Unify Low-Shear-Rate Rheology and Gel Properties of Drilling Muds: A Transient Rheological and Structural Model for Complex Well Applications”. In: IADC/SPE Drilling Conference. Miami: Society of Petroleum Engineers, 2006. DOI: 10.2118/99080-MS.

[111] R. G. Larson. “Constitutive Equations for Thixotropic Fluids”. In: *Journal of Rheology* 59.3 (May 2015), pp. 595–611. DOI: 10.1122/1.4913584.

[112] Paulo R. de Souza Mendes. “Modeling the Thixotropic Behavior of Structured Fluids”. In: *Journal of Non-Newtonian Fluid Mechanics* 164.1-3 (Dec. 2009), pp. 66–75. DOI: 10.1016/j.jnnfm.2009.08.005.

[113] S. Livescu. “Mathematical Modeling of Thixotropic Drilling Mud and Crude Oil Flow in Wells and Pipelines—A Review”. In: *Journal of Petroleum Science and Engineering* 98-99 (Nov. 2012), pp. 174–184. DOI: 10.1016/j.petrol.2012.04.026.

[114] Eric Cayeux and Amare Leulseged. "Modelling of Drilling Fluid Thixotropy". In: (2018), p. 14.

[115] Roney L. Thompson, Luiz U.R. Sica, and Paulo R. de Souza Mendes. "The Yield Stress Tensor". In: *Journal of Non-Newtonian Fluid Mechanics* (Sept. 2018). DOI: 10.1016/j.jnnfm.2018.09.003.

[116] Stuart B Savage, Robert Pfeffer, and Zhong M Zhao. "Solids Transport, Separation and Classification". In: *Powder Technology* 88.3 (1996), pp. 323–333.

[117] C. K. K. Lun, S. B. Savage, D. J. Jeffrey, and N. Chepurniy. "Kinetic Theories for Granular Flow: Inelastic Particles in Couette Flow and Slightly Inelastic Particles in a General Flowfield". In: *Journal of Fluid Mechanics* 140 (1984), pp. 223–256. DOI: 10.1017/S0022112084000586.

[118] Stuart B. Savage. "Granular Flows Down Rough Inclines - Review and Extension". In: *Studies in Applied Mechanics*. Vol. 7. Elsevier, 1983, pp. 261–282. DOI: 10.1016/B978-0-444-42192-0.50028-1.

[119] S. B. Savage and D. J. Jeffrey. "The Stress Tensor in a Granular Flow at High Shear Rates". In: *Journal of Fluid Mechanics* 110 (1981), pp. 255–272. DOI: 10.1017/S0022112081000736.

[120] P. C. Johnson and R. Jackson. "Frictional–Collisional Constitutive Relations for Granular Materials, with Application to Plane Shearing". In: *Journal of Fluid Mechanics* 176 (1987), pp. 67–93. DOI: 10.1017/S0022112087000570.

[121] David G. Schaeffer. "Instability in the Evolution Equations Describing Incompressible Granular Flow". In: *Journal of differential equations* 66.1 (1987), pp. 19–50.

[122] Isaac Goldhirsch. "Introduction to Granular Temperature". In: *Powder Technology* 182.2 (Feb. 2008), pp. 130–136. DOI: 10.1016/j.powtec.2007.12.002.

[123] Jianmin Ding and Dimitri Gidaspow. "A Bubbling Fluidization Model Using Kinetic Theory of Granular Flow". In: *AIChE Journal* 36.4 (Apr. 1, 1990), pp. 523–538. DOI: 10.1002/aic.690360404.

[124] Syamlal, M., Rogers, W., and O'Brien, T. J. *MFIX Documentation Theory Guide*. Morgantown: U.S. Department of Energy, Office of Fossil Energy, 1993. URL: http://dx.doi.org/10.2172/10145548.

[125] R. A. Bagnold. “Experiments on a Gravity-Free Dispersion of Large Solid Spheres in a Newtonian Fluid under Shear”. In: *Proceedings of the Royal Society of London. Series A. Mathematical and Physical Sciences* 225.1160 (1954), pp. 49–63. DOI: 10.1098/rspa.1954.0186.

[126] Satoru Ogawa, Akira Umemura, and Nobunori Oshima. “On the Equations of Fully Fluidized Granular Materials”. In: *Zeitschrift für angewandte Mathematik und Physik ZAMP* 31.4 (July 1980), pp. 483–493. DOI: 10.1007/BF01590859.

[127] J. L. Sinclair and R. Jackson. “Gas-Particle Flow in a Vertical Pipe with Particle-Particle Interactions”. In: *AIChE Journal* 35.9 (Sept. 1, 1989), pp. 1473–1486. DOI: 10.1002/aic.690350908.

[128] Hamzah M. Beakawi Al-Hashemi and Omar S. Baghabra Al-Amoudi. “A Review on the Angle of Repose of Granular Materials”. In: *Powder Technology* 330 (May 2018), pp. 397–417. DOI: 10.1016/j.powtec.2018.02.003.

[129] Florian R. Menter. “Two-Equation Eddy-Viscosity Turbulence Models for Engineering Applications”. In: *AIAA Journal* 32.8 (Aug. 1994), pp. 1598–1605. DOI: 10.2514/6.1993-2906.

[130] Florian R. Menter. “Zonal Two Equation K-ω Turbulence Models For Aerodynamic Flows”. In: 24th Fluid Dynamics Conference. Orlando, Florida: American lnstirute of Aeronautics and Astronautics (AIAA), July 6–9, 1993, p. 22.

[131] B. E. Launder and D. B. Spalding. *Lectures in Mathematical Models of Turbulence*. London; New York: Academic Press, 1972.

[132] David C. Wilcox. *Turbulence Modeling for CFD*. 3rd ed. La Cãnada, Calif: DCW Industries, 2006. 522 pp.

[133] C. M. Tchen. “Mean Value and Correlation Problems Connected with the Motion of Small Particles Suspended in a Turbulent Fluid”. PhD thesis. Delft: Delft University, 1947. URL: https://link.springer.com/book/10.1007/978-94-017-6101-7.

[134] Juergen O. Hinze. *Turbulence*. McGraw-Hill, 1975.

[135] C. Simonin and P. L. Viollet. “Predictions of an Oxygen Droplet Pulverization in a Compressible Subsonic Coflowing Hydrogen Flow”. In: *Numerical Methods for Multiphase Flows, FED91* (1990), pp. 65–82.

[136] GT Csanady. “Turbulent Diffusion of Heavy Particles in the Atmosphere”. In: *Journal of the Atmospheric Sciences* 20.3 (1963), pp. 201–208. DOI: 10.1175/1520-0469(1963)020<0201:TDOHPI>2.0.CO;2.

[137] Boxue Pang, Shuyan Wang, Qiujin Wang, Kai Yang, Huilin Lu, Muhammad Hassan, and Xiaoxue Jiang. “Numerical Prediction of Cuttings Transport Behavior in Well Drilling Using Kinetic Theory of Granular Flow”. In: *Journal of Petroleum Science and Engineering* 161 (Feb. 2018), pp. 190–203. DOI: 10.1016/j.petrol.2017.11.028.

[138] Emmanuel I. Epelle and Dimitrios I. Gerogiorgis. “Transient and Steady State Analysis of Drill Cuttings Transport Phenomena under Turbulent Conditions”. In: *Chemical Engineering Research and Design* (Nov. 2017). DOI: 10.1016/j.cherd.2017.11.023.

[139] Mohammadreza Kamyab and Vamegh Rasouli. “Experimental and Numerical Simulation of Cuttings Transportation in Coiled Tubing Drilling”. In: *Journal of Natural Gas Science and Engineering* 29 (Feb. 2016), pp. 284–302. DOI: 10.1016/j.jngse.2015.11.022.

[140] J. Singh, M. Rudman, and H. M. Blackburn. “The Influence of Shear-Dependent Rheology on Turbulent Pipe Flow”. In: *Journal of Fluid Mechanics* 822 (July 2017), pp. 848–879. DOI: 10.1017/jfm.2017.296.

[141] J. Singh, M. Rudman, H.M. Blackburn, A. Chryss, L. Pullum, and L.J.W. Graham. “The Importance of Rheology Characterization in Predicting Turbulent Pipe Flow of Generalized Newtonian Fluids”. In: *Journal of Non-Newtonian Fluid Mechanics* 232 (June 2016), pp. 11–21. DOI: 10.1016/j.jnnfm.2016.03.013.

[142] J. Singh, M. Rudman, and H. M. Blackburn. “The Rheology Dependent Region in Turbulent Pipe Flow of a Generalised Newtonian Fluid”. In: 20th Australasian Fluid Mechanics Conference. Perth, Australia, 2016. URL: http://users.monash.edu.au/~bburn/pdf/493.pdf.

[143] M. Rudman and H. M. Blackburn. “Turbulence Modification in Shear-Thinning Fluids: Preliminary Results for Power Law Rheology”. In: *18th Australian Fluid Mechanics Conference. Launceston, Australia*. 2012. URL: http://people.eng.unimelb.edu.au/imarusic/proceedings/18/385%20-%20Rudman.pdf.

[144] M. Rudman and H. M. Blackburn. “The Effect of Shear-Thinning Behaviour on Turbulent Pipe Flow”. In: *Third International Conference on CFD in the Minerals and Process Industries*. Vol. 1. Melbourne: CSIRO, 2003, pp. 383–390. URL: http://www.cfd.com.au/cfd_conf03/papers/044Rud.pdf.

[145] P. J. Oliveira and Fernando Tavares de Pinho. “A Qualitative Assessment of the Role of a Viscosity Depending on the Third Invariant of the Rate-of-Deformation Tensor upon Turbulent Non-Newtonian Flow”. In: *Journal of Non-Newtonian Fluid Mechanics* 78.1 (1998), pp. 1–25. DOI: 10.1016/S0377-0257(97)00107-9.

[146] Jesse Capecelatro and Olivier Desjardins. “Eulerian–Lagrangian Modeling of Turbulent Liquid–Solid Slurries in Horizontal Pipes”. In: *International Journal of Multiphase Flow* 55 (Oct. 2013), pp. 64–79. DOI: 10.1016/j.ijmultiphaseflow.2013.04.006.

[147] Dominik Kubicki and Simon Lo. “Slurry Transport in a Pipeline – Comparison of CFD and DEM Models”. In: *Ninth International Conference on CFD in the Minerals and Process Industries*. 2012. URL: http://www.cfd.com.au/cfd_conf12/PDFs/067KUB.pdf.

[148] Sandip K. Lahiri and K. C. Ghanta. “Computational Fluid Dynamics Simulation of the Solid Liquid Slurry Flow in a Pipeline”. In: Chemcon 2008. 2008. URL: https://works.bepress.com/sandip_lahiri/14/.

[149] Schalk Cloete, Stein Tore Johansen, and Shahriar Amini. “Performance Evaluation of a Complete Lagrangian KTGF Approach for Dilute Granular Flow Modelling”. In: *Powder Technology* 226 (Aug. 2012), pp. 43–52. DOI: 10.1016/j.powtec.2012.04.010.

[150] Schalk Cloete, Stein Tore Johansen, Abdelghafour Zaabout, Martin van Sint Annaland, Fausto Gallucci, and Shahriar Amini. “The Effect of Frictional Pressure, Geometry and Wall Friction on the Modelling of a Pseudo-2D Bubbling Fluidised Bed Reactor”. In: *Powder Technology* 283 (Oct. 2015), pp. 85–102. DOI: 10.1016/j.powtec.2015.04.060.

[151] Ali Khosronejad and Fotis Sotiropoulos. “Numerical Simulation of Sand Waves in a Turbulent Open Channel Flow”. In: *Journal of Fluid Mechanics* 753 (Aug. 2014), pp. 150–216. DOI: 10.1017/jfm.2014.335.

[152] Nils Reidar B. Olsen. "Three-Dimensional CFD Modeling of Self-Forming Meandering Channel". In: *Journal of Hydraulic Engineering* 129.5 (2003), pp. 366–372. DOI: 10.1061/(ASCE)0733-9429(2003)129:5(366).

[153] B. Brørs. "Numerical Modeling of Flow and Scour at Pipelines". In: *Journal of Hydraulic Engineering* 125.5 (May 1, 1999), pp. 511–523. DOI: 10.1061/(ASCE)0733-9429(1999)125:5(511).

[154] Jeff Li and Bernard Luft. "Overview Solids Transport Study and Application in Oil-Gas Industry - Theoretical Work". In: International Petroleum Technology Conference. Kuala Lumpur: International Petroleum Technology Conference, Dec. 10, 2014. DOI: 10.2523/IPTC-17832-MS.

[155] Jeff Li and Bernard Luft. "Overview of Solids Transport Studies and Applications in Oil and Gas Industry - Experimental Work". In: SPE Russian Oil and Gas Exploration & Production Technical Conference and Exhibition. Moscow: Society of Petroleum Engineers, Oct. 14, 2014. DOI: 10.2118/171285-MS.

[156] Subhash Shah, S. Naik, and I. Dosunmu. "Critical Assessment of Solids Removal Technology: Deviated and Horizontal Wells". In: *Hydraulic Fracturing Quarterly* 1.1 (2014), pp. 112–120.

[157] Sun Xiaofeng, Wang Kelin, and Yan Tie. "Review of Hole Cleaning in Complex Structural Wells". In: *The Open Petroleum Engineering Journal* 6 (2013), pp. 25–32. DOI: 10.2174/1874834101306010025.

[158] Wang Kelin, Yan Tie, Sun Xiaofeng, Shao Shuai, and Luan Shizhu. "Review and Analysis of Cuttings Transport in Complex Structural Wells". In: *The Open Fuels & Energy Science Journal* 6 (2013), pp. 9–17. DOI: /10.2174/1876973X20130610001.

[159] M. Kamyab, V. Rasouli, G. Cavanough, and S. Mandal. "Challenges of Cuttings Transport in Micro Borehole Coiled Tubing Drilling for Mineral Exploration". In: *WIT Transactions on Engineering Sciences* 81 (Dec. 4, 2012), pp. 109–120. DOI: 10.2495/PMR120101.

[160] V. C. Kelessidis, G. Mpandelis, A. Koutroulis, and T. Michalakis. "Significant Parameters Affecting Efficient Cuttings Transport in Horizontal and Deviated Wellbores in Coil Tubing Drilling: A Critical Review". In: 1st International Symposium of the Faculty

of Mines (ITU) on Earth Sciences and Engineering. Istanbul, May 16, 2002. URL: http://www.mred.tuc.gr/home/kelessidis/publications/10.pdf.

[161] AA Pilehvari, Jamal Joseph Azar, and SA Shirazi. “State-of-the-Art Cuttings Transport in Horizontal Wellbores”. In: *SPE Drilling & Completion* 14.03 (1999). DOI: /10.2118/57716-PA.

[162] J. J. Azar and R. Alfredo Sanchez. “Important Issues in Cuttings Transport for Drilling Directional Wells”. In: *Latin American and Caribbean Petroleum Engineering Conference*. Society of Petroleum Engineers, 1997. DOI: 10.2118/39020-MS.

[163] Roger Aragall Tersa. “Improvements of Cuttings Transport Models through Physical Experiments and Numerical Investigations of Solid-Liquid Transport”. PhD thesis. Clausthal-Zellerfeld: Technische Universität Clausthal, 2016. 150 pp. URL: http://d-nb.info/1101965851/34.

[164] Ebrahim Hajidavalloo, Masoud Sadeghi-Behbahani-Zadeh, and Younes Shekari. “Simulation of Gas–Solid Two-Phase Flow in the Annulus of Drilling Well”. In: *Chemical Engineering Research and Design* 91.3 (Mar. 2013), pp. 477–484. DOI: 10.1016/j.cherd.2012.11.009.

[165] Zhi-ming Wang, Xiao-le Guo, Ming Li, and Yu-kui Hong. “Effect of Drillpipe Rotation on Borehole Cleaning for Extended Reach Well”. In: *Journal of Hydrodynamics, Ser. B* 21.3 (June 2009), pp. 366–372. DOI: 10.1016/S1001-6058(08)60158-4.

[166] Ali Zakerian, Siyamak Sarafraz, Amir Tabzar, Nassim Hemmati, and Seyed Reza Shadizadeh. “Numerical Modeling and Simulation of Drilling Cutting Transport in Horizontal Wells”. In: *Journal of Petroleum Exploration and Production Technology* (Jan. 25, 2018). DOI: 10.1007/s13202-018-0435-6.

[167] S. Akbari and S. H. Hashemabadi. “Temperature and Pressure Effects of Drilling Fluid on Cutting Transport Using CFD Simulations: Effects of Drilling Fluid Using CFD Simulation”. In: *Asia-Pacific Journal of Chemical Engineering* 12.6 (Nov. 2017), pp. 980–992. DOI: 10.1002/apj.2140.

[168] Xiao-le Guo, Wen-yin Li, and Ji-lin Liu. “Simulation on Cuttings Transport with Drillpipe Rotation in Highly-Inclined Well Section”. In: 2017 International Conference on Applied Mechanics and Mechanical Automation (AMMA 2017). Hong Kong: DEStech Transactions on Engineering and Technology Research, June 23, 2017. DOI: 10.12783/dtetr/amma2017/13334.

[169] Sneha Sayindla, Bjørnar Lund, Jan David Ytrehus, and Arild Saasen. “CFD Modelling of Observed Cuttings Transport in Oil-Based and Water-Based Drilling Fluids”. In: SPE/IADC Drilling Conference and Exhibition. The Hague: Society of Petroleum Engineers, Mar. 14, 2017. DOI: 10.2118/184660-MS.

[170] E. GhasemiKafrudi and S.H. Hashemabadi. “Numerical Study on Cuttings Transport in Vertical Wells with Eccentric Drillpipe”. In: *Journal of Petroleum Science and Engineering* 140 (Apr. 2016), pp. 85–96. DOI: 10.1016/j.petrol.2015.12.026.

[171] K. Mohammadzadeh, S.H. Hashemabadi, and S. Akbari. “CFD Simulation of Viscosity Modifier Effect on Cutting Transport by Oil Based Drilling Fluid in Wellbore”. In: *Journal of Natural Gas Science and Engineering* 29 (Feb. 2016), pp. 355–364. DOI: 10.1016/j.jngse.2015.11.011.

[172] Titus Ntow Ofei. “Effect of Yield Power Law Fluid Rheological Properties on Cuttings Transport in Eccentric Horizontal Narrow Annulus”. In: *Journal of Fluids* 2016 (2016), pp. 1–10. DOI: 10.1155/2016/4931426.

[173] Siamak Akhshik, Mehdi Behzad, and Majid Rajabi. “CFD–DEM Model for Simulation of Non-Spherical Particles in Hole Cleaning Process”. In: *Particulate Science and Technology* 33.5 (Sept. 3, 2015), pp. 472–481. DOI: 10.1080/02726351.2015.1010760.

[174] Siamak Akhshik, Mehdi Behzad, and Majid Rajabi. “CFD–DEM Approach to Investigate the Effect of Drill Pipe Rotation on Cuttings Transport Behavior”. In: *Journal of Petroleum Science and Engineering* 127 (Mar. 2015), pp. 229–244. DOI: 10.1016/j.petrol.2015.01.017.

[175] Reza Rooki, Faramarz Doulati Ardejani, Ali Moradzadeh, and Mahmood Norouzi. “CFD Simulation of Rheological Model Effect on Cuttings Transport”. In: *Journal of Dispersion Science and*

Technology 36.3 (Mar. 4, 2015), pp. 402–410. DOI: 10.1080/01932691.2014.896219.

[176] Reza Rooki, Faramarz Doulati Ardejani, Ali Moradzadeh, and Mahmood Norouzi. "Simulation of Cuttings Transport with Foam in Deviated Wellbores Using Computational Fluid Dynamics". In: *Journal of Petroleum Exploration and Production Technology* 4.3 (Sept. 2013), pp. 263–273. DOI: 10.1007/s13202-013-0077-7.

[177] Reza Rooki, F D Ardejani, Ali Moradzadeh, and Mahmood Norouzi. "Cuttings Transport Modeling in Foam Drilling Using Computational Fluid Dynamics (CFD)". In: *International Journal of Petroleum & Geoscience Engineering (IJPGE)* 1.2 (2013), pp. 115–127.

[178] F. A. R. Pereira, C. H. Ataíde, and M. A. S. Barrozo. "CFD Approach Using a Discrete Phase Model for Annular Flow Analysis". In: *Latin American applied research* 40.1 (2010), pp. 53–60. URL: http://ref.scielo.org/qdggs4.

[179] Sang Mok Han, Young Kyu Hwang, Nam Sub Woo, and Young Ju Kim. "Solid-Liquid Hydrodynamics in a Slim Hole Drilling Annulus". In: *Journal of Petroleum Science and Engineering* 70.3-4 (2010), pp. 308–319. DOI: 10.1016/j.petrol.2009.12.002.

[180] Md. Wazed Ali. "A Parametric Study of Cutting Transport in Vertical and Horizontal Well Using Computational Fluid Dynamics (CFD)". Master thesis. Morgantown: West Virginia University, 2002. URL: https://libwvu.on.worldcat.org/oclc/49792545.

[181] H.I. Bilgesu, M.W. Ali, K. Aminian, and S. Ameri. "Computational Fluid Dynamics (CFD) as a Tool to Study Cutting Transport in Wellbores". In: SPE Eastern Regional Meeting. Lexington: Society of Petroleum Engineers, 2002. DOI: 10.2118/78716-MS.

[182] Meysam Naderi and Ehsan Khamehchi. "Cutting Transport Efficiency Prediction Using Probabilistic CFD and DOE Techniques". In: *Journal of Petroleum Science and Engineering* 163 (Apr. 2018), pp. 58–66. DOI: 10.1016/j.petrol.2017.12.083.

[183] Mostafa Keshavarz Moraveji, Mohammad Sabah, Ahmad Shahryari, and Ahmadreza Ghaffarkhah. "Investigation of Drill Pipe Rotation Effect on Cutting Transport with Aerated Mud Using CFD Approach". In: *Advanced Powder Technology* 28.4 (Apr. 2017), pp. 1141–1153. DOI: 10.1016/j.apt.2017.01.020.

[184] Baojiang Sun, Hengfu Xiang, Hao Li, and Xiangfang Li. “Modeling of the Critical Deposition Velocity of Cuttings in an Inclined-Slimhole Annulus”. In: *SPE Journal* 22.04 (Aug. 1, 2017), pp. 1213–1224. DOI: 10.2118/185168-PA.

[185] Gregory B. Dykes. “Cuttings Transport Implications for Drill String Design: A Study with Computational Fluid Dynamics”. Master. Golden, CO: Colorado School of Mines, 2014. URL: http://hdl.handle.net/11124/10644.

[186] M. A. Manzar and S. N. Shah. “Particle Distribution and Erosion During the Flow of Newtonian and Non-Newtonian Slurries in Straight and Coiled Pipes”. In: *Engineering Applications of Computational Fluid Mechanics* 3.3 (Nov. 2014), pp. 296–320. DOI: 10.1080/19942060.2009.11015273.

[187] Johanna Hamne. “CFD Modeling of Mud Flow around Drill Bit”. Master. Luleå: Luleå University of Technology, 2014. URL: http://urn.kb.se/resolve?urn=urn:nbn:se:ltu:diva-49453.

[188] Sun Xiaofeng, Wang Kelin, Yan Tie, Shuai Shao, and Jianjun Jiao. “Effect of Drillpipe Rotation on Cuttings Transport Using Computational Fluid Dynamics (CFD) in Complex Structure Wells”. In: *Journal of Petroleum Exploration and Production Technology* 4.3 (May 2014), pp. 255–261. DOI: 10.1007/s13202-014-0118-x.

[189] Sun Xiaofeng, Yan Tie, Li Wei, and Wu Yanze. “Study on Cuttings Transport Efficiency Affected by Stabilizer’s Blade Shape in Vertical Wells”. In: *Open Petroleum Engineering Journal* 6 (2013), pp. 7–11. DOI: 10.2174/1874834101306010007.

[190] Reza Ettehadi Osgouei, Mehmet Evren Ozbayoglu, and Tham Keat Fu. “CFD Simulation of Solids Carrying Capacity of a Newtonian Fluid Through Horizontal Eccentric Annulus”. In: ASME 2013 Fluids Engineering Division Summer Meeting. Incline Village, NV: American Society of Mechanical Engineers, July 7, 2013. DOI: 10.1115/FEDSM2013-16204.

[191] Mehmet Sorgun. “Modeling of Newtonian Fluids and Cuttings Transport Analysis in High Inclination Wellbores with Pipe Rotation”. PhD. Ankara: Middle East Technical University, 2010. URL: https://etd.lib.metu.edu.tr/upload/12612385/index.pdf.

[192] Nekkhil Mishra. "Investigation of Hole Cleaning Parameters Using Computational Fluid Dynamics in Horizontal and Deviated Wells". Master Thesis. Morgantown: West Virginia University, 2007. URL: https://libwvu.on.worldcat.org/oclc/132690399.

[193] Omid Heydari, Eghbal Sahraei, and Pål Skalle. "Investigating the Impact of Drillpipe's Rotation and Eccentricity on Cuttings Transport Phenomenon in Various Horizontal Annuluses Using Computational Fluid Dynamics (CFD)". In: *Journal of Petroleum Science and Engineering* 156 (July 2017), pp. 801–813. DOI: 10.1016/j.petrol.2017.06.059.

[194] Behnam Amanna and Mohammad Reza Khorsand Movaghar. "Cuttings Transport Behavior in Directional Drilling Using Computational Fluid Dynamics (CFD)". In: *Journal of Natural Gas Science and Engineering* 34 (Aug. 2016), pp. 670–679. DOI: 10.1016/j.jngse.2016.07.029.

[195] Yasin Demiralp. "Effects Of Drill-Pipe Whirling Motion On Cuttings Transport Performance For Horizontal Drilling". Master Thesis. Lousiana State University, 2014. URL: https://digitalcommons.lsu.edu/gradschool_theses/2238/.

[196] Titus Ntow Ofei and William Pao. "Modelling of Pressure Drop and Cuttings Concentration in Eccentric Narrow Horizontal Well Bore with Rotating Drillpipe". In: *Journal of Applied Sciences* 14.23 (2014), pp. 3263–3269. DOI: 10.3923/jas.2014.3263.3269.

[197] Titus Ntow Ofei, Sonny Irawan, and William Pao. "CFD Method for Predicting Annular Pressure Losses and Cuttings Concentration in Eccentric Horizontal Wells". In: *Journal of Petroleum Engineering* 2014 (2014), pp. 1–16. DOI: 10.1155/2014/486423.

[198] Dan Lucas. "Agglomeration and Transport of Drilling-Generated Particles in Directional Oil Wells - Numerical Simulation". AdWell Open Seminar (Stavanger). 2014.

[199] Doguhan Yilmaz. "Discrete Phase Simulations of Drilled Cuttings Transport Process in Highly Deviated Wells". Master. Baton Rouge, LA: Louisiana State University, 2012. URL: https://digitalcommons.lsu.edu/gradschool_theses/2980/.

[200] Uduak Mme and Paal Skalle. "CFD Calculations of Cuttings Transport through Drilling Annuli at Various Angles". In: *International Journal of Petroleum Science and Technology* 6.2 (2012), pp. 129–141. URL: http://www.ipt.ntnu.no/~pskalle/files/TechnicalPapers/44_CFDcuttings.pdf (visited on 06/24/2015).

[201] Hussain H. Al-Kayiem, Nadia Mohd Zaki, Muhamad Z. Asyraf, and Mahir Elya Elfeel. "Simulation of the Cuttings Cleaning During the Drilling Operation". In: *American Journal of Applied Sciences* 7.6 (2010), pp. 800–806. DOI: 10.3844/ajassp.2010.800.806.

[202] Eric Cayeux, Taiwo Mesagan, Sakti Tanripada, Mohamed Zidan, and Kjell Kåre Fjelde. "Real-Time Evaluation of Hole-Cleaning Conditions With a Transient Cuttings-Transport Model". In: *SPE Drilling & Completion* 29.01 (Mar. 1, 2014), pp. 05–21. DOI: 10.2118/163492-PA.

[203] Rolv Rommetveit, Knut S Bjorkevoll, George W Halsey, Hans Freddy Larsen, Antonino Merlo, Leslie N Nossaman, Miles N Sweep, Knut Martin Silseth, and Sven Inge Odegaard. "Drilltronics: An Integrated System for Real-Time Optimization of the Drilling Process". In: IADC/SPE Drilling Conference. Dallas, TX: Society of Petroleum Engineers (SPE), 2004, p. 8. DOI: 10.2118/87124-MS.

[204] Rolv Rommetveit, Knut Steinar Bjorkevoll, George Wesley Halsey, Erling Fjar, Sven Inge Odegaard, Mike C. Herbert, Ove Sandve, and Bjarne Larsen. "E-Drilling: A System for Real-Time Drilling Simulation, 3D Visualization and Control". In: *Digital Energy Conference and Exhibition*. Digital Energy Conference and Exhibition. Houston, Texas, U.S.A.: Society of Petroleum Engineers (SPE), 2007. DOI: 10.2118/106903-MS.

[205] Johnny Petersen, Rolv Rommetveit, Knut Steinar Bjorkevoll, and Johnny Froyen. "A General Dynamic Model for Single and Multi-Phase Flow Operations during Drilling, Completion, Well Control and Intervention". In: *IADC/SPE Asia Pacific Drilling Technology Conference and Exhibition*. IADC/SPE Asia Pacific Drilling Technology Conference and Exhibition. Jakarta, Indonesia: Society of Petroleum Engineers (SPE), 2008. DOI: 10.2118/114688-MS.

[206] Gunnar Hjelmtveit Lille. *Technologies to Improve Drilling Efficiency and Reduce Costs*. Technical report. Oslo: OG21's technology group on drilling and intervention (TTA3), 2014.

[207] Milad Khatibi, Rune W. Time, and H.A. Rabenjafimanantsoa. "Particles Falling Through Viscoelastic Non-Newtonian Flows in a Horizontal Rectangular Channel Analyzed with PIV and PTV Techniques". In: *Journal of Non-Newtonian Fluid Mechanics* 235 (Sept. 2016), pp. 143–153. DOI: 10.1016/j.jnnfm.2016.08.004.

[208] P. Doron, D. Granica, and D. Barnea. "Slurry Flow in Horizontal Pipes—Experimental and Modeling". In: *International Journal of Multiphase Flow* 13.4 (1987), pp. 535–547. DOI: 10.1016/0301-9322(87)90020-6.

[209] P. Doron and D. Barnea. "A Three-Layer Model for Solid-Liquid Flow in Horizontal Pipes". In: *International Journal of Multiphase Flow* 19.6 (1993), pp. 1029–1043. DOI: 10.1016/0301-9322(93)90076-7.

[210] P. Doron, M. Simkhis, and D. Barnea. "Flow of Solid-Liquid Mixtures in Inclined Pipes". In: *International journal of multiphase flow* 23.1993 (1997), pp. 313–323. DOI: 10.1016/S0301-9322(97)80946-9.

[211] F. Charru, H. Mouilleron, and O. Eiff. "Erosion and Deposition of Particles on a Bed Sheared by a Viscous Flow". In: *Journal of Fluid Mechanics* 519 (Nov. 25, 2004), pp. 55–80. DOI: 10.1017/S0022112004001028.

[212] Benjamin Werner. "The Influence of Drilling Fluid Rheology on Cuttings Bed Behavior". PhD. Trondheim: Norwegian University of Science and Technology, 2018. URL: http://rgdoi.net/10.13140/RG.2.2.19105.30566.

[213] A. Torsvik, V. Myrseth, N. Opedal, B. Lund, A. Saasen, and J. D. Ytrehus. "Rheological Comparison of Bentonite Based and KCl / Polymer Based Drilling Fluids". In: *Annual Transactions of the Nordic Rheology Society* 22 (2014). URL: https://nrs.blob.core.windows.net/pdfs/nrspdf-503c6b3c-2217-46cd-8fe5-d114d54ad115.pdf.

[214] J. Greener. "The Response of Viscoelastic Liquids to Complex Strain Histories: The Thixotropic Loop". In: *Journal of Rheology* 30.2 (1986), p. 285. DOI: 10.1122/1.549849.

[215] D. C.-H. Cheng. "Thixotropy". In: *International Journal of Cosmetic Science* 9.4 (Aug. 1987), pp. 151–191. DOI: 10.1111/j.1467-2494.1987.tb00472.x.

[216] F. J. Rubio-Hernández and A. I. Gómez-Merino. "Time Dependent Mechanical Behavior: The Viscoelastic Loop". In: *Mechanics of Time-Dependent Materials* 12.4 (Dec. 2008), pp. 357–364. DOI: 10.1007/s11043-008-9066-5.

[217] H. M. Laun. "Prediction of Elastic Strains of Polymer Melts in Shear and Elongation". In: *Journal of Rheology* 30.3 (June 1986), pp. 459–501. DOI: 10.1122/1.549855.

[218] Ad Hoc Committee on Official Nomenclature and Symbols. "Official Symbols and Nomenclature of The Society of Rheology". In: *Journal of Rheology* 57.4 (July 2013), pp. 1047–1055. DOI: 10.1122/1.4811184.

[219] Markus Reiner. "The Deborah Number". In: *Physics Today* 17.1 (1964), p. 62. DOI: 10.1063/1.3051374.

[220] James Lindsay White. "Dynamics of Viscoelastic Fluids, Melt Fracture, and the Rheology of Fiber Spinning". In: *Journal of Applied Polymer Science* 8.5 (Sept. 1964), pp. 2339–2357. DOI: 10.1002/app.1964.070080527.

[221] A. C. Pipkin. *Lectures on Viscoelasticity Theory*. 2nd ed. Applied Mathematical Sciences v. 7. New York: Springer-Verlag, 1986. 188 pp. URL: https://www.springer.com/de/book/9781461599708.

[222] J. M. Dealy. "Weissenberg and Deborah Numbers - Their Definition and Use". In: *Rheology Bulletin* 79 (July 2010), pp. 14–18. URL: https://www.rheology.org/sor/Publications/RheoBulletin/RB2010Jul.pdf.

[223] R. J. Poole. "The Deborah and Weissenberg Numbers". In: *The British Society of Rheology, Rheology Bulletin* 53.2 (2012), pp. 32–39. URL: http://pcwww.liv.ac.uk/~robpoole/papers/poole_45.pdf (visited on 03/29/2017).

[224] A. Acharya, R. A. Mashelkar, and J. Ulbrecht. "Flow of Inelastic and Viscoelastic Fluids Past a Sphere - I. Drag Coefficient in Creeping and Boundary-Layer Flows". In: *Rheologica Acta* 15.9 (1976), pp. 454–470. DOI: 10.1007/BF01530348.

[225] M. M. Gumulya, R. R. Horsley, and V. Pareek. “Numerical Simulation of the Settling Behaviour of Particles in Thixotropic Fluids”. In: *Physics of Fluids* 26.2 (Feb. 2014), p. 023102. DOI: 10.1063/1.4866320.

[226] Katherine Moseley, Michael Fairweather, and David Harbottle. “Settling Dynamics of Two Identical Vertically Aligned Spheres in a Thixotropic Fluid”. In: *Journal of Non-Newtonian Fluid Mechanics* 271 (Sept. 2019), p. 104146. DOI: 10.1016/j.jnnfm.2019.104146.

[227] Felix M. Exner. “Uber Die Wechselwirkung Zwischen Wasser Und Geschiebe in Flüssen”. In: *Akad. Wiss. Wien Math. Naturwiss. Klasse* 134 (2a 1925), pp. 165–204. URL: https://www.zobodat.at/pdf/SBAWW_134_2a_0165-0203.pdf.

[228] Gert Lube, Herbert E. Huppert, R. Stephen J. Sparks, and Armin Freundt. “Collapses of Two-Dimensional Granular Columns”. In: *Physical Review E* 72.4 (Oct. 4, 2005). DOI: 10.1103/PhysRevE.72.041301.

[229] Alexis Bougouin and Laurent Lacaze. “Granular Collapse in a Fluid: Different Flow Regimes for an Initially Dense-Packing”. In: *Physical Review Fluids* 3.6 (June 13, 2018). DOI: 10.1103/PhysRevFluids.3.064305.

[230] Malika Ouriemi, Pascale Aussillous, and éLisabeth Guazzelli. “Sediment Dynamics. Part 2. Dune Formation in Pipe Flow”. In: *Journal of Fluid Mechanics* 636 (Oct. 2009), p. 321. DOI: 10.1017/S0022112009007927.

[231] Malika Ouriemi, Julien Chauchat, Pascale Aussillous, Marc Médale, and Elisabeth Guazzelli. “Sediment Transport and Dunes in Pipe Flow”. In: 7th International Conference on Multiphase Flow. 2010, pp. 1–6. URL: https://hal.archives-ouvertes.fr/hal-00621110.

[232] Stein T. Johansen, Jiongyang Wu, and Wei Shyy. “Filter-Based Unsteady RANS Computations”. In: *International Journal of Heat and Fluid Flow* 25.1 (Feb. 2004), pp. 10–21. DOI: 10.1016/j.ijheatfluidflow.2003.10.005.

[233] Stein Tore Johansen and Wei Shyy. *Turbulence Modeling Using RANS Models with a Pre-Defined Filter Size*. Research Report SINTEF A27886. Trondheim: SINTEF Materials & Chemistry, 2016.

[234] K. C. Wilson and A. D. Thomas. “Analytic Model of Laminar-Turbulent Transition for Bingham Plastics”. In: *The Canadian Journal of Chemical ldots* 84 (October 2006). DOI: 10.1002/cjce.5450840502.

[235] M. Niazi Ardekani and L. Brandt. “Turbulence Modulation in Channel Flow of Finite-Size Spheroidal Particles”. In: *Journal of Fluid Mechanics* 859 (Jan. 2019), pp. 887–901. DOI: 10.1017/jfm.2018.854.

[236] Francesco Picano, Pedro Costa, Wim-Paul Breugem, and Luca Brandt. “Turbulence Modulation by Dense Suspensions in Channel Flows”. In: 10th International Symposium on Turbulence and Shear Flow Phenomena (TSFP10). Chicago, 2017, p. 6. URL: http://www.tsfp-conference.org/proceedings/2017/2/265.pdf.

[237] Iman Lashgari, Francesco Picano, Wim-Paul Breugem, and Luca Brandt. “Transition to Turbulence in the Presence of Finite Size Particles”. In: *Procedia IUTAM* 14 (2015), pp. 211–217. DOI: 10.1016/j.piutam.2015.03.042.

[238] J. Singh, M. Rudman, and H.M. Blackburn. “The Effect of Yield Stress on Pipe Flow Turbulence for Generalised Newtonian Fluids”. In: *Journal of Non-Newtonian Fluid Mechanics* 249 (Nov. 2017), pp. 53–62. DOI: 10.1016/j.jnnfm.2017.09.007.

[239] A. Maleki and I.A. Frigaard. “Axial Dispersion in Weakly Turbulent Flows of Yield Stress Fluids”. In: *Journal of Non-Newtonian Fluid Mechanics* 235 (Sept. 2016), pp. 1–19. DOI: 10.1016/j.jnnfm.2016.07.002.

[240] Angnes Ngieng Tze Tiong, Perumal Kumar, and Agus Saptoro. “Reviews on Drag Reducing Polymers”. In: *Korean Journal of Chemical Engineering* 32.8 (Aug. 2015), pp. 1455–1476. DOI: 10.1007/s11814-015-0104-0.

[241] Christopher M. White and M. Godfrey Mungal. “Mechanics and Prediction of Turbulent Drag Reduction with Polymer Additives”. In: *Annual Review of Fluid Mechanics* 40.1 (2008), pp. 235–256. DOI: 10.1146/annurev.fluid.40.111406.102156.

[242] F.T. Pinho. “A GNF Framework for Turbulent Flow Models of Drag Reducing Fluids and Proposal for a k–ε Type Closure”. In: *Journal of Non-Newtonian Fluid Mechanics* 114.2-3 (Sept. 2003), pp. 149–184. DOI: 10.1016/S0377-0257(03)00120-4.

[243] Andrey A. Gavrilov and Valeriy Ya Rudyak. “Reynolds-Averaged Modeling of Turbulent Flows of Power-Law Fluids”. In: *Journal of Non-Newtonian Fluid Mechanics* 227 (Jan. 2016), pp. 45–55. DOI: 10.1016/j.jnnfm.2015.11.006.

[244] Gianluca Iaccarino, Eric S.G. Shaqfeh, and Yves Dubief. “Reynolds-Averaged Modeling of Polymer Drag Reduction in Turbulent Flows”. In: *Journal of Non-Newtonian Fluid Mechanics* 165.7-8 (Apr. 2010), pp. 376–384. DOI: 10.1016/j.jnnfm.2010.01.013.

[245] Dhruv Mehta, Adithya Thota Radhakrishnan, Jules van Lier, and Francois Clemens. “A Wall Boundary Condition for the Simulation of a Turbulent Non-Newtonian Domestic Slurry in Pipes”. In: *Water* 10.2 (Jan. 30, 2018), p. 124. DOI: 10.3390/w10020124.

[246] Stein Tore Johansen and Sjur Mo. “Improved Fluid Control by Proper Non-Newtonian Flow Modeling”. In: Tekna Flow Assurance. Larvik, 2015. URL: https://docplayer.net/7153517-Improved-fluid-control-by-proper-non-newtonian-flow-modeling.html.

[247] Robert Sawko. “Mathematical and Computational Methods of Non-Newtonian, Multiphase Flows”. PhD thesis. Cranfield: Cranfield University, 2012. URL: https://dspace.lib.cranfield.ac.uk/handle/1826/7264.

[248] C. K. G. Lam and K. Bremhorst. “A Modified Form of the K-ε Model for Predicting Wall Turbulence”. In: *Journal of Fluids Engineering* 103.3 (Sept. 1, 1981), pp. 456–460. DOI: 10.1115/1.3240815.

[249] M. R. Malin. “Turbulent Pipe Flow of Power-Law Fluids”. In: *International Communications in Heat and Mass Transfer* 24.7 (Nov. 1997), pp. 977–988. DOI: 10.1016/S0735-1933(97)00083-3.

[250] D. W. Dodge and A. B. Metzner. “Turbulent Flow of Non-Newtonian Systems”. In: *AIChE Journal* 5.2 (June 1959), pp. 189–204. DOI: 10.1002/aic.690050214.

[251] Thomas F. Irvine. “A Generalized Blasius Equation for Power Law Fluids”. In: *Chemical Engineering Communications* 65.1 (Mar. 1988), pp. 39–47. DOI: 10.1080/00986448808940242.

[252] E. J. Novotny. “Proppant Transport”. In: *SPE Annual Fall Technical Conference and Exhibition Proceedings*. SPE Annual Fall Technical Conference and Exhibition. Denver, CO: Society of Petroleum Engineers, 1977. DOI: 10.2118/6813-MS.

[253] R. P. Chhabra and P. H. T. Uhlherr. “Sphere Motion through Non-Newtonian Fluids at High Reynolds Number”. In: *The Canadian Journal of Chemical Engineering* 58.1 (Feb. 1980), pp. 124–128. DOI: 10.1002/cjce.5450580120.

[254] A. Acharya, R. A. Mashelkar, and J. Ulbrecht. “Flow of Inelastic and Viscoelastic Fluids Past a Sphere - Part II: Anomalous Separation in the Viscoelastic Fluid Flow”. In: *Rheologica Acta* 15.9 (1976), pp. 471–478. DOI: 10.1007/BF01530349.

[255] George Gabriel Stokes. *On the Effect of the Internal Friction of Fluids on the Motion of Pendulums*. Vol. 9. Pitt Press Cambridge, 1851. URL: http://www.nawcc-index.net/Articles/Stokes-InternalFriction.pdf.

[256] D. F. McTigue, R. C. Givler, and J. W. Nunziato. “Rheological Effects of Nonuniform Particle Distributions in Dilute Suspensions”. In: *Journal of Rheology* 30.5 (Oct. 1986), pp. 1053–1076. DOI: 10.1122/1.549845.

[257] Milad Khatibi, Ekaterina Wiktorski, Dan Sui, and Rune Wiggo Time. “Experimental Study of Frictional Pressure Loss for Eccentric Drillpipe in Horizontal Wells”. In: *SPE-191046-MS*. IADC/SPE Asia Pacific Drilling Technology Conference and Exhibition. SPE: Society of Petroleum Engineers, Aug. 24, 2018, p. 18. DOI: 10.2118/191046-MS.

[258] Milad Khatibi, Rune W. Time, and Rashid Shaibu. “Dynamical Feature of Particle Dunes in Newtonian and Shear-Thinning Flows: Relevance to Hole-Cleaning in Pipe and Annulus”. In: *International Journal of Multiphase Flow* 99 (Feb. 2018), pp. 284–293. DOI: 10.1016/j.ijmultiphaseflow.2017.10.015.

[259] Sneha Sayindla, Bjørnar Lund, Jan David Ytrehus, and Arild Saasen. “Hole-Cleaning Performance Comparison of Oil-Based and Water-Based Drilling Fluids”. In: *Journal of Petroleum Science and Engineering* 159 (Nov. 2017), pp. 49–57. DOI: 10.1016/j.petrol.2017.08.069.

[260] Jan David Ytrehus, Ali Taghipour, Sneha Sayindla, Bjørnar Lund, Benjamin Werner, and Arild Saasen. “Full Scale Flow Loop Experiments of Hole Cleaning Performances of Drilling Fluids”. In: ASME, May 31, 2015, V010T11A041. DOI: 10.1115/OMAE2015-41901.

[261] Jan David Ytrehus, Bjørnar Lund, Ali Taghipour, Birgitte Ruud Kosberg, Luca Carazza, Knud Richard Gyland, and Arild Saasen. “Cuttings Bed Removal in Deviated Wells”. In: *Proceedings of the 37th International Conference on Ocean, Offshore and Arctic Engineering (OMAE2018)*. 37th International Conference on Ocean, Offshore and Arctic Engineering (OMAE2018). Madrid: American Society of Mechanical Engineers (ASME), June 17–22, 2018. DOI: 10.1115/OMAE2018-77832.

[262] A. A. Bassal. “The Effect of Drillpipe Rotation on Cuttings Transport in Inclined Wellbores”. Master’s Thesis. Department of Petroleum Engineering, University of Tulsa, 1996. URL: http://library.utulsa.edu//record=b1560102.

[263] Oney Erge, Evren M. Ozbayoglu, Stefan Z Miska, Mengjiao Yu, Nicholas Takach, Arild Saasen, and Roland May. “The Effects of Drillstring Eccentricity, Rotation, and Buckling Configurations on Annular Frictional Pressure Losses While Circulating Yield Power Law Fluids”. In: *SPE-167950-MS*. SPE: Society of Petroleum Engineers, Mar. 4, 2014. DOI: 10.2118/167950-MS.

[264] J. L. Vieira Neto, A. L. Martins, C. H. Ataíde, and M. A. S. Barrozo. “Non-Newtonian Flows in Annuli with Variable Eccentric Motion of the Inner Tube”. In: *Chemical Engineering & Technology* 35.11 (Nov. 2012), pp. 1981–1988. DOI: 10.1002/ceat.201200239.

[265] Isabele Cristina Bicalho, D.B.L. dos Santos, Carlos Henrique Ataíde, and Claudio Roberto Duarte. “Fluid-Dynamic Behavior of Flow in Partially Obstructed Concentric and Eccentric Annuli with Orbital Motion”. In: *Journal of Petroleum Science and Engineering* 137 (Jan. 2016), pp. 202–213. DOI: 10.1016/j.petrol.2015.11.029.

[266] Isabele Cristina Bicalho, José Lucas Mognon, Carlos Henrique Ataíde, and Claudio Roberto Duarte. “Fluid Dynamics Study of the Flow and Pressure Drop Analysis of a Non-Newtonian Fluid through Annular Ducts with Unusual Cross-Sections”. In: *The*

Canadian Journal of Chemical Engineering 94.2 (Feb. 2016), pp. 391–401. DOI: 10.1002/cjce.22401.

[267] Shunxin Feng, Qibing Li, and Song Fu. “On the Orbital Motion of a Rotating Inner Cylinder in Annular Flow”. In: *International Journal for Numerical Methods in Fluids* 54.2 (May 20, 2007), pp. 155–173. DOI: 10.1002/fld.1388.

[268] M. Haciislamoglu and J. Langlinais. “Non-Newtonian Flow in Eccentric Annuli”. In: *Journal of Energy Resources Technology* 112.3 (1990), pp. 163–169. DOI: 10.1115/1.2905753.

[269] Mustafa Haciislamoglu and Ulysse Cartalos. “Practical Pressure Loss Predictions in Realistic Annular Geometries”. In: *SPE-28304-MS*. SPE: Society of Petroleum Engineers, Jan. 1, 1994. DOI: 10.2118/28304-MS.

[270] M Ghazavi, M Hosseini, and M Mollanouri. “A Comparison between Angle of Repose and Friction Angle of Sand”. In: The 12th International Conference of the International Association for Computer Methods and Advances in Geomechanics (IACMAG). Goa, Oct. 1, 2008, p. 4. URL: https://citeseerx.ist.psu.edu/viewdoc/download?doi=10.1.1.384.495&rep=rep1&type=pdf.

[271] W.W. White, Zamora Mario, and C.F. Svoboda. “Downhole Measurements of Synthetic-Based Drilling Fluid in an Offshore Well Quantify Dynamic Pressure and Temperature Distributions”. In: *SPE Drilling & Completion* 12.3 (1997), pp. 12–15. DOI: 10.2118/35057-PA.

[272] Roberto Maglione, Giovanni Robotti, and Raffaele Romagnoli. “In-Situ Rheological Characterization of Drilling Mud”. In: *SPE Journal* 5 (July 2000), pp. 23–26. DOI: 10.2118/66285-PA.

[273] E. Santoyo, S. Santoyo-Gutiérrez, A. Garcia, G Espinosa, and S L Moya. “Rheological Property Measurement of Drilling Fluids Used in Geothermal Wells”. In: *Applied Thermal Engineering* 21 (2001), pp. 283–302. DOI: 10.1016/S1359-4311(00)00003-X.

[274] Yuen Philip Hoang. “A Numerical Study of Viscoelastic Flow Through an Array of Cylinders”. Master thesis. Toronto: University of Toronto, 2018. URL: https://tspace.library.utoronto.ca/handle/1807/82906.

[275] Christian Berg. “Viscoelastic Entrance Flow of Hydrolized Polyacrylamide (HPAAM)”. Master thesis. Porsgrunn: Telemark University College, 2014. URL: https://openarchive.usn.no/usn-xmlui/handle/11250/2439047 (visited on 08/28/2018).

[276] Krishna Kumar Yeleswarapu. “Evaluation of Continuum Models for Characterizing the Constitutive Behavior of Blood”. PhD thesis. Pittsburgh: University of Pittsburgh, 1996. URL: http://pittcat.pitt.edu/cgi-bin/Pwebrecon.cgi?BBID=1701699.

[277] Tejasvi Khambhampati. “A Comparative Study between Newtonian and Non-Newtonian Models in a Stenosis of a Carotid Artery”. Master thesis. College Station: Texas A&M University, 2013. URL: https://oaktrust.library.tamu.edu/handle/1969.1/151909.

[278] Zhi-Ying Zheng, Feng-Chen Li, and Juan-Cheng Yang. “Modeling Asymmetric Flow of Viscoelastic Fluid in Symmetric Planar Sudden Expansion Geometry Based on User-Defined Function in FLUENT CFD Package”. In: *Advances in Mechanical Engineering* 5 (Jan. 2013), p. 795937. DOI: 10.1155/2013/795937.

[279] P.R. Resende, K. Kim, B.A. Younis, R. Sureshkumar, and F.T. Pinho. “A FENE-P k–ε Turbulence Model for Low and Intermediate Regimes of Polymer-Induced Drag Reduction”. In: *Journal of Non-Newtonian Fluid Mechanics* 166.12 (July 1, 2011), pp. 639–660. DOI: 10.1016/j.jnnfm.2011.02.012.

[280] Simon Rogers. “Large Amplitude Oscillatory Shear: Simple to Describe, Hard to Interpret”. In: *Physics Today* 71.7 (July 2018), pp. 34–40. DOI: 10.1063/PT.3.3971.

[281] Kyu Hyun, Manfred Wilhelm, Christopher O. Klein, Kwang Soo Cho, Jung Gun Nam, Kyung Hyun Ahn, Seung Jong Lee, Randy H. Ewoldt, and Gareth H. McKinley. “A Review of Nonlinear Oscillatory Shear Tests: Analysis and Application of Large Amplitude Oscillatory Shear (LAOS)”. In: *Progress in Polymer Science* 36.12 (Dec. 2011), pp. 1697–1753. DOI: 10.1016/j.progpolymsci.2011.02.002.

[282] IM Krieger and TJ Dougherty. “A Mechanism for Non-Newtonian Flow in Suspensions of Rigid Spheres”. In: *Transactions of The Society of Rheology* III (1959), pp. 137–152. URL: http://scitation.aip.org/content/sor/journal/tsor/3/1/10.1122/1.548848.

[283] Mateus Palharini Schwalbert, Paulo Laranjeira da Cunha Lage, and Argimiro Resende Secchi. "Simulation of Non-Isothermal Non-Newtonian Flow with Multi-Region Thermal Coupling". In: 22nd International Congress of Mechanical Engineering. Ribeirão Preto, Nov. 3, 2013. URL: http://www.abcm.org.br/pt/wp-content/anais/cobem/2013/PDF/724.pdf.

[284] O. Desjardins, R.O. Fox, and P. Villedieu. "A Quadrature-Based Moment Method for Dilute Fluid-Particle Flows". In: *Journal of Computational Physics* 227.4 (Feb. 2008), pp. 2514–2539. DOI: 10.1016/j.jcp.2007.10.026.

[285] Dan Sun, Andrew Garmory, and Gary J. Page. "A Robust Two-Node, 13 Moment Quadrature Method of Moments for Dilute Particle Flows Including Wall Bouncing". In: *Journal of Computational Physics* 330 (Feb. 2017), pp. 493–509. DOI: 10.1016/j.jcp.2016.11.025.

[286] Schalk Cloete, Stein Tore Johansen, and Shahriar Amini. "Performance Evaluation of a Complete Lagrangian KTGF Approach for Dilute Granular Flow Modelling". In: *Powder Technology* 226 (Aug. 2012), pp. 43–52. DOI: 10.1016/j.powtec.2012.04.010.

[287] Andrey A. Gavrilov and Valeriy Ya. Rudyak. "A Model of Averaged Molecular Viscosity for Turbulent Flow of Non-Newtonian Fluids". In: *Journal of Siberian Federal University. Mathematics & Physics.* 7.1 (2014), pp. 46–57. URL: http://mi.mathnet.ru/jsfu345.

[288] Anshuman Roy and Ronald G. Larson. "A Mean Flow Model for Polymer and Fiber Turbulent Drag Reduction". In: *Applied Rheology* 15.6 (2005), pp. 370–389. DOI: 10.3933/ApplRheol-15-370.

[289] D. Keith Walters and Davor Cokljat. "A Three-Equation Eddy-Viscosity Model for Reynolds-Averaged Navier–Stokes Simulations of Transitional Flow". In: *Journal of Fluids Engineering* 130.12 (2008), p. 121401. DOI: 10.1115/1.2979230.

[290] Robin B. Langtry and Florian R. Menter. "Correlation-Based Transition Modeling for Unstructured Parallelized Computational Fluid Dynamics Codes". In: *AIAA Journal* 47.12 (Dec. 2009), pp. 2894–2906. DOI: 10.2514/1.42362.

[291] Josip Zoric, Stein Tore Johansen, Kristian Etienne Einarsrud, and Asbjorn Solheim. “On Pragmatism in Industrial Modeling”. In: *CFD 2014 - 10th International Conference on Computational Fluid Dynamics in the Oil & Gas, Metallurgical and Process Industries*. Ed. by Stein Tore Johansen and Jan Erik Olsen. Trondheim: SINTEF, 2014, pp. 1–16. URL: http://hdl.handle.net/11250/2464595.

[292] H.M. Blackburn and S.J. Sherwin. “Formulation of a Galerkin Spectral Element–Fourier Method for Three-Dimensional Incompressible Flows in Cylindrical Geometries”. In: *Journal of Computational Physics* 197.2 (July 2004), pp. 759–778. DOI: 10.1016/j.jcp.2004.02.013.

[293] Madhava Syamlal. *MFIX Documentation Numerical Technique*. Morgantown: U.S. Department of Energy, Office of Fossil Energy, 1998. URL: http://dx.doi.org/10.2172/656644.

[294] A. Passalacqua and R.O. Fox. “Implementation of an Iterative Solution Procedure for Multi-Fluid Gas–Particle Flow Models on Unstructured Grids”. In: *Powder Technology* 213.1-3 (Nov. 2011), pp. 174–187. DOI: 10.1016/j.powtec.2011.07.030.

[295] Cesar M. Venier, Santiago Marquez Damian, and Norberto M. Nigro. “Numerical Aspects of Eulerian Gas–Particles Flow Formulations”. In: *Computers & Fluids* 133 (July 2016), pp. 151–169. DOI: 10.1016/j.compfluid.2016.05.003.

[296] Ernst A. Meese and Stein Tore Johansen. “A Simulation Concept for Generic Simulation of Multi-Material Flow Using Staggered Cartesian Grids”. In: *Progress in Applied CFD–CFD2017 Selected Papers from 12th International Conference on Computational Fluid Dynamics in the Oil & Gas, Metallurgical and Process Industries*. Trondheim: SINTEF akademisk forlag, 2017, pp. 253–263. URL: http://hdl.handle.net/11250/2480173 (visited on 12/07/2018).

[297] Son Tung Dang, Stein Tore Johansen, and Ernst A Meese. “A Cartesian Cut-Cell Method, Based on Formal Volume Averaging of Mass, Momentum Equations”. In: *Progress in Applied CFD–CFD2017 Selected Papers from 12th International Conference on Computational Fluid Dynamics in the Oil & Gas, Metallurgical and Process Industries*. Trondheim: SINTEF akademisk forlag, 2017. URL: http://hdl.handle.net/11250/2480172.

[298] Son Tung Dang, Ernst Arne Meese, John Christian Morud, and Stein Tore Johansen. "Numerical Approach for Generic Three-phase Flow Based on Cut-cell and Ghost Fluid Methods". In: *International Journal for Numerical Methods in Fluids* (July 5, 2019), fld.4758. DOI: 10.1002/fld.4758.

List of Figures

A

Publications

A.1. Main contributions

The bibliography lists papers in the order as they appear in the text. The order at which papers are provided in the individual appendices is based on the publication type instead: Journal paper, Conference paper, Report, Manuscript.

Note that preliminary results of the papers [**I**, **II**, **VIII**] were presented at scientific conferences. The references of the respective conference papers [**IX**, **X**, **XVI**] are given in appendix A.2.

Preliminary results of this thesis were also presented at the following events:

- Equinor Hole Clearing Workshop. Equinor, Stavanger, Norway, 2018.
- Final Report Meeting of the AdWell project. IRIS, Stavanger, Norway, 2018.
- The second AdWell Open Seminar. UiS, Stavanger, 2017.

[**I**] A. Busch, A. Islam, D. Martins, F. P. Iversen, M. Khatibi, S. T. Johansen, R. W. Time, and E. A. Meese. “Cuttings Transport Modeling - Part 1: Specification of Benchmark Parameters with a Norwegian Continental Shelf Perspective”. In: *SPE Drilling & Completion* 33.2 (2018). DOI: 10.2118/180007-PA.

[**II**] Alexander Busch and Stein T. Johansen. “An Eulerian-Lagrangian CFD Study of a Particle Settling in an Orthogonal GNF Shear Flow”. In: *Journal of Non-Newtonian Mechanics* 263 (2019), pp. 77–103. DOI: 10.1016/j.jnnfm.2018.11.005.

[III] Alexander Busch, Benjamin Werner, and Stein T. Johansen. "Cuttings Transport Modeling - Part 2: Dimensional Analysis and Scaling". In: *SPE Drilling & Completion* 35.01 (2020), pp. 69–87. DOI: 10.2118/198907-PA.

[IV] Alexander Busch, Velaug Myrseth, Milad Khatibi, Paal Skjetne, Sigve Hovda, and Stein Tore Johansen. "Rheological Characterization of Polyanionic Cellulose Solutions with Application to Drilling Fluids and Cuttings Transport Modeling". In: *Applied Rheology* 28.2 (2018), pp. 1–16. DOI: 10.3933/ApplRheol-28-25154.

[V] Alexander Busch and Stein Tore Johansen. "On The Validity Of The Two-Fluid-KTGF Approach For Dense Gravity-Driven Granular Flows as Implemented in ANSYS Fluent R17.2". In: *Powder Technology* 364 (2020), pp. 429–456. DOI: 10.1016/j.powtec.2020.01.043.

[VI] Alexander Busch, Milad Khatibi, Stein T. Johansen, and Rune W. Time. "A 2D Sediment Bed Morphodynamics Model for Turbulent, Non-Newtonian, Particle-Loaded Flows". In: *Progress in Applied CFD - CFD2017*. The 12th International Conference on CFD in Oil & Gas, Metallurgical and Process Industries (CFD2017). Trondheim: SINTEF, May 30, 2017. URL: https://www.sintefbok.no/book/index/1119/progress_in_applied_cfd_cfd2017.

[VII] Alexander Busch, Are Simonsen, and Stein Tore Johansen. "DNS vs. RANS Turbulence Modeling of Turbulent Pipe and Annular Flows of Shear-Thinning Fluids". In: *Unpublished, in progress.* (2019).

[VIII] Alexander Busch and Stein Tore Johansen. "Cuttings Transport: On the Coupled Effect of Drillpipe Rotation and Lateral Motion". In: *Journal of Petroleum Science and Engineering* 191 (2020), pp. 1–27. DOI: 10.1016/j.petrol.2020.107136.

Journal paper 1 (I)

Cuttings Transport Modeling - Part 1: Specification of Benchmark Parameters with a Norwegian Continental Shelf Perspective

Alexander Busch, Aminul Islam, Dwayne Martins, Fionn P. Iversen, Milad Khatibi, Stein Tore Johansen, Rune W. Time, Ernst A. Meese

SPE Drilling & Completion, Vol. 33, Issue 2, 2018.

DOI: 10.2118/180007-PA.

Not included due to copyright restrictions

Journal paper 2 (III)

Cuttings Transport Modeling - Part 2: Dimensional Analysis and Scaling

Alexander Busch, Benjamin Werner, Stein Tore Johansen

SPE Drilling & Completion, Vol. 35, Issue 1. 2020.

DOI: 10.2118/198907-PA.

Journal paper 3 (IV)

Rheological characterization of Polyanionic Cellulose solutions with application to drilling fluids and cuttings transport modeling

Alexander Busch, Velaug Myrseth, Milad Khatibi, Paal Skjetne, Sigve Hovda, Stein Tore Johansen

Applied Rheology, Vol. 28, Issue 2, 2018.

DOI: 10.3933/ApplRheol-28-25154.

Applied Rheology | DOI: 10.3933/APPLRHEOL-28-25154 | WWW.APPLIEDRHEOLOGY.ORG

RHEOLOGICAL CHARACTERIZATION OF POLYANIONIC CELLULOSE SOLUTIONS WITH APPLICATION TO DRILLING FLUIDS AND CUTTINGS TRANSPORT MODELING

ALEXANDER BUSCH[1], VELAUG MYRSETH[2], MILAD KHATIBI[3], PAAL SKJETNE[4], SIGVE HOVDA[1],
STEIN TORE JOHANSEN[1, 4]

[1]Norwegian University of Science and Technology (NTNU), Kolbjørn Hejes Vei 1B, 7491 Trondheim, Norway
[2]SINTEF Petroleum Research AS, Thormøhlens Gate 53c, 5006 Bergen, Norway
[3]University of Stavanger (UiS), Kristine Bonnevies Vei 22, 4021 Stavanger, Norway
[4]SINTEF Materials and Chemistry, S.P. Andersens veg 15B, 7494 Trondheim, Norway

*Corresponding author: alexander.busch@alumni.ntnu.no

Received: 3.10.2017, Final version: 15.3.2018

ABSTRACT:
In petroleum drilling, aqueous Polyanionic Cellulose solutions (PAC) are often used as a drilling fluid model system in experimental laboratory studies to investigate cuttings transport. Cuttings transport refers to the transportation of drilled-off solids out of the wellbore. In these studies, PAC solutions are typically assumed to behave purely viscous, i.e. they do not show time-dependent/thixotropic and/or viscoelastic properties. In this study, a rheological characterization of PAC has been performed in combination with an evaluation of time scales characterizing the fluid to verify the conventional assumption of a purely-viscous fluid. It is found that PAC solutions are generally not purely viscous: They feature viscoelastic behavior on time scales of the order of 0.01 to 1 s, such as normal stress differences, as well as thixotropic behavior on larger time scales of the order of 10 to 1000 s because of their polymeric microstructure. If simplified to a purely viscous fluid, the degree of uncertainty in representing the measured apparent shear viscosity may increase by an order of ≈ 75 to 90 % depending on the relevant time scale. When obtaining flow curves, a sufficiently long measurement point duration (sampling time for a particular torque reading) is required to ensure that the liquid microstructure has reached its dynamic equilibrium at the desired shear rate. Due to their polymeric nature, PAC solutions feature Newtonian viscosity plateaus at both low and high shear rates. For modeling purposes, the application of a Cross/Carreau material function is recommended because it both best describes the flow curve data and minimizes extrapolation errors compared to the conventionally used Power Law material function.

KEY WORDS:
Rheological characterization, modeling, CFD, cuttings transport, flow curves, thixotropy, viscoelasticity, uncertainty, time scales

1 INTRODUCTION

Polyanionic Cellulose (PAC) is frequently used as drilling fluid viscosifier in oil drilling [1–6] and, dissolved in distilled water, as drilling fluid substitute in cuttings transport studies [7–16] or other multiphase flow studies [17–19] relevant to the oil & gas industry. Cuttings transport is the process of adequately flushing drilled-off solids (“cuttings”) out of a petroleum wellbore. Inadequate flushing of cuttings from the bore hole (poor hole cleaning) leads to accumulation of solids in the wellbore. Problems associated with cuttings transport are a major contributor to downtime during drilling operations. In drilling fluids, PAC may act as a loss agent (preventing loss of drilling fluids into permeable formations) as well as a viscosifying agent (developing viscosity depending on concentration and other variables such as water chemistry and salinity). In laboratory studies of cuttings transport, PAC is used as a drilling fluid substitute, i.e. a drilling fluid model system, since it yields transparent, non-hazardous, shear-thinning fluids when added to (distilled) water. The translucency allows for optical investigations of the flow as well as optical measurement techniques such as particle image velocimetry.

The relationship between experimental cuttings transport studies in a laboratory, the real drilling process (cuttings transport in a wellbore), and cuttings transport modeling as well as the role of rheometric testing

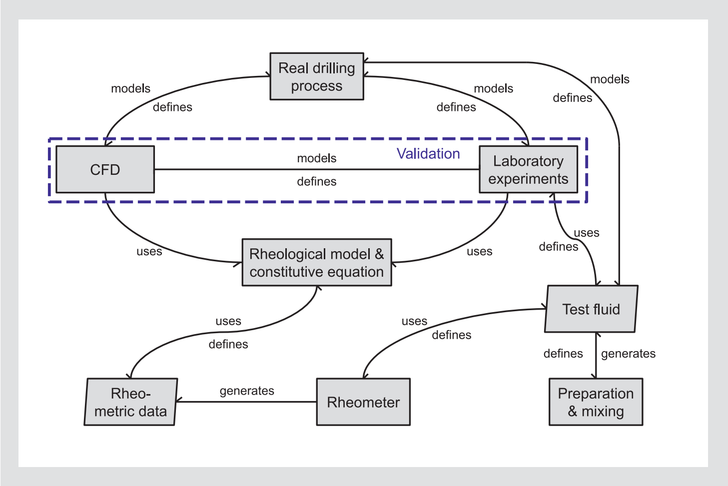

Figure 1: Overview of cuttings transport modeling via CFD and/or laboratory experiments and the role of rheometric testing.

is conceptually depicted in Figure 1. PAC may be used both in the real drilling process, e.g. as a viscosifying agent, and/or in an experimental study in a laboratory as a test fluid modeling the real drilling fluid. Numerical modeling of cuttings transport using e.g. Computational Fluid Dynamics (CFD) methods is another methodology, which may be used to investigate cuttings transport, or more generic, multiphase problems [a]. CFD results are usually validated against experimental data generated in the laboratory. CFD models require a constitutive equation describing the fluid's rheology [b]. In the petroleum industry, both on engineering and research level, drilling fluids in 3D CFD cuttings transport studies are typically modeled as incompressible and purely viscous, i.e. Generalized Newtonian Fluids (GNF), where the stress tensor of the Cauchy equations of motion is given as

$$T = -pI + 2\eta(\dot{\gamma})D \tag{1}$$

where D is the rate of deformation tensor

$$D = \frac{1}{2}\left[\nabla u_i + \left(\nabla u_j\right)^T\right] \tag{2}$$

and the shear rate $\dot{\gamma}$ is a total shear measure defined as

$$\dot{\gamma} = \sqrt{2D:D} \tag{3}$$

In Equation 1, the apparent dynamic shear viscosity $\eta(\dot{\gamma})$ of the fluid may be a function of the shear rate $\dot{\gamma}$ or is constant in case of Newtonian fluids. Commonly used models in the drilling industry to represent $\eta(\dot{\gamma})$ are the Bingham model [20] (accounting for yield stress phenomena), the Ostwald/de Waele "Power law" (PL) [21] (accounting for shear-thinning behavior) or the Herschel-Bulkley (HB) model [22] being a combination of the former two. More sophisticated models such as the Cross [23] or Carreau [24] models (accounting for limiting viscosities at both low and high shear rates) are used on a very limited basis. Higher-order fluid descriptions, i.e. constitutive equations accounting for time-dependent and/or viscoelastic behavior, have – to the awareness of the authors – not been applied in CFD cuttings transport studies.

The selection of a particular type of material function for the apparent viscosity $\eta(\dot{\gamma})$ is based on the particular rheometric data available. A rheological model for the fluid under consideration is built by fitting the material function to the rheometric data in order to obtain numerical values for the corresponding model coefficients. Rheometric data is obtained from rheometric testing, e.g. obtaining value pairs of the apparent viscosity vs. shear rate in case of a GNF, for the fluids used in the experiment. Alternatively, one may deduce rheometric data from available experimental pressure loss data using a pipe viscometer [25]. Both real drilling fluids, which may show any combination of shear-thinning, yield stress, viscoelastic and thixotropic behavior, and model drilling fluids such as e.g. aqueous PAC solutions, may be used as experimental fluids. Preparing and mixing of constituent components is important for both real and model fluids.

Polyanionic cellulose (PAC) is a water-soluble biopolymer derived from carboxymethyl cellulose (CMC, E466) with a high degree of substitution (DS) of hydroxyl groups with sodium (NaCl), i.e. PAC is a high-quality sodium CMC with higher DS and thus molecular weight (Mw) [26]. Like sodium CMC, PAC is produced from naturally occurring cellulose by etherification, where hydroxyl groups are substituted with sodium groups. The properties of the polymers, such as viscosity, and molecular weight may be tailored by substitution of other functional groups into the chain. The DS determines the specific performance. As opposed to sodium CMC ($0.4 < DS < 0.8$ [26]), PAC features a $DS > 0.9$ [27] and features less residual sodium [28]. In drilling fluids, the main advantage of PAC compared to CMC is the better resistance to salt which provides improved shale inhibition characteristics as well as filtrate control [27]. The anions stabilize clay particles which improves filter cake texture and reduce risk of swelling of clay rich formations. However, salts do have a strong impact on the rheology of PAC and may even cause transition to Newtonian be-

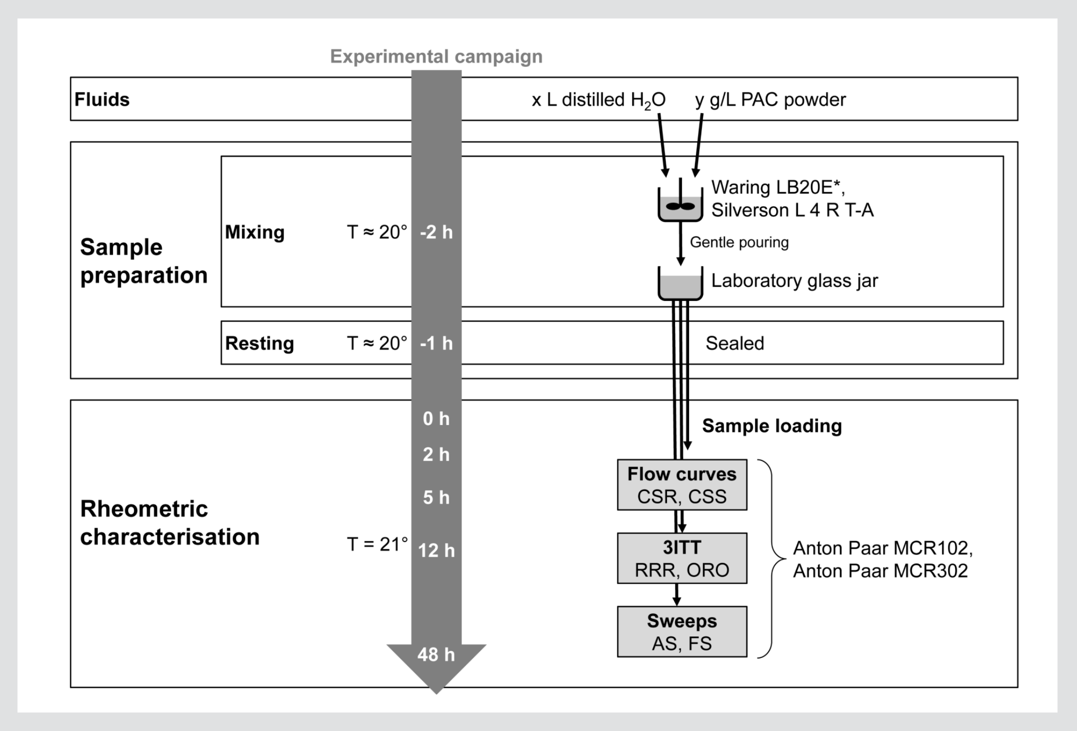

Figure 2: Test plan as applied in this study. Monitoring of natural degradation of fluid over duration of experimental campaign by obtaining flow curves at times indicated. All preparation and testing was conducted at ambient pressure, i.e. $p \approx 101325$ Pa.

havior [29]. For CMC solutions it is known that they are generally shear-thinning and viscoelastic [30, 31] and feature thixotropic-like behavior [31–33]. They generally seem to obey the Cox-Merz rule [30]. However, as a consequence of restructuring processes they deviate from the Cox-Merz rule at high shear [34]. PAC solutions have so far been investigated much less. Given their relation to CMC, it is not surprising that they feature shear-thinning and viscoelastic properties [2].

The rheological information of aqueous PAC solutions used in cuttings transport studies [7–16] is usually disclosed in the form of model coefficients, such as the Ostwald/de Waele “Power law” model [21], without any indication of the uncertainty of the measurements and model fit. PAC solutions in these studies are considered purely viscous, i.e. they are considered to feature neither viscoelastic nor time-dependent/shear-history dependent properties [7–15,17, 18, 19] and are thus modeled as GNF, most commonly employing a PL model. However, indication of viscoelastic [2, 16] and time-dependent [19, 29] behavior of PAC solutions exists, which is not surprising given the polymeric nature of PAC solutions.

This paper reports a complete rheological characterization of PAC solutions with regards to apparent viscosity, yield stress, time-dependent behavior, and viscoelastic properties. Characteristic time scales of the fluid (further referred to as ”rheological time scales”) are derived from the experimental data gathered. An estimate of the uncertainty associated with simplification of the physics of the fluid by assuming a purely shear-thinning rheology, i.e. treating it as a GNF is provided. In Section 2, we present the methodology and materials used to obtain the experimental data along with definitions of some of the rheological time scales later used in the interpretation of data. In Section 3, the different rheometric test results are presented along with the derived time scales. Section 4 provides a discussion of the rheometric testing results as well as the corresponding time scales. Finally, in Section 5, a conclusion and outlook is provided.

2 MATERIALS & METHODS

2.1 EQUIPMENT AND GENERAL RHEOMETRIC TEST PROTOCOL

Various rheometric tests were performed on different PAC solutions (generated with the same PAC granules) with two different rheometers:

- Flow curves (FC), with both controlled shear rate (CSR) and controlled shear stress (CSS)
- Amplitude sweeps (AS) with constant angular frequency as well as frequency sweeps (FS) with constant strain
- 3 interval time tests (3ITT), with rotational-rotational-rotational (RRR) interval settings

Figure 2 provides a timeline overview of this study's test protocol. The individual process steps (mixing, resting, rheometric measurements) will be presented in the following sections. To monitor phenomena such as natural degradation, fermentation, or off-gassing, additional flow curves were obtained regularly during the rheometric characterization at the times indicated in Figure 2 (0, 2, 5, 12, 48 h) with fresh samples from the prepared fluid stored in the glass jar. Due to equipment availability, different mixers and rheometers operated by different operating personnel were utilized, as depicted in Figure 2. The majority of the data was generated with the Waring LB20E*/Anton Paar MCR102 combination. Additional testing was conducted with the Silverson L4RT-A/Anton Paar MCR302 combination to supplement and cross-check the results.

The measuring systems utilized were concentric cylinders (CC27) with a gap size of 1.13 mm, conical bottom, and a nominal sample volume of 19.35 ml. The accuracy of the rheometers is specified with ± 5 % relative SD (SDr) for a torque $T > 5$ nNm for rotation and $T > 7.5$ nNm for oscillation in case of the MCR102 and $T > 1$ nNm and $T > 0.5$ nNm in case of the MCR302, respectively. An accuracy of ±1% SDr is specified for $T > 10\ \mu$Nm [35]. For the CC27 geometry utilized, the latter may be converted [36] to an apparent viscosity threshold given by

$$\eta_{min} \approx 2.02 \cdot 10^{-1}\, \dot{\gamma}^{-1} \tag{4}$$

In case of higher shear rates, i.e. rotation speeds, inertial instabilities such as Taylor vortices may develop. For the CC27 geometry utilized and a gap-dependent critical Taylor number of 1884 [37], the maximum apparent viscosity threshold to avoid Taylor vortices is then given by

$$\eta_{max} \approx 8.389 \cdot 10^{-6}\, \dot{\gamma} \tag{5}$$

2.2 FLUIDS

MI-Swaco Polypac R, as used in this study, is a white, odorless granulated powder with a molecular mass of 881.2 kDa (Mw). No treatment method such as aging [38] was applied. Three different mixtures of MI-Swaco Polypac R and distilled water as summarized in Table 1 were used for all tests. The concentrations were chosen such that a typical drilling fluid apparent viscosity range [39] is covered. Most tests were done on PAC2 and PAC4, as these concentrations represent an apparent viscosity range resulting in transitional wellbore flows.

2.3 SAMPLE PREPARATION, RESTING, AND LOADING

Two different types of mixers as given in Figure 2 were used to mix the granular PAC with distilled water. The mixers were non-compliant with ISO 10416 [38] because they did not feature the required high-speed range. To obtain homogenously mixed samples for rheometric testing with the available mixers, the mixing procedures given in Table 2 were established and followed to prepare all samples. The utilized rotational speeds of the different mixers during "Addition" and "Mixing" are a resulting best-working and mixer-dependent compromise of two contradictory requirements":

- In order to keep the developing viscosity low and ensure homogenous mixing, the rotational speed has to be as high as possible
- In order to entrain as little air as possible during mixing, the rotational speed has to be as low as possible

After mixing, air bubbles were observed in all samples. However, in the case of the Waring LB20E* mixer, the observed bubbles were considerably smaller, probably due to the higher mixing speed utilized. After the resting periods, no air bubbles were observed in either sample. The respective resting times were mainly due to laboratory availability constraints. However, a resting interval of 1 hour represents a realistic industrial time frame as applied by drilling service companies that perform onsite rheological measurements on drilling fluids on a daily basis. The fluid samples were gently poured from

Fluid	PAC concentration [wt%]	 [ppm]	 [g/L]	Mix. density [kg/m³]
PAC2	0.2	2000	2	998.0
PAC4	0.4	4000	4	998.2
PAC8	0.8	8000	8	999.0

Table 1: Fluid specification ($T = 21°C$, distilled H_2O).

Process steps	Waring LB20E*/	Silverson L4RT-A
Preparation	Depending on the concentration required, a pre-calculated amount of PAC granules was established using a laboratory scale.	
Addition	Running the mixer at low speeds (400-900 rpm), the PAC granules were slowly and evenly (in order to ensure all particles to become individually wetted) added to the first half of the distilled water using a spatula at the position of assumed highest shear over the mixing blades. After full addition of the PAC granules, the second half of water was gently added to the mixture.	Running the mixer at fairly high speed (3000 rpm), the PAC granules were slowly and evenly (in order to ensure all particles to become individually wetted) added to the first half of the distilled water using a spatula at the position of assumed highest shear over the mixing blades. After full addition of the PAC granules, the second half of water was gently added to the mixture.
Mixing	The mixer was set to higher speeds (3300 rpm) for half an hour.	The mixer was set to lower speeds (2000 rpm) for half an hour.
Resting	The solutions were transferred to glass jars, sealed and were left to rest at ambient temperature (T ≈ 20°) for a minimum of 1 hour prior to measurements.	The solutions were transferred to glass jars, sealed and were left to rest in a dark place at ambient temperature (T ≈ 20°) for a minimum of 48 hours prior to measurements.

Table 2: Sample preparation procedures.

the glass jar into the cylinder of the rheometers measuring system up to the marking line. The cylinder was inserted into its fixture on the rheometer and the measurement system/inner cylinder was lowered into the outer cylinder containing the sample. Measurements were not started until the rheometers indicated a steady temperature of 21 °C.

2.4 RHEOMETER SETTINGS

The main rheometer settings of the different tests conducted in this study are summarized in Table 3. Temperature was controlled to T = 21 °C by the rheometers in all cases. All measurements were conducted at ambient pressure. The reason is that typically cuttings transport studies are also conducted at ambient conditions and temperature scaling of polymeric solution is fairly well understood [31, 32]. No pre-shearing was conducted in any of the tests summarized in Table 3. Standard pre-shearing definitions do not exist in the petroleum industry [38, 40, 41], other than that typically Fann rheometer measurement are conducted as a downward sweep, i.e. from high to low shear rates. Pre-shearing as used in various studies has been quite subjective, and has for instance been based on the high shear rates experienced at the drill bit. As the fluids resting time at the drill bit is very short, the relevance of such high pre-shear is not clear. Moreover, our overall objective is numerical cuttings transport modeling, where the computational domain is an annular subsection quite some distance from the bit. The influence of the high shear rate at the bit (applied to the fluid in a very short time only) is not expected to be of much relevance at an arbitrary wellbore element far from the bit. Finally, any other pre-shear would either be subjective or have to be based on the wall or average shear rate of annular flow, which is a function of fluid velocity, wellbore geometry, and flow exponent n, i.e. problem-specific. Thus, we decided for the following reproducible and unified approach: After gentle pouring of the sample into the measurement cylinder all samples where subject to a resting time (≈ 30 – 90 s) until the rheometers temperature control reached the set point of T = 21 °C.

Test	Anton Paar MCR102	Anton Paar MCR302
FC	Upward and downward sweeps with $\dot{\gamma}$ = 0.01…1200 s^{-1} (typical cuttings transport shear rate range[8]) in a CSR mode with a constant measurement point duration[9] (MPD) Δt = 5 s.	As Anton Paar MCR102, but with logarithmically decreasing MPD Δt = 120…2 s log for the upward sweep and vice-versa for the downward sweep.
AS	Fixed angular frequency ω = 10 rad/s and logarithmically increasing strain γ = 0.1…1000%.	
FS	Fixed strain γ = 0.02% and logarithmically increasing angular frequency ω = 0.1…100 rad/s.	
3ITT	Low rotational shear intervals $\dot{\gamma}$ = 0.1 s^{-1} and an intermediate high rotational shear interval with $\dot{\gamma}$ = 1200 s^{-1} for 50 s and 600 s.	

Table 3: Rheometer settings.

Note that for every rheometric measurement, a fresh sample from the glass jar was loaded into the rheometer and discharged after the measurement. Hence, every measurement was performed with a sample having a relatively comparable state of microstructure, since the shearing due to pouring should be equal for all the samples used.

2.5 RHEOLOGICAL TIME SCALES OF THE FLUID

Various microscopic effects such as molecular motion (in the order of 10 – 15 seconds and therefore negligible) or structural changes may occur in a complex fluid. Consequently, there exists a corresponding variety of characteristic time scales for the respective relaxation times. Particular formulations of these fluid time scales often depend on the constitutive equations and/or material function used and may also depend on test data available. Since the degree of viscoelasticity and thixotropy is to be estimated, four rheological time scales are defined as follows [42]:

- The GNF relaxation times λ_{PL} and λ_{Cr}, which are based on the respective GNF material models, namely the Ostwald/de Waele "Power law" (PL) model [21] in its rearranged form, where the ordinary PL coefficient K_{PL} is expressed as $K_{PL} = \mu_o(\lambda)^{n_{PL}-1}$, which then yields

  $$\eta(\dot{\gamma}) = \mu_o \left(\lambda_{PL}\dot{\gamma}\right)^{n_{PL}-1} \tag{6}$$

  and the Cross (Cr) [23] model

  $$\eta(\dot{\gamma}) = \left(\mu_o - \mu_\infty\right)\left(1 + \left(\lambda_{Cr}\dot{\gamma}\right)^{n_{Cr}-1}\right) + \mu_\infty \tag{7}$$

  Note that the PL material function may be considered a special case of the Carreau [24] material function

  $$\eta(\dot{\gamma}) = \left(\mu_o - \mu_\infty\right)\left[1 + \left(\lambda_{Ca}\dot{\gamma}\right)^2\right]^{\frac{n_{Ca}-1}{2}} + \mu_\infty \tag{8}$$

  which approaches a PL material function for the case of higher shear rates and neglected infinite-shear viscosity μ_∞. Hence, the model coefficients in Equation 6 may be considered equivalent to the coefficients and fit of a Carreau material function; however, they are not exactly identical.
- The "Recoverable Shear"-based relaxation time λ_{RS}, which is constructed from the GNF PL coefficients and coefficients of a PL fit of the First Normal Stress Difference (FNSD).

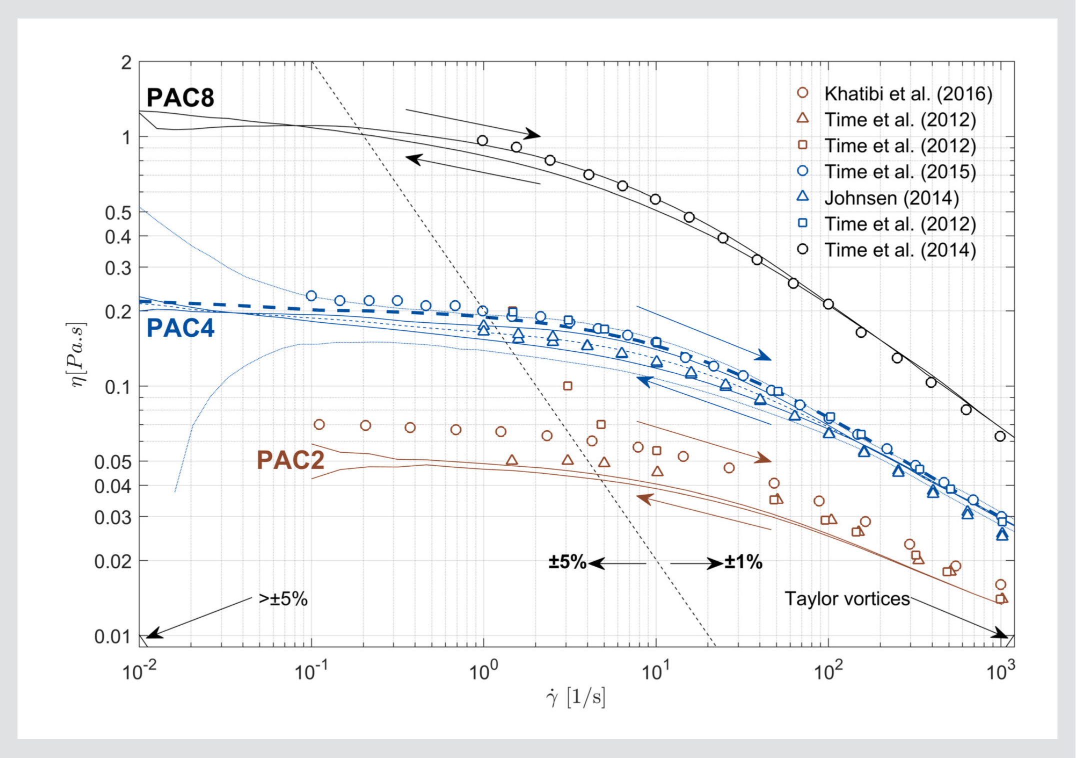

Figure 3: Flow curves (FC) for different concentrations tested and FC obtained from the literature. Solid lines are means of upward and downward sweeps, respectively (PAC4 based on 13, all others based on three consecutive measurements), the means of the two sweeps are represented by the dashed lines. Small dotted lines represent means of up-/downward sweep ± 3SD, thick dashed line represents logarithmic MPD. Colored arrows indicate direction of rheometer sweeps. The dashed black line indicates the rheometer accuracy [35] threshold as given by Equation 4, the smaller black lines in the bottom left and right corners indicate the end of the rheometer accuracy threshold and the beginning of the Taylor vortices regime as given by Equation 5, respectively.

$$\lambda_{RS} = \left(\frac{K_{FNSD}}{2K_{PL}}\right)^{\left(\frac{1}{n_{FNSD}-n_{PL}}\right)} \tag{9}$$

A PL material function does not capture the Newtonian viscosity plateaus at low and high shear rates. Therefore, PL coefficients are determined for a given point of the flow curve with the following conditions:

$$\eta_{PL}(\dot{\gamma}) = \eta_{Cr}(\dot{\gamma}) \tag{10a}$$

$$\frac{\partial \eta_{PL}(\dot{\gamma})}{\partial \dot{\gamma}} = \frac{\partial \eta_{Cr}(\dot{\gamma})}{\partial \dot{\gamma}} \tag{10b}$$

- The Maxwell relaxation time λ_{Max} which is based on the linear viscoelastic Maxwell model represents time scales on which the fluid acts in a linear viscoelastic manner.

$$\lambda_{Max}(\omega) = \frac{G'(\omega)}{\omega G''(\omega)} \tag{11}$$

Experimental FS data may be used to estimate the order of magnitude of these time scales.

- The 3ITT relaxation time λ_{3ITT} is estimated based on time-dependent changes of the apparent viscosity due to instantaneous start-up/shut-down of a steady shear flow using 3ITT data. An exponential function of the form

$$\eta(t) = \eta_\infty + (\eta_o - \eta_\infty) e^{-\frac{1}{\lambda_{3ITT}} t} \tag{12}$$

is used for this purpose, with the rheological relaxation time λ_{3ITT} being the corresponding time constant it takes to relax to 63% to the dynamic equilibrium value.

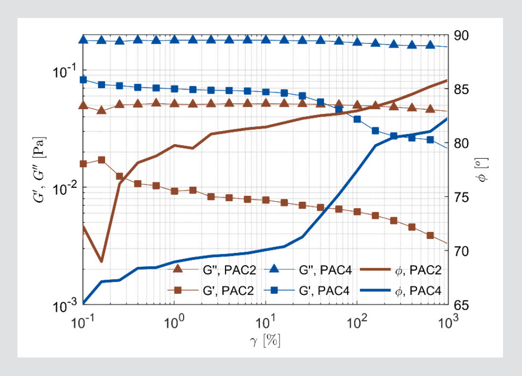

Figure 4: Amplitude sweeps (ω = 10 rad/s) for PAC2 and PAC4.

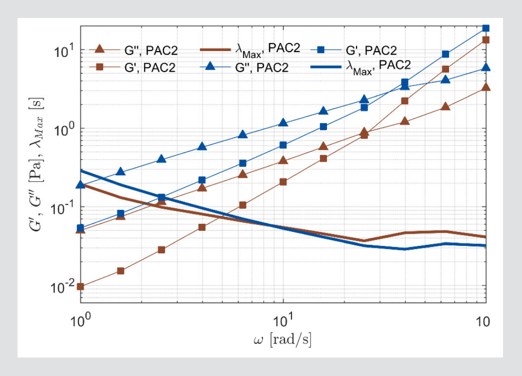

Figure 5: Frequency sweeps (γ = 0.2 %) for PAC2 and PAC4.

3 RESULTS

3.1 FLOW CURVES

A flow curve (FC) is considered to represent the equilibrium apparent shear viscosity of a fluid sample over a range of relevant shear rates. Figure 3 depicts the obtained FCs for all PAC concentrations. The apparent viscosity indicated is the mean of 13 (PAC4) and three (PAC2, PAC8) measurements. Additionally, data obtained from the literature is displayed using unfilled symbols. For all concentrations tested with a constant MPD of Δt = 5 s, a prominent hysteresis effect was found. Figure 3 shows two solid lines for each PAC solution, representing means of the upward (higher curve) and downward (lower curve) sweep respectively, the mean of these two means is represented by the solid line. The FC obtained with a logarithmically decreasing MPD of Δt = 120 - 2 s log (here depicted with a thick dashed line) shows almost no hysteresis effect and thus may be considered the equilibrium FC [43]. Most of the FC data sets from the literature do not show any hysteresis effect. However, the data of Johnsen (2014) [13] and [18] (not displayed) also indicate a small hysteresis effect for intermediate shear rates. Additionally, in the case of PAC4, the natural scatter of the whole measurement process was identified through measurements of 13 FC (Not depicted in Figure 3). Each FC was obtained with a fresh sample from the prepared mixtures. Arithmetic mean and standard deviation (SD) were established for both upward and downward sweeps separately. For PAC4, the obtained mean ± 3 SD of upward/downward sweeps are respectively indicated in Figure 3 by dotted lines.

All results indicate a constant Newtonian viscosity at low shear rates for all tested concentrations. FCs obtained with a constant MPD of Δt = 5 s show a large variance of data at very low shear rates, as indicated by the diverging dotted lines in Figure 3. Most of the FC data sets from the literature do not cover the low shear rate range ($\dot{\gamma}$ = 0.01 - 1 s^{-1}). However, Time et al. [19] and Khatibi et al. [29] have covered the shear rate range $\dot{\gamma}$ = 0.1 - 1 s^{-1} and the respective data sets also do indicate a Newtonian viscosity plateau in the low shear rate range. The different data sets plotted in Figure 3 are not coinciding for a particular fluid concentration. However, in case of PAC4, most datasets are fully enclosed by the arithmetic mean ± 3 SD boundaries of our data. The five FCs obtained in order to monitor natural degradation (as described in Figure 2, not displayed in Figure 3), are within the arithmetic mean ± 3SD boundaries. No time-dependency, i. e. different FC at different points in time, was observed over the duration of the experimental campaign. Fitting the PL, Carreau and Cross material functions (Equations 6 – 8) to the equilibrium FCs yields model coefficients as summarized in Table 4.

3.2 AMPLITUDE SWEEPS

Amplitude sweeps (AS) provide the dependence of the loss modulus G'' (characterizing the viscous property of a material sample) and storage modulus G' (characterizing the elastic property of a material sample) over a range of relevant strain for a given frequency of oscillatory motion and thus allow for quantification of the viscoelasticity of a material. Results for PAC4 and PAC2 are depicted in Figure 4. The loss modulus G'' exceeds the storage modulus G' for the entire strain range tested. While for the lower strain range, e.g. γ < 10 %, G' and G'' do have the same order of magnitude, G' and G'' differ by more than one order of magnitude for the higher strain range, e.g. γ > 500 %. The phase shift angle ϕ, defined as

$$\phi = arctan\frac{G''}{G'} \tag{13}$$

is an indication of ideal solid behavior for 0° and ideal fluid behavior for 90°. In case of the investigated PAC4 sample, the phase shift angle ϕ ranges from 66° to 70° for strains smaller than 1% and reaches 86° at a strain of 1000% (corresponding to a shear rate of $\dot{\gamma}$ = 100 s^{-1} for the set angular frequency of ω = 10 rad/s). The PAC2 phase shift angle exceeds the PAC4 phase shift angle for the entire strain range investigated.

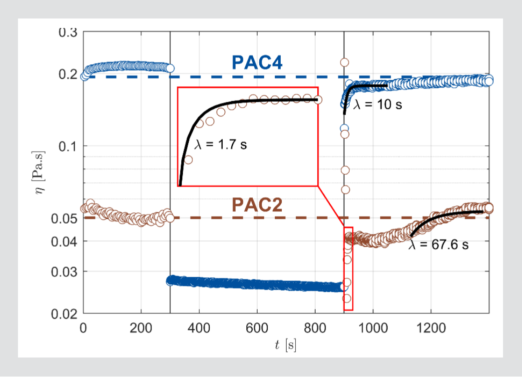

Figure 6: 3ITT-RRR, 100-50-500 test, PAC2 (partly smoothed) and PAC4 apparent viscosity η response to shear rate steps ($\dot{\gamma}$ = 0.1→1200→0.1 s^{-1}).

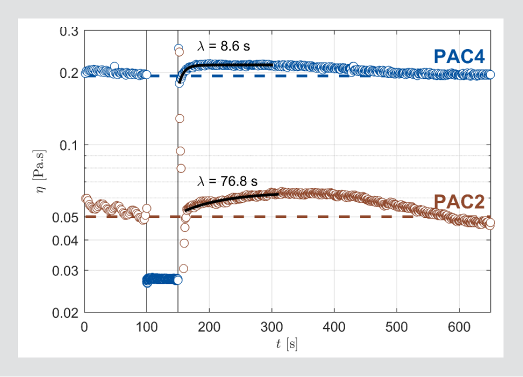

Figure 7: 3ITT-RRR, 300-600-500 test, PAC2 (partly smoothed) and PAC4 apparent viscosity η response to shear rate steps ($\dot{\gamma}$ = 0.1→1200→0.1 s^{-1}).

3.3 FREQUENCY SWEEPS

As opposed to AS, frequency sweeps (FS) provide the dependence of the storage modulus G' and the loss modulus G'' over a range of relevant oscillation frequencies for a given amplitude of strain. Results of PAC2 and PAC4 FS are depicted in Figure 5. In the low angular frequency range (ω = 0.1 - 10 rad/s), G' is smaller than G'' by almost one order of magnitude. Towards the high angular frequency range, the G' increases more than G''. Between ω = 20 rad/s and ω = 30 rad/s, the G'' equals the G' for the PAC2 data, and at ω = 20 rad/s for the PAC4 data. Based on Equation 11, the upper Maxwell time scale representing viscoelastic effects is estimated as $\lambda_{Max}(\omega = 0.1 \text{ rad/s}) \approx 0.67$ s for PAC4.

3.4 THREE INTERVAL THIXOTROPY TESTS

Three Interval Thixotropy Tests (3ITT) were conducted with PAC2 and PAC4 in order to establish the time-dependent behavior of the apparent viscosity due to microstructural changes. Figure 6 shows 3ITT-RRR (→ RRR: Three intervals of rotational shear) results for a 100-50-500 s interval definition and Figure 7 for 300-600-500 s, where the length of the third interval was limited by laboratory availability constraints. Apparent viscosity is plotted as a function of time as a response to the step-like changes of the imposed shear rate. The PAC2 data was partly smoothed with a time average filter because it featured quite some scatter, presumably due to the much lower apparent viscosity level. In all cases, the apparent viscosity follows the step change from the very low to the very high shear rate instantly. However, after the intermediate high shear-rate interval, the apparent viscosity shows a remarkable time-dependent recovery in the third interval. In the case of the 100-50-500 s intervals (Figure 6), the apparent viscosity overshoots the reference level, almost instantly for PAC 2 and exponentially for PAC4. In both cases, a second relaxation phase follows the overshoots in which the apparent viscosity develops almost back to the reference level. In the case of the 300-600-500 s intervals (Figure 7), the apparent viscosity undershoots the reference level, almost instantly for PAC 2 and exponentially for PAC4. Again, the apparent viscosity develops further and gradually increases to almost the reference value of the first interval towards the end of the experiment. For the immediate response to the step from high to low shear rate, the rheological relaxation times λ_{3ITT}, estimated based on curve fitting of Equation 12 to the experimental data and depicted in black in Figure 6 and Figure 7, are in the order of 10¹ s for the initial response of PAC 4. Zooming in to the very few seconds after the step (red subplot in Figure 7), reveals a time scale in the order of 1 s for PAC2 [c].

Fluid	Model	μ_0 [Pa·s]	μ_∞ [Pa·s]	λ [s]	n [-]	R²	SSE
	PL	0.0491	0	0.12	0.731	0.999	$3.71 \cdot 10^{-7}$
PAC2	Carreau	0.0491	0.001	0.239	0.771	0.99	$3.82 \cdot 10^{-5}$
	Cross	0.0525	0.001	0.012	0.516	-Inf	Inf
	PL	0.202	0	0.139	0.617	0.998	$1.11 \cdot 10^{-5}$
PAC4	Carreau	0.202	0.001	0.282	0.689	0.981	$3.10 \cdot 10^{-3}$
	Cross	0.212	0.001	0.029	0.574	0.999	$2.38 \cdot 10^{-4}$

Table 4: Model coefficients for PL ($\dot{\gamma} > 48$ s^{-1}), Carreau and Cross models, equations (6 - 8) for PAC2 and PAC4 data with goodness-of-fit R^2 and sum of squared errors SSE.

The second relaxation phase features much larger time scales in the order of several 10¹ s for PAC2 (Figure 7) to several 10² s for PAC4, as depicted in Figure 8, where the PAC4 3ITT data is normalized with the corresponding FC apparent viscosities. Fitting the growth function, i.e. Equation 12 to the more gentle increasing part of the third interval provides a time scale of 392 s for the 300-500-300 test and 126 s for the 100-50-500 test. The intermediate, i.e. high shear rate intervals do show time-dependent apparent viscosity as well. Using a decay function, similar to Equation 12 but with η_o and η_∞ exchanged, reveals the time constant for the second high shear rate interval of the 300-600-500 s interval case to be in the order of 615 s. In addition, Figure 8 provides a clearer picture of the first interval, the purpose of which is to establish an equilibrium reference level. The apparent viscosity readings are not stable and equal to

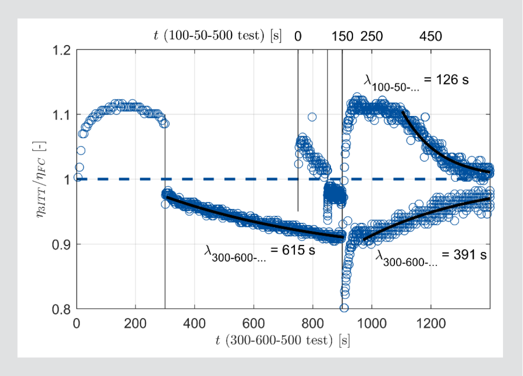

Figure 8: 3ITT-RRR, 300-600-500 test, η_{3ITT} normalized with respective FC apparent viscosity value η_{FC}.

the equilibrium FC values. Assuming that the time scale identified in the third interval is the relevant one for the low-shear situation of the first and third interval, one may conclude that the first interval needs to have a duration of approximately 1200 s ($3\lambda_{3ITT}$) in order to yield stable reference values for any initial state of the samples microstructure.

3.5 NORMAL STRESSES & COX-MERZ EMPIRISM

Since we are only interested in order of magnitude estimates, we did not directly measure normal stresses but rather exploited the FS results, namely the complex viscosity η^* as a function of the angular frequency ω, and estimated the first normal stress differences (FNSD) N_1 based on the first normal stress coefficient (FNSC) Ψ_1 using Laun's rule [44]

$$\psi_1(\dot{\gamma}) = 2\frac{G'}{\omega^2}\left[1+\left(\frac{G'}{G''}\right)^2\right]^{0.7}\Bigg|_{\dot{\gamma}=\omega} \tag{14}$$

Figure 9 shows the estimated FNSC Ψ_1 for the case of PAC2 and PAC4 as well as the corresponding time scale estimates λ_{RS} as defined in Equation 9, where the PL coefficients are determined point-wise to more closely follow the apparent viscosity function using the conditions (10). Additionally, the Cross fit of the apparent viscosity as provided in Table 4 and the complex viscosity η^* are depicted. The complex viscosity η^* is plotted over the shear rate utilizing the Cox-Merz rule [45]. The time scale estimate λ_{RS} is in the order of $5{\cdot}10^{-2}$ s for PAC2 and $2{\cdot}10^{-2}$ s for PAC4. The relevance of normal stresses and thus viscoelasticity may be judged by comparing it to the shear stress for a given shear rate. Figure 10 depicts the shear stress τ based on the Cross fit of the apparent viscosity as given in Table 4, the estimated FNSD $N_1 = \Psi_1\dot{\gamma}^2$ as well as the recoverable shear $N_1/2\tau$. The recoverable shear exceeds a value of 0.5 for shear rates larger than approximately 13 s^{-1} (PAC2) and 25 s^{-1} (PAC4).

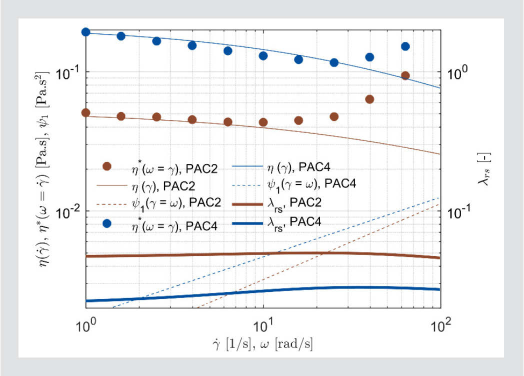

Figure 9: Cox-Merz-rule ($\eta(\dot{\gamma}) \approx \eta^*(\omega = \dot{\gamma})$) and PAC2 and PAC4 time scales λ_{rs}, where the respective coefficients are based on PL-fits of the FNSD N_1 (here plotted as PL of the FNSC $\psi_1 = N_1/\dot{\gamma}^2$) and $\eta(\dot{\gamma})$ via Equation 10.

4 DISCUSSION

4.1 RANGE OF TIME SCALES

The obtained rheological time scales for PAC2 and PAC4 are summarized in Figure 11. Two groups may be distinguished: The 3ITT time constants have the order of magnitude 10^1 - $8 \cdot 10^2$, the GNF time constants, the Maxwell relaxation time and the FNSD time constant have the orders of magnitude 10^{-3} - 1. Since the Maxwell as well as the RS time scales are characteristic for the viscoelastic behavior of the PAC solutions, we attribute these time scales range to viscoelasticity. With the same reasoning, we attribute the 3ITT time scale range to microstructural changes of the PAC solution as a consequence of accumulated shear, i.e. thixotropy. This distinction is important if one wants to design constitutive equations accounting for both the viscoelastic and thixotropic features [46]. While the RS time scales certainly indicate the correct order of magnitude, its numerical values are not correct over the entire range of shear rate. As may be seen from Figure 10, the simple FNSD fit does not accurately capture the lower shear rate range.

4.2 SHEAR-THINNING BEHAVIOR

4.2.1 Transient effects at low shear rates

The FC data indicates a transient behavior of the fluid samples at very low shear rates resulting in large uncertainty ranges of the apparent viscosity (Figure 3). As the equilibrium PAC4 FC data demonstrates, a MPD of Δt = 120 - 2 s log (or longer) is much better suited than a constant value of 5 s to allow for an equilibrium fluid microstructure at very low shear rates. This is confirmed by the 3ITT results, where a preliminary quasi-equilibrium is reached only after approximately 30 s $\approx 3\lambda_{3ITT}$ (Figure 7) for the investigated shear rate step. For the very low shear rate range $\dot{\gamma} = 10^{-2}$ - 10^{-1} s^{-1}, a MPD of Δt = 120 - 2 s log yields a total strain of γ = 1.2 - 6 as opposed

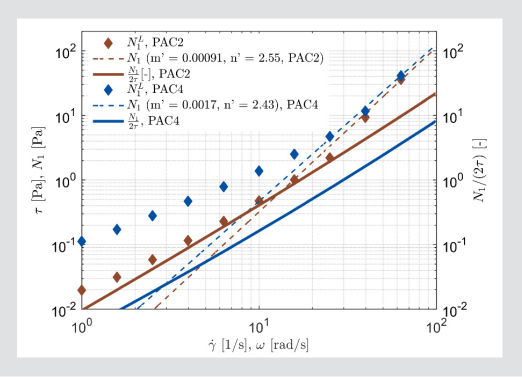

Figure 10: PAC2 and PAC4 recoverable shear $N_1/(2\tau)$, where the FNSD N_1 is based on PL fits to the FNSD $N_1^L = \psi_1\dot\gamma^2$ and the FNSC ψ_1 is obtained from FS data via Laun's rule [44].

to $\gamma = 0.05$ - 0.5 for the MPD $\Delta t = 5$ s, i.e. the logarithmic MPD used leads to much more strain and thus microstructural equilibrium. In general, a strain of $\gamma = 5$ is considered a minimum to ensure microstructural equilibration [47].

4.2.2 Hysteresis

The FCs obtained with a constant MPD consistently feature a hysteretic area indicating thixotropic [48], or more general, time/shear-history-dependent behavior. Most of the benchmarked data obtained from the literature do not show a hysteresis loop. In the case of PAC4, the logarithmic MPD and Johnsen [13] data show a much smaller degree of hysteresis in some parts of the investigated shear-rate range. Primarily, this may also be attributed to MPD settings, as described in 4.2.1. Since FCs are considered to refer to the equilibrium behavior of the fluid, a full equilibrium of the loaded sample needs to be established prior to sampling the apparent viscosity. Another important factor is the total time of shear, which varies greatly between the two MPD concepts. For instance, in the case of the constant MPD of $\Delta t = 5$ s, the total time of shear is about 150 s at $\dot\gamma = 16.1$ s^{-1} (upward sweep). In the case of the logarithmically decreasing MPD of $\Delta t = 120$ - 2 s, the corresponding total time of shear is about 663 s, which may allow for a better dynamic equilibrium of the fluid microstructure and consequently an apparent viscosity value consistent with the upward sweep.

4.2.3 Scatter of different flow curves

The SD for most of the shear rate range tested is in the order of the specified accuracy of the rheometer. When expressed as SE, the order of magnitude is consistent with the typical experimental error of 1 – 10 % for rotational rheometry [49]. The FC obtained from the literature coincide neither with each other nor with our logarithmic MPD data. The spread is consistent with technical work performed [50] to develop ISO 13500 [51], where intra-lab differences, when obtaining FC of PAC according to ISO 10416 [38], are estimated to be less than 10 % SD; however, using Fann viscometers. With reference to the elements of Figure 1, intra-lab differences may arise due to various rheometric characterization process parameters, which may differ between studies and laboratories: (i) Rheometer: Type of rheometer, measurement point duration (MPD) as in Section 4.2.2, (true) sample temperature [49], measuring systems (concentric cylinder, cone-plate), natural scatter of measurement process/accuracy and (ii) Preparation & mixing: Type of mixer, geometry of mixers utilized (blade versus jug geometry/size), mixing speed and duration, resting time, sample volume, effect of air bubbles, sample transfer, and impurities (unclean equipment, usage of non-distilled water with an effect on pH). The total difference of one FC to another is a consequence of all the possible differences of above mentioned process parameters. In case of our data, the observed test data differences may be most likely attributed to the different MPDs (see 4.2.2), but possibly also to the different mixer types, and resting times utilized.

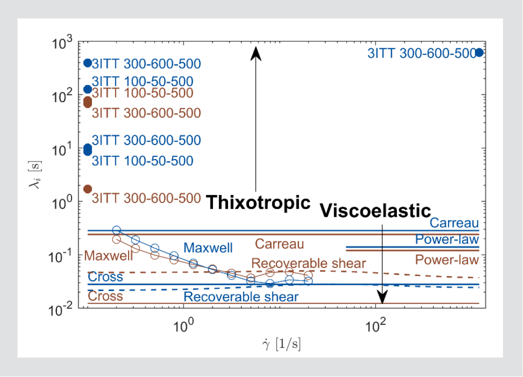

Figure 11: PAC2 and PAC4 time scales overview.

The effective shear rate and the total strain of the mixing process are a function of the mixer geometry, mixer speed and the total mixing times. The two mixing processes differ regarding the average shear rate, which is higher for the Waring LB20E* case by a factor of 1.65, regardless of whether estimated with the ratio of circumferential velocity/blade radius or impeller rotational speed times impeller geometry constant. Furthermore, the degree of turbulence generated during the mixing process is substantially higher for the Waring LB20E*/ mixer with a mixer impeller Reynolds number of the order $Re_{Imp} \approx 4650$ - 11627 versus $Re_{Imp} \approx 600$ - 1500 for the Silverson L4RT-A. Finally, cavitation may have occurred in the case of the Waring LB20E* (Cavitation number ≈ 1.5) as opposed to the Silverson L4RT-A (Cavitation number ≈ 20). Hence, the overall mixing quality of the Waring LB20E* seems to be much different from the Silverson L4RT-A. Possibly the higher degree of shear, turbulence and inception of cavitation might have altered the polymeric microstructure and affected the measurements.

The nominal resting times applied in the two preparation processes were very different (1 versus

48 h). This may have allowed further development of a higher-quality solution in the case of the 48 h samples, as diffusion processes may have further dissolved remaining granules and completely hydrated the polymer. In addition, more and smaller air bubbles (which were more likely to occur in the case of the Waring LB20E* due to the higher degree of shear and turbulence) may have left the system. For a time frame of one hour (Waring LB20E*), the cut-off size for bubbles that would have degassed from the bottom of the jar to the top (liquid height ≈ 0.1 m) is d_p = 0.1 mm, whereas d_p = 0.0146 mm for a time frame of 48 h (Silverson L4RT-A) [d]. However, the effective resting times in case of the Waring LB20E* fluid samples were substantially longer for most of the samples, as the prepared fluid was further left to rest in the sealed glass jars until the actual sample for the individual measurement was taken. No significant differences (with respect to the established SDs) were observed in the subsequent FC measurements at the times indicated in Figure 2, indicating that the discussed MPD is the primary influence on the different FC.

4.2.4 Newtonian plateau at low and high shear rates

PAC solutions feature a Newtonian viscosity plateau at low shear rates, as one would expect because of their polymeric nature. This low shear-rate Newtonian viscosity plateau requires the application of an appropriate viscosity model such as the Cross [23] and Carreau [24] family of models if one is interested in that shear-rate range, e.g. the settling of particles in drilling fluids, and a GNF rheology model is assumed to adequately describe the FC data. The same applies if one is interested in higher shear rate ranges, as the PAC solutions investigated feature a corresponding Newtonian plateau, which, in the absence of data available, may be taken equivalent to the solvent viscosity. However, precise high-shear rate data becomes important to not underestimate the laminar shear viscosity of the fluid, as it would occur using a PL material function [53].

In the context of CFD modelling, where a rheological model is required as input (Figure 1), it is also very beneficial for the computational process if a four-parameter material function of the Cross [23] and Carreau [24] family of models is used, as some control volumes in the domain will always feature low shear rates and, during the iteration process, some other might see shear rates much higher than the final value. This may increase numerical stability because iterations are based on fitted rather than extrapolated rheometric data or cut-off values. Furthermore, regions of low shear are ubiquitous in every flow problem. In addition, the high shear rate region above the range of interest is important when it comes to turbulent flow modeling in order to avoid extrapolation errors of the laminar shear viscosity [53]. In addition, for higher shear rate ranges, extensional viscosity effects may lead to turbulent drag reduction (DR) because of stretching of polymer molecule chains. This is well understood for CMC, where comparable concentrations may lead to DR of 10 – 35 % [54]. If relevant, one may account for DR by appropriate models, e.g. [55].

4.3 VISCOELASTIC BEHAVIOR

4.3.1 Relevance of elastic properties

The investigated PAC solutions exhibited relevant viscoelastic properties for very low strains (Figure 4) or high frequencies (Figure 5), since both loss and storage modulus were of the same order of magnitude. However, elasticity seems negligible for continuous deformation, i.e. strains larger than 1000 %, since the phase shift angle ϕ at a strain of 1000 % has a value of 82.5° for PAC4 and 86° for PAC2, with a phase shift angle ϕ = 90° representing purely viscous behavior. In that sense, PAC2 is less viscoelastic because the phase shift angle is exceeding the one of PAC4 over the entire range of strain, i.e. for a given strain PAC2 is more fluid-like than PAC4. Hence, PAC4 represents a worst-case in terms of viscoelasticity. If continuous deformation, i.e. flow over a sufficient amount of time and therefore large strain, takes place, the elastic response of the microstructure seems negligible. This is the case in a steady-state drilling operation; hence, PAC solutions used to investigate such operations may be treated as purely viscous. However, in regions of low deformation, for instance the interstitial drilling fluid in a cuttings bed, viscoelasticity may not be negligible.

On the other hand, normal stresses, which are caused by strain-induced microscopic anisotropy where polymer molecules depart from their equilibrium shape, become more relevant at higher shear rates, as depicted in Figure 10. The recoverable shear $N_1/(2\tau)$ is usually considered as a degree of elasticity, where a value of larger than ½ indicates high elastic behavior [56]. The effect of normal stresses on particle settling is well-known and may have to be accounted for in case of high settling shear rates using the estimated viscoelastic time scales provided in Figure 11 and an appropriate model [57]. The estimated viscoelastic time scale range λ_{Max} is only valid for small deformations as it is based on the Maxwell model. The Maxwell model does not describe the data completely as the slopes of both G' and G'' in the FS are not equal to 2 and 1, respectively [48]. However, comparing the FC apparent viscosity with the results from the FS by utilizing the Cox-Merz rule (Figure 9), we find that the two curves do reasonably well coincide for the lower shear rate range, i.e. the

Maxwell-based time scales may serve as a first approximation. However, like CMC solutions [34], PAC solutions deviate from the Cox-Merz-empiricism for higher shear rates as a consequence of the internal restructuring processes. Viscoelasticity is relevant on short timescales. This is also apparent from Figure 8, where viscosity and corresponding stress overshoots are observable just after the shear rate step from interval two to three. These overshoots do have a quite large amplitude; hence, on these short time scales, elastic effects are both present and significant quantitatively.

4.3.2 Yield stress

No yield stress is evident for the strain range investigated since the loss modulus G'' always exceeds the storage modulus G' and no crossing of the two moduli occurs (Figure 4). In addition, the CSS FC tests (not depicted) did not show any evidence of yielding. This may seem conflicting with other studies stating that PAC increases the yield point/yield stress in drilling fluids [1, 3, 5, 6] or, more generally, that anionic surfactants affect the yield stress of Bentonite slurries [58]. However, as opposed to this study, where purely PAC in an aqueous solution is used to create a model drilling fluid, the above cited studies actually investigated drilling fluid systems, where PAC is one of multiple additives to e.g. Bentonite-based suspensions. Here, the PAC anions may stabilize the clay particles and thus stabilize the suspension and indeed increase an existing yield stress. In addition, as per drilling industry convention, all these studies have applied either the HB or the Bingham [20] material function to their data, which were obtained with Fann viscometers. Thus, yield point/yield stress as employed in these studies and defined in the drilling industry [40] is to some extent a model artefact rather than a feature of the obtained rheometric data since it is purely based on the two conventionally taken data points at Fann viscometer speeds θ_{300} and θ_{600} (Bingham model) or θ_3 and θ_6 (Herschel-Bulkley model) [40]. A more firm (but also more time-consuming and complex) approach may be taken by adopting a material function which better describes the data, e.g. HB instead of Bingham, and by determining a yield stress based on e.g. crossover points in the AS test or performing shear stress sweeps in a CSS mode and plotting stress versus strain [59]. For higher concentrations or smaller strains than the ones investigated in this study, i.e. 8 g/L a yield stress may develop in pure PAC solutions. However, for higher polymer concentrations, the resulting increase in apparent viscosities disqualifies such high concentrations for use as they are exceeding the typical range of drilling fluid viscosities [39].

4.4 TIME-DEPENDENT BEHAVIOR

The tested PAC fluids generally show time-dependent, or more precisely shear-history dependent behavior. After the step from low to high shear rates, stress/viscosity jumps almost instantly to a new preliminary equilibrium value; however, followed by a transient behavior of stress/viscosity with large rheological relaxation times in the order of 10^3 s. From high to low shear rates, transient behavior and relaxation are observed with a rheological relaxation time in the order of 10^0 s (PAC2) and 10^1 s (PAC4), with a second subsequent transient behavior of stress/viscosity with large rheological relaxation times in the order of 10^2 s (PAC2) and 10^3 s (PAC4). The observed dynamics are not a result of the change of the flow field (high to low shear rate step and subsequent change of the velocity field) as the time scale associated with the change of the velocity field is in the order of $< 10^{-2}$ seconds [e].

The general change of apparent viscosity with time in the second and third 3ITT intervals confirms the time-dependent behavior of the investigated PAC fluids, as indicated by the hysteretic flow curves. Physically, this may be attributed to the interaction of the long-chain PAC molecules and the break-down/development of a three-dimensional structure in the solution. The high deformational load in the second interval will cause the polymer chains to align with the shear forces, resulting in a decreasing viscosity. In the transition to the recovery interval, the high load may have initiated a spontaneous rearrangement or crystallization of the polymer chains, which may further entangle over time, leading to an increase in viscosity. This may already be observed in the reference values of the 3ITT, where a transient behavior of the sample is visible indicating time-dependent behavior of the apparent viscosity. An even longer first interval, i.e. a sufficient amount of strain as described in Section 4.2.1, is required to get rid of all dynamics in the sample and reach dynamic equilibrium, i.e. stable reference values. A large scatter of the amplitude of viscosity occurs in the third interval of the 3ITT. We consider this a consequence of the apparent viscosity levels (in particular regarding PAC2) as well as a MPD setting issue since the MPD in the third test interval is just 0.5 s, whereas the MPD in the first interval is 5 s and thus acting as a time filter. Strikingly, PAC2 shows more pronounced over- and undershoots than PAC4, even though it can build less microstructure due to its lower concentration. Within this study, the described time-dependent behavior has been observed for two different concentrations as well as two shear rate steps only. A more comprehensive test matrix combined with much longer time intervals seems required and thus further work is needed to investigate the time-dependency of PAC solutions.

4.4.1 Long-term behavior

Within the time frames of our experiments, we could not observe a full structural recovery of the viscosity under- and overshoots. Viscosity overshoots have also been observed with oil-based drilling fluids. However, these fluids may fully relax to the reference value after sufficient time [59]. This is also observed in the case of the 100-50-500 3ITT data, where the apparent viscosity eventually relaxes back to the reference value (Figure 8). However, this relaxation takes place on even larger time scales than the ones describing the initial transient response given in Figure 7. The large time scales identified in the 3ITT tests ($\lambda_{3ITT} \approx 391 - 615$ s) indicate that even the FC obtained with a logarithmically MPD is not yet fully representing the dynamic equilibrium: For small shear rates such as $\dot{\gamma} = 0.1$ s^{-1}, the apparent viscosity changes by ≈ 8 % with $\lambda_{3ITT} = 391$ s (Third interval, Figure 8) and for large shear rates such as $\dot{\gamma} = 1200$ s^{-1}, the apparent viscosity changes by ≈ 5 % with $\lambda_{3ITT} \approx 615$ s (Second interval, Figure 8). These time scales also show that the sample's resting time in the measurement device could have been longer in order to ensure better structural reformation after the pouring process.

4.4.2 Thixotropic versus time-dependent behavior

The fluid samples behavior is of classic thixotropic nature because the change in viscosity is fully reversible, which is associated with a microstructure breakdown and complete reformation [48]. However, the observation of complete structural reformation depends on the time frame of the experiment. If the time scale of observation is chosen to be shorter, for instance in the order of the initial transient response (Figure 7), the reformation process is still occurring and the apparent viscosity difference is in the order of 10 %.

4.4.3 Simplification to viscous behaviors

We have shown that PAC solutions generally feature time-dependent behavior. For small deformations and/or high frequencies, a linear viscoelastic behavior is evident; for high shear rates normal stresses differences may become important. Furthermore, PAC solutions show thixotropic behavior on larger time scales, with a nonlinear increase of the time scale as a function of the concentration. In principle, a simplified treatment of the investigated PAC solutions as GNF is to be justified with respect to the actual flow problem as it depends on the ratio of i) the elastic or microstructural rheological time scales and ii) the characteristic process time scales and the time of observation in a Deborah number sense [60]. For very short process time scales, elastic effects are relevant, especially as they apparently may result in large amplitudes. For longer process time scales, the thixotropic microstructural effects become relevant. However, here the corresponding amplitude ratios are much less pronounced, as may be verified both from the FC hysteresis (Figure 3) and normalized 3ITT apparent viscosity plots (Figure 8). For the PAC4 hysteresis, the downward sweep mean apparent viscosity at an intermediate shear rate is 83 – 90 % of the upward sweep mean apparent viscosity. For the PAC4 3ITT relaxation, the apparent viscosity values reach 95 % of the reference value in $2\lambda_{3ITT}$ by definition and for the PAC4 examples given in Figure 7, the apparent viscosity has reached approximately 80 % of the final value in Δt = 5 to 7 s, which corresponds well with the apparent viscosity ratio of the FC downward and upward sweep given above.

For a PAC4 flow problem where the relevant time scale is in the order of the MPD $\Delta t = 5$ s, e.g. particles falling out of suspension and settling to the lower part of a horizontal wellbore section, the hysteretic FC presented in Figure 3 may be used to estimate the increase of uncertainty if the observed hysteretic loop, i.e. the change in time-dependent apparent viscosity due to change of the microstructure is neglected. For modeling purposes, one may represent this hysteretic FC with the mean of the upward and downward sweep means, i.e. the dotted line in Figure 3 plus/minus a respective tolerance. For the given example, these tolerances may be estimated from the extremes as a result of natural scatter (Dotted lines of PAC4 FC in Figure 3). Thus, instead of having one FC, which may be used to fit a material function, one now has a FC with an increased uncertainty accounting for time-dependent effects.

For the given FC example, the relative standard uncertainty of both the upward and downward sweep is in the order of ≈ ± 5 % for $\dot{\gamma} > 140$ s^{-1} and ≈ ± 10 % for $\dot{\gamma} < 30$ s^{-1} (based on respective means (solid lines) depicted in Figure 3 ± 3SD) [f]. If the hysteresis loop is neglected, the dashed lines are taken as ± 3SD and hence the uncertainty for this mean of the upward and downward sweep mean (dotted line) increases to ≈ ± 15 % for $\dot{\gamma} < 30$ s^{-1} and ≈ ± 18 % for $\dot{\gamma} < 5$ s^{-1}, which is a relative increase of 75 to 90 %. The uncertainty of the range $\dot{\gamma} > 140$ s^{-1} remains the same and for shear rates $\dot{\gamma} < 0.3$ s^{-1} there is no reliable uncertainty estimate possible as the MPD effect (see 4.2.1) overshadows and thus increases the hysteretic loop uncertainty intervals. In addition, the 3SD interval is approximately equal to the range of scatter representing intra-lab differences. Figure 3 shows that the uncertainty estimate (dashed lines) encloses the PAC4 results obtained from the literature as well as the assumed equilibrium FC. Thus, for the case of MPD Δt = 5 s, intra-lab differences (which may be due to one or a combination of the factors given in 4.2.3) lead to an apparently equivalent uncertainty magnitude as time-dependent effects.

It is important to note that this uncertainty estimate additionally includes the natural scatter of the FC measurement process as well as discussed factors such as MPD, mixing process and resting times as it is based on 3SD of both the upward and downward sweeps. Note also that the order of magnitude of the FC hysteresis is dependent on the MPD, i.e. the time scale of observation, as well as the shear rate step. The latter is small for a FC sweep, in case of larger shear rate gradients the above given uncertainty range may underestimate the apparent viscosity. Hence, performing 3ITT tests for different shear rate steps will provide a better understanding of how uncertainty scales with shear rate steps and the time scale of observation. However, a better approach for modeling activities obviously is to use the equilibrium FC instead of averaging the hysteretic FC. This imposes a constraint on experimental modeling in order to minimize the uncertainty when it comes to validation as indicated in Figure 1. Proper dynamic equilibrium i.e. a constant apparent viscosity needs to be ensured prior to sampling the variables of interest. Given the largest time scales identified (λ_{3ITT} = 615 s), this may not be practically possible as it yields very long laboratory times.

Finally, with respect to CFD modeling, the total uncertainty associated with a rheological model utilized may be estimated with the root of the sum of the squares of individual uncertainties of every process step required to construct the rheological model. With reference to Figure 1, the fluid may feature more complex physics, which if neglected, increase uncertainty by potentially 75 to 90 % as described above. The preparation process may increase uncertainty due to the various reasons mentioned in 4.2.3, in particular mixing procedures and resting times. The measurement process as such provides scattered data with a certain SD, here ± 1 to ± 5 %, and is sensitive to the measurement settings (Sections 4.2.1 and 4.2.2). Uncertainty will further increase (at least for certain ranges of shear rate) if an inappropriate material function is selected to represent the data as discussed in Sections 4.2.4 and 4.3.2. The fit of the material function to the rheometric data by regression may further increase uncertainty (Table 4).

4.5 SUBSTITUTION OF DRILLING FLUIDS IN LABORATORY STUDIES

In general, the investigated PAC solutions seem capable of serving as model systems for drilling fluids in laboratory cuttings transport studies (referring to "Test fluid" in Figure 1) since they feature shear-thinning behavior, and also show viscoelastic and thixotropic behavior. The identified large thixotropic time scales ($\lambda_{3ITT} \approx 10^2$ - 10^3 s) do have the same order of magnitude as water-based drilling fluids (WBDF) such as bentonite [43, 61] and KCl [61] dispersions, as well as oil-based drilling fluids (OBDF) [59]. Moreover, the relative change in amplitude is also comparable to the behavior of WBDF [43, 61] and OBDF [59]. However, as opposed to bentonite-based WBDF, the investigated PAC solutions do show a much smaller thixotropic time scale ($\lambda_{3ITT} \approx 10$ s) for the first part of the microstructure build-up after stress relieve [43]. PAC solutions do not show a yield stress for the concentrations investigated. Regardless of how to define and measure a yield stress, a yield stress is assumed a desirable property of a drilling fluid, keeping particles in suspensions at zero flow. The addition of Xanthan gum may be one way to develop a yield stress and keeping translucency as it is known to add viscoelasticity (but may also further increase shear thinning) [62]. Another important parameter to consider is density, which is basically equal to water for the investigated PAC solutions. The variations in relative fluid density between drilling fluids and rock may vary with a factor of 1 to 3 [39]. However, relative density effects are well understood and there is no need to match relative density in experiments as long as the variation is smaller than one order of magnitude [g]. It is more important to match the sedimentation velocities of cuttings which may be controlled by the particle size.

5 CONCLUSIONS

Aqueous PAC solutions apparently feature linear viscoelastic properties in case of low strains and/or high frequencies and exhibit relevant normal stress differences in case of high shear rates, but no yield stress. They further show time-dependent, or more precisely shear-history dependent behavior. When performing flow curve measurements, sufficiently long measurement point durations over the entire range of shear rates are required to obtain a microstructural equilibrium in the sample. This is critical in order to minimize the uncertainty due to thixotropic effects and to obtain the most reliable fit to applied rheological models. For cuttings transport modeling purposes, it seems reasonable to treat PAC solutions as purely viscous, shear-thinning, fluids as long as:

- small deformations and/or large frequencies as well as higher shear rates are not relevant for the problem, hence neglecting elastic properties
- the time of observation is sufficiently longer than the fluids rheological relaxation times, i.e. that an equilibrium of the problem with respect to the fluids flow field and microstructure is achieved, hence time-dependent restructuring effects are becoming irrelevant

If this is not satisfied, the overall uncertainty of the rheometric flow curve data, i.e. square root of sum of squares of the general experimental uncertainty and an additional uncertainty associated with the purely viscous interpretation of the data and corresponding model coefficients may increase by an order of ≈ 75 to 90 %. Further work is required to detail this estimate with regards to the time scale of observation as well as shear rate steps and relate it to specific cutting transport process time scales. Instead of a yield stress, pure PAC solutions feature a low-shear viscosity plateau and require a corresponding material function, e.g. Cross/Carreau if the low shear rate range ($\dot{\gamma} < 1\ s^{-1}$) is relevant for the particular problem investigated. For modeling purposes, the application of a Cross/Carreau material function is beneficial because it minimizes the negative effects of extrapolation of the conventionally used Power Law material function.

ACKNOWLEDGEMENTS

The project Advanced Wellbore transport Modeling (AdWell) with its sponsor, PETROMAKS 2/the Research Council of Norway (project 228391) and its partners Statoil, Neptune Energy Norge AS, IRIS, UiS, NTNU and SINTEF are gratefully acknowledged for funding and supporting this work. We thank the reviewers and editors of Applied Rheology for their valuable suggestions to improve the manuscript.

REFERENCES

[1] Mahto V, Sharma VP: Rheological study of a water based oil well drilling fluid, J. Pet. Sci. Eng. 45 (2004) 123 – 128.

[2] Benyounes K, Mellak A, Benmounah A, Oubraham C: Effect of polymer concentration on the rheological properties of polyelectrolyte solutions, 14th SGEM GeoConference on Science and Technologies in Geology, Exploration and Mining, Surveying Geology & Mining Ecology Management (SGEM), Sofia (2014) 703 – 710.

[3] Elemam AE, Hussien RA, Ibrahim AA, Mohamed SA: Impacts of polyanionic cellulose polymer (PAC-LV) on drilling fluids properties, SUST J. Eng. Comput. Sci. JECS 16 (2015) 30 – 36.

[4] Kok MV, Alikaya T: Effect of polymers on the rheological properties of KCl/polymer type drilling fluids, Energy Sources 27 (2005) 405 – 415.

[5] Olatunde AO, Usman MA, Olafadehan OA, Adeosun TA, Ufot OE: Improvement of rheological properties of drilling fluid using locally based materials, Pet. Coal 54 (2012) 65 – 75.

[6] Razi MM, Razi FM, Saadati H: Modification of rheological and API fluid loss of bentonine-based drilling fluids using polyanionic Cellulose (PAC), Proceedings of the 3rd Iranian Petroleum Conference, IPEC, Teheran (2012).

[7] Ramadan A, Saasen A, Skalle P: Application of the minimum transport velocity model for drag-reducing polymers, J. Pet. Sci. Eng. 44 (2004) 303 – 316.

[8] Ramadan A, Skalle P, Johansen ST, Svein J, Saasen A: Mechanistic model for cuttings removal from solid bed in inclined channels, J. Pet. Sci. Eng. 30 (2001) 129 – 141.

[9] Noah AZ: Optimizing drilling fluid properties and flow rates for effective hole cleaning at high-angle and horizontal wells, J. Appl. Sci. Res. 9 (2013) 705 – 718.

[10] Nguyen TN, Miska SZ, Yu M, Takach NE, Ramadan A: Experimental study of hydraulic sweeps in horizontal wells, Wiert. Nafta Gaz 27 (2010) 307 – 331.

[11] Rabenjafimanantsoa HA, Time RW, Saasen A: Flow regimes over particle beds – Experimental studies of particle transport in horizontal pipes, Annu. Trans. Nord. Rheol. Soc. 13 (2005) 99 – 106.

[12] Garcia-Hernandez AJ, Miska SZ, Yu M, Takach NE, Zettner CM: Determination of cuttings lag in horizontal and deviated wells, SPE Annual Technical Conference and Exhibition, Society of Petroleum Engineers, Anaheim, CA (2007).

[13] Johnsen MS: Particle transport and hole cleaning in wells during drilling, Master thesis, University of Stavanger (2014).

[14] Adari RB, Miska S, Kuru E, Bern P, Saasen A: Selecting drilling fluid properties and flow rates for effective hole cleaning in high-angle and horizontal wells, SPE Annual Technical Conference and Exhibition, Society of Petroleum Engineers, Dallas (2000).

[15] Sorgun M: Modeling of Newtonian fluids and cuttings transport analysis in high inclination wellbores with pipe rotation, PhD thesis, Middle East Technical University, Ankara (2010).

[16] Khatibi M, Time RW, Rabenjafimanantsoa HA: Particles falling through viscoelastic non-Newtonian flows in a horizontal rectangular channel analyzed with PIV and PTV techniques, J. Non-Newton. Fluid Mech. 235 (2016) 143 – 153.

[17] Time RW, Rabenjafimanantsoa AH: Splitting mechanisms and dynamics of taylor bubbles in non-Newtonian fluids in annuli with relevance to gas-kicks in petroleum wells, Annu. Trans. Nord. Rheol. Soc. 20 (2012) 79 – 88.

[18] Rabenjafimanantsoa AH, Time RW, Paz T: Dynamics of expanding slug flow bubbles in non-Newtonian drilling fluids, Annu. Trans. Nord. Rheol. Soc. 19 (2011) 69 – 76.

[19] Time RW, Rabenjafimanantsoa HA: Dynamics of stagnant taylor bubbles in vertical upward pipe flow with venturi obstruction and non-Newtonian liquids, Annu. Trans. Nord. Rheol. Soc. 23 (2015) 69 – 77.

[20] Bingham EC: Fluidity and plasticity, Vol. 2. McGraw-Hill Book Company, Inc. (1922).

[21] Ostwald W: Über die Geschwindigkeitsfunktion der Viskosität disperser Systeme, Colloid Polym. Sci. 36 (1925) 99 – 117.

[22] Herschel W, Bulkley R: Konsistenzmessungen von Gummi-Benzollösungen, Kolloid Z. 39 (1926) pp 291 – 300.

[23] Cross MM: Rheology of non-Newtonian fluids: a new flow equation for pseudoplastic systems, J. Colloid Sci. 20 (1965) 417 – 437.

[24] Carreau PJ: Rheological equations from molecular network theories, PhD thesis, University of Wisconsin-Madison (1968).

[25] Metzner AB, Reed JC: Flow of non-newtonian fluids-correlation of the laminar, transition, and turbulent-flow regions, AIChE J. 1 (1955) 434 – 440.
[26] Hughes TL, Jones TG, Houwen OH: Chemical characterization of CMC and its relationship to drilling-mud rheology and fluid loss, SPE Drill. Complet. 8 (1993) 157 – 164.
[27] Palumbo S, Giacca D, Ferrari M, Pirovano P: The development of potassium cellulosic polymers and their contribution to the inhibition of hydratable clays, SPE International Symposium on Oilfield Chemistry, Society of Petroleum Engineers (1989).
[28] PAC – Schlumberger Oilfield Glossary, http://www.glossary.oilfield.slb.com/Terms/p/pac.aspx
[29] Khatibi M, Potokin N, Time RW: Experimental investigation of effect of salts on rheological properties of non-Newtonian fluids, Annu. Trans. Nord. Rheol. Soc. 24 (2016).
[30] Florjancic U, Zupancic A, Zumer M: Rheological characterization of aqueous polysaccharide mixtures undergoing shear, Chem. Biochem. Eng. Q. 16 (2002) 105 – 118.
[31] Vais AE, Palazoglu TK, Sandeep K p., Daubert CR: Rheological characterization of carboxymethylcellulose solution under aseptic processing conditions, J. Food Process Eng. 25 (2002) 41 – 61.
[32] Abelrahim KA, Ramaswamy HS, Doyon G, Toupin C: Effects of concentration and temperature on carboxymethylcellulose rheology, Int. J. Food Sci. Technol. 29 (1994) 243 – 253.
[33] Benchabane A, Bekkour K: Rheological properties of carboxymethyl cellulose (CMC) solutions, Colloid Polym. Sci. 286 (2008) 1173 – 1180.
[34] Kulicke W-M, Reinhardt U, Fuller GG, Arendt O: Characterization of the flow properties of sodium carboxymethylcellulose via mechanical and optical techniques, Rheol. Acta 38 (1999) 26 – 33.
[35] Jan Schaffer (Anton Paar): Personal communication (2017).
[36] Irgens F: Rheology and non-Newtonian fluids, Springer International Publishing, Cham (2014).
[37] Barnes HA: A handbook of elementary rheology, Univ. of Wales, Institute of Non-Newtonian Fluid Mechanics, Aberystwyth (2000).
[38] ISO/TC 67, SC 3: ISO 10416:2008 - Petroleum and natural gas industries – Drilling fluids – Laboratory testing, International Organization for Standardization (2008).
[39] Busch A, Islam A, Martins D, Iversen FP, Khatibi M, Johansen ST, Time RW, Meese EA: Cuttings transport modeling – Part 1: Specification of benchmark parameters with a Norwegian continental shelf perspective, SPE Drill. Complet. in press (2018).
[40] API RP 13D: Rheology and hydraulics of oil-well drilling fluids, American Petroleum Institute, Washington, D.C. (2010).
[41] ISO/TC 67, SC 3: ISO 10414-1:2008 - Petroleum and natural gas industries – Field testing of drilling fluids – Part 1 – Water-based fluids.pdf, International Organization for Standardization (2008).
[42] Bird RB, Armstrong RC, Hassager O: Dynamics of polymeric liquids. Volume 1: Fluid Mechanics, New York (1987).
[43] Tehrani A: Thixotropy in water-based drilling fluids, Annu. Trans. Nord. Rheol. Soc. 16 (2008).
[44] Laun HM: Prediction of elastic strains of polymer melts in shear and elongation, J. Rheol. 30 (1986) 459 – 501.
[45] Cox WP, Merz EH: Correlation of dynamic and steady flow viscosities, J. Polym. Sci. 28 (1958) 619 – 622.
[46] Larson RG: Constitutive equations for thixotropic fluids, J. Rheol. 59 (2015) 595 – 611.
[47] Wagner CE, Barbati AC, Engmann J, Burbidge AS, McKinley GH: Apparent shear thickening at low shear rates in polymer solutions can be an artifact of non-equilibration, Appl. Rheol. 26 (2016) 54091.
[48] Mezger TG: The rheology handbook, Vincentz Network, Hannover (2014).
[49] Laun M, Auhl D, Brummer R, Dijkstra DJ, Gabriel C, Mangnus MA, et al.: Guidelines for checking performance and verifying accuracy of rotational rheometers: Viscosity measurements in steady and oscillatory shear (IUPAC Technical Report), Pure Appl. Chem. 86 (2014) 945 – 1968.
[50] Balestrini A, Maas A, Seheult M, Morton EK: Advances in API/ISO Standard Grade Purified Poly-Anionic Cellulose (PAC) and Drilling Grade Xanthan Gum (XG) Test Procedure and Specifications Definition, 2009 SPE/IADC Drilling Conference and Exhibition, Amsterdam (2009).
[51] ISO/TC 67, SC 3: ISO 13500:2008 – Petroleum and natural gas industries – Drilling fluid materials – Specifications and tests, International Organization for Standardization (2008).
[52] Schiller L, Naumann A: Über die grundlegenden Berechnungen bei der Schwerkraftaufbereitung, Z. Verein Deutsch. Ing. 77 (1933) 318 – 320.
[53] Singh J, Rudman M, Blackburn HM, Chryss A, Pullum L, Graham LJW: The importance of rheology characterization in predicting turbulent pipe flow of generalized Newtonian fluids, J. Non-Newton. Fluid Mech. 232 (2016) 11 – 21.
[54] Deshmukh SR, Sudhakar K, Singh RP: Drag-reduction efficiency, shear stability, and biodegradation resistance of carboxymethyl cellulose-based and starch-based graft copolymers, J. Appl. Polym. Sci. 43 (1991) 1091 – 1101.
[55] Roy A, Larson RG: A mean flow model for polymer and fiber turbulent drag reduction, Appl. Rheol. 15 (2005) 370 – 389.
[56] Barnes HA, Hutton JF, Walters K: An introduction to rheology, Elsevier Science, Amsterdam (1989).
[57] Acharya A, Mashelkar RA, Ulbrecht J: Flow of inelastic and viscoelastic fluids past a sphere – I. Drag coefficient in creeping and boundary-layer flows, Rheol. Acta 15 (1976) 454 – 470.
[58] Güngör N: Effect of the adsorption of surfactants on the rheology of Na-bentonite slurries, J. Appl. Polym. Sci. 75 (2000) 107 – 110.
[59] Oltedal VM, Werner B, Lund B, Arild Saasen, Ytrehus JD: Rheological properties of oil based drilling fluids and base oils, Proceedings of the ASME 2015 34th International Conference on Ocean, Offshore and Arctic Engineering OMAE2015, American Society of Mechanical Engineers, St. John's, Newfoundland (2015).
[60] Reiner M: The Deborah number, Phys. Today 17 (1964) 62.
[61] Torsvik A, Myrseth V, Opedal N, Lund B, Saasen A, Ytrehus JD: Rheological comparison of bentonite based and KCl/polymer based drilling fluids, Annu. Trans. Nord. Rheol. Soc. 22 (2014).

[62] Benyounes K, Mellak A, Benchabane A: The effect of carboxymethylcellulose and xanthan on the rheology of bentonite suspensions, Energy Sources Part Recovery Util. Environ. Eff. 32 (2010) 1634 – 1643.

[63] Barnes HA: Thixotropy – a review, J. Non-Newton. Fluid Mech. 70 (1997) 1 – 33.

[64] Taghipour MA, Lund B, Sandvold I, Opedal N: Experimental study of rheological properties of model drilling fluids, Annu. Trans. Nord. Rheol. Soc. 20 (2012).

FOOTNOTES

[a] CFD methods are hereafter considered as multiphase finite volume Reynolds Averaged Navier Stokes models, where the particles are either treated as point masses (Eulerian-Lagrangian) or second continuum (Eulerian-Eulerian). Hence, various closures are required, such as considered particle forces as well as turbulence and rheology models.

[b] A constitutive equation is considered as a mathematical expression relating stress and strain and/or strain rates, or even other flow/material properties. A rheological model comprises a particular constitutive equation as well as certain assumptions made for a set of experimental data to fit material functions such as shear viscosity and first normal stress coefficient. However, in many cases these terms are used interchangeably.

[c] The rheological relaxation time λ_{3ITT} may alternatively be defined as the time it takes to fully relax to an equilibrium state. Here, the definition of a time constant is used as described in Equation 9. The applied definition of λ_{3ITT} therefore represents the time it takes to relax to ≈ 63 % of its final value.

[d] Based on zero shear rate viscosity h_0 of the system and Schiller-Naumann [52] drag law.

[e] This estimate may be obtained by rearranging the momentum balance for pure shear flow in the rheometer gap and inserting the two extremes of apparent viscosity h = 0.0275 Pas and h = 0.2 Pas, the density r = 999 kg/m^3 and the rheometer gap size y = 1.013 mm.

$$\frac{\partial u}{\partial t} = \frac{\eta \partial^2 u}{\rho \partial y^2} \rightarrow \delta t \approx \frac{\rho y^2}{\eta}$$

The inverse of the RHS yields the corresponding time scales $dt_{(h\,=\,0.0275\ \mathrm{Pas})} = 0.046$ s and $dt_{(h\,=\,0.2\ \mathrm{Pas})} = 0.0064$ s for the change in velocity dt as a result of the change in shear rate d γ.

[f] Usually, standard uncertainty is based on SD. Here, we base it on 3 • SD as this encompasses 99 % of the scattered data and is consistent with Figure 3.

[g] Besides scaling the problem, addition of Laponite may be considered in order to increase density and further develop time-dependent behaviour [63] by keeping the required translucency [64].

Journal paper 4 (V)

On The Validity Of The Two-Fluid-KTGF Approach For Dense Gravity-Driven Granular Flows as implemented in ANSYS Fluent R17.2

Alexander Busch, Stein Tore Johansen

Powder Technology, Vol. 364, Special Issue CPT-2018-Melbourne, 2020.

DOI: 10.1016/j.powtec.2020.01.043.

Powder Technology 364 (2020) 429–456

Contents lists available at ScienceDirect

Powder Technology

journal homepage: www.elsevier.com/locate/powtec

On the validity of the two-fluid-KTGF approach for dense gravity-driven granular flows as implemented in ANSYS Fluent R17.2

Alexander Busch [a,*], Stein Tore Johansen [a,b]

[a] *Norwegian University of Science and Technology (NTNU), Trondheim, Norway*
[b] *SINTEF Industry, Trondheim, Norway*

ARTICLE INFO

Article history:
Received 25 June 2019
Received in revised form 4 January 2020
Accepted 15 January 2020
Available online 22 January 2020

Keywords:
Cliff collapse
Two fluid model
KTGF
Frictional
CFD

ABSTRACT

As a subproblem of solid transport in wellbores, we have investigated the cliff collapse problem by means of the Two-Fluid-Model (TFM), where the rheological description of the second phase (sand) is governed by the Kinetic Theory of Granular Flows (KTGF) and additional closures from soil mechanics for dense (frictional) regions of the solid phase. Using ANSYS Fluent R17.2, we have studied the influence of the aspect ratio and scale of the initial cliff, the scale of the particle size, four different interstitial fluids (air, water, and two viscous but shear-thinning solutions), and the role of the initial condition (IC) of the solid volume fraction. The latter was evaluated by two different strategies: (1) Let solids settle to establish a compacted granular bed in dynamic equilibrium prior to allow the cliff to collapse and (2) simply patch the solid volume fraction into the computational domain at $t = 0$.

While most of the simulations produced a final deposit featuring a slope, validation with experimentally obtained scaling laws from the literature was not comprehensively successful. The primary reason identified is that, at steady-state, for which a sloped deposit must exist, a thin layer at the top of the sediment bed remains flowing, yielding a scale-dependent disintegration of the cliff over longer periods of time which ultimately results in a flat bed. We suspect this phenomenon, hereafter termed *top bed velocity defect*, to be a consequence of the numerical solutions strategy of Fluent which may result in some momentum solid flux imbalance at top-bed regions where the gradient of the solids kinetic/collisional pressure is high.

Comprehensive model tuning is required to yield a better physical representation of the IC. In addition, alternative closures for both solid frictional pressure and solid viscosity may be helpful to better replicate the experimental data. On the other hand, experimental spread and missing experimental data for the shear-thinning fluids requires more comprehensive experimental data for validation purposes.

If the model in its current form is used for transport modeling of cuttings in wellbore flows, the velocity defect will lead to an unknown overestimation of the mass flux of solids. When it comes to the modeling of dune migration, the *top bed velocity defect* will likely cause disintegration of the dune over longer periods of time.

1. Introduction

Granular cliff collapse, i.e. the disintegration of a pile of granular material over time because of gravity, is an often-researched problem because it represents the physics of landslides and it is a comparatively simple problem to study on a laboratory scale. When it comes to modeling, it is the granular flow analog to the dambreak problem in fluid mechanics. Our motivation, however, is slightly different: we are concerned with wellbore flow modeling, where the transported solids may form a bed at the bottom of the annular conduit. Depending on the local inclination of the wellbore and on operational parameters (e.g. fluid throughput, drill pipe rotation, and inclination), ripples and dunes and even avalanches may occur. Due to the scale of the actual wellbore, model validation is often difficult. Hence, we apply our modeling approach, the Two-Fluid-Model (TFM) with closures from the Kinetic Theory of Granular Flows (KTGF) and additional closures from soil mechanics (SM) to handle dense granular regions, to

---

Abbreviations: 2D-3D, Two-Three dimensional in space; BC, Boundary Condition; CFD, Computational Fluid Dynamics; CCP, Cliff Collapse Problem; DEM, Discrete Element Method; FFR, Free Fall regime; IR, Inertial regime; KTGF, Kinetic Theory of Granular Flows; PAC, Polyanionic Cellulose; RHS, Right Hand Side; SPH, Smooth Particle Hydrodynamics; SM, Soil Mechanics; TFM, Two Fluid Model; VR, Viscous regime.

[*] Corresponding author.

E-mail addresses: alexander.busch@ntnu.no, alexander.busch@alumni.ntnu.no (A. Busch).

https://doi.org/10.1016/j.powtec.2020.01.043

the Cliff Collapse Problem (CCP), which constitutes an extreme case of what might happen in a inclined wellbore in the absence of flow and pipe rotation.

Nomenclature

Greek symbols

α	Volume fraction
$\dot{\gamma}$	Shear rate, total shear measure
Δ	Difference
η	Apparent shear viscosity
κ	Bulk viscosity
λ	Parameter in Cross material function and cliff collapse scaling law
μ	Newtonian shear viscosity
ϕ	Angle of internal friction
ρ	Density
Θ	Granular temperature

Latin symbols

a	Aspect ratio
c	Coefficient
d	Diameter
$\mathbf{D}$	Rate of deformation tensor
e	Coefficient of restitution
f	Functional
$\mathbf{f}$	Force vector
g	Radial distribution function
$\mathbf{g}$	Gravity
I	Inertial number
$\mathbf{I}$	Identity tensor
k	Granular conductivity
K	Interphase exchange coefficient
n	Parameter in Cross material function and cliff collapse scaling law
p	Pressure
r	Square root of the fluid-solid density ratio
Re	Reynolds number
St	Stokes number
t	Time
T	Relaxation time
$\mathbf{T}$	Stress tensor
$\mathbf{u}$	Phase velocity
V	Volume
w	Width
x, y	Spatial dimension

Indices

0	Zero, initial, $t = 0, \dot{\gamma} \to 0$
∞	Infinity, $\dot{\gamma} \to \infty$
c	Collisional
Cr	Cross
D	Drag
f	Fluid (if used as first index), Frictional (if used as second index, e.g. $_{s,f}$)
i, j	Index
k	Kinetic
mpd	Maximum packing density of the model
n	Non-dimensional
p	Particle
s	Solid
T	Transposed

1.1. From cuttings transport modeling to the CCP

When decomposing cuttings transport in wellbores into smaller and simpler cases, one retrieves the classic CCP. Here, a granular column with an initial with x_0, height y_0 and solid volume fraction $\alpha_{s,0}$, as conceptually depicted in Fig. 1, disintegrates under the influence of gravity as soon as one of the side walls, here the Right Hand Side (RHS), is removed.

At *steady-state*, the final shape features the final run-out length x_f, the final deposit height y_f and an inclination angle in the order of the angle of repose of the respective granular material. A review of granular flows in general and dam-break granular flows and the CCP in particular was recently provided by Delannay et al. [1], who pointed out deficiencies of conventional modeling approaches and conclude that only very limited modeling work is available which has actually addressed problems encompassing flows in which dense and dilute regions coexist.

1.2. Experimental work

The CCP has been intensively researched throughout the years as it is both a numerical test case as well as a real-world problem (e.g. land slides, avalanches). While various specific scaling laws for x_f and y_f have been suggested in the literature, some depending on the experimental setup and/or interstitial fluid [2–7], a universal trend is a power-law dependence on the aspect ratio $a = y_0/x_0$. Distinct behaviors are found at small and large a, as well as for different interstitial fluids. A generic non-dimensional framework [1] for x_f and y_f is given as

$$x_{n,f} = \lambda_x a^{n_x} \tag{1}$$

and

$$y_{n,f} = \lambda_y a^{n_y - 1} \tag{2}$$

respectively, where the dimensionless x-coordinate is defined as

$$x_n = \frac{x - x_0}{x_0} \tag{3}$$

and the dimensionless y-coordinate is defined as

$$y_n = \frac{y}{y_0} \tag{4}$$

where the index 0 denotes the initial configuration at flow time $t = 0$.

The coefficients λ_i may account for granular material properties and experimental setups [3], and the exponents n_i account for large aspect ratio effects [3], and both may also account for the granular fluid flow regime [2]. In addition, in case of interstitial liquids, λ_i and n_i may also account for the then relevant role of the initial solid volume fraction [2].

Various experimental studies have shown that in case of dry granular media the CCP scales predominantly with the initial aspect ratio [1–3,6,8,9]. For instance, Lube et al. [3][1] determined for[2]

$$\begin{array}{llll} a < 1.8: & \lambda_x = 1.6 & \& & n_x = 1 \\ a > 2.8: & \lambda_x = 2.2 & \& & n_x = \dfrac{2}{3} \end{array} \tag{5}$$

for the scaling law (1) and for

---

[1] The parameter values of Lube et al. were determined with quartz sand (\rho_p = 2600 kg/m£, d_p = {0.15, 1.5} mm and \alpha_repose = 29.5°. In addition, rice and sugar were used. Concerning the nondimensional run-out length, there was no difference between the different particles. However, the deposit height for the fine quarts sand (d_p = 0.15 mm) is better described with \lambda_y = 1.1.

[2] Note that in the scaling framework of both Lube et al. [3] and Bougouin and Lacaze [2], $y_n = y/x_0$. Hence, to suit the scaling law definition as used in this study, these $y_n(a)$ scaling laws of have to be divided by the aspect ratio a which then yields the coefficients as given in Eqs. (6) and (8)

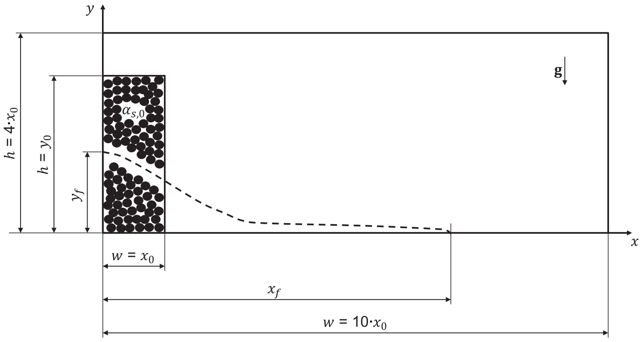

Fig. 1. Conceptual sketch of the CCP with dimensions used in this study. Solid line rectangle filled with particles represents initial condition at $t = 0$, dashed line represent a possible final shape. Large black solid line rectangle represents the dimensions of the computational domain.

$$\begin{aligned} a < 1.15: &\quad \lambda_y = 1 \quad \& \quad n_y = 0 \\ a > 1.15: &\quad \lambda_y = 1 \quad \& \quad n_y = -\frac{2}{5} \end{aligned} \tag{6}$$

for the scaling law (2), in contrast to Bougouin and Lacaze [2],[3] who recently established for the scaling law (1)

$$\begin{aligned} a < 2: &\quad \lambda_x = 2.7 \pm 0.3 \quad \& \quad n_x = 1 \\ a > 2: &\quad \lambda_x = 3.7 \pm 0.3 \quad \& \quad n_x = 0.64 \pm 0.02 \end{aligned} \tag{7}$$

and for the scaling law (2)

$$\begin{aligned} a < 0.75: &\quad \lambda_y = 1 \quad \& \quad n_y = 0 \\ a > 0.75: &\quad \lambda_y = 0.80 \pm 0.07 \quad \& \quad n_y = -0.65 \pm 0.04 \end{aligned} \tag{8}$$

The CCP with an interstitial liquid has been far less investigated. The final run-out length and deposit height does not differ much from the dry case [8]. However, the initial solid volume fraction arises as a relevant parameter [10,11]. Rondon et al. [10] showed that the initial solid volume fraction of the cliff (for instance $\alpha_{s,\,0} = 0.55$ corresponding to a loose state as a result of plain sedimentation vs. $\alpha_{s,\,0} = 0.60$ corresponding to a dense state as a result of enforced precompaction) is a major parameter affecting the dynamics of the collapse. The loose configurations collapse rapidly on time scales proportional to the initial heights and result in elongated final deposits with a decreasing slope for decreasing volume fractions. Dense configurations feature much smaller dynamics on time scales that increase with increasing volume fractions. For instance, for initially loose beds ($\alpha_s = 0.55$) of sand collapsing in a fluid, the time to steady-state of the collapsing cliff is in the order of 1 s, whereas for initially dense beds ($\alpha_s = 0.60$), it takes about 30–40 s until the final state is reached [10]. The final slopes of these deposits are approximately constant and equal to the material's angle of repose. A physical explanation is that for the dense cliff to flow the solids need too dilate first, which results in liquid flowing into the cliff due to a negative pore pressure opposing the disintegration. By contrast, the loose column ejects liquid because of positive pore pressure which enhances the disintegration of the cliff.

Recently, Bougouin and Lacaze [2] showed that collapses of a granular column and the corresponding flow regimes may be characterized by a Stokes number in the form of

$$St = \frac{\sqrt{0.5\rho_s \Delta\rho \|\mathbf{g}\| d_s^3}}{18\eta} \tag{9}$$

and the square root of the fluid-solid density ratio

$$r = \sqrt{\frac{\rho_s}{\rho_f}} \tag{10}$$

and may be consequently categorized into one of the following granular flow regimes:

- **Free Fall Regime** (FFR) for $St \gg 1$ and $r \gg 1$, typically the dry case, where the ambient fluid has no effect on the collapse.
- **Inertial Regime** (IR) for $St \gg 1$ and $r \ll 1$, where the individual grain reaches its inertial limit velocity and gravity is balanced by fluid drag force.
- **Viscous Regime** (VR) for $St \ll 1$, where the individual grain reaches its Stokes limit velocity.

Furthermore, Bougouin and Lacaze [2] showed that the coefficients given in Eq. (7) and (8) only apply to the FFR and the IR. The VR features different coefficients instead. The coefficients for the VR run-out length are

$$\begin{aligned} a < 2: &\quad \lambda_x = 1.5 \pm 0.1 \quad \& \quad n_x = 1 \\ a > 2: &\quad \lambda_x = 1.9 \pm 0.1 \quad \& \quad n_x = 0.64 \pm 0.02 \end{aligned} \tag{11}$$

and for the deposit height

$$\begin{aligned} a < 0.75: &\quad \lambda_y = 1 \quad \& \quad n_y = 0 \\ a > 0.75: &\quad \lambda_y = 0.87 \pm 0.03 \quad \& \quad n_y = -0.52 \pm 0.02 \end{aligned} \tag{12}$$

1.3. Modeling work

Two major modeling approaches are typically utilized for the rheological description of the granular matter:

1. Simplifying the granular media to a single phase yet complex fluid, a so-called $\eta(I)$-rheology, where the viscosity coefficient is a function of the inertial number $I = 2\dot{\gamma} d_s / \sqrt{p/\rho_s}$ and goes from a minimum value for low I characterizing the quasi-static regime to an asymptotical finite value for large values of I [1,12–16].
2. Using a Two-Fluid-Model framework and assuming additivity [17], the solid stress tensor is decomposed into two contributions, the first, namely $\mathbf{T}_{s,k/c}$, based on the Kinetic Theory of Granular Flows (KTGF) developed by Savage [18–20] handling the loose, i.e. the collisional/kinetic regime1F[4] ($\alpha_s < \alpha_{s,f}$) and the second, namely $\mathbf{T}_{s,f}$, utilizing closures from soil mechanics describing the dense regime

---

[3] Bougouin and Lacaze used spherical glass beads with \rho_p = {2500, 2230} and d_p ≈ {1, 3} mm, respectively.

[4] By some researchers referred to as inertial regime or viscous regime.

$(\alpha_s > \alpha_{s,f})$[5], where frictional contacts dominate. Various closure laws exist for the solid pressure $p_{s,k/c}$ [20] and solid viscosity $\eta_{s,\ k/c}$ [20] being mainly a function of the granular temperature θ and the solid volume fraction α_s. Some closures exist for the frictional pressure $p_{s,f}$ [21,22] and frictional viscosity $\eta_{s,f}$ [22,23] being a function of the solid volume fraction α_s and the magnitude of the solid shear rate tensor $\dot{\gamma}_s = \|\dot{\boldsymbol{\gamma}}_s\|$ as well as the solid pressure p_s,.respectively.

The inertial number dependent rheology may be considered much more general than the TFM-KTGF-SM framework. The former accounts for the transition between frictional and collisional regimes in a continuous and physical manner (It can be correlated to physical parameters like particle diameter, inter-particle friction and particle stiffness) while the latter is simply based on a discrete solid volume fraction threshold. Recently, inertial number dependent rheology formulations have been successfully applied to the TFM approach [24,25]. However, such models have not yet found its way into commercial codes.

CFD cuttings transport studies typically employ the second approach. For the sake of completeness, relevant alternative approaches to describe granular flows are Discrete Element Modeling (DEM), e.g. [9,26], where individual particles or parcels are tracked in a Lagrangian manner in addition to the continuum modeling of the carrier phase and Smooth Particle Hydrodynamics (SPH) [27]. DEM methods are however severely limited by affordable and available computational power for larger systems and SPH has not yet gained wide application in industrial environments yet.

The inclusion of the frictional regime is particularly relevant when heap building is of relevance [28]. For instance, when modeling the hour glass problem, heap building in the lower chamber does not occur if the solid stress tensor does not include $\mathbf{T}_f$ with a solid viscosity material function accounting for plasticity [28]. A widely used model is the one of Schaeffer [23], which is based on a Mohr-Coulomb yield criteria and produces large frictional viscosities in case of vanishing shear rates and high solid pressures such that flow is effectively blocked.

For small aspect ratios, the frictional viscosity is dominating the dynamics [29], while for larger aspect ratios, where inertia and velocity magnitudes become much larger, the inclusion of either a $\eta(I)$-description [15] or a KTGF-description [30] appears required to account for the different dynamics.

Savage et al. [31] recently showed that a mixture model approach with the inclusion of the Schaeffer [23] frictional viscosity model is a suitable alternative to model the collapse of granular media for both air and water as interstitial fluid. However, for three-dimensional cuttings transport modeling, the mixture model is not as suited as the TFM because of very heterogeneous solid concentrations.

1.4. Scope and structure

Recent studies [32,33] question the applicability of the classical Schaeffer frictional viscosity model [23] and found that different yield criteria and frictional viscosity closures are required. In contrast, the inclusion of these models is required to properly describe dense granular shearing flows with the KTGF [30].To evaluate the validity of the prescribed modeling approach for cuttings transport problems, where dense sediment beds may form at the lower wall of the annular flow domain, we investigate the cliff collapse problem for granular media (sand in air, water and two shear-thinning aqueous polymer solutions) on nine different spatial scales (respective combinations of three domain sizes and three particle diameters) for different initial aspect ratios and solid volume fractions of the cliff.

The important question is whether in the absence of external flow, i.e. the drilling fluid flushing the annulus, the solid phase behaves like a true granular matter under the pure influence of gravity and eventually stops flowing by building a static bed, satisfying a prescribed angle of repose.

We first provide a description of the physical model, followed by all relevant information on the various cases investigated and the CFD setup and numerical method. We then present all results, where we compare the numerical findings with the aforementioned scaling laws of Lube et al. [3] and Bougouin and Lacaze [2]. In the following discussion, we focus on the observed differences between scaling laws and numerical results as well as the role of the initial solid volume fraction in case of liquid interstitial fluids and the computational procedure utilized.

2. Materials & methods

2.1. Physical model

In the TFM, both the fluid (index f) and the solid (index s) phase are treated as a continuum and assumed both isothermal and incompressible3F[6]. Hence, for an arbitrary volume element V_i, the phase volume fractions α_i must sum to one, i.e.

$$V_i = \int_V \alpha_i dV \quad \wedge \quad \sum_i \alpha_i = 1 \quad \wedge \quad i \in \{f, s\} \tag{13}$$

and mass conservation is given by

$$\frac{\partial}{\partial t}(\alpha_i \rho_i) + \nabla \cdot (\alpha_i \rho_i \mathbf{u}_i) = 0 \tag{14}$$

where the index $i \in \{f,s\}$ and ρ_i and $\mathbf{u}_i$ denote the intrinsic volume averages of density and velocity, respectively.

Both phases obey a general form of the Cauchy momentum transport equation of the form, which for the fluid and solid phase respectively reads

$$\begin{aligned}\frac{\partial}{\partial t}\left(\alpha_f \rho_f \mathbf{u}_f\right) + \nabla \cdot \left(\alpha_f \rho_f \mathbf{u}_f \mathbf{u}_f\right) = {} & -\alpha_f \nabla p_f + \nabla \cdot (\alpha_f \boldsymbol{\tau}_f) \\ & + \alpha_f \rho_f \mathbf{g} - \frac{1}{V} \sum_{p \in V} \mathbf{f}_j\end{aligned} \tag{15}$$

$$\begin{aligned}\frac{\partial}{\partial t}(\alpha_s \rho_s \mathbf{u}_s) + \nabla \cdot (\alpha_s \rho_s \mathbf{u}_s \mathbf{u}_s) = {} & -\alpha_f \nabla p_f - \nabla p_s + \nabla \cdot \boldsymbol{\tau}_s + \alpha_s \rho_s \mathbf{g} \\ & + \frac{1}{V} \sum_{p \in V} \mathbf{f}_j\end{aligned} \tag{16}$$

where $\boldsymbol{\tau}_i$ is the phasic deviatoric stress tensor comprising some constitutive equation, here a compressible Generalized Newtonian Fluid (GNF) and phase-dependent material functions for the shear and bulk viscosities, η_i and κ_i,

$$\boldsymbol{\tau}_i = 2\eta_i \mathbf{D}_i + \left(\kappa_i - \frac{2}{3}\eta_i\right)(\nabla \cdot \mathbf{u}_i)\mathbf{I} \tag{17}$$

where $\mathbf{D}_i$ is the symmetric part of the fluid or solid velocity gradient (also known as the rate of deformation tensor, or alternatively the rate of strain tensor)

$$\mathbf{D}_i = \frac{1}{2}\left(\nabla \mathbf{u}_i + \nabla \mathbf{u}_i{}^T\right) \tag{18}$$

and the shear rate $\dot{\gamma}_i$ is the magnitude of the rate of deformation tensor $\mathbf{D}_i$,

---

[5] By some researchers referred to as plastic regime or frictional regime.

[6] Note that the solid phase may feature some closure law which accounts for the compressibility of granular matter.

Table 1
Overview of solid phase state equations and material functions used to model the kinetic/collisional (index *k*/*c*) and frictional (index *f*) regimes.

Regime	Quantity	Closure law	Source
Kinetic/collisional (***j*** = ***k***/***c***)	Pressure	$p_{s,k/c} = \alpha_s \rho_s \Theta_s + 2{\alpha_s}^2 \rho_s \Theta_s \left(1 + e_{ss}\right) g_{0,ss} \quad (31)$	[20]
	Shear viscosity (collisional)	$\eta_{s,c} = \frac{4}{5}{\alpha_s}^2 \rho_s d_s g_{0,ss} (1 + e_{ss}) \left(\frac{\Theta_s}{\pi}\right)^{\frac{1}{2}} \quad (32)$	[20]
	Shear viscosity (kinetic)	$\eta_{s,k} = \frac{10 \rho_s d_s \sqrt{\Theta_s \pi}}{96(1 + e_{ss}) g_{0,ss}} \left(1 + \frac{4}{5}\alpha_s \left(1 + e_{ss}\right) g_{0,ss}\right)^{\frac{1}{2}} \quad (33)$	[34]
	Bulk viscosity	$\kappa_{s,c/k} = \frac{4}{3} {\alpha_s}^2 \rho_s d_s g_{0,ss} (1 + e_{ss}) \left(\frac{\Theta_s}{\pi}\right)^{\frac{1}{2}} \quad (34)$	[20]
Frictional (***j*** = ***f***)	Pressure	$p_{s,f} = 0.05 \, \frac{(\alpha_s - \alpha_{s,f})^2}{(\alpha_{s,mpd} - \alpha_s)^5} \quad (35)$	[21]
	Shear viscosity	$\eta_{s,f} = \frac{p_s \, \sin\phi_s}{\sqrt{2} \Vert \mathbf{D}_s \Vert} \quad (36)$	[23]
	Bulk viscosity	n/a	n/a

$$\dot{\gamma}_i = \sqrt{2\mathbf{D}_i : \mathbf{D}_i} \tag{19}$$

The closures for the granular viscosities are provided in Section 2.3 and the rheological closure of the fluid is given in Section 2.2.

The last term in Eqs. (15) and (16) represents the momentum transfer of one phase to the other, where the force sum is to be taken over all particles in the volume *V*. We here only consider the drag force $\mathbf{f}_D$, which is typically modeled based on the relative velocity

$$\mathbf{u}_r = \mathbf{u}_s - \mathbf{u}_f \tag{20}$$

as

$$\frac{1}{V} \sum_{p \in V} \mathbf{f}_j = K \mathbf{u}_r \tag{21}$$

where the interphase exchange coefficient *K* is generically expressed as

$$K = \frac{\alpha_s \rho_s f}{T_s} \tag{22}$$

with the Stokes relaxation time T_s written as

$$T_s = \frac{\rho_s {d_s}^2}{18 \eta_f} \tag{23}$$

The functional *f* in Eq. (22) includes specific a drag function $c_d(Re_p)$ and depends on the particular model utilized. We use the formulation of Gidaspow [34], which is a combination of the Wen and Yu model [35] and the Ergun equation [36], where the interphase exchange coefficient *K* is given as

$$\begin{aligned} \alpha_s \le 0.2: \quad & K = c_D \frac{3 \alpha_s \rho_f \Vert \mathbf{u}_r \Vert}{4 {\alpha_f}^{0.65} d_s} \\ \alpha_s > 0.2: \quad & K = 150 \, \frac{{\alpha_s}^2 \eta_f}{\alpha_f {d_s}^2} + 1.75 \, \frac{\alpha_s \rho_f \Vert \mathbf{u}_r \Vert}{d_s} \end{aligned} \tag{24}$$

where the coefficient of drag is defined as

$$c_D = \frac{24}{\alpha_f \, \mathrm{Re}_p} \left(1 + 0.15 \left(\alpha_f \, \mathrm{Re}_p\right)^{0.687}\right) \tag{25}$$

and the particle Reynolds number is defined as

$$\mathrm{Re}_p = \frac{\rho_f d_s \Vert \mathbf{u}_r \Vert}{\eta_f} \tag{26}$$

2.2. Fluid rheological properties

We here limit the rheological description of a drilling fluid model system to purely shear-thinning behavior. Often, experimental cuttings transport studies utilize polymeric solutions because these are easy to produce, non-hazardous and translucent. The shear viscosity of polymeric solutions is well-characterized by the Cross (Cr) [37] material function

$$\eta_f = \frac{\mu_0 - \mu_\infty}{1 + \left(\lambda_{Cr} \dot{\gamma}_f\right)^{n_{Cr}}} + \mu_\infty \tag{27}$$

because this represents the shear viscosity data much better for a wider shear rate range since it accounts for Newtonian viscosities at both low and high shear rates [38]. Here, μ_0 is the zero-shear viscosity, μ_∞ is the infinite-shear viscosity, λ_{Cr} is the Cross time constant and n_{Cr} is the Cross exponent. Moreover, this model collapses to the simple Newtonian case for e.g. $\mu_0 = \lambda_{Cr} = n_{Cr} = 0$.

The fluid phase is assumed incompressible and consequently the bulk viscosity in Eq. (17) becomes zero.

2.3. Solid rheological properties

As mentioned in the introduction, the KTGF framework developed by Savage [18–20] is used to describe the loose, i.e. the collisional/kinetic regime4F[7] (solid volume fraction $\alpha_s < \alpha_{s,f} = 0.55$) and additionally closures from soil mechanics are applied to describe the dense regime ($\alpha_s \ge \alpha_{s,f}$) of the solids.

Assuming additivity [17], the entire solid stress tensor, namely Eq. (17) with index *s* and including the solid pressure p_s, is then given by the sum of collisional/kinetic and frictional components

$$\begin{aligned} \mathbf{T}_s &= \mathbf{T}_{s,k/c} + \mathbf{T}_{s,f} \\ &= \sum_{j \in \{k/c,f\}} \left[\left(-p_{s,j} + \left(\kappa_{s,j} - \frac{2}{3} \eta_{s,j} \right) \nabla \cdot \mathbf{u}_s \right) \mathbf{I} + 2 \eta_{s,j} \mathbf{D}_s \right] \end{aligned} \tag{28}$$

Even though the general stencil is that of a compressible Newtonian fluid, namely Eq. (17), the rheological properties of the solid phase given by the respective material functions as summarized in Table 1 are highly non-linear. They depend on a variety of parameters and variables such as the granular temperature Θ_s as a measure for the degree of random particle motion (granular fluctuations due to individual particle collisions), for which the general transport equation reads [39].

---

[7] In the literature, these regimes are alternatively known as the inertial or viscous regime and the plastic or frictional regime, respectively.

Table 2
Fluid densities and rheological model coefficients at room temperature (21 °C) and atmospheric pressure (1.01 bar).

Fluid	ρ_f [kg/m^3]	Cross model coefficients			
		μ_0 [Pa·s]	μ_∞ [Pa·s]	λ_{Cr} [1/s]	n_{Cr} [−]
Air	$1.225{\cdot}10^{0}$	0	$1.79{\cdot}10^{-5}$	0	0
H_2O	$9.980{\cdot}10^{2}$	0	$1.002{\cdot}10^{-3}$	0	0
PAC2	$1.000{\cdot}10^{3}$	$7.210{\cdot}10^{-2}$	$1.002{\cdot}10^{-3}$	$1.090{\cdot}10^{-2}$	0.586
PAC4	$1.000{\cdot}10^{3}$	$2.140{\cdot}10^{-1}$	$1.002{\cdot}10^{-3}$	$2.610{\cdot}10^{-2}$	0.608

$$\frac{3}{2}\left[\frac{\partial}{\partial t}(\alpha_s\rho_s\Theta_s)+\nabla\cdot(\alpha_s\rho_s\mathbf{u}_s\Theta_s)\right]=\mathbf{T}_s:\nabla\mathbf{u}_s+\nabla\cdot(k_{\Theta_s}\nabla\Theta_s)-D_{\Theta_s}+K_{fs} \tag{29}$$

where k_{Θ_s} is the granular conductivity [e.g. 21] and the two final terms in Eq. (29) are the collisional dissipation of energy [20] and the interphase exchange between the particle fluctuations and the fluid phase [34].The granular temperature Θ_s is defined as

$$\Theta_s=\frac{1}{3}\langle u_{s,i}{}' u_{s,i}{}'\rangle \tag{30}$$

where $u_{s,i}{}'$ is the i-th fluctuating component of the solids velocity and the bracket represents an ensemble average of the fluctuating velocities of all particles within a finite volume [39].

Eq. (29) is simplified to an algebraic equation by neglecting the convection and diffusion terms—an often used assumption in dense, slow moving fluidized beds where the local generation and dissipation of granular temperature far outweigh the transport by convection and diffusion.

In Eqs. (31)–(34), e_{ss} is the coefficient of restitution for particle collisions and

$$g_{0,ss}=\left[1-\left(\frac{\alpha_s}{\alpha_{s,\,\max}}\right)^{\frac{1}{3}}\right]^{-1} \tag{37}$$

is the radial distribution function accounting for the probability of particle collisions, which has been used frequently in the history of granular flows [20,40–42] in the form presented in Eq. (37).

2.4. Test matrix

We investigated the influence of the aspect ratio and scale of the initial cliff ($a = y_0/x_0 = 1, 2, 3$, and $x_0 = 0.1, 1, 10$ m, respectively), the scale of the particle size ($d_s = 10^{-4}, 10^{-3}, 10^{-2}$ m), four different interstitial fluids (air, water, and two viscous but shear-thinning polymer solutions, namely Polyanionic Cellulose with concentrations of 2 g/L and 4 g/L, hereafter termed PAC2 and PAC4, respectively, all material data provided in Table 2), and the role of the initial conditions (ICs) such as solid volume fraction $\alpha_{s,\,0}$ and solid pressure fields. Fig. 2 provides the logical relationship of the investigated parameters for the example of $a = 3$.

By letting the solids settle and establish a granular bed in a pre-simulation, smooth fields for $\alpha_{s,\,0}$ (average $\alpha_{s,\,0} \approx 0.59$) and p_s as well as other quantities are obtained which allow for a smooth simulation start when the RHS wall of the cliff is being removed instantly. The alternative is to simply patch the respective $\alpha_{s,\,0}$ into the computational domain, which we have also investigated for a $\alpha_{s,\,0} = \{0.55, 0.60\}$, as depicted in Fig. 2.

For each IC, we investigated the role of four different interstitial fluids (see Table 2) and nine different cases. The latter are spatial combinations of the particle diameter range and the initial cliff scale, as provided in Table 3 and depicted in Fig. 2.

In all cases, the solid phase was replicating sand, represented by mono-sized spherical particles with a density $\rho_s = 2560$ kg/m^3. In the frictional closures, namely Eqs. (35) and (36), the angle of internal friction ϕ_s was assumed to be 45° in order to yield an angle of repose of the final deposit of approximately 25°…30° [28], the coefficient of restitution for particle collisions e was taken as 0.9, the maximum packing density of the solid phase $\alpha_{s,mpd}$ was defined as 0.63 and the solid volume fraction threshold for the dense regime, where the frictional model activates, was $\alpha_{s,\,f} = 0.50$.

2.5. CFD setup & numerics

For the three cliff scales investigated, three structured quadrilateral 2D meshes with an initial grid size $\Delta x = 0.002, 0.02, 0.2$ m were generated. In order to precisely track the evolution of the collapsing cliff, adaptive meshing was used throughout the simulations to refine the mesh based on the magnitude of the solid volume fraction gradient $\|\nabla\alpha_s\|$ every fifth timestep. Depending on the fluid type, simulations were run for 4 s (air, $\Delta t = 10^{-4}$ s) or 100 s (all liquids, $\Delta t = 10^{-3}$ s) to obtain the final solution.

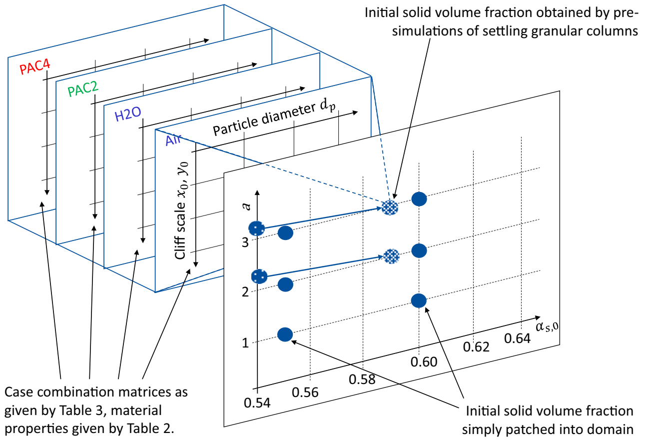

Fig. 2. Different cases investigated. For each combination of aspect ratio a and initial volume fraction $\alpha_{s,\,0}$, the nine spatial combinations provided in Table 3 where simulated for each fluid phase indicated.

Table 3
Investigated combinations of spatial scales for initial cliff and particle. The matrix given by Table 3 is the framework of each of the individual materials for a given aspect ratio as depicted by Fig. 2. The symbols indicated are respectively used in all remaining figures of the paper (unless indicated otherwise).

		Particle scale		
		Small ($d_s = 0.0001$ m)	Medium ($d_s = 0.001$ m)	Large ($d_s = 0.01$ m)
Cliff scale	Small ($w = 0.1$ m, $y_0 = 0.04$ m, $\Delta x = 0.002$ m)	1 / ○	2 / ○	3 / ○
	Medium ($w = 1$ m, $h = 0.4$ m, $\Delta x = 0.02$ m)	4 / ◇	5 / ◇	6 / ◇
	Large ($w = 10$ m, $h = 4$ m, $\Delta x = 0.2$ m)	7 / □	8 / □	9 / □

We used ANSYS Fluent R17.2, a commercial Finite Volume code and hereafter simply termed Fluent, to solve the physical model. The flow fields were solved using the Phase-Coupled SIMPLE scheme [43] in a segregated manner (but coupled by phases) with conservative underrelaxation factors, as conceptually shown in Fig. 3.

A shared pressure correction equation is solved, based on total continuity. Fluent is based on a collocated grid and uses a “Rhie and Chow type of scheme to calculate volume fluxes” [45,46]. The solid volume fraction is solved for the secondary phase and the primary phase value is then obtained from the constraint (13). After solving the granular temperature Eq. (29), the solid pressures (31) and (35) are obtained from the solid volume fractions.

The QUICK scheme [44] was applied for spatial discretization and the Green-Gauss node-based gradient scheme to evaluate all gradients. The term ∇p_s in the momentum equation of the granular phase, namely Eq. (15) with index s in combination with Eq. (28), is numerically resolved by $\nabla p_s \approx \partial p_s / \partial \alpha_s \nabla \alpha_s$. The time discretization was implicit second order. The algebraic multigrid method with the Gauss-Seidel solver was used to solve the system of discretized equation.

3. Results

First, we provide a mapping of our investigated cases on the flow regime map of Bougouin and Lacaze [2] because the scaling laws to use for model validation depend on the granular flow regime. Our numerical results are subsequently presented in the following manner: For each of the first phase fluids and initial solid volume fractions investigated, we depict the numerical results in the form of the dimensionless final run-out length and final deposit height per aspect ratio a together with the scaling laws of Lube et al. [3] and Bougouin and Lacaze [2]. Examples of the dimensional final shapes of the deposit, together with the initial shapes and snapshots of the evolution of the cliff disintegration using the matrix framework given in Table 3 and Fig. 2 are provided in Appendix A.

Both the dimensional final run-out length and the dimensional final deposit height were determined based on the maximum of the volume fraction gradient, with restrictions imposed on the y- and x-coordinate, respectively:

$$\begin{aligned} x_f &= x(\max\|\nabla\alpha_s(x, y \geq d_s)\|) \\ y_f &= y(\max\|\nabla\alpha_s(\Delta x, y)\|) \end{aligned} \tag{38}$$

3.1. Granular flow regimes

By expressing our design space in terms of the quantities defining the granular flow regime of Bougouin and Lacaze [2], namely eqs. (9) and (10), we can identify the respective granular flow regimes for the individual cases as depicted on Fig. 4.

The spatial scale of the cliff is not a parameter in the space of Bougouin and Lacaze [2], hence the different spatial scales of the cliff as investigated in this study collapse on one single point, respectively.

The granular flow regime mapping shows that when it comes to the scaling laws of Bougouin and Lacaze [2], the correct scaling benchmark for the air numerical results are given by the coefficients (7) and (8). For the H2O and PAC2 cases, the coefficients (7) and (8) as well as (11) and (12) apply, however, depending on the particle diameter. The PAC4 cases are entirely covered by the coefficients (11) and (12).

3.2. Sand in air

Fig. 5 provides the dimensionless final run-out length and final deposit height for $\alpha_{s,\,0} \approx 0.59$, i.e. where the IC conditions of the

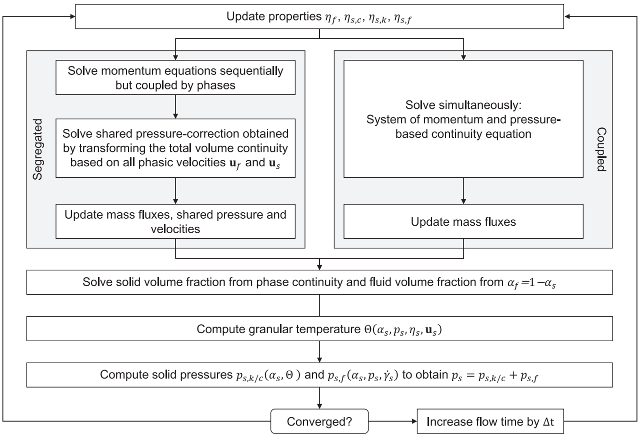

Fig. 3. Computational sequences of ANSYS Fluent R17.2, adapted from [45,46].

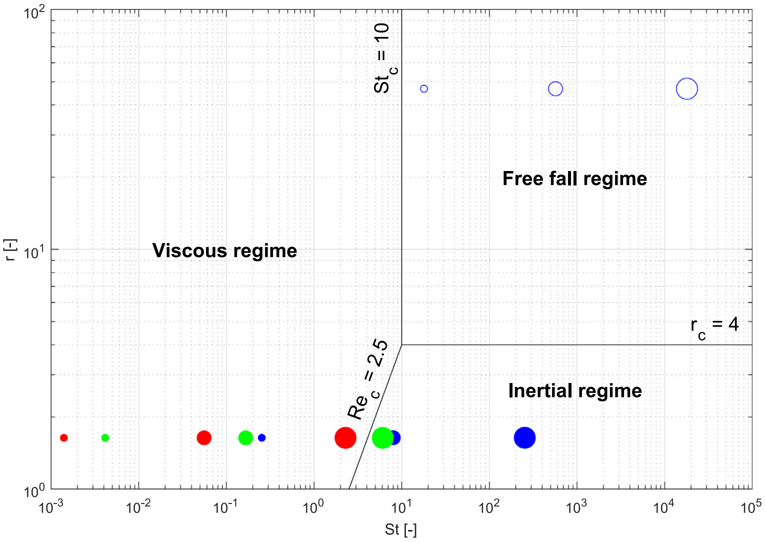

Fig. 4. Different cases investigated mapped on granular fluid flow regime map (square root of grain density ratio r vs. Stokes number St) of Bougouin and Lacaze [2]. Colors indicate fluids as defined in Fig. 2 (blue circled = air, blue filled = H2O) and sizes of data points represent the three different particle diameters. Note that the different symbols as defined in Table 3 fall onto one point because the spatial size of the cliff is not part of the r-St-space of Bougouin and Lacaze [2]. (For interpretation of the references to colour in this figure legend, the reader is referred to the web version of this article.)

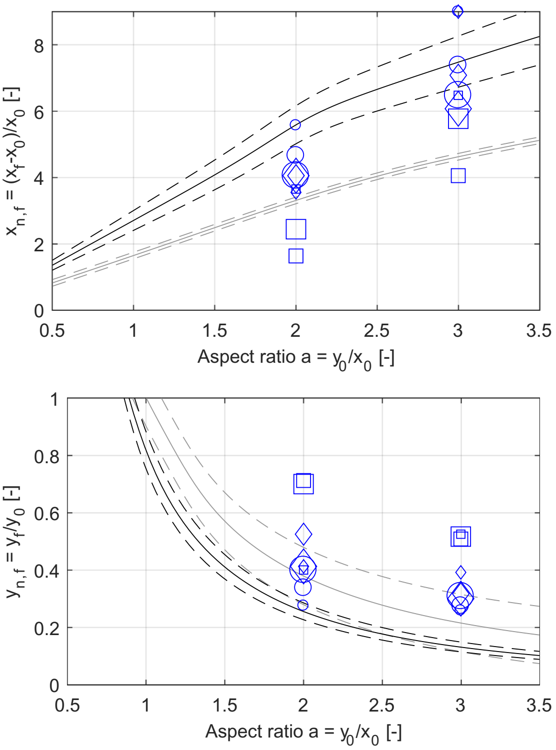

Fig. 5. Final non-dimensional run-out $x_{n,f}$ (left) and height $y_{n,f}$ (right) for sand in air with $\alpha_{s,0} \approx 0.59$. The data points correspond to the dimensional x_f and y_f values depicted in A.1.1. Grey solid lines represent the scaling of Lube et al. [3] with dashed lines indicating ± 10%, black solid lines the scaling of Bougouin and Lacaze [2] for the FFR with dashed lines indicating uncertainty given in [2].

simulation where obtained by letting a pile of sand settle in air in order to obtain steady and smooth fields for all quantities. Figs. 6 and 7 depict the dimensionless final run-out length and final deposit height for $\alpha_{s,0} = 0.55$ and $\alpha_{s,0} = 0.60$, respectively. Here, the IC were given by the constant $\alpha_{s,0}$ only, which was simply patched into the computational domain.

Most of the numerical run-out length data falls between the two scaling curves of Lube et al. [3] and Bougouin and Lacaze [2]. Exceptions are for instance the small particle diameters for the intermediate and large cliff scale for $a = 1$ in case of the patched solid volume fraction $\alpha_{s,0} = 0.55$ (Fig. 6 left) as well as the intermediate and large particle diameters for the large cliff scale for $a = 2$ in case of the pre-simulated solid volume fraction $\alpha_{s,0} \approx 0.5$ (Fig. 5 left).

Both exceptions are represented in the respective deposit height plots, were in case of the latter the data points fall above (Fig. 5 right) and in case of the former the data points fall below the scaling laws (Fig. 6 right).The deposit height data for the large cliff scale cases fall consistently on top of the scaling laws, i.e. the numerically obtained deposit height is always larger than the experimentally obtained as represented by the scaling laws.

For the non-dimensional run-out length $x_{n,f}$, some data points coincide at the maximum value. This is the end of the computational where solids where stopped by the boundary wall.

On a more general note, for a particular aspect ratio all results feature a spread in the order of up to ± ≈ 50% for the run-out distances and ± ≈ 50% for the deposit heights.

3.3. Sand in water

Fig. 8 provides the dimensionless final run-out length and final deposit height for $\alpha_{s,0} \approx 0.59$, i.e. where the IC conditions of the simulation where obtained by letting a pile of sand settle in air in order to obtain steady and smooth fields for all quantities. Figs. 9 and 10 depict the dimensionless final run-out length and final deposit height for $\alpha_{s,0} = 0.55$ and $\alpha_{s,0} = 0.60$, respectively. Here, the IC were given by the constant $\alpha_{s,0}$ only, which was simply patched into the computational domain.

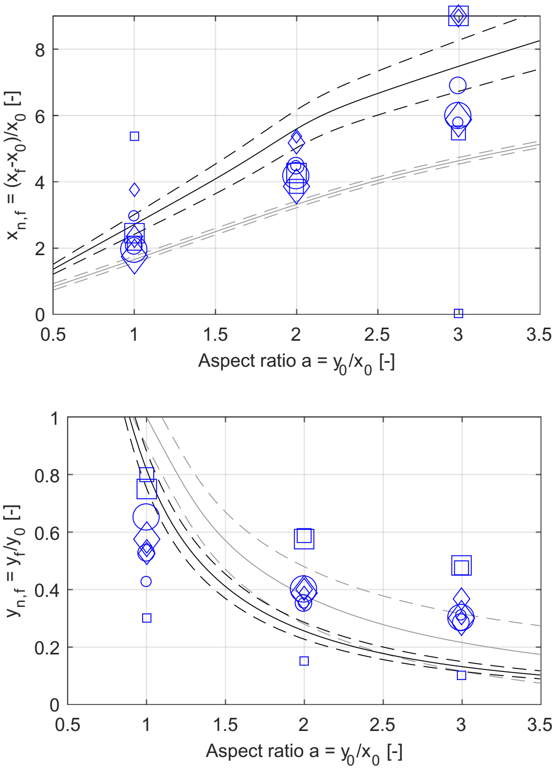

Fig. 6. Final non-dimensional run-out $x_{n,\,f}$ (left) and height $y_{n,\,f}$ (right) for sand in air with $\alpha_{s,\,0} = 0.55$. The data points correspond to the dimensional x_f and y_f values depicted in A.2.1. For further description see caption of Fig. 5.

In contrast to the air results, most of the numerical run-out length data is much more scattered. However, the majority falls between the scaling curves for the VR and the IR of Bougouin and Lacaze [2]. Exceptions are for instance the small particle diameters for $a = \{1, 2\}$ in case of the patched solid volume fraction $\alpha_{s,\,0} = 0.55$ (Fig. 9 left) as well as the small particle diameters in case of the pre-simulated solid volume fraction $\alpha_{s,\,0} \approx 0.59$ (Fig. 8 left).

The numerical results for the deposit height are much less scattered than the run-out length results, except for $a = 1$, where the small particle diameter data is only about 25% of the scaling law magnitude. Consistently, for all $\alpha_{s,\,0}$, the large particle diameter cases fall above, and the small particle diameter cases fall below the scaling laws. Furthermore, the large cliff scale (represented by squared boxes) produces the largest deposit heights, while the intermediate and small cliff scales (represented by diamonds and circles, respectively) produce smaller deposit heights and lie close together.

The corresponding dimensional results show that for some combinations, e.g. $\alpha_{s,\,0} \approx 0.59$ and $a = 2$, cases 1, 4, 7, 8 (Fig. A.11), the cliff has entirely disintegrated and the steady-state is a flat sediment bed. In some other cases, e.g. $\alpha_{s,\,0} \approx 0.59$ and $a = 3$, case 7 (Fig. A.12), it appears as if the simulation time was to short and no steady-state has been reached yet. For these two phenomena, our implementation of Eq. (38) has difficulties capturing the final run-out length correctly, as may be seen from e.g. $\alpha_{s,\,0} \approx 0.59$ and $a = 2$, case 4 (Fig. A.12).

While the scaling laws state that the VR run-out lengths are shorter than the IR ones, this is not represented by the numerical data. As depicted on Fig. 4, the intermediate and large particle diameters cases fall into the IR and the small ones into the viscous regime. However, the order of the run-out length depicted on Figs. 8–10 is vice-versa in most cases when compared to the respective scaling laws.

The same applies to the deposit heights, where small diameters almost consistently feature the smallest deposit heights. However, as opposed to the run-out lengths the virtual difference between the deposit height scaling laws for the IR and VR is negligible.

3.4. Sand in PAC

For PAC, the same observations can be made as for the previously discussed water cases. However, the scatter of the data is worse. Hence, we only briefly summarize the major points of the PAC results[8]:

Many of the PAC2 results also fall between the two scaling laws for the run-out length. The large particle diameter cases produce deposit heights larger than what the scaling law predicts, and the order of the numerical results does not reflect the order of the flow regime dependent scaling laws.

An entirely leveled-out sediment bed also occurs for the small particle diameter cases. The not-occurred disintegration of the cliff occurs for almost the same cases.

3.5. Initial conditions in case of $\alpha_{s,\,0} \approx 0.59$

For all the cases $\alpha_{s,\,0} \approx 0.59$, i.e. where the IC conditions of the simulation where obtained by letting a pile of sand settle in the respective fluid in order to obtain steady and smooth fields for all quantities, the obtained fields showed a very inconsistent picture when it comes to smoothness.

For instance, in cases of the liquids where the cliff collapsed entirely and eventually yielded a horizontal deposit, initial conditions obtained by settling solids in a granular column do not feature a smooth frictional viscosity field. Fig. 11 depicts contour plots of the frictional viscosity, granular pressure and granular temperature at $t = 4$ s for $a = 2$ and case 1.

While the latter two appear smooth, the frictional viscosity shows regions of comparatively low viscosities in the lower center part and walls of the granular column and especially at the top of the bed.

3.6. Non-zero velocity at top of sediment bed

For all cases investigated, including the pre-simulations to obtain IC in case of $\alpha_{s,\,0} \approx 0.59$, the top-cells of the steady-state5F[9] sediment bed features a non-zero solid velocity, regardless of how long simulations are ran. Zooming in on the near-bed region of a pre-simulation as depicted in Fig. 12, it becomes clear that some of the cells feature a positive vertical solid velocity.

These are corelated with large changes of the kinetic/collisional solid pressure $p_{s,\,k/c}$, as shown in Fig. 12 (right) or more in Fig. B.7 in Appendix B, which shows the y-component of the gradient of the kinetic/collisional solid pressure $p_{s,\,k/c}$ displayed in Fig. 12 (right).

A more comprehensive set of field plots covering all relevant quantities is provided in Appendix B.

4. Discussion

At first glance, the numerical results appear to not scale well with the scaling laws of Lube et al. [3] and Bougouin and Lacaze [2]. In the following, we will first discuss the issue of non-zero velocities at the top of the deposit bed, which overshadows the results, and provide potential

---

[8] See https://www.youtube.com/playlist?list=PLfeJTTWUNqAXyvNppPBEMm5_I531YQV2p for some PAC2 CCP results and https://www.youtube.com/playlist?list=PLfeJTTWUNqAUFGIO9Gz-wFzHJxmTg1-cm for some PAC4 CCP results.

[9] Here steady-state is a relative term as the discussion will show. For now, it refers to the final state as obtained in the simulations at maximum flow time. More generally, and with respect to real world experiments, it is a state, where the deposit flow has completely stopped and the final shape is a deposit slope.

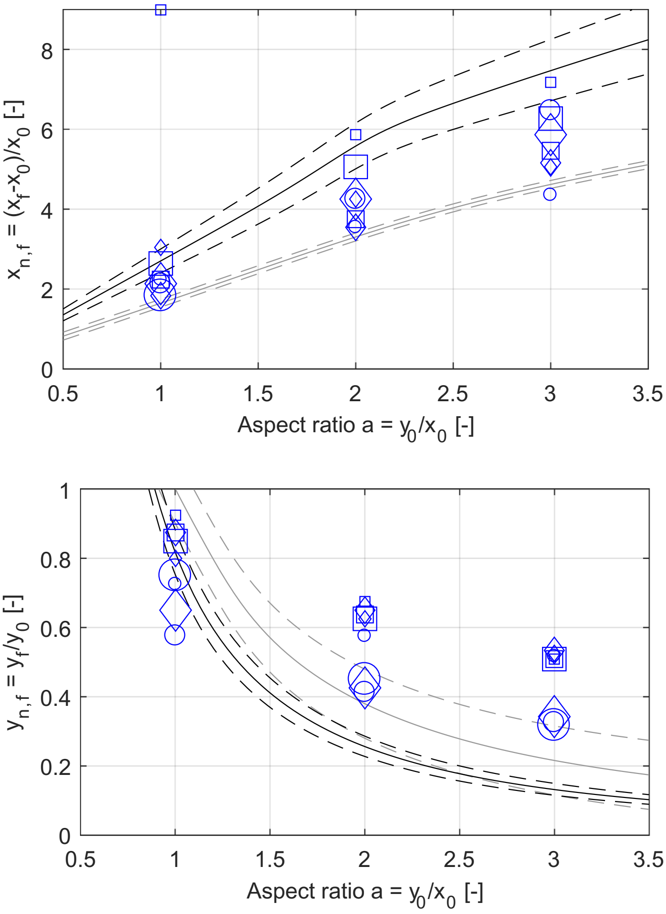

Fig. 7. *Final non-dimensional run-out* $x_{n,\,f}$ *(left) and height* $y_{n,\,f}$ *(right) for sand in air with* $\alpha_{s,\,0} = 0.60$*. The data points correspond to the dimensional* x_f *and* y_f *values depicted in A.3.1. For further description see caption of* Fig. 5.

explanations linked to the computational procedure. After briefly focusing on the relevance of the utilized closures laws for the solid stress tensor, we discuss the numerical results with respect to the scaling laws of Lube et al. [3] and Bougouin and Lacaze [2]. Finally, we comment on the applicability of the employed modeling approach for hydraulic conveying applications such as cuttings transport in wellbores and dune migration.

4.1. Non-zero velocity at top of bed

Because of the non-zero velocity in the grid cells at the top of the deposit bed, the entire top-layer of the granular bed remains in a—in the framework of the TFM—low-viscosity-like state and thus keeps flowing over long periods of time. Hence, the non-zero velocity in the grid cells close to the top of the deposit bed is affecting the final run-out length and deposit height because solids are continuously redispersed into the fluid layer on top of the sediment bed and settle back down. The top-layer of the sediment bed is a region of high shear and thus the frictional viscosity is very low leading to the top layer of the sediment bed remaining in a low-viscosity-like state, regardless of the total simulation time. In case of the cliff collapse problem, this leads to a small but continuous downslope flow of sediment, which over longer time scales further reduces the deposit height and consequently increases the run-out length. It is important to realize that this hereafter called *top bed velocity defect* not only avoids a steady-state (The system does not really reach a true steady-state as the top layer of the granular bed remains in a dynamic state) but also affects the dynamics of the granular collapse by a small degree.

The reason for this positive solid velocity component as shown in Fig. 12 is the internal switching of Fluent when it comes to the computation of the solid stress tensor, namely Eq. (28): For cells where $\alpha_s < \alpha_{s,f} = 0.5$, only the kinetic/collisional part $\mathbf{T}_{s,\,k/c}$, is computed and the frictional part $\mathbf{T}_{s,f}$ is zero, i.e., the solid phase in these cells is not subject to the frictional models as given by eqs. (35) and (36), and is only governed by the KTGF. However, the non-consideration of the frictional viscosity $\eta_{s,f}$ leads to very low values of the solid viscosity η_s and thus results in a liquid-like state of the solids phase. Apparently, in these cells the solid pressure gradient $\nabla p_{s,k/c}$ (which is determined based on Eq. (31) and not by pressure-velocity coupling) is then large enough to overcome the effect of gravity and provide enough momentum to lift the solids.

In case of an inclined bed, for instance the states of the cliff collapse system after collapse and when reaching a first quasi steady state where the deposit shape features an angle of repose, α_s in the top layer cells may have any numerical value between 0 and $\alpha_{s,mpd}$ because the cell is not necessarily entirely filled with the dense bed. While this is

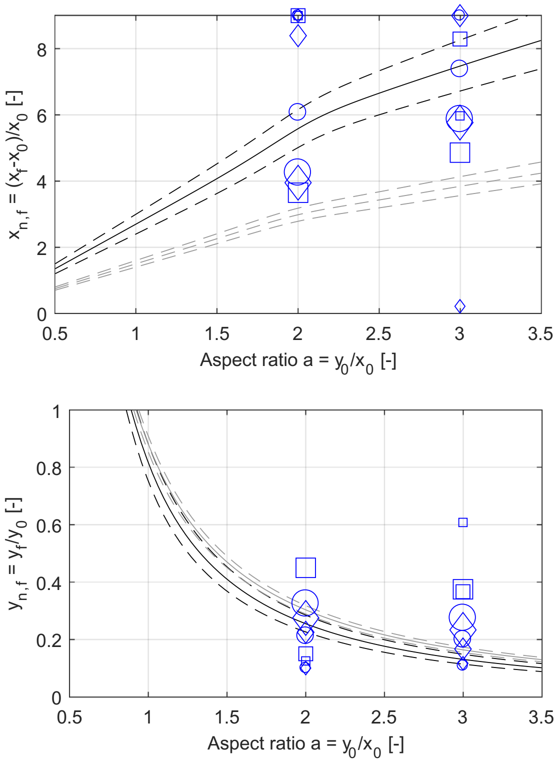

Fig. 8. Final non-dimensional run-out $x_{n,\,f}$ (left) and height $y_{n,\,f}$ (right) for sand in water with $\alpha_{s,\,0} \approx 0.59$. The data points correspond to the dimensional x_f and y_f values depicted in A.1.2. Grey solid lines represent the scaling of Bougouin and Lacaze [2] for the VR and black solid lines the scaling of Bougouin and Lacaze [2] for the IR, with dashed lines indicating uncertainty given in [2], respectively.

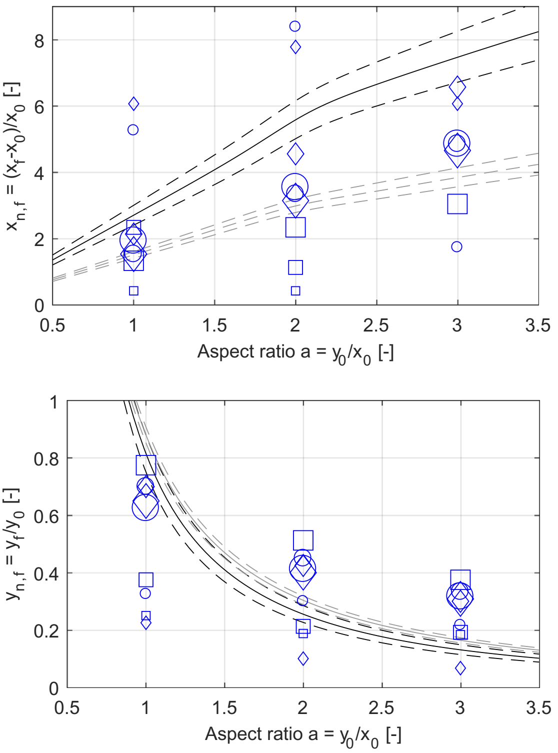

Fig. 9. Final non-dimensional run-out $x_{n,\,f}$ (left) and height $y_{n,\,f}$ (right) for sand in water with $\alpha_{s,\,0} = 0.55$. The data points correspond to the dimensional x_f and y_f values depicted in A.2.2. For further description see caption of Fig. 8.

perfectly representing the current shape of the deposit for the current point in time, the numerical values lead to a granular rheological behavior entirely governed by the KTGF because the frictional closures are only activated for $\alpha_s > \alpha_{s,fric} = 0.5$. Hence this top layer sees some self-induced flow due to the KTGF-governed cells.

4.2. Computational procedure

In order to better understand the described *top bed velocity defect* phenomena, we tried alternative numerical approaches such as implicit and explicit volume fraction treatment and the coupled (including coupled with volume fractions) solving approach. However, the same *top bed velocity defect* occurred. Letting the solver compute two volume fractions instead of exploiting constraint (13) led to divergence. Disactivating the KTGF state equation for the solid pressure, i.e. Eq. (31), led to a significant reduction of the *top bed velocity defect*. The granular temperature decreased significantly to very low levels.

Therefore, our hypothesis is that the observed phenomena is due to a checker-board-like issue arising in the multiphase pressure-velocity-coupling (PVC) concept employed by Fluent on a collocated grid which does not fully account for the KTGF solid pressure. While details of the “Rhie and Chow type of scheme to calculate volume fluxes” are not disclosed [45,46], it appears that volume fractions are held constant and the shared pressure is used as a basis. However, the Rhie and Chow interpolation procedure [47] used to compute the normal flux velocity components on the cell faces is known to produce collocated velocities under certain circumstances e.g. the presence of strong body forces such as when explicit solid pressure or gravity become strong [48]. In the top-layer region where the *top bed velocity defect* occurs, the solid pressures (31) and (35), which act as source term in the momentum equations, are strongly dependent on the solid volume fraction and hence should be considered in the pressure corrections step [48].

In earlier versions of Fluent, a second pressure correction equation appears to have been solved for the solid pressure [28,49]. In that case, the introduction of the additional state equations $p_s = p_{s,c/k}(\alpha_s,\ldots) + p_{s,f}(\alpha_s,\ldots)$ results in an overdetermined system [28]. Obtaining α_s from p_s instead is one way to remedy this problem [28] and led to the Compressible Disperse Phase (CDP) method, which was effectively applied to simulate the hour glass problem without any *top bed velocity defect* phenomena and staple slopes of granular heaps [28]. Later, it was unsuccessfully attempted to implement the CDP method using a co-located mesh (A collocated mesh lead to negative pressures for some solid volume fractions, while a staggered arrangement ensured positivity for all solid fractions) [50].

More recently, Passalacqua and Fox [51] and Venier et al. [52] developed numerical approaches to handle granular flows for the open-source CFD code OpenFoam, where the particle pressure contribution to the solid flux is considered and two phasic pressure correction equations are solved. Both successfully employed a settling bed of solids as test case, however, only solid volume fraction and no velocity plots were disclosed.

An alternative explanation for the observed phenomena is the concept of numerical storms due to unbalanced numerical schemes [53]. Well-balanced here refers to the property of conserving the

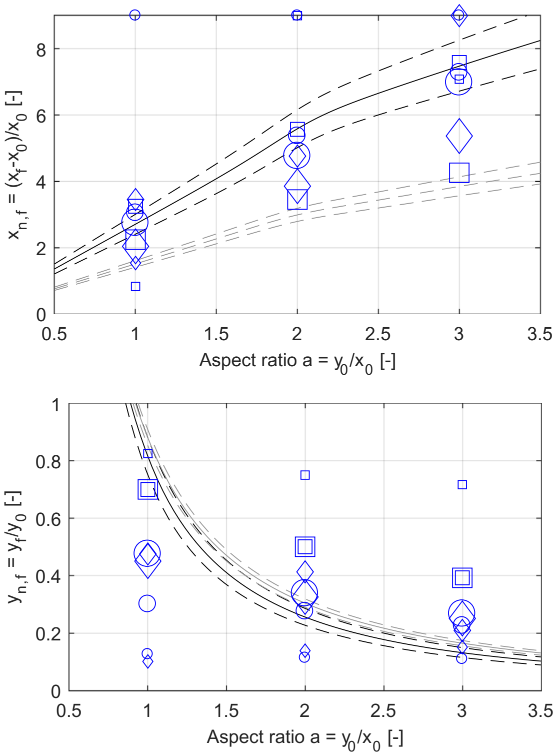

Fig. 10. Final non-dimensional run-out $x_{n,\,f}$ (left) and height $y_{n,\,f}$ (right) for sand in water with $\alpha_{s,\,0} = 0.60$. The data points correspond to the dimensional x_f and y_f values depicted in A.3.2. For further description see caption of Fig. 8.

fundamental balance of hydrostatic pressure and gravitational acceleration down a slope at steady-state at a discrete level [53]. If this is not the case, it can be shown that for the shallow-water equations, a lake at rest will feature spurious oscillations of the water surface [53]. A much finer grid will help to minimize the numerical artefacts and may correspondingly be beneficial in reducing the order of magnitude of the velocity defect seen in our simulations.

4.3. Relevance of solid closure laws

The form of the stress tensor, namely Eq. (28), in combination with the closure law for viscosity, namely Eq. (36), must allow a quasi-static solution, where the fluid is so highly viscous that it does not flow with respect to our time scales 1..0.100 s. For vanishing shear rates in the frictional regime, a Bingham-type flow behavior is obtained due to the yield feature inherent in Eq. (36). For instance, for the thin layer flow at the top of the sediment, u_s becomes smaller with a decreasing bed slope and thus also the shear rate and the stress become small. However, the viscosity η_f is based on the magnitude of the deformation rate tensor **D** in the denominator whereas a particular stress component of the stress tensor **T** is a direct function of the corresponding component of **D**. Now, the magnitude of **D** is always larger than the magnitude of the individual components of **D**, which eventually should lead to the cut-off viscosity (default cut-off value 10^5 Pa·s in Fluent) and to the above mentioned quasi-static state.

Another relevant factor contributing to the observed flowing state of the deposit top layer may be the combination of frictional viscosity and frictional pressure models describing the solid phase in dense regions. Venier et al. [52] showed that the application of the Schaeffer frictional model [23] in combination with the solid frictional pressure formulation of Syamlal et al. [22] produces much higher levels of solid volume fraction in the region just below the sediment top-layer, with a very sharp drop at the top of the sediment bed. Venier et al. [52] distinguish between the

- "Schaeffer model" (the solid frictional pressure formulation of Syamlal et al. [22] in combination with the frictional viscosity model of Schaeffer [23] as employed in this study).
- "Johnson and Jackson model" (the solid frictional pressure model of Johnson and Jackson [21] as employed in this study and the frictional viscosity model of Johnson and Jackson [21] which, in contrast to the model of Schaeffer [23], is independent of the shear rate).

However, it is the solid pressure formulation which in fact makes the difference because the solid frictional pressure formulation of Syamlal

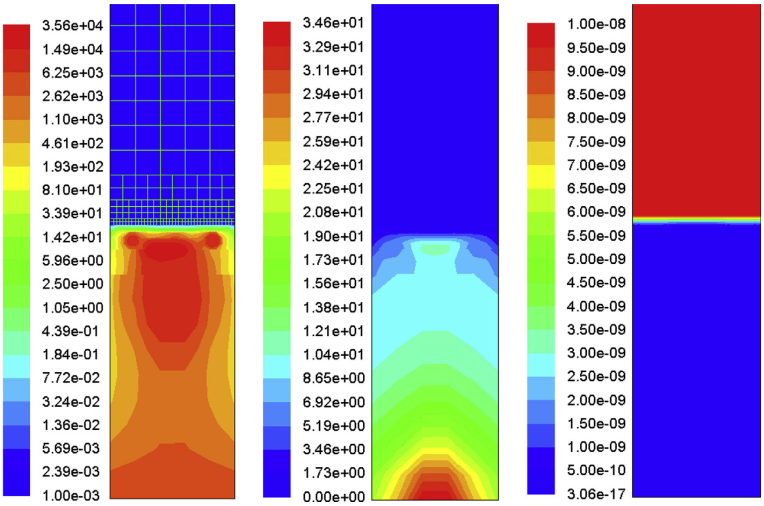

Fig. 11. Result of pre-simulation ($t = 4$ s for air, $a = 2$, case 1), from left to right: frictional viscosity, granular pressure, granular temperature.

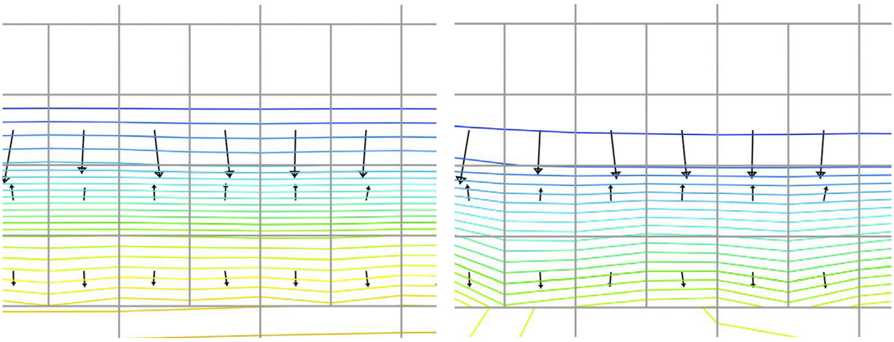

Fig. 12. Zoom of the top-bed region of the pre-simulation of air #5, air, a = 3 (For full field plots see Fig. B.1 and Fig. B.6 in Appendix B). Black arrows denote solid velocity. Left: Colored horizontal lines represent constants of solid volume fraction. Right: Colored horizontal lines represent constants of kinetic/collisional solid pressure.

et al. [22] diverges to levels of several magnitudes larger than the one of Johnson and Jackson [21]. Hence, the combination of the solid frictional pressure formulation of Syamlal et al. [22] and the frictional viscosity model of Schaeffer [23] may be a viable option in order to decrease the magnitude of the liquid-like state of the solid phase below the top of the sediment bed. However, the frictional pressure formulation of Syamlal et al. [22] is available as a solid frictional pressure model in Fluent but its application does also lead to the velocity field disturbance at the top of the sediment bed, as described in sections 3.7 and 4.1.

If an alternative material function is utilized for the frictional viscosity, for instance the one put forward by Laux [28], heap building is generally enhanced because the material functions of Laux and the one Schaeffer [23] differ by one order of magnitude.

4.4. Numerical results vs. scaling of experimental data

Major factors affecting the comparison of numerical and experimental results are:

- The previously mentioned *top bed velocity defect* which leads to an ongoing flow of the outer layer after the deposit has reached a first quasi steady-state similar to the angle of repose of the material. This flow continuously decreases the deposit height, increases the run-out length and ultimately leads to an entirely flat bed for sufficiently long flow times.
- Factors not taken into account in the scaling laws of of Bougouin and Lacaze [2] and Lube et al. [3] such as the materials angle of internal friction, the particle diameter and the scale of the cliff as well as initial conditions.
- The performance of the closures, in particular the frictional pressure and stress models, utilized to describe the solid phase.

If the solid phase is simply patched into the domain, it is crucial to identify the solid volume fraction of the model which relates to the solid volume fraction in the real world. In case of water as the interstitial fluid, the collapse happens in about 2–3 s. For a liquid first phase, the initial solid volume fraction of the cliff is known to have a drastic effect on the dynamics of the collapse [10]. From a logical standpoint, our results obtained with the pre-simulated settled solid bed in dynamic equilibrium ($\alpha_{s,\,0} \approx 0.59$) and more so our $\alpha_{s,\,0} = 0.60$ results are equivalent with the loose solid bed ($\alpha_{s,\,0} \approx 0.55$) of Rondon et al. (2011) [10] because the plain settling of solids in our numerical pre-simulation is precisely how Rondon et al. (2011) [10] obtained the initial granular column in their experiments. Hence, the numerical model needs to be tuned such that the pre-simulations result in settled beds with $\alpha_{s,\,0} \approx 0.55$, for instance by adjusting the maximum packing density $\alpha_{s,\,mpd}$ and the beginning of the frictional regime $\alpha_{s,\,f}$.

Now, considering our $\alpha_{s,\,0} = 0.55$ results, the full collapse of the small particle size cliffs may be explained by the fact that the $\alpha_{s,\,0} = 0.55$ in our simulations corresponds to an unsettled and hence uncompacted state in the real world. Therefore, in the framework of the model, no significant frictional viscosity build-up could occurs within the time scale of the collapse. Frictional viscosity builds up over time because of the developing compaction process in the remaining cliff. This process occurs on a certain time scale as the liquid must flow out of the bed. This outflow process takes much longer in case of smaller particles because the Stokes settling velocity scales with the square of the particle diameter and so does the permeability of a packed bed of solids. Hence, flow dynamics are governed by the liquid because of the low Stokes numbers and the collapse of the granular column is thus dominated by fluid inertia rather than the particles itself. Once liquid is ejected from the granular pile and the granular collapse occurs small particles do have insufficient inertia to resist the liquid flow and counteract the collapse. The build-up of frictional pressure and thus frictional viscosity does not occur sufficiently within the time scale of the collapse. The granular media thus remains in a flowing state and may level out prior to reaching sufficient frictional viscosity levels to represent the Mohr-Coulomb yield criterion inherent in the Schaeffer [23] frictional viscosity model. The role of particle and fluid inertia also explains the different order of the various particle diameter results when compared to the VR and IR scaling laws: Smaller particles follow the flow and therefore less deposit height and smaller run-out length may occur.

Therefore, to first compact the solid phase under the pure influence of gravity is the preferred strategy to obtain correct IC, with sufficiently accurate profiles of volume fraction, solid pressure, and frictional viscosity. The failure of these in some simulations is attributed to the aforementioned *top bed velocity defect*, which, as shown in Fig. 11, may negatively affect the solid frictional viscosity field.

Various spatial scales seem to lead to different non-dimensional deposit heights and run-out lengths. Apparently, these two quantities are not universal for a given granular material in the utilized modeling framework. The *top bed velocity defect* is contributing to this effect because the ratio of the outer layer flow thickness to the scale of the cliff varies. In addition, the frictional pressure may also play a role. In case of larger spatial scales, a more compacted bed is produced which then yields higher average levels of the frictional viscosity. For instance, $\alpha_{s,\,pack}$, defined as the maximum packing density observed in the entire domain, is larger for large systems ($\alpha_{s,\,pack} \approx 0.625$) and smaller for smaller systems ($\alpha_{s,\,pack} \approx 0.605$). As the build-up and break down of the frictional viscosity occurs on time scales in the order of the initial collapse of the cliff, the different average frictional viscosity levels may also contribute to the cliff scale being a factor.

The scaling laws are based on 3D experiments in a channel and may thus be affected by the z-dimension in terms of friction between particles and the channel side walls. The 2D simulations assume an infinitely wide channel.

With all these factors in mind, the performance of the numerical model is much better than it seems at first glance. While in its present form it does not allow accurate quantitative predictions of the final run-out length and final deposit height it may be tuned with regards to the solid frictional pressure and frictional viscosity formulations as well as numerical coefficients such as the angle of internal friction to yield better quantitative results. However, the time-dependency of the results due to the *top bed velocity defect* remains an issue and needs further attention.

4.5. Consequences for modeling of hydraulic conveying

In general, the TFM-KTGF modeling framework as utilized in this study seems capable of modeling hydraulic conveying on a qualitative basis. However, due to several factors such as the *top bed velocity defect* as well as the required tuning of model parameters, quantitative results will most likely be incorrect. Especially the artificial agitation of the bed surface will lead to an overestimation of transported solids. Presence of flow will thus immediately result in transport of solids in the streamwise direction although physics dictate a critical value of bed shear stress to be exceeded to mobilize grains and transport solids. For the very same reason, modeling of dune migration is not adequately possible, at least on larger time scales. While the occurrence of reverse flow at the lee side of the dune may help to sustain the dune shape, the *top bed velocity defect* will cause a disintegration of the dune over extended flow times.

5. Conclusions & outlook

We have investigated the CCP for different fluids, initial solid volume fractions, aspect ratios as well as particle and cliff scale combinations with the TFM-KTGF-SM framework.

At steady-state, the model does not yield an accurate physical representation of a stable deposit close to the angle of repose of the material. Instead, a thin layer at the top of the sediment remains flowing, yielding a scale-dependent disintegration of the cliff over longer periods of time. We suspect this phenomenon to be a consequence of the numerical solutions strategy of Fluent which may result in some solid flux imbalance at top-bed regions where the gradient of the solids kinetic/collisional pressure is high.

Model tuning based on calibration of parameters (angle of internal friction, solid volume fraction threshold for the frictional regime, maximum packing density) and possibly alternative closures for both solid frictional pressure and solid viscosity are required to match the solid volume fraction of the model with the solid volume fraction of the real world and better replicate the experimental data. On the other hand, experimental spread and missing experimental data for the shear-thinning fluids require more comprehensive experimental data for validation purposes.

If the model in its current form is used for transport modeling of cuttings in wellbore flows, the *top bed velocity defect* will lead to an unknown overestimation of transported solids. When it comes to the modeling of dune migration, the *top bed velocity defect* will likely cause disintegration of the dune over longer periods of time.

Declaration of Competing Interest

None.

Acknowledgements

The project Advanced Wellbore transport Modeling (AdWell) with its sponsor, PETROMAKS 2/the Research Council of Norway (project 228391) and its partners Equinor, Neptune Energy AS, IRIS, UiS, NTNU and SINTEF are gratefully acknowledged for funding and supporting this work. In addition, we are very grateful for the computational resources provided at NTNU by UNINETT Sigma2 AS, as part of the national infrastructure for computational science in Norway. Finally, we thank Tore Halsne Flåtten for his input on the numerical part.

Appendix A. Dimensional final deposit shapes

A.1. Initial solid volume fraction $\alpha_{s,0} \approx 0.59$

A.1.1. Air

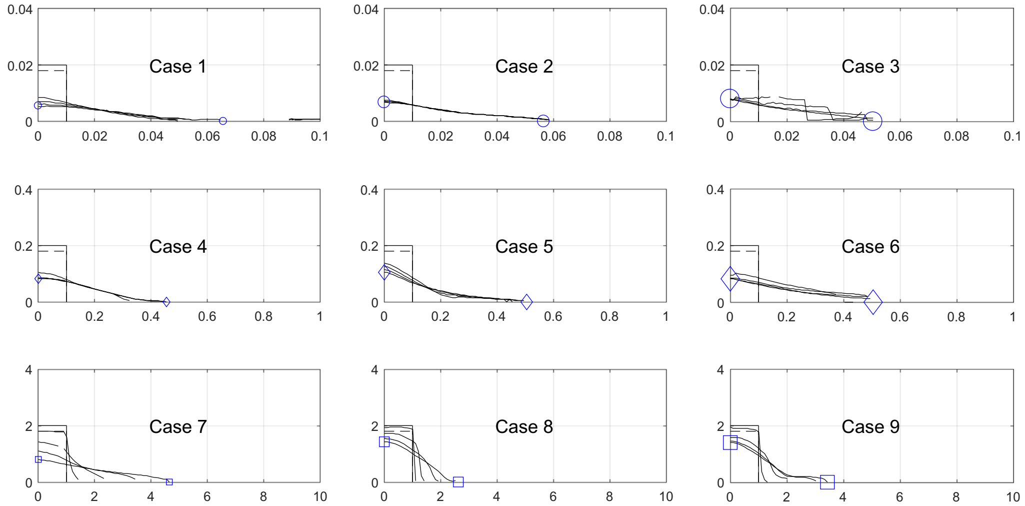

Fig. A.1. Time evolution of dimensional shapes (x and y positions of the cliff boundary) of sand in air for initial solid volume fraction $\alpha_{s,0} \approx 0.59$ and aspect ratio $a = 2$ as given by Table 3. The individual shapes represent the collapsing cliff at $t = 0, 1, 2, 3{,}4$ s. The final values of $x_f = x(t = 4\ \mathrm{s})$ and $y_f = y(t = 4\ s)$ *are highlighted and correspond to the values depicted in* Fig. 5.

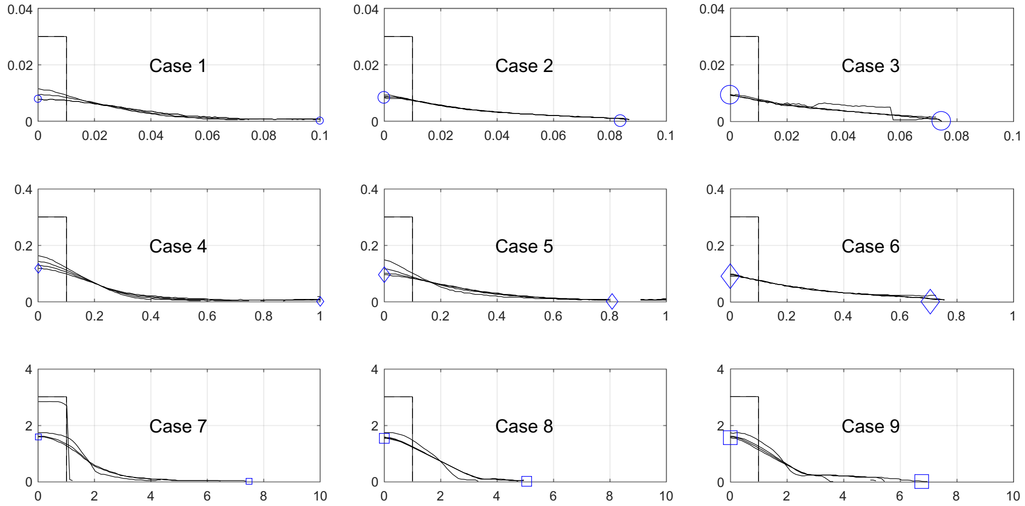

Fig. A.2. Time evolution of dimensional shapes (x and y positions of the cliff boundary) of sand in air for initial solid volume fraction $\alpha_{s,0} \approx 0.59$ and aspect ratio $a = 3$. For further description see caption of Fig. A.1. *Videos available here: https://www.youtube.com/playlist?list=PLfeJTTWUNqAWQZ6mgCWEXgR7_IpCQdfOo.*

A.1.2. H2O

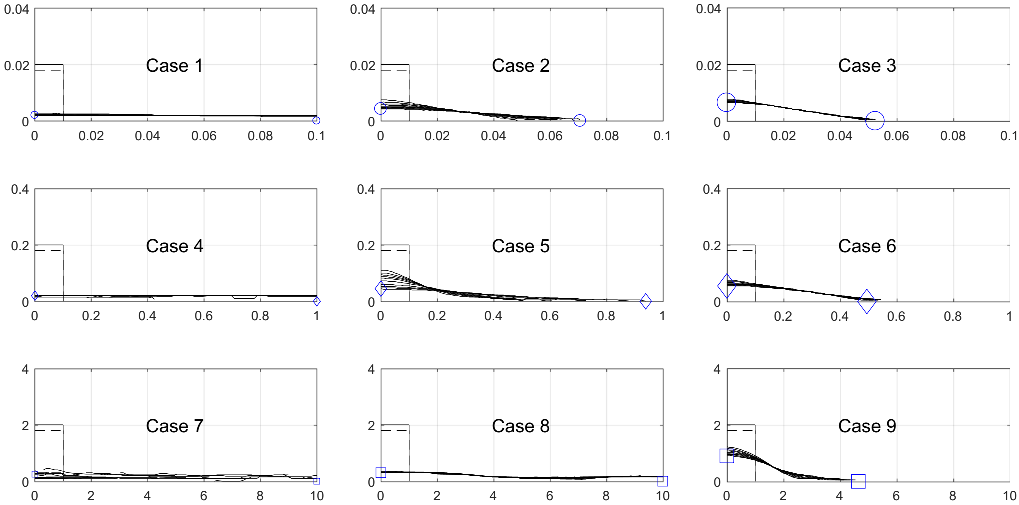

Fig. A.3. Time evolution of dimensional shapes (x and y positions of the cliff boundary) of sand in water for initial solid volume fraction $\alpha_{s,0} \approx 0.59$ and aspect ratio $a = 2$ and the different cases as given by Table 3. The individual shapes represent the collapsing cliff at $t = 0, 10, 20, \ldots, 100$ s. The final values of $x_f = x(t = 100$ s) and $x_f = y(t = 100$ *s) are highlighted and correspond to the values depicted in* Fig. 8.

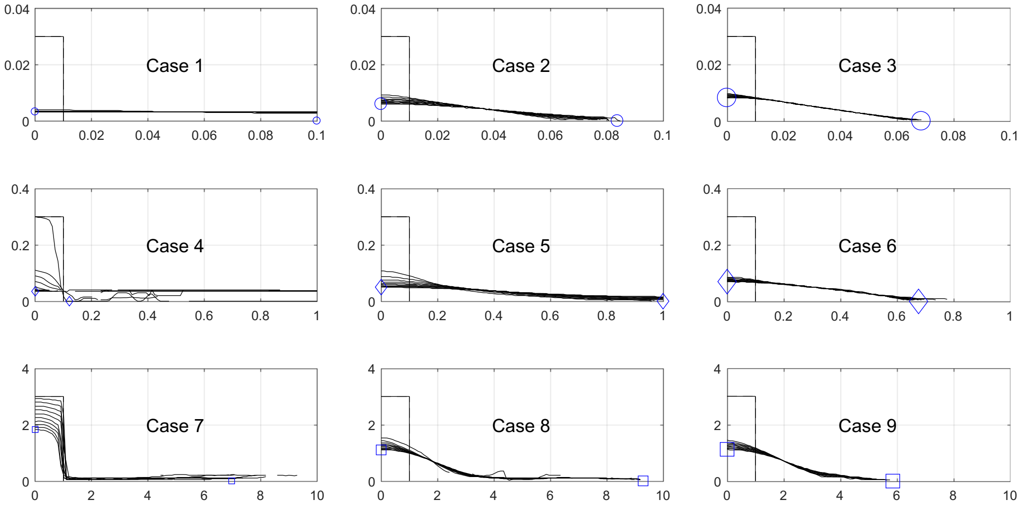

Fig. A.4. Time evolution of dimensional shapes (x and y positions of the cliff boundary) of sand in water for initial solid volume fraction $\alpha_{s,0} \approx 0.59$ and aspect ratio $a = 3$. For further description see caption of Fig. A.3. *Videos available here.: https://www.youtube.com/playlist?list=PLfeJTTWUNqAVyrW3M9QMmxhN9v3jz9knq.*

A.2. Initial solid volume fraction $\alpha_{s,0} = 0.55$

A.2.1. Air

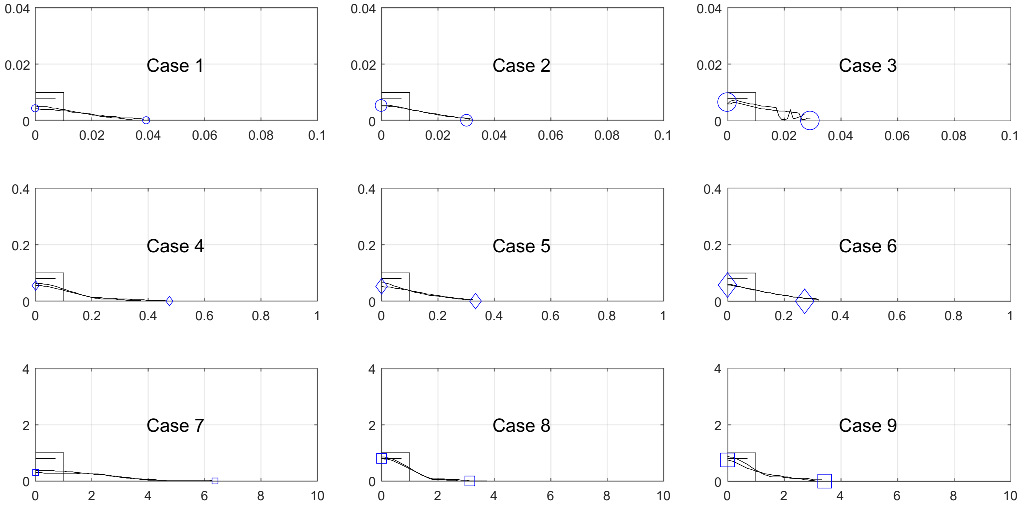

Fig. A.5. Time evolution of dimensional shapes (x and y positions of the cliff boundary) of sand in air for initial solid volume fraction $\alpha_{s,0} = 0.55$ and aspect ratio $a = 1$ and the different cases as given by Table 3. The individual shapes represent the collapsing cliff at $t = 0, 1, 2$ s. The final values of $x_f = x(t = 2\ \text{s})$ and $y_f = y(t = 2\ \text{s})$ *are highlighted and correspond to the values depicted in* Fig. 6.

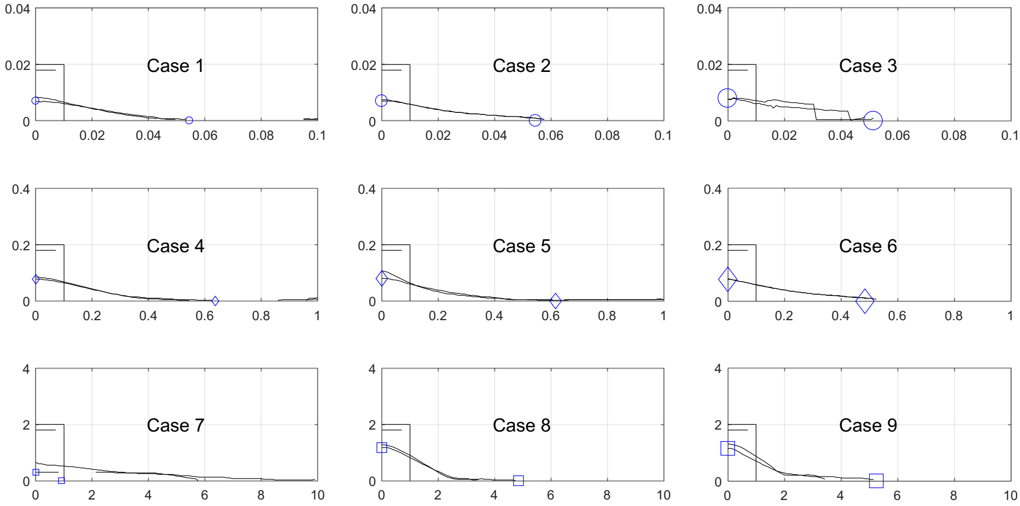

Fig. A.6. Time evolution of dimensional shapes (x and y positions of the cliff boundary) of sand in air for initial solid volume fraction $\alpha_{s,0} = 0.55$ and aspect ratio $a = 2$. For further description see caption of Fig. A.5.

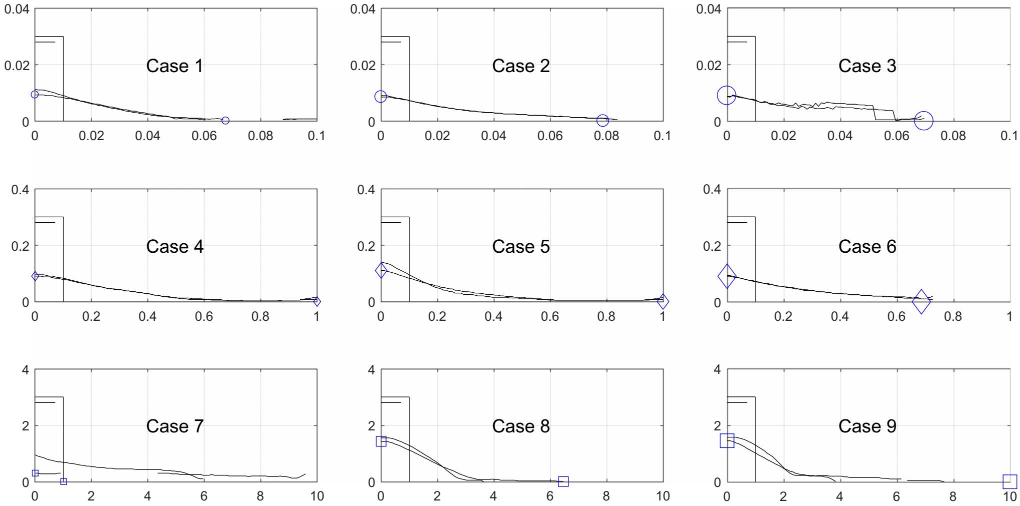

Fig. A.7. Time evolution of dimensional shapes (x and y positions of the cliff boundary) of sand in air for initial solid volume fraction $\alpha_{s,0} = 0.55$ and aspect ratio $a = 3$. For further description see caption of Fig. A.5.

A.2.2. H2O

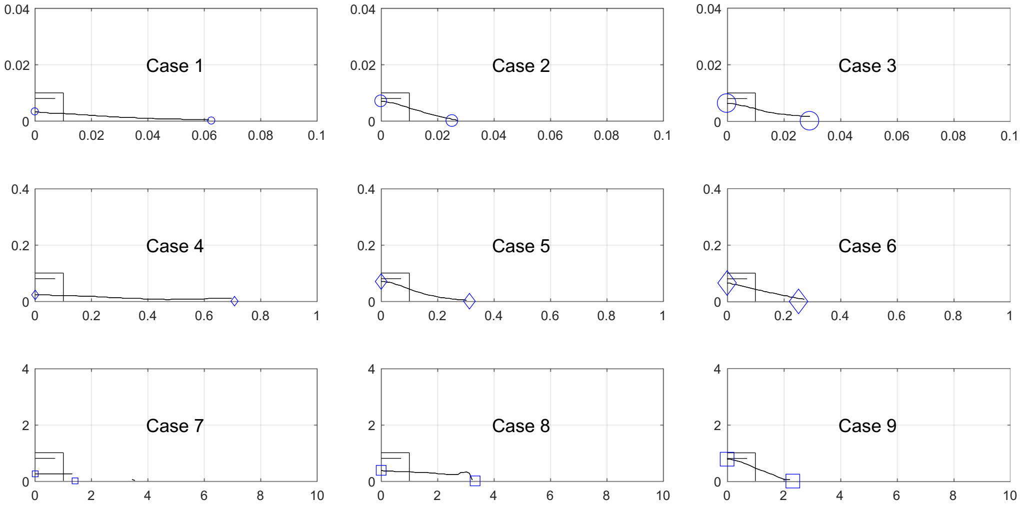

Fig. A.8. Time evolution of dimensional shapes (x and y positions of the cliff boundary) of sand in water for initial solid volume fraction $\alpha_{s,0} = 0.55$ and aspect ratio $a = 1$ and the different cases as given by Table 3. The individual shapes represent the collapsing cliff at $t = 0, 1, 2$ s. The final values of $x_f = x(t = 2\text{ s})$ and $y_f = y(t = 2\ s)$ *are highlighted and correspond to the values depicted in* Fig. 9.

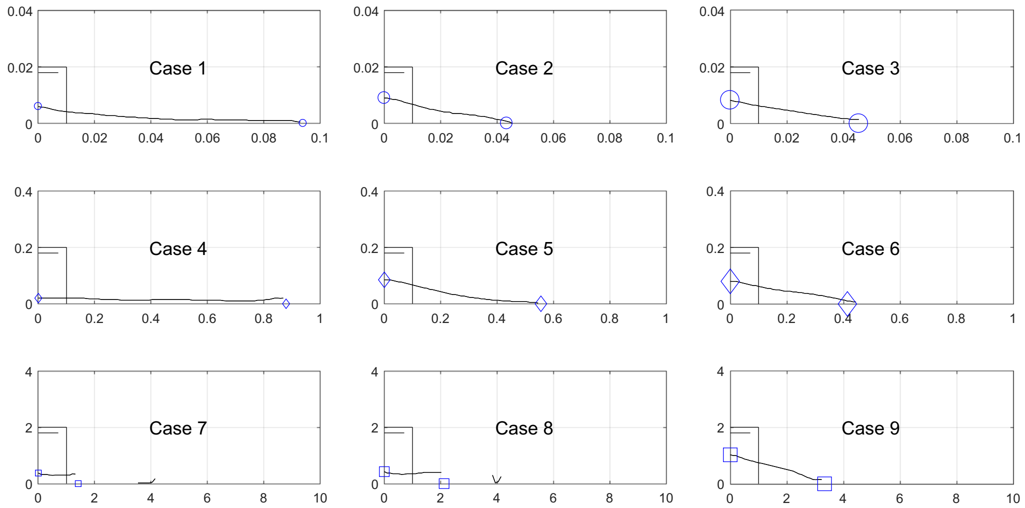

Fig. A.9. Time evolution of dimensional shapes (*x* and *y* positions of the cliff boundary) of sand in water for initial solid volume fraction $\alpha_{s,0} = 0.55$ and aspect ratio $a = 2$. For further description see caption of Fig. A.8.

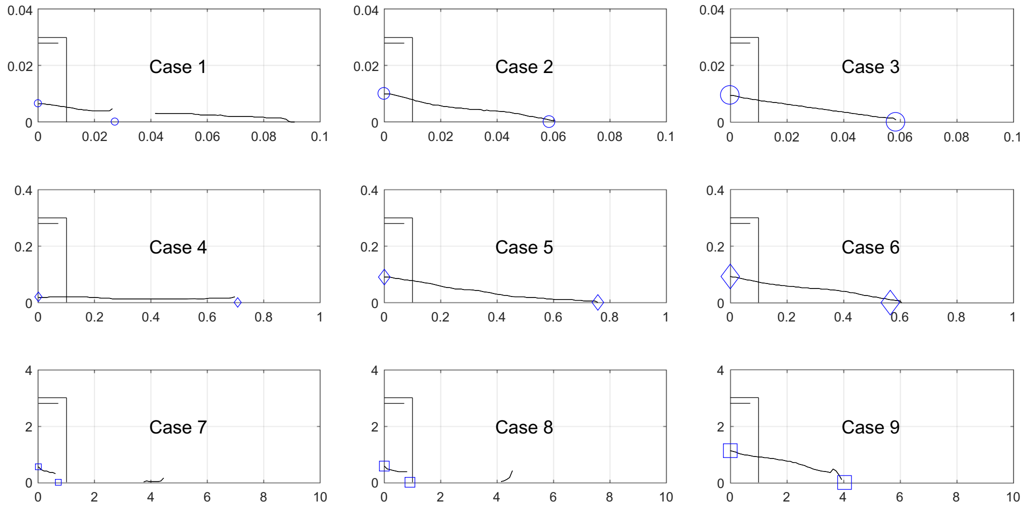

Fig. A.10. Time evolution of dimensional shapes (*x* and *y* positions of the cliff boundary) of sand in water for initial solid volume fraction $\alpha_{s,0} = 0.55$ and aspect ratio $a = 3$. For further description see caption of Fig. A.8.

A.3. . Initial solid volume fraction $\alpha_{s,\,0} = 0.60$

A.3.1. Air

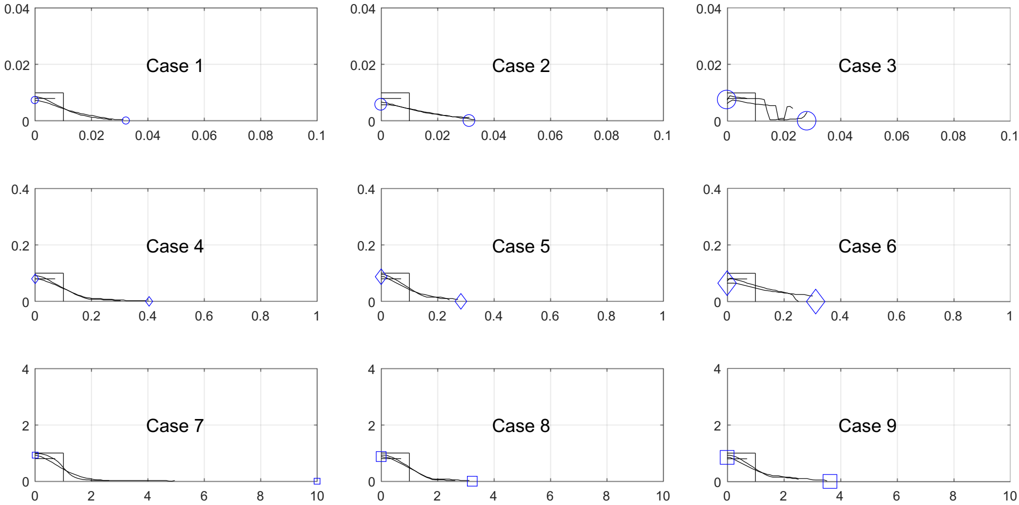

Fig. A.11. Time evolution of dimensional shapes (x and y positions of the cliff boundary) of sand in air for initial solid volume fraction $\alpha_{s,\,0} = 0.60$ and aspect ratio $a = 1$ and the different cases as given by Table 3. The individual shapes represent the collapsing cliff at $t = 0, 2$ s. The final values of $x_f = x(t = 2\text{ s})$ and $y_f = y(t = 2\text{ s})$ *are highlighted and correspond to the values depicted in* Fig. 7.

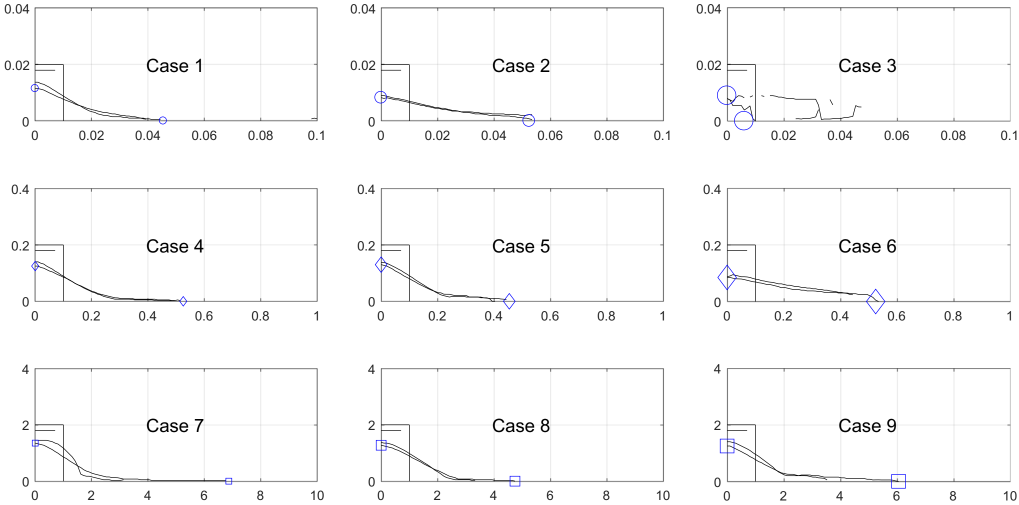

Fig. A.12. Time evolution of dimensional shapes (x and y positions of the cliff boundary) of sand in air for initial solid volume fraction $\alpha_{s,\,0} = 0.60$ and aspect ratio $a = 2$. For further description see caption of Fig. A.11.

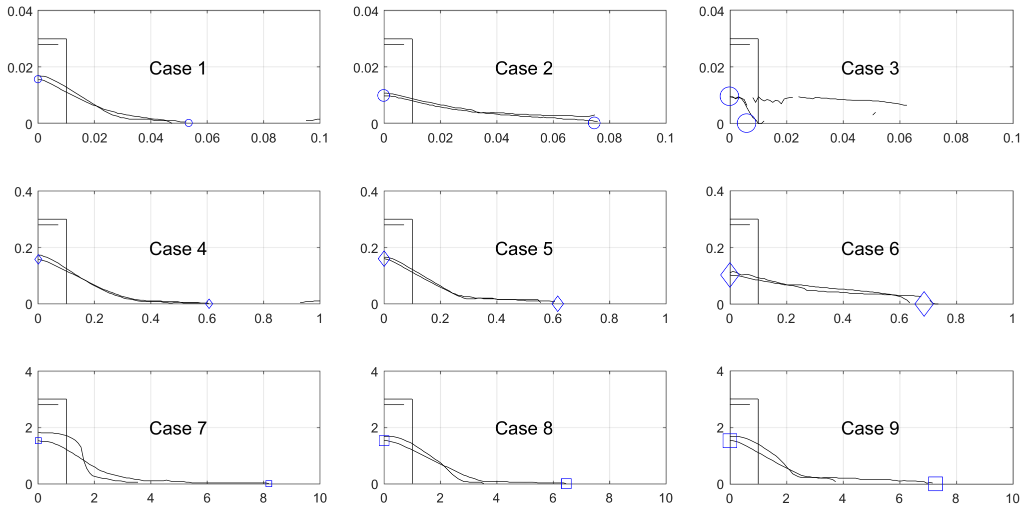

Fig. A.13. Time evolution of dimensional shapes (x and y positions of the cliff boundary) of sand in air for initial solid volume fraction $\alpha_{s,0} = 0.60$ and aspect ratio $a = 3$. For further description see caption of Fig. A.11.

A.3.2. H2O

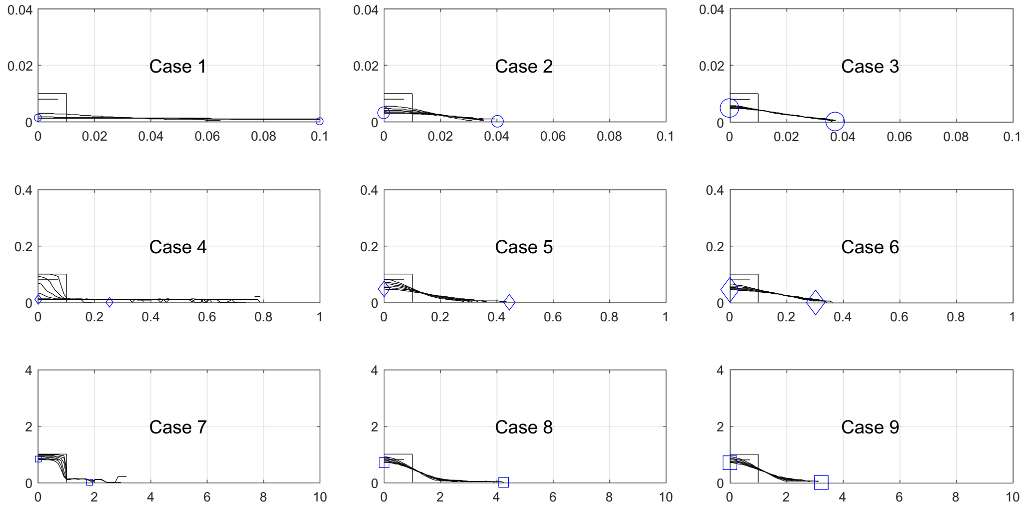

Fig. A.14. Time evolution of dimensional shapes (x and y positions of the cliff boundary) of sand in water for initial solid volume fraction $\alpha_{s,0} = 0.60$ and aspect ratio $a = 1$ and the different cases as given by Table 3. The individual shapes represent the collapsing cliff at $t = 0, 10, 20, \ldots, 60$ s. The final values of $x_f = x(t = 60\,\text{s})$ and $x_f = y(t = 60\,\text{s})$ *are highlighted and correspond to the values depicted in* Fig. 10.

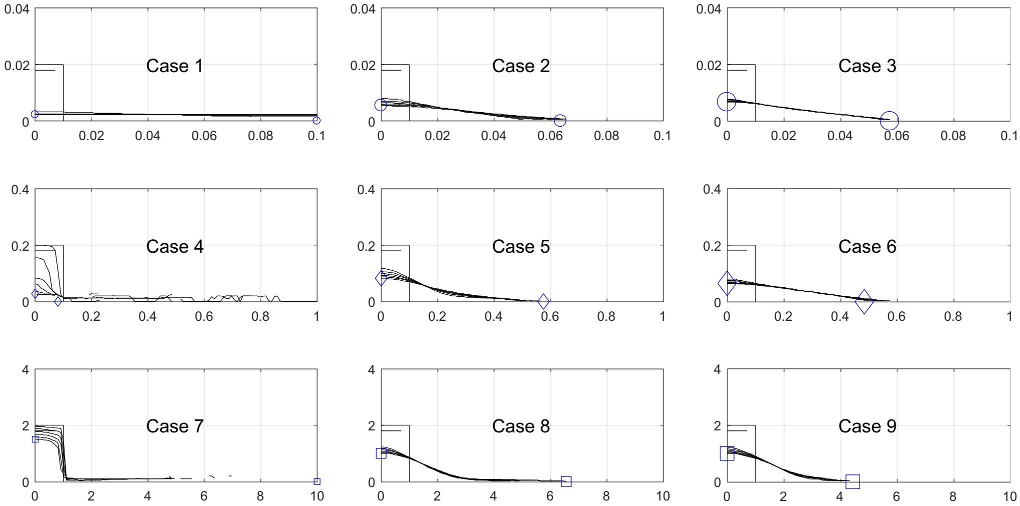

Fig. A.15. Time evolution of dimensional shapes (x and y positions of the cliff boundary) of sand in water for initial solid volume fraction $\alpha_{s,\,0} = 0.60$ and aspect ratio $a = 2$. For further description see caption of Figure Fig. A.14.

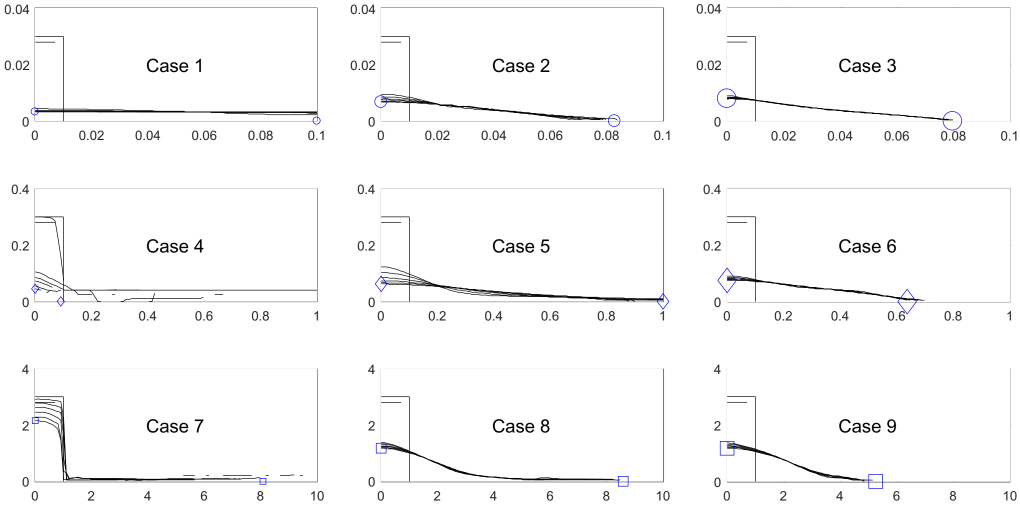

Fig. A.16. Time evolution of dimensional shapes (x and y positions of the cliff boundary) of sand in water for initial solid volume fraction $\alpha_{s,\,0} = 0.60$ and aspect ratio $a = 3$. For further description see caption of Fig. A.14.

Appendix B. Field plots for $\alpha_{s,0} \approx 0.59$, $a = 3$, air, #5

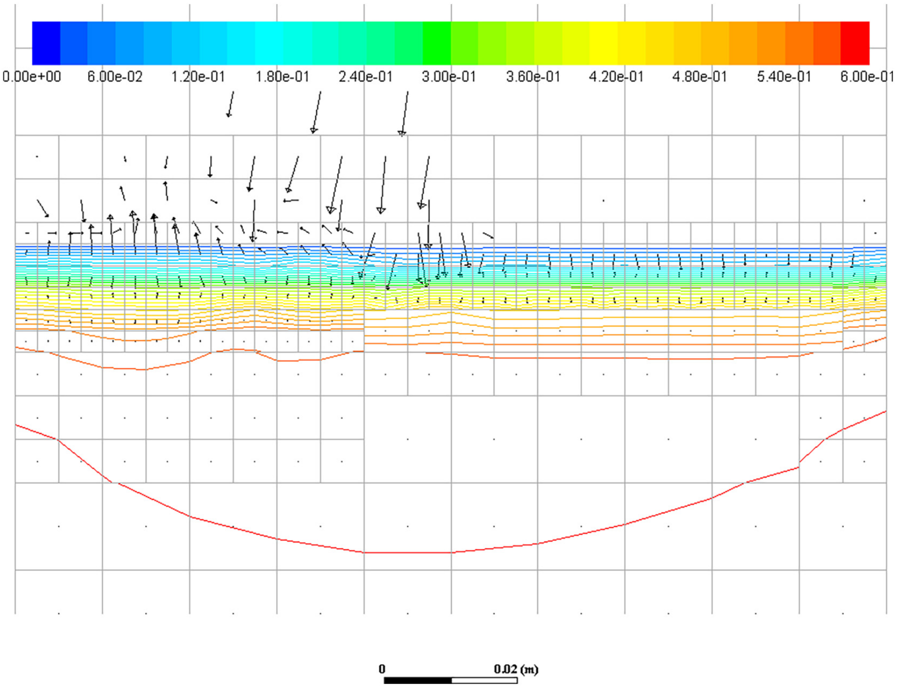

Fig. B.1. Solid volume fraction and solid velocity (result of $\alpha_{s,0} \approx 0.59$, $a = 3$, air, #5 pre-simulation, zoom on top of bed, maximum solid velocity 0.47 m/s).

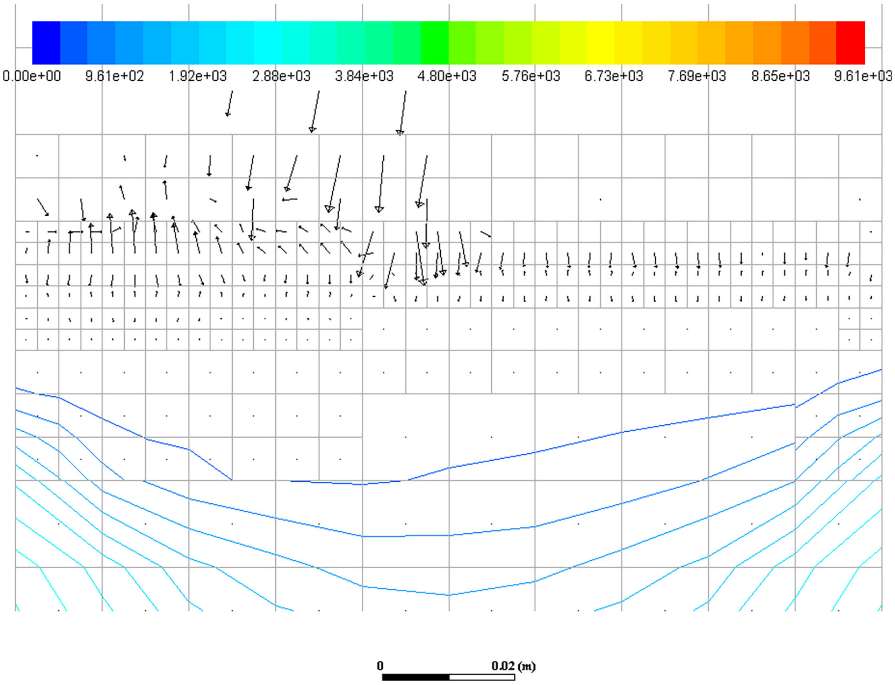

Fig. B.2. Solid pressure and solid velocity (result of $\alpha_{s,0} \approx 0.59$, $a = 3$, air, #5 pre-simulation, zoom on top of bed, maximum solid velocity 0.47 m/s).

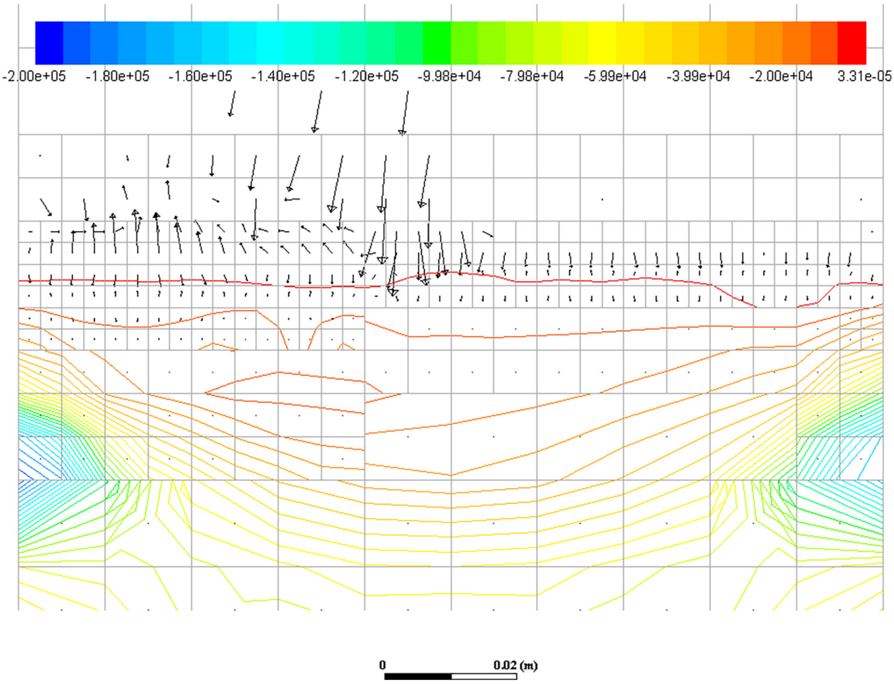

Fig. B.3. y-component of solid pressure gradient (result of $\alpha_{s,0} \approx 0.59$, $a = 3$, air, #5 pre-simulation, zoom on top of bed, maximum solid velocity 0.47 m/s).

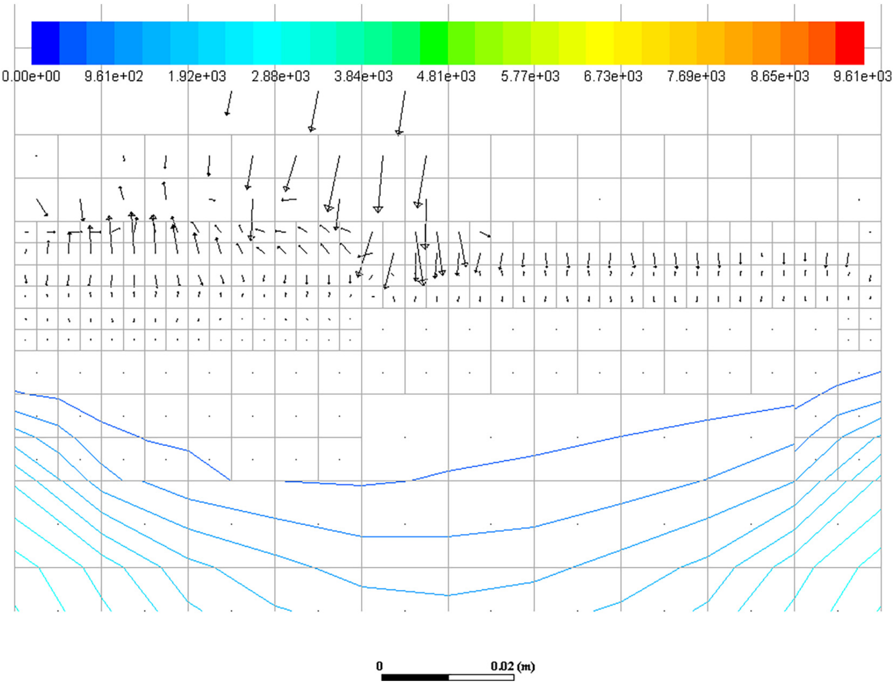

Fig. B.4. Frictional pressure and solid velocity (result of $\alpha_{s,0} \approx 0.59$, $a = 3$, air, #5 pre-simulation, zoom on top of bed, maximum solid velocity 0.47 m/s).

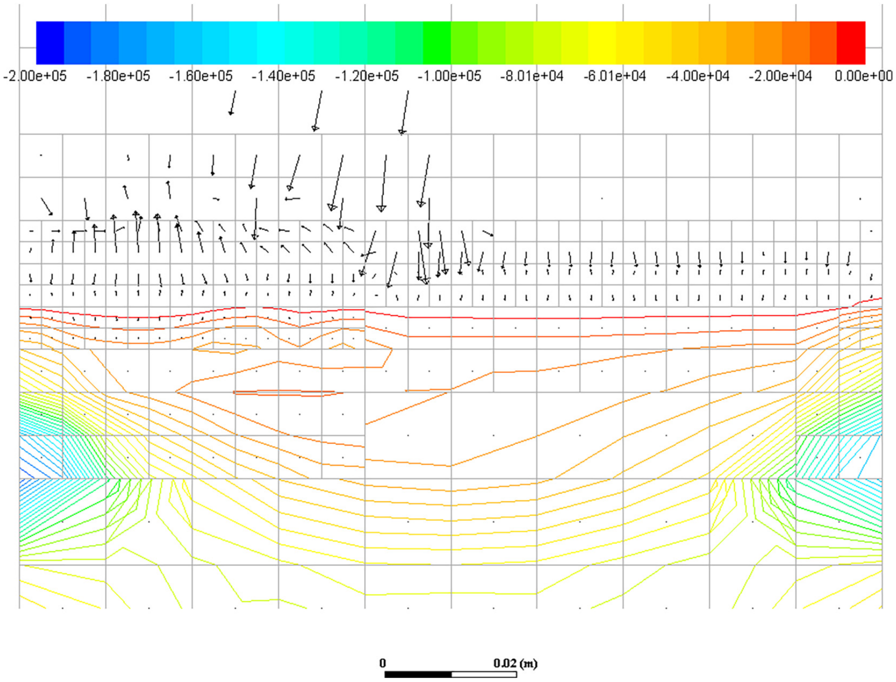

Fig. B.5. y-component of frictional pressure gradient (result of $\alpha_{s,0} \approx 0.59$, $a = 3$, air, #5 pre-simulation, zoom on top of bed, maximum solid velocity 0.47 m/s).

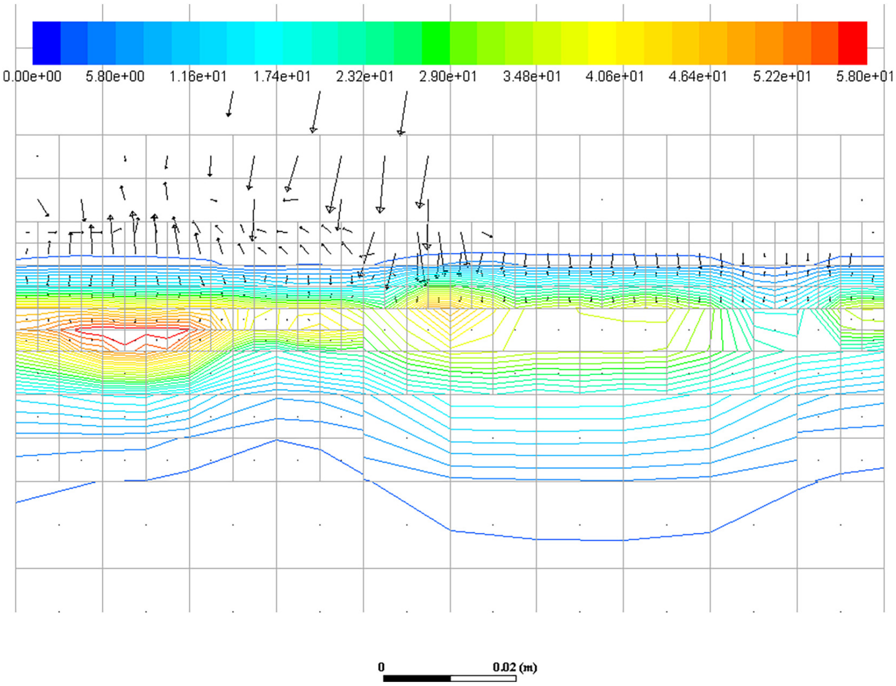

Fig. B.6. Kinetic/collisional pressure and solid velocity (result of $\alpha_{s,0} \approx 0.59$, $a = 3$, air, #5 pre-simulation, zoom on top of bed, maximum solid velocity 0.47 m/s).

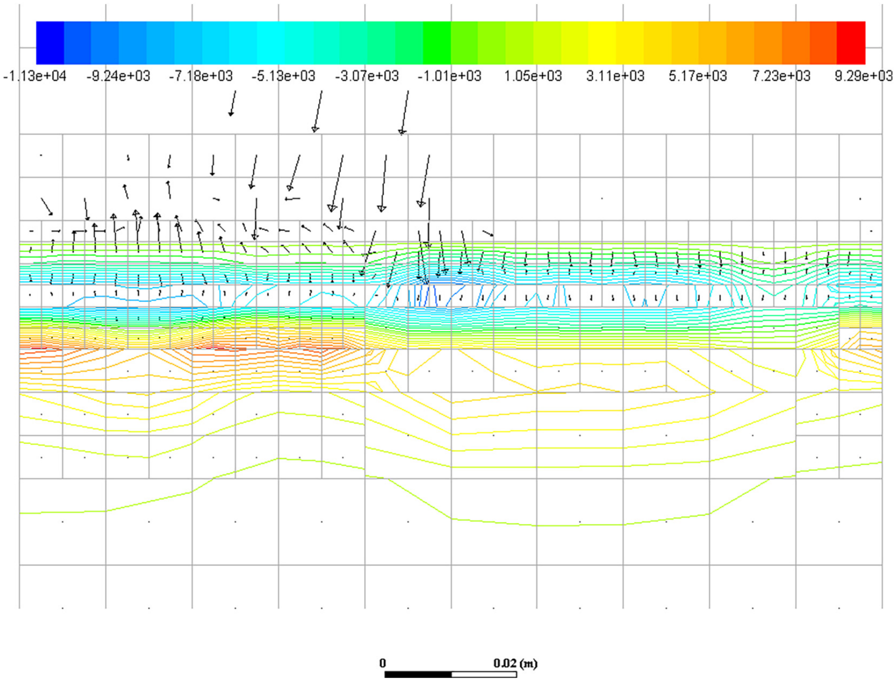

Fig. B.7. y-component of kinetic/collisional pressure gradient and solid velocity (result of $\alpha_{s,0} \approx 0.59$, $a = 3$, air, #5 pre-simulation, zoom on top of bed, maximum solid velocity 0.47 m/s).

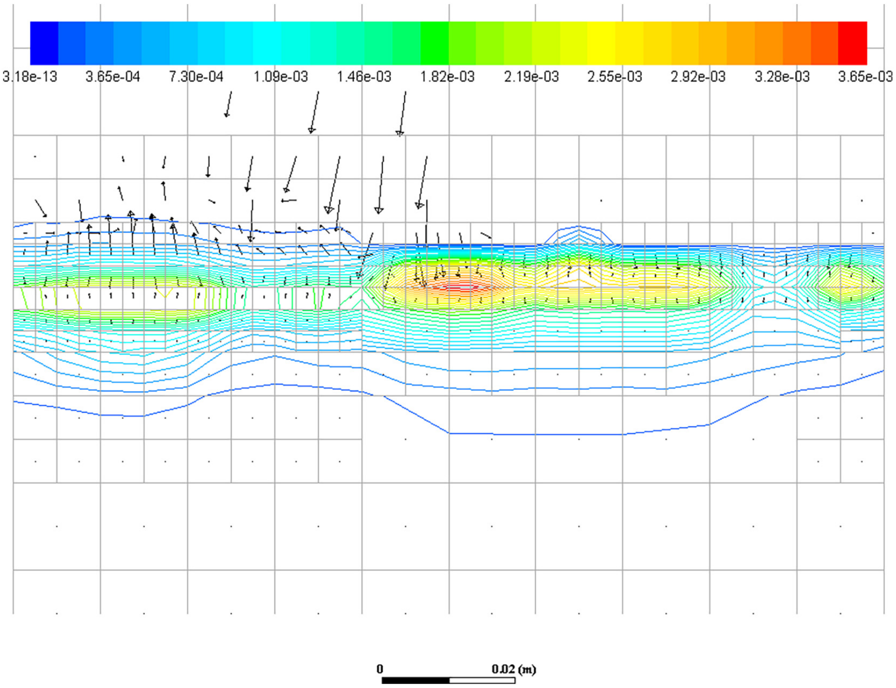

Fig. B.8. Granular temperature and solid velocity (result of $\alpha_{s,0} \approx 0.59$, $a = 3$, air, #5 pre-simulation, zoom on top of bed, maximum solid velocity 0.47 m/s).

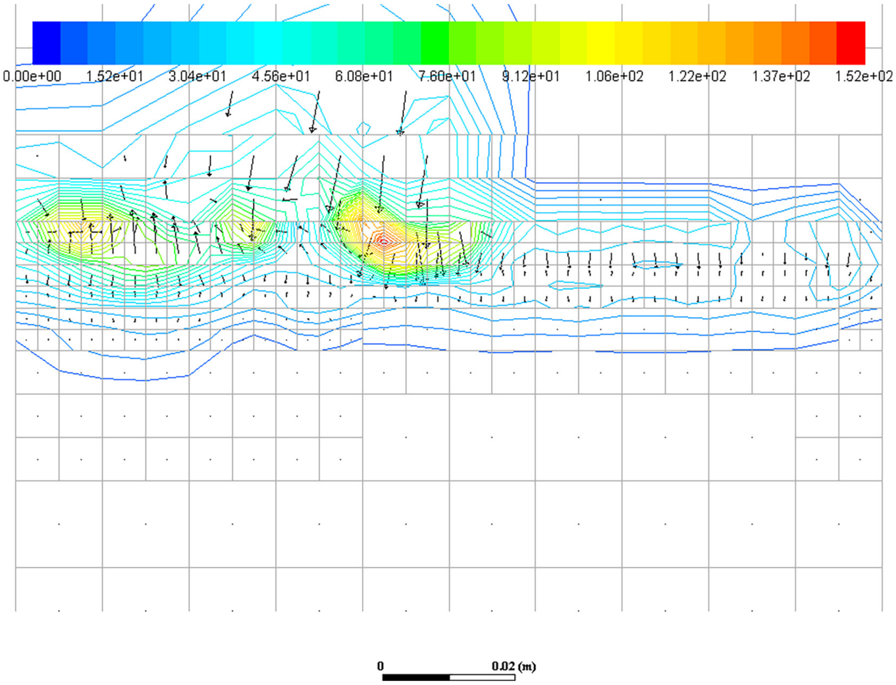

Fig. B.9. Solid strain rate and solid velocity (result of $\alpha_{s,0} \approx 0.59$, $a = 3$, air, #5 pre-simulation, zoom on top of bed, maximum solid velocity 0.47 m/s).

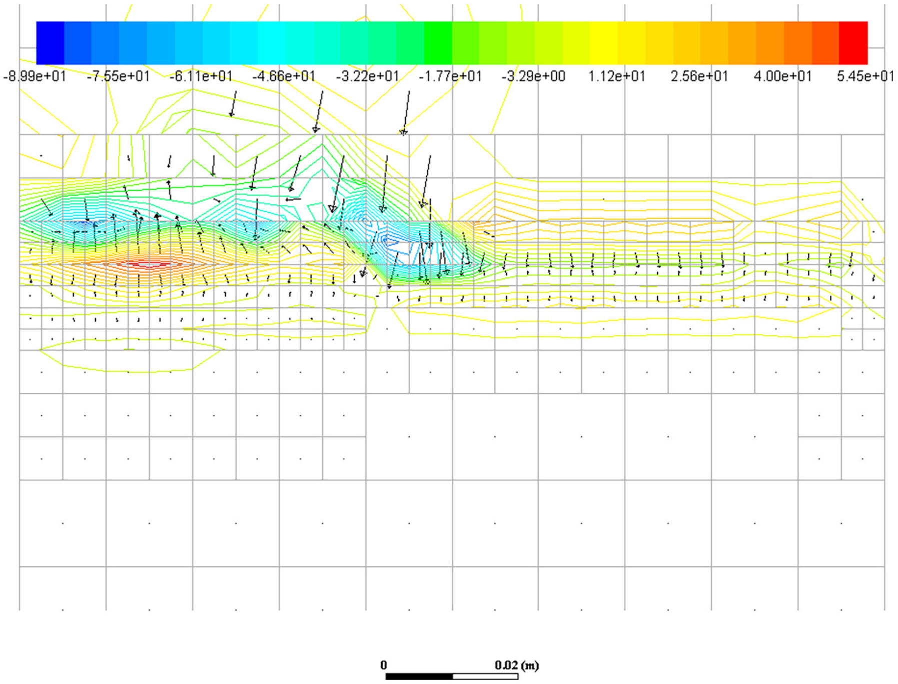

Fig. B.10. Solid ∂u/∂y and solid velocity (result of $\alpha_{s,0} \approx 0.59$, $a = 3$, air, #5 pre-simulation, zoom on top of bed, maximum solid velocity 0.47 m/s).

References

[1] R. Delannay, A. Valance, A. Mangeney, O. Roche, P. Richard, Granular and particle-laden flows: from laboratory experiments to field observations, J. Phys. D. Appl. Phys. 50 (5) (Feb. 2017), 053001.

[2] A. Bougouin, L. Lacaze, Granular collapse in a fluid: different flow regimes for an initially dense-packing, Physical Review Fluids 3 (6) (Jun. 2018).

[3] G. Lube, H.E. Huppert, R.S.J. Sparks, A. Freundt, Collapses of two-dimensional granular columns, Phys. Rev. E 72 (4) (Oct. 2005).

[4] A. Mangeney, O. Roche, O. Hungr, N. Mangold, G. Faccanoni, A. Lucas, Erosion and mobility in granular collapse over sloping beds, J. Geophys. Res. 115 (F3) (Sep. 2010).

[5] S.J. de Vet, B. Yohannes, K.M. Hill, J.R. de Bruyn, Collapse of a rectangular well in a quasi-two-dimensional granular bed, Phys. Rev. E 82 (4) (Oct. 2010).

[6] S.J. de Vet, J.R. de Bruyn, Shape of impact craters in granular media, Phys. Rev. E 76 (4) (Oct. 2007).

[7] S. Siavoshi, A. Kudrolli, Failure of a granular step, Phys. Rev. E 71 (5) (May 2005).

[8] E.L. Thompson, H.E. Huppert, Granular column collapses: further experimental results, J. Fluid Mech. 575 (Mar. 2007) 177.

[9] L. Lacaze, J.C. Phillips, R.R. Kerswell, Planar collapse of a granular column: experiments and discrete element simulations, Phys. Fluids 20 (6) (Jun. 2008), 063302.

[10] L. Rondon, O. Pouliquen, P. Aussillous, Granular collapse in a fluid: role of the initial volume fraction, Phys. Fluids 23 (7) (Jul. 2011), 073301.

[11] M. Pailha, et al., Initiation of Submarine Granular Avalanches: Role of the Initial Volume Fraction, 1027, 2008 935–937.

[12] P. Jop, Rheological properties of dense granular flows, Comptes Rendus Physique 16 (1) (Jan. 2015) 62–72.

[13] P. Jop, Y. Forterre, O. Pouliquen, A constitutive law for dense granular flows, Nature 441 (7094) (Jun. 2006) 727–730.

[14] F. da Cruz, S. Emam, M. Prochnow, J.-N. Roux, F. Chevoir, Rheophysics of dense granular materials: discrete simulation of plane shear flows, Phys. Rev. E 72 (2) (Aug. 2005).

[15] P.-Y. Lagrée, L. Staron, S. Popinet, The granular column collapse as a continuum: validity of a two-dimensional Navier–stokes model with a $\mu(I)$-rheology, J. Fluid Mech. 686 (Nov. 2011) 378–408.

[16] T. Barker, D.G. Schaeffer, M. Shearer, J.M.N.T. Gray, Well-posed continuum equations for granular flow with compressibility and $\mu(I)$-rheology, Proc. R. Soc. A 473 (2201) (May 2017), 20160846.

[17] S.B. Savage, Granular flows down rough inclines - review and extension, Studies in Applied Mechanics, vol. 7, Elsevier 1983, pp. 261–282.

[18] S.B. Savage, R. Pfeffer, Z.M. Zhao, Solids transport, separation and classification, Powder Technol. 88 (3) (1996) 323–333.

[19] S.B. Savage, D.J. Jeffrey, The stress tensor in a granular flow at high shear rates, J. Fluid Mech. 110 (1981) 255–272.

[20] C.K.K. Lun, S.B. Savage, D.J. Jeffrey, N. Chepurniy, Kinetic theories for granular flow: inelastic particles in Couette flow and slightly inelastic particles in a general flowfield, J. Fluid Mech. 140 (1984) 223–256.

[21] P.C. Johnson, R. Jackson, Frictional–collisional constitutive relations for granular materials, with application to plane shearing, J. Fluid Mech. 176 (1987) 67–93.

[22] M. Syamlal, W. Rogers, T.J. O'Brien, *MFIX Documentation Theory Guide*. Morgantown: U.S. Department of Energy, Office of Fossil Energy, 1993.

[23] D.G. Schaeffer, Instability in the evolution equations describing incompressible granular flow, Journal of differential equations 66 (1) (1987) 19–50.

[24] S. Schneiderbauer, A. Aigner, S. Pirker, A comprehensive frictional-kinetic model for gas–particle flows: analysis of fluidized and moving bed regimes, Chem. Eng. Sci. 80 (Oct. 2012) 279–292.

[25] S. Chialvo, S. Sundaresan, A modified kinetic theory for frictional granular flows in dense and dilute regimes, Phys. Fluids 25 (7) (2013), 070603.

[26] K. Kumar, J.-Y. Delenne, K. Soga, Mechanics of granular column collapse in fluid at varying slope angles, Journal of Hydrodynamics, Ser. B 29 (4) (Aug. 2017) 529–541.

[27] C. Wang, Y. Wang, C. Peng, X. Meng, Two-fluid smoothed particle hydrodynamics simulation of submerged granular column collapse, Mech. Res. Commun. 79 (Jan. 2017) 15–23.

[28] H. Laux, "Modeling of Dilute and Dense Dispersed Fluid-Particle Two-Phase Flow," PhD Dissertation, Norwegian University of Science and Technology, Norway, Trondheim, 1998.

[29] I.R. Ionescu, A. Mangeney, F. Bouchut, O. Roche, Viscoplastic modeling of granular column collapse with pressure-dependent rheology, J. Non-Newtonian Fluid Mech. 219 (May 2015) 1–18.

[30] B.H. Ng, Y. Ding, M. Ghadiri, Assessment of the kinetic–frictional model for dense granular flow, Particuology 6 (1) (Feb. 2008) 50–58.

[31] S.B. Savage, M.H. Babaei, T. Dabros, Modeling gravitational collapse of rectangular granular piles in air and water, Mech. Res. Commun. 56 (Mar. 2014) 1–10.

[32] A. Nikolopoulos, N. Nikolopoulos, N. Varveris, S. Karellas, P. Grammelis, E. Kakaras, Investigation of proper modeling of very dense granular flows in the recirculation system of CFBs, Particuology 10 (6) (Dec. 2012) 699–709.

[33] E. Ghadirian, H. Arastoopour, Numerical analysis of frictional behavior of dense gas–solid systems, Particuology 32 (Jun. 2017) 178–190.

[34] D. Gidaspow, R. Bezburuah, J. Ding, Hydrodynamics of circulating fluidized beds: kinetic theory approach, *Fluidization VII, Proceedings of the 7th Engineering Foundation Conference on Fluidization*, Gold Coast, 1992.

[35] C.Y. Wen, Y.H. Yu, "Mechanics of fluidization," presented at the Chem. Eng. Prog., Symp. Ser, 62, 1966 100–111.

[36] S. Ergun, Fluid flow through packed columns, Chem. Eng. Prog. 48 (1952) 89–94.

[37] M.M. Cross, Rheology of non-Newtonian fluids: a new flow equation for pseudoplastic systems, J. Colloid Sci. 20 (5) (1965) 417–437.

[38] A. Busch, V. Myrseth, M. Khatibi, P. Skjetne, S. Hovda, S.T. Johansen, Rheological characterization of Polyanionic cellulose solutions with application to drilling fluids and cuttings transport modeling, Appl. Rheol. 28 (2) (2018) 1–16.

[39] J. Ding, D. Gidaspow, A bubbling fluidization model using kinetic theory of granular flow, AICHE J. 36 (4) (Apr. 1990) 523–538.

[40] R.A. Bagnold, Experiments on a gravity-free dispersion of large solid spheres in a Newtonian fluid under shear, Proceedings of the Royal Society of London. Series A. Mathematical and Physical Sciences 225 (1160) (1954) 49–63.

[41] S. Ogawa, A. Umemura, N. Oshima, On the equations of fully fluidized granular materials, Zeitschrift für angewandte Mathematik und Physik ZAMP 31 (4) (Jul. 1980) 483–493.

[42] J.L. Sinclair, R. Jackson, Gas-particle flow in a vertical pipe with particle-particle interactions, AICHE J. 35 (9) (Sep. 1989) 1473–1486.

[43] S. Vasquez, A phase coupled method for solving multiphase problems on unstructured mesh, Presented at the ASME 200 Fluids Engineering Division Summer Meeting, 2000.

[44] B.P. Leonard, A stable and accurate convective modelling procedure based on quadratic upstream interpolation, Comput. Methods Appl. Mech. Eng. 19 (1) (1979) 59–98.

[45] Inc ANSYS, ANSYS Fluent User Guide R17, vol. 2, ANSYS, Inc., Canonsburg, PA, 2016.

[46] Inc ANSYS, ANSYS Fluent Theory Guide R17, vol. 2, ANSYS, Inc., Canonsburg, PA, 2016.

[47] C.M. Rhie, W.L. Chow, Numerical study of the turbulent flow past an airfoil with trailing edge separation, AIAA J. 21 (11) (Nov. 1983) 1525–1532.

[48] H. Karema, Numerical treatment of inter-phase coupling and phasic pressures in multi-fluid modelling, VTT PUBLICATIONS 4 (5) (2002) 8.

[49] M. Syamlal, MFIX Documentation Numerical Technique. Morgantown, U.S. Department of Energy, Office of Fossil Energy, 1998.

[50] E.A. Meese, S.T. Johansen, A simulation concept for generic simulation of multi-material flow using staggered cartesian grids, *Progress in Applied CFD–CFD2017 Selected papers from 12th International Conference on Computational Fluid Dynamics in the Oil & Gas, Metallurgical and Process Industries*, Trondheim 2017, pp. 253–263.

[51] A. Passalacqua, R.O. Fox, Implementation of an iterative solution procedure for multi-fluid gas–particle flow models on unstructured grids, Powder Technol. 213 (1–3) (Nov. 2011) 174–187.

[52] C.M. Venier, S. Marquez Damian, N.M. Nigro, Numerical aspects of Eulerian gas–particles flow formulations, Comput. Fluids 133 (Jul. 2016) 151–169.

[53] S. Noelle, N. Pankratz, G. Puppo, J.R. Natvig, Well-balanced finite volume schemes of arbitrary order of accuracy for shallow water flows, J. Comput. Phys. 213 (2) (2006) 474–499.

Journal paper 5 (II)

An Eulerian-Lagrangian CFD study of a particle settling in an orthogonal GNF shear flow

Alexander Busch, Stein Tore Johansen

Journal of Non-Newtonian Mechanics, Vol. 263, 2019.

DOI: 10.1016/j.jnnfm.2018.11.005.

For the UDF source code, please see appendix B.2.

Journal of Non-Newtonian Fluid Mechanics 263 (2019) 77–103

Contents lists available at ScienceDirect

Journal of Non-Newtonian Fluid Mechanics

journal homepage: www.elsevier.com/locate/jnnfm

An Eulerian-Lagrangian CFD study of a particle settling in an orthogonal shear flow of a shear-thinning, mildly viscoelastic fluid

Alexander Busch[a,*], Stein Tore Johansen[a,b]

[a] Norwegian University of Science and Technology (NTNU), Trondheim, Norway
[b] SINTEF Materials and Chemistry, Trondheim, Norway

ARTICLE INFO

Keywords:
Particle settling
Orthogonal shear flow
GNF
Shear-thinning
Viscoelastic
Thixotropic
CFD
Eulerian-Lagrangian
DPM
Drag
Lift
Drilling
Cuttings transport

ABSTRACT

For improving CFD models of particle transport in wellbore flows, i.e. *cuttings transport*, we have extended the Lagrangian Discrete-Particle-Model model of the commercial code ANSYS Fluent 17.2 to describe the motion of a particle settling in an orthogonal shear flow of a shear-thinning, mildly viscoelastic fluid. Essentially, the fluid strain rate as the magnitude of the fluid deformation rate tensor is corrected by a particle-induced shear rate. This corrected strain rate is used to compute an apparent viscosity. The fluid is treated as a Generalized Newtonian Fluid using Cross and Carreau material functions. Different drag laws are investigated, including one which accounts for the fluids viscoelastic wake structure behavior via a correction term. We validate the model with eight different particle trajectories representing different combinations of particle diameters, fluid flow rates and rheological properties (water and polymeric solutions) provided by Khatibi et al. [1].

In general, the experimental trajectories are satisfactorily replicated by the CFD model. However, for small particles a trajectory mismatch is observed close to the lower channel wall. We find this mismatch to be a consequence of unexpectedly high particle x-velocities in the experimental data. Various possible causes are identified and discussed. More detailed experimental near-wall data of both particle and fluid velocities as well as more sophisticated modeling of the fluids rheology, including the rheology effect on the forces acting on the particles, may be required to minimize the mismatch.

In addition, we further conclude that in case of the polymeric solutions particle drag is the dominant particle force, that the viscoelastic wake of the particle is not significantly affecting the trajectories, and that a Newtonian drag law may be used as long as the particle-induced shear rate is estimated with $\|\mathbf{v}_r\|/d_p$ and a material function accounting for the limiting zero-shear Newtonian viscosity is applied.

1. Introduction

Particle transport in complex non-Newtonian flows is an important problem in the oil and gas industry. In wellbore flows, shear-thinning (and often additionally viscoelastic and thixotropic) drilling fluid systems are used to transport drilled-off particles also known as *cuttings* back to the surface.

In recent years, Real-Time (RT) models have gained importance, especially when it comes to automated drilling. Computational-Fluid-Dynamics (CFD) simulations have just as well become increasingly important in recent years as they may contribute with a better understanding of the complex flow physics involved and provide input for closure laws required for the one-dimensional (1D) RT models.

A sub-problem of above mentioned complex wellbore flows and a comparatively simple benchmark for a CFD model would be a single, spherical, non-neutrally buoyant particle advected in a shear flow of a shear-thinning fluid. In fact, single non-buoyant particles in orthogonal shear flows (of shear-thinning and/or viscoelastic fluids) have been intensively researched for years, e.g. [1–14].

1.1. State of the art of particles subjected to non-Newtonian shear flows

Acharya et al. [2] proposed an empirical correlation to correct the drag coefficient of a settling sphere for elastic effects. This correlation has been satisfactorily applied in subsequent works, e.g. [3,4,15]. The latter have shown that the increase in settling velocity for lower Weissenberg numbers followed by a decrease for higher Weissenberg numbers known for Boger fluids is also observable in shear-thinning fluids.

Novotny et al. [8] distinguished between settling in a quiescent shear-thinning fluid and settling in a shear flow of the same fluid. For the latter case, they computed an effective shear rate as the vector magnitude of the fluids and particles shear rate, respectively. Experimental results showed that the settling velocity dramatically increases as a con-

---

[*] Corresponding author.
E-mail addresses: alexander.busch@ntnu.no, alexander.busch@alumni.ntnu.no (A. Busch).

https://doi.org/10.1016/j.jnnfm.2018.11.005
Received 9 February 2018; Received in revised form 29 August 2018; Accepted 11 November 2018

Nomenclature

Greek symbols

γ	Strain.
$\dot{\gamma}$	Shear rate, total shear measure.
β	Confinement ratio.
Δ	Difference.
η	Apparent shear viscosity.
λ	Rheological time scale, parameter in Cross and Carreau material functions.
μ	Newtonian shear viscosity.
ρ	Density.
Ψ	First Normal Stress Coefficient.

Latin symbols

A	Surface area.
c	Coefficient.
d	Diameter.
$\mathbf{D}$	Rate of deformation tensor.
f	Functional.
$\mathbf{F}$	Force vector.
g	Gravity.
K	Parameter in PL, PL Consistency Index.
l	Length.
m	Mass.
n	Parameter in PL , PL Exponent.
N	Normal stress difference.
p	Pressure.
Re	Reynolds number.
t	Time.
T	Transposed.
$\mathbf{T}$	Stress tensor.
$\mathbf{u}$	Fluid velocity.
U	Fluid bulk velocity.
$\mathbf{v}$	Particle velocity.
V	Volume.
w	Width.
Wi	Weissenberg number as defined by [2]:$\mathrm{Wi} = \lambda_f \|\mathbf{v}_r\|/d_p$
x, y, z	Spatial dimensions.

Indices

0	Zero, $\dot{\gamma} \to 0$.
∞	Infinity, $\dot{\gamma} \to \infty$.
Ca	Carreau.
Cr	Cross.
D	Drag.
f	Fluid.
f, c	Fluid, as computed by the CFD code per grid cell.
RL	Rotational Lift.
p	Particle.
PL	Power-Law.
r	Relative.
VM	Virtual mass.

Abbreviations

2D, 3D	Two-, Three dimensional in space.
CFD	Computational Fluid Dynamics.
CMC	Sodium Carboxymethyl Cellulose.
FC	Flow Curve.
FNSC	First Normal Stress Coefficient.
FNSD	First Normal Stress Difference.
GNF	Generalized Newtonian Fluid.
PAC	Polyanionic Cellulose.
PL	Power-Law.

sequence of the additional shear and its effect on the local viscosity as seen by the particle.

Roodhart [11] as well as Highgate and Worlow [16] introduced the concept of horizontal and vertical viscosities (corresponding to velocities and respective shear rates), i.e. an anisotropy of viscosity, as a consequence of alignment and/or stretching of polymer molecule chains due to imposed shear.

Van den Brule and Gheisary [5,13] showed that the settling of a sphere in a viscoelastic orthogonal shear flow is retarded, i.e. the drag is enhanced, in line with newer results [6,9,12,17]. The retardation may be attributed to different elastic stresses in the converging flow ahead of the particle and diverging flow in the wake of the particle due to elastic relaxation processes [17], wall effects and/or inadequate rheological data [6], breakage of stress-symmetry [9], or due to lift-generating normal stress differences [12].

Renaud et al. [18] investigated the flow of a Power-Law (PL) fluid over a sphere and provided analytical equations for a Reynolds Number and a drag coefficient. Based on Stokes stream function and the rate of energy dissipation, they derived an average shear rate of a particle as $\sqrt{6}v_p/d_p$.

Talmon and Husman [19] showed that for particles settling in shear flows of a viscoplastic fluid co-rotation of particles with the flow as well as equilibrium of forces in the vertical direction fully determine the settling velocity. Their derived settling equation, however, is only valid for cases were the particle-induced shear rate is smaller than the shear rate of the background flow field.

Pereira et al. [20] computed trajectories of a single particle in an annular viscoplastic flow by means of CFD. They used a Lagrangian-Eulerian approach where the solid phase was modelled using the “Discrete Phase Model” (DPM) using Fluent 6.2.16. The fluid was modeled with a yield-power-law/Herschel-Bulkley [21] material function and the drag coefficient was modeled with an empirical correlation using an “effective viscosity”–based Reynolds number and experimental data of previous studies. However, as the advected particle was neutrally-buoyant, no settling occurred and hence no particle-induced shear.

Padhy et al. [10] showed that shear-thinning and elasticity are counteracting effects: the shear-thinning property of the polymers used tended to decrease the drag coefficient whereas the elastic property of the polymers used tended to increase the drag coefficient.

Hu et al. [7] measured the settling velocity of a single particle in orthogonal shear using a transparent Couette cell and a shear-thinning fluid. Based on the work of Tanner et al. [12], they determined a ratio of the elastic and viscous contributions to the particle settling velocity. Increase of viscosity, elastic lift and elastic instability may enhance particle suspension as a function of the shear rate and fluid relaxation time.

Childs et al. [22] analytically investigated settling of small particles in shear flows of shear-thinning fluids, where the fluids apparent viscosity is assumed to be primarily determined by the background flow. They showed, that a “kinematic barrier” in the center of the flow, i.e. regions where the velocity gradients become small and hence the apparent viscosity large, effectively slows down the settling process and thus greatly affects particle trajectories.

Khatibi et al. [1] and Zoric et al. [14] have both experimentally and numerically investigated the trajectories of a single particle in a laminar channel flow of an aqueous polymeric solution with shear-thinning (and minor viscoelastic) properties. Their CFD simulations did not fit the experimental results; the conclusion drawn was that the simulations did not consider the local flow field and thus viscosity as seen by the particle.

1.2. *Purpose, scope and structure of this paper*

To improve cuttings transport RT modeling by enhanced CFD models, we develop a comparatively simple non-Newtonian Eulerian-Lagrangian model accounting for the particle-induced shear rate by applying the shear rate magnitude concept introduced by Novotny et al. [8].

As a simplified test case, we study the trajectory of a single, spherical, non-buoyant particle in a shear-thinning and mildly viscoelastic polymer solution and water. Specifically, the role of three different drag law formulations is investigated as well as the effect of the fluids viscoelasticity on the drag coefficient. The model is implemented in Fluent R17.2 and validation is conducted with the experimental results of Khatibi et al. [1].

In the following sub-section, the standard Fluent Eulerian-Lagrangian DPM is briefly summarized. In Section 2, our amendments to Fluents' DPM are presented, followed by a short description of the implementation in Fluent R17.2. In addition, a reassessment of the experimental results [1] is provided, as well as a summary of all relevant parameters investigated in this study. Finally, descriptions of the CFD setup and the numerics used are given. In Section 3, a selection of relevant results is presented. The focus here is on the core of the model, i.e. the shear rate and drag law formulation. A critical and comprehensive discussion of possible influences not accounted for in the actual model is provided in Section 4. A conclusion and outlook are given in the last section.

1.3. The Eulerian-Lagrangian equations of motion

Based on the Cauchy equations of motion and assuming an isothermal system, a fluid phase is described by mass and momentum conservation in an Eulerian frame of reference in an appropriate control volume. For an incompressible fluid, mass conservation is simply given by $\nabla(\rho_f \mathbf{u}) = 0$, where ρ_f is the fluids constant and homogeneous density and $\mathbf{u}$ denotes intrinsic volume averages of the fluid velocity. The momentum balance for the fluid phase reads

$$\frac{\partial}{\partial t}\left(\rho_f \mathbf{u}\right) + \nabla\cdot\left(\rho_f \mathbf{u}\mathbf{u}\right) = -\nabla p - \nabla\cdot\mathbf{T}_f + \rho_f \mathbf{g} + \frac{1}{V}\sum_{p\in V}\mathbf{F}_i, \tag{1}$$

where p is the static pressure and $\mathbf{T}_f$ is the deviatoric stress tensor comprising some constitutive equation and material function(s) for the fluid. The last term in Eq. (1) is representing the momentum effect of the particles on the fluid, where the force sum is to be taken over all particles in the volume V. As one of the necessary requirements of the DPM is that the solid volume fraction is low, no fluid volume fraction $\alpha_f = 1 - \alpha_s$ is considered in the momentum balance of the fluid phase, i.e. Eq. (1).

Newton's second law for an arbitrary inert particle subjected to a flow reads

$$m_p \dot{\mathbf{v}} = \mathbf{F}_D + \mathbf{F}_{G,B} + \sum \mathbf{F}_j, \tag{2}$$

where m_p is the mass of the particle, $\mathbf{v}$ its Lagrangian velocity, $\mathbf{F}_D$ and $\mathbf{F}_{G/B}$ are the drag and combined gravity and buoyancy forces, respectively,

$$\mathbf{F}_D = \frac{1}{2}\rho_f A_p c_D \|\mathbf{v}_r\|\mathbf{v}_r, \tag{3}$$

$$\mathbf{F}_{G/B} = \left(m_p - m_f\right)\mathbf{g}. \tag{4}$$

Here, $A_p = \pi \mathrm{d}_\mathrm{p}^2/4$ is the particles projected area, c_D is the drag coefficient and $\mathbf{v}_r = \mathbf{u} - \mathbf{v}$ the relative velocity of the particle. The term $\sum \mathbf{F}_j$ in Eq. (2) may include other forces such as Magnus and Saffman lift, virtual mass and Basset/history.

Alternatively, using $m_i = \rho_i V_p$ and assuming sphericity ($\leftrightarrow A_p = \pi \mathrm{d}_\mathrm{p}^2/4$ and $V_p = \pi \mathrm{d}_\mathrm{p}^3/6$) the particles equation of motion may be rewritten in a per unit mass manner as

$$\dot{\mathbf{v}} = \frac{3}{4}\frac{\rho_f}{\rho_p}\frac{c_D}{d_p}\|\mathbf{v}_r\|\mathbf{v}_r + \left(1 - \frac{\rho_f}{\rho_p}\right)\mathbf{g} + \sum\frac{\mathbf{F}_j}{\rho_p V_p}$$
$$\leftrightarrow \quad \dot{\mathbf{v}} = \underbrace{\frac{\mathbf{u}-\mathbf{v}}{\tau_p}}_{\mathbf{F}_D/m_p} + \underbrace{\frac{\mathbf{g}\left(\rho_p - \rho_f\right)}{\rho_p}}_{\mathbf{F}_{GB}/m_p} + \frac{\sum\mathbf{F}_j}{m_p} \tag{5}$$

The denominator of the drag force per unit mass $\mathbf{F}_D/m_p$ is the particle relaxation time τ_p

$$\tau_p = \frac{4\rho_p {d_p}^2}{3\eta_f c_D \mathrm{Re}_p}. \tag{6}$$

Hence, the drag force per unit mass $\mathbf{F}_D/m_p$ may be expressed as

$$\frac{\mathbf{F}_D}{m_p} = \frac{3c_D \mathrm{Re}_p \eta_f \mathbf{v}_r}{4\rho_p {d_p}^2}. \tag{7}$$

In Fluent, the apparent viscosity of the fluid phase η_f showing up in Eq. (7) as well as in the particle Reynolds number Re_p and the drag coefficient $c_D = f(\mathrm{Re}_p)$ is based on the apparent viscosity of the background shear flow field of the fluid without consideration of the additional shear induced by the slip velocity of the particle. For further distinction, this apparent viscosity is hereafter referred to as the—in a CFD sense—cell-based apparent viscosity of the fluid $\eta_{f,\,c}$. In addition, we will hereafter refer to Eq. (7), where the viscosity is purely based on the resolved fluid rate of deformation tensor $\mathbf{D}_f$ in conjunction with the Schiller-Naumann drag law [23] and a particular rheology model such as the Cross [24] model as the *Fluent state-of-the-art*.

In general, the drag coefficient $c_d = f(\mathrm{Re}_p)$ is a function of the particle Reynolds number

$$\mathrm{Re}_p = \frac{\rho_f \|\mathbf{v}_r\| d_p}{\eta_f}. \tag{8}$$

where η_f is the fluids apparent viscosity.

For small particle Reynolds numbers, i.e. $Re_p \ll 1$, the particle is subjected to Stokes flow and the settling velocity becomes

$$v_{set} = \frac{{d_p}^2 g\left(\rho_p - \rho_f\right)}{18\eta_f}. \tag{9}$$

The drag coefficient beyond the Stokes regime, i.e. $Re_p \gg 1$, may be iteratively computed by utilizing a drag law, e.g. Schiller and Naumann [23].

For the special case of a particle settling under the pure influence of gravity in dynamic equilibrium, the LHS and the RHS sum term $\sum \boldsymbol{F}_j/\rho_p V_p$ in Eq. (5) become zero. Rearranging provides expressions for the steady-state settling velocity v_{set} and the drag coefficient c_D, respectively,

$$v_{set} = \sqrt{\frac{4d_p g}{3c_D}\left(\frac{\rho_f}{\rho_p} - 1\right)} \quad \leftrightarrow \quad c_D = \frac{4d_p g}{3{v_{set}}^2}\left(\frac{\rho_f}{\rho_p} - 1\right). \tag{10}$$

Hence, an increase of the drag coefficient c_D leads to a decrease of the settling velocity v_{set}.

2. Materials and methods

The first three subsections of this section describe the model used in the CFD simulations, followed by a brief explanation of the implementation of the model in Fluent R17.2. The last sections provide further information such as all case parameters and numerical settings.

2.1. Rheological model

For a shearing flow of an incompressible and purely viscous (here shear-thinning) fluid, i.e. no viscoelastic and time-dependent microstructural/thixotropic fluid properties, i.e. a Generalized Non-Newtonian Fluid (GNF), the deviatoric stress tensor $\mathbf{T}_f$ of the Cauchy momentum equation reads

$$\mathbf{T}_f = -2\eta_f(\dot{\gamma})\mathbf{D}_f, \tag{11}$$

where $\mathbf{D}_f$ is the symmetric part of the fluid velocity gradient (also known as the rate of deformation tensor, or alternatively the rate of strain tensor)

$$\mathbf{D}_f = \frac{1}{2}\left(\nabla\mathbf{u} + \nabla\mathbf{u}^T\right). \tag{12}$$

For a GNF, the fluids apparent viscosity η_f in Eq. (11) is purely a function of the *shear rate* $\dot{\gamma}$, which is the magnitude of the fluids instantaneous rate of deformation tensor $\mathbf{D}_f$,

$$\eta_f = f\left(\dot{\gamma}_f\right) \quad \text{with} \quad \dot{\gamma}_f = \sqrt{2\mathbf{D}_f : \mathbf{D}_f} = \sqrt{2\left({D_{11}}^2 + {D_{12}}^2 + \ldots\right)}, \tag{13}$$

where the functional f may be modeled with an appropriate GNF material function.

For a particle settling in a shear flow of a shear-thinning fluid and in the realm of the DPM, the viscosity needs to be determined based on: (1) the pure shear of the fluid due to the mean fluid velocity $\mathbf{u}$, and (2) the additional shear due to the relative velocity vector $\mathbf{v}_r$ because of the local shear field induced by the moving particle, which is not considered/computed by the CFD solver.

Dropping indices for the fluid phase f, the rate of deformation tensor $\mathbf{D}$ may correspondingly be decomposed into two parts describing the rate of deformation as introduced above

$$\mathbf{D} = \underbrace{\mathbf{D}_f}_{1.} + \underbrace{\mathbf{D}_p}_{2.}, \tag{14}$$

where the index f now denotes the background flow field without presence of the particle.

The total shear rate $\dot{\gamma}$ may thus be generally computed as

$$\begin{aligned}\dot{\gamma} &= \sqrt{2\mathbf{D} : \mathbf{D}} = \sqrt{2\left(\mathbf{D}_f + \mathbf{D}_p\right) : \left(\mathbf{D}_f + \mathbf{D}_p\right)} \\ &= \sqrt{2\left(\mathbf{D}_f : \mathbf{D}_f + \mathbf{D}_p : \mathbf{D}_p + 2\mathbf{D}_p : \mathbf{D}_f\right)}.\end{aligned} \tag{15}$$

For a laminar and simple 2D shear flow with $\mathbf{u} = (u_x, 0, 0)$ and $\mathbf{v}_r = (0, v_y, 0)$, where the velocity components and hence the induced shear are normal to each other, the total shear rate $\dot{\gamma}$ may be written as [8]

$$\dot{\gamma} = \sqrt{\left(\dot{\gamma}_f\right)^2 + \left(\dot{\gamma}_p\right)^2}. \tag{16}$$

This is a subcase of Eq. (15), as it represents the first and second tensor contractions only. The mixed contraction computes to zero due to the orthogonal shear flow.

In case of DPM-CFD simulations, the shear rate of the background flow field $\dot{\gamma}_f$ is provided by the CFD code. The particle-induced shear rate, however, must be estimated. Based on Stokes stream function, the surface-averaged shear rate induced by a particle d_p with relative velocity $\mathbf{v}_r$ may be estimated with $\dot{\gamma}_p = 2\ \|\mathbf{v}_r\|/d_p$ [25]. Although, many alternative formulations exist, e.g. $\dot{\gamma}_p = 0.39f\ \|\mathbf{v}_r\|/d_p$ [26], where f is a functional correcting for wall, density or particle shape effects or $\dot{\gamma}_p = \sqrt{6}\ \|\mathbf{v}_r\|/d_p$ [18], which is also an averaged shear rate based on Stokes stream function but representative for the rate of energy dissipation instead. In the petroleum industry, a standard definition [27] is $\dot{\gamma}_p = 12\ \|\mathbf{v}_r\|/d_p$. However, in many non-Newtonian drag law studies [28], the shear rate is taken to be

$$\dot{\gamma}_p = \frac{\|\mathbf{v}_r\|}{d_p}, \tag{17}$$

which also conforms to dimensional analysis of a sphere settling in a PL fluid [29] and will be used primarily in this study unless indicated otherwise.

The most simple material function accounting for shear-thinning behavior is the Ostwald material function [30], also known as Power Law (PL), here given in a time constant formulation [31]

$$\eta_f(\dot{\gamma}) = \eta_0\left(\lambda_{PL}\dot{\gamma}\right)^{n_{PL}-1}. \tag{18}$$

Note, that the ordinary PL coefficient K_{PL} may be obtained as $K = \eta_0\lambda_{PL}^{n_{PL}-1}$, which then gives

$$\eta_f(\dot{\gamma}) = K_{PL}\dot{\gamma}^{n_{PL}-1}. \tag{19}$$

In case of a polymeric solution, however, the functional f in Eq. (13) is best-expressed with the Cross (Cr) [24] material function

$$\eta_f(\dot{\gamma}) = \frac{\mu_0 - \mu_\infty}{1 + \left(\lambda_{Cr}\dot{\gamma}\right)^{n_{Cr}}} + \mu_\infty \tag{20}$$

because this represents the apparent viscosity data much better for a wider shear rate range since it accounts for Newtonian viscosities at both low and high shear rates. Here, μ_0 is the zero-shear viscosity, μ_∞ is the infinite-shear viscosity, λ_{Cr} is the Cross time constant and n_{Cr} is the Cross exponent.

As an alternative, the Carreau (Ca) [32] material function

$$\eta_f(\dot{\gamma}) = \left(\mu_0 - \mu_\infty\right)\left(1 + \left(\lambda_{Ca}\dot{\gamma}\right)^2\right)^{\frac{n_{Ca}-1}{2}} + \mu_\infty \tag{21}$$

may be used. Here, again μ_0 is the zero-shear viscosity, μ_∞ is the infinite-shear viscosity, λ_{Ca} is the Carreau time constant and n_{Ca} is the Carreau exponent.

Note that the Carreau material function collapses to a PL, i.e. Eq. (18), for the case of higher shear rates and neglected infinite-shear viscosity μ_∞. The PL coefficients characterizing the low shear rate, i.e. Newtonian region and the intermediate shear rate, i.e. shear-thinning region may be obtained from the Carreau material function as follows:

- Newtonian region

$$\dot{\gamma} < \frac{1}{\lambda_{Ca}} \quad \rightarrow \quad n_{PL} = 1, \quad K_{PL} = \mu_0, \tag{22}$$

- Shear-thinning region

$$\dot{\gamma} > \frac{1}{\lambda_{Ca}} \quad \rightarrow \quad n_{PL} = n_{Ca}, \quad K_{PL} = \mu_0{\lambda_{Ca}}^{(n_{Ca}-1)}. \tag{23}$$

Correspondingly, in case of the Cross material function, one may infer PL coefficients for any given point of the flow curve $\eta_f = f(\dot{\gamma})$ by requiring:

$$\begin{aligned}\eta_{PL}(\dot{\gamma}) &= \eta_{Cr}(\dot{\gamma}) \\ \frac{\partial\eta_{PL}(\dot{\gamma})}{\partial\dot{\gamma}} &= \frac{\partial\eta_{Cr}(\dot{\gamma})}{\partial\dot{\gamma}}.\end{aligned} \tag{24}$$

Since the aqueous PAC solutions used in the experiments [1] are expected to show minor viscoelastic behavior only, we here restrict ourselves to the GNF formulations presented, especially because the channel flow is fully established and steady. However, when it comes to particle settling, elastic properties of the fluid may become relevant for higher Weissenberg numbers $Wi = (\tau_{11} - \tau_{22})/(2\tau_{12})$ and may be considered by applying corrections to the drag law utilized.

2.2. Non-Newtonian drag laws

The standard way [28] of constructing drag laws for non-Newtonian fluids is to apply a correction factor $Y = f(n_{PL})$ to the Stokes formula to account for the Stokes drag to be a function of the PL exponent n_{PL}. Correspondingly, one may rewrite Eq. (7) with Stokes' drag force $\mathbf{F}_D = 3\pi d_p\eta_f\mathbf{v}_r$ as

$$c_D = Y\frac{24}{\mathrm{Re}_p}. \tag{25}$$

For the case of a PL fluid, the particle Reynolds number Re_p may be manipulated by applying the PL, i.e. Eq. (19), expressing the shear rate as $\|\mathbf{v}_r\|/d_p$, i.e. Eq. (17), and simplifying to yield a Metzner-Reed-type [33] particle Reynolds number

$$\mathrm{Re}_{p-MR} = \frac{\rho_f\|\mathbf{v}_r\|^{2-n_{PL}}{d_p}^{n_{PL}}}{K_{PL}}. \tag{26}$$

If $\dot{\gamma} = 2\ \|\mathbf{v}_r\|/d_p$ is used instead for the shear rate, one obtains the Reynolds number as given in (26) with an additional factor $2^{n_{PL}-1}$ in the denominator. Both Re_p formulations, amongst others, have been used in many drag laws available in the literature.

For more sophisticated GNF material functions such as Cross or Carreau, it may be convenient to express the Reynolds number Re_p based on the Newtonian zero-shear viscosity μ_0 instead [34],

$$\mathrm{Re}_{p0} = \frac{\rho_f\|\mathbf{v}_r\|d_p}{\mu_0}. \tag{27}$$

Table 1
Non-Newtonian drag law formulations used in this study.

#	Drag law and applicability range	Fluid model	Re_p	Drag co-efficient c_D	Drag law coefficients $Y_1,\ Y_2,\ Y_3$
1	Schiller and Naumann [23] ($Re_p < 800$) [35]	Carreau or Cross based on Eq. (17)	(8)	$\frac{24Y_1}{\mathrm{Re}_{p0}} + \frac{Y_2}{\mathrm{Re}_{p0}{}^{Y_3}}$	$Y_1 = 1$ $Y_2 = 3.6Y_1$ $Y_3 = 0.313$
2	Chhabra and Uhlherr [34] ($Re_p < 394$)	Carreau based on $\dot\gamma = 2\ \mathbf{v}_r/d_p$	(27)	$\frac{24Y_1}{\mathrm{Re}_{p0}} + \frac{Y_2}{\mathrm{Re}_{p0}{}^{Y_3}}$	$Y_1 = 1 + 0.65(n_{Ca} - 1)\Lambda^{0.2}$ $Y_2 = 3.6Y_1$ $Y_3 = 0.313$ $\Lambda = \lambda_{Ca}\frac{2\lvert\mathbf{v}_r\rvert}{d_p}$
3	Acharya et al. [2] ($Re_p < 1000$)	PL based on Carreau via Eqs. (22) and (23), and Eq. (17)	(26)	$\frac{24Y_1}{\mathrm{Re}_p} + \frac{Y_2}{\mathrm{Re}_p{}^{Y_3}}$	$Y_1 = 3^{\frac{3n_{PL}-3}{2}}\left(\frac{-22n_{PL}{}^2+29n_{PL}+2}{n_{PL}(n_{PL}+2)(2n_{PL}+1)}\right)$ $Y_2 = 10.5n_{PL} - 3.5$ $Y_3 = 0.32n_{PL} + 0.13$

While a large variety of non-Newtonian drag laws exists in the literature, most of them are based on the PL model and therefore require n_{PL} and K_{PL} as an input, which maybe obtained via conditions (24) in case of a Cross material function or Eqs. (22) and (23) in case of a Carreau material function. However, in this study, three different concepts are employed as follows and briefly summarized in Table 1:

1. an apparent viscosity concept, i.e. Eqs. (16), (17), e.g. (20), and (8) in conjunction with the Newtonian Schiller-Naumann drag law [23],
2. the Chhabra and Uhlherr drag law [34], which is explicitly designed for the Carreau [32] material function
3. and the Acharya drag law [2], which is based on the PL material function and additionally features a viscoelastic drag correction factor.

The Acharya drag law [2] additionally features a correction factor for viscoelastic effects such as normal stress differences, as the latter may significantly affect the drag coefficient:

$$c_{D-VE} = c_D\left(1 - 0.18\left(\mathrm{WiRe}_{p-MR}\right)^{0.19}\right), \tag{28}$$

where the Weissenberg number Wi is given as $\mathrm{Wi} = \lambda_f\|\mathbf{v}_r\|/d_p$ and Re_{p-MR} is the Generalized Reynolds number [33] for the particle given by Eq. (26). Wi in Eq. (28) is based on the time scale definition introduced by Leider and Bird [36], where a time scale λ_f is formed from PL fits of the shear viscosity and the first normal stress difference $N_1 = \tau_{11} - \tau_{22}$:

$$\lambda_f = \frac{K_{FNSD}}{2K_{PL}}^{\frac{1}{n_{FNSD}-n_{PL}}}. \tag{29}$$

Here, K and n are the coefficients of a shear viscosity data fit (Index *PL*) and a normal stress difference data fit (Index *FNSD*). Depending on whether one starts with the stress ratio N_1/τ_{12} or the recoverable shear $\mathrm{N}_1/(2\tau_{12})$, the factor 2 appears in the denominator of Eq. (29) or not.

2.3. Other relevant forces $\mathbf{F}_j$

Other contributing forces $\mathbf{F}_j$ to the particle equation of motion (2) are for instance the virtual mass force representing the required acceleration of fluid mass displaced by the accelerating particle and lift forces as a consequence of velocity gradients acting on the particle and particle rotation.

We will only investigate the relevance of these forces for a Newtonian case, assuming that in case of shear-thinning fluids the much higher apparent viscosity will lead to domination of the drag force.

As the density ratio in the experiments of [1] is $\rho_f/\rho_f > 0.1$, the mass of the fluid displaced by the moving particle is considered via the virtual mass force

$$\mathbf{F}_{VM} = c_{VM}\rho_f\frac{m_p}{\rho_p}\left(\frac{D\mathbf{u}}{Dt} - \dot{\mathbf{v}}\right), \tag{30}$$

where the virtual mass coefficient c_{VM} is taken as 0.5.

Because of the hydrostatic pressure gradient, a particle feels the differing pressure on opposite sides of itself and will be subject to a net force in the opposite direction of the pressure gradient given by the pressure gradient force

$$\mathbf{F}_P = -\frac{m_p}{\rho_p}\nabla p, \tag{31}$$

Since both shear gradients and rotation are present, both the low $\mathrm{Re_p}$ Saffman [37,38] and the high $\mathrm{Re_p}$ Magnus [39] lift force may be of relevance. The rotation rate of a spherical particle in non-Newtonian flows is of the (Newtonian) order $\omega = \dot\gamma/2$, but decreases with increasing viscoelasticity of the fluid [40]. This in principle indicates a relevance of lift due to particle rotation, i.e. the Magnus force as given by Rubinow and Keller [41]

$$\mathbf{F}_{Ma} = c_{RL}\frac{\pi}{8}d_p{}^3\rho_f(\mathbf{u} - \mathbf{v}) \times \left(\frac{1}{2}\nabla \times \mathbf{u} - \boldsymbol{\omega}\right), \tag{32}$$

where $\boldsymbol{\omega}$ is the particles' angular velocity and the rotational lift coefficient c_{RL} may be used to correct for higher particle Reynolds numbers and/or particle shape[1]. In addition, the shear flow as such indicates a relevance of lift due to velocity gradients on the particle surface, i.e. the Saffman [37,38] force, hereafter given in a tensorial form as a 3D extension [42] to Saffman's original formulation [37,38].

$$\mathbf{F}_{Sa} = 3.23\frac{d_p{}^2\sqrt{\mu_f\rho_f}\mathbf{D}_f}{\sqrt{\dot\gamma_f}}(\mathbf{u} - \mathbf{v}). \tag{33}$$

2.4. DPM implementation

In Fluent, the drag force per unit mass $\mathbf{F}_D/m_p$ is defined according to Eq. (7). The available macro DEFINE_DPM_DRAG allows to specify the drag coefficient c_D. To additionally correct the purely cell-based apparent viscosity of the fluid $\eta_{f,\,c}$ in Eq. (7), the following form is used

$$c_{DPM} = \frac{\eta_f}{\eta_{f,c}}\frac{3c_D\mathrm{Re}_p}{4}. \tag{34}$$

In Eq. (34), the actual apparent viscosity of the fluid $\eta_f(\dot\gamma)$, the total shear rate is $\dot\gamma$ computed from Eq. (16), the particle Reynolds number $\mathrm{Re}_p(\eta_f)$, and the drag coefficient $c_D(\mathrm{Re}_p)$ are evaluated using one of the concepts summarized in Table 1.

2.5. Reassessment of the experimental setup and data

2.5.1. Dimensions of the experimental setup

Fig. 1 provides a conceptual sketch of the laboratory setup of Khatibi et al. [1].

The actual test section starts with the particle injection point (7) and features a 1.5 m long section (6) with particle traps (8). Here, the particle trajectories were obtained via Particle Tracking Velocimetry (PTV) and velocity profiles were determined via Particle Image Velocimetry (PIV)

---

[1] In case of Magnus lift, an additional ordinary differential equation for the particles' angular momentum is solved which balances rotational drag and the particle's moment of inertia.

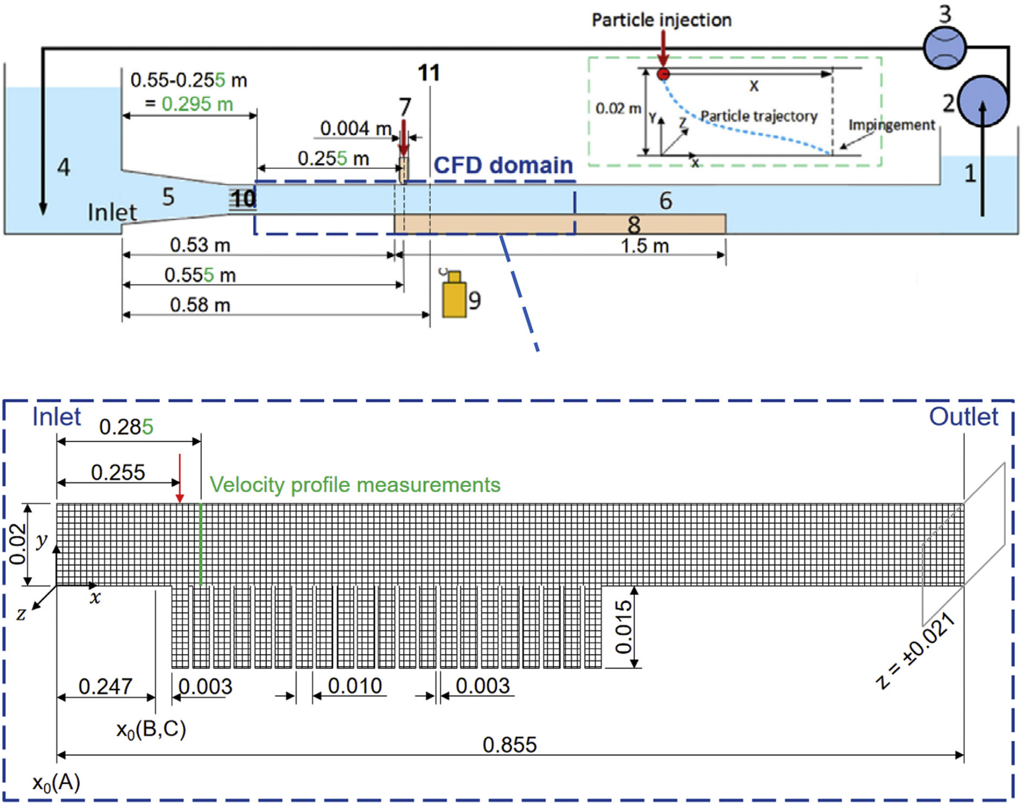

Fig. 1. Laboratory setup of [1] adapted from [1]. CFD domain of this study indicated with dashed blue line. Green numbers indicate a difference between actual numbers [43] and numbers reported in [1]. A, B, C refers to specific CFD cases introduced in Section 2.7. (For interpretation of the references to colour in this figure legend, the reader is referred to the web version of this article.)

at positions (9) and (11), respectively. Upstream of the test section, the experimental setup featured a converging section (5) fed from a tank (4) followed by a honeycomb-like [43] flow straightener (10). From a computational view point, the flow field at the exit of this straightener may be approximated with a uniform bulk velocity. Hence, the general CFD domain as used in this study (dashed blue rectangle in Fig. 1) encompasses the entire section from the straightener via the particle injection point to a point well downstream of the particle traps (1.5 m in total).

The particle traps (8) on the bottom channel wall do affect the channel (6) flow field. Hence, for the CFD computations it is vital to inject the particles at the correct position relative to these traps. The actual particle injection point (7) in the experiments [1] was at 0.255 m after the flow straightener [43].

2.5.2. Particle diameter

The particles used for the settling experiments were glass beads. The diameters reported [1] represent the mean diameter of a distribution [43]; i.e. there is some uncertainty associated with the nominal particle diameters [1]. In case of the smallest particle diameter used for the H_2O experiments, the nominal particle diameter was $d_p = 0.00116\,\text{m}$ [43].

2.5.3. Fluid properties

The flow curve (FC) data of Khatibi et al. [1] has been refitted with both Cross and Carreau material functions as depicted in Fig. 2; a tabulated overview is provided in Table 4 in the Appendix.

Polymeric solutions often feature elastic properties and in particular normal stress differences, which may lead to an increase of the drag coefficient compared to an inelastic fluids [2,12]. For the PAC fluids used in the experiments [1], we showed that, for higher shear rates, these polymeric solutions feature significant normal stress differences in the order of the shear stresses [44]. For the particular case of PAC4, second-order PL coefficients K_{FNSD} and n_{FNSD} for first normal stress data N_1 are available [44] and may be used to construct a characteristic fluid time scale λ_f as given by Eq. (29). However, our normal stress data [44] was estimated based on Laun's rule [45], and no direct measurements of normal stresses were conducted. As an alternative, either the Cross or Carreau time constants, λ_{Cr} and λ_{Ca} respectively, may be used [46]. This is not identical to the normal stress based time scale λ_f as given by Eq. (29); however, it is of the same order of magnitude [44].

The rheometric uncertainty is unknown [1]. However, for identical concentrations of the very same PAC granules, the uncertainty of the rheometric data is ≈ ± 5% SD [44]. The additional uncertainty introduced by the regression to either the Cross or Carreau material function is given in Table 4 in the Appendix; however, the uncertainty of the rheometric data is much larger.

2.5.4. Velocity profiles

The experimental channel flow x-velocity profiles [1] (reprinted as circles in Fig. 3) do not provide wall-near information because this would have required higher resolution techniques [1]. Interestingly, they feature some degree of non-ideal parabolic curvature as well as

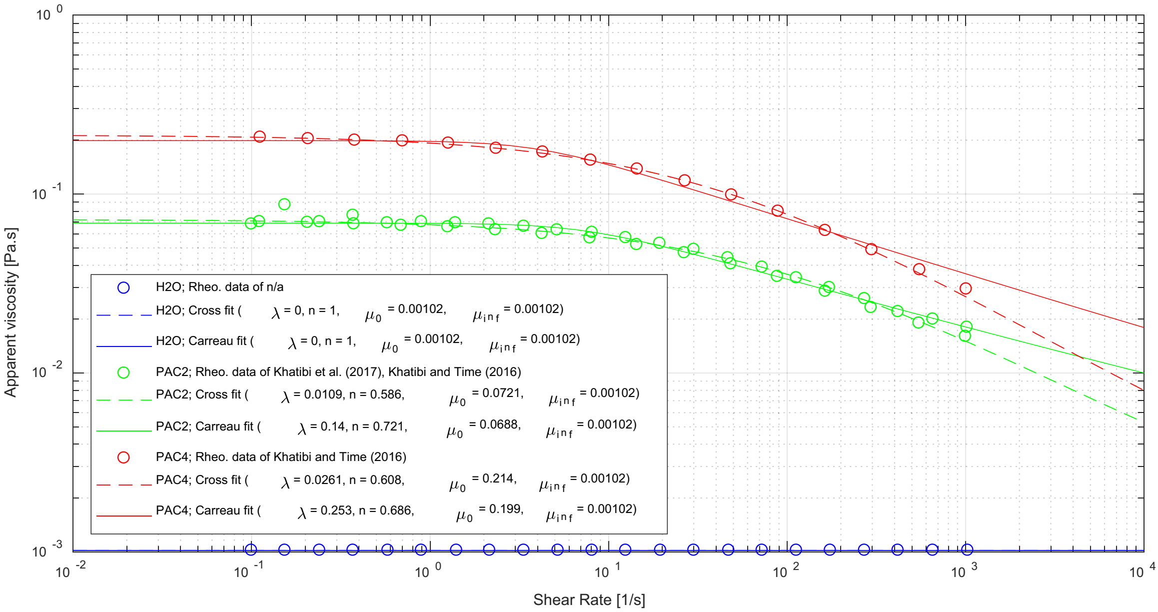

Fig. 2. Experimental flow curves (FC) [1] (circles) and corresponding Cross (dashed lines) and Carreau (solid lines) fits based on Eqs. (20) and (21), respectively. The Cross model fits the data slightly better (see numerical values of R^2 in Table 4 in the Appendix).

skewness. This may be a consequence of experimental scatter or possibly indicating wall slip, a phenomenon well-known for polymeric liquids [47,48].

Fitting polynomials of order two for the PAC solutions and order five for the water case[2] and extrapolating to the wall yields estimates for the slip velocities as indicated in Fig. 3.

While for the bottom wall the particle traps will effectively act as a slip-boundary for the channel flow and may thus explain a slip velocity this is not the case for the top wall. Sodium Carboxymethyl Cellulose (CMC) solutions — which are chemically and rheologically strongly related to the PAC solutions utilized in the experiments [1] — show wall slip for fairly low concentrations [49]. The PAC solutions may lead to wall slip; however, this is certainly not the case for H_2O. Nevertheless, the polynomial fits along with the slip velocities indicated in Fig. 3, hereafter termed “experimental velocity profiles”, are further used in the simulations in order to minimize the effect of an incorrect fluid velocity profile on the particle trajectory.

Note that the wall slip values indicated in Fig. 3 are totally subjective as they are based on the extrapolation of the polynomial fits. Using only e.g. the first few data points of the H_2O profile and extrapolating to the wall yields twice as large slip velocities.

2.5.5. *Particle injection conditions*

The initial velocities of the particle at the particle injection point provided by Khatibi et al. [1] were determined based on an average of the y-velocity components of the entire particle trajectory data [43].

The particle injection point, (7) in Fig. 1, is the end of a small pipe of diameter d and length z. In the experiments [1] the particle was inserted at the top, settled through the pipe and entered the channel at the pipe end [43]. Hence, at the injection point, one would expect the particle velocity to be equal to the terminal settling velocity corrected by wall effects as the confinement ratios $\beta_i = d_{p,i}/d$ for the different particle diameters ranges are 0.29, 0.5 and 0.75, respectively. However, we simply estimated initial particle velocities based on a differential of the first two data points of the experimental trajectory data [1], as provided in Table 2.

Table 2
Test matrix [1], fluid density $\rho_f = 1000\,\mathrm{kg/m^3}$, particle density $\rho_p = 2560\,\mathrm{kg/m^3}$.

Case	Fluid	U	d_p	v_{x0}	v_{y0}
1	H_2O	0.085	0.00116	5.95E-06	−0.00014
2	H_2O	0.085	0.002	0	−0.00031
3	PAC2	0.048	0.002	0	−2.75E-05
4	PAC2	0.048	0.003	0	−5.75E-05
5	PAC4	0.048	0.002	0	−1.04E-05
6	PAC4	0.048	0.003	0	−4.55E-05
7	PAC4	0.085	0.002	0	−1.57E-05
8	PAC4	0.085	0.003	0	−5.69E-05

2.6. *Test matrix*

Table 2 summarizes the main parameters, namely the fluid type, the fluids bulk velocity **U** and the particle diameter d_p, which have been varied in the experimental campaign [1]. Additionally, Table 2 provides the initial particle velocities estimated from the experimental data [1]. The rheological model coefficients for the various fluids may be inferred from Fig. 2 or Table 4 in the Appendix, alternatively.

The bulk velocity-based channel Reynolds number for the water case is 2294. However, as the entrance length of the flow is relatively short (the distance between injection point (7) and flow straightener (9) as depicted in Fig. 1 is just 0.255 m), we consider the flow at the trajectory section laminar. Due to the much higher apparent viscosity of PAC, all the PAC cases are also treated as laminar.

---

[2] While this is physically reasonable for the PAC solutions because of the laminar flow regime, the 5th order polynomial fit was chosen purely because it best-fits the observed velocity profile.

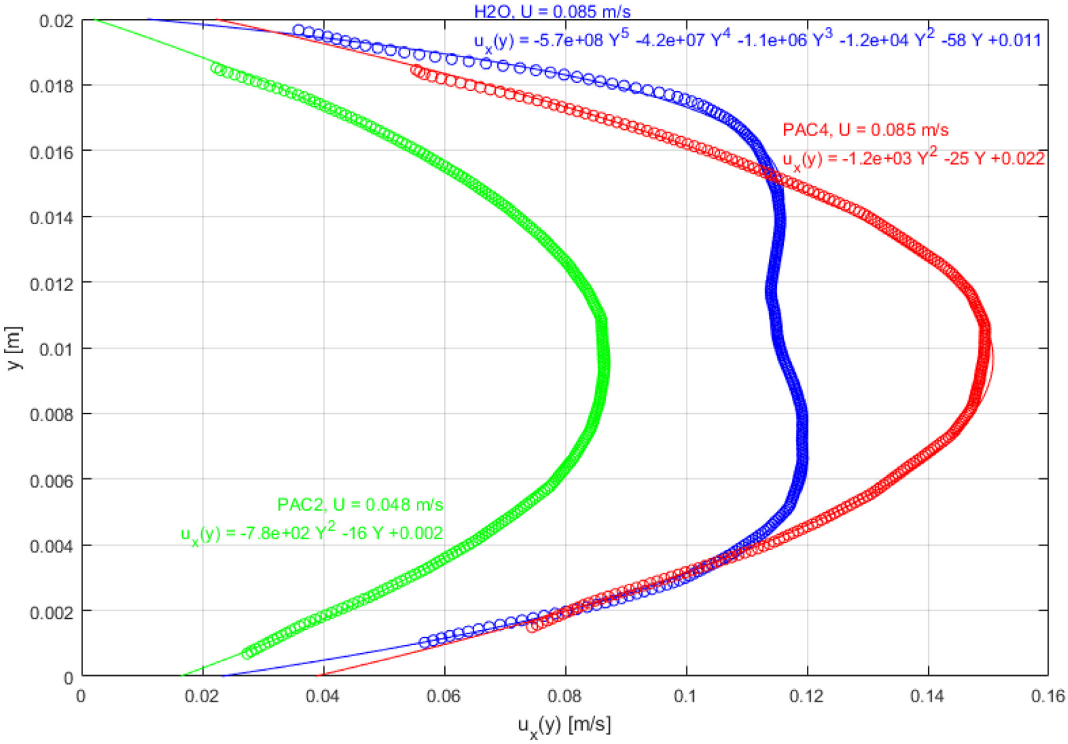

Fig. 3. Boundary slip velocity estimate based on extrapolation of polynomial fits (PAC solutions → degree 2, H_2O → degree 5) to experimental velocity profiles [1]. As the dependent variable of the polynomials is defined as $\boldsymbol{Y} = \boldsymbol{y} - 0.02$, the last terms readily provide the boundary slip velocities at the channel top wall. Since for the PAC4, $\boldsymbol{U} = 0.048$ m/s case no velocity profile is available [1], this may be scaled from the PAC4, $\boldsymbol{U} = 0.085$ m/s case based on superficial velocities.

2.7. CFD setup

To investigate the effect of 2D vs. 3D as well as the effect of the particle traps at the bottom channel wall, three different setups were used as depicted in Fig. 4.

Case A fully represents the laboratory setup in 3D. In contrast to the 3D mesh depicted in the Appendix of Khatibi et al. [1], the particle injection pipe was not part of the computational domain because the injection conditions were based on the experimental data, see Section 2.5.5. Cases B and C are shortened by 0.247 m, i.e. the distance from the inlet to the first trap is 3 mm and to the particle injection point is 8 mm.

In case of A, uniform velocity profiles, i.e. the superficial liquid velocities as given in Table 2, were specified at the inlet. In case of B and C, either parametrized parabolic velocity profiles with the mean velocity equal to the bulk velocities given in Table 2, or the actual experimental velocity profiles[3] [1], see Section 2.5.4, were specified at the inlet. B and C were used for 2D simulations, whereas A was additionally used for 2D and 3D simulations.

The domain was entirely meshed with a structured quadrilateral grid. The mesh size was 1 mm in the inlet and outlet part of the domain and 0.5 mm in the settling test section, i.e. in the part of the test section were particle traps were located. Fig. 4 additionally provides the total number of cells for the individual cases. The meshes as specified above were found sufficiently fine to provide mesh-independent results.

2.8. Numerics

For the fluid phase, the SIMPLE scheme was used for pressure-velocity coupling and second order spatial discretization was applied. Gradients were evaluated using the Green-Gauss node-based gradient scheme. The algebraic multigrid method utilizing the Gauss-Seidel solver with default under-relaxation factor settings were used to solve the discretized equation systems.

The particle force balance Eq. (2) was integrated using the automatic scheme selection feature of Fluent, where a high-order semi-implicit trapezoidal scheme and a low-order unconditionally stable implicit Euler scheme is used depending on the required accuracy, the stability range of the high-order scheme, and actual particle velocity and relaxation time. Both one-way and two-way coupling were used, depending on the cases defined in Fig. 4. However, as there is just one single particle advected through the domain, one-way coupling is sufficient. As the hydrodynamic flow is steady and no particle break-up and/or collision may occur in the single-particle problem studied here, a steady flow particle tracking concept was applied.

Note that the cases investigated somewhat violate the usual assumption that the particle size d_p is smaller than the grid size, i.e. Δx, Δy, and Δz. This may lead to a significant error in regions of high fluid velocity gradients since particle forces, for instance drag, will be computed merely based on the cell values where the center of the particles is located.

3. Results

We first briefly describe results of various pre-investigations which were conducted to either simplify the actual computations or reduce

---

[3] The experimental velocity profiles of case 5 and 6 were not provided in [1] and were therefore scaled from cases 7 and 8 based on the ratio of superficial velocities.

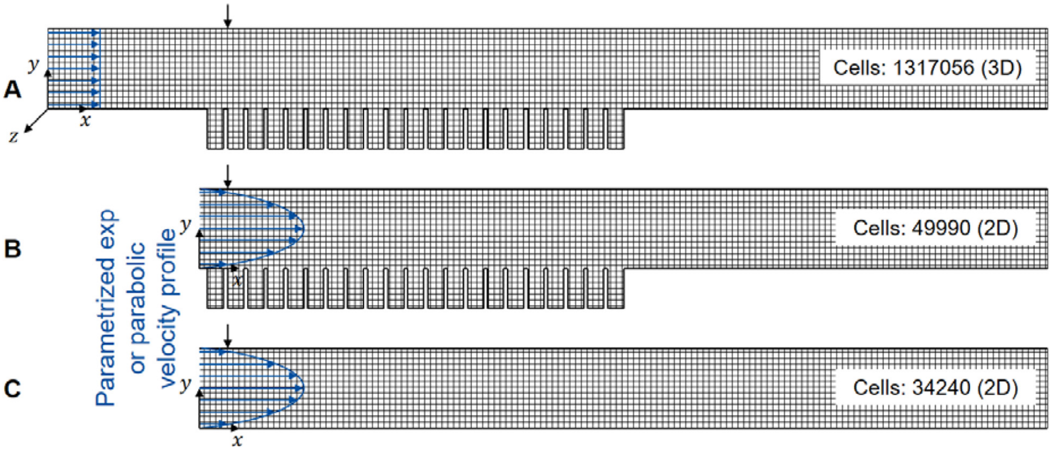

Fig. 4. Different CFD cases used in this study.

the CFD test matrix. This is followed by presenting the actual results, both particle trajectories $y = f(x)$ and particle velocity components v_x and v_y as a function of the channel height y, for the different drag law formulations investigated.

3.1. Pre-investigations

There is very little difference between a 2D and a 3D trajectory if the correct velocity profile is specified. If a 2D variant of Case A is utilized, a uniform velocity specification at the inlet yields a wrong velocity profile at the test section, as the boundary conditions (BC) incorporate a periodic BC in the z-direction, i.e. the channel is infinitely wide. If a parabolic profile is specified instead, the difference 2D vs. 3D is almost non-existent. The 3D simulations feature a secondary flow because of the particle traps at the lower channel wall. While the corresponding fluid y-velocity component is two orders of magnitude smaller than the particle y-velocity component in case of H_2O (Fig. A1 in the Appendix) it is in the same order of magnitude in case of PAC4 (Fig. A2 in the Appendix). In addition, shear rate and viscosity fields are affected by the traps and secondary flows (Figs. A3 and A4 in the Appendix). However, the effect on the actual particle trajectories of the viscous PAC cases is virtually non-existent (Fig. A5 vs. Fig. A7 in the Appendix)[4].

Regarding the x-velocity components, it is important to either include these particle traps in the computational domain or, alternatively, specify corresponding slip velocities as BCs. Because of the particle traps, the $u_x(y)$ velocity field features an effective slip velocity at $y = 0.0$ m. This may be verified from Fig. 3, where the boundary slip velocity of the lower channel wall is significantly larger than the one at the top wall.

To rule out the effect of the velocity profiles on the trajectory, the results presented hereafter are purely based on the specification of tuned velocity profiles as described in 2.5.4. Both for the uniform inlet velocity profile BC (case A) and the parabolic velocity BC (cases B and C), the CFD velocity profiles in the test section do not match the experimental profiles. While the general magnitude is the same and the maximum velocities are matching well, the values differ close to the top and bottom channel walls. It is unclear whether this is due to polymeric wall slip or not[5].

The effect of the other particle forces $\mathbf{F}_j$, namely Eqs. (30)–(33), on the particle trajectories is most prominent after the injection in the upper half of the channel. Fig. 5 depicts the particle x-coordinate ratio (obtained x-coordinate with consideration of $\mathbf{F}_j$ divided by obtained x-coordinate without consideration of $\mathbf{F}_j$) for the case of water as a function of the channel height y for two particle sizes.

The difference between consideration and neglection of the other forces is up to 70% for the larger particle. As the larger particles inertia will reduce the effect of lift and drag, we expect this large difference to be primarily a consequence of the virtual mass force. However, the actual difference in trajectories is quite small as may be verified from Figs. A5 to A8 provided in the Appendix.

The large and small particles show opposite behavior shortly after the injection point. As the smaller particle features less inertia, the effect of virtual mass is smaller and the effect of streamwise lift is larger leading to additional acceleration into the flow direction.

For the non-Newtonian PAC solutions, the effect of the other particle forces $\mathbf{F}_j$ is less prominent because of the higher apparent viscosities and the thus over-proportional increasing drag force: The drag force scales linearly with viscosity for Stokes flow, whereas the Saffman force scales with the square root of viscosity. The other forces are independent of viscosity. Hence, we neglect $\mathbf{F}_j$ in the particle force balance for the hereafter presented results.

3.2. Particle trajectories

In this section, we present results for the three different models summarized in Table 1. All results are based on Case C, with a case setup as depicted in Fig. 6.

As mentioned in Sections 2.5.4 and 3.1, the experimental velocity profiles specified at the inlet were tuned with the slip velocities indicated (Fig. 6, left), which explains the good match between CFD and experimental profiles (Fig. 6, right).

Fig. 7 shows the numerically obtained trajectories for the apparent viscosity concept using the Cross model for all the different cases of

---

[4] This holds for the geometry and dimensions as specified in Figure 1 and for any other position of the injection point relative to the traps. Figure A2 to Figure A4 in the Appendix suggest that a shift of the position of the injection point relative to the traps may lead to a much further advected particle because that particle may end up just upstream of a trap tooth where fluid y-velocity components may be sufficiently large to transport it to the next trap instead. However, for any injection point variation in x, the simulations predict an almost identical shift of the impingent point.

[5] No pressure data was obtained during the experimental campaign [1]. If pressure data for different flow rates is available, one can determine the slip velocity [49].

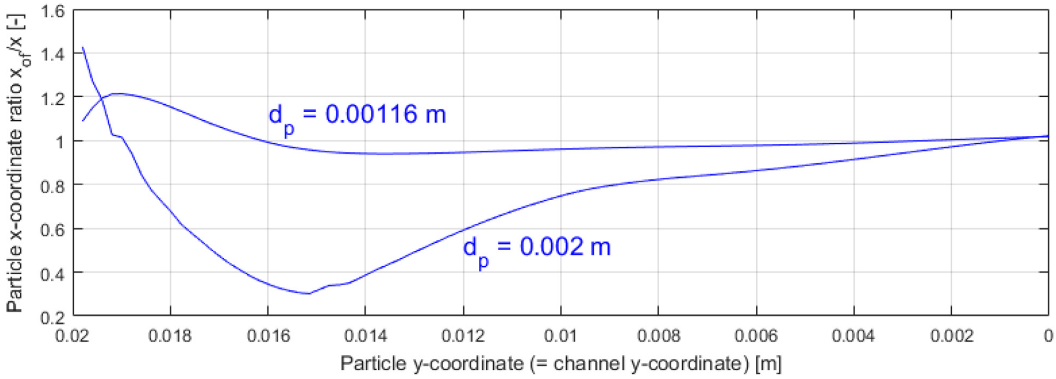

Fig. 5. Relevance of other forces $\boldsymbol{F_j}$ expressed as particle $\boldsymbol{x}$-coordinate ratio (obtained $\boldsymbol{x}$-coordinate with consideration of $\boldsymbol{F_j}$ divided by obtained $\boldsymbol{x}$-coordinate without consideration of $\boldsymbol{F_j}$) for the H_2O case. CFD case C, slip velocities and experimental fluid velocity profiles as given in Fig. 3, Fluent-state-of-the-art.

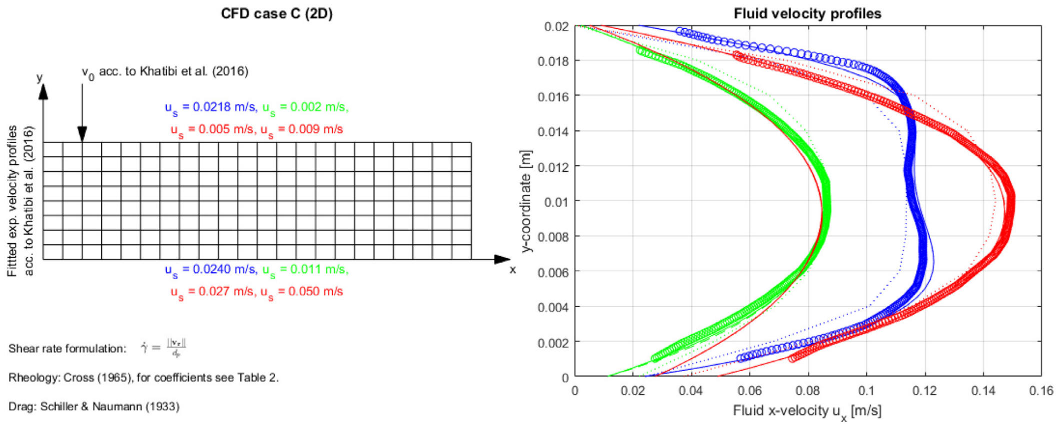

Fig. 6. Case setup for CFD case C (left) and fluid velocity profiles (right). Circles indicate the experimental velocity profiles [1] at $x_{CFD}(C) = 0.038$ m, solid lines are our CFD profiles obtained at $x_{CFD}(C) = 0.038$ m, dotted lines are the CFD profiles [1] obtained at $x_{CFD}(C) = 0.015$ m. For color codes see Fig. 2/Fig. 3.

Table 2 (solid lines), together with the experimental data (large circles represent the large particle diameter, small circles the smaller size) [1].

In addition, the CFD trajectories obtained by Khatibi et al. [1] are provided with dotted lines and trajectory results based on the Fluent state-of-the-art as are provided with dashed lines.

The smaller particle trajectories do coincide with the experimental data reasonably well. The larger particle trajectories do coincide roughly until the channel centerline. The lower part of the larger particle trajectories, however, is overestimated in the H_2O case and underestimated in most PAC cases.

In case of H_2O, the Fluent state-of-the-art results (dashed lines) coincide with the apparent viscosity model results, as expected. For many PAC cases, the Fluent state-of-the-art results over-predict the experimental trajectories, i.e. in the simulations the settling of the particle happens slower than in the experiments, in particular at the center of the flow.

Results for the concept #2, i.e. the Chhabra and Uhlherr [34] drag law as provided in Table 1, are depicted in Fig. 8. The same qualitative trajectory trend as predicted by the apparent viscosity concept is observed, namely that CFD and experimental trajectories coincide reasonably well apart from the lower channel half in case of the small particle sizes.

For the H_2O cases, the Fluent state-of-the-art results coincide with the apparent viscosity model results.

Results for the concept #3 are depicted in Fig. 9. Compared to the apparent viscosity concept results depicted in Fig. 7, the PAC2 results show drag reduction as the impingement point has shifted towards the injection point. The PAC4 results show drag enhancement as the impingement point has moved further downstream. Small differences are also noticeable for the water cases, which may be due to comparatively high particle Reynolds numbers (see Table 3 in the Appendix) and a possibly limited accuracy of the Acharya [2] drag law in that range[6].

3.3. Velocity components

In order to further analyze the trajectory results of the apparent viscosity concept #1 provided in Fig. 7, the velocity components of the particle velocity vector **v**, namely v_x and v_y, were computed based on point-by-point differentials, i.e. $\Delta x/\Delta t$ and $\Delta y/\Delta t$, from the time series data for both the numerical results of this study and the experimental data [1]. In case of the experimental data [1], we additionally computed

---

[6] In the paper of Acharya [2], the applicable range of Reynolds numbers is given as $10^{-3} < Re_p < 10^3$. However, the validation of the drag law is only disclosed up to $Re_p \approx 50$ (Fig. 9 in [2]) without any associated quantitative uncertainty.

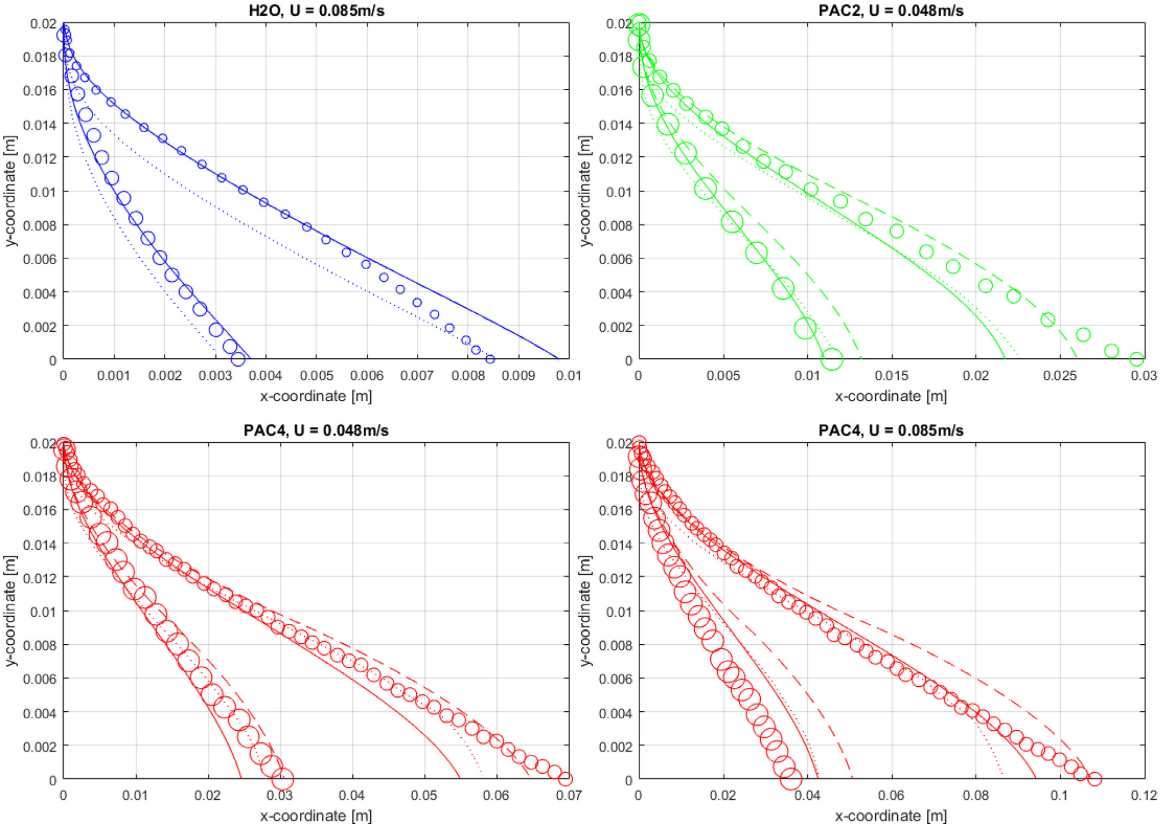

Fig. 7. Apparent viscosity concept #1 CFD trajectories (solid lines; Schiller and Naumann drag law [23] with Cross [24] model coefficients as given in Fig. 2) vs. experimental particle trajectories (circles) [1]. Circle sizes represent particle diameters according to Table 2. Dashed lines represent Fluent's state-of-the-art, dotted lines represent CFD results of Khatibi et al. [1].

a time-averaged velocity based on the 9 nearest neighbor experimental data points.

The x-velocity components normalized with the respective fluid x-velocity component $u_x(y)$ of all the cases of Fig. 7 are depicted in Fig. 10 as a function of the channel y-coordinate. A normalized velocity value of $(\Delta x/\Delta t)/u_x = 1$ represents equal fluid and particle velocities. Some CFD results feature small spikes which is a consequence of the numerics of Fluent.

For the case of H_2O (left subfigures in Fig. 10), both numerical and experimental results match reasonably well. For the PAC cases with small particle diameter (three top right subfigures in Fig. 10), however, large mismatches in the lower part of the channel, i.e. $y < 0.01$ m, are observed. In the experiments, the particle moves faster than the fluid by a factor of 1.5 to up to 4-6 for $y < 0.004$ m, whereas in the simulations, the velocity ratio is about 1.1 for the PAC4 cases, and 1.1-1.8 for the PAC2 case. For the large particle PAC cases (three bottom right subfigures in Fig. 10), the match between experimental and numerical velocity ratios is slightly better. However, in the case of PAC4, $U = 0.048$ m/s (second-right bottom subfigure in Fig. 10), the velocity ratio difference is of the same order as in the small diameter cases. For the case of PAC4, $U = 0.085$ m/s (right bottom subfigure in Fig. 10), the velocity ratio difference is comparatively small close to the lower wall but larger in the center part of the channel flow. The PAC4 cases feature a velocity ratio in the order of 1 for the most part of the upper channel half, with the notable exception of the PAC4, $U = 0.085$ m/s case (right bottom subfigure in Fig. 10), where the experimental velocity ratio is in the order of 0.5 for the upper channel half.

The particles y-velocity components of all the apparent viscosity concept cases presented in Fig. 7 are depicted in Fig. 11 as a function of the channel y-coordinate. While the y-velocity based on the raw experimental data (dots in Fig. 11) is very scattered, the time-averaged experimental velocity provides a clearer picture of the y-velocity (dotted lines in Fig. 11).

The overall magnitude matches well in all cases; however, the numerical results (solid lines in Fig. 11) shows curvatures which may not be directly seen in the experimental data. Two different types of curvature are to be distinguished: (1) Initial relaxation effects and (2), in the case of PAC, more prominent subsequent effects of varying shear rate and thus viscosity as well as possible relevance of other forces such as lift.

Regarding (1), for the H_2O cases (left subfigures in Fig. 11), the particles y-velocity component approaches the steady-state value of a single particle settling in a quiescent fluid based on the apparent viscosity concept #1, see Table 1. However, in case of the larger particle, the y-velocity component is larger than the terminal velocity. This is a consequence of the initial particle velocity specified in the simulations, see Section 2.5.5. The PAC cases show a corresponding velocity relaxation effect; however, much of this relaxation occurs, as expected, much faster than in the case of H_2O.

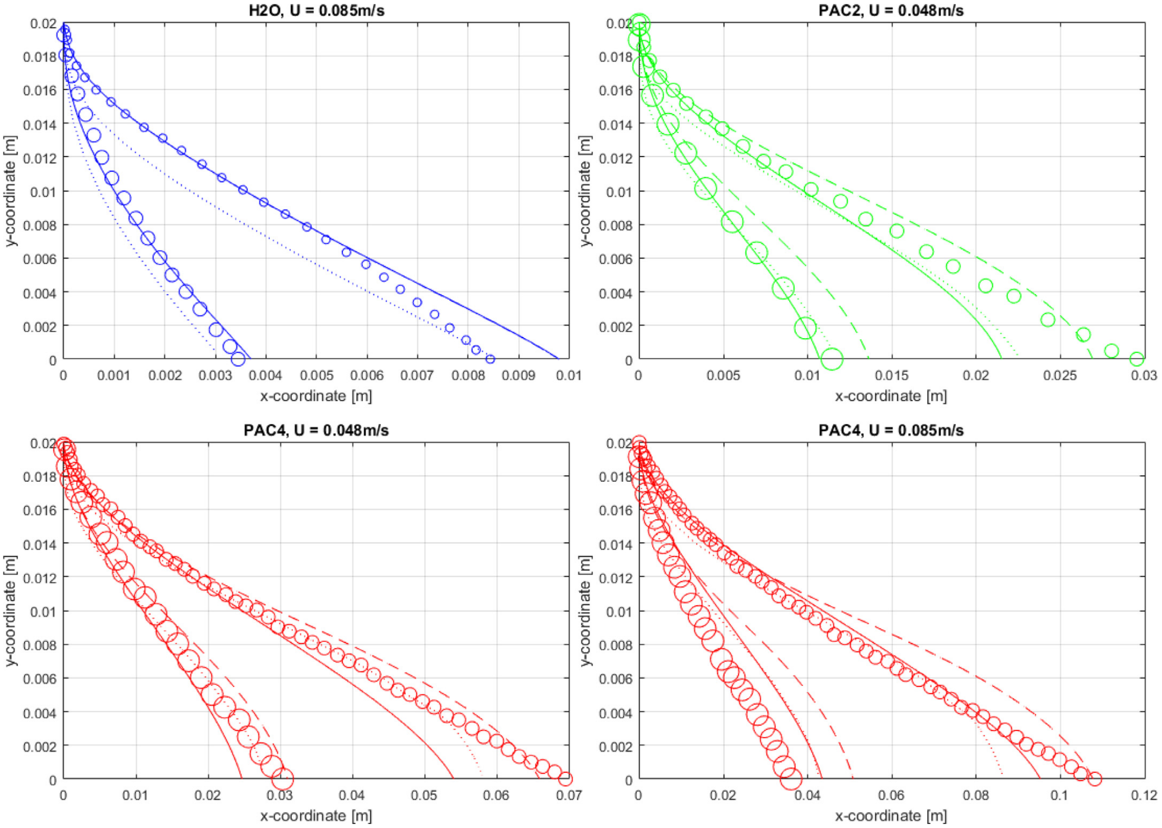

Fig. 8. Concept #2 CFD trajectories (solid lines; Chhabra and Uhlherr drag law [34] with Carreau [32] model as given in Fig. 2) vs. experimental particle trajectories (circles) [1]. For further information see caption of Fig. 7.

Regarding (2), in case of the numerical PAC results, a prominent curvature of the $\Delta y/\Delta t$-curve is observed over the entire channel y-coordinate, with y-velocity minima (in magnitude) at the channels centerline. Due to the channel shear flow and the corresponding change in shear rate and hence viscosity in the y-direction, one would expect that the experimental y-velocity component of the particles is varying along the channel y-direction. Unfortunately, this may not be directly inferred from the time-averaged experimental y-velocity component.

The minimum particle y-velocity is the same for different fluid bulk velocities. This is to be expected as in the center of the channel the mean flow strain is vanishing and the apparent viscosity is purely determined by the particle induced shear rate.

Another possibility of analyzing the results is to plot the ratio of the relative velocity components, i.e. $(v_x - u_x)/(v_y - u_y)$ over the channel height y, as depicted in Fig. 12. While in the H_2O and the large particle diameter PAC2 cases, the experimental data and the CFD results coincide fairly well, this is not so for the other PAC cases.

A general trend is that close to the channel top wall, the relative velocity ratio is positive, as both the nominator and denominator are positive due to the particle lacking behind both the fluid velocity in the x- and y-direction. In the lower part of the channel, the particle x-velocity component is larger than the fluid x-velocity component, and hence the relative velocity ratio becomes negative.

Towards the lower channel wall, the experimental ratio (dotted lines) becomes smaller than minus one for all but the $U = 0.048\,\mathrm{m/s}$, $d_p = 3\,\mathrm{mm}$ PAC case as the positive horizontal slip velocity $(v_x - u_x)$ becomes larger in magnitude than the negative vertical slip $(v_y - u_y)$. This is not so for the numerical results (solid lines). For the two $U = 0.085\,\mathrm{m/s}$ PAC4 cases, the experimental ratio becomes larger than one both in the upper half and center of the channel. This implies that the negative horizontal slip velocity $(v_x - u_x)$ becomes larger in magnitude than the negative vertical slip $(v_y - u_y)$.

4. Discussion

Macroscopically, the experimental trajectories [1] and the numerical trajectories of this study match reasonably well for the drag law concepts #1 and #2 given in Table 1 (and even for concept #3, if the Cross time constant or, alternatively, no viscoelastic correction, i.e. Eq. (28), is used). While the S-shaped numerical trajectories are qualitatively in agreement with the analytical results of Childs et al. [22], there exists a large mismatch between the S-shaped numerical trajectories of this study and the J-shaped experimental trajectories [1] for the lower channel wall region, i.e. $y < 0.008\,\mathrm{m}$, in particular for all the small particle diameter cases. In principle, possible reasons for such a mismatch may be due to:

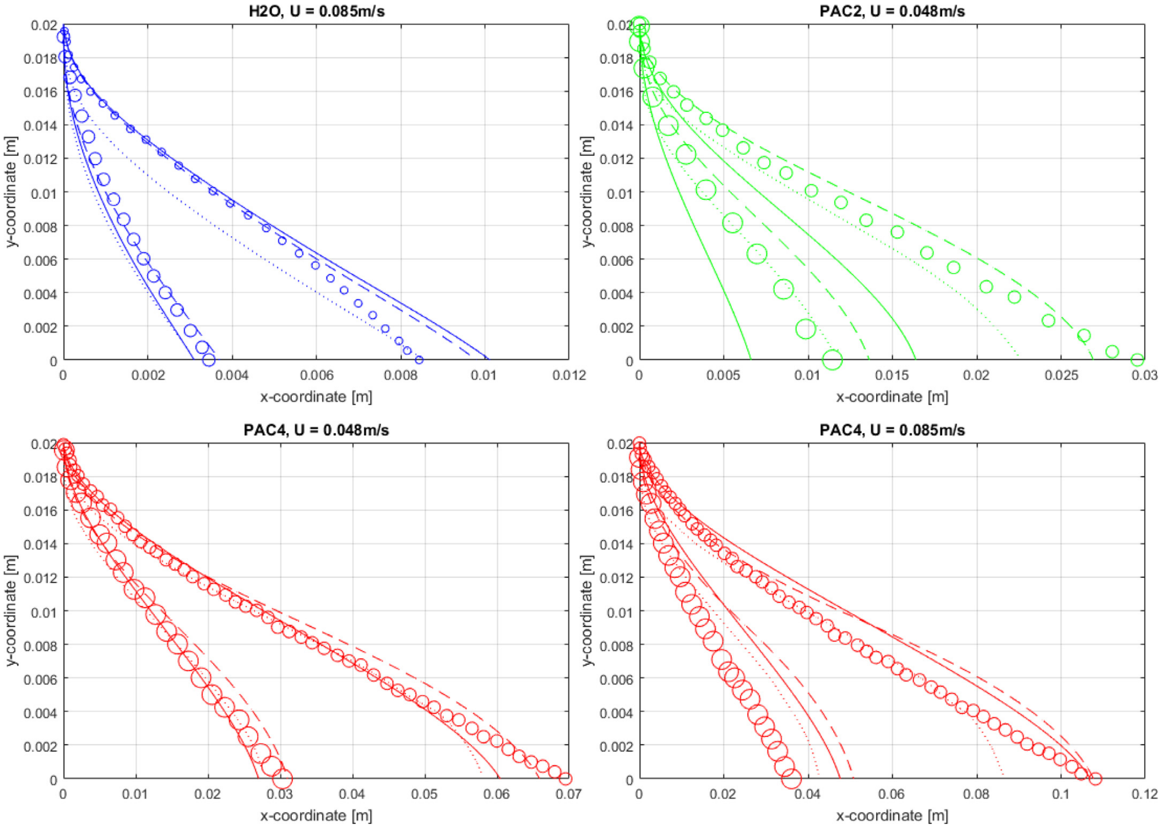

Fig. 9. Concept #3 CFD trajectories (solid lines; Acharya [2] drag law with time scale $\lambda = \lambda_{Ca}$ and PL-coefficients obtained from Carreau [32] model coefficients as given in Fig. 2 using conditions (22) and (23)) vs. experimental particle trajectories (circles) [1]. [1]. For further information see caption of Fig. 7.

1. Shear rate model and effect of particle-induced shear.
2. Rheological description of the fluid.
3. Wall presence.
4. Anisotropic viscosity due to polymer chains.
5. Drag law formulation.
6. Other relevant forces than drag.
7. Shape of fluid velocity profile at particle settling test section.
8. Initial velocity of particles at injection.
9. Uncertainty of all parameters.
10. Experimental measurement errors.

The points 1 to 10 will be individually discussed in the following subsections.

4.1. Shear rate model and effect of particle-induced shear

For the case of orthogonal shear, the validity of Eq. (16) has been proven in many studies so far, (see Section 1.1). Macroscopically, this is also the case for the problems investigated in this study. However, microscopically, close to the channel walls, the relative velocity of the particle does have a significant x-component (see Fig. 10), which may lead to non-orthogonal velocities violating the orthogonal shear rate assumption of Eq. (16). Furthermore, Eq. (16) may not straightforwardly be used for arbitrary 3D problems where fluid and relative particle velocities and shear rates may have any angle with respect to each other. For such cases, $\mathbf{D}_p$ in Eq. (15) needs to be detailed by e.g. expressing Eq. (17) in a tensorial form to yield an expression for $\mathbf{D}_p$.

The particle-induced shear rate estimate $\dot{\gamma} = \|\mathbf{v}_r\|/d_p$ appears to represent the correct order of magnitude because the y-velocity components are reasonably well met in case of the apparent viscosity concept (Fig. 11). The same applies for the other drag law formulations investigated.

4.2. Rheological description of the fluid

It is known that PAC solutions feature mild viscoelastic and thixotropic behavior [44], the former for short time scales in the order of < 1 s, the latter for larger time scales in the order of 10 to 800 s [44]. Viscoelasticity in the form of normal stress differences may also affect the steady-state velocity profiles in the channel close to a flow extension as well as the force balance acting on a particle moving relative to the fluid flow.

Moreover, the rheological properties of the experimental fluids are generally subject to temperature influence. While “the rheology of water, PAC 2 g/l and PAC 4 g/l did not change before and after the experiment” [1], the in-situ temperature of the fluid in the channel flow is not known. The experiments were conducted at ambient room temperature, which may not have been exactly 21°C. In addition, the shearing of the fluid in the components of the flow loop, in particular in the centrifugal pump, may have raised the in-situ fluid temperature.

We think that viscoelastic effects are not playing a major role. The PAC solutions used in the experiments [1] feature elastic properties [44], which is known to affect the wake structure of a moving par-

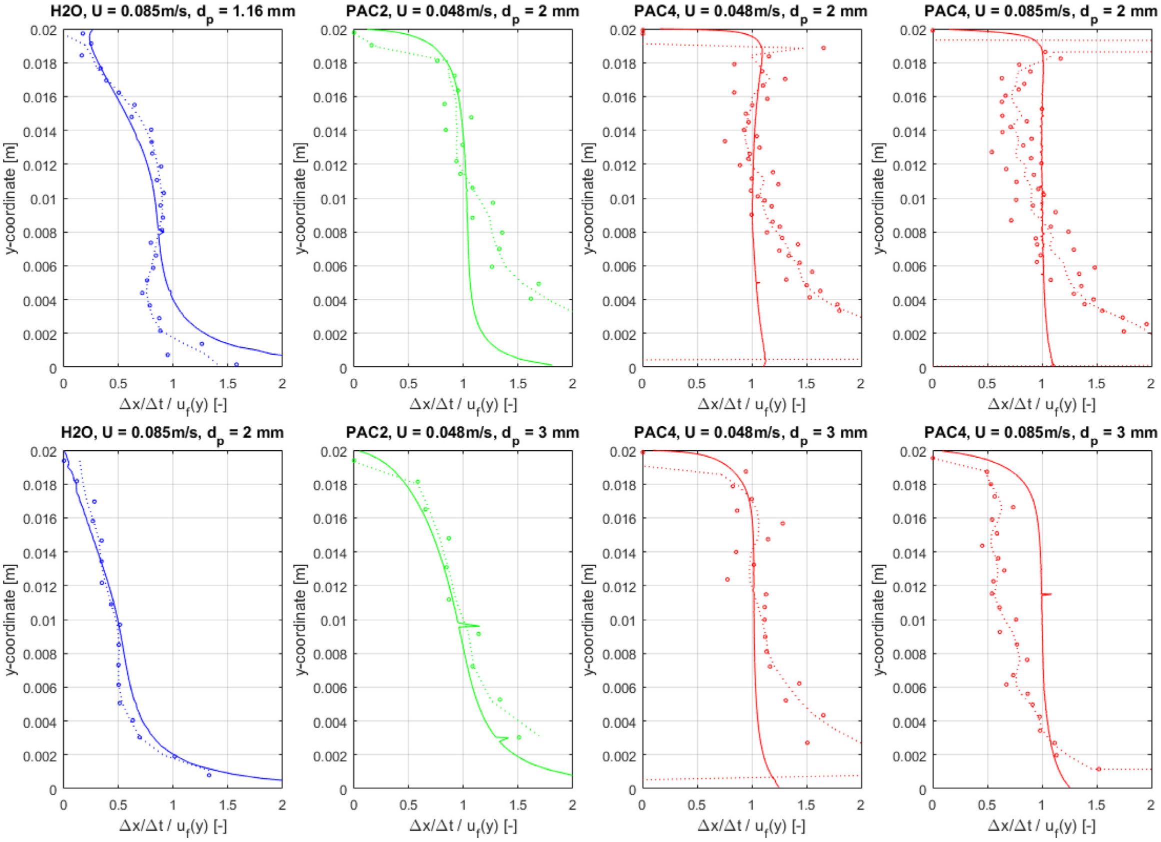

Fig. 10. Particle $\boldsymbol{x}$-velocity components normalized with fluid $\boldsymbol{x}$-velocity components for the cases presented in Fig. 7 as function of the channel $\boldsymbol{y}$-coordinate. CFD (solid lines) vs. experimental particle trajectories (circles) [1]. Dotted lines represent time-averaged experimental data.

ticle [2,50]. However, a corresponding correction of the drag coefficient, namely Eq. (28) applied in drag concept #3, does not significantly change the trajectories, if the time scale used is equal to the time constant of the Cross model (not shown here). If the Carreau time constant is used, however, the numerical results indeed show drag enhancement (see Fig. 9), which results in a better trajectory match close to the lower channel wall for PAC4. But it also leads to increased mismatch in the centerline for the PAC4 cases as well as significant drag reduction and thus mismatch in the PAC2 cases. While it is debatable which one is the more correct time scale to use, the Cross time constant represents the magnitude of the time scale defined by Eq. (29) much better than the Carreau time constant [44]. Hence, we expect the Cross time constant to be a valid representation and conclude that viscoelastic wake is of minor significance for the cases investigated. As may be verified from Eq. (29), elastic effects due to normal stress differences are shear rate dependent and the shear rates experienced by the particle are apparently not large enough to significantly change the drag and correspondingly the particles trajectory.

However, taking a microscopic view, thixotropic effects may indeed have played a role because the in-situ apparent viscosity might change from the flow straightener to the particle settling test section. The flow straightener essentially leads to a contraction flow, where a fluid element experiences a sudden high shear rate in the straightener rapidly followed by a comparatively low shear rate after the straightener in the channel. For large shear rate steps, PAC4 shows thixotropic behavior with very large time scales of the order of ≈ 10-800 s [44]. The relative difference in apparent viscosity, i.e. the ratio of instantaneous apparent viscosity to microstructural steady-state apparent viscosity, ranges between 80% to 95% for the two time scales mentioned [44]. Hence, even though the shear rate step from the flow straightener to the channel flow is probably not as large as in shear rate step tests used to evaluate thixotropic response [44], the apparent viscosity might have changed by a certain unknown percentage in the order of 0…80% because the time scale for a fluid element traveling from the flow straightener to the test section is of the order $\dot{\gamma} = x/U = 3\text{-}5.3\,\mathrm{s}$, where $x = 0.255\,\mathrm{m}$ is the distance (Fig. 1) and U is the respective fluid bulk velocity. From a macroscopic viewpoint, thixotropy should not have played any role in the experiments [1] as trajectory measurements were obtained > 35 minutes after initializing the channel flow [1], hence in full flow-dynamic and microstructural equilibrium.

Another mechanism for increased drag is based on acting normal stress differences which may contribute to particle lift acting against the direction of the particle relative velocity [12]. This mechanism, however, would have yielded slower settling velocities (which in fact match quite well the experimental data) and much faster relaxation of the particle velocity in the x-direction.

Normal stress presence may also significantly change the velocity profiles [51–53]. However, since we have used the actual experimental velocity profiles it does not explain the trajectory mismatch. On the other hand normal stresses could reduce the observed downward velocities on the lee of a particle trap tooth, i.e. reduce the downward drag.

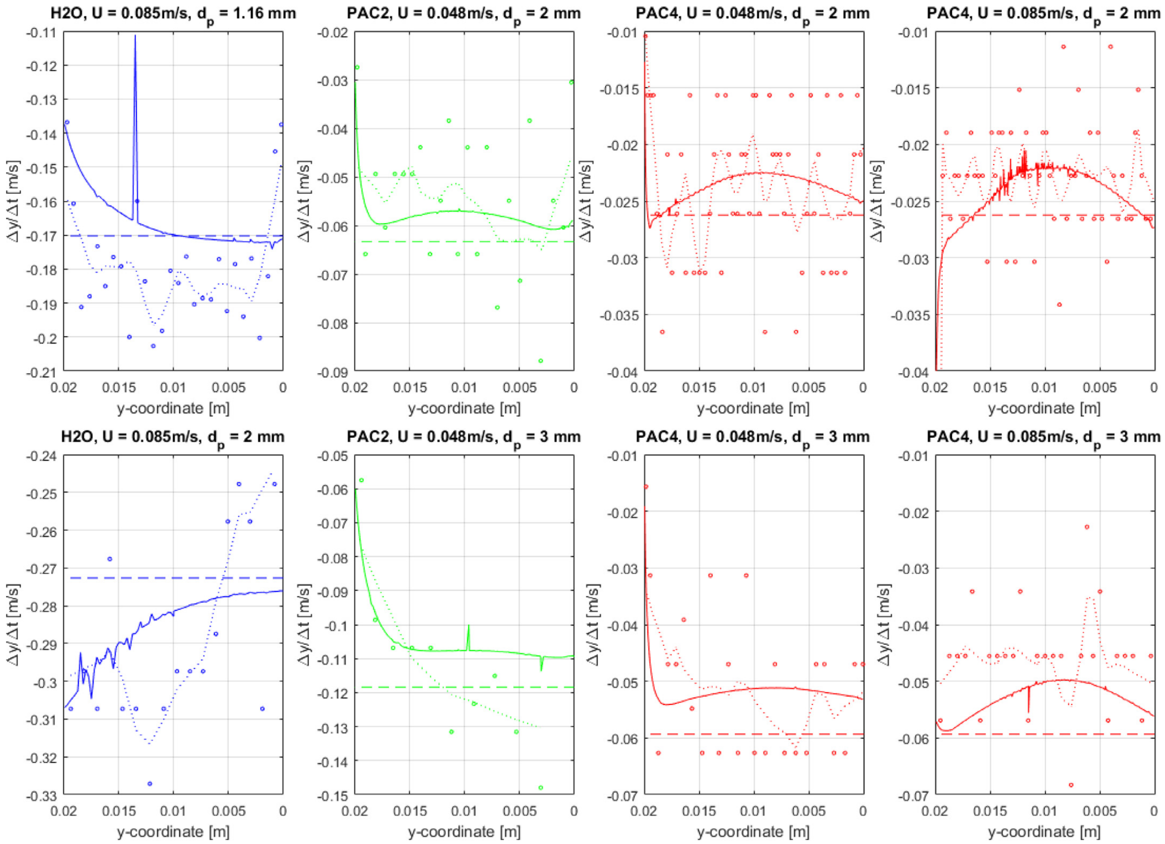

Fig. 11. Particle $\boldsymbol{y}$-velocity components for the cases presented in Fig. 7 as function of the channel $\boldsymbol{y}$-coordinate. CFD (solid lines) vs. experimental particle trajectories (circles) [1]. Dotted lines represent time-averaged experimental data, dashed lines represent the steady-state, i.e. terminal velocity of a single particle settling in a quiescent fluid based on the apparent viscosity concept #1 as given in Table 1.

4.3. Wall presence

It is well known that the presence of a wall affects the drag coefficient, both for a particle moving along a wall [54,55] and approaching a wall [56], as well as for particles settling in confined geometries such as a tube [28].

In case of the channel side walls, the confinement ratios $\beta_i = d_{p,i}/w$ for the different particle diameters are 0.028, 0.0748, and 0.074, respectively, with the channel width $w = 0.042$ m. These values correspond to a wall factor $f = v_{set,w}/v_{set}$ of approximately 0.97 to 0.9 in case of creeping flow [28], i.e. a particle settling in a tube with confinement ratios β_i would feature settling velocities of 90-97 % compared to the unconfined case. However, as the channel walls represent a far less confinement than a tubular geometry, side wall effects may be considered irrelevant for the here studied case.

In case of horizontal walls, the vertical drag may increase by 50% when a 3 mm diameter particle is 6 mm away from the bottom channel wall [56]. Indeed, the time-averaged experimental particle y-velocity components of the two water cases and the 2 mm PAC2 case depicted in Fig. 11 show some decrease of the settling velocity close to $y = 0$. However, this is not clearly seen in the other cases depicted in Fig. 11. Furthermore, the scatter of the experimental data is relatively large near the bottom wall of the channel, featuring the particle traps. These traps are much larger (10 mm) than the remaining wall elements (3 mm). Moreover, as opposed to the horizontal velocity components (Fig. 10), the numerical particle y-velocity components are actually coinciding reasonably well with the experiments (Fig. 11) indicating that the vertical drag is predicted fairly correct.

4.4. Anisotropic viscosity

Roodhart [11] conceptually introduced the idea of an “anisotropic apparent viscosity”, i.e. “horizontal” and “vertical” apparent viscosity components and correspondingly different drag, representing the arrangement of the polymeric molecules (alignment or stretching) due to imposed shear. For CMC solutions, Gheissary and Van den Brule [5] also attributed this phenomenon to flow-induced anisotropy of viscosity because CMC solutions shear-thin due to molecule alignment.

Because of the strong rheological relationship between CMC and PAC (PAC is basically a higher quality CMC with a higher degree of substitution), an “anisotropic viscosity” effect might indeed have occurred in the experiments [1]. However, three considerations lead us to believe that this is not the primary factor when it comes to the mismatch of CFD and experimental trajectories:

First, for larger particles the mismatch close to the lower wall seems less prominent than for smaller particles. However, larger particles induce higher shear rates and the anisotropic viscosity is a high-shear rate effect [5,11], so one would expect an even larger mismatch for larger particles.

Second, the apparent viscosity function used by the CFD code is based on rheometer shear flow data, which corresponds to the x-velocity

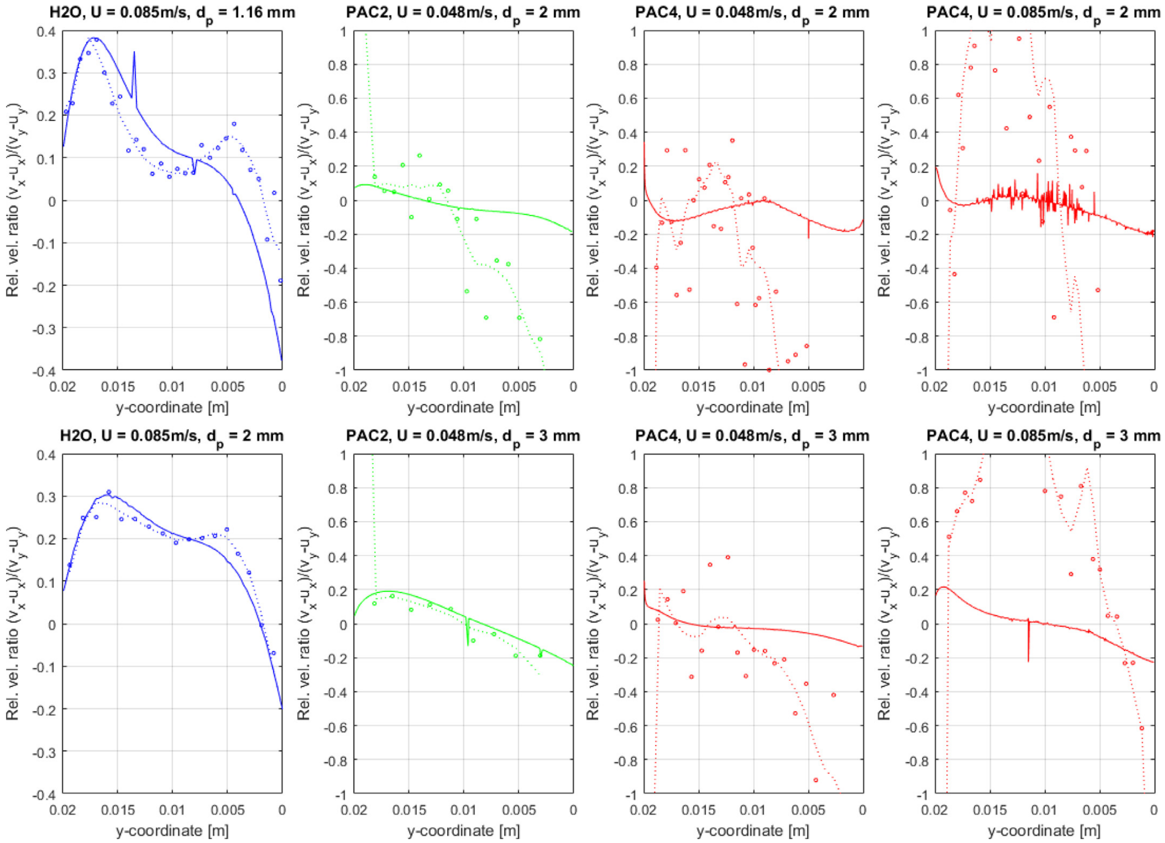

Fig. 12. Relative velocity components $(\boldsymbol{v}_x - \boldsymbol{u}_x)/(\boldsymbol{v}_y - \boldsymbol{u}_y)$ of the cases presented in Fig. 7 over the channel height $\boldsymbol{y}$. CFD (solid lines) vs. experimental particle trajectories (circles) [1]. Dotted lines represent time-averaged experimental data. As experimental $\boldsymbol{u}_y$-data is not available, $\boldsymbol{u}_y$ was assumed to be zero.

profile of the channel shear flow. If the anisotropic viscosity hypothesis is correct, than the apparent viscosity function should correctly predict the apparent viscosity in the x-direction. Hence, the particle x-velocities should match well and the experimental particle y-velocities should differ from the numerical velocities; however, the opposite is the case.

Third, plotting the absolute particle x-velocities vs. channel y-coordinate (see Fig. A9 in the Appendix) reveals that for the lower part of the channel the particle is advected with a fairly constant velocity being roughly equal to the fluids maximum velocity in the channel centerline. However, even in the case of an anisotropic viscosity there should occur deceleration of the particle as a consequence of drag, corresponding to the particle acceleration in the upper part of the channel.

4.5. Drag law formulation

In general, non-Newtonian drag laws may substantially differ from each other for three reasons: First, they are based on possibly different sets of experimental data and different Reynolds number definitions and shear rate estimates may have been used to construct non-Newtonian drag laws. Second, many of them are based on the PL material function which is not valid over a larger range of shear rates because it does not account for limiting viscosities. Third, in some cases the fluids used for drag law studies may have featured some relevant viscoelastic behavior overshadowing the GNF drag [28].

For the examples investigated here, the trajectories obtained with drag law concept #1 and #2 (see Table 1) are virtually identical. As discussed in Section 4.2, even concept #3 does yield the same trajectories if the viscoelastic drag correction, i.e. Eq. (28), is based on the Cross time constant or neglected. It seems that in contrast to common perception [28], an apparent viscosity concept (#1 in Table 1) based on a Newtonian drag law may just as well be used if the particle-induced shear rate is estimated with Eq. (16) and the apparent viscosity is computed based on a material function, here the Cross or Carreau models, describing the fluid correctly over the relevant range of shear.

In addition to the vicoelastic drag correction utilized, further drag coefficient corrections may be applied to account for wall effects and anisotropy as discussed in Sections 4.3 and 4.4.

4.6. Other relevant forces than drag

The pre-investigations indicate that the other forces than drag, $\mathbf{F}_j$, are to be expected of small relevance in the non-Newtonian cases. However, it is not clear whether the simplistic assumption of an apparent viscosity also holds for the viscosity of the Newtonian lift laws and the rotational drag law required in the additional Lagrangian angular momentum equation for the particle to determine the particle's rotation rate. Furthermore, the Saffman lift force model [37,38] is limited to a certain range of particle, shear and rotational Reynolds numbers. Even though it was later extended to suit a larger regime of particle Reynolds numbers [57], its validity is still restricted by both the shear and rotation Reynolds numbers.

The usual DPM assumption that independent of grid size the particle experiences the undisturbed velocity field at the mass center of the particle may lead to wrong computational results for the drag and lift forces because the particle spans multiple grid cells and experiences non-linear velocity gradients across its virtual surface. A higher-resolution and yet computational affordable approach is to explicitly account for the particles volume in the computational domain, e.g. by using a macroscopic particle model [58,59], a dynamic deforming mesh in conjunction with a six degrees-of-freedom Rigid Body Dynamics solver [60], or, more generally, an immersed boundary method approach [61].

However, the time-averaged experimental y-velocity components of the particle indicate a relatively constant settling velocity fairly in accordance with the numerical results of this study and hence indicates that lift may only play a minor role.

In the non-Newtonian case of PAC solutions, rotation slip will additionally contribute to the shear rate as seen by the particle and thus affect the drag coefficient [62]. However, as lift and hence rotation is expected to play a minor role, the effect on the shear rate and the coefficient of drag is also expected to be minor.

The difference between the CFD trajectories of Khatibi et al. [1] and the ones computed in this study may be explained with the additional forces used by Khatibi et al. [1]. They used an apparent viscosity concept without the particle-induced shear rate correction, i.e. Eq. (16), as well as Newtonian Saffman lift and turbulent dispersion. However, besides the discussion of the Saffman lift force as given above, we do not expect turbulent dispersion playing a crucial role here, as the channel flow is well in the laminar regime based on the channel Reynolds number (see Section 2.6).

4.7. Shape of fluid velocity profiles at particle settling test section

While specifications of a uniform velocity profile (case A) or parabolic velocity profiles (cases B and C) at the inlet of the respective computational domains do not exactly yield the experimental velocity profiles [1], the latter may be reasonably well reproduced by specification of the actual experimental velocity profile in conjunction with slip velocity tuning, as described in Sections 2.5.4. Hence, for the trajectories computed numerically, the velocity profiles should not contribute significantly to any trajectory mismatch, assuming the experimental velocity profiles [1] are representing the true in-situ velocity $v_x(y)$.

As the experimental velocity profile for PAC2 is unavailable [1], it is possible that the scaled (based on superficial velocity ratios) velocity profile of the PAC2 cases is somewhat incorrect and hence the particle is not advected far enough downstream until it impinges on the lower wall.

It is unclear whether the PAC fluids used in combination with the acrylic wall really feature wall slip or whether this is just an artefact of the unresolved PIV-velocity profiles close to the wall. If the former is true, it does apparently not influence the shape of the trajectories a lot as the difference between the slip and no-slip trajectories is not to prominent, see Fig. A5 to Fig. A8 provided in the Appendix.

The particle traps at the bottom channel wall do lead to local flow field disturbances and may be effectively represented by slip velocities, see Section 2.5.4. Hence, the effect of the traps appears to be accounted for by the numerical model and does not explain the particle trajectory mismatch close to the lower channel wall. However, the traps may have an end-effect on the velocity profiles as discussed in Section 4.2 due to the role of normal stresses. Further investigation of this effect requires high-resolution wall-near experimental velocity profiles at the position of the particle.

As the experimental and numerical y-velocity components reasonably well coincide; any mismatch in trajectories may be attributed to the x-velocity component. This is confirmed by the normalized x-velocity component plots provided in Fig. 10, which show that close to the lower channel wall small particles are advected much faster than the fluid.

A particle being faster than the fluid may be explained with the higher momentum that the particle carries from its former mid-channel position. However, comparing specific cases shows that the orders of magnitude, i.e. the velocity ratios being in the range 1.5-5, appear very unphysical. For instance, comparing the H_2O, $U = 0.085\,\mathrm{m/s}$, $d_p = 0.002\,\mathrm{m}$ case (bottom left subfigure of Fig. 10, $(\Delta x/\Delta t)/u_x(y) = 1\text{-}3$ for $y < 0.002\,\mathrm{m}$) with the corresponding PAC case (top right subfigure of Fig. 10, $(\Delta x/\Delta t)/u_x(y) > 2$ for $y < 0.002\,\mathrm{m}$) shows that in case of PAC4 the particle should relax to the fluids velocity a lot faster, i.e. the velocity ratio $(\Delta x/\Delta t)/u_x(y)$ should be smaller than that of H_2O for $y < 0.002\,\mathrm{m}$, as the viscosity magnitude of PAC4 is much higher than that of H_2O. Instead, the particle is a lot faster than the fluid and does not relax in the time scale of the experiment. Another example is the comparison of the two PAC4, $U = 0.085\,\mathrm{m/s}$ cases (Right subfigures of Fig. 10). For the smaller particle one would again expect a much faster relaxation as the particles inertia, i.e. its momentum carrying capacity, is much smaller than the one of the bigger particle.

For the H_2O cases, both the CFD and experimental ratios of slip velocities (left subfigures of Fig. 12) indicate that the slip velocity component in the y-direction always dominates because the ratios are smaller/larger than plus/minus one. As expected, the horizontal particle velocity lags behind the horizontal fluid velocity until the particle is quite close to the bottom due to the initially very low horizontal slip. However, this is very different for some of the PAC cases. Here the experimental data shows ratios larger/smaller than plus/minus one. In the experimental data of the PAC4, U = 0.048 m/s case (Fig. 10), we see that the horizontal slip is, as expected, smaller than for water in the upper part of the channel, while the particle starts to move significantly faster than the fluid horizontally in the lower half of the channel (2 mm diameter case). For the PAC4, U = 0.085 m/s case, the particles are expected to have approximately twice as large horizontal slip due to the larger velocity gradients. This effect is seen in the simulations. However, in the experiments the horizontal slip is increased by an order of magnitude or more. We see that for five out of the six PAC4 cases the experimental data shows ratios larger/smaller than plus/minus one. These experimental results are hard to explain without additional higher-resolution near-wall measurements of the fluid and particle velocities. All PAC CFD cases show ratios smaller than the span of the Newtonian case, which is what one would expect due to the higher apparent viscosity levels and hence shorter particle relaxation times.

4.8. Initial velocity of particles at injection

Particle initial velocities may influence trajectories quite largely [14]. However, this effect has been mitigated in this study by specifying the actual particle velocities as initial conditions, see Section 2.5.5.

As may be verified from Fig. 11, in case of the PAC solutions the relaxation process is very fast and, given the scatter of the experimental data, the y-velocity components coincide reasonably well. The two unphysical results (bottom left and top right subfigure of Fig. 11) where the particle is actually entering the channel with a settling velocity much faster than the steady-state velocity (dashed lines in Fig. 11) is a direct consequence of utilizing the first two experimental data [1] points as initial condition.

4.9. Uncertainty of parameters

In principle, all physical parameters such as those given in Fig. 2/Table 4 are subject to natural scatter when measured and thus uncertain, either because of real different instances of the physical objects or because of measurement process immanent inaccuracies. Furthermore, simplifications such as representing the complex rheological behavior with a GNF constitutive equation or closures such as the application of non-Newtonian/high Reynolds number drag laws may increase the uncertainty. For instance, the pure flow curve measurements of PAC solutions show an uncertainty range of ≈ ± 5% for

$\dot{\gamma} > 140\ s^{-1}$ and $\approx \pm 10\%$ for $\dot{\gamma} < 30\ s^{-1}$ [44]. The Schiller-Naumann drag law [23] utilized in the apparent viscosity concept #1 features an uncertainty of $\pm 5\%$ [63] with regards to the standard Newtonian drag curve [35]. Up to $\mathrm{Re}_p < 100$, Newtonian drag laws such as the Schiller-Naumann drag law [23] may be used instead of dedicated non-Newtonian drag laws [28]. However, the degree of uncertainty may be larger ($\pm 30\%$) [28]. The #2 drag law has an uncertainty of $\pm 3.5\%$ [34]. Another unknown is the actual particle diameter since the nominal values [1] in fact represent a distribution. The particle diameter d_p acts quadratic on the settling velocity, see Eq. (9). Hence, knowledge of the actual particle diameter in settling experiments is important and may be established by e.g. the use of a particle size analyzer.

Quantifying the combined effect of multiple uncertain parameters on the trajectories, for instance by application of polynomial chaos theory [14], requires knowledge of uncertainty ranges for all the relevant parameters and is a study of its own kind. Nevertheless, in principle, uncertainty propagation of one or more parameters may significantly affect computed trajectories. However, we do not expect this to be the major reason for the observed mismatch between experiments and simulation as any uncertain quantity would affect the entire numerically computed trajectory and not just the lower near-wall part.

4.10. Experimental measurement errors

As discussed in Sections 4.3 and 4.8, the experimental PTV trajectory data [1] shows some anomalies, namely that the particle becomes much faster than the fluid close to the lower wall for the small particle diameter and that in two cases the particle initially is actually faster than the steady-state settling velocity. In addition, the experimental PIV velocity profile data [1] shows a non-parabolic profile with deviations close the channel walls. Given the geometrical dimensions and the 2D PTV technique used [1], two possible errors may be prevalent in the determination of the position of the particle and hence the experimental trajectories reported by Khatibi et al. [1].

First, optical distortion, i.e. a parallax error, may have led to an under-prediction of the x-position. However, in the PTV pictures, the position was determined by scaling the particle channel height and the distances of the particle traps as length units [43]. Even on distorted pictures with relevant refraction, the position would be determined correctly as the identical distortion and refraction would occur to the scale used for determining the particle position.

Second, an over-prediction of the particles position might have occurred due to refraction of light as it travels through the fluid, the acrylic wall and air. However, estimating the relative difference based on the geometrical camera setup (positioned between 0.3 to 0.5 m away from the channel) [43] and the different refraction indices of air, acryl and H_2O/PAC gives a maximal relative error < 5 %.

4.11. Summary

Some of the possible factors discussed in Sections 4.1–4.10 may have affected either the experimental results or CFD trajectories by an unknown percentage. The relevance of each effect is unknown; however, some are certainly more relevant than others. For instance, we expect the correct rheological description to be crucial and much more important than temperature effects because realistically the temperature variations in the experiments is within a couple of degrees Celsius.

An important indication for the possible relevance of improper rheological modeling (Section 4.2), incorrect velocity profiles (Section 4.6), the neglected lift forces (Section 4.6), and incorrect trajectory data (Section 4.10) is the local mismatch observed between CFD and experimental trajectories close to the lower channel wall. Hence, more detailed and accurate near-wall experimental data (velocity profiles and trajectories, in-situ rheological properties via pipe viscometry) and modeling work (3D formulation of Eq. (16), particle lift laws for shear-thinning fluids, more sophisticated constitutive equations and material functions accounting for time-dependency and/or normal stress differences) are required to minimize the observed mismatch.

5. Conclusion

In our simulations of a particle settling in a orthogonal shear flow of a shear-thinning, mildy viscoelastic fluid, we have accounted for the particle-induced shear rate and the corresponding effect on viscosity by applying a shear rate vector magnitude concept. This yields particle trajectories, which in principle coincide well with the experimentally obtained trajectories of Khatibi et al. [1]. However, a significant mismatch is observed in the lower channel wall region, primarily for small particle sizes, and is a consequence of the particles x-velocity components. In the available experimental data [1], the particles x-velocity components are unphysically faster than the respective fluid velocity at the particle position, if Generalized Newtonian Fluid behavior is assumed. This may be a consequence of improper modeling, namely a too simple rheological description by neglecting normal stress differences and/or thixotropic behavior or the non-consideration of particle lift laws (for which no shear-thinning formulation is yet validated). In addition, inaccurate near-wall experimental data, namely velocity profiles and particle trajectories may be the cause. More research dedicated to these issues is required to eliminate the trajectory mismatch.

Furthermore, we find that for the investigated cases particle drag appears to be the major particle force, that viscoelastic effects of the polymeric solutions are not dominant when it comes to particle settling, and that standard Newtonian drag laws (e.g. Schiller-Naumann) may be used in an apparent viscosity concept as long as the particle-induced shear rate is estimated with $\|\mathbf{v}_r\|/d_p$.

Acknowledgements

The project Advanced Wellbore Transport Modeling (AdWell) with its sponsor, PETROMAKS 2/the Research Council of Norway (project 228391) and its partners Equinor, Neptune Energy Norge AS, IRIS, UiS, NTNU and SINTEF are gratefully acknowledged for funding and supporting this work. Furthermore, we thank our colleagues Milad Khatibi and Rune W. Time from the University of Stavanger for the experimental data shared and valuable discussions. Finally, we thank our colleagues Aminul Islam (Equinor) and Dwayne Martins (Neptune Energy Norge AS) for reviewing the paper and providing valuable input.

Supplementary materials

Supplementary material associated with this article can be found, in the online version, at doi:10.1016/j.jnnfm.2018.11.005.

Appendix

Table 3
Maximum particle Reynolds numbers Re_p for Fluent's state-of-the-art ($Re_{p,\ old}$) and the apparent viscosity concept #1 ($Re_{p,\#1}$) as well as the drag law concept #3 ($Re_{p,\#3}$).

Case	1	2	3	4	5	6	7	8
$\boldsymbol{Re_{p,\ old}}$	212	618	2.67	7.19	0.434	1.38	0.823	1.66
$\boldsymbol{Re_{p,\#1}}$	212	618	2.18	5.89	0.39	1.11	0.822	1.54
$\boldsymbol{Re_{p,\#3}}$	204	632	3.12	10.17	0.35	1.13	0.90	1.68

Table 4
Fluid densities and rheological model coefficients based on fits to the rheometric data of [1] as depicted in Fig. 2, at room temperature (21°C) and atmospheric pressure (1.01 bar).

Fluid	ρ_f [kg/m^3]	Cross (goodness-of-fit R^2 = 0.9986)				Carreau (goodness-of-fit R^2 = 0.9813)			
		μ_0 [Pa·s]	μ_∞ [Pa·s]	λ_{Cr} [1/s]	n_{Cr} [-]	μ_0 [Pa·s]	μ_∞ [Pa·s]	λ_{Ca} [1/s]	n_{Ca} [-]
H_2O	998	0	0.001	0	0	0	0.001	0	0
PAC2	1000	0.0721	0.001	0.0109	0.586	0.0688	0.001	0.1400	0.7210
PAC4	1000	0.214	0.001	0.0261	0.608	0.1989	0.001	0.2528	0.6861

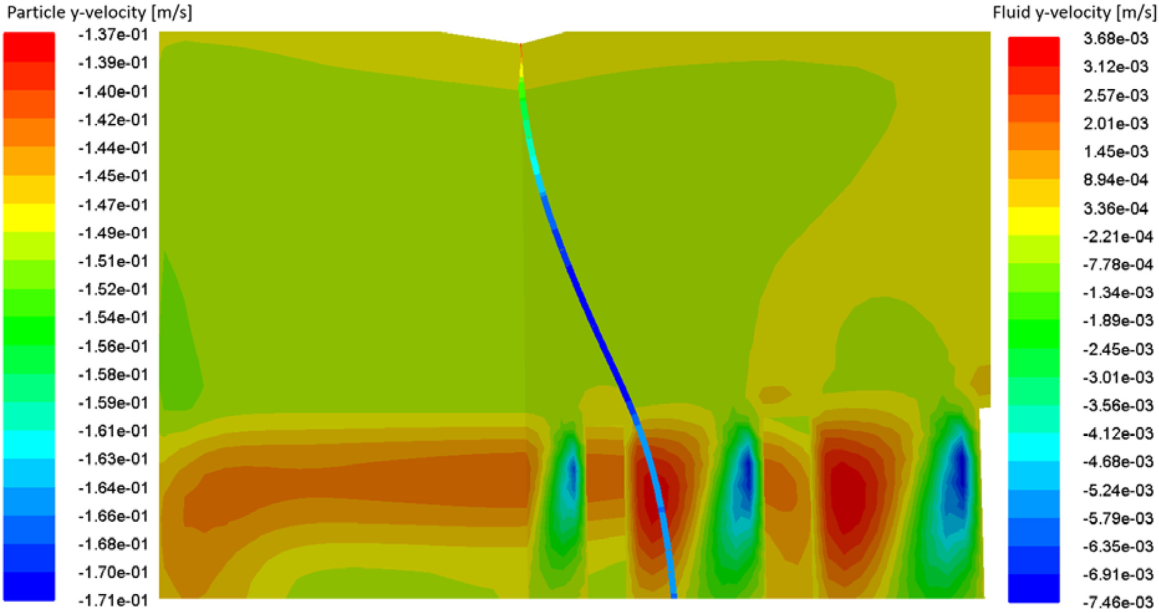

Fig. A1. Secondary flows because of the particle traps for test case 1 as given in Table 2. CFD case A with no-slip BC and all particle forces.

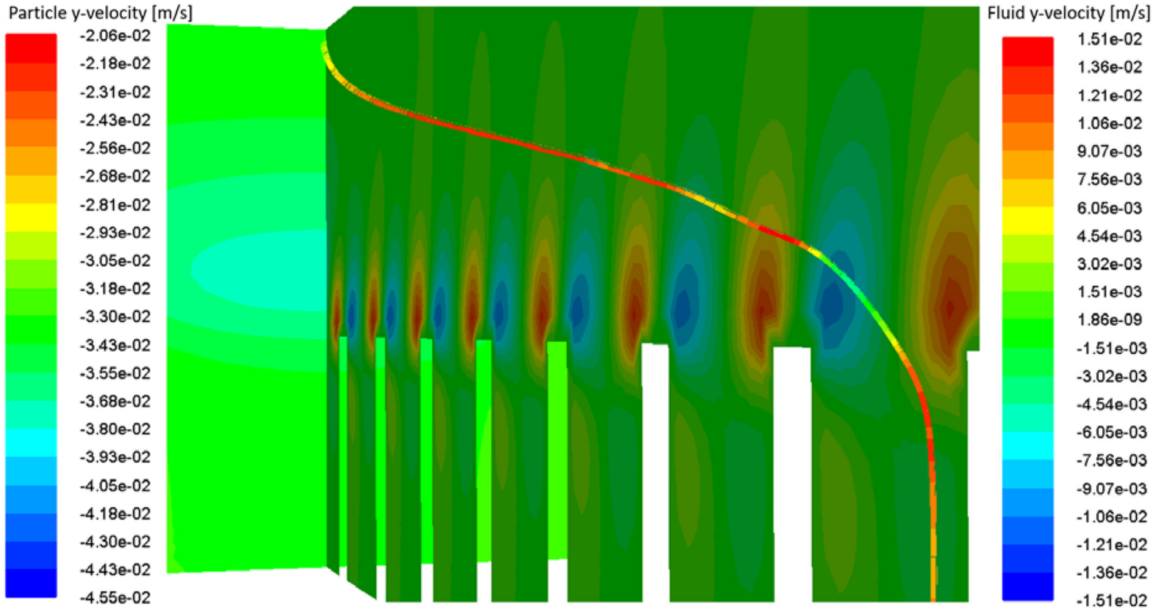

Fig. A2. Secondary flows because of the particle traps for test case 7 as given in Table 2. CFD case A with no-slip BC and all particle forces. Drag concept #1 with $\dot{\gamma}$ based on Eq. (16) and cross material function.

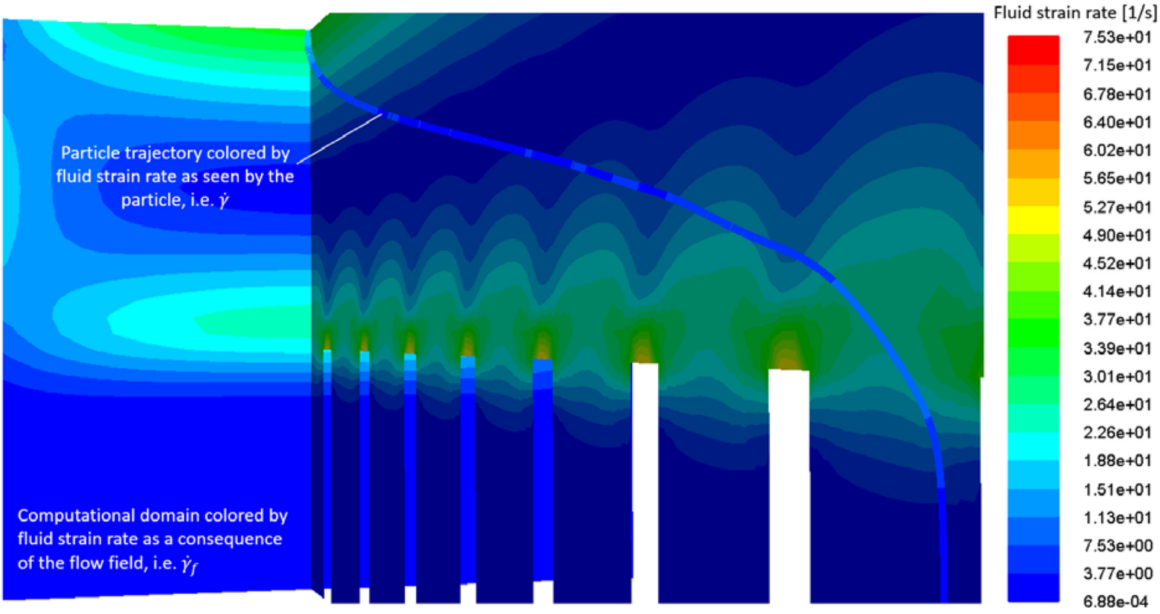

Fig. A3. Effect of particle traps on strain rate for test case 7 as given in Table 2. CFD case A with no-slip BC and all particle forces. Drag concept #1 with $\dot{\gamma}$ based on Eq. (16) and cross material function.

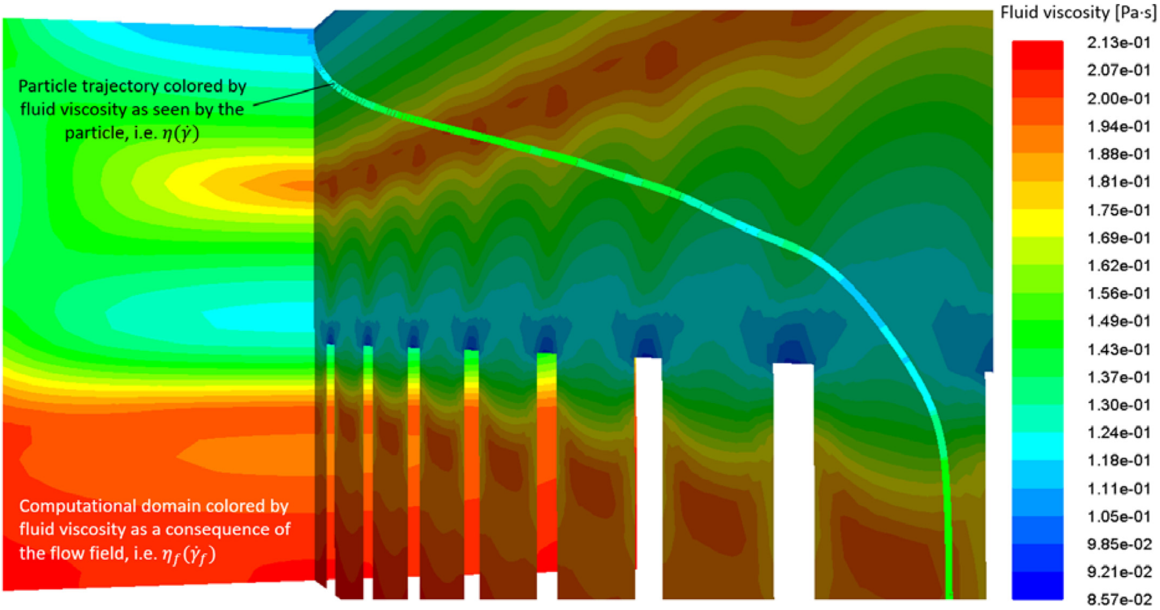

Fig. A4. Effect of particle traps on viscosity for test case 7 as given in Table 2. CFD case A with no-slip BC and all particle forces. Drag concept #1 with $\dot{\gamma}$ based on Eq. (16) and cross material function.

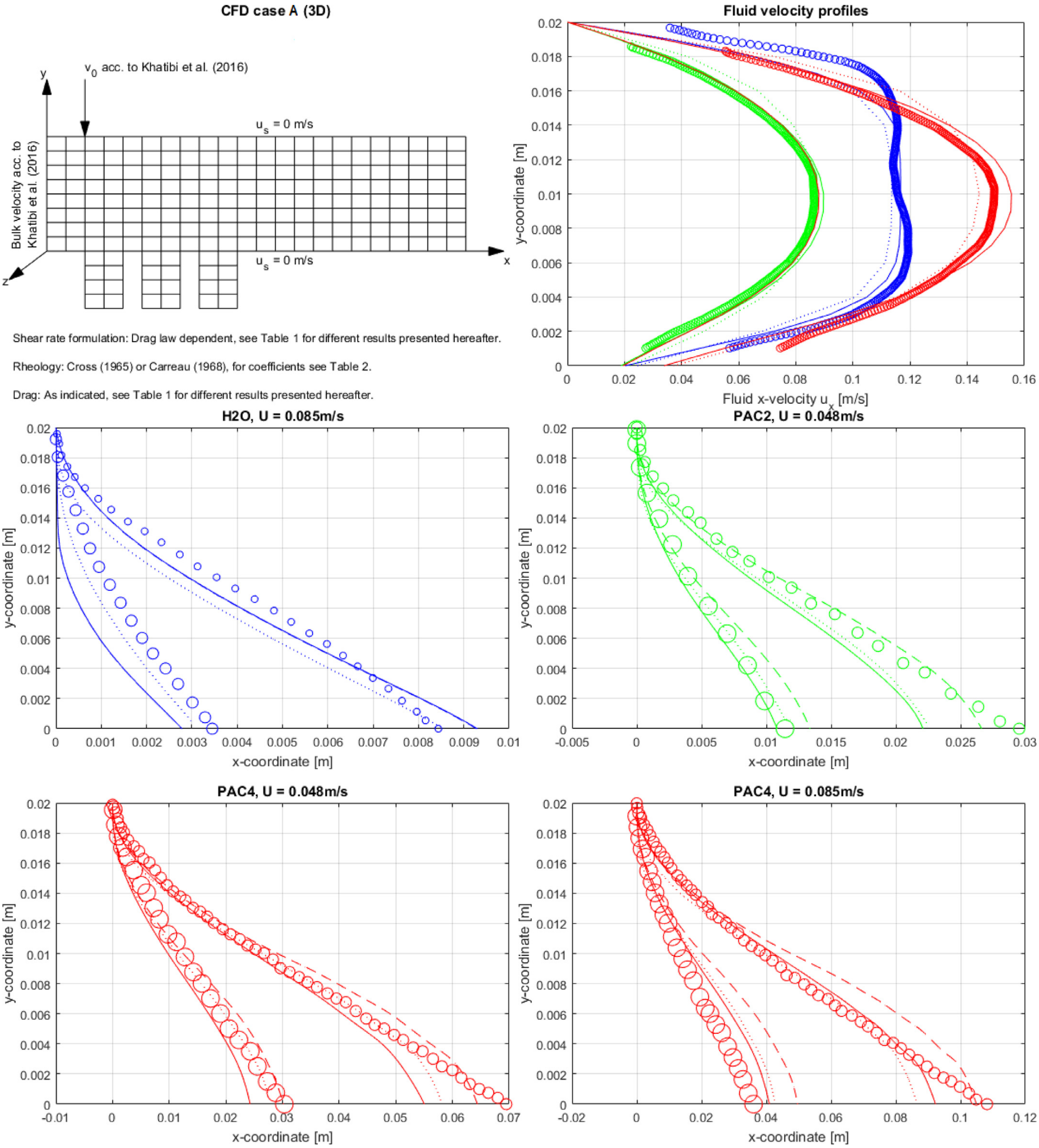

Shear rate formulation: Drag law dependent, see Table 1 for different results presented hereafter.

Rheology: Cross (1965) or Carreau (1968), for coefficients see Table 2.

Drag: As indicated, see Table 1 for different results presented hereafter.

Fig. A5. Pre-investigation, role of particle forces, CFD case A (3D), no-slip BC, drag force and all particle forces as described in Section 2.3.

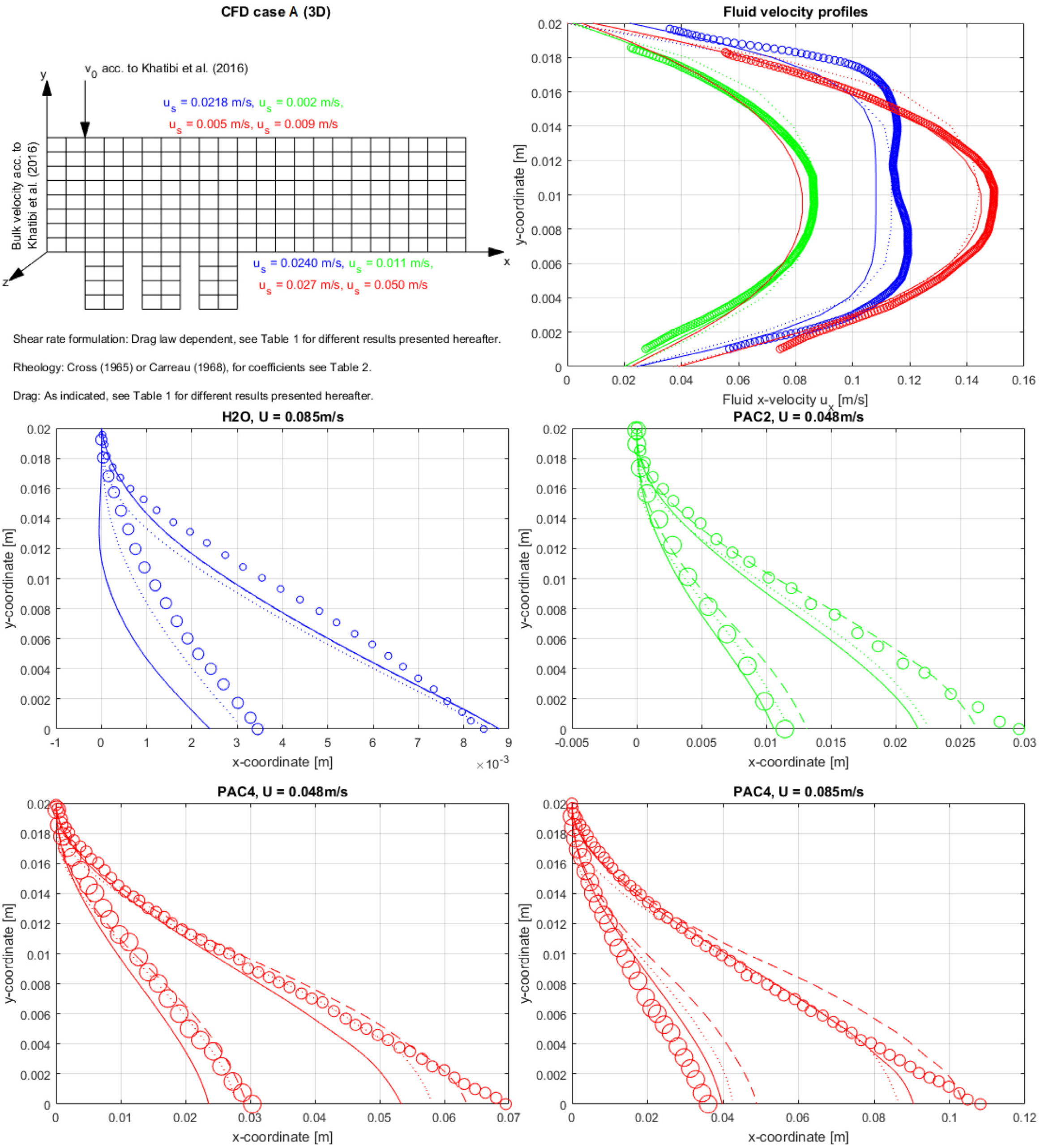

Fig. A6. Pre-investigation, role of particle forces, CFD case A (3D), slip BC, drag force and all particle forces as described in Section 2.3.

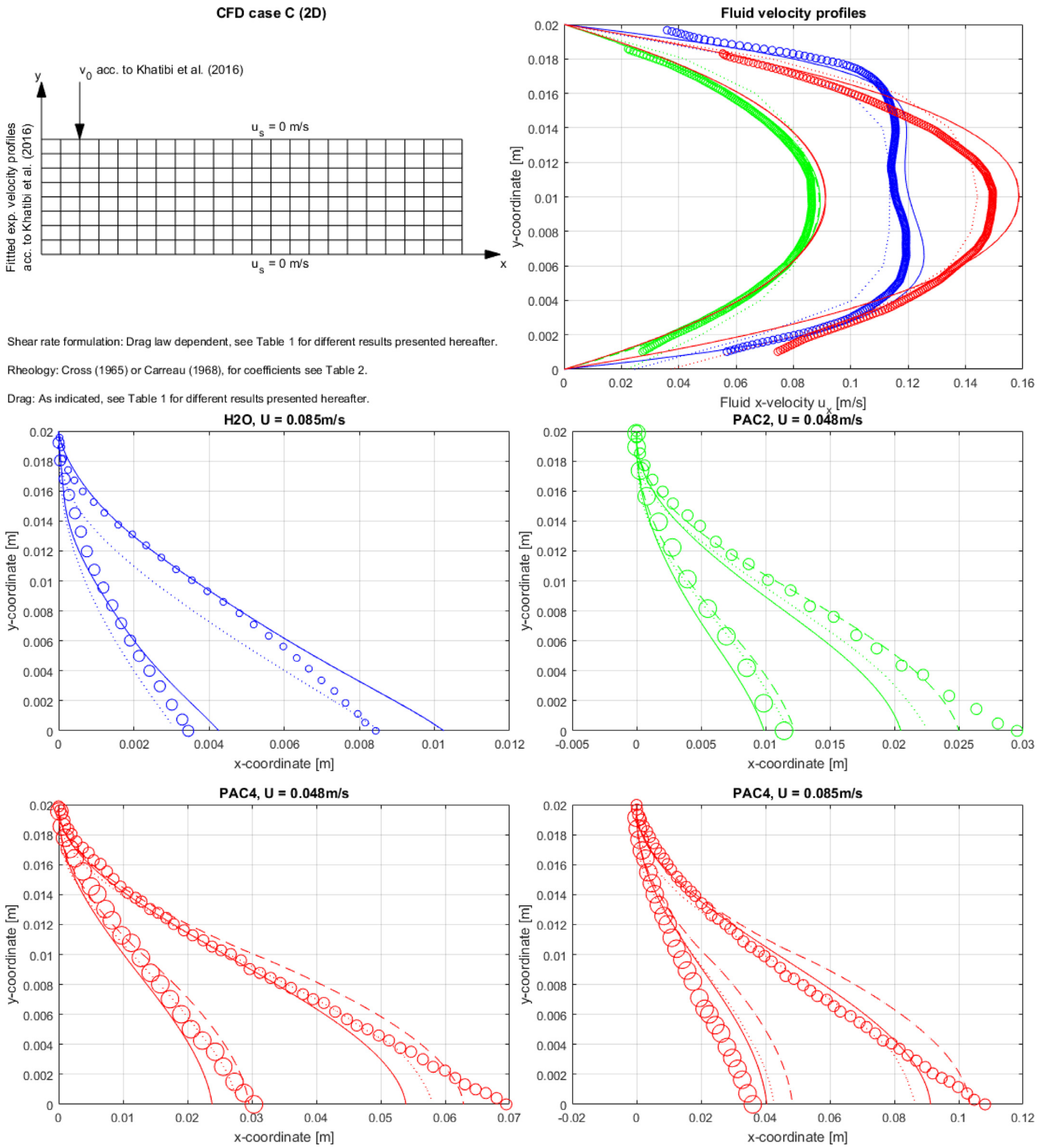

Fig. A7. Pre-investigation, role of particle forces, CFD case C (2D), no-slip BC, drag force and all particle forces as described in Section 2.3.

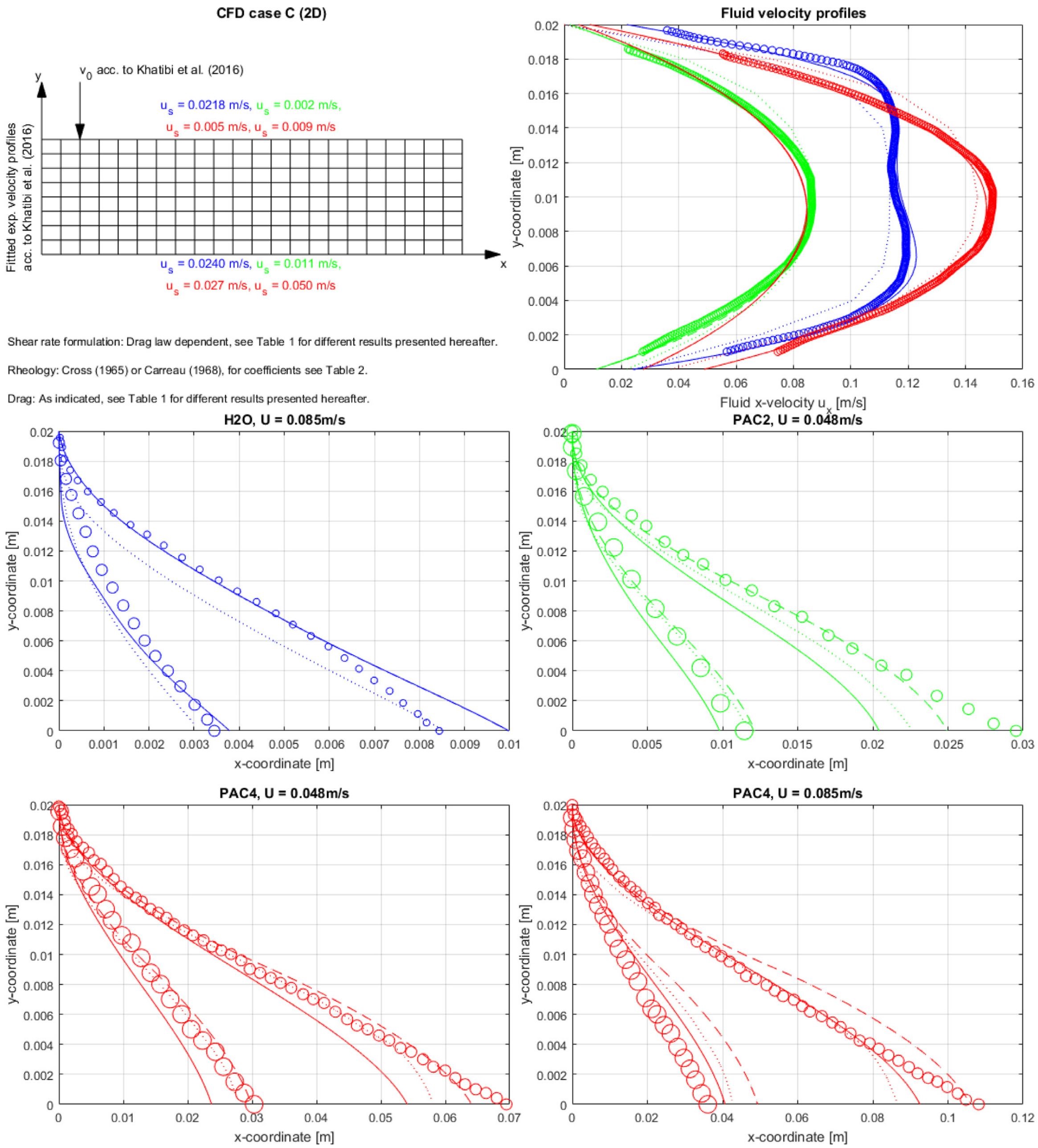

Fig. A8. Pre-investigation, role of particle forces, CFD case C (2D), slip BC, drag force and all particle forces as described in Section 2.3.

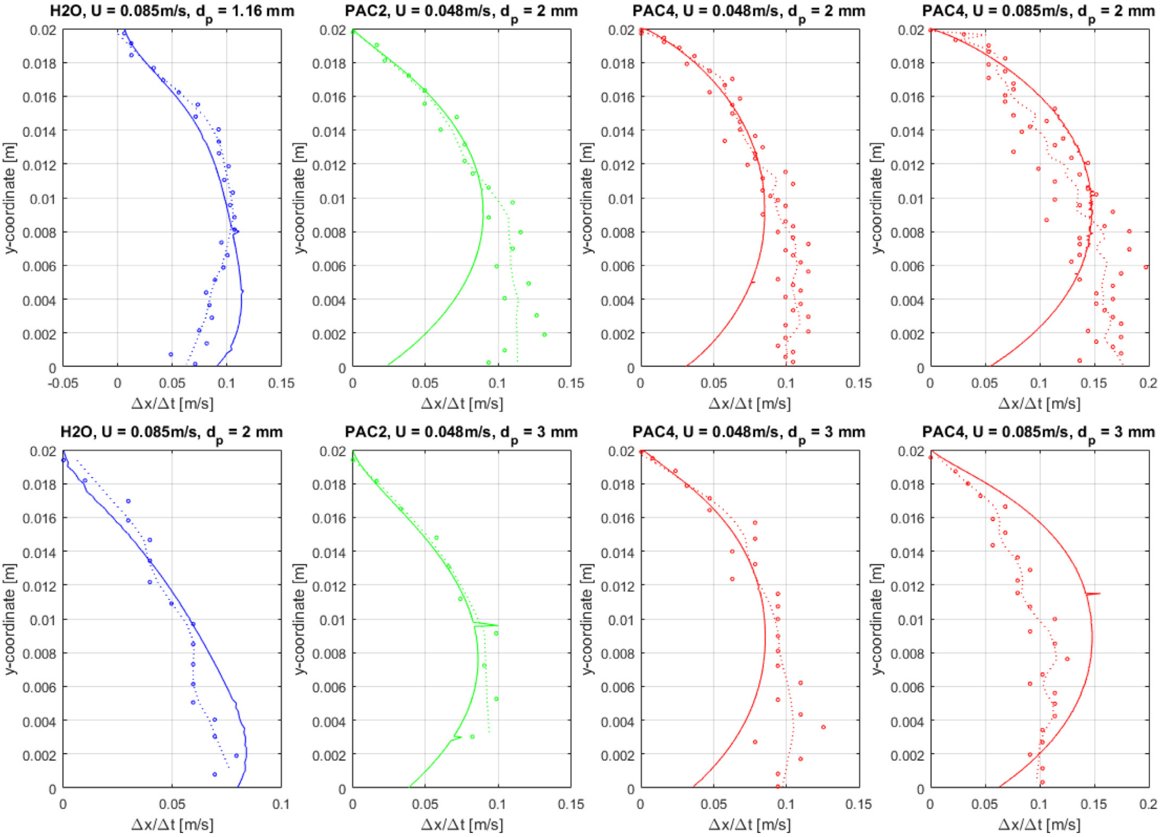

Fig. A9. Particle x-velocity components for the cases presented in Fig. 7 as function of the channel y-coordinate. CFD (solid lines) vs. experimental particle trajectories (circles) [1]. Dotted lines represent time-averaged experimental data.

References

[1] M. Khatibi, R.W. Time, H.A. Rabenjafimanantsoa, Particles falling through viscoelastic non-Newtonian flows in a horizontal rectangular channel analyzed with PIV and PTV techniques, J. Non Newton. Fluid Mech. 235 (2016) 143–153, doi:10.1016/j.jnnfm.2016.08.004.

[2] A. Acharya, R.A. Mashelkar, J. Ulbrecht, Flow of inelastic and viscoelastic fluids past a sphere - I. Drag coefficient in creeping and boundary-layer flows, Rheol. Acta 15 (1976) 454–470.

[3] A.R. Acharya, Viscoelasticity of crosslinked fracturing fluids and proppant transport, SPE Product. Eng. 3 (1988), doi:10.2118/15937-PA.

[4] A.R. Acharya, Particle transport in viscous and viscoelastic fracturing fluids, SPE Product. Eng. 1 (1986) 104–110, doi:10.2118/13179-PA.

[5] G. Gheissary, B. Van den Brule, Unexpected phenomena observed in particle settling in non-Newtonian media, J. Non Newton. Fluid Mech. 67 (1996) 1–18.

[6] K.D. Housiadas, R.I. Tanner, The drag of a freely sedimentating sphere in a sheared weakly viscoelastic fluid, J. Non Newton. Fluid Mech. 183–184 (2012) 52–56, doi:10.1016/j.jnnfm.2012.07.002.

[7] Y.T. Hu, H. Chung, J.E. Maxey, What is more important for proppant transport, viscosity or elasticity?, In: SPE hydraulic fracturing technology conference proceedings, Society of Petroleum Engineers, The Woodlands, TX, 2015, doi:10.2118/173339-MS.

[8] E.J. Novotny, Proppant transport, in: SPE annual fall technical conference and exhibition proceedings, Society of Petroleum Engineers, Denver, CO, 1977, doi:10.2118/6813-MS.

[9] S. Padhy, E.S.G. Shaqfeh, G. Iaccarino, J.F. Morris, N. Tonmukayakul, Simulations of a sphere sedimenting in a viscoelastic fluid with cross shear flow, J. Non Newton. Fluid Mech. 197 (2013) 48–60, doi:10.1016/j.jnnfm.2013.02.003.

[10] S. Padhy, M. Rodriguez, E.S.G. Shaqfeh, G. Iaccarino, J.F. Morris, N. Tonmukayakul, The effect of shear thinning and walls on the sedimentation of a sphere in an elastic fluid under orthogonal shear, J. Non Newton. Fluid Mech. 201 (2013) 120–129, doi:10.1016/j.jnnfm.2013.07.007.

[11] L.P. Roodhart, Proppant settling in non-Newtonian fracturing fluids, in: SPE/DOE low permeability gas reservoirs symposium proceedings, Society of Petroleum Engineers, Denver, 1985, doi:10.2118/13905-MS.

[12] R.I. Tanner, K.D. Housiadas, F. Qi, Mechanism of drag increase on spheres in viscoelastic cross-shear flows, J. Non Newton. Fluid Mech. 203 (2014) 51–53, doi:10.1016/j.jnnfm.2013.10.007.

[13] B. Van den Brule, G. Gheissary, Effects of fluid elasticity on the static and dynamic settling of a spherical particle, J. Non Newton. Fluid Mech. 49 (1993) 123–132.

[14] J. Zoric, A. Busch, E.A. Meese, M. Khatibi, R.W. Time, S.T. Johansen, H.A. Rabenjafimanantsoa, On pragmatism in industrial modeling - part ii: workflows and associated data and metadata, in: in: The 11th International Conference on CFD in the Minerals and Process Industries, CSIRO Publishing, Melbourne, 2015.

[15] S. Malhotra, M.M. Sharma, A general correlation for proppant settling in VES fluids, in: SPE hydraulic fracturing technology conference proceedings, Society of Petroleum Engineers, The Woodlands, 2011, doi:10.2118/139581-MS.

[16] D.J. Highgate, R.W. Whorlow, The viscous resistance to motion of a sphere falling through a sheared non-Newtonian liquid, Br. J. Appl. Phys. 18 (1967) 1019.

[17] A.V. Bazilevskii, D.A. Koroteev, A.N. Rozhkov, A.A. Skobeleva, Sedimentation of particles in shear flows of viscoelastic fluids, Fluid Dyn. 45 (2010) 626–637, doi:10.1134/S0015462810040125.

[18] M. Renaud, E. Mauret, R.P. Chhabra, Power-law fluid flow over a sphere: average shear rate and drag coefficient, Can. J. Chem. Eng. 82 (2004) 1066–1070.

[19] A.M. Talmon, M. Huisman, Fall velocity of particles in shear flow of drilling fluids, Tunnell. Underground Space Technol. 20 (2005) 193–201, doi:10.1016/j.tust.2004.07.001.

[20] F.A.R. Pereira, C.H. Ataíde, M.A.S. Barrozo, CFD Approach using a discrete phase model for annular flow analysis, Latin Am. Appl. Res. 40 (2010) 53–60.

[21] W. Herschel, R. Bulkley, Konsistenzmessungen von Gummi-Benzollösungen, Kolloid-Zeitschrift 39 (1926) 291–300, doi:10.1007/BF01432034.

[22] L.H. Childs, A.J. Hogg, D. Pritchard, Dynamic settling of particles in shear flows of shear-thinning fluids, J. Non Newton. Fluid Mech. 235 (2016) 83–94, doi:10.1016/j.jnnfm.2016.07.011.

[23] L. Schiller, A. Naumann, Über die grundlegenden Berechnungen bei der Schwerkraftaufbereitung, Z. Ver. Dtsch. Ing. 77 (1933) 318–320.

[24] M.M. Cross, Rheology of non-Newtonian fluids: a new flow equation for pseudoplastic systems, J. Colloid Sci. 20 (1965) 417–437, doi:10.1016/0095-8522(65)90022-X.

[25] P.H.T. Uhlherr, T.N. Le, C. Tiu, Characterisation of inelastic power-law fluids using falling sphere data, Can. J. Chem. Eng. 54 (1976) 497–502, doi:10.1002/cjce.5450540603.

[26] C.H. Ataide, F.A.R. Pereira, M.A.S. Barrozo, Wall effects on the terminal velocity of spherical particles in Newtonian and non-Newtonian fluids, Braz. J. Chem. Eng. 16 (1999) 387–394, doi:10.1590/S0104-66321999000400007.

[27] API RP 13D, Rheology and hydraulics of oil-well drilling fluids, American Petroleum Institute (API), Washington, D. C., 2010.

[28] R. Chhabra, Bubbles, drops, and particles in non-Newtonian fluids, Taylor & Francis Group, LLC, Boca Raton, 2007 http://sutlib2.sut.ac.th/sut_contents/H110625.pdf.

[29] S.N. Shah, Y. El Fadili, R.P. Chhabra, New model for single spherical particle settling velocity in power law (visco-inelastic) fluids, Int. J. Multiphase Flow 33 (2007) 51–66, doi:10.1016/j.ijmultiphaseflow.2006.06.006.

[30] W. Ostwald, Ueber die Geschwindigkeitsfunktion der Viskosität disperser Systeme, Colloid Polymer Sci. 36 (1925) 99–117.

[31] R.B. Bird, R.C. Armstrong, O. Hassager, Dynamics of polymeric liquids, Fluid Mechanics, 1, 2nd ed, New York, 1987.

[32] P.J. Carreau, 1939-, Rheological equations from molecular network theories 1968 (1968). https://search.library.wisc.edu/catalog/999638316602121.

[33] A.B. Metzner, J.C. Reed, Flow of non-Newtonian fluids-correlation of the laminar, transition, and turbulent-flow regions, AIChE J. 1 (1955) 434–440, doi:10.1002/aic.690010409.

[34] R.P. Chhabra, P.H.T. Uhlherr, Sphere motion through non-newtonian fluids at high reynolds number, Can. J. Chem. Eng. 58 (1980) 124–128, doi:10.1002/cjce.5450580120.

[35] R. Clift, J.R. Grace, M.E. Weber, Bubbles, drops, and particles, Academic Press, New York, 1978.

[36] P.J. Leider, R.B. Bird, Squeezing flow between parallel disks. I. Theoretical analysis, Indust. Eng. Chem. Fundament. 13 (1974) 336–341.

[37] P.G.T. Saffman, The lift on a small sphere in a slow shear flow, J. Fluid Mech. 22 (1965) 385–400.

[38] P. Saffman, Corrigendum to “The lift on a small sphere in a slow shear flow, J. Fluid Mech. 31 (1968) 624.

[39] G. Magnus, Über die Abweichung der Geschosse, und: Über eine auffallende Erscheinung bei rotierenden Körpern, Annalen der Physik und Chemie 164 (1853) 1–29, doi:10.1002/andp.18531640102.

[40] G. D’Avino, P.L. Maffettone, Particle dynamics in viscoelastic liquids, J. Non Newton. Fluid Mech. 215 (2015) 80–104, doi:10.1016/j.jnnfm.2014.09.014.

[41] S.I. Rubinow, J.B. Keller, The transverse force on a spinning sphere moving in a viscous fluid, J. Fluid Mech. 11 (1961) 447–459.

[42] D.F. McTigue, R.C. Givler, J.W. Nunziato, Rheological effects of nonuniform particle distributions in dilute suspensions, J. Rheol. 30 (1986) 1053–1076, doi:10.1122/1.549845.

[43] M. Khatibi, Personal communication, (2017).

[44] A. Busch, V. Myrseth, M. Khatibi, P. Skjetne, S. Hovda, S.T. Johansen, Rheological characterization of Polyanionic Cellulose solutions with application to drilling fluids and cuttings transport modeling, Appl. Rheol. 28 (2018) 1–16, doi:10.3933/ApplRheol-28-25154.

[45] H.M. Laun, Prediction of elastic strains of polymer melts in shear and elongation, J. Rheol. 30 (1986) 459–501, doi:10.1122/1.549855.

[46] R.B. Bird, Experimental tests of generalised newtonian models containing a zero-shear viscosity and a characteristic time, Can. J. Chem. Eng. 43 (1965) 161–168, doi:10.1002/cjce.5450430402.

[47] H.A. Barnes, A review of the slip (wall depletion) of polymer solutions, emulsions and particle suspensions in viscometers: its cause, character, and cure, J. Non Newton. Fluid Mech. 56 (1995) 221–251, doi:10.1016/0377-0257(94)01282-M.

[48] Y. Cohen, A.B. Metzner, Apparent slip flow of polymer solutions, J. Rheol. 29 (1985) 67–102.

[49] H. Abchiche, M. Mellal, A. Bensakhria, M. Trari, Comparative study of correction methods of wall slip effects for CMC solutions, Comptes Rendus M?Canique 343 (2015) 322–330, doi:10.1016/j.crme.2015.02.006.

[50] A. Acharya, R.A. Mashelkar, J. Ulbrecht, Flow of inelastic and viscoelastic fluids past a sphere - part ii: anomalous separation in the viscoelastic fluid flow, Rheol. Acta 15 (1976) 471–478.

[51] M. Gottlieb, R.B. Bird, Exit effects in non-newtonian liquids. an experimental study, Ind. Eng. Chem. Fund. 18 (1979) 357–368, doi:10.1021/i160072a013.

[52] R.M. Ybarra, R.E. Eckert, Effect of velocity profile rearrangement in a slit on measured normal stress of polymer solutions, J. Rheol. 32 (1988) 585–591, doi:10.1122/1.550001.

[53] B.C. Eu, Normal-stress effects in tube flow of a non-Newtonian fluid, Phys. Rev. A. 40 (1989) 1497–1506, doi:10.1103/PhysRevA.40.1497.

[54] A.J. Goldman, R.G. Cox, H. Brenner, Slow viscous motion of a sphere parallel to a plane wall—I motion through a quiescent fluid, Chem. Eng. Sci. 22 (1967) 637–651.

[55] A.J. Goldman, R.G. Cox, H. Brenner, Slow viscous motion of a sphere parallel to a plane wall—II Couette flow, Chem. Eng. Sci. 22 (1967) 653–660.

[56] H. Brenner, The slow motion of a sphere through a viscous fluid towards a plane surface, Chem. Eng. Sci. 16 (1961) 242–251.

[57] R. Mei, An approximate expression for the shear lift force on a spherical particle at finite Reynolds number, Int. J. Multiphase Flow 18 (1992) 145–147.

[58] M. Agrawal, A. Bakker, M.T. Prinkey, Macroscopic particle model - tracking big particles in CFD, in: The Proceeding of AIChE 2004 Annual Meeting, AIChE, Austin, TX, 2004 http://www.nt.ntnu.no/users/skoge/prost/proceedings/aiche-2004/pdffiles/papers/268b.pdf accessed April 8, 2016.

[59] D. Wadnerka, M. Agrawal, V. Pareek, Prediction of terminal velocity of a particle falling in non-Newtonian fluids using the macroscopic particle model, in: in: 7th Lnternational Conference on Multiphase Flow Proceedings, Tampa, FL, 2010.

[60] S.V. Ghatage, M. Shakhaoath Khan, Z. Peng, E. Doroodchi, B. Moghtaderi, N. Padhiyar, J.B. Joshi, G.M. Evans, S. Mitra, Settling/rising of a foreign particle in solid-liquid fluidized beds: Application of dynamic mesh technique, Chem. Eng. Sci. 170 (2017) 139–153, doi:10.1016/j.ces.2017.01.064.

[61] S. Ghosh, J.M. Stockie, Numerical simulations of particle sedimentation using the immersed boundary method, Commun. Comput. Phys. 18 (2015) 380–416, doi:10.4208/cicp.061113.050115a.

[62] F.A. Godínez, E. de la Calleja, E. Lauga, R. Zenit, Sedimentation of a rotating sphere in a power-law fluid, J. Non Newton. Fluid Mech. 213 (2014) 27–30, doi:10.1016/j.jnnfm.2014.08.013.

[63] C. Crowe, J. Schwarzkopf, M. Sommerfeld, Y. Tsuji, Multiphase flows with droplets and particles, CRC Press Taylor & Francis Group, Boca Raton, 2012.

Journal paper 6 (VIII)

Cuttings transport: On the coupled effect of drillpipe rotation and lateral motion on the cuttings bed

Alexander Busch, Stein Tore Johansen

Journal of Petroleum Science and Engineering, Vol. 191, 2020.

DOI: 10.1016/j.petrol.2020.107136.

For the UDF source code, please see appendix B.3.

Journal of Petroleum Science and Engineering 191 (2020) 107136

Contents lists available at ScienceDirect

Journal of Petroleum Science and Engineering

journal homepage: http://www.elsevier.com/locate/petrol

Cuttings transport: On the effect of drill pipe rotation and lateral motion on the cuttings bed

Alexander Busch[a,*], Stein Tore Johansen[a,b]

[a] Norwegian University of Science and Technology (NTNU), Trondheim, Norway
[b] SINTEF Industry, Trondheim, Norway

A R T I C L E I N F O

Keywords:
Cuttings transport
Hole cleaning
Drilling
CFD
Rotation
Whirling
Orbital motion

A B S T R A C T

Drill pipe rotation is considered a relevant factor for cuttings transport and hole cleaning. However, in the term “rotation” is often used as a moniker for the combination of plain drill pipe rotation around its own axis and more complex lateral motion, as many laboratory setups feature an unconstrained drill string. Lateral motion is generally considered to benefit the transports of cuttings due to increased bed agitation. By means of Computational Fluid Dynamics, we have investigated the effect of synchronous and asynchronous whirling drill string motion on the cuttings bed and cuttings transport for water and a more viscous, shear-thinning fluid using the Two Fluid Model in conjunction with the Kinetic Theory Of Granular Flows and closures from soil mechanics to rheologically describe granular matter. The dynamic mesh capability of ANSYS Fluent R17.2 is exploited to account for the orbital motion of the drill string. In addition, three base cases (negative eccentric, concentric, and positive eccentric) are investigated for comparison. Whirling motion helps tremendously to disperse the solids into the main flow region and hence improves the quality of cuttings transport and hole cleaning, with synchronous whirl by far outperforming asynchronous whirl due to the cumulative tangential and radial velocities. The effect is much more prominent for water than for the more viscous, shear-thinning fluid because the latter already shows a comparatively good cuttings transport performance. Moreover, in case of the more viscous, shear-thinning fluid, the positive eccentric annulus provides an even better cuttings transport capability, if comparison is made on equivalent pressure gradients. Because of the higher viscosity level, the whirling motion reduces the axial throughput, which despite the increased bed agitation results in worse performance compared to the positive eccentric case.

1. Introduction

In petroleum drilling, solid particles (cuttings) are generated by the drill bit which is being pushed downhole with a certain rate of penetration (ROP). The cuttings are subsequently transported by the often shear-thinning drilling fluid through the annular space (created by the drill pipe[1] in a wellbore) to the surface, as qualitatively depicted in Fig. 1.

Adequate cuttings transport is required for proper hole cleaning, i.e. the absence of a critical cuttings bed to avoid costly downtimes in drilling due to e.g. stuck pipes. The quality of solids transport depends on many factors (A. Busch et al., 2018a, Busch et al., 2019), two of which are drill pipe rotation and eccentricity. Due to the relevance of cuttings transport to the drilling industry, these have been the subject of many experimental studies (Avila et al., 2008; e.g. Han et al., 2010; Larsen, 1990; Sanchez et al., 1999; Tomren et al., 1986) over the last decades as well as numerical, or more precisely Computational Fluid Dynamics (CFD) studies (e.g. Akhshik et al., 2015; Epelle and Gerogiorgis, 2017; Heydari et al., 2017; Pang et al., 2019, 2018) in recent years.

1.1. Effect of parameters on cuttings transport and hole cleaning

Negative[2] eccentricity increases the accumulation of particles at the

---

* Corresponding author.
E-mail addresses: alexander.busch@ntnu.no, alexander.busch@alumni.ntnu.no (A. Busch).

[1] Strictly speaking, one needs to distinguish between individual drill pipe elements and the drill string made up of several drill pipe elements. However, for simplicity and because we here focus on an annular element with length L $<$ 10 m, we use the terms interchangeably.

[2] The coordinate system employed in this study is depicted in Fig. 1 and defined as follows: Assuming a horizontal wellbore, i.e. an inclination of 90° as used in the petroleum industry, the streamwise direction is positive x, the vertical direction against gravity is positive y, and the direction out of the plane is positive z. Thus, negative eccentricity is characterizing a drill pipe out-of-center towards the lower side of the annulus, whereas positive eccentricity is the opposite.

https://doi.org/10.1016/j.petrol.2020.107136
Received 19 June 2019; Received in revised form 26 February 2020; Accepted 28 February 2020

Nomenclature

Greek symbols

α	Volume fraction
γ	Shear rate, total shear measure
Δ	Difference
ε	Turbulent dissipation rate
η	Apparent shear viscosity
κ	Bulk viscosity
μ	Newtonian shear viscosity
ω	Specific turbulent dissipation rate
ϕ	Inclination
φ	Angle of internal friction
Π	Non-dimensional quantity
ρ	Density
σ	Prandtl number
τ	Deviatoric stress tensor
θ	Circumferential coordinate
Θ	Granular temperature

Latin symbols

A	Surface area, Amplitude
c	Coefficient
d	Diameter, Differential
D	Rate of deformation tensor
e	Non-dimensional eccentricity, coefficient of restitution
E	Dimensional eccentricity
f	Functional
f	Force vector
g	Radial distribution function
g	Gravity
I	Identity tensor
k	Turbulent kinetic energy, Granular conductivity
K	Power-law parameter (also known as Consistency Index), interphase exchange coefficient
l	Limiter coefficient
L	Length
m	Mass
n	Parameter in Power-law (PL), also known as PL exponent
N	Normal stress difference
p	Pressure
Q	Volumetric flow rate
Re	Reynolds number
r	Radial, Rock
t	Time.
T	Relaxation time.
Ta	Taylor number
T	Stress tensor
u	Phase velocity
U	Fluid bulk velocity
v	Particle velocity
V	Volume
w	Width
x	Spatial dimension
y	Spatial dimension
z	Spatial dimension

Indices

0	Zero, $\gamma \to 0$
∞	Infinity, $\gamma \to \infty$
c	Collisional
D	Drag
f	Fluid, Frictional
i, j,k	Index
i	Inner
j	Joint
k	Kinetic
MR	Metzner-Reed
o	Outer
p	Pipe.
PL	Power Law
r	Relative.
s	Solid, Slip (Subscript), Superficial (Superscript)
t	Turbulent
T	Transposed.
VM	Virtual mass
w	Whirl

Abbreviations

2D, 3D	Two-, Three dimensional in space
AW	Asynchronous Whirl
BC	Boundary Condition
CFD	Computational Fluid Dynamics
CMC	Sodium Carboxymethyl Cellulose
CTR	Cuttings Transport Ratio
DEM	Discrete Element Method
FC	Flow Curve
GNF	Generalized Newtonian Fluid
HB	Herschel-Bulkley
KTGF	Kinetic Theory of Granular Flows
MP	Multi-Phase
PAC	Polyanionic Cellulose
PL	Power-Law
RPM	Revolutions Per Minute
ROP	Rate Of Penetration
SP	Single-Phase
SST	Shear Stress Transport
SW	Synchronous Whirl
TFM	Two Fluid Model

lower side of the annulus (leading to a sediment or cuttings bed) because the narrower gap results in a local reduction in fluid velocity (Bicalho et al., 2016a; Heydari et al., 2017). At the same time, pressure loss decreases because the effective cross-sectional flow area increases. This also holds for the single-phase (SP) case, regardless of fluid type or flow regime (McCann et al., 1995). Rotation on the other hand generally increases the transport of cuttings (Duan et al., 2010; Han et al., 2010), in particular in the cases off negative eccentric configurations because the tangential velocity of the rotating pipe is acting at the position of high solid volume fractions, i.e. at the cuttings bed (Bicalho et al., 2016a; Heydari et al., 2017; Xiaofeng et al., 2014). However, this effect is dependent on the particle size as small particles will be re-entrained much easier than large ones (Duan et al., 2008; Sifferman et al., 1992) as well as the annular diameter ratio, as the effect of rotation becomes much more relevant for smaller annular gaps (Peden et al., 1990). By reducing an existing cuttings bed and thereby increasing the effective flow area, drill pipe rotation leads to a decrease in pressure loss, which is different to the SP case where rotation may increase or decrease pressure losses, depending on the flow regime and fluid (Sorgun et al., 2011). For instance, pressure losses increase with rotation for turbulent flows and decrease for laminar flows of Power-Law (PL) fluids because of the shear-thinning property of the fluid (Johansen et al., 2003; McCann et al., 1995). On the other hand, for the case of Yield-Power-Law (YPL)/Herschel-Bulkley (HB) fluids, Erge et al. (2015, 2014) observed no significant effect of rotation for turbulent flows and a pressure loss increase or decrease in the laminar and transitional regime, depending on the magnitude of inertial forces, i.e. the spatial dimensions of the annulus as well as the viscosity level of the fluid.

Often, in cuttings transport studies, the drill string is assumed to rest in a fixed position, which may be either concentric or eccentric. However, this is rarely the case in wellbores (Ahmed et al., 2010; Saasen, 2014), where the drill pipe may feature complex lateral motion patterns (Gao, 2010; Leine et al., 2002; Shyu, 1989). Rotation is a necessary requirement for lateral motions. For a given rate of rotation, a variety of lateral motion patterns may be observed depending on the three-dimensional (3D) wellbore trajectory and the particular point of the wellbore one focuses on. The flexibility of the drill pipe (Xiao et al., 2003) and the buckling of the drill string (Erge et al., 2015, 2014), as a consequence of the axial force applied on the string and the bit, i.e. weight on bit, determine the local eccentricity and in combination with the drill string rotation and its experienced torque (Leine et al., 2002) as well as the hydrodynamic pressure and viscous forces of the drilling fluid (Leine et al., 2002; Xiao et al., 2003) lead to a specific lateral motion.

In general, a drill pipe rotating in a wellbore with an angular velocity ωp = 2π rpmp/60 may feature a variety of lateral/orbital motion patterns, which include the absence of lateral motion, i.e. pure rotation, snaking motion, where the drill pipes climbs the annular wall to a certain extent and then falls back due to gravity, irregular motion, and whirling motion, where the drill pipe rolls or slides on the surface of the outer pipe in an clockwise or anti-clockwise manner, as detailed further in section 2.1 (Gao, 2010).

While specific types of lateral motion of the drill string may cause material wear and damage (Cayeux et al., 2018) as well as an increase in average pressure drop (Erge et al., 2015, 2014; Khatibi et al., 2018a, 2018b) and pressure oscillations (Khatibi et al., 2018a), it is also reasonable to expect an increased transport of cuttings because the motion of the drill pipe additionally agitates the bed and entrains particles into the bulk of the liquid flow. However, only a very limited number of research activities have focused on the specific effect of lateral drill string motion on cuttings transport.

1.2. *State of the art of lateral drill string motion experiments*

In experimental studies, both rotation and eccentricity have been extensively investigated and in many laboratory setups rotation and eccentricity are truly independent parameters (e.g. Duan et al., 2010; Peden et al., 1990; Sifferman et al., 1992). However, in many other laboratories (e.g. Avila et al., 2008; Khatibi et al., 2018a, 2018b; Sanchez et al., 1999; Sayindla et al., 2017; Ytrehus et al., 2018, 2015) the drill string is not entirely constrained and hence lateral, orbital and/or whirling motion may occur. Thus, the eccentricity at the point of observation is time-dependent and a function of the aforementioned parameters and, unfortunately, often undisclosed.

In a review conducted by Pilehvari et al. (1999), the relevance of the role of lateral drill pipe motion is first mentioned as “the manner in which the drill string behaves dynamically” and attributed to the study of Bassal (1996) in the sense that “all previous experimental studies had limitations in simulating the real dynamics of the drill pipe”. At the same time, many of these results were disseminated by Sanchez et al. (1999).

In the experiments of Sanchez et al. (1999), the drill string was only constrained at its end and hence was able to move freely in the middle where flow observations were made. Sanchez et al. (1999) showed that not the pure rotation but rather the resulting orbital motion is the reason for significant improvement of hole cleaning, both during actual drilling and after drilling when cuttings generation has ceased.

1.3. *State of the art of lateral drill string motion modelling*

Recently, Computational Fluid Dynamics (CFD) has been increasingly used to study wellbore flows (e.g. Bicalho et al., 2016a; Bilgesu et al., 2002; Epelle and Gerogiorgis, 2017; Hajidavalloo et al., 2013; Heydari et al., 2017; Mme and Skalle, 2012; Ofei et al., 2014; Ofei and Pao, 2014; Pang et al., 2018, 2019; Pereira et al., 2007; Rooki et al., 2013a, 2013b; Wang et al., 2009; Xiaofeng et al., 2014). Typically, rotation is treated as plain drill string rotation and simply accounted for by specifying a tangential no-slip velocity at the drill pipe wall. The role of whirling motion, however, has gained much less attention.

Very recently, Pang et al. (2019) studied orbital drill pipe motion by means of CFD for the case of a PL fluid and showed that orbital motion increases the cuttings transport ratio (CTR) while decreasing the pressure drop (However, higher rotating speeds cause a sharp increase in pressure drop in particular when the drill pipe orbits in the opposite direction to its self-rotation). The larger the radius of the orbital motion, the better for the CTR. Orbital motion periodically stirrs up the cutting bed by causing the core zone of the axial bulk velocity following the orbital motion (though lagging behind that) and producing secondary tangential flows and eddies. Pang et al. (2019) utilized the Eulerian-Eulerian Two Fluid Model (TFM) in combination with the Kinetic Theory of Granular Flows (KTGF), though no additional closures were employed to account for frictional effects within the dense granular media, i.e. the cuttings bed. The sliding mesh method of ANSYS Fluent R14.0 was employed to realize the orbital motion of the drill pipe. Self-rotational speed ωp and orbital speed ωw were considered to be equivalent in magnitude, i.e. ωw = ωp and ωw = -ωp, and investigated in the range 0–200 rpm.

Recently, Cayeux et al. (2018) investigated the special case of

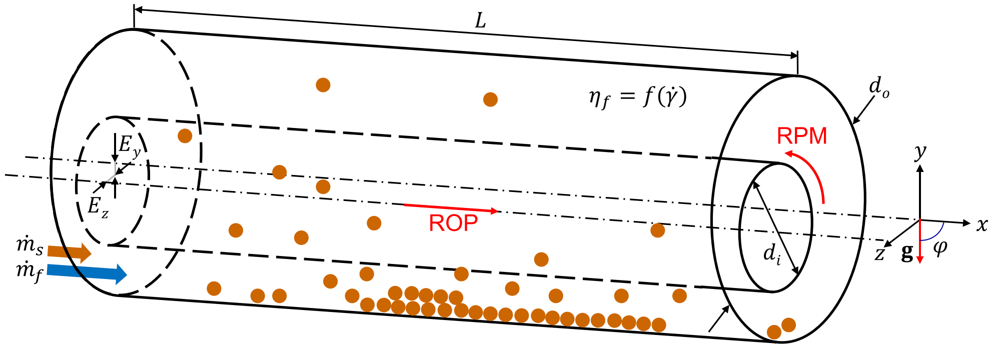

Fig. 1. Cuttings transport process on an annular scale.

synchronous whirl, where the drill string angular frequency equals the angular frequency of the whirling motion and the pipe always faces the same side towards the outer wall of the annulus, comprising the cases of SP laminar flow of Newtonian, PL, and HB fluids. Based on the methodology used by Feng et al. (2007) they inverted the annular system by considering the outer cylinder rotating around the inner and accounted for centrifugal and Coriolis forces. The whirling motion contributes to the total pressure gradient for all fluids investigated. However, in case of the HB fluid the pressure gradient of the pure rotational cases exceeds the one of the whirling cases at approximately 80 rpm for all volumetric flow rates investigated, presumably because the whirling motion avoids plug regions at higher rotational speeds (Cayeux et al., 2018).

Both Vieira Neto et al. (2012) and (Bicalho et al., 2016b, 2016a) experimentally investigated the flow of laminar xanthan gum solutions in annuli with orbital inner pipe motion. In addition, they simulated the pressure drop using the dynamic meshing (Neto et al., 2012) and sliding mesh capabilities (Bicalho et al., 2016a, 2016b) of ANSYS Fluent and obtained a good fit between experimental and numerical results. Rotation and corresponding orbital motion of the inner tube results in more uniform flow distributions in the annulus, preventing flow stagnation in the narrow-gap regions in cases of eccentric configurations. Therefore, in the case of a partially blocked annulus with eccentricity, increasing drill pipe rotation and orbital motion is considered to improve the transport of cuttings (Bicalho et al., 2016a).

For a negative eccentricity of a highly shear thinning fluid, Demiralp (2014) investigated the effect of different whirl patterns on cuttings transport. A two-way coupling between solids and fluid by means of CFD and the Discrete Element Method (DEM) and presumably (The details of the whirling motion implementation are not disclosed) the dynamic meshing capabilities of ANSYS Fluent were employed to investigate hole cleaning for different fluid superficial velocities and drill pipe rotations. Solids concentration decreases with increasing whirling speed in all flow regimes, with synchronous whirl yielding the highest solid superficial velocity.

1.4. Purpose, scope and structure of this paper

While some numerical studies investigated the impact of whirling motion on the flow hydrodynamics (Bicalho et al., 2016a; Cayeux et al., 2018; Feng et al., 2007; Neto et al., 2012), the effect of drill pipe whirl on cuttings transport has—to our knowledge—not been quantitatively investigated, with the notable exceptions of the thesis of Demiralp (2014) and the recent study of Pang et al. (2019). Experimental investigations have often featured a laterally moving drill string; however, the lateral motion is usually a consequence of the system and the controlling parameter is simply the rotational rate of the drill pipe. Unfortunately, no clear distinction is made in the literature between plain drill pipe rotation and additional lateral, orbital, or whirling motion, in particular when it comes to the interpretation and quantification of experimental results. Even recent review papers combine these under the umbrella rotation (Kelin et al., 2013; Li and Luft, 2014a, 2014b; Ofei et al., 2015; Xiaofeng et al., 2013). In addition, we are not aware of any study where the modes of and the parameters describing orbital motion were disseminated. This hinders quantitative comparisons.

We numerically investigate the effect of two classical whirling motion cases, namely forward and backward whirl (detailed definitions are provided in the following section 2.1), on cuttings transport for water and a more viscous, shear-thinning fluid. We then compare these results to eccentric and concentric cases with plain drill string rotation.

In the following section, a description of the drill string whirl cases as well as all relevant other parameters investigated is presented, followed by a brief summary of the physical CFD model along with required closures. SP results are then presented and compared to the experiments of Khatibi et al. (2018a, 2018b), followed by the presentation of cuttings transport simulation results. In the subsequent discussion, we provide explanations for the observed phenomena as well as an analysis of the strength and weaknesses of our investigations. Finally, a brief summary and outlook is given.

2. Materials and Methods

2.1. Drill string whirl

In general, four patterns of drill pipe motion may be characterized as follows (Shyu, 1989):

1. Synchronous whirl (SW), also known as forward whirl, where the tool joint is sliding on the hole/casing wall in such a manner that it always faces the same side towards the outer wall. Consequently, the drill pipe rotation and its whirling motion show identical angular velocities, i.e. ωw = ωp.
2. Asynchronous whirl (AW), also known as backward whirl, where the tool joint is rolling on the hole/casing wall without any slip. Consequently, the whirling motion occurs in opposite direction of the drill pipe rotation and the angular velocity of the whirl motion is given by ωw = -dj/doωp, where dj is the diameter of the tool joints.
3. More complex whirl, where there is slip between the surfaces such that ωw = csωp, where cs is different from 1 or -dj/da, not necessarily constant and may even be different for the y and z-direction such that the motion pattern becomes a Lissajou curve.
4. Any other (seemingly chaotic) motion, where e.g. the drill string does not always remain in contact with the wellbore wall (at all times) and/or where there is slip between the surfaces of tool joints and wellbore wall.

We here focus on plain whirling motion, i.e. type 1 and 2 as characterized above, because it is easiest to parametrize. A generic framework for the whirling motion is given by a 2D oscillation equation in y and z:

$$y_w = \left(E_y + A_y\right) - A_y \cos\left(\omega_y t\right), \tag{1}$$

$$z_w = E_z + A_z \sin\left(\omega_z t\right), \tag{2}$$

where Ei are the dimensional eccentricities, Ai the dimensional amplitudes, and ωi the angular velocities (which are here taken as ωw = ωy = ωz), as depicted in Fig. 2.

While SW and AW may be straightforwardly parametrized as described above, this is not so in many experimental setups because the drill string is free to move in the test section. For instance, in the experiments of Khatibi et al. (2018a, 2018b), the eccentricity and amplitude are functions of the drill pipe's rotation rate and the superficial fluid velocity. The drill pipe consisted of several acrylic elements connected with flexible joints, the diameter of which was slightly larger than the drill pipe (see Fig. 17 in Appendix C). One end was connected to a dual current motor while the other end was not constrained and hence free to move. Therefore, the flexible drill string arrangement was subject to lateral motion because of the enforced rotation at one end and the systems mechanical properties (compliances of individual drill string elements and flexible joints, Coulomb and viscous friction). Khatibi et al. (2018b) showed, that in their SP experiments the observed change in vertical eccentricity Ey is largely dependent on the rotation rate of the drill pipe and to a smaller extent on the Reynolds number of the flow. We curve-fitted second-order polynomials to the available dimensional data (Khatibi, 2018), the coefficients of which are presented in Table 1.

In the experiments of Khatibi et al. (2018a, 2018b), the horizontal amplitude Az as well as the angular velocity ω_W were not determined explicitly. However, the latter may be estimated with $2\pi\, rpm/60$ based on the frequency spectra analysis of pressure readings (Khatibi, 2018; Khatibi et al., 2018a), while the former may be roughly estimated by $A_y/2$ (Khatibi, 2018).

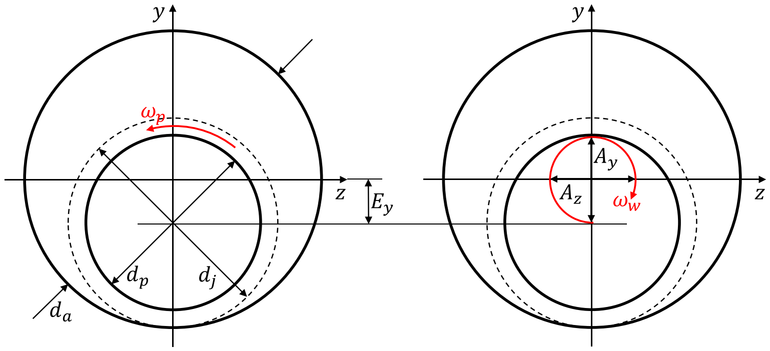

Fig. 2. Geometrical and kinematical system quantities, downstream orientation. Left: Geometrical dimensions of drill pipe, tool joints and outer wall of wellbore as well as drill pipe rotation around its own axis. Right: Kinematic quantities describing whirling motion of drill pipe in wellbore.

Table 1
Coefficients for second-order polynomials c1+c2rpmp + c3Qf + c4rpmp2+c5rpmpQf + c6Qf2 describing Ey = f(rpmp, Qf) and Ay = f(rpmp, Qf) in the SP experiments of Khatibi et al. (2018a, 2018b). It is assumed that for rpmp = 0 and Qf > 0 the datapoints show the same trend as for rpmp = 0 and Qf = 0 (red marked in Table 6 in Appendix C).

Case	c1	c2	c3	c4	c5	c6
Ey	−0.007085	2.916e-06	0.04796	1.891e-08	0.003387	845.2
Ay	0.0003163	5.074e-05	−0.8467	−1.526e-07	−0.001904	560

Table 2
SP test matrix following the experiments of Khatibi et al. (2018a, 2018b). In case of non-zero drill pipe speed, whirling acc. to equations (1) and (2) as well as Table 1 was additionally specified.

Case	Fluid	Eccentricity	ω_p [RPM]
1	H_2O	0	0
2	H_2O	−0.95	0
3	H2O	−0.88	100
4	H2O	−0.77	200
5	H2O	−0.60	300
6	PAC	0	0
7	PAC	−0.95	0

Table 3
MP test matrix. In case of e_y = {SW, AW} a whirling motion acc. to equations (1) and (2) was additionally specified.

Case	Fluid	e_y [-]	ω_p [RPM]	dp/dx [Pa/m]
1	H_2O	−0.54	0, 30, 60, 100, 130	−100, −200, −300, −400, −500
2	H_2O	0.00		
3	H2O	0.54		
4	H2O	AW	30, 60, 100, 130	
5	H2O	SW		
6	PAC	−0.54	0, 30, 60, 100, 130	
7	PAC	0.00		
8	PAC	0.54		
9	PAC	AW	30, 60, 100, 130	
10	PAC	SW		

2.2. Test matrix

Table 2 summarizes the SP cases investigated for rotational and lateral-motion model validation.

For the cuttings transport multiphase (MP) simulations, a horizontal 8.5 in wellbore section ($d_o = 0.216$ m) with a 5.0 inch drill pipe ($d_p = 0.127$ m and tool joint diameter $d_j = 0.168$ m) was assumed. Different fluids, eccentricities/whirl types, pressure gradients and drill pipe rotation rates were investigated as summarized by Table 3 in order to represent field values.

For the sake of clarity, Fig. 3 details column e_y of Table 3, where the drill pipe's AW and SW motion is defined as described in section 2.1 and equations (1) and (2).

The properties of the two types of fluids investigated in this study are given in Table 4.

In all cases, following Khatibi et al. (2018a, 2018b), the solids were simplified as spherical particles with diameter $d_s = 1.2$ mm, density $\rho_s = 2650$ kg/m^3 and angle of internal friction $\alpha_{if} = 45^\circ$. The solid loading was determined such that without flow and rotation, the solids bed was filling the lower clearance for the smaller eccentricity $e_y = -0.54$, which yields $\alpha_s = 0.047$.

2.3. Physical model

As a MP flow model, we here apply the TFM in combination with the KTGF developed by Savage (Lun et al., 1984; Savage et al., 1996; Savage and Jeffrey, 1981) handling the loose, i.e. the collisional/kinetic regime[3] (solid volume fraction $\alpha_s < \alpha_{s,f} = 0.55$) and closures from soil mechanics describing the dense regime ($\alpha_s > \alpha_{s,f}$) of the cuttings, hereafter termed solids. The two phases are considered as interpenetrating continua and mass continuity and momentum transport equations along with closures for the fluids and solids material functions, turbulence, and the momentum exchange terms are used to model the system. The full model description is given in 5 Appendix A.

As previous investigators (e.g. Epelle and Gerogiorgis, 2017; Pang et al., 2019, 2018; Zakerian et al., 2018), we utilize the model implementation of ANSYS Fluent (ANSYS, Inc., 2016a, 2016b), a broadly used commercial CFD code.

---

[3] In the literature, these regimes are alternatively known as the inertial or viscous regime and the plastic or frictional regime, respectively.

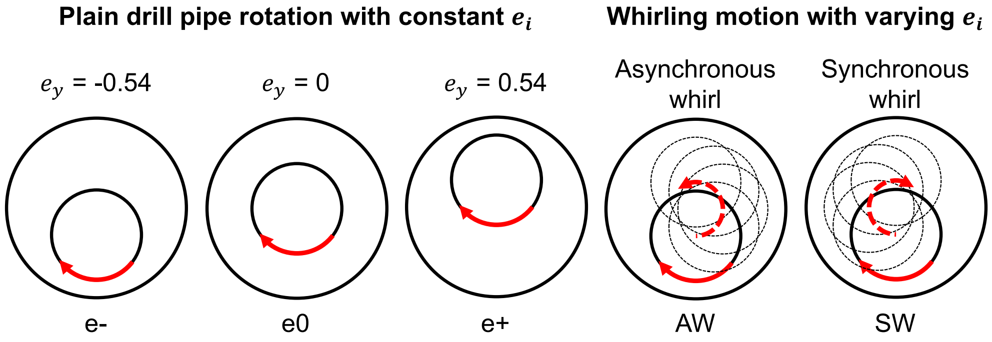

Fig. 3. *Overview of different systems investigated in terms of eccentricity e_i, plain drillpipe rotation around the drill pipe axis, and whirling motion of the drill pipe.*

Table 4
Fluid rheological model coefficients and density for different cases investigated based on the experiments of Khatibi et al. (2018a, 2018b).

Fluid	n_{PL} [-]	K_{PL} [Pa·s^n]	ρ_f [kg/m^3]
H_2O	1	0.001002	1000
PAC (PL)	0.86	0.025	

2.4. CFD setup & numerics

For the SP simulations, a variety of meshes of varying eccentricity based on Table 1 were created. Table 7 in Appendix E provides an overview of the relevant mesh parameters and Fig. 4 provides an eccentric example of the “Intermediate (MP)” case.

The dependency of the numerical solution on the mesh resolution was firstly evaluated with SP simulations (without rotation) as depicted in Fig. 19 in Appendix E. For all meshes, the r -spacing was non-uniform in order to obtain a higher resolution close to the walls. Periodic boundary conditions (BC), i.e., what leaves the domain enters the domain, were applied to either end of the annular element in order to reduce computational efforts. The length of the computational domain was chosen as $L = d_o$ for the SP, and $L = 3d_o$ for the MP simulations (such that any periodicity in the solution is not influenced by the BC).[4]The “Coarse (High Re)” mesh and the “Superfine (Low Re)” mesh results differ by only 1%, while the “Intermediate” mesh result differs from the “Superfine (Low Re)” mesh result by 3.8%. However, the “Intermediate” mesh does feature a much smaller first layer more suited for larger flows/pressure gradients (and thus steeper wall gradients) and it represents the experimental data best. Fig. 20 in Appendix E shows transient results for a MP case for the “Intermediate (MP)” and “Fine” meshes. In the near-steady-state time period, the difference between the two meshes is <1% for U_f and about 5% for U_s. The selected mesh quality “Intermediate” provided a fair compromise between sufficiently accurate results in the form of time-averaged integral quantities (Goldschmidt et al., 2004) such as superficial velocities/mass flow rates and associated computational effort and is comparable to similarly sized grids in other studies (e.g. Epelle and Gerogiorgis, 2017; Rooki et al., 2013b, 2013a; Zakerian et al., 2018).

The plain rotation of the drill pipe around its own axis was defined as a slip velocity of the inner wall, i.e., the fluid velocity at the wall is not zero but has a magnitude and direction equivalent to the wall rotational speed of the drill pipe. In case of SP simulations, we specified a mass flow rate, while in case of MP simulations a mixture pressure gradient $\Delta p/\Delta x$ along with the solid volume fraction α_s was specified.Fluent’s dynamic meshing capability was employed to deform the mesh and simulate the orbital motion of the inner pipe. The latter was defined by an User-Defined-Function (UDF) which is simply an implementation of the time derivative of equations (1) and (2) and provides the velocities of the center of gravity of the orbital motion of the drill pipe to the solver. The spring-based smoothing method, were the cell edges are treated as elastic springs, was used to update the mesh every time step.

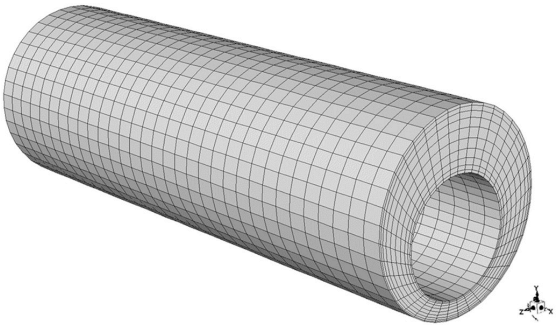

Fig. 4. Initial grid for negative eccentric and whirling motion cases. Full video showing trajectory of drill string whirling motion available at https://youtu.be/vV-0C9GXkWM.

All simulations but the SP mesh dependence cases depicted in Fig. 19 in Appendix E were performed in a transient manner, as exemplarily depicted in Fig. 20 in Appendix E. The time step was 10^{-3} s to 10^{-4} s and a second-order implicit scheme was employed. The (Phase-Coupled) SIMPLE scheme (Vasquez, 2000) was used for pressure-velocity coupling. The QUICK scheme (Leonard, 1979) was used for second-order spatial discretization and the Green-Gauss node-based gradient scheme was used to evaluate all gradients. The time discretization was implicit second order. The algebraic multigrid method with the Gauss-Seidel solver and conservative under-relaxation factor settings were used to solve the system of discretized equation.

At t = 0 the solids were patched into the domain and then allowed to settle over time until a partly moving-partly stationary bed is built up, resulting in an quasi-steady state of U_f and U_s, as illustrated by Fig. 20. Simulations were then continued for at least five orbital motions for the purpose of data sampling.

Pre-studies showed that the mesh deformation works fine for a couple of orbital motions only. After six to twelve orbital cycles, the

---

[4] Even though a RANS framework is adopted, we did not know whether the drill string dynamics would generate any irregular solid particle motions in the streamwise direction. Therefore, we decided to employ a domain where, for the given dimensions, the length is about 14.5 times the mean gap. This is about 4.3 times the largest gap occurring in the eccentric cases studied. However, no streamwise dependency of any flow quantities where observed.

mesh starts to deform non-uniformly and eventually highly skewed cells lead to negative volume and divergence. We therefore simply replaced the mesh after a preset number of orbital cycles (two to four) with the initial, where the solver transfers the current solution from the old to the new mesh using interpolation schemes. Reducing the time step size did not rectify the mesh deterioration.

3. Results

We first present results which to some extent validate the CFD model with available experimental data. Secondly, we present results for the industrially relevant 8.5 inch wellbore section flow case where we focus on the effect of whirling motion on cuttings transport and the transitional flow regime.

3.1. Validation with single-phase experimental data

For validating the CFD model we hereafter present SP results benchmarked with respective experimental data and friction factor correlations. We use the experimental data of Khatibi et al. (2018a, 2018b) because besides containing data for transitional flow of PL fluids, this data set also contains data for whirling drill string motion. In their experiments, Khatibi et al. (2018a, 2018b) used water and a shear-thinning 1 g/L polyanionic cellulose solution (PAC). A broad variety of friction factor correlations for turbulent concentric and eccentric annular flow is available in the literature. For instance, for the fully eccentric annular turbulent flow of different concentrations of drag-reducing guar gum solutions, explicit friction factor correlations as a function of the generalized Reynolds number, diameter ratio, and relative roughness are available (Dosunmu and Shah, 2015; Ogugbue and Shah, 2011). Other examples are the works of Kelessidis et al. (2011) and Pilehvari and Serth (2009) for the flow of bentonite suspensions. However, to our knowledge, no dedicated friction factor correlation for PAC solutions exists. For the case of PAC, we therefore utilize the correlations of Dodge and Metzner (1959) and Irvine (1988), which are corrected for eccentricity (Haciislamoglu and Cartalos, 1994; Haciislamoglu and Langlinais, 1990), if required.

Fig. 5shows CFD results for the flow of water in a concentric and fully eccentric annulus without pipe rotation.

The results are benchmarked with the aforementioned friction factor correlations from the literature. In addition, experimental data (Khatibi et al., 2018a, 2018b) is depicted. The reason for choosing this particular experimental data set is that it also contains data for whirling drill string motion.

While the CFD predictions adequately fit the empirical relations for both the concentric and eccentric annular configurations, the experimental data for the eccentric case falls slightly on top of the concentric flow data.

A zoom on the low superficial velocity range of Fig. 5 (black box) is depicted in Fig. 6.

In addition, CFD results for three different whirling motion cases are depicted along with the corresponding experimental results (Khatibi et al., 2018b). Note that the maximum eccentricity and the predefined whirling motion parameters for these cases are functions of the drill pipe rotational speed and the superficial fluid velocity and only valid for the experimental setup of Khatibi et al. (2018a, 2018b). With increasing rotational speed and the corresponding change of whirling motion, the respective pressure gradient increases. Interestingly, the aforementioned difference between CFD and experimental results is not observed for the 100 and 200 rpm cases. However, the 300 rpm cases are heavily underpredicted by the CFD simulations.

Finally, Fig. 7 provides pressure gradient vs. superficial fluid velocity results for the flow of PAC, both for the concentric and the eccentric case.

While there is good agreement between the friction factor correlations, CFD results and, in the eccentric case, the experimental data in the lower (laminar) range of superficial fluid velocities, this is not so for the higher (transitional) range. Compared to the friction factor correlations, the CFD results overpredict the transitional regime by up to 40%. In case of the eccentric configuration, CFD and experimental results show good agreement up to $U_{f,x} = 1.4$ m/s, where the experimental results start to deviate from the CFD results and approach the friction factor correation at higher $U_{f,x}$.

3.2. Validation with multi-phase experimental data

Concerning MP flows, the physical model as presented in Appendix A and its implementation in Fluent as used in this study has been validated to a good extent by several other researchers as depicted in Fig. 8 for the case of non-whirling flow cases and based on the non-dimensional Π-space of Busch et al. (2019). Except for the Cuttings Transport Ratio (CTR) and, to some extent, the Taylor number *Ta*, our parameter space as given by Tables 3 and 4 is encompassed in the spaces of previous studies. The lower CTR is a consequence of our comparatively high fluid superficial velocities. Most previous studies have validated their models with cases where the drill pipe is not rotating ($\rightarrow Ta = 0$), the reason is—from our point of view—that in many experimental studies the drill pipe is actually allowed to move freely but unfortunately this is often not clearly communicated. Therefore, high-quality experimental data suited for validation purposes is scarce.

3.3. Cuttings transport studies

While there are many ways to quantify the efficiency of cuttings transport and hole cleaning (A. Busch et al., 2018a), we here apply the *CTR* as the ratio of the two superficial phasic velocities (Bourgoyne et al., 1991, p. 178), i.e.

$$CTR = \frac{U_s^s}{U_f^s}, \tag{3}$$

where the superficial velocities are defined as

$$U_i^s = \frac{1}{A}\int_A \left(\alpha_i(y,z) \quad u_i(y,z) \right) dA, \quad i \in \{f, s\}, \tag{4}$$

where u_i are the respective phasic x -velocity components and A is the cross-sectional area.[5]

This *CTR* choice is mainly motivated by the specification of the mixture pressure gradient $\Delta p/\Delta x$ and the solid volume fraction α_s as input parameters in our numerical simulations due to the periodicity of our computational domain. Hence, the latter constitutes a fixed mass of solids and hence predetermined bed height in the absence of flow. Therefore, the superficial velocities and the pressure gradient constitute the response of the system. For clarity, it is important to realize that the results presented do compare to each other in terms of dp/dx equivalence only and not in terms of equivalence of U_f^s (or U_s^s). While the latter is often used in the literature and is beneficial because the flow rate is known a priori, from a controls engineering point of view the former is sounder: While the volumetric fluid flow rate may be the primary variable to manipulate during operations, it is the pressure gradient which is monitored and to be kept below critical values.

For the different cases defined and depicted in Table 3 and Fig. 3, respectively, and H2O as the fluid phase, Fig. 9 shows the *CTR* plotted vs. drill pipe rotation and dp/dx.

In the absence of whirling motion, the *CTR* is highest for the positive eccentricity and lowest for the negative eccentricity. The effect of plain

---

[5] Note that as the phases are incompressible the definition of the superficial velocities provided in equation is equivalent to the volumetric flow rates, i.e. Ui = Qi = ρimi.

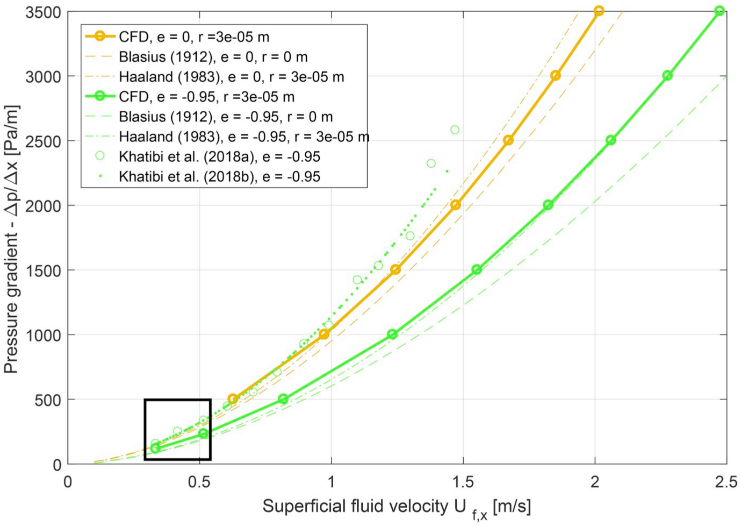

Fig. 5. CFD (solid lines) and experimental (marker symbols) pressure gradient $\Delta p/\Delta x$ vs. bulk velocity $U_{f,x}$ comparison for the e = −0.95, 0 rpm H_2O case of Khatibi et al. (2018a, 2018b). In addition, CFD results for a concentric annulus are depicted. Empirical correlations for both the concentric and eccentric—corrected for eccentricity (Haciislamoglu and Cartalos, 1994; Haciislamoglu and Langlinais, 1990)—case are plotted with dashed lines. The black box highlights the area depicted in Fig. 6.

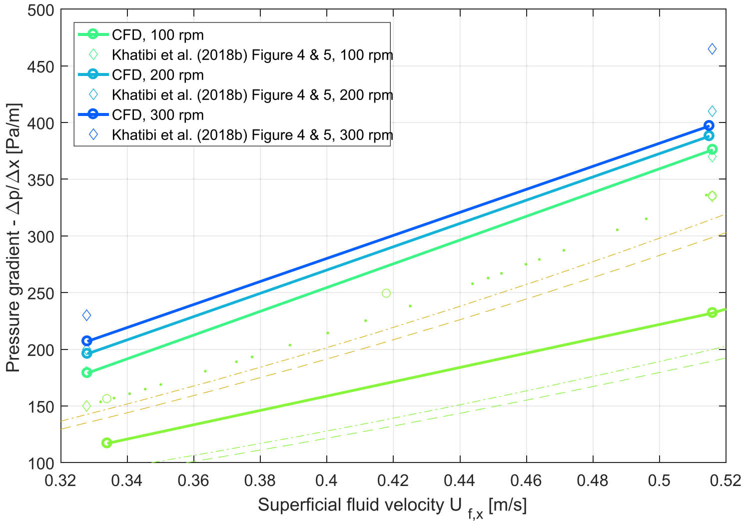

Fig. 6. CFD and experimental (time-averaged) data (Khatibi et al., 2018b) for various rpm cases. With regards to the non-rotating cases depicted in Figs. 5 and 6 depicts a zoom on the low $U_{f,x}$ -region of Fig. 5. For the respective legend information see Fig. 5.

drill pipe rotation is generally highest in the case of negative eccentricity. However, for higher pressure gradients, it similarly increases the *CTR* for the positive eccentricity case.

The presence of whirling motion significantly increases the *CTR* for rotational rates faster than 60 … 100 rpm. AW leads to *CTR* levels between concentric and positive eccentric drill pipe arrangements, while SW is outperforming all other cases for rotational rates faster than 60 … 100 rpm.

For the different cases depicted in Fig. 3 and PAC as the fluid phase, Fig. 10 shows the *CTR* plotted vs. drill pipe rotation and $dp/\ dx$.

As in the Newtonian case, the CTR is highest for SW, given that rotational rates larger than 60 … 100 rpm are maintained. As opposed to the Newtonian case, the AW case falls between the negative and concentric cases for the entire range of rotational rates.

The effect of plain drill pipe rotation is largest for the negative eccentric case and virtually non-existent for the positive eccentricity. For the concentric case, the *CTR* jumps from one level to another between 30 and 60 rpm.

In addition to the $CTR = f(rpm, dp/dx)$, we provide the results in the form $ROP = f(rpm, dp/dx)$, where *ROP* is related to the superficial solid velocity as the nominator of the *CTR* as follows: In a real field scenario at steady-state (with respect to all input parameters such as U_f^s and *ROP*), the superficial velocity of the solids U_s^s is determined by the *ROP*, the bit diameter D_o, and the rock porosity α_r as a consequence of mass conservation.

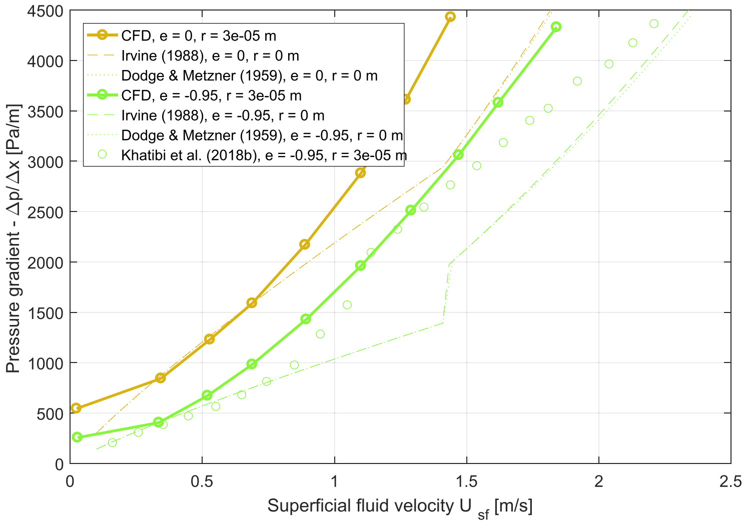

Fig. 7. CFD (solid lines) and experimental (marker symbols) pressure gradient $\Delta p/\Delta x$ vs. bulk velocity $U_{f,x}$ comparison for the e = −0.95, 0 rpm PAC case (Khatibi et al., 2018a). In addition, CFD results for a concentric annulus are depicted. Empirical PL correlations for both the concentric and eccentric—corrected for eccentricity (Haciislamoglu and Cartalos, 1994; Haciislamoglu and Langlinais, 1990)—case are plotted with dashed/dotted lines.

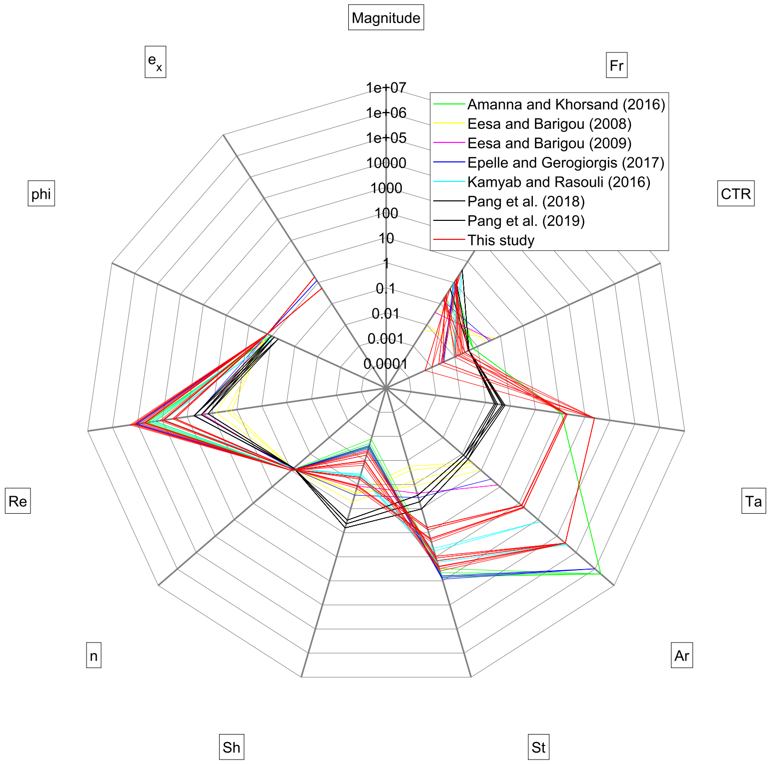

Fig. 8. Validation works of the physical model as summarized in 5 Appendix A and its implementation in ANSYS Fluent vs. this study based on the Π -space of the non-whirling flow case (Busch et al., 2019).

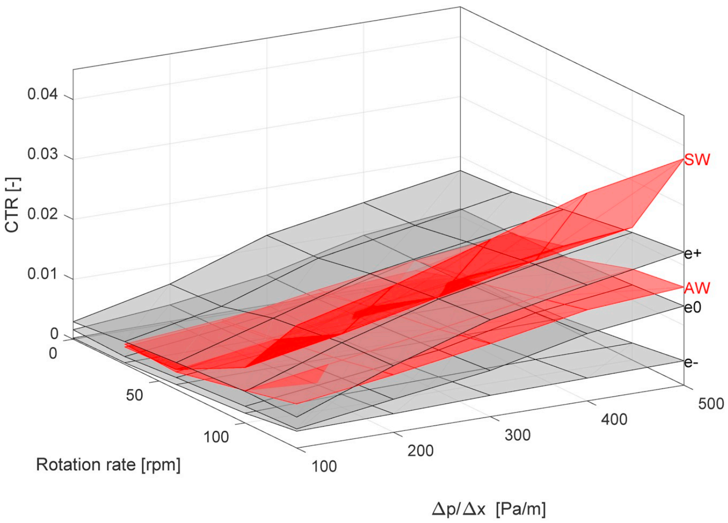

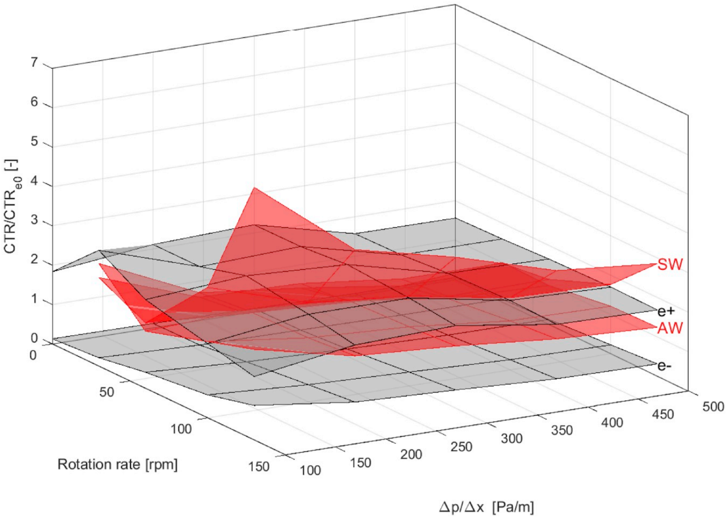

Fig. 9. Top: Absolute CTR vs. drill pipe rotation rate and pressure gradient for H2O and the systems defined in Fig. 3. Bottom: Relative change of the CTR based on the concentric system e0.

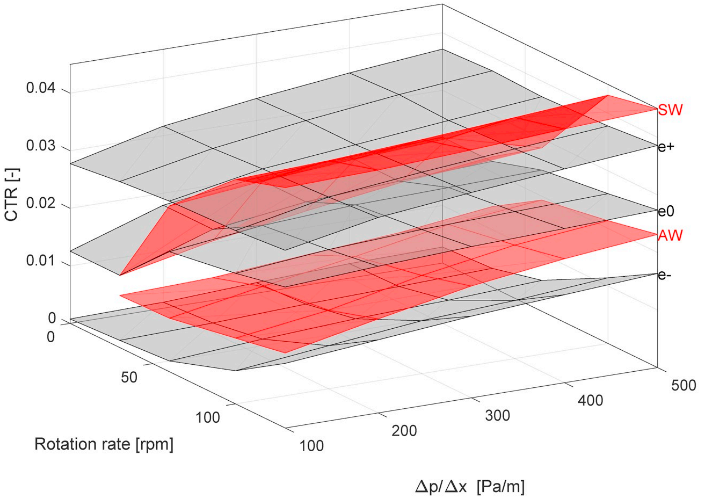

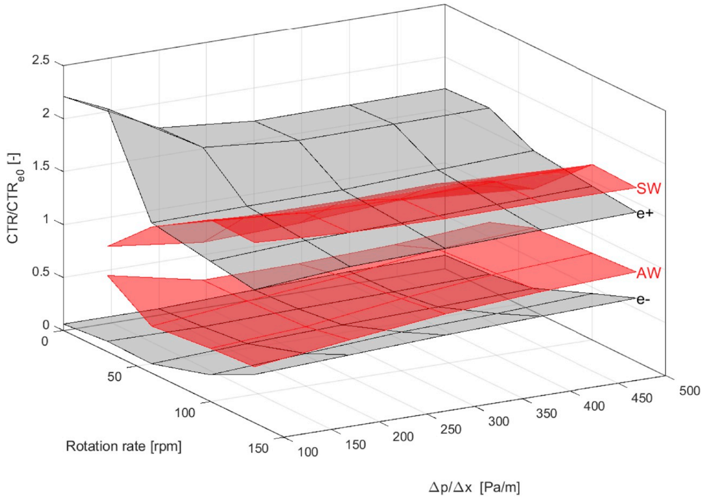

Fig. 10. Top: Absolute CTR vs. drill pipe rotation rate and pressure gradient for PAC and the systems defined in Fig. 3. Bottom: Relative change of the CTR based on the concentric system e0.

$$\frac{\pi D_o^2}{4} ROP(1-\alpha_r) = \frac{\pi\left(D_o^2 - D_i^2\right)}{4} U_s^s \tag{5}$$

While we find the same qualitative results for the case of H2O (Fig. 11), this is not so for the case of PAC (Fig. 12), where in contrast to the $CTR = f(rpm, dp/dx)$ presentation of Fig. 10 the positive eccentricity yields the highest ROP for the entire range of rotational rates considered and hence performs best in terms of hole cleaning.

To further illustrate the effect of the varied parameters on the results, we additionally depict the fluid superficial velocities for H2O and PAC in Fig. 13 and Fig. 14, respectively.

As expected, due to the different viscosity magnitudes, the fluid throughputs of PAC consistently fall under the levels of H2O for a given dp/dx.

For the concentric and positive eccentric cases, the effect of rotation is a bit more pronounced at lower dp/dx, and correspondingly fluid superficial velocities. For the negative eccentric case, as opposed to the H2O, a plateau exists for rotation rates >100 rpm in case of the PAC solution.

For any given pressure gradient, orbital motion results in a significantly reduced throughput for the entire range of rotational rates considered.

4. Discussion

4.1. Validation with single-phase experimental data

For the SP H2O base case (Re = 4900, $e = -0.95$, 0 rpm) of Khatibi et al. (2018a), the CFD results do fairly well fit the empirical pressure drop correlation (Blasius, 1912; Haaland, 1983) with the eccentricity correction (Haciislamoglu and Cartalos, 1994) applied. However, the experimental results (Khatibi et al., 2018a) exceed the CFD results by

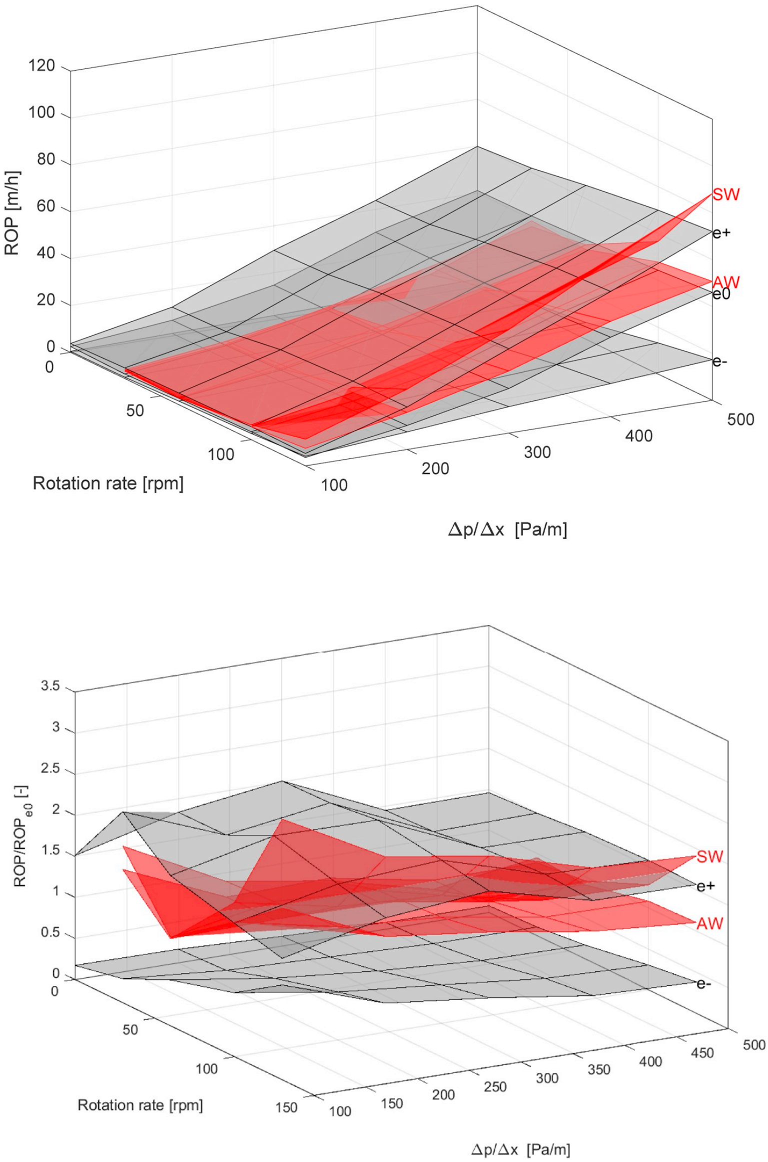

Fig. 11. Top: Absolute ROP vs. drill pipe rotation rate and pressure gradient for H2O and the systems defined in Fig. 3. Bottom: Relative change of the ROP based on the concentric system e0.

50% and do coincide with the fully concentric CFD results, which also match well with the empirical correlation (Blasius, 1912; Haaland, 1983). The significantly larger pressure drops found in the experiments may be a result of different factors. First, the computational domain assumes periodicity along x, which is not necessarily the case because of development length effects and a likely skewed whirling motion of the drill string.

The predefined whirling motion of the drill string is not necessarily describing the motion of the drill string for every x -location of the annulus. In the CFD model, we assume that the axis of the string and the outer pipe are parallel. However, due to the compliance of the drill pipe material as well as the flexible joints and the concentric fixation of the drill string at the motor end it is very likely that the drill string in the experiments features more complex whirling motion, which additionally varies in the streamwise direction, i.e. is skewed along x. Closer to the motor end it will naturally feature a more concentric and less whirling motion while further away of the motor it may move more freely and hence feature more complex elliptic motion patterns as indicated in Fig. 1 of Khatibi et al. (2018a). This is corroborated by the geometrical constraints introduced by the flexible drill string section joints with an outer diameter $d_j = 0.031$ m (Khatibi, 2018) which yields a dimensionless eccentricity $e = -0.6$, whereas the factual eccentricity for the no flow/no rotation situation as reported by Khatibi et al. (2018b) was $e = -0.94$ (see tabulated data in Table 6/Appendix C). In addition, the

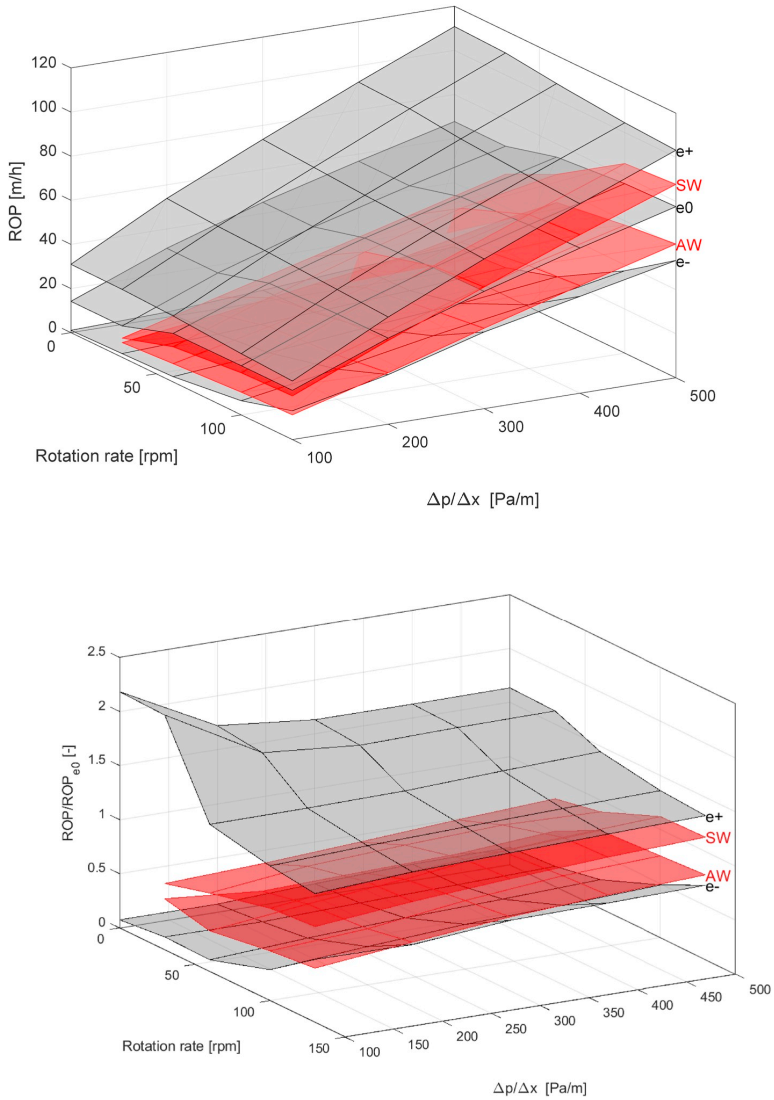

Fig. 12. Top: Absolute ROP vs. drill pipe rotation rate and pressure gradient for PAC and the systems defined in Fig. 3. Bottom: Relative change of the ROP based on the concentric system e0.

parameters characterizing the whirling motion of the drill pipe, namely the y - and z -amplitude and the frequency, were not precisely measured but rather estimated based on the obtained experimental data. The data characterizing the vertical eccentricity and amplitude of the drill string does not cover the entire parameter space and was obtained by graphical analysis of the PIV pictures. Both the horizontal amplitude and the frequency of the whirling motion where simply estimated based on visual observations rather than directly measured.

Furthermore, hydrodynamic entrance effects may be of relevance. For the laminar flow of water in a concentric annulus with $d_i/\,d_o > 0.5$, the development length may be estimated with $x_d = d_h/2(1 - 0.119\ln(d_i\,/d_o))(0.631^{1.6} + (0.0442\mathrm{Re})^{1.6})^{1/1.6}$ (Poole, 2010), which gives 1.71 m for the Re = 4900 case and 2.69 m for the Re = 7700 case. In contrast, in case of turbulent flow, the development length is much shorter and may be estimated with $4.4 d_h \mathrm{Re}^{1/6}$ (Çengel and Cimbala, 2006), which yields only 0.27 m and 0.29 m, respectively. However, Lien et al. (2004) recommend $150 d_h/2$, which yields 1.25 m.

In any case, here we are dealing with transitional flow, which is intermittent in the sense that both laminarization and development of turbulence are competing. In the experiments of Khatibi et al. (2018a, 2018b), the distance from the beginning of the annular section to the first pressure transducer is 1.4 m, and 1.52 m from the first to the second pressure transducer. Moreover, 0.3 m prior to the first pressure transducer, the first flexible joint with an outer diameter $d_j = 0.031$ m (Khatibi, 2018) significantly reduces the cross-sectional flow area and hence introduces a flow disturbance. Thus, the flow may still have been of developing nature in the section where pressure measurements were taken.

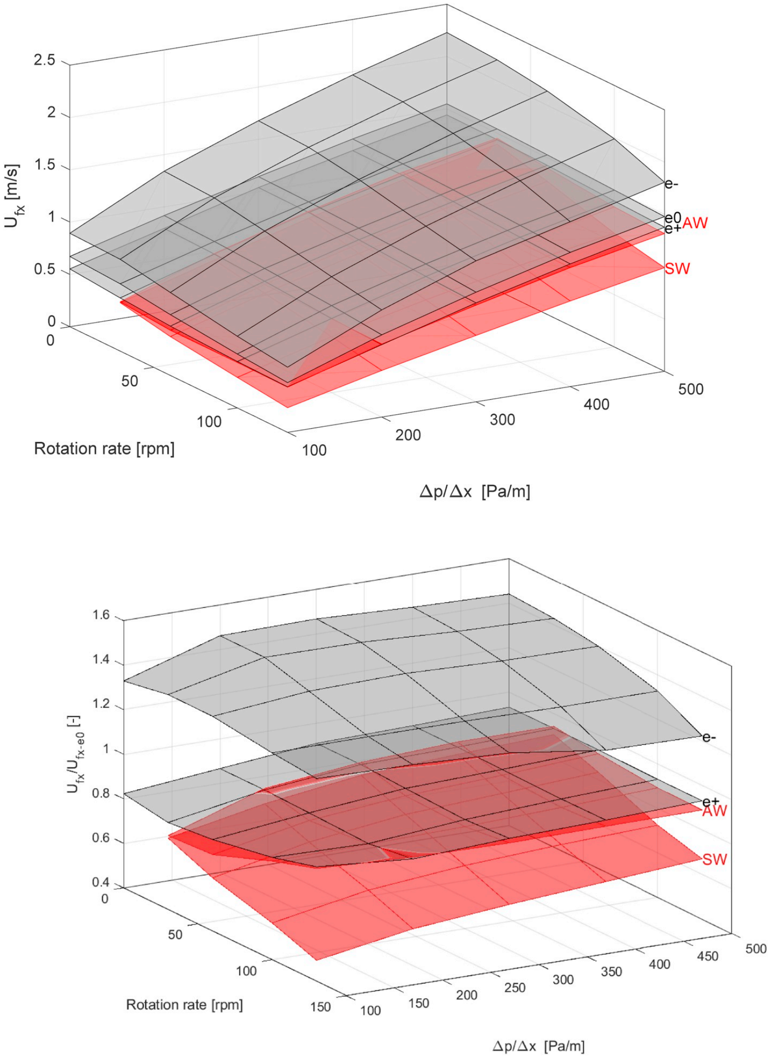

Fig. 13. Top: Absolute fluid superficial velocity vs. drill pipe rotation rate and pressure gradient for H2O and the systems defined in Fig. 3. Bottom: Relative change of the fluid superficial velocity based on the concentric system e0.

Finally, in the case of PAC, the discrepancies between CFD and experimental results as well as the friction factor correlations may be attributed to the viscoelastic and/or drag-reducing capabilities of the PAC solutions utilized (Alexander Busch et al., 2018b). The Generalized Newtonian Fluid framework with the PL material function does neither account for normal stress differences nor for elongational viscosity, both of which affect flows in eccentric annuli with the latter also affecting rotational flows (Escudier et al., 2002). Moreover, while the employed k-ω SST model is versatile regarding $y+$ values it does neither consider n_{PL} -dependent damping functions (e.g. Malin, 1997) nor non-Newtonian wall functions (e.g. Johansen and Mo, 2015) in the $y+ < 1$ and $y+ > 30$ regimes, respectively.

4.2. Cuttings transport – plain drill pipe rotation

Focusing on the plain drill pipe rotation cases first, the positive eccentric case generally leads to much better hole cleaning than the eccentric case, in line with other studies (Bicalho et al., 2016a; Heydari et al., 2017). The more clearance between the drill pipe and the cuttings bed, the better the hole cleaning because of the higher fluid velocities below the drill pipe and on top of the sediment bed. Consequently, the shear stress acting on the bed is much higher for a positive eccentric drill pipe than for a negative eccentric one, hence the better *CTR* and *ROP* values. This is physically sound and in accordance with the often-stated order when it comes to the relevance of individual cuttings transport parameters: Volumetric fluid flow rate is typically considered the most important parameter, simply because it is just the axial flow components which transports solids. Drill pipe rotation is an additional contributing factor which depends on the flow regime, fluid rheological parameters, and, as shown, eccentricity. It is important to note that the results were obtained for a total solid volume fraction $\alpha_s = 0.047$. Larger values will lead to a higher cuttings bed in the computational domain, which will

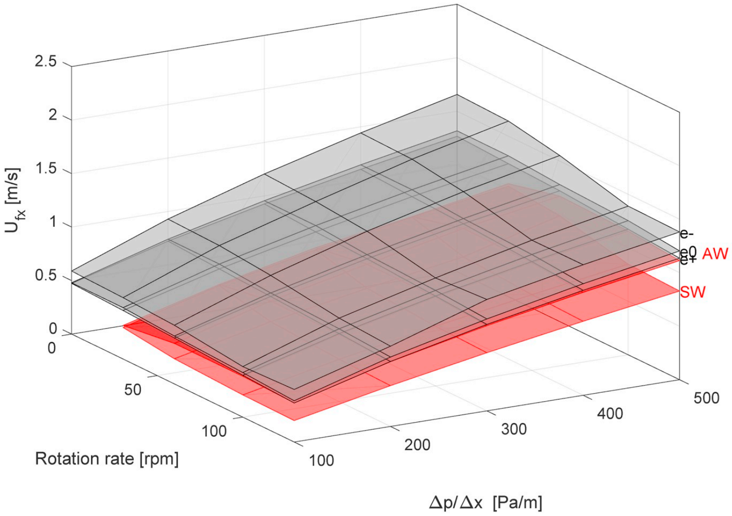

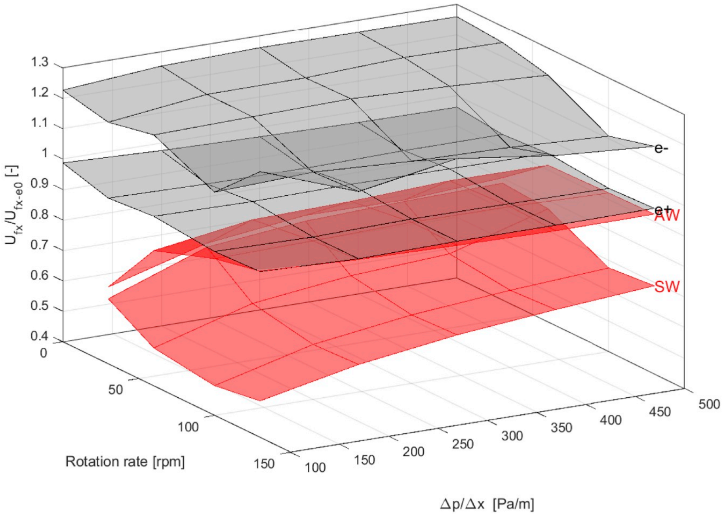

Fig. 14. Top: Absolute fluid superficial velocity vs. drill pipe rotation rate and pressure gradient for PAC and the systems defined in Fig. 3. Bottom: Relative change of the fluid superficial velocity based on the concentric system e0.

change the picture.

The effect of plain drill pipe rotation is highest for the negative eccentricity because the corresponding tangential velocities of the fluid and subsequently the solid phase act directly on the bed, agitate the bed and disperse solids into regions of higher fluid velocity, where they are easily transported downstream. This effect is less prominent in the other configurations. However, it is also less relevant for hole cleaning in the other configurations because of the aforementioned role of the locally higher fluid streamwise velocities and the higher shear stresses acting on the bed.

For a shear-thinning fluid in laminar flow, rotation may generally reduce the pressure gradient, i.e. increase the throughput for a given dp/dx. In contrast, in turbulent flow, rotation may increase the pressure gradient, i.e. decrease the throughput for a given dp/dx, as it increases the degree of turbulence. For the investigated shear-thinning PAC solution, this effect is very small, presumably because shear-thinning and turbulence generation are counteracting each other as the flow is in fact transitional rather than fully turbulent (see Fig. 18 in Appendix D). In addition, the presence of solids certainly overshadows this SP effect.

4.3. *Cuttings transport – whirling motion*

Assuming a concentric drill pipe as the base case, the presence of whirling motion generally increases both the *CTR* and the *ROP*. The same mechanism as for plain drill pipe rotation applies: The additional whirling motion leads to an increase in tangential and here additionally radial (with respect to the streamwise flow direction) velocities which help to agitate the sediment bed and disperse cuttings into the main flow regions and thus enhance cuttings transport. Note that in case of the shear-thinning PAC, the SW and AS *ROP* is less than for the concentric case and only for higher $\Delta p/\Delta x$ SW outperforms the concentric arrangement. The orbital drill pipe motion leads to two counteracting effects: (1) A reduction of the viscosity due to the additional applied shear and (2) the agitation of the bed due to the increase of turbulence and increased tangential/radial velocities, the.second one becoming dominant for higher $\Delta p/\Delta x$.

The SW significantly outperforms the AW because in case of SW both the tangential velocity induced by the drill pipe motion around its own axis and the radial velocity induced by the drill pipe orbital motion act in the same direction and are therefore additive. In case of AW, the plain drill pipe rotation is in the opposite direction of the drill pipe orbital motion and the respective velocities to some extent counteract each other.

In case of the PAC, the solids transport is highest for the positive eccentric case. For this geometrical arrangement, the rotation of the drill pipe around its own axis leads only to a minor shift of the cuttings bed towards the side of the annulus (Fig. 16 (top) in 5 Appendix A), with the majority of the helical flow pattern occurring on top of the main flow field. This is not so for the SW case (Fig. 16 (bottom) in 5 Appendix A), where the orbital motion of the drill pipe leads to a circumferentially alternating helical flow pattern affecting the entire volume of the annulus. While this is generally considered a positive feature in the sense of bed agitation, it also leads to a reduction in fluid throughput because much more fluid obeys the induced helical motion (Fig. 14). This is also the case for H2O SW (Fig. 13), where the difference lies in the magnitude of velocities and viscosities associated with the two fluids. In case of H2O SW, the circumferentially alternating helical flow pattern leads to much less tangential flow (Fig. 15 in 5 Appendix A) and hence allows for more throughput. This indicates that (synchronous) whirling motion is most effective in enhancing cuttings transport in presence of low viscosity fluids and larger rotation rates. However, more comprehensive data is required in order to adequately assess the coupled effect of whirling motion and fluid rheological properties.

An operational challenge currently discussed in the drilling industry is drilling with an *ROP* of 60 m/h and a drill pipe rotation rate of 60 rpm (Iversen and Islam, 2018). Figs. 11 and 12 suggest that this may be achieved by ensuring a positive eccentricity or SW state of the drill string in the wellbore in combination with a $dp/dx > 500$ Pa/m for H2O and $dp/dx > 250$ Pa/m for PAC. However, the quantitative results presented in Figs. 11 and 12 may not simply be applied to field scenarios because the modelling framework used is, for the multiphase part, neither validated nor tuned with experimental data.

4.4. *Strength and weaknesses*

The presented model and computational approach is a comparatively simple tool to analyze the effect of orbital drill pipe motion. As applied in this study, it allows for quantification of the effect of whirling motion on cuttings transport and qualitatively confirms the conclusion of Sanchez et al. (1999) that (if compared to an negative eccentric drill string arrangement) the orbital motion of the drill pipe is the major reason for significant improvement of cuttings transport.

While the model and code implementation as utilized in this study has been validated to a good extent by several other researchers (e.g. Amanna and Khorsand Movaghar, 2016; Epelle and Gerogiorgis, 2017; Kamyab and Rasouli, 2016; Pang et al., 2019, 2018) for the case of non-whirling flow cases (see Fig. 8), further validation work is required for the whirling cases. However, this requires experimental data where the kinematics of the orbital drill pipe motions are clearly quantified. i.e., a precise description of the drill string orbital motion is provided. If this is not so, any then required estimate of motion-relevant parameters likely leads to bad model predictions as the comparison of SP simulations and experimental results of Khatibi et al. (2018a, 2018b) has shown.

The design space must be analyzed more comprehensively. In terms of fluid rheological properties, more viscous fluids have to be investigated as well as the role of a potential yield stress in the presence of whirling motion. In addition, solid volume fractions, solid particle diameters, the pipe-hole-diameter combination and inclination, which is a critical parameter as it defines the potential for avalanches, is to be varied in order to obtain a broader quantitative picture of the relevance of whirling motion. Given enough data, one may then also transform the data easily into the more common $(\alpha_s, dp/dx) = f(U_f, \ldots)$ framework. More complex motion patterns need to be studied as we have just focused on easy-to-parametrize forward and backward whirl. Any slip between the drill pipe collars and the wellbore wall as well as detachment may occur in the wellbore. Furthermore, the presence of the cuttings bed will likely change the circular or elliptical orbital motion patterns typically utilized in the industry (due to their simple mathematical description). However, a bidirectional coupling of moving drill pipe structure and flow of fluid and solid phases is not reasonably possible on the annular scale as the structural deformation and associated non-flow forces depend on information up- and downstream of the annular domain under investigation.

While the applied GNF framework is the state-of-the-art in cuttings transport research, it does not account for potentially relevant physics such as thixotropy and viscoelasticity. Laboratory fluids such as CMC and PAC are known to act thixotropic and viscoelastic (Alexander Busch et al., 2018b), and the viscoelastic properties of drilling fluid systems as used in the field may lead to sediment bed cohesion (Werner, 2018) that is not captured by the GNF framework.

For higher superficial velocities, the model does not replicate pressure drop quantitatively well. Two effects come into play: (1) Too high values of the fluids viscosity are to be expected due to the utilized turbulence modelling approach, which will reduce particle settling and the mass flow rate for a given pressure gradient. As briefly mentioned in 5A.4, the RANS framework of commercial solvers in general and Fluent specifically does not account for the viscosity as a varying quantity. Generally, in RANS turbulence models, the rate of strain is defined as the symmetric part of the mean velocity field gradient. This neglects any additional variation due to the velocity fluctuations, which will lead to an underestimation of the rate of strain magnitude and thus overestimation of the fluid viscosity. Note that the same holds for other two-equation models such as the often-utilized k-ε-model. (2) The high-Re approach taken is based on Newtonian wall functions which will likely produce incorrect estimates of the respective near-wall quantities in the non-Newtonian case.

The transport rate of solids through the domain may be overestimated by an unknown extent. The Eulerian-Eulerian method employed in this study, i.e. the Two Fluid Model (TFM) continuum approach with the Kinetic Theory of Granular Flow (KTGF) and additional closures to handle the dense granular regime, as implemented in Fluent R17.2, does not produce angle of repose satisfying conditions in the absence of flow under all conditions (Busch and Johansen, 2018). Even for a horizontal bed under the sole influence of gravity, the top-layer always remains in a liquid-like state regardless of flow time. The KTFG dynamics act in a checkerboard-like manner ensuring a very low viscous solid phase, which in the concept of the TFM continuum approach should feature high solid viscosity levels representing the non-flowing sediment bed. According to these observations, it is expected that the solids bed will behave as “fluidized” in the simulations and that the solids flux may be overestimated. An alternative and with respect to the above mentioned overestimation of the solids transport rate better-suited modelling approach is the CFD-DEM framework (e.g. Akhshik et al., 2015; Zhang et al., 2016), which if combined with the periodic BC approach as used in this study may also allow reasonable computation times.

Another issue with the TFM-KTGF-SM approach is the potential violation of its inherent continuum assumption for specific combinations of system sizes and particle sizes (Goldschmidt et al., 2004). For instance, the smallest mesh size as a consequence of the dynamic meshing technique employed is approx. 1.04 mm, which is in the order of the particle size d_p. This may lead to an error in regions of high fluid velocity or pressure gradients since interaction forces between phases will be simply computed based on the respective cell values. However, the same applies for Lagrangian methods. Alternatives, such as Fluent’s Macroscopic Particle Model (Agrawal et al., 2004), are not fit for purpose due to the associated computational effort for the systems under consideration here.

The employed mesh moving feature of Fluent R17.2 led to severe mesh deformation with time. Depending on the orbital frequency, the mesh had to be replaced (i.e. the current solution is interpolated to a new mesh) after several seconds of flow time in order to avoid grid deterioration. The mesh motion feature of Fluent is not meant to be used for high rotational mesh deformation, therefore a sliding mesh approach as employed by Bicalho et al. (2016a, 2016b) may be the better choice.

The accuracy of the results may be increased by refining the mesh. This may be achieved at no additional computational costs by significantly shortening the domain since no streamwise development of any quantity was observed.

5. Conclusions & outlook

We have numerically investigated the role of whirling drill string motion on cuttings transport by means of CFD and a dynamic mesh technique. The essential findings are:

- In case of a negative eccentric annulus, whirling motion helps tremendously to disperse the solids into the main flow region and hence improves the quality of cuttings transport and hole cleaning. The effect is much more relevant for water than for the investigated more viscous, shear-thinning fluid because the latter already shows a good cuttings transport performance.
- Synchronous whirl is much better suited to agitate the bed and disperse cuttings than asynchronous whirl because the tangential and radial velocities add to each other.
- For the investigated parameter values, the positive eccentric annulus provides an even better cuttings transport capability for PAC being the carrier fluid. Whirling motion reduces the axial throughput, which despite the increased bed agitation results in worse performance compared to the positive eccentric case.
- The classical view of rotation being a relevant parameter for cuttings transports needs to be detailed: The cuttings transport research community needs to distinguish between plain drill pipe rotation around its own axis and rotation involving different types of whirling motion or more complex lateral motion patterns. Experimentalists are advised to carefully design their laboratory setups such that occurring whirling motion can be quantified.
- More research is required to explore the entire industry-relevant design space, i.e. other numerical values of the solid volume fraction, other fluids, inclination, and orbital motions. In addition, the laminar flow regime needs to be addressed. However, a bi-partisan approach is need where experimental work is conducted in order to validate and improve the simulation work.

CRediT authorship contribution statement

Alexander Busch: Conceptualization, Data curation, Formal analysis, Investigation, Methodology, Resources, Software, Validation, Visualization, Writing - original draft, Writing - review & editing. **Stein Tore Johansen:** Conceptualization, Formal analysis, Funding acquisition, Methodology, Project administration, Resources, Supervision, Writing - review & editing.

Acknowledgements

The project Advanced Wellbore transport Modeling (AdWell) with its sponsor, PETROMAKS 2/the Research Council of Norway (project 228391) and its partners Equinor, Neptune Energy Norge AS, NORCE, UiS, NTNU and SINTEF are gratefully acknowledged for funding and supporting this work. In addition, we are grateful for the computational resources provided at NTNU by UNINETT Sigma2 AS. Further, we thank the unknown reviewers for providing valuable input and improving the paper quality.

Appendix ASupplementary data

Supplementary data to this article can be found online at https://doi.org/10.1016/j.petrol.2020.107136.

Appendix A. Physical model

Appendix A1. The Cauchy equations of motion for a two-phase flow

In the TFM framework, the fluid (index f) as well as the solid (index s), phase are described as interpenetrating continua. Both fluid and solid are considered isothermal and incompressible.[6] For an arbitrary volume element V_i, the phase volume fractions α_i must therefore sum to one.

$$V_i = \int_V \alpha_i dV \quad \wedge \quad \sum_i \alpha_i = 1 \quad \wedge \quad i \in \{f, s\} \tag{6}$$

Mass conservation is given by

$$\frac{\partial}{\partial t}(\alpha_i \rho_i) + \nabla \cdot (\alpha_i \rho_i u_i) = 0 \tag{7}$$

where the index $i \in \{f, s\}$ and ρ_i and $\mathbf{u}_i$ denote the intrinsic volume averages of density and velocity, respectively.

Both phases obey a general form of the Cauchy momentum transport equation, which for the fluid and solid phase respectively reads

$$\frac{\partial}{\partial t}(\alpha_f \rho_f \mathbf{u}_f) + \nabla \cdot (\alpha_f \rho_f \mathbf{u}_f \mathbf{u}_f) = -\alpha_f \nabla p_f + \nabla \cdot (\alpha_f \boldsymbol{\tau}_f) + \alpha_f \rho_f \mathbf{g} - \frac{1}{V} \sum_{p \in V} \mathbf{f}_j, \tag{8}$$

$$\frac{\partial}{\partial t}(\alpha_s \rho_s \mathbf{u}_s) + \nabla \cdot (\alpha_s \rho_s \mathbf{u}_s \mathbf{u}_s) = -\alpha_s \nabla p_f - \nabla p_s + \nabla \cdot \boldsymbol{\tau}_s + \alpha_s \rho_s \mathbf{g} + \frac{1}{V} \sum_{p \in V} \mathbf{f}_j, \tag{9}$$

where $\boldsymbol{\tau}_i$ is the phasic deviatoric stress tensor comprising some constitutive equation, here a compressible Generalized Newtonian Fluid (GNF) and phase-dependent material functions for the shear and bulk viscosities, η_i and κ_i,

$$\boldsymbol{\tau}_i = 2\eta_i \mathbf{D}_i + \left(\kappa_i - \frac{2}{3}\eta_i\right)(\nabla \cdot \mathbf{u}_i)\mathbf{I}, \tag{10}$$

where $\mathbf{D}_i$ is the symmetric part of the fluid or solid velocity gradient (also known as the rate of deformation tensor, or alternatively the rate of strain tensor)

$$\mathbf{D}_i = \frac{1}{2}\left(\nabla \mathbf{u}_i + \nabla \mathbf{u}_i^T\right) \tag{11}$$

and the shear rate $\dot{\gamma}_i$ is the magnitude of the rate of deformation tensor $\mathbf{D}_i$,

$$\dot{\gamma}_i = \sqrt{2D_i : D_i} \tag{12}$$

The closures for the granular phase are provided in section A.3 and the rheological closures of the fluid are provided in section A.2.

As we are not solving these balance equations to the smallest length scales of the flow, the phenomenon of turbulence is to be modeled. Performing Reynolds averaging (Reynolds, 1895) of the instantaneous balance equations for mass and momentum, a so-called Reynolds stress term $\nabla \cdot (-\rho \overline{\mathbf{u}' \mathbf{u}'})$ arises in the now ensemble-averaged momentum conservation equation. The Reynolds or turbulent stress tensor $\boldsymbol{\tau}_{i,t} = -\rho_i \overline{\mathbf{u}_i' \mathbf{u}_i'}$ is usually assumed symmetric and may be modeled by applying the Boussinesque (1877) hypothesis, also known as the gradient diffusion hypothesis, to relate the Reynolds stresses to the mean velocity gradients and the turbulent viscosity in the form of

$$\tau_{i,t} = -2\mu_{i,t} D_i \tag{13}$$

The employed closures for the turbulent (or eddy) viscosity $\mu_{i,t}$ used in the constitutive equation for the turbulent stress tensor $\boldsymbol{\tau}_{i,t}$ are further detailed in section A.4.

The last terms in equations (8) and (9) are representing the momentum transfer of one phase to the other, where the force sum is to be taken over all particles in the volume V. We here only consider the drag force $\mathbf{f}_D$, which is typically modeled based on the relative velocity

$$\mathbf{u}_r = \mathbf{u}_s - \mathbf{u}_f \tag{14}$$

as

$$\frac{1}{V} \sum_{p \in V} \mathbf{f}_j = K \mathbf{u}_r, \tag{15}$$

To model the interphase exchange coefficient K, we apply the formulation of Gidaspow et al. (1992), which is a combination of the Wen and Yu (1966) model and the Ergun (1952) equation, where the interphase exchange coefficient K is given as

---

[6] Note that the solid phase may feature some closure law which accounts for the compressibility of granular matter.

$$\begin{aligned} \alpha_s \leq 0.2: \quad & K = c_D \frac{3\alpha_s \rho_f \|\mathbf{u}_r\|}{4\alpha_f^{0.65} d_s} \\ \alpha_s > 0.2: \quad & K = 150 \frac{\alpha_s^2 \eta_f}{\alpha_f d_s^2} + 1.75 \frac{\alpha_s \rho_f \|\mathbf{u}_r\|}{d_s} \end{aligned} \tag{16}$$

with the coefficient of drag described as

$$c_D = \frac{24}{\alpha_f \mathrm{Re}_p} \left(1 + 0.15 \left(\alpha_f \mathrm{Re}_p\right)^{0.687}\right), \tag{17}$$

and the particle Reynolds number defined as

$$\mathrm{Re}_p = \frac{\rho_f d_s \|u_r\|}{\eta_f} \tag{18}$$

Appendix A.2. Rheological closures of the fluid phase

We are here concerned with either Newtonian (constant viscosity, e.g. $\eta_f = 0.001002$ Pa s for water) or purely shear-thinning fluids which obey the GNF constitutive equation (10) with $\kappa_f = 0$ assuming incompressibility. In case of shear-thinning fluids the most simple formulation of the viscosity η_f accounting for shear-thinning behavior is the Ostwald (1925) material function, also known as power law (PL),

$$\eta_f(\dot{\gamma}) = K_{PL} \dot{\gamma}^{n_{PL}-1} \tag{19}$$

Drilling fluids may feature a yield stress and are therefore typically described with the Herschel and Bulkley (1926) material function, also known as Yield Power Law (YPL). However, we here limit ourselves to PL fluids as the experimental data used for SP validation is based on a PL fluid.

Appendix A.3. Rheological closures of the solid phase

If the TFM-KTGF framework is used to describe dense granular flows, the entire solid stress tensor, namely equation (10) with index s and including the solid pressure p_s, is given by the sum of collisional/kinetic and frictional components (Savage, 1983)

$$T_s = T_{s,k/c} + T_{s,f} = \sum_{j \in \{k/c,\ f\}} \left[\left(-p_{s,j} + \left(\kappa_{s,j} - \frac{2}{3} \eta_{s,j} \right) \nabla \cdot u_s \right) I + 2 \eta_{s,j} D_s \right] \tag{20}$$

Even though the general stencil is that of a compressible Newtonian fluid, namely equation (10), the rheological properties of the solid phase given by the respective material functions as summarized in Table 5 are highly non-linear as they depend on a variety of variables.

Table 5
Overview of solid phase state equations and material functions used to model the kinetic/collisional (index k/c) and frictional (index f) regimes.

Regime	Quantity	Equation	Source
Kinetic and collisional ($j = k/\ c$)	Pressure	$p_{s,k/c} = \alpha_s \rho_s \Theta_s + 2\alpha_s^2 \rho_s \Theta_s (1 + e_{ss}) g_{0,ss}$ (21)	Lun et al. (1984)
	Shear viscosity	$\eta_{s,c} = \frac{4}{5} \alpha_s^2 \rho_s d_s g_{0,ss} (1 + e_{ss}) \left(\frac{\Theta_s}{\pi}\right)^{\frac{1}{2}}$ (22)	Lun et al. (1984)
	Shear viscosity	$\eta_{s,k} = \frac{10 \rho_s d_s \sqrt{\Theta_s \pi}}{96(1 + e_{ss}) g_{0,ss}} \left(1 + \frac{4}{5} \alpha_s (1 + e_{ss}) g_{0,ss}\right)^{\frac{1}{2}}$ (23)	Gidaspow et al. (1992)
	Bulk viscosity	$\kappa_{s,c/k} = \frac{4}{3} \alpha_s^2 \rho_s d_s g_{0,ss} (1 + e_{ss}) \left(\frac{\Theta_s}{\pi}\right)^{\frac{1}{2}}$ (24)	Lun et al. (1984)
Frictional ($j = f$)	Pressure	$p_{s,f} = 0.05 \frac{\left(\alpha_s - \alpha_{s,f}\right)^2}{\left(\alpha_{s,mpd} - \alpha_s\right)^5}$ (25)	Johnson and Jackson (1987)
	Shear viscosity	$\eta_{s,f} = \frac{p_s \sin \varphi_s}{\sqrt{2} \|\mathbf{D}_s\|}$ (26)	Schaeffer (1987)
	Bulk viscosity	n/a	n/a

For instance, for vanishing shear rates in the frictional regime, a

Bingham-type flow behavior is obtained due to the yield feature inherent in equation (26). The kinetic/collisional closures given in Table 5 are functions of the granular temperature Θ_s as a measure for the degree of random particle motion, for which the transport equation reads (Ding and Gidaspow, 1990)

$$\frac{3}{2}\left[\frac{\partial}{\partial t}(\alpha_s\rho_s\Theta_s)+\nabla\cdot(\alpha_s\rho_s u_s\Theta_s)\right]=T_s:\nabla u_s+\nabla\cdot(k_{\Theta_s}\nabla\Theta_s)-D_{\Theta_s}+K_{fs} \tag{27}$$

where k_{Θ_s} is the granular conductivity (e.g. Syamlal et al., 1993) and the granular temperature Θ_s, a measure for the granular fluctuations due to individual particle collisions, is defined as

$$\Theta_s=\frac{1}{3}\langle u_{s,i}^{'}u_{s,i}^{'}\rangle \tag{28}$$

Here, $u_{s,i}$' is the i -th fluctuating component of the solids velocity in the Cartesian coordinate system and the bracket represents an ensemble average of the fluctuating velocities of all particles within a finite volume and time period (Ding and Gidaspow, 1990).

The partial differential equation (21) can be simplified to an algebraic equation by neglecting the convection and diffusion terms – an often used assumption in dense, slow moving fluidized beds, where the local generation and dissipation of granular temperature far outweigh the transport by convection and diffusion. The two final terms in equation (21) are the collisional dissipation of energy (Lun et al., 1984) and the interphase exchange between the particle fluctuations and the liquid phase (Gidaspow et al., 1992).

In equations (21)-(24), $e_{ss}=0.9$ is the coefficient of restitution for particle collisions and

$$g_{0,ss}=\left[1-\left(\frac{\alpha_s}{\alpha_{s,\max}}\right)^{\frac{1}{3}}\right]^{-1} \tag{29}$$

is the radial distribution function accounting for the probability of particle collisions, which has been used frequently in the history of granular flows (Bagnold, 1954; Lun et al., 1984; Ogawa et al., 1980; Sinclair and Jackson, 1989) in the form presented in equation (23).

Appendix A.4. Turbulence closures

Concerning the fluid phase, we here use the Shear Stress Transport (SST) k - ω model (Menter, 1994, 1993), because of its suitability for swirling flows, the possibility to either integrate it to the laminar sublayer or apply wall functions, and because it correctly collapses to the laminar solution in case of laminar flows.

Dropping the fluid index f, the turbulent viscosity is defined as

$$\mu_t=l\frac{\rho k}{\omega} \tag{30}$$

where l is a limiter coefficient ensuring that overprediction of the turbulent viscosity is avoided and therefore enabling the SST k - ω model to better predict the onset and amount of flow separation from smooth surfaces.

The two transport equations for the turbulent kinetic energy k and the specific dissipation ω are

$$\frac{\partial}{\partial t}(\rho k)+\frac{\partial}{\partial x_i}(\rho k u_i)=\frac{\partial}{\partial x_j}\left[\left(\mu+\frac{\mu_t}{\sigma_k}\right)\frac{\partial k}{\partial x_j}\right]+G_k-Y_k \tag{31}$$

and

$$\frac{\partial}{\partial t}(\rho\omega)+\frac{\partial}{\partial x_i}(\rho\omega u_i)=\frac{\partial}{\partial x_j}\left[\left(\mu+\frac{\mu_t}{\sigma_\omega}\right)\frac{\partial\omega}{\partial x_j}\right]+G_\omega-Y_\omega+D_\omega \tag{32}$$

where σ_i are the respective turbulent Prandtl numbers, G_i are respective production terms, Y_i are respective dissipation terms and D_ω is a cross diffusion term, which arises in equation (26) as a consequence of the blending of the standard k - ω model and the standard k - ε model (converted to a k - ω formulation). For further details as well as all relevant closures of the model, the reader is referred to Menter (1994, 1993).

The solid phase turbulence is also described with a turbulent viscosity, i.e. equation (13). However, the turbulence quantities of the solid phase are obtained from the fluid phase by applying the Tchen theory of dispersion of discrete particles by homogenous turbulence.as given by Simonin and Viollet (1990).

To our knowledge, no non-Newtonian modifications—for instance in the form of damping functions as for the k - ε model (Malin, 1997) or in the form of additional closures for averaged apparent viscosity and turbulent cross-correlations with fluctuating viscosity as a consequence of Reynolds-averaging of the non-constant viscosity (Gavrilov and Rudyak, 2016)—have so far been developed for the k - ω family of models. Hence, we employ the SST k - ω model as implemented in Fluent, and some inaccuracy is expected in the case of non-Newtonian liquids.

Appendix B. CFD velocity field plots

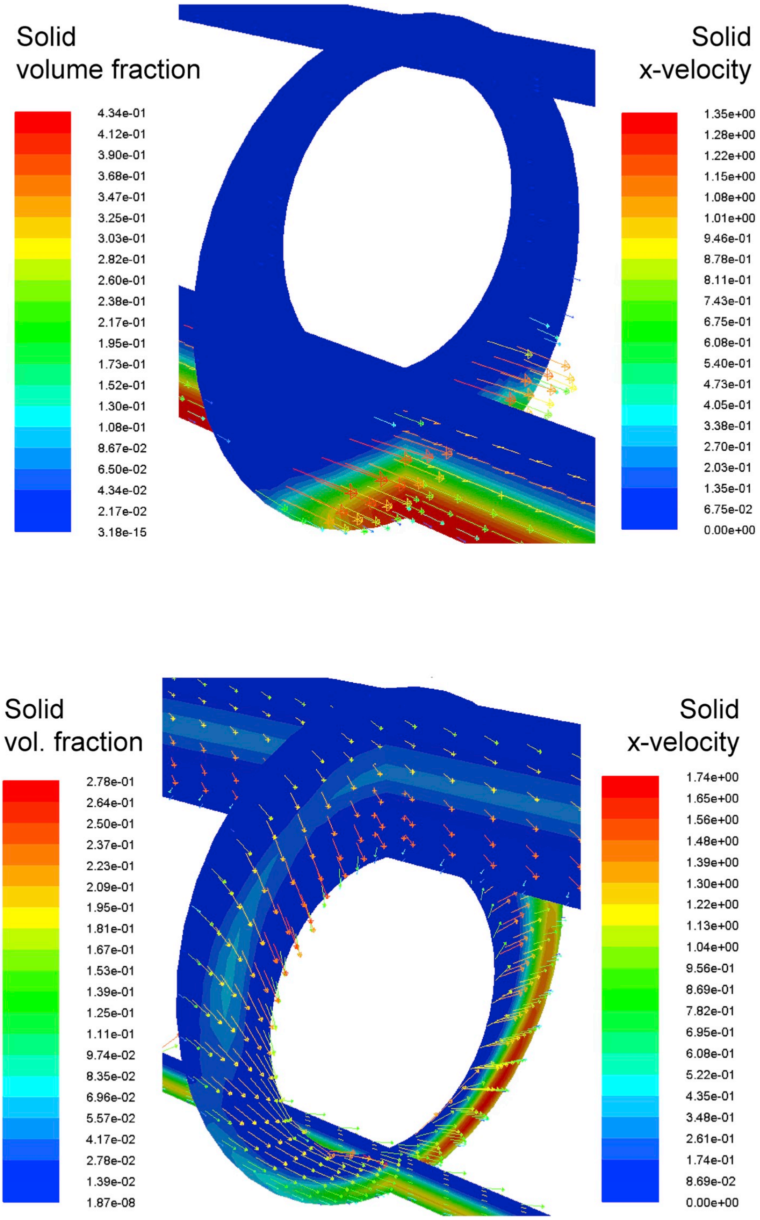

Fig. 15. α_s and $\boldsymbol{u}_s$ fields for e+ (top) and SW (bottom, lower drill pipe position depicted, full video available at https://youtu.be/vw4LUL3dF-c), H2O, $dp/\ dx = -500$ Pa/m and 130 rpm.

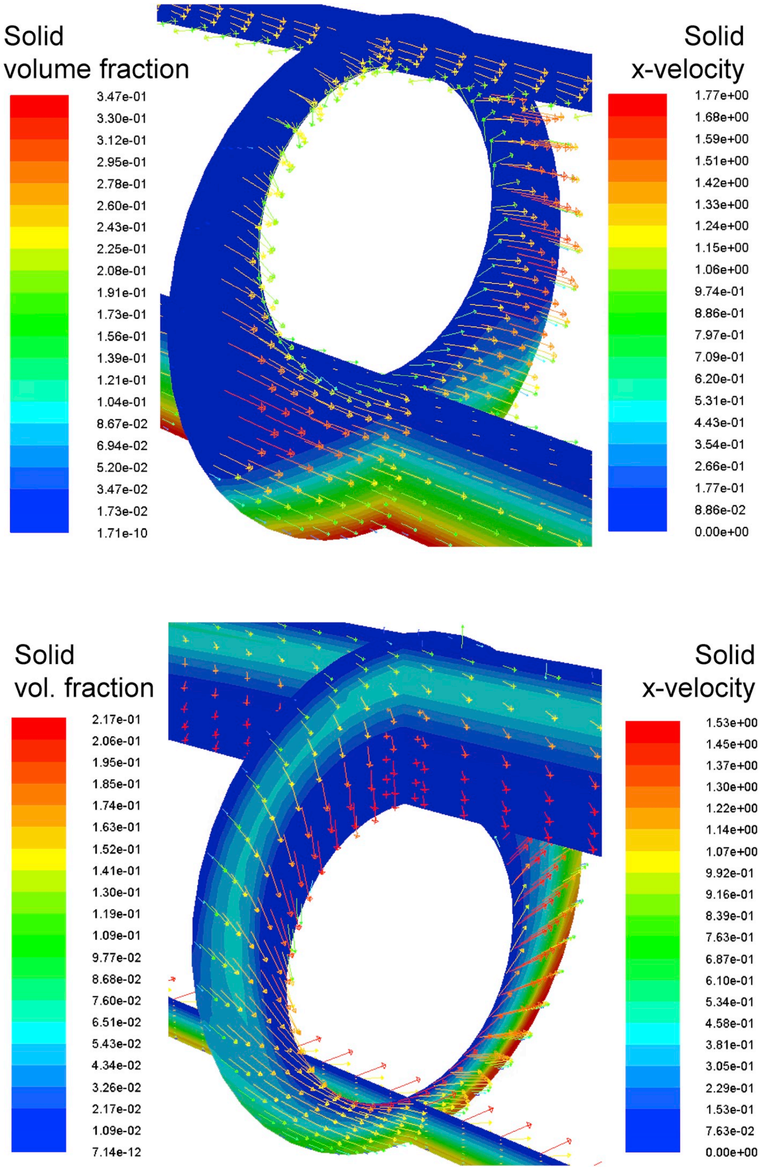

Fig. 16. α_s and $\boldsymbol{u}_s$ fields for e+ (top) and SW (bottom, lower drill pipe position depicted, full video available at https://youtu.be/bbkj9hh8rYw), PAC, $dp/\,dx = -500$ Pa/m and 130 rpm.

Appendix C. Experimental data

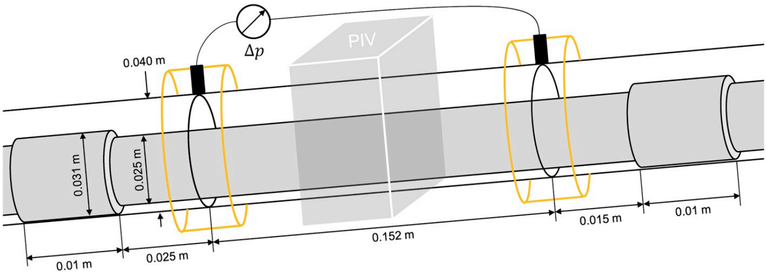

Fig. 17. Annular test section of (Khatibi et al., 2018a, 2018b).

Table 6
Eccentricity E_y and amplitude A_y as observed by (Khatibi et al., 2018a, 2018b) and courtesy of Khatibi (2018).

Q_f [m^3/s]	U_{sf} [m/s]	*rpm* [1/min]	E_y [m]	A_y [m]	$E_y + A_y$ [m]	e_{max} [-]	e_{min} [-]
0.000E+00	0.0000	0.0000	−0.0071	0.0000	−0.0071	−0.94	−0.94
0.000E+00	0.0000	100.0000	−0.0065	0.0046	−0.0019	−0.86	−0.25
0.000E+00	0.0000	200.0000	−0.0058	0.0038	−0.0020	−0.78	−0.27
0.000E+00	0.0000	300.0000	−0.0045	0.0016	−0.0028	−0.60	−0.38
2.600E-04	0.3395	0.0000	−0.0069	0.0000	−0.0069	−0.93	−0.93
2.600E-04	0.3395	100.0000	−0.0064	0.0041	−0.0023	−0.85	−0.31
2.600E-04	0.3395	200.0000	−0.0057	0.0043	−0.0014	−0.76	−0.18
2.600E-04	0.3395	300.0000	−0.0042	0.0022	−0.0020	−0.56	−0.27
4.100E-04	0.5354	0.0000	−0.0069	0.0000	−0.0069	−0.93	−0.93
4.100E-04	0.5354	100.0000	−0.0064	0.0038	−0.0026	−0.85	−0.34
4.100E-04	0.5354	200.0000	−0.0050	0.0027	−0.0023	−0.67	−0.31
4.100E-04	0.5354	300.0000	n/a	n/a	n/a	n/a	n/a
9.400E-04	1.2275	0.0000	−0.0061	0.0000	−0.0061	−0.82	−0.82
9.400E-04	1.2275	100.0000	−0.0056	0.0035	−0.0020	−0.74	−0.27
9.400E-04	1.2275	200.0000	n/a	n/a	n/a	n/a	n/a
9.400E-04	1.2275	300.0000	n/a	n/a	n/a	n/a	n/a

Appendix D. Flow regimes

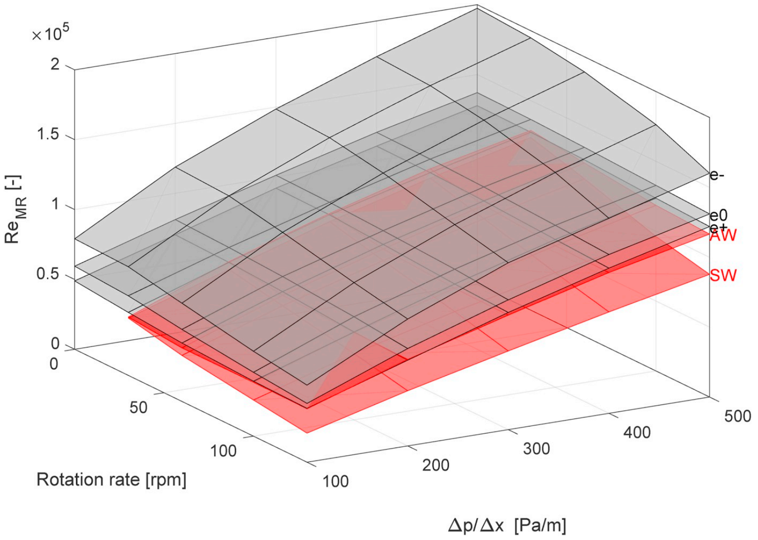

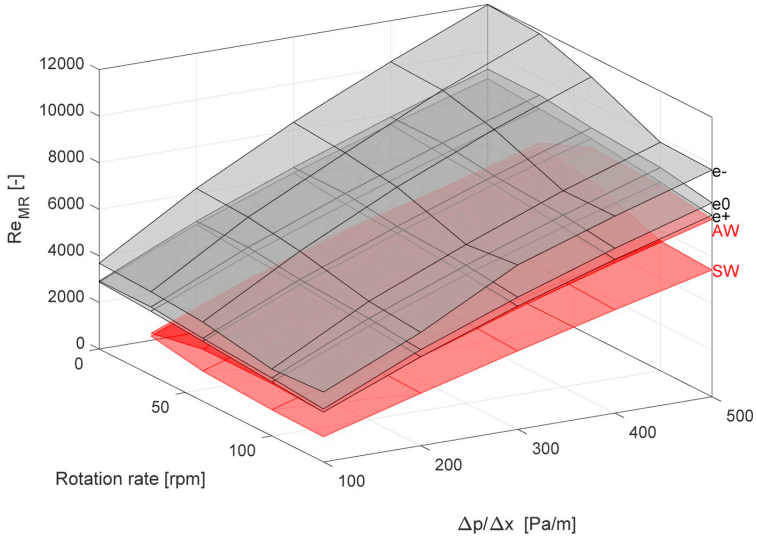

Fig. 18. Metzner and Reed (1955) Reynolds number vs. drill pipe rotation rate and pressure gradient for H2O (top) and PAC (bottom). See Table 3 and Fig. 3 for the test matrix and the system definition, respectively.

Appendix E. Mesh dependence

Table 7
Parameters of the different meshes ($d_i = 0.127$ m, $d_o = 0.216$ m, $L = 0.1$ m $e_y = e_z = 0$) used for the mesh dependency investigation. The coarse mesh is a so-called high Reynolds number mesh where wall functions are used, the superfine mesh is a so-called low Reynolds number mesh, where the wall layer is fully resolved.

	Coarse (High Re)	Intermediate (SP)	Intermediate (MP)	Fine	Superfine (Low Re)
Cells in x-direction	5	10	32	20	40
Cells in r-direction	5	10	10	20	40
Cells in θ-direction	20	40	40	40	160
Δx [m]	0.0200	0.0100	0.0203	0.0050	0.0025
Δr [m]	0.0089	0.0045	0.0045	0.0022	0.0011

(*continued on next page*)

Table 7 (*continued*)

	Coarse (High Re)	Intermediate (SP)	Intermediate (MP)	Fine	Superfine (Low Re)
Δ θ [m]	0.0269	0.0135	0.0135	0.0135	0.0034
1st layer height [m]	0.0075	0.002	0.001	0.00085	0.00025
Total cells	500	4000	12800	16000	256000

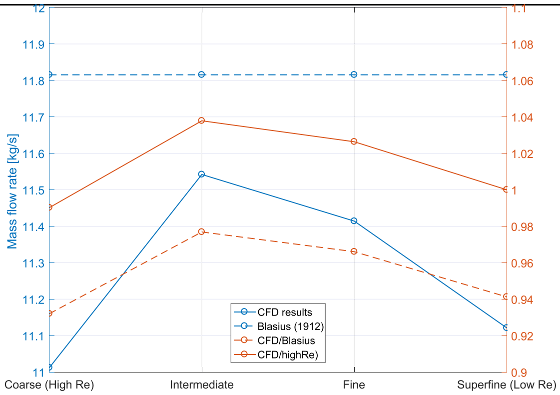

Fig. 19. Mesh dependency of SP water flow (no rotation) for the meshes defined in Table 7 and a pressure difference of $\Delta p/\Delta x = 30$ Pa/m. When comparing the CFD results to the Blasius friction factor correlation, the difference is in the order of −3 … -6% (dashed brown curve). When comparing the simulation results to the low Reynolds number superfine mesh where the wall layer is fully resolved, the difference is in the order of −1 … 4% (solid brown curve). (For interpretation of the references to colour in this figure legend, the reader is referred to the Web version of this article.).

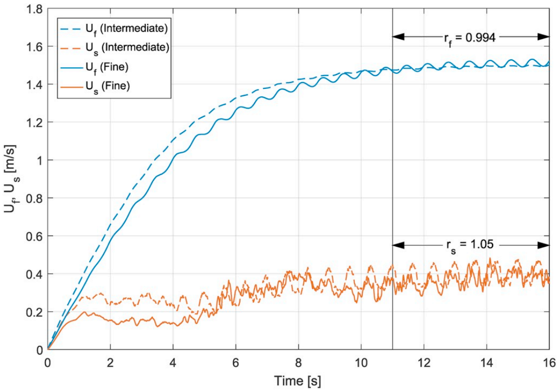

Fig. 20. Mesh dependency of MP water-solid flow for the Coarse and Intermediate meshes defined in Table 7 and a pressure difference of $\Delta p/\ \Delta x = 500$ Pa. For the time interval 11 … 16 s, the quantity r_i represents the ratio of U_i^{Coarse}/U_i^{Fine}.

References

Agrawal, M., Bakker, A., Prinkey, M.T., 2004. Macroscopic particle model - tracking big particles in CFD. In: The Proceeding of AIChE 2004 Annual Meeting. Presented at the AIChE 2004 Annual Meeting. AIChE, Austin, TX.

Ahmed, R.M., Enfis, M.S., El Kheir, H.M., Laget, M., Saasen, A., 2010. The effect of drillstring rotation on equivalent circulation density: modeling and analysis of field measurements. In: SPE Annual Technical Conference and Exhibition. Presented at the SPE Annual Technical Conference and Exhibition. Society of Petroleum Engineers, Florence, Italy. https://doi.org/10.2118/135587-MS.

Akhshik, S., Behzad, M., Rajabi, M., 2015. CFD–DEM approach to investigate the effect of drill pipe rotation on cuttings transport behavior. J. Petrol. Sci. Eng. 127, 229–244. https://doi.org/10.1016/j.petrol.2015.01.017.

Amanna, B., Khorsand Movaghar, M.R., 2016. Cuttings transport behavior in directional drilling using computational fluid dynamics (CFD). J. Nat. Gas Sci. Eng. 34, 670–679. https://doi.org/10.1016/j.jngse.2016.07.029.

ANSYS, Inc, 2016. ANSYS Fluent User Guide R17.2. ANSYS, Inc., Canonsburg, PA.

ANSYS, Inc, 2016. ANSYS Fluent Theory Guide R17.2. ANSYS, Inc., Canonsburg, PA.

Avila, R.J., Pereira, E.J., Miska, S.Z., Takach, N.E., 2008. Correlations and analysis of cuttings transport with aerated fluids in deviated wells, pp. 132–141. https://doi.org/10.2118/87180-PA. SPE-87180-PA 23.

Bagnold, R.A., 1954. Experiments on a gravity-free dispersion of large solid spheres in a Newtonian fluid under shear. Proc. Roy. Soc. Lond. Math. Phys. Sci. 225, 49–63. https://doi.org/10.1098/rspa.1954.0186.

Bassal, A.A., 1996. The Effect of Drillpipe Rotation on Cuttings Transport in Inclined Wellbores (Master's Thesis). Department of Petroleum Engineering, University of Tulsa.

Bicalho, I.C., dos Santos, D.B.L., Ataíde, C.H., Duarte, C.R., 2016a. Fluid-dynamic behavior of flow in partially obstructed concentric and eccentric annuli with orbital motion. J. Petrol. Sci. Eng. 137, 202–213. https://doi.org/10.1016/j.petrol.2015.11.029.

Bicalho, I.C., Mognon, J.L., Ataíde, C.H., Duarte, C.R., 2016b. Fluid dynamics study of the flow and pressure drop analysis of a non-Newtonian fluid through annular ducts with unusual cross-sections. Can. J. Chem. Eng. 94, 391–401. https://doi.org/10.1002/cjce.22401.

Bilgesu, H.I., Ali, M.W., Aminian, K., Ameri, S., 2002. Computational fluid dynamics (CFD) as a tool to study cutting transport in wellbores. In: Presented at the SPE Eastern Regional Meeting. Society of Petroleum Engineers, Lexington. https://doi.org/10.2118/78716-MS.

Blasius, H., 1912. Das Aehnlichkeitsgesetz bei Reibungsvorgängen. Z. Des. Vereines Dtsch. Ingenieure 19, 639.

Bourgoyne, A.T., Millheim, K.K., Chevenert, M.E., Young Jr., F.S., 1991. Applied Drilling Engineering, second ed. SPE Textbook Series. Society of Petroleum Engineers, Richardson, TX.

Boussinesque, J., 1877. Essai sur la theories des eaux courantes. Tome XXIII (1).

Busch, A., Islam, A., Martins, D., Iversen, F.P., Khatibi, M., Johansen, S.T., Time, R.W., Meese, E.A., 2018a. Cuttings transport modeling - Part 1: specification of benchmark parameters with a Norwegian continental shelf perspective, 33. SPE Drilling & Completion. https://doi.org/10.2118/180007-PA.

Busch, A., Johansen, S.T., 2018. On the validity of the two-fluid-KTGF approach for dense gravity-driven granular flows. In: Book of Abstracts. Presented at the the 2nd International Symposium on Computational Particle Technology (CPT-2018), CSIRO. Monash University, Melbourne.

Busch, Alexander, Myrseth, V., Khatibi, M., Skjetne, P., Hovda, S., Johansen, S.T., 2018b. Rheological characterization of Polyanionic Cellulose solutions with application to drilling fluids and cuttings transport modeling. Appl. Rheol. 28, 1–16. https://doi.org/10.3933/ApplRheol-28-25154.

Busch, A., Werner, B., Johansen, S.T., 2019. Cuttings transport modeling - Part 2: dimensional analysis and scaling. SPE Drilling & Completion Preprint. https://doi.org/10.2118/198907-PA.

Cayeux, E., Skadsem, H.J., Carlsen, L.A., Stokland, L.M., Cruikshank, S., 2018. Analysis of asymmetric tool-joint wear while drilling long horizontal sections. In: SPE Norway One Day Seminar. Presented at the SPE Norway One Day Seminar. Society of Petroleum Engineers, Bergen, Norway. https://doi.org/10.2118/191339-MS.

Çengel, Y.A., Cimbala, J.M., 2006. Fluid mechanics: fundamentals and applications, McGraw-Hill Series in Mechanical Engineering. McGraw-HillHigher Education, Boston.

Demiralp, Y., 2014. Effects of Drill-Pipe Whirling Motion on Cuttings Transport Performance for Horizontal Drilling. Master Thesis. Lousiana State University.

Ding, J., Gidaspow, D., 1990. A bubbling fluidization model using kinetic theory of granular flow. AIChE J. 36, 523–538. https://doi.org/10.1002/aic.690360404.

Dodge, D.W., Metzner, A.B., 1959. Turbulent flow of non-Newtonian systems. AIChE J. 5, 189–204. https://doi.org/10.1002/aic.690050214.

Dosunmu, I.T., Shah, S.N., 2015. Friction pressure prediction for annular flow of power law fluids. Chem. Eng. Commun. 202, 1380–1388. https://doi.org/10.1080/00986445.2014.938806.

Duan, M., Miska, S., Yu, M., Takach, N.E., Ramadan, A., Hallman, J.H., 2010. Experimental study and modeling of cuttings transport using foam with drillpipe rotation. SPE Drill. Complet. 25 https://doi.org/10.2118/116300-PA.

Duan, M., Miska, S.Z., Yu, M., Takach, N.E., Ramadan, A., Zettner, C.M., 2008. Transport of small cuttings in extended-reach drilling. SPE Drill. Complet. 23 https://doi.org/10.2118/104192-PA.

Epelle, E.I., Gerogiorgis, D.I., 2017. Transient and steady state analysis of drill cuttings transport phenomena under turbulent conditions. Chem. Eng. Res. Des. https://doi.org/10.1016/j.cherd.2017.11.023.

Erge, O., Ozbayoglu, E.M., Miska, S., Yu, M., Takach, N., Saasen, A., May, R., 2015. The effects of drillstring-eccentricity, -rotation, and -buckling configurations on annular frictional pressure losses while circulating yield-power-law fluids. SPE Drill. Complet. 30, 257–271. https://doi.org/10.2118/167950-PA.

Erge, O., Ozbayoglu, E.M., Miska, S.Z., Yu, M., Takach, N., Saasen, A., May, R., 2014. The effects of drillstring eccentricity, rotation, and buckling configurations on annular frictional pressure losses while circulating yield power law fluids. In: SPE-167950-MS. Society of Petroleum Engineers. https://doi.org/10.2118/167950-MS. SPE.

Ergun, S., 1952. Fluid flow through packed columns. Chem. Eng. Prog. 48, 89–94.

Escudier, M.P., Oliveira, P.J., Pinho, F.T., 2002. Fully developed laminar flow of purely viscous non-Newtonian liquids through annuli, including the effects of eccentricity and inner-cylinder rotation. Int. J. Heat Fluid Flow 23, 52–73. https://doi.org/10.1016/S0142-727X(01)00135-7.

Feng, S., Li, Q., Fu, S., 2007. On the orbital motion of a rotating inner cylinder in annular flow. Int. J. Numer. Methods Fluid. 54, 155–173. https://doi.org/10.1002/fld.1388.

Gao, G., 2010. Dynamic buckling and snaking motion of rotating drilling pipe in a horizontal well. SPE J. 11.

Gavrilov, A.A., Rudyak, V.Y., 2016. Reynolds-averaged modeling of turbulent flows of power-law fluids. J. Non-Newtonian Fluid Mech. 227, 45–55. https://doi.org/10.1016/j.jnnfm.2015.11.006.

Gidaspow, D., Bezburuah, R., Ding, J., 1992. Hydrodynamics of circulating fluidized beds: kinetic theory approach. In: Fluidization VII, Proceedings of the 7th Engineering Foundation Conference on Fluidization. Presented at the 7th International Conference on Fluidization, Gold Coast.

Goldschmidt, M.J.V., Beetstra, R., Kuipers, J.A.M., 2004. Hydrodynamic modelling of dense gas-fluidised beds: comparison and validation of 3D discrete particle and continuum models. Powder Technol. 142, 23–47. https://doi.org/10.1016/j.powtec.2004.02.020.

Haaland, S.E., 1983. Simple and explicit formulas for the friction factor in turbulent pipe flow. J. Fluid Eng. 105, 89–90. https://doi.org/10.1115/1.3240948.

Haciislamoglu, M., Cartalos, U., 1994. Practical pressure loss predictions in realistic annular geometries. In: SPE-28304-MS. Society of Petroleum Engineers. https://doi.org/10.2118/28304-MS. SPE.

Haciislamoglu, M., Langlinais, J., 1990. Non-Newtonian flow in eccentric annuli. J. Energy Resour. Technol. 112, 163–169. https://doi.org/10.1115/1.2905753.

Hajidavalloo, E., Sadeghi-Behbahani-Zadeh, M., Shekari, Y., 2013. Simulation of gas–solid two-phase flow in the annulus of drilling well. Chem. Eng. Res. Des. 91, 477–484. https://doi.org/10.1016/j.cherd.2012.11.009.

Han, S.M., Hwang, Y.K., Woo, N.S., Kim, Y.J., 2010. Solid-liquid hydrodynamics in a slim hole drilling annulus. J. Petrol. Sci. Eng. 70, 308–319. https://doi.org/10.1016/j.petrol.2009.12.002.

Herschel, W.H., Bulkley, R., 1926. Konsistenzmessungen von Gummi-benzollösungen. Kolloid Z. 39, 291–300. https://doi.org/10.1007/BF01432034.

Heydari, O., Sahraei, E., Skalle, P., 2017. Investigating the impact of drillpipe's rotation and eccentricity on cuttings transport phenomenon in various horizontal annuluses using computational fluid dynamics (CFD). J. Petrol. Sci. Eng. 156, 801–813. https://doi.org/10.1016/j.petrol.2017.06.059.

Irvine, T.F., 1988. A generalized Blasius equation for power law fluids. Chem. Eng. Commun. 65, 39–47. https://doi.org/10.1080/00986448808940242.

Iversen, F.P., Islam, A., 2018. Hole Cleaning/Cuttings Transport Workshop Meeting Summary. Equinor, Stavanger.

Johansen, S.T., Mo, S., 2015. Improved Fluid Control by Proper Non-newtonian Flow Modeling. Presented at the Tekna Flow Assurance, Larvik.

Johansen, S.T., Skalle, P., Sveen, J., 2003. A generic model for calculation of frictional losses in pipe and annular flows. J. Can. Petrol. Technol. 42 https://doi.org/10.2118/03-06-01.

Johnson, P.C., Jackson, R., 1987. Frictional–collisional constitutive relations for granular materials, with application to plane shearing. J. Fluid Mech. 176, 67–93. https://doi.org/10.1017/S0022112087000570.

Kamyab, M., Rasouli, V., 2016. Experimental and numerical simulation of cuttings transportation in coiled tubing drilling. J. Nat. Gas Sci. Eng. 29, 284–302. https://doi.org/10.1016/j.jngse.2015.11.022.

Kelessidis, V.C., Dalamarinis, P., Maglione, R., 2011. Experimental study and predictions of pressure losses of fluids modeled as Herschel–Bulkley in concentric and eccentric annuli in laminar, transitional and turbulent flows. J. Petrol. Sci. Eng. 77, 305–312. https://doi.org/10.1016/j.petrol.2011.04.004.

Kelin, W., Tie, Y., Xiaofeng, S., Shuai, S., Shizhu, L., 2013. Review and analysis of cuttings transport in complex structural wells. Open Fuel Energy Sci. J. 6, 9–17. https://doi.org/10.2174/1876973X20130610001.

Khatibi, M., 2018. Personal Communication.

Khatibi, M., Time, R.W., Shaibu, R., 2018a. Dynamical feature of particle dunes in Newtonian and shear-thinning flows: relevance to hole-cleaning in pipe and annulus. Int. J. Multiphas. Flow 99, 284–293. https://doi.org/10.1016/j.ijmultiphaseflow.2017.10.015.

Khatibi, M., Wiktorski, E., Sui, D., Time, R.W., 2018b. Experimental study of frictional pressure loss for eccentric drillpipe in horizontal wells. In: SPE-191046-MS. Presented at the IADC/SPE Asia Pacific Drilling Technology Conference and Exhibition. Society of Petroleum Engineers, SPE, p. 18. https://doi.org/10.2118/191046-MS.

Larsen, T.I.F., 1990. A Study of the Critical Fluid Velocity in Cuttings Transport for Inclined Wellbores (Master). Department of Petroleum Engineering, University of Tulsa, Tulsa.

Leine, R.I., van Campen, D.H., Keultjes, W.J.G., 2002. Stick-slip whirl interaction in drillstring dynamics. J. Vib. Acoust. 124, 209. https://doi.org/10.1115/1.1452745.

Leonard, B.P., 1979. A stable and accurate convective modelling procedure based on quadratic upstream interpolation. Comput. Methods Appl. Mech. Eng. 19, 59–98.

Li, J., Luft, B., 2014a. Overview of Solids Transport Studies and Applications in Oil and Gas Industry. In: Experimental Work. Presented at the SPE Russian Oil and Gas Exploration & Production Technical Conference and Exhibition. Society of Petroleum Engineers, Moscow. https://doi.org/10.2118/171285-MS.

Li, J., Luft, B., 2014b. Overview Solids Transport Study and Application in Oil-Gas Industry - Theoretical Work. In: Presented at the International Petroleum Technology Conference, International Petroleum Technology Conference, Kuala Lumpur. https://doi.org/10.2523/IPTC-17832-MS.

Lien, K., Monty, J.P., Chong, M.S., Ooi, A., 2004. The entrance length for fully developed turbulent channel flow. In: Presented at the 15th Australasian Fluid Mechanics Conference. The University of Sydney, Sydney, p. 4.

Lun, C.K.K., Savage, S.B., Jeffrey, D.J., Chepurniy, N., 1984. Kinetic theories for granular flow: inelastic particles in Couette flow and slightly inelastic particles in a general flowfield. J. Fluid Mech. 140, 223–256. https://doi.org/10.1017/S0022112084000586.

Malin, M.R., 1997. Turbulent pipe flow of power-law fluids. Int. Commun. Heat Mass Tran. 24, 977–988. https://doi.org/10.1016/S0735-1933(97)00083-3.

McCann, R.C., Quigley, M.S., Zamora, M., Slater, K.S., 1995. Effects of high-speed pipe rotation on pressures in narrow annuli. SPE Drill. Complet. 10 https://doi.org/10.2118/26343-PA.

Menter, F.R., 1994. Two-equation eddy-viscosity turbulence models for engineering applications. AIAA J. 32, 1598–1605. https://doi.org/10.2514/6.1993-2906.

Menter, F.R., 1993. Zonal Two Equation K-ω Turbulence Models for Aerodynamic Flows. In: Presented at the 24th Fluid Dynamics Conference. American lnstirute of Aeronautics and Astronautics (AIAA), Orlando, Florida, p. 22.

Metzner, A.B., Reed, J.C., 1955. Flow of non-Newtonian fluids-correlation of the laminar, transition, and turbulent-flow regions. AIChE J. 1, 434–440. https://doi.org/10.1002/aic.690010409.

Mme, U., Skalle, P., 2012. CFD calculations of cuttings transport through drilling annuli at various angles. Int. J. Petrol. Sci. Technol. 6, 129–141.

Neto, J.L.V., Martins, A.L., Ataíde, C.H., Barrozo, M.A.S., 2012. Non-Newtonian flows in annuli with variable eccentric motion of the inner tube. Chem. Eng. Technol. 35, 1981–1988. https://doi.org/10.1002/ceat.201200239.

Ofei, T.N., Irawan, S., Pao, W., 2015. Drilling Parameter Effects on Cuttings Transport in Horizontal Wellbores: A Review. In: Awang, M., Negash, B.M., Md Akhir, N.A., Lubis, L.A. (Eds.), ICIPEG 2014. Springer Singapore, Singapore, pp. 199–207. https://doi.org/10.1007/978-981-287-368-2_18.

Ofei, T.N., Irawan, S., Pao, W., 2014. 2014. CFD method for predicting annular pressure losses and cuttings concentration in eccentric horizontal wells. J. Petrol. Eng. 1–16. https://doi.org/10.1155/2014/486423.

Ofei, T.N., Pao, W., 2014. Modelling of pressure drop and cuttings concentration in eccentric narrow horizontal well bore with rotating drillpipe. J. Appl. Sci. 14, 3263–3269. https://doi.org/10.3923/jas.2014.3263.3269.

Ogawa, S., Umemura, A., Oshima, N., 1980. On the equations of fully fluidized granular materials. ZAMP (Z. Angew. Math. Phys.) 31, 483–493. https://doi.org/10.1007/BF01590859.

Ogugbue, C.C., Shah, S., 2011. Laminar and turbulent friction factors for annular flow of drag-reducing polymer solutions in coiled-tubing operations. SPE-130579-PA. https://doi.org/10.2118/130579-PA.

Ostwald, W., 1925. Über die Geschwindigkeitsfunktion der Viskosität disperser Systeme. Colloid Polym. Sci. 36, 99–117.

Pang, B., Wang, S., Jiang, X., Lu, H., 2019. Effect of orbital motion of drill pipe on the transport of non-Newtonian fluid-cuttings mixture in horizontal drilling annulus. J. Petrol. Sci. Eng. 174, 201–215. https://doi.org/10.1016/j.petrol.2018.11.009.

Pang, B., Wang, S., Wang, Q., Yang, K., Lu, H., Hassan, M., Jiang, X., 2018. Numerical prediction of cuttings transport behavior in well drilling using kinetic theory of granular flow. J. Petrol. Sci. Eng. 161, 190–203. https://doi.org/10.1016/j.petrol.2017.11.028.

Peden, J.M., Ford, J.T., Oyeneyin, M.B., 1990. Comprehensive experimental investigation of drilled cuttings transport in inclined wells including the effects of rotation and eccentricity. In: European Petroleum Conference. Society of Petroleum Engineers, The Hague. https://doi.org/10.2118/20925-MS.

Pereira, F. a R., Barrozo, M. a S., Ataide, C.H., 2007. CFD predictions of drilling fluid velocity and pressure profiles in laminar helical flow. Braz. J. Chem. Eng. 24, 587–595. https://doi.org/10.1590/S0104-66322007000400011.

Pilehvari, A., Azar, J.J., Shirazi, S., 1999. State-of-the-art cuttings transport in horizontal wellbores. SPE Drill. Complet. 14 https://doi.org/10.2118/57716-PA.

Pilehvari, A., Serth, R., 2009. Generalized hydraulic calculation method for axial flow of non-newtonian fluids in eccentric annuli. SPE-111514-PA. https://doi.org/10.2118/111514-PA.

Poole, R.J., 2010. Development-length requirements for fully developed laminar flow in concentric annuli. J. Fluid Eng. 132, 4. https://doi.org/10.1115/1.4001694.

Reynolds, O., 1895. On the dynamical theory of incompressible viscous fluids and the determination of the criterion. Phil. Trans. Roy. Soc. Lond. 186, 123–164.

Rooki, R., Ardejani, F.D., Moradzadeh, A., Norouzi, M., 2013a. Cuttings transport modeling in foam drilling using computational fluid dynamics (CFD). Int. J. Petrol. Geosci. Eng. (IJPGE) 1, 115–127.

Rooki, R., Ardejani, F.D., Moradzadeh, A., Norouzi, M., 2013b. Simulation of cuttings transport with foam in deviated wellbores using computational fluid dynamics. J. Petrol. Expl. Prod. Technol. 4, 263–273. https://doi.org/10.1007/s13202-013-0077-7.

Saasen, A., 2014. Annular frictional pressure losses during drilling - predicting the effect of drillstring rotation. J. Energy Resour. Technol. 136, 034501 https://doi.org/10.1115/1.4026205.

Sanchez, R.A., Azar, J.J., Bassal, A.A., Martins, A.L., 1999. Effect of drillpipe rotation on hole cleaning during directional-well drilling. SPE J. 4 https://doi.org/10.2118/56406-PA.

Savage, S.B., 1983. Granular flows down rough inclines - review and extension. In: Studies in Applied Mechanics. Elsevier, pp. 261–282. https://doi.org/10.1016/B978-0-444-42192-0.50028-1.

Savage, S.B., Jeffrey, D.J., 1981. The stress tensor in a granular flow at high shear rates. J. Fluid Mech. 110, 255–272. https://doi.org/10.1017/S0022112081000736.

Savage, S.B., Pfeffer, R., Zhao, Z.M., 1996. Solids transport, separation and classification. Powder Technol. 88, 323–333.

Sayindla, S., Lund, B., Ytrehus, J.D., Saasen, A., 2017. Hole-cleaning performance comparison of oil-based and water-based drilling fluids. J. Petrol. Sci. Eng. 159, 49–57. https://doi.org/10.1016/j.petrol.2017.08.069.

Schaeffer, D.G., 1987. Instability in the evolution equations describing incompressible granular flow. J. Differ. Equ. 66, 19–50.

Shyu, R.-J., 1989. Bending Vibration of Rotating Drill Strings (PhD Thesis). Massachusetts Institute of Technology (MIT).

Sifferman, T.R., Becker, T.E., others, 1992. Hole cleaning in full-scale inclined wellbores. SPE Drill. Eng. 7, 115–120.

Simonin, C., Viollet, P.L., 1990. Predictions of an oxygen droplet pulverization in a compressible subsonic coflowing hydrogen flow. Num. Methods Multiphase Flows FED91, 65–82.

Sinclair, J.L., Jackson, R., 1989. Gas-particle flow in a vertical pipe with particle-particle interactions. AIChE J. 35, 1473–1486. https://doi.org/10.1002/aic.690350908.

Sorgun, M., Aydin, I., Ozbayoglu, M.E., 2011. Friction factors for hydraulic calculations considering presence of cuttings and pipe rotation in horizontal/highly-inclined wellbores. J. Petrol. Sci. Eng. 78, 407–414. https://doi.org/10.1016/j.petrol.2011.06.013.

Syamlal, M., Rogers, W., O'Brien, T.J., 1993. MFIX Documentation Theory Guide. U.S. Department of Energy, Office of Fossil Energy, Morgantown.

Tomren, P.H., Iyoho, A.W., Azar, J.J., 1986. Experimental study of cuttings transport in directional wells. SPE Drill. Eng. 1, 43–56. https://doi.org/10.2118/12123-PA.

Vasquez, S., 2000. A phase coupled method for solving multiphase problems on unstructured mesh. In: Presented at the ASME 200 Fluids Engineering Division Summer Meeting.

Wang, Z., Guo, X., Li, M., Hong, Y., 2009. Effect of drillpipe rotation on borehole cleaning for extended reach well. J. Hydrodynam., Ser. B 21, 366–372. https://doi.org/10.1016/S1001-6058(08)60158-4.

Wen, C.Y., Yu, Y.H., 1966. Mechanics of fluidization. Present. Chem. Eng. Prog., Symp. Ser. 100–111.

Werner, B., 2018. The Influence of Drilling Fluid Rheology on Cuttings Bed Behavior (PhD). Norwegian University of Science and Technology, Trondheim.

Xiao, W., Zhang, Y., Zhong, Y., 2003. Annulus whirling motion analysis of the rotary drill string by the action of hydrodynamic pressure and friction force. In: 19th Biennial Conference on Mechanical Vibration and Noise, Parts A, B, and C. Presented at the ASME 2003 International Design Engineering Technical Conferences and Computers and Information in Engineering Conference, vol. 5. ASME, Chicago, Illinois, USA, pp. 1003–1010. https://doi.org/10.1115/DETC2003/VIB-48423.

Xiaofeng, S., Kelin, W., Tie, Y., 2013. Review of hole cleaning in complex structural wells. Open Petrol. Eng. J. 6, 25–32. https://doi.org/10.2174/1874834101306010025.

Xiaofeng, S., Kelin, W., Tie, Y., Shao, S., Jiao, J., 2014. Effect of drillpipe rotation on cuttings transport using computational fluid dynamics (CFD) in complex structure wells. J. Petrol. Expl. Prod. Technol. 4, 255–261. https://doi.org/10.1007/s13202-014-0118-x.

Ytrehus, J.D., Lund, B., Taghipour, A., Kosberg, B.R., Carazza, L., Gyland, K.R., Saasen, A., 2018. Cuttings bed removal in deviated wells. In: Proceedings of the 37th International Conference on Ocean, Offshore and Arctic Engineering (OMAE2018). Presented at the 37th International Conference on Ocean, Offshore and Arctic Engineering (OMAE2018). American Society of Mechanical Engineers (ASME), Madrid. https://doi.org/10.1115/OMAE2018-77832.

Ytrehus, J.D., Taghipour, A., Sayindla, S., Lund, B., Werner, B., Saasen, A., 2015. Full scale flow loop experiments of hole cleaning performances of drilling fluids. ASME. https://doi.org/10.1115/OMAE2015-41901. V010T11A041.

Zakerian, A., Sarafraz, S., Tabzar, A., Hemmati, N., Shadizadeh, S.R., 2018. Numerical modeling and simulation of drilling cutting transport in horizontal wells. J. Petrol. Expl. Prod. Technol. https://doi.org/10.1007/s13202-018-0435-6.

Zhang, G., Gutierrez, M., Li, M., 2016. A coupled CFD-DEM approach to model particle-fluid mixture transport between two parallel plates to improve understanding of proppant micromechanics in hydraulic fractures. Powder Technol. https://doi.org/10.1016/j.powtec.2016.11.055.

Conference paper 1 (VI)

A 2D sediment bed morphodynamics model for turbulent, non-Newtonian, particle-loaded flows

Alexander Busch, Milad Khatibi, Stein Tore Johansen, Rune W. Time

In: Progress in Applied CFD - Proceedings of the 12th International Conference on CFD in Oil & Gas, Metallurgical and Process Industries (CFD2017). Trondheim, Norway, 2017.

URL:
https://www.sintefbok.no/book/index/1119/progress_in_applied_cfd_cfd2017.

For the UDF source code, please see appendix B.1.

A 2D SEDIMENT BED MORPHODYNAMICS MODEL FOR TURBULENT, NON-NEWTONIAN, PARTICLE-LOADED FLOWS

Alexander BUSCH[1*], Milad KHATIBI[2], Stein T. JOHANSEN[1,3], Rune W. TIME[2]

[1] Norwegian University of Science and Technology (NTNU), Trondheim, NORWAY

[2] University of Stavanger (UiS), Stavanger, NORWAY

[3] SINTEF Materials and Chemistry, Trondheim, NORWAY

* E-mail: alexander.busch@ntnu.no

1. ABSTRACT

In petroleum drilling, cuttings transport problems, i.e. an accumulation of drilled of solids in the wellbore, are a major contributor to well downtime and have therefore been extensively researched over the years, both experimentally and through simulation. In recent years, Computational Fluid Dynamics (CFD) has been used intensively due to increasing available computational power. Here, the problem of cuttings transport is typically investigated as a laminar/turbulent, potentially non-Newtonian (purely shear-thinning) multiphase problem. Typically, an Eulerian-Eulerian two-fluid model concept is utilized, where the particle phase is treated as a second continuous phase. Optionally, a granular flow model, based on the Kinetic Theory of Granular Flow (KTGF), may be used to account for the dense granular flow properties of cuttings forming a sediment bed. One issue of the state of the art CFD approach as described above is the proper resolution of the bed interface, as this may not be accurately resolved in an industrial-relevant CFD simulation.

In this paper, an alternative approach is taken based on modeling concepts used in environmental sediment transport research (rivers, deserts). Instead of including the sediment bed in the computational domain, the latter is limited to the part of the domain filled with the particle-loaded continuous fluid phase. Consequently, the bed interface becomes a deformable domain boundary, which is updated based on the solution of an additional scalar transport equation for the bed height, which is based on the so-called Exner equation (Exner, 1925), a mass conservation equation accounting for convection, and additionally deposition and erosion in the bed load layer. These convective fluxes are modeled with closures relating these fluxes to flow quantities.

As a first step, a 2D model was implemented in ANSYS Fluent R17.2 using Fluent's dynamic mesh capabilities and User-Defined Function (UDF) interfaces. The model accounts for local bed slope, hindered settling, and non-Newtonian, shear-thinning viscosity of the fluid phase as well as turbulence. Model results are benchmarked with experimental data for five different operating points. Most probably due to the utilized unsteady Reynolds-Averaging framework (URANS), the model is not capable of predicting flow-induced dunes; however, it does predict bed deformation as a consequence of for instance non-equilibrium boundary conditions. Other model issues such as e.g. non-Newtonian formulations of the closures are identified and discussed.

Keywords: Drilling, cuttings transport, particle transport, sediment transport, bed load, turbulence, non-Newtonian, multiphase, deforming mesh, CFD.

2. NOMENCLATURE

Greek Symbols

α	Volume fraction, [-].
β	Local bed slope, [rad].
$\dot{\gamma}$	Shear rate, mag. of deformation rate tensor, [1/s].
ρ	Mass density, [kg/m^3].
μ	Dynamic viscosity, [kg/m.s].
ν	Kinematic viscosity, [kg/m.s].
τ	(Wall) Shear stress, [Pa].
ϕ	Angle of repose, [rad].
θ	Non-dimensional shear stress, Shields number, [-].
ω	Specific dissipation rate [1/s].

Latin Symbols

c	Coefficient of drag, [-].
C	Bed slope model constant, ≈ 1.5, [-].
d	Diameter, [m].
D	Deposition, [m/s].
$\mathbf{D}$	Rate of deformation tensor, [m/s^2].
E	Entrainment, [m/s].
F	Momentum exchange term, [kg/s^2.m^3].
$\mathbf{g}$	Gravitational acceleration, [m/s^2].
h	Bed height, [m].
k	Turbulent kinetic energy, [m^2/s^2].
n	Exp. in rheo. models & hind. settling function, [-].
q	Vol. bed load transport rate per unit width, [m^3/s.m].
s	Ratio of solid and fluid densities, [-].
S	Source term, [kg/s.m^3].
t	Time, [s].
$\mathbf{T}$	Stress tensor, [kg.m/s^2.m^3].
$\mathbf{u}$	Velocity vector, [m/s].
v	Vertical velocity component, [m/s].
V	Volume, [m^3].

Sub/superscripts

0	Horizontal or initial or zero.
$*$	Non-dimensional.
b	Bed.
cr	Critical/Treshold.
CR	Cross.
D	Drag.
f	Fluid.
i	Phase index.
PL	Power-law.
s	Solid.
t	Turbulent.
T	Transposed.
x	x-direction in space.
y	y-direction in space.
z	z-direction in space.

Abbreviations

2D	Two-dimensional in space.
3D	Three-dimensional in space.
CFD	Computational Fluid Dynamics.

H_2O	Water.
KTGF	Kinetic theory of granular flow.
PAC	Polyannionic cellulose.
OBM	Oil-based muds.
UDF	User-Defined Function.
URANS	Unsteady Reynolds-Averaged-Navier-Stokes.
SST	Shear Stress Transport.
VLES	Very Large-Eddy Simulation.
WBM	Water-based muds.

3. INTRODUCTION

Existing research body and praxis

Cuttings transport in wellbores, herein termed wellbore flows, is a multiscale problem, both in space and time but also regarding the different levels of physical complexity. In general, wellbore flows incorporate non-Newtonian rheology, dispersed and potentially dense packed solids (cuttings forming a sediment bed) and the flow may be turbulent. The domain of interest is an annulus, formed by the drill pipe, which may also rotate, inside the wellbore.

Conceptually, the flow may be categorized into three layers: (1) A flowing mixture layer, where particles are transported in a heterogeneous suspension. (2) An intermediate layer, where particles roll and slide on top of each other, which is just a few particle diameters thick. (3) Depending on the various parameters involved, a densely packed, and in most cases stationary, cuttings bed may form at the lower part of the annulus.

Several scientists, e.g. Doron and Barnea (1993); Savage et al. (1996) or more recently Bello et al. (2011); Nossair et al. (2012); Goharzadeh et al. (2013); Corredor et al. (2016), have experimentally investigated wellbore flows in laboratory flow loops. Corredor et al. (2016) determined the critical velocities for the initiation of particle movement with rolling, saltation, and suspension. They found that the fluctuation of pressure gradient is due to the dune movement. Nossair et al. (2012) found a significant influence of pipe inclination on flow structure as a consequence of liquid-particle interaction at the bed interface and the suspension layer. Goharzadeh et al. (2013) found that an increased bed height in a horizontal pipe reduces the effective cross-sectional flow area and results in higher local liquid velocity, which is leading to higher shear forces at the solid-liquid interface. For solid particles, the dominant factors to induce the movement is the fluid shear force at the solid-liquid interface and the gravity force.

In recent years, CFD has been increasingly used to model wellbore flows. Different levels of complexity may be addressed by incorporating adequate models for multiphase flows, non-Newtonian fluid rheology, turbulence, and more physics. Mainly, the Eulerian-Eulerian two-fluid model has been used in recent research activities, for instance by Ofei et al. (2014); Sun et al. (2014); Manzar and Shah (2014); Han et al. (2010), where the fluid and solid phase are treated as two interpenetrating continua. In wellbore flows, a cuttings bed may form under different conditions. Solids are not kept entirely in suspension, but settle out and agglomerate on the lower part of the annulus forming a stationary packed bed with maximum packing density ($\alpha_s \approx 0.63$) and a moving dense layer ($\alpha_s \approx 0.55$), where particles roll and slide on top of each other. This layer is usually only a few particle diameters thick. In terms of CFD modeling, the formation of a cuttings bed may be accounted for by incorporating the kinetic theory of granular flow (KTGF), as for instance used by Han et al. (2010). The KTGF describes the granular flow in the dense packed bed, where solid pressure and granular temperature become important flow variables.

Position and Motivation

Utilizing the KTGF is computationally more expensive as additional transport equations have to be solved. Furthermore, the fine layer on top of the stationary cuttings bed, where particle roll and slide on top of each other, may not be resolved properly. Finally, the cuttings bed interface[1] may not be tracked properly, as interpolation of the various solids volume fraction values of different cells is required to yield the approximate position based on a threshold such as e.g. $\alpha_s = 0.55$.

In sediment transport research, CFD models usually utilize the so-called “Exner equation”, derived by Exner (1925), in order to track the development of the sediment bed height. The sediment bed height is usually taken as the distance from some reference level to the top or bottom of the so-called “bed load” layer. The "bed load" layer is located on top of the static bed and comprises a thin layer containing sediment flux, characterized by sliding and rolling particles. The dispersed solids are usually modelled by an additional species transport equation. Empirical formulas are used to model the bed load transport rate, where a variety of models exists to account for the deposition and entrainment fluxes. Examples of such a modeling approach are Solberg et al. (2006); Brørs (1999) or more recently Khosronejad et al. (2011); Khosronejad and Sotiropoulos (2014).

In order to simplify numerical cuttings transport studies, we will apply a combination of a multiphase treatment of the particle-loaded, potentially non-Newtonian flow and the Exner equation approach for tracking the bed interface. A two-dimensional (2D) model is implemented in ANSYS Fluent 17.2 and results are compared with respective experimental data for a set of different case parameters.

Structure of this work

In section 4, we present a description of the modeling concept as well as the general flow and bed load models, along with different important model elements. Section 5 provides an overview of the experimental setup and measurement techniques. In section 6, both numerical and experimental results will be presented. A discussion of the results and comparison of CFD and experimental results is provided in section 7. Finally, section 8 provides a conclusion and outlook.

---

[1] This is an ambiguous term. In this study, it is considered to be the top of the sliding/rolling particle layer, where saltation processes just start to occur.

4. NUMERICAL MODEL

This section provides a description of the general methodology used to model the evolution of the cuttings bed as well as a detailed description of the CFD model used in this study.

As a first step, the CFD model is built for a two-dimensional (2D) channel flow, where the domain is discretized with a structured hexagonal grid as depicted in Figure 1.

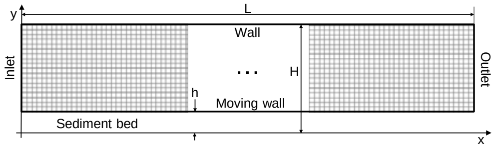

Figure 1: 2D channel domain.

Here, an initial cuttings or sediment bed is depicted. However, the cuttings bed is not part of the discretized domain. Instead, it is accounted for by setting the coordinate system appropriately, such that, in the given example, the y-coordinate is zero at the channel bottom, equal to the bed height at the lower end of the mesh and equal to the channel height at the top end of the mesh.

General modeling concept

An overview of the general modeling concept is provided in Figure 2.

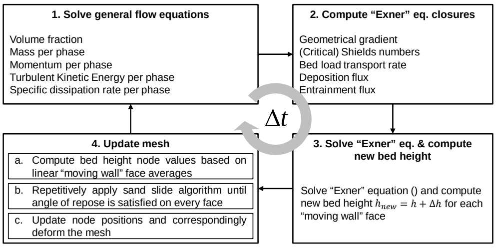

Figure 2: Overview of general modeling concept.

Four major steps per computational CFD time step are performed as follows:

1. Within the discretized domain of Figure 1, an Eulerian-Eulerian two fluid model is solved, where both the solvent and the dispersed phase are treated as interpenetrating continua.
2. Based on the solution, certain quantities required for modeling the evolution of the sediment bed are straightforwardly computed.
3. The evolution of the bed interface is described by the so-called “Exner equation”, first introduced by Exner (1925). It is based on conservation of mass applied to a control volume, where the height of the volume may change with time due to the gain or loss of mass in the control volume. The evolution equation for the bed height h is:

$$\frac{\partial h}{\partial t} = -\frac{1}{(1-\alpha_{fb})}\left(\frac{\partial q_{bx}}{\partial x} + E - D\right) \qquad (1)$$

   Here, q_{bx} is the volumetric bed load transport rate per unit width, i.e. the amount of solids being transported in the bed load layer along the bed interface, and E and D are source terms representing volumetric entrainment and deposition fluxes of solids, respectively. The solution of equation (1) leads to a change in bed height for a given time step and grid cell.
4. Ensuring that the solids angle of repose is not violated and transferring face to node positions, the mesh is updated accordingly. Figure 3 shows a zoom of the near-bed region of Figure 1 at two subsequent time steps and illustrates that the computed change in bed height is used to accordingly deform the mesh on a per node and per time step basis.

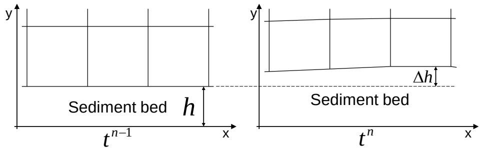

Figure 3: Mesh-deformation.

The CFD model, as further detailed in the next two subsections, is implemented in ANSYS Fluent R17.2 using its dynamic mesh capabilities and UDF functionalities.

Flow field

The flow field, i.e. both the fluid and solid phase flowing through the discretized domain (Step 1. in Figure 2), is described in an Eulerian-Eulerian and unsteady Reynolds-Averaged (URANS) framework. Both the fluid and the solid phase are considered isothermal and incompressible. Hence, for an arbitrary volume element, the phase volume fractions have to sum to one.

$$V_i = \int_V \alpha_i dV \quad \wedge \quad \sum_i \alpha_i = 1 \quad \wedge \quad i \in \{f,s\} \qquad (2)$$

Transport of mass

The continuity equation for phase $i \in \{f,s\}$ is expressed as

$$\frac{\partial}{\partial t}(\alpha_i \rho_i) + \nabla(\alpha_i \rho_i \mathbf{u}_i) = S_i \qquad (3)$$

The source term S_i on the RHS is generally zero. However, in cells at the sediment bed interface, i.e. wall-adjacent cells of the bottom domain boundary “moving wall”, mass may be added or removed as a consequence of solid deposition and entrainment processes taking place at the sediment bed interface.

Transport of momentum

The momentum balance for the phase $i \in \{f,s\}$ reads

$$\begin{aligned} &\frac{\partial}{\partial t}(\alpha_i \rho_i \mathbf{u}_i) + \nabla \cdot (\alpha_i \rho_i \mathbf{u}_i \mathbf{u}_i) \\ &= \alpha_i \nabla \mathbf{T}_i + 2\nabla(\alpha_i \mu_{t-i} \mathbf{D}_i) + \alpha_i \rho_i \mathbf{g} + K(\Delta \mathbf{u}_i) + \sum F_s \end{aligned} \qquad (4)$$

The stress tensor $\mathbf{T}$ for a generalized Newtonian fluid is

$$\mathbf{T}_i = -p\mathbf{1} + 2\mu_i(\dot{\gamma})\mathbf{D}_i \qquad (5)$$

where $\mathbf{D}_i$ is the rate of deformation tensor

$$\mathbf{D}_i = \frac{1}{2}\left(\nabla \mathbf{u}_i + \nabla \mathbf{u}_i^T\right) \qquad (6)$$

and the shear rate $\dot{\gamma}$ is a total shear measure defined as

$$\dot{\gamma} = \sqrt{2\mathbf{D}:\mathbf{D}} \qquad (7)$$

The turbulent Reynolds stresses are modelled using the gradient diffusion hypothesis (Boussinesq hypothesis), where turbulent Reynolds stresses are related to the mean velocity gradients and the turbulent viscosity μ_{t-i}.

In the drag term, K is the interphase momentum exchange coefficient

$$K = \frac{A_i \rho_s}{6\tau_s} f(c_D) \qquad (8)$$

with the particle relaxation time

$$\tau_s = \frac{\rho_s d_s}{18\mu_f} \tag{9}$$

and where the function $f(c_D)$ represents the effect of a particular interphase momentum exchange model. Here, the model of Schiller and Naumann (1933) has been used. Other momentum exchange terms include lift, virtual mass, turbulent dispersion and turbulent interaction

$$\sum F = F_L + F_{VM} + F_{TD} + F_{TI} \tag{10}$$

where the standard Fluent formulation for the virtual mass force is used and lift is described by the model of Saffman (1965), turbulent dispersion by the model of Simonin and Viollet (1990b), and turbulent interaction as described by Simonin and Viollet (1990a).

Note, that, in accordance with the source term in the mass transport equation (3), the momentum equation (4) should feature a corresponding momentum source term to account for momentum exchange in the wall-adjacent grid cells. However, compared to the other terms in equation (4), the momentum source term due to mass exchange is expected to be of negligible order of magnitude.

Fluid rheology

Drilling fluids are either pure water (H_2O) or so-called H_2O or oil based muds (WBM, OBM). The first is a simple Newtonian fluid, the latter are generally engineered non-Newtonian (shear thinning, viscoelastic and thixotropic) fluid systems. However, usually, drilling fluids are modelled as generalized Newtonian fluids, i.e. purely viscous without elastic and time-dependent properties. Hence, the fluid apparent viscosity becomes only a function of the second invariant of the rate of deformation tensor, see equation (5), and may be expressed with different models depending on the fluids properties. In this study, experiments were performed for H_2O and an aqueous solution of Poly-Anionic Cellulose with a concentration of 1 g/L (PAC1) as a WBM model system. PAC solutions are both shear-thinning and translucent which qualifies them for usage as WBM model systems in optical investigations. Preparation of the PAC1 solution and rheology measurements were described in previous studies, see Khatibi et al. (2016a), (2016b). Figure 4 shows the apparent dynamic viscosity $\mu(\dot{\gamma})$ of H_2O and PAC1 versus shear rate $\dot{\gamma}$.

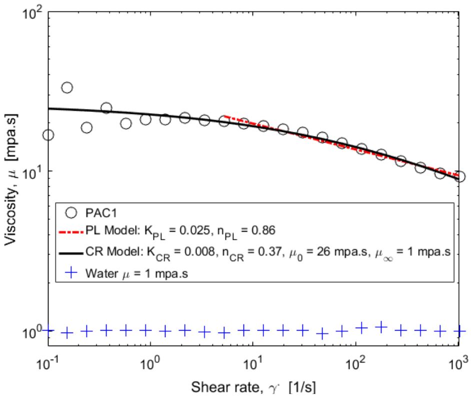

Figure 4: Rheology of water and PAC 1 g/l at 21 °C.

Power-law (*PL*) and Cross (*CR*) models, equations (11) and (12) respectively, were used for curve fitting of the PAC1 rheometric data; however, only the *CR* model was used in the CFD computations.

$$\mu_{PL}(\dot{\gamma}) = K_{PL}\dot{\gamma}^{n_{PL}-1} \tag{11}$$

$$\mu_{CR}(\dot{\gamma}) = \frac{\mu_0 - \mu_\infty}{1 + (K_{CR}\dot{\gamma})^{n_{CR}}} + \mu_\infty \tag{12}$$

Density of H_2O and PAC1 were approximately 1000 kg/m³. All liquids were measured at room temperature (21 °C) and atmospheric pressure (1.01 bar).

Dispersed phase

In order to model drill cuttings, two different types of spherical glass beads with median diameters $d_s = 0.3$ mm and $d_s = 1.2$ mm were used in this study, with solids density $\rho_s = 2500$ kg/m³.

Turbulence

As an URANS approach is taken to model the fluid flow, a turbulence model is required in order to compute the turbulent viscosity $\mu_{t\text{-}i}$. Here, the k-ω SST model of Menter (1994) is used to model the two turbulent quantities, namely the turbulent kinetic energy k and the inverse turbulence time scale ω. Roughness of a non-moving sand bed may be directly represented by the particle diameter. However, due to the moving sand particles, which may also slide, roll and saltate, bed roughness is taken to be equivalent to $2d_s$.

Bed load layer

As illustrated in Figure 3, the lower wall of the computational domain may deform based on the solution of the bed height transport equation (1). In order to solve equation (1), three closures are required, namely models for the volumetric bed load transport rate per unit width, the volumetric deposition flux and the volumetric entrainment flux (Step 2. in Figure 2).

Incipient motion

Bed load transport and entrainment only take place if the fluid has sufficient momentum to overcome a critical bed shear stress threshold, characterized by the Shields number. The Shields number is a non-dimensional shear stress acting on the bed and may also be seen as the ratio of shear force to gravitational force, acting on a particle at the top of the bed.

$$\theta = \frac{|\tau_b|}{g d_s (\rho_s - \rho_f)} \tag{13}$$

For a horizontal bed, the critical Shields number to overcome for bed load transport and entrainment to take place, may be estimated using an empirical expression of Soulsby (1997)

$$\theta_{cr,0} = \frac{0.24}{d_*} + 0.055\left(1 - e^{-0.02 d_*}\right) \tag{14}$$

where d_* is a dimensionless particle diameter

$$d_* = \left(\frac{g(s-1)}{\nu_f^{\,2}}\right)^{\frac{1}{3}} d_s \tag{15}$$

Applying a force balance to a particle on a slope yields, for the 2D case, where shear stress always acts in the bed slope direction,

$$\theta_{cr} = \theta_{cr,0} \frac{\sin(\beta + \phi)}{\sin(\phi)} \qquad (16)$$

where ϕ is the solids angle of repose and β is the local bed slope.

Bed load transport rate

The bed load transport rate is mainly a function of the shear stress acting on the bed. Various empirical bed load formulas exist for different flow patterns and sediments. In this study, the expression of Nielsen (1992) is used,

$$q_{bx-0} = \begin{cases} 0 & if \quad \theta \le \theta_{cr} \\ 12\sqrt{g(s-1)d_s{}^3\theta}\,(\theta - \theta_{cr}) & if \quad \theta > \theta_{cr} \end{cases} \qquad (17)$$

which is valid for a zero-slope bed. Following Struiksma and Crosato (1989), a slope correction term is introduced as

$$q_{bx} = q_{bx-0}\left(\frac{u_f}{|u_f|} - C\frac{\partial h}{\partial x}\right) \qquad (18)$$

where C is a constant and the direction of q_{bx} is assumed to be equivalent to the x-direction of the fluid velocity u_f in the wall-adjacent grid cell.

Deposition

The deposition flux D, i.e. particles leaving suspension and depositing on the bed, may be modeled as the product of the solid volume fraction and the suspension hindered settling velocity of Richardson and Zaki (1957)

$$D = \alpha_s\left(\alpha_f{}^n v_{set}\right) \qquad (19)$$

where v_{set} is the settling velocity of an individual particle estimated with

$$v_{set} = -\sqrt{\frac{4(\rho_s - \rho_f)d_p g}{3\rho_f c_D}} \qquad (20)$$

based on the drag coefficient c_D of Schiller and Naumann (1933). According to Garside and Al-Dibouni (1977), the exponent n in equation (19) is given by

$$n = \frac{0.27\,\mathrm{Re}_p{}^{0.9} + 5.1}{0.1\,\mathrm{Re}_p{}^{0.9} + 1} \qquad (21)$$

Entrainment/Erosion

Following Celik and Rodi (1988), the entrainment flux E, i.e. particles leaving the bed and entering suspension due to near-bed turbulent eddies, may be expressed with the near-bed Reynolds flux of solids

$$E = \frac{\overline{\alpha_s' u_j'}}{\rho_s} \approx -\frac{\mu_T}{\rho_s Sc_T}\frac{\partial \alpha_s}{\partial y} \qquad (22)$$

which may be modeled using the ratio of turbulent viscosity and the turbulent Schmidt number times the solid fraction gradient.

Sand slide

A pile of granular material will, under the pure influence of gravity, settle in such a way that the angle between its slope and the horizontal plane is equal to the materials angle of repose. The solution of equation (1) may lead to a violation of the angle of repose. Hence, a sand slide algorithm is required to avoid local violation of the angle of repose. The algorithm of Liang et al. (2005) is applied, where a face gradient is readjusted in a mass-conservative manner if the face slope is violating the angle of repose (Step 4. in Figure 2).

Boundary and initial conditions

Initially, the bed height is 5 mm in the entire domain and all the flow variables in the domain are zero.

At the inlet, a laminar velocity profile, which is adjusted to the potentially changing inlet size between step (4) and step (1) in Figure 2, is utilized for both the solid and the fluid phase. The velocity profile is defined in such a manner that the superficial velocities of the 2D channel flow CFD model and 3D pipe flow experiments match.

A zero bed load transport rate gradient is used as a BC for the volumetric bed load transport rate.

The solid volume fraction is assumed constant across the inlet. Reasonable values for the in-situ solid volume fraction were estimated based on the ratio of experimental superficial velocities

$$\alpha_s = \frac{U_{ss}}{U_{ss} + U_{sl}} \qquad (23)$$

where the superficial particle velocity was calculated from the solids collection/injection rate as described in section 5 and the superficial liquid velocity was calculated based on logged data from a Coriolis flow meter.

Implementation in ANSYS Fluent R17.2

With reference to Figure 2, the implementation in ANSYS Fluent R17.2 is as follows:

1. The flow field is solved in a standard manner using the Phase-Coupled SIMPLE scheme, spatial discretization is second order, with the exception of volume fraction where the QUICK scheme has been used. The time discretization is implicit second order.
2. After the flow field variables are available, the three closures (18), (19), and (22) are calculated using an EXECUTE_AT_END UDF.
3. In the same UDF, the bed height evolution equation (1) is solved with a first-order upwind scheme

   $$h_x^{t+\Delta t} = h_x^t - \frac{\Delta t}{(1-\alpha_{fb})\Delta x}\left(q_x^t - q_{x-\Delta x}^t\right) - \frac{\Delta t}{(1-\alpha_{fb})}(E - D) \quad (24)$$

   Note, that the volumetric transport rate q_x is a function of the transported property h. However, changes of the bed height h occur on a much larger time scale than changes of flow field variables such as velocity. Since the first-order upwind scheme, i.e. equation (24), is solved at the end of each CFD time step, no numerical instabilities are to be expected.

   The net solid and fluid fluxes into/out of the wall-adjacent cell leads to a source term in these cells, as given in equation (3).
4. Finally, the computational domain is then updated by individual node movement using a DEFINE_GRID_MOTION UDF, where the new node positions are computed based on linear face position averages and the whole bed is repetitively swept with the sand slide algorithm until the angle of repose is satisfied at all bed faces. ANSYS Fluent's dynamic mesh capability is used to deform the mesh correspondingly. Here, the spring-based smoothing method is used, where the individual node displacements are obtained by treating the mesh as a network of connected springs. Displacements of the boundary nodes computed via equation (24) will be transmitted through the mesh by calculating adjacent node displacements based on Hooke’s law.

5. EXPERIMENTS

Flow loop

The experiments were carried out in a medium-scale flow loop at the University of Stavanger. The flow loop, shown in Figure 5, is a closed loop, where the particles are separated and re-injected continuously to the test sections after collection in a hydrocyclone (10).

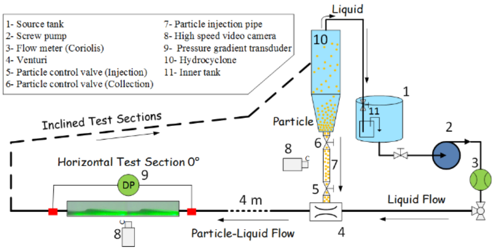

Figure 5: Medium-scale flow loop.

The flow loop features both a horizontal and an inclined test section, where the pipe is made of transparent plexiglas. The inner pipe diameter is 0.04 m, the total length of the horizontal test section is 6 m, with an upstream entrance length of 4 m. The test fluid was stored in a 350 L source tank (1). A PCM Moineau 2515 screw pump (2), regulated by a frequency invertor, provided the flow. Liquid flow rate and temperature were monitored by a Promass 80F DN50 Coriolis flow meter (3). The glass beads were mixed into the liquid through a Venturi shaped injector (4). The test section was located 4 m downstream of the injection point to minimize entrance flow effects and to let the particle-liquid patterns become fully developed. The pressure gradient data was measured over a length of 1.52 m by a Rosemount 3051 transducer (9). At the same position, flow pattern images were recorded using two high speed video cameras (8): A Basler camera with 500 fps at full resolution of 800x600 and a SpeedCam Mini e2 camera with 2500 fps at full resolution of 512x512 pixels. Particles and liquid were separated in the hydrocyclone (10), just after the inclined test section. The particles are then re-injected through the injection pipe (7) and the liquid is returned to the tank (1).

Estimate of CFD boundary conditions

The solid superficial velocity required to specify the in-situ solid volume fraction used as a BC in the CFD model, i.e. equation (23), was estimated by measuring the injection and collection rate of particles. A time series of images of the injection pipe (7) was obtained, where one of the control valves (5, 6) was closed and the other one was open to collect or inject the particles. The changes of the packed particles height were calculated by analyzing the images in Matlab.

Test matrix

Table 1 summarizes the relevant parameters used in the experiments (and corresponding simulations).

In all cases, glass beads with a density of 2500 kg/m³ were used as solids.

The global α_s represents the total volumetric loading of solids in the flow loop, whereas the in-situ α_s represents the estimated solid volume fraction of moving solids according to equation (23) used as a BC in the CFD simulations.

Table 1: Test matrix

Case	#1	#2	#3	#4	#5
Fluid	H_2O	H_2O	H_2O	PAC1	PAC1
U_{sl} [m/s]	0.26	0.43	0.44	0.45	0.81
μ_0 [mPa.s]	-	-	-	26	26
μ_∞ [mPa.s]	1	1	1	1	1
K_{CR} [Pa.s^{nCR}]	-	-	-	0.008	0.008
n_{CR} [-]	-	-	-	0.37	0.37
d_s [mm]	0.3	0.3	1.2	1.2	1.2
α_S [-] global	0.08	0.08	0.12	0.12	0.12
α_S [-] in-situ	≈ 0.0015	≈ 0.0015	≈ 0.001	≈ 0.001	≈ 0.001

Pipe inclination was 0° in all cases, i.e. only the data from the horizontal test section was used in this study.

6. RESULTS

Numerical Modeling (CFD)

In the case of H_2O, solids eventually accumulate into a pile at the inlet due to a developing recirculation zone, blocking more than half the inlet. For case #1, as depicted in Figure 6, and at approximately x ≈ 1 m, a static bed begins to form where the solids concentration profile as well as the bed height is constant with respect to x.

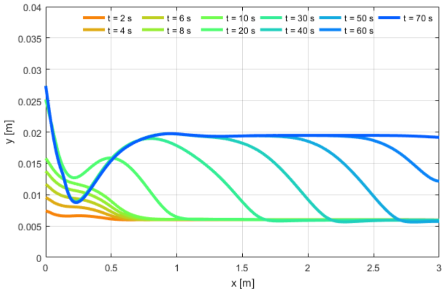

Figure 6: Bed height as a function of time, case #1.

For case #2, as illustrated in Figure 7, a large pile of solids develops in the domain (here depicted at t = 50 s), which eventually is eroded.

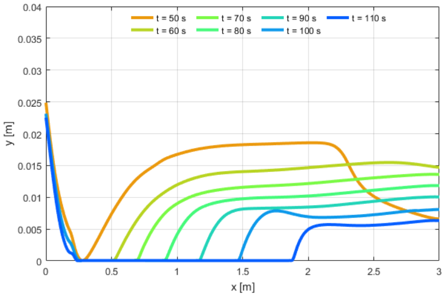

Figure 7: Bed height as a function of time, case #2.

For case #3, simulations were always diverging for a big variety of solver settings. Using time steps < 0.0005 s lead to stable simulations; however, no results were obtained due to currently unavailable computational power required.

In case of PAC1, no pile build-up is observed at the inlet in either case. For case #4, as depicted in Figure 8, a dune starts to grow at x ≈ 0.5 m and eventually the bed approaches a steady-state with a bed height h = 0. 0136 m.

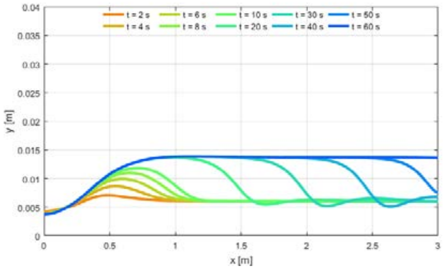

Figure 8: Bed height as a function of time, case #4.

For case #5, as illustrated in Figure 9, the bed is eroded from the start and yields a semi-steady-state bed height towards the outlet.

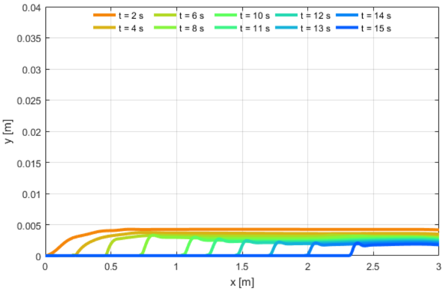

Figure 9: Bed height as a function of time, case #5.

However, the bed is eroded continuously, leading to zero bed height after the small dune traveling through the domain in the flow wise direction.

No moving sand dunes were observed in the simulations.

Experiments

In this study, only a subset of experimental results relevant for validation of CFD simulations are presented (horizontal test section, moving bed flow pattern).

Figure 10 to Figure 14 show the corresponding experimental results for the cases #1 to #5.

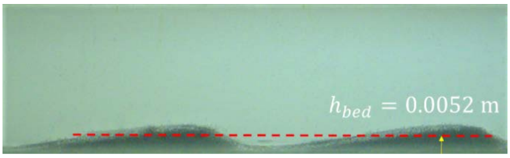

Figure 10: Exp. result case #1.

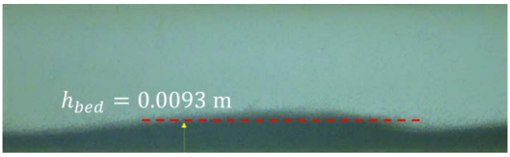

Figure 11: Exp. result case #2.

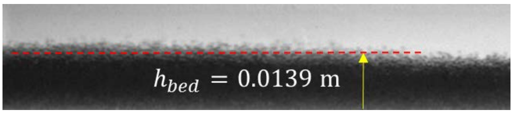

Figure 12: Exp. result case #3.

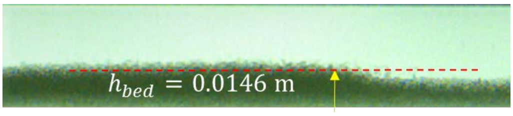

Figure 13: Exp. result case #4.

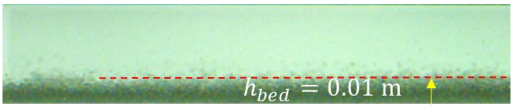

Figure 14: Exp. result case #5.

For case #1, #2 and #3, the fluid as well as particle properties are the same; with the only difference that the particle diameter d_s is 4 times larger in case #3 compared to case #1 and #2. Increasing the liquid superficial velocity U_{sl} leads to a higher bed height (case #2, Figure 11 vs. case #1, Figure 10), and changing the solids particle diameter d_s causes an even higher bed height (case #3, Figure 12).

For case #4 and #5, PAC1 was used as a fluid, having shear-thinning properties as shown in Figure 4. Changing the fluid properties from H_2O to the more viscous and shear-thinning PAC1 (case #4, Figure 8), changes the flow pattern and causes the bed to become much flatter but with a slightly higher bed height. By increasing the liquid superficial velocity U_{sl} (case #5, Figure 14), the bed height is reduced, and the flow pattern changes to stratified flow with more particles in suspension near the bed.

7. DISCUSSION

First, the numerical results are discussed with a focus on model issues, followed by a brief discussion of the experimental results. Finally, numerical and experimental results are compared with each other.

Numerical Modeling (CFD)

Dynamic bed forms and URANS concept

Even though simulation results predict bed changes with respect to space and time, no dynamic bed forms such as dunes are observed. For case #1 and #4, a sediment bed with constant height in dynamic equilibrium with the interacting flow is obtained in the second half of the computational domain. For case #1 and #4, the bed seems to be eventually eroded; however, also no dunes are observed. The lack of dynamic morphodynamic bed shapes may be a direct consequence of the URANS concept employed. Here, only averaged turbulent quantities are considered. Hence, no flow-induced perturbations of the sand bed are observed away from the inlet. Similar results have also been obtained by other researchers in sediment transport research, e.g. Khosronejad et al. (2015). Hence, a URANS concept may only be used to predict an averaged bed height. A capability to resolve large scale turbulent structures seems required in order to obtain flow-induced bed perturbations and dune dynamics. One computationally affordable concept may be the Very Large Eddy Scale (VLES) model introduced by Johansen et al. (2004), an approach that is currently investigated.

Bed erosion & steady-state

For case #2 and #5, the simulation results indicate a vanishing bed, i.e. the bed is eroding over time. Here, the solid transport capacity of the flow seems to be high enough to eventually transport all solids out of the domain, which is consistent with the comparatively high superficial velocity of the cases. However, as will be further discussed in section “Comparison of CFD and experimental results”, this is not in accordance with experiments, where a steady-state bed height is observed. Further simulation time is required to finally develop a full dynamic equilibrium, since, as Figure 7 and Figure 9 indicate, the eroding bed eventually leads to a fully flushed channel.

Numerical instabilities

For case #3, no converging solution could be obtained. In this case we have particles of d_s = 1.2 mm in H_2O. The settling velocity becomes large ($v_{set} \approx 0.1$ m/s), imposing a considerable time step limitation. The problems observed here are expected to be related to the relative large hydrodynamic relaxation times of the larger particles leading to high deposition fluxes. These lead to short timescales for the Exner equation and consequently affect the numerical stability of our coupled equations.

Bed load transport rate closure

The used bed load transport rate is an empirical formula obtained for sand-water mixtures. Even though it is based on the non-dimensionalised wall shear stress in the form of the Shields number, it may not be adequate to quantify bed load transport for closed channel flows.

Furthermore, the applicability of bed load transport rate formulas for shear-thinning apparent viscosities is questionable.

The critical Shields number as the threshold for incipient motion was experimentally determined by Shields (1936) for a constant ratio of water-sand densities as well as a, with respect to the shear rate, constant water viscosity. Thus, for density ratios other than water-sand, as may be encountered in wellbore flows, and/or the varying apparent viscosity of drilling fluids, the standard Shields curve may not represent the correct threshold of motion.

Node position update

The updated node positions are computed based on a simple face-averaging. In cases where the two neighboring faces of an arbitrary face do have a y-coordinate larger or smaller than the y-coordinate of the current face, the used averaging concept is not fully mass-conservative under all conditions. This may be easily deduced from Figure 3, where the third cell may be considered a local maximum. Since both the downstream and upstream face do have smaller y-coordinates, averaging node positions as described will lead to a new face value smaller than the actual computed face value. Ideally, the new node positions could be interpolated using e.g. splines with the constraint of mass conservation.

BC & model parameters

Appropriate BC as well as correct estimates of model parameters are major issues in all CFD simulations. Here, concerning BC, the transfer of a pipe cross-sectional geometry to a channel cross-sectional geometry is not fully consistent with regards to all parameters: Superficial velocities are matched; however, due to the different cross-sections, wall shear stress and Reynolds numbers are different.

For all cases, in the first half of the computational domain, the sand bed height changes with respect to space and time because of the various solid (bed load, deposition and entrainment) and corresponding fluid fluxes having different orders of magnitude and direction. This is mainly a consequence of the BC, i.e. the specified parabolic velocity profile and constant solid volume fraction across the inlet. These conditions do not represent a dynamic equilibrium. Since the velocity profile is updated based on the bed change at the inlet, a recirculation zone develops and the flow field and accordingly the sediment bed develop over an entrance length approximately equal to half the channel length. This may be circumvented by setting the first grid point constant, i.e. non-deforming. The two most prominent uncertain parameters are probably the estimated in-situ solid volume fraction given by equation (23) as well as the bed roughness required for the turbulence model. A sensitivity study may be required to identify the quantitative effect of these parameters on bed height.

Regarding solid fraction, a profile, for instance based on the Rouse concentration profile of suspended sediments, may be used. Together with a more realistic turbulent velocity profile, this may help to considerably reduce the required entrance length and thus speed up computations.

Non-Newtonian rheology

The apparent viscosity is based on the shear rate of the background fluid. For testing purposes, local, particle-induced shear rate and thus viscosity changes were taken into account for the settling velocity of solids in the wall-adjacent bed cells. However, this needs to be implemented into drag law formulations as well as shear-rate dependent force terms used in the two-fluid model. If not, solid velocities of the two fluid model and settling velocities of the bed load model would be inconsistent.

The utilized non-Newtonian rheology description as a generalized non-Newtonian fluid does not account for interdependencies of non-Newtonian fluid rheology and turbulence. Non-Newtonian rheology is only taken into account via the molecular viscosity, i.e. equation (5) and (12) whereas the effect of turbulence is only taken into account by the corresponding models affecting the turbulent viscosity $\mu_{t\text{-}i}$. This is due to the conventional but simplified RANS treatment where the viscosity is first considered constant and later made variable by relating it to the shear rate, again see equation (5) and (12). Thus, terms representing the impact of fluctuations in strain rate on the fluids molecular viscosity as shown by Pinho (2003) as well as Gavrilov and Rudyak (2016) are ignored.

Adequate wall treatment for non-Newtonian fluids is not available so far, as the wall functions in ANSYS Fluent are based on the common Newtonian log-law concept.

Hence, the boundary layer needs to be resolved down to y+ < 1 into the laminar sublayer or non-Newtonian wall laws have to be developed, e.g. based on Johansen (2015).

Drag, other momentum exchange terms and settling models utilized are based on Newtonian fluids. Here, further work is needed to account for non-constant viscosities, using available modeling concepts such as e.g. Childs et al. (2016); Ceylan et al. (1999); Li et al. (2012); Renaud et al. (2004); Shah et al. (2007); Shah and others (1986).

Experiments

Recording of experimental data started after a flow stabilization sequence of 30 min, in order to yield dynamic equilibrium. An entrance length of 4 m upstream of the test section was sufficient to yield a well-developed particle-liquid flow in test section of the horizontal pipe, where the video images were recorded. The camera frame rate was sufficient to capture and track the movement of individual particles inside the test section.

Bed heights were measured from the video images and are in agreement with conventional theory.

Theoretically, the bed height should decrease with increasing liquid flowrate due to increased shear stress against the bed. Thus, both bed load and suspended load increase, which may be directly seen in Figure 13 and Figure 14 for the case of PAC1. However, in the case of H_2O, an increase in bed height is observed, which may be explained by flow pattern transition from a rather stationary bed, where dunes are moving very slowly (case #1) to a moving bed, where dunes move much faster (case #2). In addition, beyond a threshold velocity, particle dunes disappear and the bed becomes flatter.

For constant particle mass density, the bed height increases with increasing particle diameter, due to increase in settling velocity, and decrease in entrainment rate.

Increased viscosity of shear-thinning fluid leads to decrease in bed height due to the increased solids transport capacity of the flow. This is mainly due to reduced settling velocity and consequently less deposition. It also leads to higher shear-stress acting on the bed and consequently more bed-load transport.

Comparison of CFD and experimental results

As pointed out, the URANS-based numerical modeling approach does not yield any bed dynamics such as dunes. Therefore, comparison of CFD and experimental results may only be conducted based on a time/spatial average of the steady-state bed height.

Table 2 provides a quantitative comparison of the bed heights predicted by CFD simulations and the averaged bed heights obtained from experiments.

In case of the experiments, the averaged bed height was determined using Matlab Pixel-Viewer. By considering the grayscale color of each pixel (0 = black…255 = white), the interface of the sediment bed was determined and averaged over a sufficient length.

In case of the CFD results, the bed heights of case #2 and #5 are not representing the final steady state, as may be seen from the respective time series given in Figure 7 and Figure 9.

Table 2: CFD vs. experimental averaged bed heights

[#]	h_{bed} (CFD) [m]	h_{bed} (Exp) [m]	Ratio [-]
1	0.019	0.0052	3.65
2	0.0056	0.0093	0.60
3	n/a	0.0139	n/a
4	0.0136	0.0146	0.93
5	0.00157	0.0100	0.16

These time series actually indicate an eroding bed, which may eventually entirely vanish from the domain. This may be explained by (1) an overprediction of the solid transport capacity of the numerical model or (2) by an underestimation of the amount of solids entering the domain. In the case of (1), the bed load transport formula may need improvement with regards to the confined domain, non-Newtonian rheology or tuning of its model constants. The two latter aspects may also be valid for the entrainment model. Interestingly, the simulation result of case #1, does not support overprediction of solid transport capacity, as the bed height obtained from CFD simulations is 3.65 times the corresponding experimentally obtained bed height (see Table 2). In the case of (2), the amount of solids entering the domain could only be estimated based on equation (23) and corresponding experimental data. However, the estimated superficial velocities are global values, representing the respective superficial velocities on the entire flow loop system level. In order to improve on this BC estimate, measurements of the local superficial velocities at the test section inlet, or alternatively the solids concentration profile, would be required.

In general, comparison of the results is further complicated by the two different domains utilized in this study. In the experiments, a pipe geometry has been used, whereas in the CFD simulations, a 2D channel (with an infinitesimal long z-coordinate) has been used. As pointed out in subsection “BC & model parameters” of section 7, it is not straightforward to match these two different geometries with regards to BC.

Due to the uncertainties and shortcomings of the current status of the numerical model, as described in the subsection “Numerical Modeling” of section 7, a valid comparison of bed heights obtained from experiments and CFD simulations is not possible yet.

8. CONCLUSION

1. The model developed so far does have major shortcomings when it comes to prediction of dunes as it may only predict the steady-state average bed height. A simplified LES approach, e.g. the VLES concept currently investigated, may lead to a model capable of describing flow-induced dynamic bed shapes such as travelling dunes.
2. The numerical model apparently does not correctly predict the transport capacity of the flow. An improved bed load transport model, together with a more realistic entrainment model, may yield more realistic transport capacities and consequently better predict the steady-state bed shape.
3. Improved inlet boundary conditions, in particular an inlet turbulent velocity profile together with a solid volume fraction profile, may considerably shorten

entrance length effects and consequently speed up computations.

4. Further modeling work is required to adequately describe the effect of non-Newtonian rheology on various elements of the model: Non-Newtonian formulations for closures such as the bed load formula, the drag coefficient, the (critical) Shields number, and the hindered settling effect as well as non-Newtonian turbulence interdependencies may improve the model.
5. An investigation of the model's sensitivity with respect to bed roughness and in-situ solid volume fraction at the inlet is necessary in order to understand the effect of these two uncertain parameters.
6. An extension of the model to 3D will extend the applicability of the model for pipe flows, annular flows and potentially even more complex flows.

9. ACKNOWLEDGEMENTS

The project *Advanced Wellbore transport Modelling (AdWell)* with its sponsor, the Research Council of Norway and its partners Statoil, GDF SUEZ E&P Norge, IRIS, UiS, NTNU and SINTEF are gratefully acknowledged for funding and supporting part of this work.

10. REFERENCES

Bello, K. O. et al., (2011), "Minimum Transport Velocity Models for Suspended Particles in Multiphase Flow Revisited." *In* SPE Annual Technical Conference and Exhibition Society of Petroleum Engineers.

Brørs, B., (1999), "Numerical Modeling of Flow and Scour at Pipelines." *Journal of Hydraulic Engineering* 125:511–523.

Celik, I., and Rodi, W., (1988), "Modeling Suspended Sediment Transport in Nonequilibrium Situations." *Journal of Hydraulic Engineering* 114:1157–1191.

Ceylan, K. et al., (1999), "A theoretical model for estimation of drag force in the flow of non-newtonian fluids around spherical solid particles." *Powder Technology* 103:286–291.

Childs, L. H. et al., (2016), "Dynamic settling of particles in shear flows of shear-thinning fluids." *Journal of Non-Newtonian Fluid Mechanics* 235:83–94.

Corredor, R. et al., (2016), "Experimental investigation of cuttings bed erosion in horizontal wells using water and drag reducing fluids." *Journal of Petroleum Science and Engineering* 147:129–142.

Doron, P., and Barnea, D., (1993), "A three-layer model for solid-liquid flow in horizontal pipes." *International Journal of Multiphase Flow* 19:1029–1043.

Exner, F. M., (1925), "Uber die Wechselwirkung zwischen Wasser und Geschiebe in Flüssen." *Akad. Wiss. Wien Math. Naturwiss. Klasse* 134:165–204.

Garside, J., and Al-Dibouni, M. R., (1977), "Velocity-Voidage Relationships for Fluidization and Sedimentation in Solid-Liquid Systems." *Industrial & Engineering Chemistry Process Design and Development* 16:206–214.

Gavrilov, A. A., and Rudyak, V. Y., (2016), "Reynolds-averaged modeling of turbulent flows of power-law fluids." *Journal of Non-Newtonian Fluid Mechanics* 227:45–55.

Goharzadeh, A. et al., (2013), "Experimental Characterization of Slug Flow on Solid Particle Transport in a 1 Deg Upward Inclined Pipeline." *Journal of Fluids Engineering* 135:081304.

Han, S. M. et al., (2010), "Solid-liquid hydrodynamics in a slim hole drilling annulus." *Journal of Petroleum Science and Engineering* 70:308–319.

Johansen, S. T., (2015), "Improved fluid control by proper non-Newtonian flow modeling." *In* Tekna – Flow Assurance Larvik.

Johansen, S. T. et al., (2004), "Filter-based unsteady RANS computations." *International Journal of Heat and Fluid Flow* 25:10–21.

Khatibi, M. et al., (2016a), "Experimental Investigation of Effect of Salts on Rheological Properties of Non-Newtonian Fluids." *In* Nordic Rheology Conference, University of Helsinki, Finland.

Khatibi, M. et al., (2016b), "Particles Falling Through Viscoelastic Non-Newtonian Flows in a Horizontal Rectangular Channel Analyzed with PIV and PTV Techniques." *Journal of Non-Newtonian Fluid Mechanics* 235:143–153.

Khosronejad, A. et al., (2011), "Curvilinear immersed boundary method for simulating coupled flow and bed morphodynamic interactions due to sediment transport phenomena." *Advances in Water Resources* 34:829–843.

Khosronejad, A. et al., (2015), "Numerical simulation of large dunes in meandering streams and rivers with in-stream rock structures." *Fluvial Eco-Hydraulics And Morphodynamics* 81:45–61.

Khosronejad, A., and Sotiropoulos, F., (2014), "Numerical simulation of sand waves in a turbulent open channel flow." *Journal of Fluid Mechanics* 753:150–216.

Li, S. et al., (2012), "The viscosity distribution around a rising bubble in shear-thinning non-newtonian fluids." *Brazilian Journal of Chemical Engineering* 29:265–274.

Liang, D. et al., (2005), "Numerical modeling of flow and scour below a pipeline in currents - Part II. Scour simulation." *Coastal Engineering* 52:43–62.

Manzar, M. A., and Shah, S. N., (2014), "Particle Distribution and Erosion During the Flow of Newtonian and Non-Newtonian Slurries in Straight and Coiled Pipes." *Engineering Applications of Computational Fluid Mechanics* 3:296–320.

Menter, F. R., (1994), "Two-equation eddy-viscosity turbulence models for engineering applications." *AIAA Journal* 32:1598–1605.

Nielsen, P., (1992), "Coastal bottom boundary layers and sediment transport." World Scientific Publishing Co Inc.

Nossair, A. M. et al., (2012), "Influence of Pipeline Inclination on Hydraulic Conveying of Sand Particles." *In* ASME 2012 International Mechanical Engineering Congress and Exposition pp. 2287–2293. American Society of Mechanical Engineers.

Ofei, T. N. et al., (2014), "CFD Method for Predicting Annular Pressure Losses and Cuttings Concentration in Eccentric Horizontal Wells." *Journal of Petroleum Engineering* 2014:1–16.

Pinho, F. T., (2003), "A Model for the Effect of Turbulence on the Molecular Viscosity of Generalized Newtonian Fluids." *In* 17th International Congress of

Mechanical Engineering, Brazilian Society of Mechanical Sciences and Engineering (ABCM), Sao Paulo.

RENAUD, M. ET AL., (2004), "Power-Law Fluid Flow Over a Sphere: Average Shear Rate and Drag Coefficient." *The Canadian Journal of Chemical Engineering* 82:1066–1070.

RICHARDSON, J. F., AND ZAKI, W. N., (1957), "Sedimentation and fluidisation: Part I." *Chemical Engineering Research and Design* 75:S82–S100.

SAFFMAN, P. G., (1965), "The lift on a small sphere in a slow shear flow." *Journal of Fluid Mechanics* 22:385.

SAVAGE, S. B. ET AL., (1996), "Solids transport, separation and classification." *Powder technology* 88:323–333.

SCHILLER, L., AND NAUMANN, A., (1933), "Über die grundlegenden Berechnungen bei der Schwerkraftaufbereitung." *Z. Ver. Dtsch. Ing* 77:318–320.

SHAH, S. N. ET AL., (2007), "New model for single spherical particle settling velocity in power law (visco-inelastic) fluids." *International Journal of Multiphase Flow* 33:51–66.

SHAH, S. N., AND OTHERS, (1986), "Proppant-settling correlations for non-Newtonian Fluids." *SPE Production Engineering* 1:446–448.

SHIELDS, A., (1936), "Anwendung der Aehnlichkeitsmechanik und der Turbulenzforschung auf die Geschiebebewegung."

SIMONIN, C., AND VIOLLET, P., (1990a), "Predictions of an oxygen droplet pulverization in a compressible subsonic coflowing hydrogen flow." *Numerical Methods for Multiphase Flows, FED91*:65–82.

SIMONIN, O., AND VIOLLET, P., (1990b), "Modelling of turbulent two-phase jets loaded with discrete particles." *FG Hewitt, et al., Phenomena in multiphase yow*:259.

SOLBERG, T. ET AL., (2006), "CFD modelling of scour around offshore wind turbines in areas with strong currents." *In* Offshore Wind Turbines situated in Areas with Strong Currents Offshore Center Danmark, Esbjerg.

SOULSBY, R., (1997), "6. Threshold of motion." *In* Dynamics of marine sands pp. 97–110. Thomas Telford Publishing.

STRUIKSMA, N., AND CROSATO, A., (1989), "Analysis of a 2-D bed topography model for rivers." *In* Water Resources Monograph (S. Ikeda and G. Parker, eds.) pp. 153–180. American Geophysical Union, Washington, D. C.

SUN, X. ET AL., (2014), "Effect of drillpipe rotation on cuttings transport using computational fluid dynamics (CFD) in complex structure wells." *Journal of Petroleum Exploration and Production Technology* 4:255–261.

Manuscript 1 (VII)

DNS vs. RANS turbulence modeling of turbulent pipe and annular flows of shear-thinning fluids

Alexander Busch, Are Simonsen, Stein Tore Johansen

In progress.

DNS vs. RANS turbulence modeling of turbulent pipe and annular flows of shear-thinning fluids

Alexander Busch[1,*], Are Simonsen[2], Stein Tore Johansen[1, 2]

[1] Norwegian University of Science and Technology (NTNU), Trondheim, Norway

[2] SINTEF Materials and Chemistry, Trondheim, Norway

*Corresponding author: alexander.busch@ntnu.no, alexander.busch@alumni.ntnu.no

Keywords: Turbulence, GNF, shear-thinning, drilling, annular, pipe, CFD, RANS, DNS, non-Newtonian.

Abstract

This manuscript summarizes work conducted in the AdWell project by SINTEF personnel and me regarding the quality of Reynolds-Averaged-Navier-Stokes (RANS) turbulence modelling when investigating wellbore flow cases in the industrially relevant Metzner-Reed (1955) Reynolds number range Re_{MR} ≈ 226…25160. Both pipe and annular Direct Numerical Simulations (DNS) for different fluids as well as eccentricities and inner pipe rotation rates were conducted by SINTEF. The respective specifications were used to run RANS simulations were turbulence was modelled with models typically used in the industry. Three different turbulence models were investigated, the Lam-Bremhorst (1981) variant of the Standard k-ϵ model, the Marin (1997) modification of the latter suited for Power-Law (PL) fluids, and the k-ω SST model, all of which are standard models in the commercial code Fluent and comparetively cheap to use in terms of computational power.

So far, a limited set of cases has been investigated. However, preliminary results show, that all models have pros and cons: While the k-ω SST model can cover the Reynolds number range down to the laminar regime, it overpredicts turbulence, in particular when rotation is present. For a Newtonian fluid, the Lam-Bremhorst (1981) variant of the Standard k-ϵ model performs better than the k-ω SST model for Re_{MR} < 10000. For a shear-thinning fluid, the former underpredicts the mass flow rate for a given pressure drop. For the case of a Power-Law material function, the Marin (1997) modification of the Lam-Bremhorst (1981) variant of the Standard k-ϵ model performs very well, both with respect to DNS results and friction factor correlations (Dodge & Metzner 1959, Irvine 1988).

However, several inconsistencies are present in the data sets generated so far and thus the DNS data is currently re-analyzed by SINTEF personnel. Furthermore, a broader parameter range of the design space must be investigated (e.g. more annular PL simulations must be conducted for eccentricities of e = {0, 0.25, 0.75} and a broader variety PL coefficients) until final conclusions regarding the performance of the turbulence models investigated may be drawn.

Contents

Nomenclature

Greek symbols

γ	Strain.
$\dot{\gamma}$	Shear rate, total shear measure.
Δ	Difference.
ϵ	Turbulent dissipation rate.
η	Apparent shear viscosity.
λ	Rheological time scale, parameter in Cross and Carreau model.
μ	Newtonian shear viscosity.
ω	Specific turbulent dissipation rate
ρ	Density.

Latin symbols

A	Surface area.
c	Coefficient.
d	Diameter.
$\mathbf{D}$	Rate of deformation tensor.
f	Functional.
g	Gravity.
K	Parameter in Power-law, also known as Consistency Index.
l	Length.
m	Mass.
n	Parameter in Power-law (PL), also known as PL exponent.
p	Pressure.
Re	Reynolds number.
t	Time.
T	Transposed.
$\mathbf{T}$	Stress tensor.
$\mathbf{u}$	Fluid velocity.
U	Fluid bulk velocity.
v	Particle velocity.
V	Volume.
w	Width.

x	Spatial dimension.
y	Spatial dimension.
z	Spatial dimension.

Indices

0	Zero, $\dot{\gamma} \rightarrow 0$.
∞	Infinity, $\dot{\gamma} \rightarrow \infty$.
Ca	Carreau.
Cr	Cross.
f	Fluid.
PL	Power Law.
t	Turbulent.
τ	Friction

Abbreviations

2D, 3D	Two-, Three dimensional in space.
CFD	Computational Fluid Dynamics.
FC	Flow Curve.
GNF	Generalized Newtonian Fluid.
PL	Power-Law.

1 Introduction

The turbulent flow of shear-thinning fluids is an important problem in the oil and gas industry. For instance, in wellbore flows, shear-thinning (and often additionally viscoelastic and thixotropic) drilling fluid systems are used to transport drilled-off particles also known as "cuttings" back to the surface. Focusing on the single-phase subproblem of hydrodynamics, a relevant question is "For a given domain of interest—typically a (drill) pipe or a (concentric or eccentric) annulus, where the inner pipe may rotate or not—and a given flow rate, what is the pressure gradient dp/dx (or vice-versa, what is the flow rate as a function of dp/dx)? While the modeling of Newtonian turbulent flows has matured to a satisfactory level for industrially-relevant problems this is less so for non-Newtonian fluids.

In recent years, Real-Time (RT) models have gained importance in the drilling industry, which are typically based on simple one-dimensional (1D) mechanistic/phenomenological models. Computational-Fluid-Dynamics (CFD) simulations have just as well become increasingly important in recent years because they may contribute with a better understanding of the complex rheological and flow physics involved and provide input for closure laws required for the 1D RT models.

Depending on the required information and the available computational speed, one may in principle distinguish between (1) simple (empirical) correlations providing the Fanning friction factor f as a function of a to-be-defined Reynolds number Re, (2) the aforementioned and more sophisticated CFD models, where the entire flow field in a typically three-dimensional domain of interest (pipe, annuli) is being computed utilizing closures to handle turbulence, and Direct Numerical Simulations (DNS), where turbulence is resolved on all length and time scales without the need for modeling.

1.1 Friction factor correlations for turbulent flows of shear-thinning fluids

Various Newtonian friction factor correlations, e.g. [1], [2], [3] exist and produce quite accurate results for turbulent flows. For non-Newtonian fluids, mainly power-law (PL) based correlations, e.g. [4–7] and more recently [8,9], for pipes and e.g. [10] for non-circular ducts such as annuli, exist. Some of these correlations are not consistent, which may partly be a consequence of the inherent Generalized Non-Newtonian Fluid (GNF) assumption of the PL model, which ignores any thixotropic and/or viscoelastic effects that may have been present in the underlying experiments. Various GNF friction factor laws and also Reynolds number definitions were evaluated by e.g. [11] [12] [13]. The hydraulic diameter concept is best-suited to correlate data in case on an annulus [11]. However, a generic framework for annuli is given by the work of Kozicke et al. [14] and Delplace and Leuliet [15], who defined a Reynolds number for PL fluids accounting for the hydraulic diameter as well as the diameter ratio.

1.2 RANS modeling of turbulent flows of shear-thinning fluids

A broad variety of turbulence models exist these days, the most relevant ones available in commercial CFD codes are the standard k-ϵ model along with its many variants and the more versatile k-ω SST model as the industrial workhorse of modern CFD codes. Historically, these models were developed for turbulent flows of Newtonian fluids. However, assuming a Generalized Newtonian Fluid (GNF), i.e. instantaneous adaption of viscosity to change in shear rate and hence no elastic and/or thixotropic properties, several non-Newtonian variants of low Reynolds number k-ϵ models were developed over the years, for instance for PL fluids in pipes [16][17] [18,19] [20,21], Herschel-Buckley fluids in annuli [22], or drag-reducing fluids in pipes [23] [24].

Several studies have focused on the evaluation of the performance of turbulence models, e.g. Newtonian fluids in concentric and eccentric annuli [25], Generalized Newtonian Fluids (GNF) in pipes [26] and concentric annuli [27] as well as more complex geometry [28].

1.3 Direct numerical simulations of turbulent flows of shear-thinning fluids

DNS of GNF is a relatively new research field. The first simulations on pipe flow were published in 2002 [29], two decades after the emergence of Newtonian DNS. The early results [30] [31] reproduced many of the experimentally observed characteristics of GNF flows such as reduced skin friction, lower turbulence intensities, and delayed transition for shear thinning fluids compared to their Newtonian counterpart. The results also showed that these effects increased with the degree of shear thinning. However, a major uncertainty with regard to the accuracy of the DNS were that the level of skin friction was overpredicted by 10-15% compared to measured data [32]. Later this was contributed to the lack of rheology characterization at high shear rates [33] and new flow experiments backed up by rheogram data covering the high shear rate end gave a skin friction comparison within 1% between experiments and DNS. As in the case for Newtonian flow, DNS has given new and detailed insight into the details of turbulent GNF flows [34] [35] [36] [37] [38] and will continue to do so in the future. There is a lack of DNS with GNF for other geometries than circular pipe, and a full comparison with experiments between cross sectionals profiles of mean flow and turbulence statistics is still missing.

1.4 Purpose, scope and structure of this paper

To improve cuttings transport RT modeling by enhanced CFD models, we investigate the performance of industrially available turbulence models, namely the standard k-ε in (1) its original definition [39], (2) in a low-Re formulation [40], and (3) in a non-Newtonian modification of the latter [17] as well as the k-ω SST model [41,42] by CFD simulations of various industrially relevant flow cases in both a pipe and an annular domain. For the later, the effects of drill pipe (= inner pipe) rotation and eccentricity are investigated. Additionally, Direct Numerical Simulations (DNS) are conducted for the very same cases. We compare the obtained CFD and DNS results and benchmark our results with data available in the literature [30,33,43].

Hereafter we briefly present the flow model with its rheological and turbulence model closures and provide the relevant parameters for all cases investigated. In section 3, we present the results in dimensional (pressure gradient dp/dx as a function of mass flow rate $\dot{m}$) as well as in non-dimensional

(Fanning friction factor f as a function of Metzner-Reed (MR) Reynolds number Re_{MR} [4])[1] form. The performance of the different turbulence models is discussed in section 4, supplemented with non-dimensional velocity profiles (both x-velocity divided by bulk velocity as a function of the radial coordinate y divided by the radius R and classical u+-y+-plots) and a conclusion is provided in section 5. Supplemental material such as the scaling concepts utilized is provided in the Appendix.

2 Materials and Methods

2.1 The Eulerian equations of motion

Assuming an isothermal system, a fluid may be described by mass and momentum conservation in an Eulerian frame of reference in an appropriate control volume based on the Cauchy equations of motion. For an incompressible fluid, mass conservation is simply given by $\nabla \cdot (\rho \mathbf{u}) = 0$, where ρ is the fluids constant and homogenous density and $\mathbf{u}$ the velocity field. The momentum balance is given by

$$\frac{\partial}{\partial t}(\rho \mathbf{u}) + \nabla \cdot (\rho \mathbf{u}\mathbf{u}) = -\nabla p - \nabla \cdot \mathbf{T} + \rho \mathbf{g} \quad , \tag{1}$$

where $\mathbf{T}$ is the deviatoric stress tensor comprising some constitutive equation and material function(s) for the fluid and p is the thermodynamic pressure. Unless these balance equations are solved to the smallest length scales, the phenomenon of turbulence is to be modelled. As a consequence of performing Reynolds averaging [44] of the instantaneous balance equations for mass and momentum a so-called Reynolds stress term $\nabla\left(-\rho\overline{\mathbf{u}'\mathbf{u}'}\right)$ arises in the—now ensemble-averaged—momentum conservation equation. The Reynolds stress tensor $-\rho\overline{\mathbf{u}'\mathbf{u}'}$ is typically assumed symmetric and may be modeled with dedicated Reynolds-Stress-Models (RSM) or, alternatively, employing the Boussinesque hypothesis [45] to relate the Reynolds stresses to the mean velocity gradients and the turbulent viscosity based on the concept of the gradient diffusion hypothesis. This leads to a deviatoric stress tensor $\mathbf{T} = \mathbf{T}_v + \mathbf{T}_t$, where $\mathbf{T}_v$ and $\mathbf{T}_t$ denote viscous and turbulent stresses, respectively.

For a shearing flow of an incompressible and purely viscous (here shear-thinning) fluid, i.e. no viscoelastic and/or time-dependent microstructural/thixotropic fluid properties, i.e. a Generalized Non-Newtonian Fluid (GNF), the deviatoric viscous stress tensor $\mathbf{T}_v$ of the Cauchy momentum equation reads

$$\mathbf{T}_v = -2\eta(\dot{\gamma})\mathbf{D} \; , \tag{2}$$

where $\mathbf{D}$ is the symmetric part of the fluid velocity gradient (also known as the rate of deformation tensor, or alternatively the rate of strain tensor)

---

[1] The MR Reynolds number is based friction factor equivalence of a Newtonian and a non-Newtonian fluid in the laminar regime and is therefore convenient to use when the bulk velocity is known a priori. However, in case of the bulk velocity being the solution of a specified pressure gradient, usage of a Generalized Reynolds number Re_G based on the wall shear stress and wall viscosity is more suitable. We briefly describe the differences of these two scaling approaches in section 4.3.

$$\mathbf{D}=\frac{1}{2}\left(\nabla\mathbf{u}+\nabla\mathbf{u}^{T}\right). \tag{3}$$

For a GNF, the fluids apparent viscosity η in equation (2) is purely a function of the magnitude of the fluids instantaneous rate of deformation tensor $\mathbf{D}$**,** the *shear rate* $\dot{\gamma}$

$$\eta=f\left(\dot{\gamma}\right) \quad \text{with} \quad \dot{\gamma}=\sqrt{2\mathbf{D}:\mathbf{D}}=\sqrt{2\left(D_{11}{}^{2}+D_{12}{}^{2}+\ldots\right)}\ , \tag{4}$$

where the functional f may be modeled with an appropriate GNF material function, e.g. [46].

The Boussinesq hypothesis [45] in the form of

$$\mathbf{T}_t=-2\mu_t\mathbf{D}\ , \tag{5}$$

is the underlying basis of all computationally cheap and hence industrially-used one and two equation turbulence models, such as the k-ϵ and k-ω family of models. Here, the turbulent viscosity μ_t is defined by the turbulent kinetic energy k, and the dissipation rate ϵ or the specific dissipation rate ω, all of which are described by additional transport equations.

2.2 Rheological closures

We are here concerned with pure shear-thinning fluids which obey the GNF constitutive equation (2). The most simple formulation accounting for shear-thinning behavior is the Ostwald material function [47], also known as power law (PL), here given in a time constant formulation [48]

$$\eta_f\left(\dot{\gamma}\right)=\eta_0\left(\lambda_{PL}\dot{\gamma}\right)^{n_{PL}-1}\ . \tag{6}$$

Note, that the ordinary PL coefficient K_{PL} may be obtained as $K=\eta_0\lambda_{PL}^{n_{PL}-1}$.

In case of a polymeric solution, however, the functional f in equation (4) is best-expressed with the Cross (Cr) [46] material function

$$\eta_f\left(\dot{\gamma}\right)=\frac{\mu_0-\mu_\infty}{1+\left(\lambda_{Cr}\dot{\gamma}\right)^{1-n_{Cr}}}+\ \mu_\infty\ . \tag{7}$$

This represents the apparent viscosity data much better for a wider shear rate range because it accounts for Newtonian viscosities at both low and high shear rates. Here, μ_0 is the zero-shear viscosity, μ_∞ is the infinite-shear viscosity, λ_{Cr} is the Cross time constant and n_{Cr} is the Cross exponent[2]. One may infer PL coefficients for any given point of the flow curve $\eta_f=f(\dot{\gamma})$ by requiring:

---

[2] Note the subtle difference between the original Cross [46] formulation, where the exponent of $(\lambda_{Cr}\dot{\gamma})$ is just n_{Cr} and the definition used here where the exponent is defined as $1-n_{Cr}$ to ensure that in the limit of high shear rates but absence of a high-shear-rate Newtonian viscosity plateau equation (6) is obtained. However, the model constants for the Cross case are defined to fulfill equation (8) in the inflection point of the Cross flow curve.

$$\begin{aligned} \eta_{PL}(\dot{\gamma}) &= \eta_{Cr}(\dot{\gamma}) \\ \frac{\partial \eta_{PL}(\dot{\gamma})}{\partial \dot{\gamma}} &= \frac{\partial \eta_{Cr}(\dot{\gamma})}{\partial \dot{\gamma}} . \end{aligned} \tag{8}$$

Note that the inverse of Cross time constant $1/\lambda_{Cr}$ is equivalent to the shear rate where the respective Newtonian zero-shear viscosity region and the shear-thinning region intersect.

For this study, a set of fluids (Newtonian, Power Law (PL), and Cross (Cr), all with density ρ = 1 kg/m³, were designed such that the respective flow curves (FC) all intersect in the same τ_w = $\eta_w \dot{\gamma}_w$ = 0.0036 Pa as depicted in Figure 1.

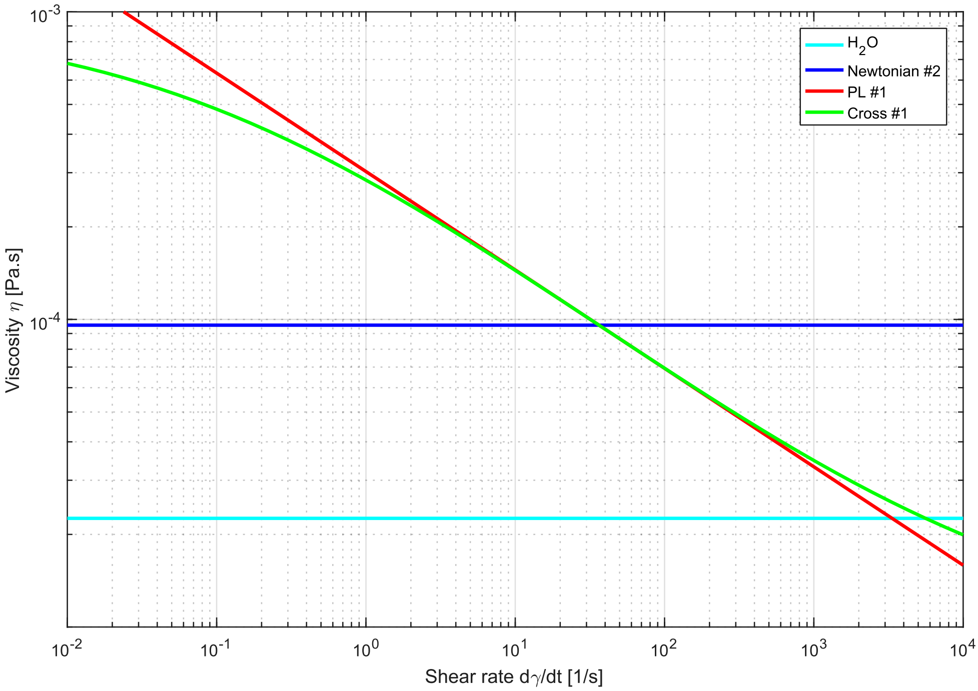

Figure 1: Flow curves for the scaled model coefficients given in Table 1. Newtonian = Ne2 and PL = PL1 and Cross = Cr1.

This corresponds to a pressure gradient dp/dx = 0.01447 Pa/m, for which, if scaled based on Reynolds number equivalence, DNS data from the literature is available [33] for the PL case. The scaling was done such that both the scaled density and hydraulic diameter are equal to unity (see 5C.4), as this is a requirement of the DNS code. The inflection point of the Cross FC coincides with the η_w of the Newtonian fluid, and the lower and upper Cross viscosity plateaus were specified as η_w/10 and 10·η_w, respectively. The model coefficients are provided in Table 1.

Fluid	Scaled				
	$\boldsymbol{\mu_0}$ [Pa·s]	$\boldsymbol{\mu_\infty}$ [Pa·s]	$\boldsymbol{\lambda_i}$ [1/s]	$\boldsymbol{n_i}$ [-]	$\boldsymbol{K_i}$ [Pa·s]

H_2O[3]	2.25e-5	n/a	n/a	1	2.25e-5
Newtonian #1	1.25e-4	n/a	n/a	1	1.25e-4
Newtonian #2	9.58e-5	n/a	n/a	1	9.58e-5
PL #1	n/a	n/a	n/a	0.68	3.02e-4
Cross #1	9.48e-4	9.48e-6	9.5825	0.60861	n/a

Table 1: Scaled rheological model coefficients for the different fluids investigated. All simulations (DNS and CFD) were performed with the coefficients scaled in manner such that ρ = 1 kg/m³. The scaling concept is based on Reynolds number and described in Appendix 5C.4 and the respective flow curves are depicted in Figure 1.

For purpose of validation, the investigated Newtonian #1 case corresponds to the annular case of Nikitin et al. [43] with a Reynolds number Re = 8000 and a friction Reynolds number $Re_\tau = \rho u_\tau d_h/(2\eta)$ = 260, the PL #1 case corresponds to the pipe case of Sing et al. [33] with Re = 10500 and Re_τ = 630, while the Newtonian #2 case is based on the PL #1 case in terms of equivalent wall shear stress and rheology.

2.3 Turbulence closures

In case of CFD modeling, additional closures for the Reynolds stress term are required, while in case of DNS, turbulence is resolved on all length and time scales. The former is achieved by applying equation (5) in conjunction with a turbulence model.

Defined by Launder and Spalding [39,49], turbulence in the k-ε model family is modelled by the two transported properties turbulent kinetic energy k and its dissipation rate ε, for which the respective transport equations read

$$\frac{\partial}{\partial t}(\rho k)+\frac{\partial}{\partial x_i}(\rho k u_i)=\frac{\partial}{\partial x_j}\left[\left(\mu+\frac{\mu_t}{\sigma_k}\right)\frac{\partial k}{\partial x_j}\right]+G_k-\underbrace{\rho\varepsilon}_{Diss}, \tag{9}$$

$$\frac{\partial}{\partial t}(\rho \varepsilon)+\frac{\partial}{\partial x_i}(\rho \varepsilon u_i)=\frac{\partial}{\partial x_j}\left[\left(\mu+\frac{\mu_t}{\sigma_\varepsilon}\right)\frac{\partial \varepsilon}{\partial x_j}\right]+\underbrace{C_{1\varepsilon}\frac{\varepsilon}{k}G_k}_{\mathrm{Prod}}-\underbrace{C_{2\varepsilon}\rho\frac{\varepsilon^2}{k}}_{Diss}. \tag{10}$$

with the turbulent (or eddy) viscosity

$$\mu_t=\rho f_\mu C_\mu\frac{k^2}{\varepsilon}, \tag{11}$$

the generation of turbulent kinetic energy due to the mean velocity gradients

$$G_k\overset{def}{=}-\rho\overline{u_i'u_j'}\frac{\partial u_j}{\partial x_i}=\mu_t\dot{\gamma}^2, \tag{12}$$

---

[3] While it is physically more reasonable to define H_2O as μ_∞ = 0.00102 Pa (because it represents the solvent viscosity, i.e. the limiting high-shear-rate Newtonian viscosity plateau, for liquids obeying the Cross material functions such as polymeric solutions), we have tabulated the model coefficients to be mathematically consistent with the PL and Cross material functions utilized.

and the empirically derived model constants $C_{1\varepsilon}$= 1.44, $C_{2\varepsilon}$ = 1.92, C_μ = 0.09 and the turbulent Prandtl numbers σ_k = 1 and σ_ϵ = 1.3.

The eddy viscosity (11) is determined from a single turbulence length scale, so the calculated turbulent diffusion is that which occurs only at the specified scale, whereas in reality all scales of motion will contribute to the turbulent diffusion.

The standard k-ε model does not adequately describe complex flows involving severe and/or or adverse pressure gradients and separation and/or strong streamline curvature and shows numerical stiffness when equations are integrated through the viscous sublayer which are treated with damping functions that have stability issues [41,42].

Several low-Re versions of the k-ε model exist, where the turbulent viscosity μ_t is damped in the near-wall region using a damping function f_μ. Industrially relevant turbulent flow of non-Newtonian fluids typically occurs at low Reynolds numbers hence several non-Newtonian modifications of low-Re k-ε models are also available in the literature, see e.g. [16] for an overview. We here investigate the formulation of Malin [17], who; for flows of PL fluids in smooth circular pipes, amended the Lam-Bremhost low-Reynolds number k-ϵ model variant [40] by introducing a dependency of the eddy viscosity near-wall damping function f_μ on the PL coefficient n, namely

$$f_\mu = \left(1 - \exp\left(-0.0165\,\mathrm{Re}_n / n^{0.25}\right)\right)^2 \left(1 + 205/\mathrm{Re}_t\right) . \tag{13}$$

The two Reynolds numbers are defined as

$$\mathrm{Re}_n = \frac{\rho\sqrt{k}\,y}{\mu} \tag{14}$$

and

$$\mathrm{Re}_t = \frac{\rho k^2}{\mu\varepsilon} , \tag{15}$$

where y is the normal distance to the wall.

Besides the definition of f_μ, the Lam-Bremhost low-Reynolds number k-ϵ model variant [40] deviates from the k-ϵ model by redefining the model coefficients $C_{1\varepsilon}$ and $C_{2\varepsilon}$ as damping functions f_1 and f_2, respectively:

$$f_1 = 1 + \left(0.05 / f_\mu\right)^3 , \tag{16}$$

$$f_2 = 1 + \exp\left(-\mathrm{Re}_t{}^2\right) , \tag{17}$$

Introduced by Wilcox [50], the k-ω model consists of one equation for the turbulent kinetic energy k and a second equation for the specific turbulent dissipation rate (or turbulent frequency) ω, which can also be thought of as the ratio of ε to k. The major difference to the k-ε family of models is that the k-ω model can be integrated through the viscous sublayer due to an automatic switch from a wall function to a low-

Reynolds number formulation based on grid spacing and therefore allows for a more accurate near wall treatment.

Compared to the k-ϵ model, the k-ω model demonstrates superior performance for wall-bounded and low Reynolds number flows, shows potential for predicting transition and performs significantly better under adverse pressure gradient conditions. However, it underpredicts the amount of separation for severe adverse pressure gradient flows [41,42].

The baseline (BSL) k-ω model is a variant of the standard k-ω model combining the original Wilcox [50] k-ω model for use near walls and the standard k-ϵ model (converted into a k-ω formulation) away from walls using a blending function [41,42]. This eliminates the standard k-ω model's strong sensitivity to free stream conditions without sacrificing near-wall performance.

In addition to all the BSL k-ω model features, the Shear Stress Transport (SST) k-ω model [41,42] accounts for turbulent shear stress transport in the definition of the turbulent viscosity. This makes the SST k-ω more suitable for a wider range of flow problems, for instance the onset and the amount of flow separation under adverse pressure gradient flows as well as airfoils or transonic shock waves [41,42].

For the SST k–ω model, the two transport equations for k and ω are

$$\frac{\partial}{\partial t}(\rho k)+\frac{\partial}{\partial x_i}(\rho k u_i)=\frac{\partial}{\partial x_j}\left[\Gamma_k \frac{\partial k}{\partial x_j}\right]+G_k-Y_k\,, \tag{18}$$

and

$$\frac{\partial}{\partial t}(\rho \omega)+\frac{\partial}{\partial x_i}(\rho \omega u_i)=\frac{\partial}{\partial x_j}\left[\Gamma_\omega \frac{\partial \omega}{\partial x_j}\right]+G_\omega-Y_\omega+D_\omega\,, \tag{19}$$

respectively, with the effective diffusivities

$$\Gamma_k=\mu+\frac{\mu_t}{\sigma_k} \tag{20}$$

and

$$\Gamma_\omega=\mu+\frac{\mu_t}{\sigma_\omega}\,, \tag{21}$$

where, in contrast to the standard k-ω model, the turbulent viscosity is defined as

$$\mu_t=l\,\frac{\rho k}{\omega}\,. \tag{22}$$

The limiter coefficient

$$l=\max\left[\frac{1}{\alpha^*},\quad \frac{\dot{\gamma} F_2}{a_1\omega}\right], \tag{23}$$

with

$$F_2 = \tanh\left({\Phi_2}^2\right) \tag{24}$$

and

$$\Phi_2 = \max\left[\frac{2\sqrt{k}}{0.09\omega y},\quad \frac{500\eta}{\rho\omega y^2}\right], \tag{25}$$

where y is the distance to the next surface, ensures that overprediction of the turbulent viscosity is avoided and therefore enables the SST k-ω model to better predict the onset and amount of flow separation from smooth surfaces.

In case of the low-Reynolds number variant, the damping factor

$$\alpha^* = {\alpha^*}_\infty \frac{{\alpha^*}_0 + \mathrm{Re}_t / R_k}{1 + \mathrm{Re}_t / R_k} \tag{26}$$

with α_∞^* = β_i/3 damps the turbulent viscosity at low turbulent Reynolds numbers

$$\mathrm{Re}_t = \frac{\rho k}{\mu\omega}, \tag{27}$$

whereas in the high-Reynolds number variant, all damping coefficients yield unity, i.e. $\alpha = \alpha_\infty = \alpha^* = \alpha_\infty^* = 1$.

While the turbulent Prandtl numbers for k and ω are σ_k = σ_ω = 2 in the classic k-ω model, in the SST k-ω model they are respectively defined as

$$\sigma_k = \frac{1}{F_1/\sigma_{k,1} + \left(1 - F_1\right)/\sigma_{k,2}} \tag{28}$$

and

$$\sigma_\omega = \frac{1}{F_1/\sigma_{\omega,1} + \left(1 - F_1\right)/\sigma_{\omega,2}}, \tag{29}$$

where the blending function

$$F_1 = \tanh\left({\Phi_1}^4\right) \tag{30}$$

with

$$\Phi_1 = \min\left[\max\left[\frac{\sqrt{k}}{0.09\omega y},\quad \frac{500\eta}{\rho\omega y^2}\right],\quad \frac{4\rho k}{\sigma_{\omega,2} D_\omega^{+,\lim} y^2}\right], \tag{31}$$

y being is the distance to the next surface and the limited positive portion of the cross-diffusion term

$$D_\omega^{+,\lim} = \max\left[D_\omega^+,\quad 10^{-10}\right], \tag{32}$$

switches between the models.

The cross diffusion term D_ω, which arises in equation (19) as a consequence of the blending of the standard k-ω model and the standard k-ϵ model (converted to a k-ω formulation), reads

$$D_\omega = \left(1 - F_1\right) D_\omega^+ , \tag{33}$$

with the positive part

$$D_\omega^+ = \frac{2\rho}{\sigma_{\omega,2}\omega} \frac{\partial k}{\partial x_j} \frac{\partial \omega}{\partial x_j} . \tag{34}$$

The generation of the turbulent kinetic energy due to the mean velocity gradients is identical to equation (12) and, in contrast to the standard k-ω model, the production of ω is given by

$$G_\omega = \frac{\rho \alpha \alpha^*}{\mu_t} G_k , \tag{35}$$

with the damping coefficient

$$\alpha = \frac{\alpha_\infty}{\alpha^*} \frac{\alpha_0 + \mathrm{Re}_t / R_\omega}{1 + \mathrm{Re}_t / R_\omega} . \tag{36}$$

In the standard k-ω model, α_∞ = 0.52, whereas in the SST k-ω model

$$\alpha_\infty = F_1 \alpha_{\infty,1} + \left(1 - F_1\right) \alpha_{\infty,2} , \tag{37}$$

with the limits

$$\alpha_{\infty,1} = \frac{\beta_{i,1}}{\beta_\infty^*} - \frac{\kappa^2}{\sigma_{\omega,1}\sqrt{\beta_\infty^*}} \tag{38}$$

and

$$\alpha_{\infty,2} = \frac{\beta_{i,2}}{\beta_\infty^*} - \frac{\kappa^2}{\sigma_{\omega,2}\sqrt{\beta_\infty^*}} . \tag{39}$$

The dissipation of k is given by

$$Y_k = \rho \beta^* f_{\beta^*} k \omega , \tag{40}$$

where f_{β^*} = 1, instead of being a piecewise function as in the standard k-ω model formulation.

The dissipation of ω is given by

$$Y_\omega = \rho \beta_i f_\beta \omega^2 , \tag{41}$$

where

$$\beta_i = F_1 \beta_{i,1} + \left(1 - F_1\right) \beta_{i,2} , \tag{42}$$

instead of being a constant as in the standard k-ω model formulation. However, in the case of the low-Reynolds number SST k-ω model variant, α_0^* in equation (26) is nevertheless defined with β_i = 0.072.

In addition, in equation (41) f_β is simply unity, instead of being a function of vorticity as in the standard k-ω model formulation.

The model constants are $\alpha_\infty^* = 1$, $\alpha_\infty = 0.52$, $\alpha_0 = 1/9$, $a_1 = 0.31$, $\beta_\infty^* = 0.09$, $\beta_{i,1} = 0.075$, $\beta_{i,2} = 0.0828$, $\kappa = 0.41$, $R_\beta = 8$, $R_k = 6$, $R_\omega = 2.95$, $\sigma_{k,1} = 1.176$, $\sigma_{\omega,1} = 2$, $\sigma_{k,2} = 1$, $\sigma_{\omega,2} = 1.168$.

To our knowledge, no non-Newtonian modifications—for instance in the form of damping functions as for the k-ϵ model [17] or in the form of additional closures for averaged apparent viscosity and turbulent cross-correlations with fluctuating viscosity as a consequence of Reynolds-averaging of the non-constant viscosity [19]—have so far been developed for the k-ω family of models. Hence, we employ the SST k-ω model as is and some inaccuracy is expected in the case of non-Newtonian liquids.

2.4 Test matrix

Table 2 summarizes the investigated combinations of turbulence models and non-Newtonian material functions. Not every combination has been investigated so far. For instance, the annular PL simulations have been conducted at e = 0.5 only.

Geometry	Rheology model	e	ω [rad/s]	Turbulence model
Pipe	H2O, Newtonian, PL, Cross	n/a	n/a	k-ϵ Standard, low Re [40] k-ϵ Standard, low Re [40], nN mod. [17] k-ω SST [41,42]
Annulus		0, 0.25, 0.5, 0.75	0, 0.234, 0.5, 1.0	

Table 2: Test matrix.

The non-dimensional eccentricity is defined as $e = 2E/d_h$, where E is the dimensional offset of the axis of the inner pipe from the outer pipe.

In most cases, RANS simulations where run at specified pressure gradients following the DNS specifications, where the pipe cases were run with dp/dx = 0.001, 0.0025, 0.005, 0.01, 0.013, 0.01447, 0.018, 0.02, 0.03, 0.04 Pa/m and the annular cases were run with dp/dx = 0.0005; 0.001; 0.00235; 0.0047; 0.0094; 0.014; 0.047; 0.06 Pa/m. In some RANS cases, convergence was difficult to obtain when specifying the pressure gradient, here the mass flow rate was estimated and specified instead.

2.5 CFD setup & numerics

Regardless of the geometry (pipe vs annulus), the computational domain was spatially discretized with hexahedral cells and periodic boundary conditions (BC) were applied at the inlet and outlet. Depending on geometry and the turbulence modelling approach utilized, the near wall layer was resolved down to y+ = 1 (annulus example depicted in Figure 2).

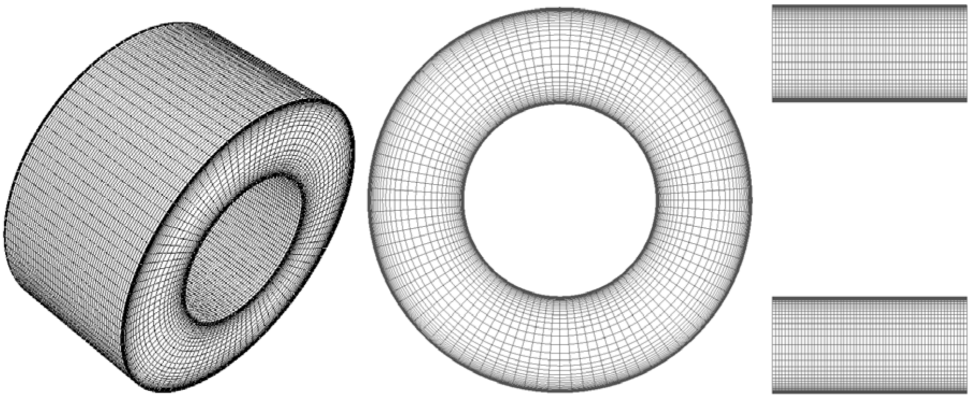

Figure 2: Low-Re mesh example for annular case.

In case of the standard k-ω STT model, a pressure gradient dp/dx was specified (as was in all DNS). However, it was not always possible to obtain a solution for the k-ϵ family of models in case of a dp/dx-specification, therefore the respective DNS mass flow rate $\dot{m}$ was specified instead. This leads to dp/dx being the solution for some k-ϵ simulations. While this is not a problem when comparing arrays of $\dot{m}$-dp/dx-data, it complicates u+-y+-comparisons because the dimensional quantities used for computing the plus-values, namely, dp/dx, τ_w, u_τ, η_w differ.

The SIMPLEC scheme was used for pressure-velocity coupling and second order spatial discretization was applied. Gradients were evaluated using the Green-Gauss node-based gradient scheme. The algebraic multigrid method utilizing the Gauss-Seidel solver with default under-relaxation factor settings were used to solve the discretized equation systems.

2.6 DNS setup & numerics

A spectral element-Fourier DNS code [51] adapted to Non-Newtonian flow described in [31] is used to solve Eq. (1) for an incompressible GNF flow in cartesian coordinates. The code uses spectral elements of arbitrary order over the pipe cross section and a Fourier expansion in the axial direction. The flow is driven by a body force equal to the mean axial pressure gradient. Table 3 provides the values of the general mesh and domain related parameters and the meshes are depicted in Figure 3. The mesh was designed to be adequate for the highest Re_τ and used in all simulations. Spatial resolution and domain size follows the recommendations of [52] and experience of [53] based on the same DNS code. The domain length of the annular geometry is in the lower range of the recommendations. It should also be noted that typically the axial length scales of non-Newtonian flows increase with shear thinning and thereby lower the criteria of axial grid points as well as being more restrictive on domain length.

Parameter	Circular	Annular	Comment
Δx^+	12	15	Axial resolution (viscous length scales)
$(\mathrm{R}\Delta\theta)^+$	7	7	Circumferential resolution at wall
Δr^+	0.6	0.5	Radial resolution at wall

Δs^+	6	12	Max edge length in cross section
$\{\mathrm{L}, \mathrm{L}^+\}$	$\{4\pi\mathrm{D}, 7900\}$	$\{4\pi\mathrm{D_h}, 3200\}$	Length in outer and viscous length scale
Spectral elements	845	679	Spectral elements in cross section
$\mathrm{N_p}$	6	10	Spectral element order
$\mathrm{N_x}$	640	216	Number of Fourier planes in axial direction

Table 3. Essential numbers for circular and annular geometries mesh.

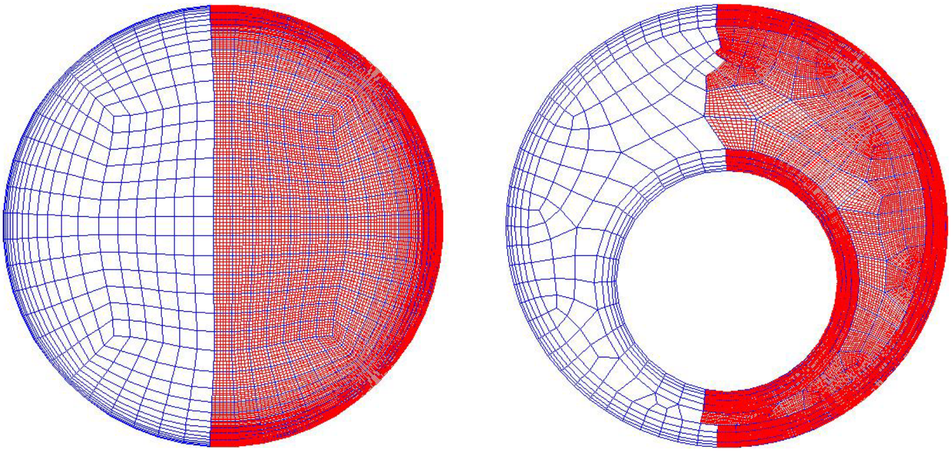

Figure 3. Spectral elements are shown on the left side of the depicted geometries and the real mesh is shown on the right. Left: Pipe geometry consisting of 845 6th-order spectral elements, and 640 Fourier planes in the axial direction. Right: Annular geometry, D_i/D_o= 0.5, e=0.5, consisting of 679 10th-order spectral elements and 216 Fourier planes in the axial direction.

The solution methodology was to run the simulations until the mean shear stress at the walls had stabilized and collect data for statistics for ~10 flow-through times.

3 Results

We first provide the results for the pipe case, where the data is presented both in dimensional and non-dimensional form. Additionally, velocity profiles are presented, both in standard and near-wall form.

3.1 Pipe

Figure 4 depicts all pipe cases investigated so far.

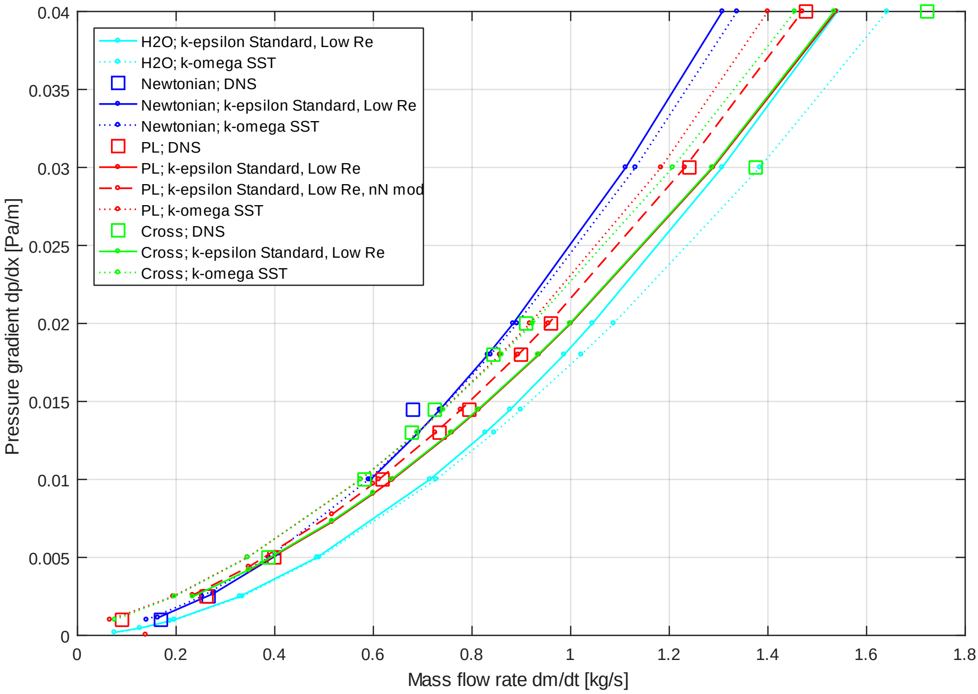

Figure 4: Pressure gradient vs. mass flow rates for all investigated pipe cases.

The Newtonian DNS data is too scarce for the time being and therefore comparison with CFD results is of not much use. However, focusing on CFD results only, the k-ω SST results underpredict the k-ϵ results for both the Newtonian and the H2O case at higher flow rates.

For the PL result, the low-Re k-ϵ non-Newtonian modification of [17] fits the DNS data best. However, when specifying the pressure gradient as input, no solution could be obtained for the first three data points. The low-Re k-ϵ without the non-Newtonian modification of f [17] slightly underpredicts the DNS data, while the k-ω SST results slightly overpredict the DNS data.

Interestingly, the two highest DNS Cross results are very much off the general trend of the DNS results and are not at all represented by the CFD data.

While Cross and PL DNS results do not coincide, the CFD results do coincide for the different turbulence models studied. However, for the higher flow rate range, the respective k-ω SST results deviate from each other.

Figure 5 shows the same data as presented in Figure 4, but replotted based on the definitions of the Fanning friction factor and the Metzner-Reed Reynolds number [4].

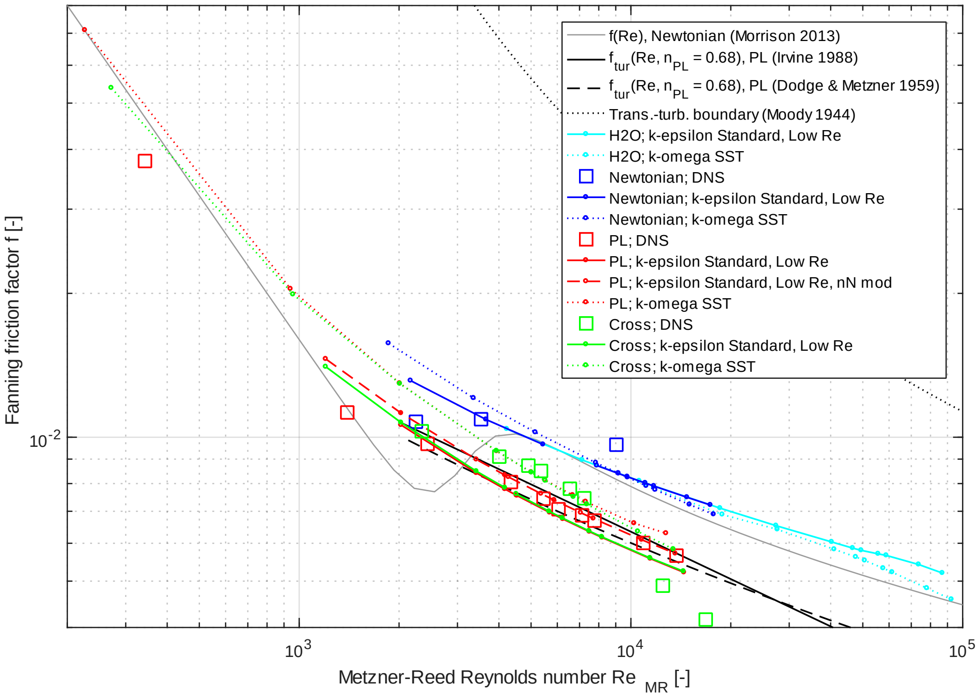

Figure 5: Fanning friction factor vs. Metzner-Reed Reynolds number for all investigated pipe cases.

While the Newtonian CFD results slightly overpredict the friction factor correlation, the three DNS results do not fit the picture. As in the dimensional plot in Figure 4, the PL DNS results scale well with the corresponding low-Re k-ϵ non-Newtonian modification of [17] and with the two PL friction factor correlations. The k-ω SST results correctly approach the laminar friction factor at lower Re, while this is not so for the k-ϵ model variants (not displayed).

For the design point of the fluids, non-dimensionalized velocity profiles for the H2O case are depicted in Figure 6 and for the Newtonian case in Figure 7.

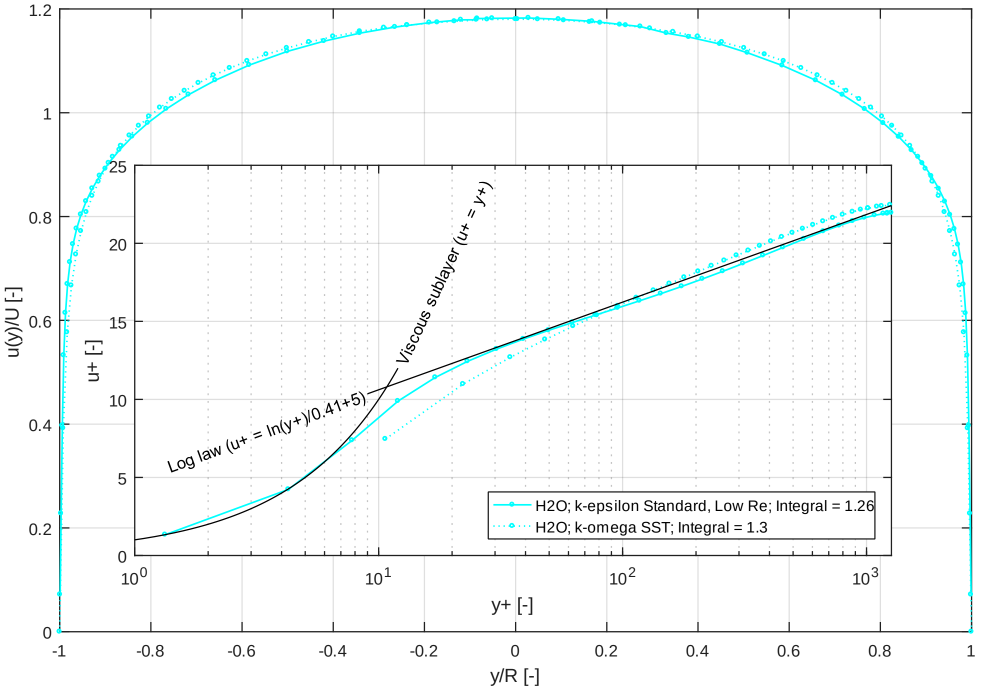

Figure 6: Velocity profiles u(y)/U vs. y/R and u+ vs. y+ for the H2O and dp/dx = 0.01447 Pa/m pipe case.

The numerical value of the integral (B3), which in terms of the perfect Newtonian solution evaluates to one, is provided in every legend entry.

In both cases, the CFD results very well coincide with the viscous and logarithmic law-of-the wall (hereafter log-law). However, the DNS results show two remarkable features: a small defect in the form of a dip at $y+$ = 90 and a positive deviation from the log-law for $y+$ < 90. This is represented by the k-ω SST model; however, not by the k-ϵ Standard, Low-Re model, which returns to the log-law at $y+$ = 120.

Clearly, the H2O k-ω SST simulation depicted in Figure 6 was insufficiently resolved in terms of y^+ values because the first data point is at $y^+ \approx 10$ and hence the integral (B3) evaluates to 0.503 only.

Figure 8 and Figure 9 depict the velocity profiles of the PL1 and Cr1 cases, respectively. Both the DNS and all but the k-ω Standard, Low-Re model overpredict the Newtonian log-law. The DNS data and the results for the low-Re k-ϵ non-Newtonian modification of [17] coincide very well.

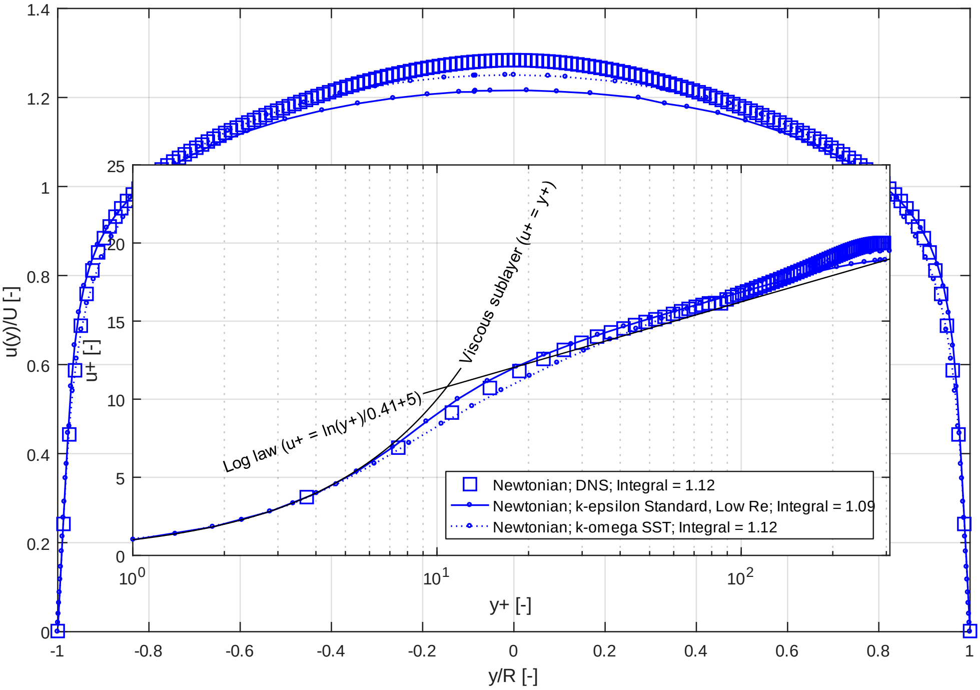

Figure 7: Velocity profiles u(y)/U vs. y/R and u+ vs. y+ for the Ne2 and dp/dx = 0.01447 Pa/m pipe case.

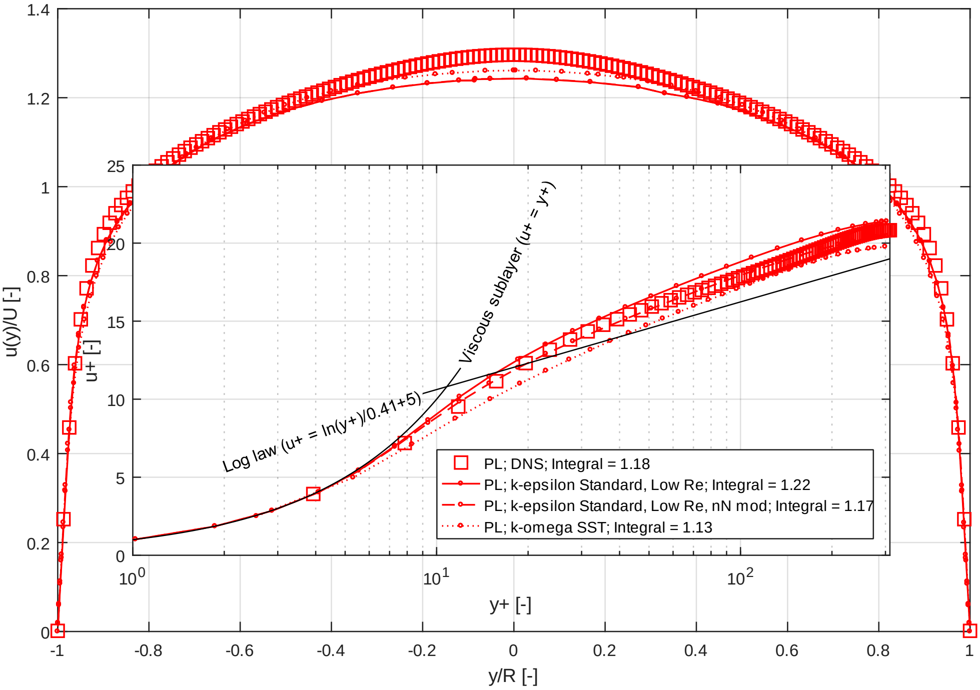

Figure 8: Velocity profiles u(y)/U vs. y/R and u+ vs. y+ for the PL1 and dp/dx = 0.01447 Pa/m pipe case.

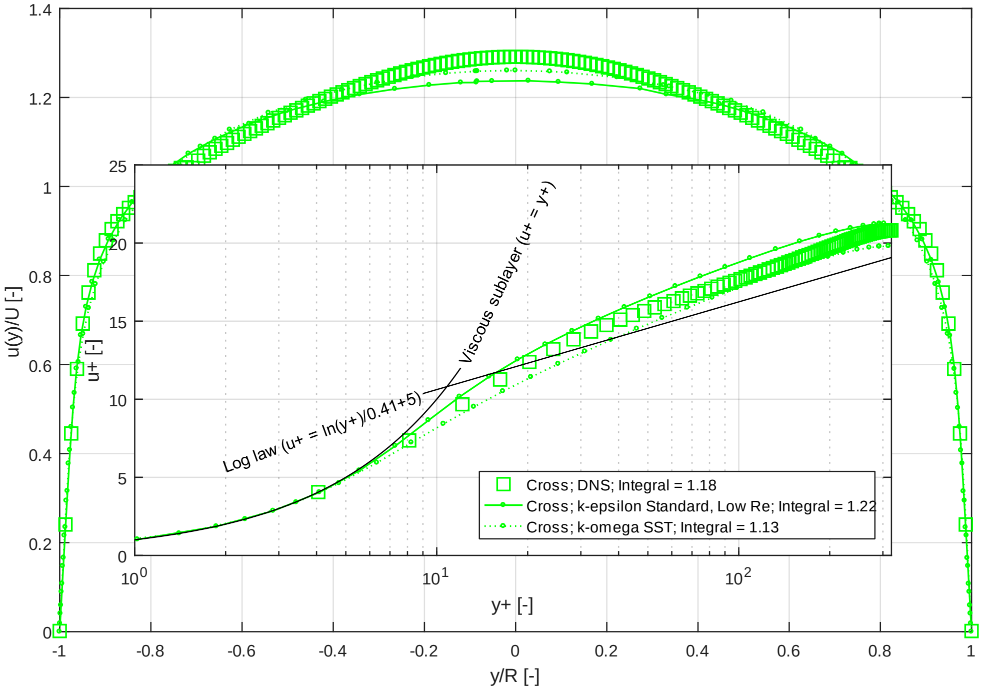

Figure 9: Velocity profiles u(y)/U vs. y/R and u+ vs. y+ for the Cr1 and dp/dx = 0.01447 Pa/m pipe case.

3.2 Annulus

Figure 10 provides limited results for two different concentric annular cases without inner pipe rotation. The Newtonian results were obtained for $d_{h,a}$ = 2 (d_o = 4, d_i = 2) whereas the H2O, PL and Cross cases were obtained for $d_{h,a}$ = $d_{h,p}$ = 1 (d_o = 2, d_i = 1), for which no DNS data is available so far.

While the Newtonian DNS and CFD data apparently do coincide well when plotted in the dimensional manner presented in Figure 10, this is clearly not so when replotting the data in non-dimensional f-Re_{MR}-form as displayed in Figure 11.

The Newtonian and H2O CFD results coincide for overlapping Re_{MR}. Furthermore, the PL and Cross results also coincide, both in the dimensional plot of Figure 10 and the non-dimensional plot of Figure 11, with the only exception being the first PL data point.

No further DNS data for the concentric annular case without rotation is available for the time being. Especially DNS of a range of PL fluids are required to evaluate prediction capability/quality of the various turbulence models for shear-thinning behavior.

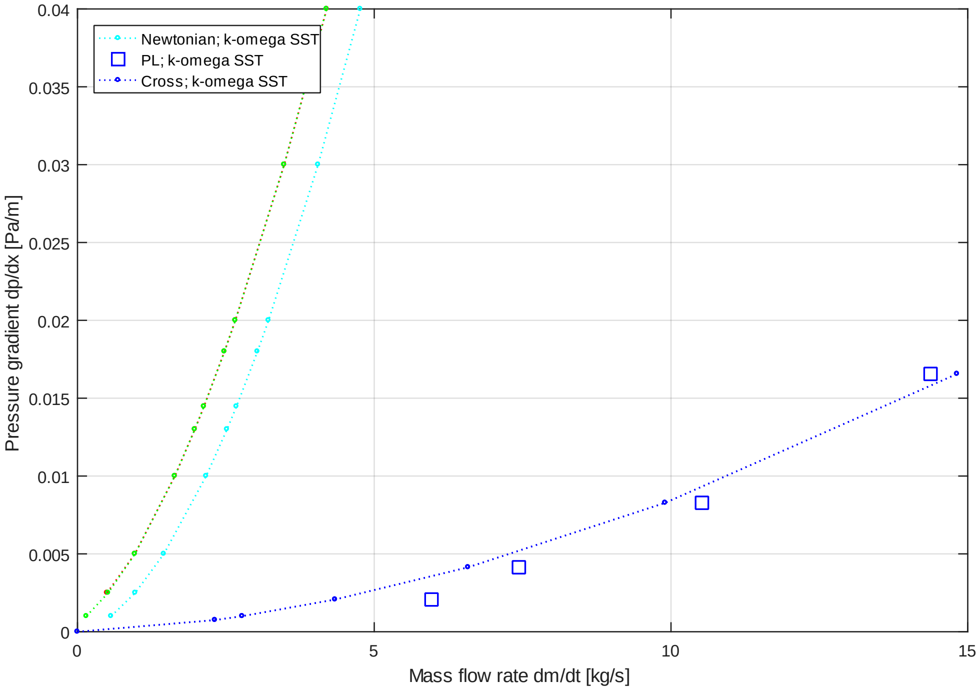

Figure 10: Pressure gradient vs. mass flow rates for concentric Newtonian cases.

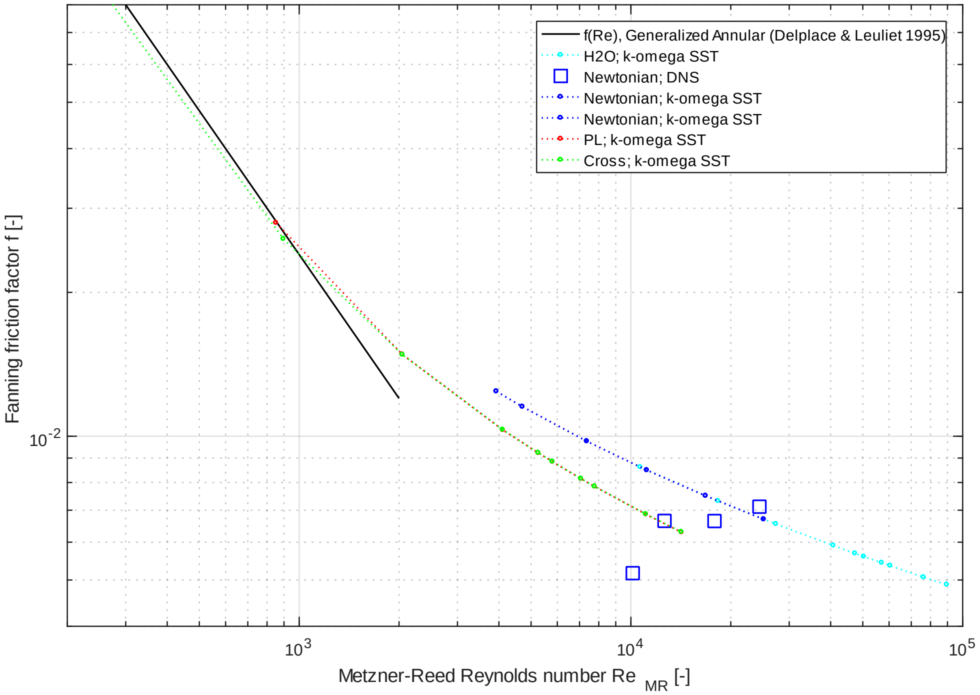

Figure 11: Fanning friction factor vs. Metzner-Reed Reynolds number for concentric annular cases.

Figure 12 depicts the effect of rotational speed of the inner pipe on the effective mass flow rate for different non-dimensional eccentricities and a fixed pressure gradient $\Delta \mathrm{p}/\Delta \mathrm{x}$ = 0.0083 Pa/m for the Newtonian fluid case. Hence, the 0 rpm, e = 0 case data is equivalent with the third Newtonian data point displayed in Figure 10.

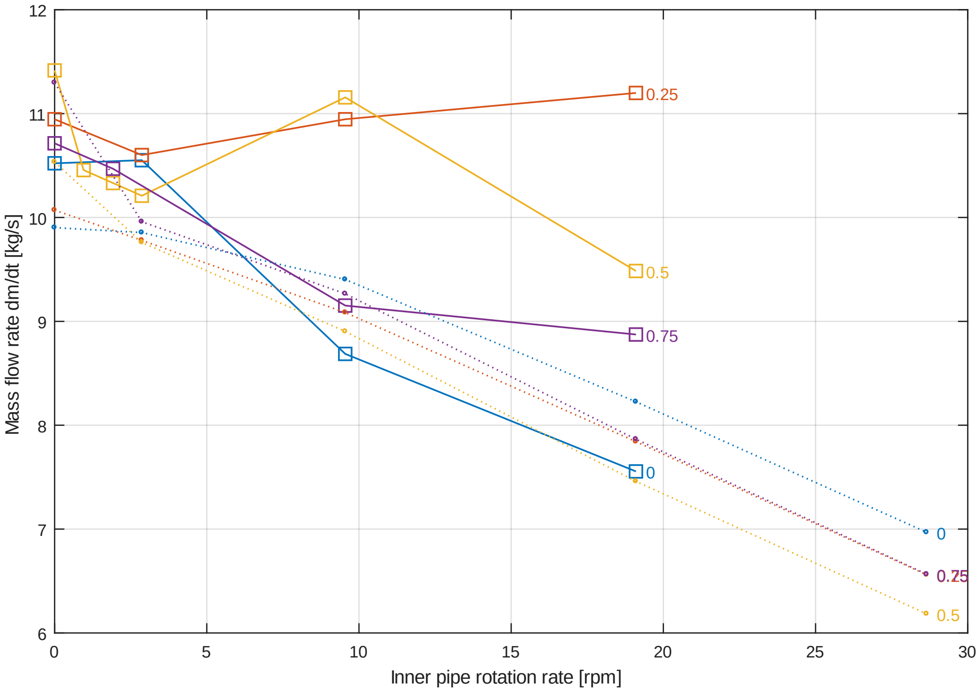

Figure 12: Mass flow rates vs. inner pipe rotational speed for concentric Newtonian case $\Delta p/\Delta x$ = 0.0083 Pa/m. Solid lines/squares represent DNS results, doted lines/filled circles represent results obtained with the k-ω SST model.

While in general the is no match between CFD and DNS results, for 0 rpm both show the same trend, that is an increase of $\dot{m}$ with increasing eccentricity e, with the exception of the e = 0.75 DNS case. However, this trend is reversed in case of the CFD results (with the notable exception of the e = 0.25 and e = 0.75 results becoming equal for higher pipe rotations), whereas the DNS results show a much more inconsistent pattern. For instance, except for 2.9 rpm, the e = 0 data points are the lowest although the e = 0.25 to e = 0.75 data points show a decrease in $\dot{m}$ with increasing eccentricity e for higher pipe rotations.

Figure 13 provides an overview of both Newtonian and PL results for an eccentricity e = 0.5 and different inner pipe rotational rates. For the 0 rpm case, a Newtonian [3] and two PL [5,7] friction factor correlations, corrected for eccentricity [54,55], are additionally displayed.

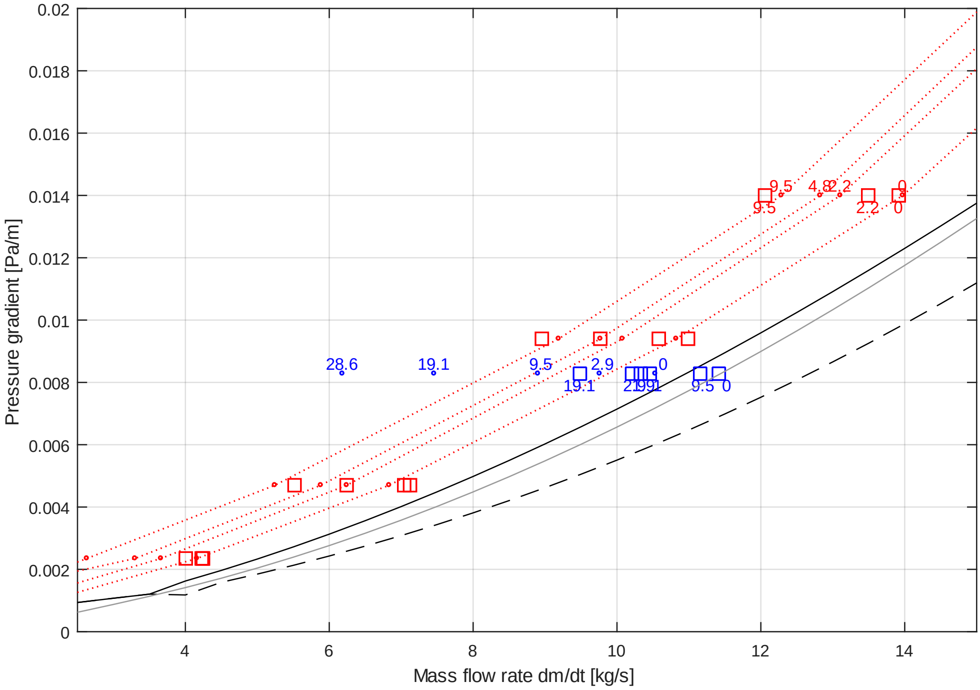

Figure 13: Pressure gradient vs. mass flow rate for eccentric (e = 0.5) Newtonian and PL cases. For legend information see Figure 4.

For both fluids, pipe rotation reduces the effective mass flow rate. However, in case of the Newtonian fluid, the effect is much more pronounced in the CFD results, where turbulence is modeled. Furthermore, even the 0 rpm case is not well predicted by the CFD model. In contrast, in case of the PL fluid, the CFD results fit the DNS data much better for most of the pressure gradients investigated. Interestingly, the DNS results for dp/dx = 0.00235 Pa/m almost coincide at $\dot{m}$ ≈ 4 kg/s.

4 Discussion

4.1 Pipe

Some of the DNS results are incorrect, most likely the resolution of these cases was insufficient. For instance, even though the Newtonian DNS data is scarce, we may conclude from the f-Re_{MR}-plot (Figure 5) that the Re_{MR} = 2248 and Re_{MR} = 9040 simulations are not coinciding with the Newtonian friction factor correlation. Furthermore, the first PL data point is well of the analytical solution f = 16/Re_{MR} and the last two Cross data points do not fit the general pattern of the obtained Cross results. An alternative explanation for the latter could be the shear-thinning property of the Cross fluids, which for high shear rates results in viscosities lower than the one of H2O (Figure 1). The obtained DNS data is currently reanalyzed by SINTEF personnel.

The CFD results appear to be independent of the choice of a turbulence model for the lower Re_{MR}regime. For higher Re_{MR}, the results deviate from each other as the turbulence is increasingly affecting the overall pressure drop.

If simulations employing the k-ϵ family of models are conducted with a dp/dx specification, i.e. the mass flow rate is the seeked solution, a certain degree of turbulence is required in order to obtain a converged and physical meaningful solution. For instance, in case of the low-Re k-ϵ non-Newtonian modification [17], no solutions could be obtained for Re_{MR} < 4280 (dp/dx = 0.01 Pa/m), whereas if the mass flow rate was specified instead solutions could be obtained down to much lower Re_{MR}. On the other hand, the k-ω SST simulations are successfully approaching the laminar limit f = 16/Re_{MR} for lower Re_{MR} and are therefore much more suited for the range Re_{MR} = 1000…4000.

The PL-Cross difference indicated by the DNS results is not replicated by the CFD simulations indicating that the description of non-Newtonian turbulence is insufficient. The non-Newtonian rheology is only considered via the molecular viscosity whereas the effect of turbulence is only taken into account by the corresponding models affecting the turbulent viscosity and thus no interdependencies of non-Newtonian fluid rheology and turbulence are considered. This is a direct result of the conventional Reynolds-averaging process utilized to derive the ensemble-averaged equations of motion, which is purely based on the velocity as the only instantaneous quantity. The viscosity, however, is considered constant and only later made a variable by relating it to the shear rate as shown in equation (2). Hence, Reynolds-averaging terms representing the impact of fluctuations in strain rate on the “laminar” viscosity are ignored [19,56].

Focusing on the fluids design point, the pressure gradient dp/dx = 0.01447 Pa/m, the DNS results show a somewhat counterintuitive order of results: The least viscous fluid (Newtonian) yields the lowest mass flow rate and the most viscous fluid (PL) yields the highest as depicted in Figure 14.

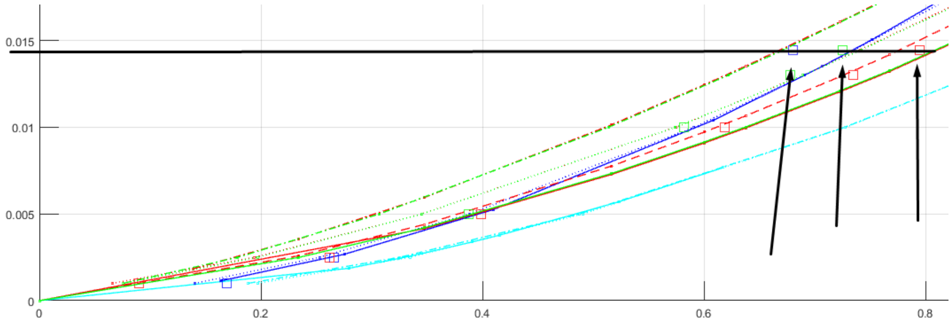

Figure 14: Zoom of the low $\dot{m}$ region of Figure 4.

This is not what one would expect from the FC (Figure 1) because the integration from the design point to the center of the pipe, i.e. towards $\dot{\gamma}$ = 0, means that the highest mass flow rate is produced by the least viscous fluid. In fact, this is well represented by the data for $\dot{m}$ < 0.3 kg/s. In case of higher throughputs, however, the degree of turbulence produced by the low viscous (compared to PL and Cross cases) Newtonian fluid is so large that the actual velocity profiles and correspondingly the bulk velocities/mass flow rates are very different. This pattern is also reproduced by the CFD simulations. The CFD turbulence models produce equivalent results close to the design point, but deviate from each other for higher pressure losses even though wall shear stress is identical and one would expect the same wall viscosity. For the design point dp/dx = 0.01447 Pa/m, the wall shear rates in the CFD simulations are all close to 40 s^{-1}, regardless of the material function utilized. This is not so for larger dp/dx values. For instance, for dp/dx = 0.04 Pa/m, the wall shear rates in the PL CFD simulations are about 110 s^{-1}, whereas for the Cross model the wall shear rates are about 170 s^{-1}. This leads to different wall viscosities and therefore different bulk velocities for the same pressure gradient.

The Cross and PL DNS results differ with respect to each other, however, the respective CFD results do not deviate from each other much. Why?

4.2 Annulus

The CFD simulations with the k-ω SST are correctly approaching the laminar limit for annular geometries, namely f = 24/Re_{MR}. Dedicated friction factor correlation for annular flow? Hydraulic diameter concept does not lead to a match with results.

Again, the DNS results for the Newtonian base case (Figure 10, Figure 11) indicate that the DNS resolution was insufficient in some cases. This is corroborated by the pattern-less picture of the DNS results displayed in Figure 12. However, the 0 rpm case seems ok because it coincides with the Newtonian friction factor correlation (Figure 13).

The PL DNS results for the e = 0.5 annulus (Figure 13), however, show reasonable results because the XXX

Apparently, the utilized k-ω SST model overestimates the degree of turbulence for higher rotational rates (e.g. Newtonian case in Figure 13). However, the For lower mass flow

4.3 Scaling of results

Very often, non-dimensionalized results presented in the literature are based on the Reynolds number definition of Metzner & Reed [4], hereafter abbreviated with MR. Some researchers have expressed their criticism of the MR Reynolds number approach [57,58], in particular if it is applied to the turbulent flow regime [57]. In Appendix 5C.2, we provide a very brief overview of the MR concept, which is essentially based on Newtonian and Non-Newtonian friction factor equivalence and a definition of the shear rate derived by Metzner & Reed [4] based on the earlier work of Rabinowitsch [59] and Mooney [60] leading to a bulk velocity dependent equation for the viscosity. Additionally, Appendix 5C.2 provides an alternative, which is based on the wall shear stress instead and hence leads to a pressure gradient dependent definition of the effective wall viscosity

$$\eta_w = \left(\frac{\Delta p d_h}{\Delta x 4}\right)^{\left(1-\frac{1}{n}\right)} K^{\frac{1}{n}}. \tag{43}$$

For the laminar regime, these two definitions produce identical results (16/Re for the pipe and 24/Re for the annular case). However, for the turbulent regime, these two approaches deviate from each other. In Figure 15 and Figure 16 we have reprinted the data of Figure 5 and Figure 11 based on the Generalized Reynolds number Re_G, where the viscosity is defined by equation (43) instead.

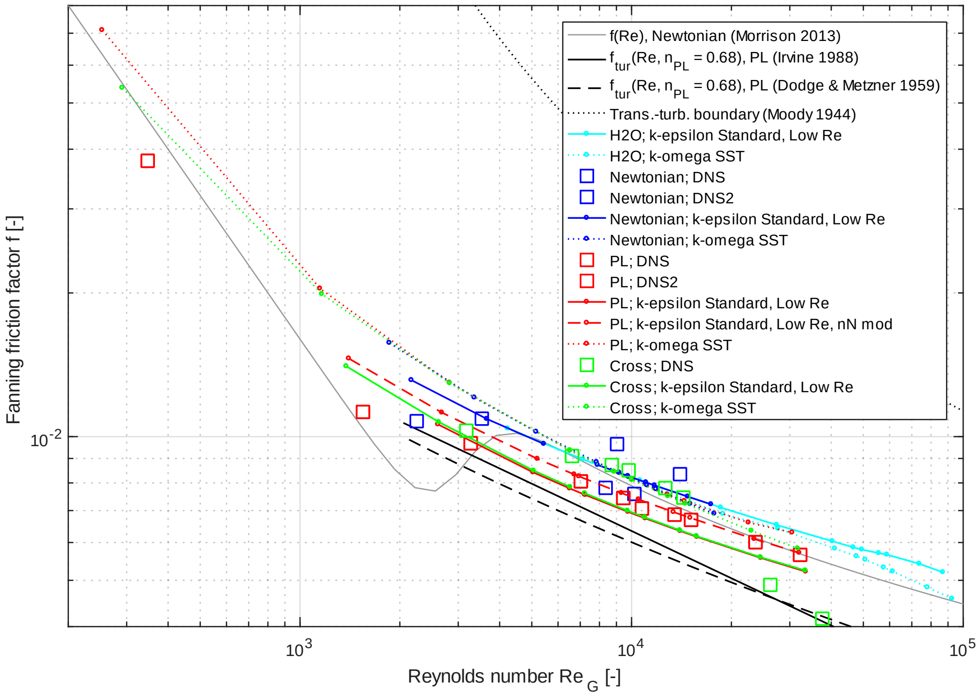

Figure 15: Fanning friction factor vs. Generalized Reynolds number for pipe cases.

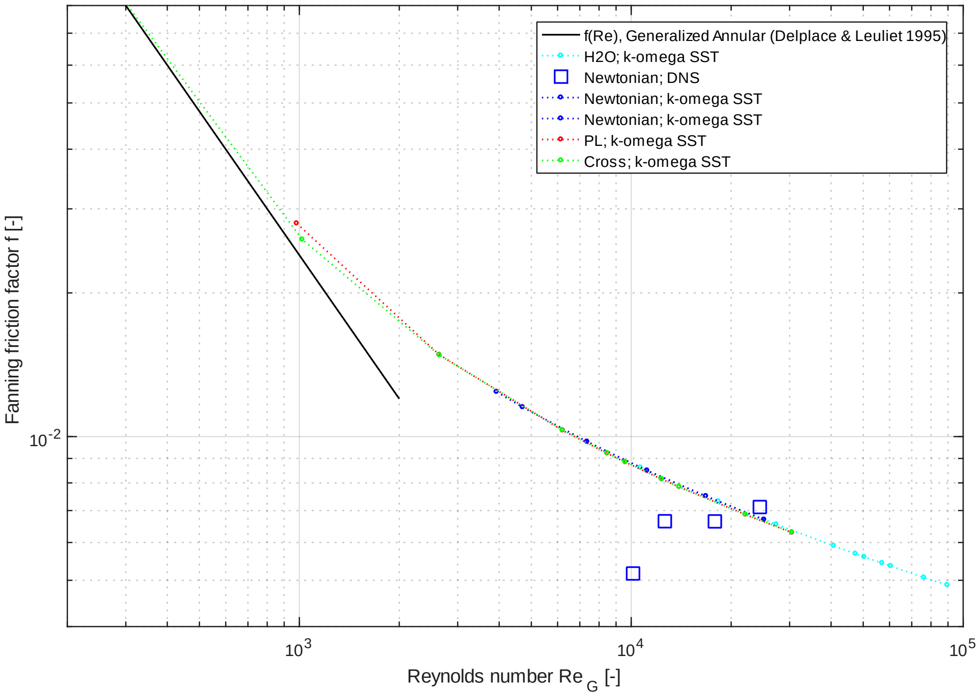

Figure 16: Fanning friction factor vs. Generalized Reynolds number for concentric annular cases.

Comparing the different scaling approaches, it appears as if the second concept where the viscosity is based on the pressure gradient and thus wall shear stress, is more universal as it collapses the PL data (as well as the data which produces identical results, e.g. the annular Cross k-ω SST) on the conventional Newtonian friction factor correlation. The wall shear-stress based approach per definition produces the correct viscosity at the wall. However, the MR concept is based on the assumption of laminar flow and a laminar velocity profile and its application therefore results in a non-correct wall viscosity. Consequently, if extended to the turbulent regime, one obtains non-unique f-Re_{MR} curves for different PL fluids.

Compare also with Haaland and Blasius.

5 Conclusions

Acknowledgements

The project Advanced Wellbore transport Modeling (AdWell) with its sponsor, PETROMAKS 2/the Research Council of Norway (project 228391) and its partners Equinor, Neptune Energy Norge AS, IRIS/NORCE, UiS, NTNU and SINTEF are gratefully acknowledged for funding and supporting this work. In addition, we are grateful for the computational resources provided at NTNU by UNINETT Sigma2 AS.

References

[1] H. Blasius, Das Aehnlichkeitsgesetz bei Reibungsvorgängen., Zeitschrift Des Vereines Deutscher Ingenieure. 19 (1912) 639.

[2] S.E. Haaland, Simple and Explicit Formulas for the Friction Factor in Turbulent Pipe Flow, Journal of Fluids Engineering. 105 (1983) 89–90. doi:10.1115/1.3240948.

[3] F.A. Morrison, Data Correlation for Friction Factor in Smooth Pipes, (2013). http://www.chem.mtu.edu/~fmorriso/DataCorrelationForSmoothPipes2013.pdf.

[4] A.B. Metzner, J.C. Reed, Flow of non-newtonian fluids-correlation of the laminar, transition, and turbulent-flow regions, AIChE Journal. 1 (1955) 434–440. doi:10.1002/aic.690010409.

[5] D.W. Dodge, A.B. Metzner, Turbulent flow of non-newtonian systems, AIChE Journal. 5 (1959) 189–204. doi:10.1002/aic.690050214.

[6] K.C. Wilson, A.D. Thomas, A New Analysis of the Turbulent Flow of Non-Newtonian Fluids, The Canadian Journal of Chemical Engineering. 63 (1985). doi:10.1002/cjce.5450630403.

[7] T.F. Irvine, A Generalized Blasius Equation for Power Law Fluids, Chemical Engineering Communications. 65 (1988) 39–47. doi:10.1080/00986448808940242.

[8] H.R. Anbarlooei, D.O.A. Cruz, F. Ramos, A.P. Silva Freire, Phenomenological Blasius-type friction equation for turbulent power-law fluid flows, Physical Review E. 92 (2015). doi:10.1103/PhysRevE.92.063006.

[9] K.T. Trinh, Logarithmic Correlations For Turbulent Pipe Flow Of Power Law Fluids, ArXiv Preprint ArXiv:1007.0789. (2010) 13.

[10] M. Kostic, J.P. Hartnett, Predicting turbulent friction factors of non-newtonian fluids in noncircular ducts, International Communications in Heat and Mass Transfer. 11 (1984) 345–352. doi:10.1016/0735-1933(84)90062-9.

[11] I.T. Dosunmu, S.N. Shah, Evaluation of friction factor correlations and equivalent diameter definitions for pipe and annular flow of non-Newtonian fluids, Journal of Petroleum Science and Engineering. 109 (2013) 80–86. doi:10.1016/j.petrol.2013.02.007.

[12] R. Haldenwang, a. P.N. Sutherland, V.G. Fester, R. Holm, R.P. Chhabra, Sludge pipe flow pressure drop prediction using composite power-law friction factor-Reynolds number correlations based on different non-Newtonian Reynolds numbers, Water SA. 38 (2012) 615–622. doi:http://dx.doi.org/10.4314/wsa.v38i4.17.

[13] E.J. GARCIA, J.F. STEFFE, COMPARISON of FRICTION FACTOR EQUATIONS FOR NON-NEWTONIAN FLUIDS IN PIPE FLOW, Journal of Food Process Engineering. 9 (1986) 93–120.

[14] W. Kozicki, C.H. Chou, C. Tiu, Non-Newtonian flow in ducts of arbitrary cross-sectional shape, Chemical Engineering Science. 21 (1966) 665–679.

[15] F. Delplace, J.C. Leuliet, Generalized Reynolds number for the flow of power law fluids in cylindrical ducts of arbitrary cross-section, The Chemical Engineering Journal and the Biochemical Engineering Journal. 56 (1995) 33–37. doi:10.1016/0923-0467(94)02849-6.

[16] K. Ro, H. Ryou, Development of the modified k-ε turbulence model of power-law fluid for engineering applications, Science China Technological Sciences. 55 (2012) 276–284. doi:10.1007/s11431-011-4664-x.

[17] M.R. Malin, Turbulent pipe flow of power-law fluids, International Communications in Heat and Mass Transfer. 24 (1997) 977–988. doi:10.1016/S0735-1933(97)00083-3.

[18] A.A. Gavrilov, V.Ya. Rudyak, A Model of Averaged Molecular Viscosity for Turbulent Flow of Non-Newtonian Fluids, Journal of Siberian Federal University. Mathematics & Physics. 7 (2014) 46–57.

[19] A.A. Gavrilov, V.Y. Rudyak, Reynolds-averaged modeling of turbulent flows of power-law fluids, Journal of Non-Newtonian Fluid Mechanics. 227 (2016) 45–55. doi:10.1016/j.jnnfm.2015.11.006.

[20] D.O.A. Cruz, C.E. Maneschy, E.N. Macedo, J.N.N. Quaresma, A TURBULENCE MODEL FOR COMPUTING THE FLOW OF POWER-LAW FLUIDS WITHIN CIRCULAR TUBES, Hybrid Methods in Engineering. 2 (2000) 13. doi:10.1615/HybMethEng.v2.i1.10.

[21] D.O. de Almeida Cruz, J.N.N. Quaresma, C.E. Maneschy, E.N. Macêdo, A turbulence model for non-Newtonian power-law fluids in ducts, in: Sao Paulo, 1999. http://www.abcm.org.br/app/webroot/anais/cobem/1999/pdf/AAABDA.pdf (accessed August 26, 2015).

[22] E.V. Podryabinkin, V.Ya. Rudyak, Modeling of turbulent annular flows of Hershel-Bulkley fluids with eccentricity and inner cylinder rotation, Journal of Engineering Thermophysics. 23 (2014) 137–147. doi:10.1134/S1810232814020064.

[23] D.O. a Cruz, F.T. Pinho, Turbulent pipe flow predictions with a low Reynolds number k-e model for drag reducing fluids, Journal of Non-Newtonian Fluid Mechanics. 114 (2003) 109–148. doi:10.1016/S0377-0257(03)00119-8.

[24] M.T. Dhotre, K. Ekambara, J.B. Joshi, CFD Simulation of the Flow Pattern for Drag Reducing Fluids in Turbulent Pipe Flows, JOURNAL OF CHEMICAL ENGINEERING OF JAPAN. 40 (2007) 304–311. doi:10.1252/jcej.40.304.

[25] I. Azouz, S.A. Shirazi, Evaluation of several turbulence models for turbulent flow in concentric and eccentric annuli, Journal of Energy Resources Technology. 120 (1998) 268–275.

[26] P. Csizmadia, C. Hős, Predicting the friction factor in straight pipes in the case of Bingham plastic and the power-law fluids by means of measurements and CFD simulation, Periodica Polytechnica Chemical Engineering. 57 (2013) 79. doi:10.3311/PPch.2174.

[27] M. Bizhani, E. Kuru, Modeling Turbulent Flow of Non-Newtonian Fluids Using Generalized Newtonian Models, in: American Society of Mechanical Engineers, 2015: p. V002T08A001-V002T08A001.

[28] B. Wu, Computational fluid dynamics investigation of turbulence models for non-newtonian fluid flow in anaerobic digesters., Environmental Science & Technology. 44 (2010) 8989–8995. doi:10.1021/es1010016.

[29] M. Rudman, L.J.W. Graham, H.M. Blackburn, L. Pullum, Non-Newtonian Turbulent and Transitional Pipe Flow, (2002). http://lionelpullum.com/pdf files/1850.pdf.

[30] M. Rudman, H.M. Blackburn, L.J.W. Graham, L. Pullum, Turbulent pipe flow of shear-thinning fluids, Journal of Non-Newtonian Fluid Mechanics. 118 (2004) 33–48. doi:10.1016/j.jnnfm.2004.02.006.

[31] M. Rudman, H.M. Blackburn, Direct numerical simulation of turbulent non-Newtonian flow using a spectral element method, Applied Mathematical Modelling. 30 (2006) 1229–1248. doi:10.1016/j.apm.2006.03.005.

[32] D.W. Dodge, A.B. Metzner, Turbulent flow of non-newtonian systems, AIChE Journal. 5 (1959) 189–204. doi:10.1002/aic.690050214.

[33] J. Singh, M. Rudman, H.M. Blackburn, A. Chryss, L. Pullum, L.J.W. Graham, The importance of rheology characterization in predicting turbulent pipe flow of generalized Newtonian fluids, Journal of Non-Newtonian Fluid Mechanics. 232 (2016) 11–21. doi:10.1016/j.jnnfm.2016.03.013.

[34] J. Singh, M. Rudman, H.M. Blackburn, The effect of yield stress on pipe flow turbulence for generalised newtonian fluids, Journal of Non-Newtonian Fluid Mechanics. 249 (2017) 53–62. doi:10.1016/j.jnnfm.2017.09.007.

[35] J. Singh, M. Rudman, H.M. Blackburn, Reynolds number effects in pipe flow turbulence of generalized Newtonian fluids, Physical Review Fluids. 3 (2018). doi:10.1103/PhysRevFluids.3.094607.

[36] J. Singh, M. Rudman, H.M. Blackburn, The influence of shear-dependent rheology on turbulent pipe flow, Journal of Fluid Mechanics. 822 (2017) 848–879. doi:10.1017/jfm.2017.296.

[37] N. Zhen, R.A. Handler, Q. Zhang, C. Oeth, Evolution of a hairpin vortex in a shear-thinning fluid governed by a power-law model, Physics of Fluids. 25 (2013) 101703. doi:10.1063/1.4824457.

[38] J. Olsthoorn, M. Stastna, D. Steinmoeller, On the dynamics of vortex-wall interaction in low viscosity shear thinning fluids, Physics of Fluids. 26 (2014) 013101. doi:10.1063/1.4857675.

[39] B.E. Launder, D.B. Spalding, Lectures in mathematical models of turbulence, Academic Press, London; New York, 1972.

[40] C.K.G. Lam, K. Bremhorst, A Modified Form of the k-ε Model for Predicting Wall Turbulence, Journal of Fluids Engineering. 103 (1981) 456–460. doi:10.1115/1.3240815.

[41] F.R. Menter, Two-equation eddy-viscosity turbulence models for engineering applications, AIAA Journal. 32 (1994) 1598–1605. doi:10.2514/6.1993-2906.

[42] F.R. Menter, Zonal Two Equation k-ω Turbulence Models For Aerodynamic Flows, in: American Institure of Aeronautics and Astronautics (AIAA), Orlando, Florida, 1993: p. 22.

[43] N. Nikitin, H. Wang, S. Chernyshenko, Turbulent flow and heat transfer in eccentric annulus, Journal of Fluid Mechanics. 638 (2009) 95. doi:10.1017/S002211200900812X.

[44] O. Reynolds, On the Dynamical Theory of Incompressible Viscous Fluids and the Determination of the Criterion, Philosophical Transactions of the Royal Society of London. 186 (1895) 123–164.

[45] J. Boussinesque, Essai sur la theories des eaux courantes, Tome XXIII. XXIII (1877). https://www.irphe.fr/~clanet/otherpaperfile/articles/Boussinesq/N0003328_PDF_1_770.pdf.

[46] M.M. Cross, Rheology of non-Newtonian fluids: a new flow equation for pseudoplastic systems, Journal of Colloid Science. 20 (1965) 417–437. doi:10.1016/0095-8522(65)90022-X.

[47] W. Ostwald, Über die Geschwindigkeitsfunktion der Viskosität disperser Systeme, Colloid & Polymer Science. 36 (1925) 99–117.

[48] R.B. Bird, R.C. Armstrong, O. Hassager, Dynamics of Polymeric Liquids. Volume 1: Fluid Mechanics, 2nd ed., New York, 1987.

[49] B.E. Launder, D.B. Spalding, The numerical computation of turbulent flows, Computer Methods in Applied Mechanics and Engineering. 3 (1974) 21. doi:10.1016/0045-7825(74)90029-2.

[50] D.C. Wilcox, Turbulence modeling for CFD, DCW industries La Canada, CA, 1998.

[51] H.M. Blackburn, S.J. Sherwin, Formulation of a Galerkin spectral element–Fourier method for three-dimensional incompressible flows in cylindrical geometries, Journal of Computational Physics. 197 (2004) 759–778. doi:10.1016/j.jcp.2004.02.013.

[52] G.N. Coleman, R.D. Sandberg, A Primer on Direct Numerical Simulation of Turbulence – Methods, Procedures and Guidelines, (n.d.) 21.

[53] C. Chin, A.S.H. Ooi, I. Marusic, H.M. Blackburn, The influence of pipe length on turbulence statistics computed from direct numerical simulation data, Physics of Fluids. 22 (2010) 115107. doi:10.1063/1.3489528.

[54] M. Haciislamoglu, U. Cartalos, Practical Pressure Loss Predictions in Realistic Annular Geometries, in: SPE-28304-MS, Society of Petroleum Engineers, SPE, 1994. doi:10.2118/28304-MS.

[55] M. Haciislamoglu, J. Langlinais, Non-Newtonian flow in eccentric annuli, Journal of Energy Resources Technology. 112 (1990) 163–169. doi:10.1115/1.2905753.

[56] F.T. Pinho, A Model for the Effect of Turbulence on the Molecular Viscosity of Generalized Newtonian Fluids, in: 17th International Congress of Mechanical Engineering, Brazilian Society of Mechanical Sciences and Engineering (ABCM), Sao Paulo, 2003. http://www.abcm.org.br/app/webroot/anais/cobem/2003/html/pdf/COB03-0295.pdf (accessed August 17, 2015).

[57] G.G. Duffy, Misapplication of the Metzner-Reed Non-Newtonian Correlation Method, Chemical Engineering Communications. 191 (2004) 182–188. doi:10.1080/00986440490261836.

[58] U. Björkman, Reflections over Metzner's method, Annual Transactions of the Nordic Rheology Society. 16 (2008). http://wwwnysv.sik.se/nrs/Open_transactions/2008/Oral presentations/Rheology and Health/Bjorkman.pdf http://projekt.sik.se/nrs/Open_transactions/2008/Oral presentations/Rheology and Health/Bjorkman.pdf.

[59] B. Rabinowitsch, Über die Viskosität und Elastizität von Solen, Z. Phys. Chem. A. 145 (1929) 1–26.

[60] M. Mooney, Explicit Formulas for Slip and Fluidity, Journal of Rheology. 2 (1931) 210–222. doi:http://dx.doi.org/10.1122/1.2116364.

[61] R.P. Chhabra, J.F. Richardson, Non-Newtonian flow and applied rheology: engineering applications, Butterworth-Heinemann, 2011. http://books.google.com/books?hl=en&lr=&id=_6nnoh9PtF0C&oi=fnd&pg=PP2&dq=%22simple+shear,+the+flow+behaviour+of+this+class+of+materials+may+be+described+by%22+%22or+shear-thinning,+characterized+by+an+apparent+viscosity+which%22+%22to+model+shear-thinning+characteristics%3B+some+of+these+are%22+&ots=mJXwXsfQhO&sig=1ucq8mT6I6DVwgkUVrH5UXVis5w (accessed June 24, 2015).

Appendix A Definitions

Mass flow is converted to volume flow rate

$$Q = \frac{\dot{m}}{\rho} \tag{A1}$$

Bulk velocity in x-direction

$$U = \frac{Q}{A} \tag{A2}$$

The cross-sectional area

$$A = \frac{\pi}{4}\left(d_o^{\,2} - d_i^{\,2}\right) \tag{A3}$$

where d_o is the outer and d_i is the inner diameter of an annulus, with d_i=0 for the pipe case.

The wetted perimeter

$$P = \pi\left(d_o + d_i\right) \tag{A4}$$

The hydraulic diameter

$$d_h = \frac{4A}{P} = d_o - d_i \tag{A5}$$

The pressure gradient is the pressure force per volume

$$\frac{\Delta p}{\Delta x} = \frac{\Delta p A}{A \Delta x} = \frac{F_p}{V} \tag{A6}$$

The shear stress at the wall (= mean wall shear stress)

$$\tau_w = \frac{\Delta p}{\Delta x}\frac{d_h}{4} \tag{A7}$$

The friction velocity

$$u_\tau = \sqrt{\frac{\tau_w}{\rho}} \tag{A8}$$

The Fanning friction factor

$$f = \frac{\tau_w}{\frac{1}{2}\rho U^2} \tag{A9}$$

Dimensionless wall distance y^+, also known as the local Reynolds number

$$y^+ = \left(R - r\right)\frac{\rho u_\tau}{\eta_w} \tag{A10}$$

where the factor $\delta = \eta_w/(\rho u_\tau)$ is the viscous layer.

Dimensionless velocity u^+

$$u^+ = \frac{u}{u_\tau} \tag{A11}$$

Dimensionless shear rate $\dot{\gamma}^+$

$$\dot{\gamma}^+ = \dot{\gamma}\frac{\eta_w}{\rho {u_\tau}^2} \tag{A12}$$

Revolutions per Minute (RPM)

$$RPM = \frac{60}{2\pi}\omega \tag{A13}$$

where the angular frequency ω is given by

$$\omega = \frac{U}{r} \tag{A14}$$

Typically, U and r are defined as $U = u(r = d_i/2)$ and $r = d_i/2$. However, in accordance with the bulk velocity used in the Reynolds number a better definition might be $U = U_r = u(r = d_i/2 + (d_o/2 - d_i/2)/2$ and $r = d_i/2$.

Appendix B Inner scaling

Mass conservation implies

$$\dot{m} = \rho\left(UA\right) = \int_A \rho\, u(r)\, dA \tag{B1}$$

where r is the radial coordinate with r = 0 at the center of the conduit.

Isolated for the superficial velocity U, this yields

$$U = \frac{\int_A \rho\, u(r)\, dA}{\rho\, A} = \frac{\int_0^R \rho\, u(r)\, 2\pi r\, dr}{\rho\, \pi R^2} = \frac{2}{R^2}\int_0^R \rho\, u(r)\, r\, dr \tag{B2}$$

where a pipe geometry is assumed.

Using the definitions (A10) and (A11), where R and r are nondimensionalized in the same manner as $y = R - r$, and after some manipulation, one obtains

$$U^+ = \frac{2}{\left(R^+\right)^2}\int_0^{R^+} u^+ y^+\, dy^+ \tag{B3}$$

Appendix C Outer scaling

C.1 Friction factor

With the concept of the hydraulic diameter $d_h = 4A/S$ as the ratio of x-sectional area A and wetted perimeter S, the wall shear stress may be developed from a force balance of pressure and viscous ("frictional") forces to

$$\tau_W = \frac{\Delta p d_h}{4\Delta x} \tag{C1}$$

The same result is obtained if one rearranges the laminar flow equation of a Newtonian fluid to

$$\frac{\Delta p d_h}{4\Delta x} = \mu \frac{8U}{d_h} \tag{C2}$$

where $8U/d_h$ is the Newtonian wall shear rate and $\Delta p d_h/4\Delta L$ is the wall shear stress.

Non-dimensionalising with a dynamic pressure yields the Fanning friction factor

$$f = \frac{\frac{\Delta p d_h}{4\Delta x}}{\rho \frac{U^2}{2}} \tag{C3}$$

which may also be obtained by manipulating equation (C2) to yield

$$f = \frac{16}{\mathrm{Re}} \tag{C4}$$

which is equivalent with (C3) and highlights the friction factor being a ratio of viscous and momentum stresses.

The Reynolds number in (C4) is defined as

$$\mathrm{Re} = \frac{\rho U D}{\mu} \tag{C5}$$

where μ is a Newtonian viscosity or an apparent viscosity of a GNF fluid.

C.1.1 Friction factor correlations for single phase, Newtonian flows

Morrison [3] (laminar & turbulent, smooth walls)

$$f = \frac{16}{\mathrm{Re}} + \frac{0.0076\left(\frac{3170}{\mathrm{Re}}\right)^{0.165}}{1+\left(\frac{3170}{\mathrm{Re}}\right)^{7}} \tag{C6}$$

Haaland [2] (turbulent, rough walls, s = roughness)

$$f = \frac{1}{4\left(-1.8\log_{10}\left(\left(\frac{s}{3.7d_h}\right)^{1.11} + \frac{6.9}{\mathrm{Re}}\right)\right)^2} \tag{C7}$$

Blasius [1] (turbulent, smooth walls)

$$f = \frac{0.316\,\mathrm{Re}^{-0.25}}{4} \tag{C8}$$

C.1.2 Friction factor correlations for single phase, GNF fluid flows

Dodge-Metzner [5]

$$\frac{1}{\sqrt{f}} = \frac{4}{n^{0.75}}\log\left(\mathrm{Re}\; f^{\left(1-\frac{n}{2}\right)}\right) - \frac{0.4}{n^{1.2}} \tag{C9}$$

Irvine [7]

$$f = \left(\frac{2^{(n+4)}}{7^{7n}}\left(\frac{4n}{3n+1}\right)^{3n^2}\mathrm{Re}^{-1}\right)^{\left(\frac{1}{3n+1}\right)} \tag{C10}$$

C.2 Generalized Reynolds number

Using the Re definition as given in equation (C5) but with the viscosity at the wall $\eta_w(\dot{\gamma}_w)$ instead yields the generalized Reynolds number. Computing the correct viscosity η_w is, however, not straightforward because one must know the shear rate at the wall.

For the case of a pipe, the following computational approaches are available as summarized in Table 4:

- Based on pressure gradient
- Based on bulk velocity (or flow rate), equivalent to [4]

The first one is more general because it accounts for the transitional/turbulent regime. For the laminar flow regime, these two approaches should lead to identical results because the pressure gradient is purely defined by the laminar viscosity and corresponding stress. However, for the transitional/turbulent flow regime, the pressure gradient is a consequence of the laminar stress as well as turbulent stresses.

	Based on pressure gradient	Based on bulk velocity (or flow rate)
1	$\frac{\Delta p}{\Delta x}$	U
2	$\tau_w = \frac{\Delta p d_h}{\Delta x 4}$	
3	$\eta_w = \frac{\tau_w}{\dot{\gamma}_w}$	$\eta_w = K\dot{\gamma}_w^{\;n-1}$

4	$\dot{\gamma}_w = \left(\frac{\tau_w}{K}\right)^{\frac{1}{n}}$	$\dot{\gamma}_w = \frac{8U}{d_h}\left(\frac{3n+1}{4n}\right)^{\frac{n}{n-1}}$
5	$\eta_w = \left(\frac{\Delta p d_h}{\Delta x 4}\right)^{\left(1-\frac{1}{n}\right)} K^{\frac{1}{n}}$	$\eta_w = K\left(\frac{8U}{d_h}\right)^{n-1}\left(\frac{3n+1}{4n}\right)^{n}$

Table 4: Computational approaches for defining a viscosity at the wall.

C.3 Generalized Reynolds number for PL fluid

C.3.1 Pipes

Based on a rheology-independent expression for the shear-rate at the wall of a fluid developed by [59] and [60], [4] defined a **generalized Reynolds number for non-Newtonian fluids**

$$\mathrm{Re}_G = \frac{\rho U^{2-n'} D^{n'}}{K' 8^{n'-1}} \tag{C11}$$

with the denominator, termed “effective viscosity” by [61] and “generalized viscosity coefficient” by [4]

$$\eta = K' 8^{n'-1} \tag{C12}$$

the dimensionless exponent n' defined as a derivative representing the slope of a logarithmic plot of the shear stress at the wall $d_h \Delta p / 4 \Delta p x$ (of a pipe) vs. the corresponding Newtonian shear rate $8U/d_h$

$$n' = \frac{d\left[\ln\left(\frac{d_h \Delta p}{4\Delta x}\right)\right]}{d\left[\ln\left(\frac{8U}{d_h}\right)\right]} \tag{C13}$$

termed flow-behavior index and describing the degree of non-Newtonian behavior of the fluid.

the dimensionless coefficient K'

$$K' = \frac{\frac{d_h \Delta p}{4\Delta x}}{\left(\frac{8U}{d_h}\right)^{n'}} \tag{C14}$$

termed fluid consistency index and describing the consistency, i.e. the degree of the apparent viscosity, of the fluid.

Equation (C11) is valid for all time-independent, purely viscous material functions if n' and K' are evaluated on small enough increments in an $d_h \Delta p / 4 \Delta x$ vs. $8U/d_h$ plot, as they in general are not necessarily constants.

However, in the case of power-law (pl) fluids as defined by [47]

$$\tau = K\dot{\gamma}^n \quad \leftrightarrow \quad \eta_{app} = \frac{\tau}{\dot{\gamma}} = K\dot{\gamma}^{n-1} \tag{C15}$$

n' and K' are in fact constants and may be related to the PL coefficients n and K as follows

$$n' = n$$
$$K' = K\left(\frac{3n+1}{4n}\right)^n \tag{C16}$$

yielding a Reynolds number Re_{pl} for power–law fluids

$$\mathrm{Re}_{pl} = \frac{\rho U^{2-n} D^n}{K\left(\frac{3n+1}{4n}\right)^n 8^{n-1}} \tag{C17}$$

which, after some manipulation[4], may be related to the Newtonian Reynolds number, equation (C5), as follows

$$\mathrm{Re}_{pl} = \frac{\mathrm{Re}}{\frac{3n+1}{4n}} \tag{C18}$$

C.3.2 Concentric annuli

Following [14] and [15], two amendments need to be undertaken in order to obtain a consistent Reynolds number for concentric annuli

As with Newtonian fluids, the diameter needs to be replaced by an equivalent diameter, e.g. the hydraulic diameter:

$$d_h = \frac{4A}{S} = d_o - d_i \tag{C19}$$

A redefinition of the shear rate and corresponding generalized Re number is required to account for geometrical effects. [14] provided a generalized Re number based on two geometric factors a and b and [15] introduced a functional β = b/a, generalized the friction factor $f = 48/\beta/Re_G$ and replaced the factor 8^{n-1} in equation (C17) with $(24/\beta)^{n-1}$.

The generalized Re number Re_G for a power-law fluid in a non-circular duct is obtained as

$$\mathrm{Re}_{pl-a} = \frac{\rho U^{2-n} D_h^{\,n}}{\left(\frac{24}{\beta}\right)^{n-1} K\left(\frac{1+n\beta}{n+n\beta}\right)^n} \tag{C20}$$

Considering a concentric annulus, two limiting cases can be distinguished. For

- Di → 0 (↔ Circular pipe of diameter D with Dh = D, β = 3 ↔ a = ¼ & b = ¾) equation (C20) reduces to equation (C17).
- Di →1 (↔narrow slot of hydraulic diameter Dh = Do-Di, β = 2 ↔ a = ½ & b = 1) equation (C20) yields

---

[4] Inserting the non-Newtonian shear rate at the wall into the PL apparent viscosity equation, and again inserting into the Newtonian Reynolds number, namely equation (C5), and rearranging/simplifying.

$$\mathrm{Re}_{pl-ns} = \frac{\rho U^{2-n} D_h^{\,n}}{12^{n-1} K \left(\frac{2n+1}{3n} \right)^n} \tag{C21}$$

	Newtonian, e.g. H2O	Non-Newtonian, e.g. PAC
Pipe	$\beta = 3$ $n = 1$ $K = 0.00102$	$\beta = 3$ n = f(Rheology) K = f(Rheology)
Annulus	$\beta = 2$ $n = 1$ $K = 0.00102$	$\beta = 2$ n = f(Rheology) K = f(Rheology)

Table 5: Overview of flow cases.

	Newtonian, e.g. H2O	Non-Newtonian, e.g. PAC
Pipe	$f_{n-p} = \frac{16}{\mathrm{Re}_{n-p}}$ $\mathrm{Re}_{n-p} = \frac{\rho U D}{\mu}$	$f_{nn-p} = \frac{16}{\mathrm{Re}_{nn-p}}$ $\mathrm{Re}_{nn-p} = \frac{\rho U^{2-n} D^n}{8^{n-1} K \left(\frac{3n+1}{4n} \right)^n}$
Annulus	$f_{n-a} = \frac{24}{\mathrm{Re}_{n-a}}$ $\mathrm{Re}_{n-a} = \frac{\rho U D_h}{\mu}$	$f_{nn-a} = \frac{24}{\mathrm{Re}_{nn-a}}$ $\mathrm{Re}_{nn-a} = \frac{\rho U^{2-n} D_h^{\,n}}{12^{n-1} K \left(\frac{2n+1}{3n} \right)^n}$

Table 6: Overview of friction factor and Reynolds number definitions.

C.3.3 Eccentric annuli

Correction factors are available for eccentric annuli, both for the laminar [55] and the turbulent flow regime [54].

C.4 PL scaling based on Reynolds similarity

Based on Reynolds similarity $\mathrm{Re}_1 = \mathrm{Re}_2$, for a for a Newtonian fluid

$$\frac{\rho_2 U_2 d_{h2}}{\mu_2} = \frac{\rho_1 U_1 d_{h1}}{\mu_1} \tag{C22}$$

Rearranging

$$\mu_2 = \mu_1 \frac{\rho_2 U_2 d_{h2}}{\rho_1 U_1 d_{h1}} \tag{C23}$$

For the pipe DNS simulations, d_h=1m and ρ=1kg/m^3. Assuming water (ρ=998.2kg/m^3, μ=0.001002Pa·s) and d_h=0.045 [33] yields

$$\mu_2 = 0.001002 \frac{1 U_2 1}{998.2 U_1 0.045} = 2.23 \cdot 10^{-5} \tag{C24}$$

For a PL fluid, regardless of starting out with the Metzner-Reed Reynolds number or with a Generalized Reynolds number with an apparent viscosity based on a shear rate estimate of the order U/d, one obtains

$$K_2 = K_1 \frac{\rho_2 U_2^{\ 2-n} d_{h2}^{\ n}}{\rho_1 U_1^{\ 2-n} d_{h1}^{\ n}} \tag{C25}$$

where $n = n_1 = n_2$ because identical shear-thinning behavior is required.

However, if a Generalized Reynolds number with an apparent viscosity based on the wall shear stress is used instead, one obtains

$$K_2 = K_1 \left(\frac{\rho_2 U_2 d_{h2}}{\rho_1 U_1 d_{h1}} \right)^n \left(\frac{\tau_1}{\tau_2} \right)^{n-1} \tag{C26}$$

Appendix D Estimates

D.1 Bulk velocity U for given pressure gradient dp/dx

Turbulent flow regime, use Blasius [1] friction factor correlation, i.e. equation (C8), with definition of friction factor, namely equation (C3)

$$\frac{0.316\,\mathrm{Re}^{-0.25}}{4} = \frac{\dfrac{\Delta p d_h}{4\Delta x}}{\rho\dfrac{U^2}{2}} \tag{D1}$$

Apply definition of Re and raise to fourth power, isolate U

$$U = \sqrt[7]{\frac{16\left(\dfrac{\Delta p}{\Delta x}\right)^4 d_h{}^5}{0.316^4\,\rho^3\eta}} \tag{D2}$$

D.2 First layer cell height

Rearrange definition of dimensionless wall distance y^+ and insert definition of friction velocity u_τ and rearranged Fanning friction factor f

$$\Delta_1 y = y^+\frac{\eta}{\rho u_\tau} = y^+\frac{\eta}{\rho U\sqrt{\dfrac{f}{2}}} \tag{D3}$$

A.2. Additional contributions

The bibliography lists papers in the order as they appear in the text. The order at which papers are provided in the individual appendices is based on the publication type instead: Journal paper, Conference paper, Report, Manuscript.

Note that papers [IX, X, XVI] describe preliminary results presented at the conferences indicated and are thus not attached to this thesis. The reader is instead referred to the respective full papers [I, II, VIII].

[IX] Alexander Busch and Stein Tore Johansen. "On The Validity Of The Two-Fluid-KTGF Approach For Dense Gravity-Driven Granular Flows". In: *Book of Abstracts*. The 2nd International Symposium on Computational Particle Technology (CPT-2018). Vol. 2. Melbourne: CSIRO, Monash University, Dec. 4–8, 2018. URL: http://www.cfd.com.au/cfdconf/pdf/2nd%20CPT%20and%2013th%20CFD-Booklet.pdf.

[X] A. Busch, A. Islam, D. Martins, F. P. Iversen, M. Khatibi, S. T. Johansen, R. W. Time, and E. A. Meese. "Cuttings Transport Modeling - Part 1: Specification of Benchmark Parameters with a Norwegian Continental Shelf Perspective". In: SPE Bergen One Day Seminar 2016. Bergen: Society of Petroleum Engineers, Apr. 20, 2016. DOI: 10.2118/180007-MS.

[XI] Alexander Busch. "Conversion of Engineering Oil Field Rheological Model Parameters to SI Model Parameters". Trondheim, 2015.

[XII] Ulf Jakob F. Aarsnes and Alexander Busch. "Transient Modeling of One-Dimensional Solid-Liquid Flow in Conduits". In: *International Journal of Multiphase Flow* 105 (August 2018 2018). Additional, pp. 102–111. DOI: 10.1016/j.ijmultiphaseflow.2018.03.023.

[XIII] Alexander Busch and Stein Tore Johansen. *Estimating the Level of Turbulence and Dunes in Wellbore Flows by Means of Bulk Flow Quantities*. Trondheim: AdWell project, 2018.

[XIV] Alexander Busch and Stein Tore Johansen. "Judging the Generalized Newtonian Fluid Assumption for Cuttings Transport Modelling by Applying Time Scale Comparisons". In: *The Transactions of the Nordic Rheology Society*. The 27th Nordic Rheology

Conference. Vol. 26. Trondheim: Nordic Rheology Society, June 15, 2018, p. 9. URL: http://nordicrheologysociety.org/transactions/.

[XV] Josip Zoric, Alexander Busch, Ernst A. Meese, Milad Khatibi, Rune W. Time, Stein T. Johansen, and H. A. Rabenjafimanantsoa. "On Pragmatism in Industrial Modeling - Part II: Workflows and Associated Data and Metadata". In: *The 11th International Conference on CFD in the Minerals and Process Industries*. The 11th International Conference on CFD in the Minerals and Process Industries. Melbourne: CSIRO Publishing, 2015. URL: http://www.cfd.com.au/cfd_conf15/PDFs/032JOH.pdf.

[XVI] Alexander Busch and Stein Tore Johansen. "Implementation and Validation of a DPM Model Accounting for Shear-Thinning Fluid Viscosity". In: 15th Multiphase Flow Conference & Short Course. Dresden: ANSYS Germany GmbH, Helmholtz-Zentrum Dresden-Rossendorf, Nov. 16, 2017. DOI: 10.13140/RG.2.2.12028.23684.

[XVII] Milad Khatibi, Rune Wiggo Time, Alexander Busch, Stein Tore Johansen, Dwayne Werner Martins, Md. Aminul Islam, and Fionn Iversen. "Investigation of Suspended Particles Around an Obstacle in Vertical Pipe Flow: Comparison Study Experimental and Simulation". In: *ASME 2017 36th International Conference on Ocean, Offshore and Arctic Engineering*. ASME 2017 36th International Conference on Ocean, Offshore and Arctic Engineering. ASME, June 25, 2017, V008T11A067. DOI: 10.1115/OMAE2017-62244.

Journal paper 7 (XII)

Transient modeling of one-dimensional solid-liquid flow in conduits

Ulf Jakob F. Aarsnes, Alexander Busch

International Journal of Multiphase Flow, Vol. 105, pp. 102–111, 2018.

DOI: 10.1016/j.ijmultiphaseflow.2018.03.023.

International Journal of Multiphase Flow 105 (2018) 102–111

Contents lists available at ScienceDirect

International Journal of Multiphase Flow

journal homepage: www.elsevier.com/locate/ijmulflow

Transient modeling of one-dimensional solid-liquid flow in conduits

Ulf Jakob F. Aarsnes[a,*], Alexander Busch[b]

[a] International Research Institute of Stavanger (IRIS), Oslo, Norway
[b] Norwegian University of Science and Technology (NTNU), Trondheim, Norway

ARTICLE INFO

Article history:
Received 24 October 2017
Revised 26 March 2018
Accepted 31 March 2018
Available online 5 April 2018

Keywords:
Particle transport
PDE
Real-Time
Drilling
Cuttings transport
Layer model

ABSTRACT

We consider the transient modeling of liquid-solid flow in conduits. Current models available in the literature are typically based on a three layer – two phase representation which, for the general transient case, results in a six-field model, entailing significant complexity in analysis and implementation. In this paper, we propose a transient three layer model represented by three equations (a third order PDE) by assuming a static momentum balance and then exploiting certain properties of the continuity relations. We illustrate how the transient model can be completed by introducing deposition–erosion closure relations from the literature, and describe its implementation by an upwind numerical scheme. Finally, some of the transient properties of the model are illustrated in six simulations comparing the simulated trends with six cuttings transport experiments found in the literature, motivated by application to horizontal drilling.

1. Introduction

Solid-liquid flow in pipes and other conduits, for instance annuli and channels, find numerous applications such as slurry flows in waste handling, sediment transport in hydrology, and cuttings (drilled-off particles) transport in drilling (Tomren et al., 1986; Larsen et al., 1997; Philip et al., 1998). Here, transient cuttings transport models can improve drilling operations by optimizing transient procedures such as connections and back-reaming, and may be utilized as Real-Time (RT) models on the drill rig to provide on-line monitoring of hole cleaning (adequate flushing of cuttings from the wellbore) (Florence and Iversen, 2010). An overview of cuttings transport modeling is given by Pilehvari et al. (1999), and more recently, by Li and Luft (2014), while more general reviews of two-phase, solid-liquid flows are for instance given by Drew (1983) and Peker and Helvaci (2008).

Inherently, cuttings transport is a transient, spatial three-dimensional (3D) problem because the conduit is an annulus, where the inner drill pipe may be off-center (or even laterally moving) and rotating, and where a bed of cuttings may form at the lower wall in inclined and horizontal sections. For lower inclinations this bed is typically stationary but features a small layer of sliding and rolling particles (referred to as *bed load* in environmental particle transport modeling and hydrology) between the usually stationary bed and the bulk of the fluid-solid flow. However, for most simulation purposes, resolving the full 3D flow field may be too cumbersome, due to the complex interaction between the phases. In particular, calculating the temporal evolution of the interface between the phases, and the transfer momentum across it, may be too computationally costly, especially when Real-Time (RT) application of the model is desired. While 3D Computational Fluid Dynamics (CFD) methodologies have been used to investigate specific cuttings transport problems and further understand the interdependencies of parameters in and on the 3D flow field, todays available computational power limits 3D CFD approaches to a scale of the order of 10^0 m, whereas the wellbore scale is of the order of 10^3 m. As such, the full 3D CFD simulations are relegated to enhancing experimental work in deriving models for closure relations (such as slip velocities as well as deposition and entrainment rates) (Kaushal et al., 2012; Capecelatro and Desjardins, 2013; Busch et al., 2017), rather than providing RT models in themselves. In any case, for fast-computing requirements on the wellbore scale such as previously mentioned RT applications, a 3D formulation of the multiphase flow problem is to be simplified using local equilibrium assumptions and a complete spatial average over the cross-sectional area, leaving only the flow direction as a spatial dimension. The resulting coarse-grained one-dimensional in space (1D) models may still feature (relatively) high complexity depending on the number of phases considered and closures utilized.

Typically, 1D solid transport models in conduits are based on a two- or three layer formulation introduced by Doron and Barnea (1993), Doron and Barnea (1996) and Doron et al. (1997),

---

[*] Corresponding author.
E-mail addresses: ujfa@iris.no (U.J.F. Aarsnes), alexander.busch@alumni.ntnu.no (A. Busch).

https://doi.org/10.1016/j.ijmultiphaseflow.2018.03.023

where the layers describe the above mentioned (stationary) bed, the (moving, in the sense of rolling and sliding particles) bed load and the flowing mixture of the transporting liquid with solids in suspension. Usually, balance equations are solved for mass and momentum for the solid and fluid phases in the individual layers. However, many models based on the layered approach are steady-state models, i.e. disregarding the transient terms.

Various transient 1D cuttings transport models have been proposed in the literature (Martins et al., 1998; Doan et al., 2003; Ramadan et al., 2005; Salazar-Mendoza and Espinosa-Paredes, 2009; Wang et al., 2010; Cayeux et al., 2014; Zhang et al., 2016) and have been shown capable of delivering significant value in field applications (Cayeux et al., 2016; Naganawa et al., 2017).

The closures utilized in these models may encompass comparatively simple single-phase *Reynolds number-friction factor*-relationships, slip velocity models (Chien, 1994), empirical correlations accounting for inclination, drill pipe rotation, or eccentricity (Larsen, 1990) and even numerical solutions of the cross-sectional flow field in order to capture secondary flows as a consequence of the solids bed (Girolami et al., 2016).

Existing transient 1D models are, however, relatively complicated and cumbersome to implement and analyze, and this complexity can limit the range of possible applications of the models, in particular with regards to model based estimation techniques (Aarsnes et al., 2016b). In addition, simplified mechanistic 1D models with semi-implicit or explicit solvers and closures are required to satisfy computational speed requirements (Florence and Iversen, 2010).

Based on these considerations, the present paper proposes a simple, phenomenological, modeling approach where considerations on time-scales and dominating dynamics are leveraged into formulating the complete model as a system of two or three hyperbolic equations, depending on the number of solid-liquid layers considered, completed by closure relations giving the suspended cuttings slip velocity as well as settling and erosion rates of the cuttings bed interface. The closure relations of the resulting model can be fitted to existing steady-state correlations to inherit the steady-state accuracy of previously published results, of which there are many (Tomren et al., 1986; Li and Walker, 2001). As such, the goal of the present paper is to provide a transient 1D simulation model, to enhance the applicability of existing steady-state results to cases where a RT-model is required. I.e., with this paper we wish to bridge this gap by providing a framework to make a steady-state model, or experimentally developed closure relations, into a transient simulation model, similarly to what was done with the Drift Flux Model in the 70‘s for liquid-gas flow.

Towards this goal, our hypothesis is that, firstly, a low order transient model (a PDE with two or three states) is sufficient to represent the transient dynamics on the time scale of the cuttings transportation. And, secondly, using steady-state flow closure relations from the literature, a transient model can be obtained without having to re-derive such closure relations specifically for the transient case.

To address this hypothesis, we give some general considerations on the continuity relations in Section 2, where under the assumption that the hydrodynamic time scale is much faster than that of the change of the bed height, the continuity of the six fields can be represented by three equations. Then, to illustrate the merit of this approach, transient simulations are performed and compared with experimental testing from cuttings transport in petroleum research where the model is shown to give a good qualitative representation of the dynamic behavior seen in experiments.

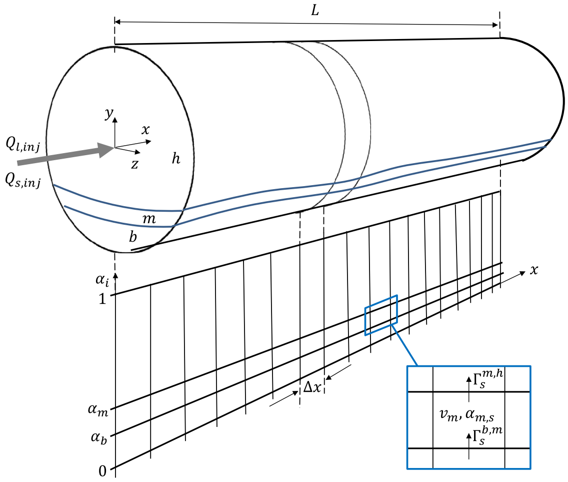

Fig. 1. Schematic of the three-layered model.

2. Starting point model

Consider a 3D field over the independent space variables *x, y, z*, and time, $t \in \mathbb{R}^+$. We denote by α_i, ρ_i, v_i the averaged volume fraction, density and velocity over a computational control volume, covering the *y, z* directions and with the infinitesimal small axial length Δx, schematically depicted in Fig. 1. Assuming the phase density ρ_i as constant, the continuity and momentum preservation equations (averaged over a computational control volume) read for the x-direction:

$$\frac{\partial \alpha_i}{\partial t} + \frac{\partial \alpha_i v_i}{\partial x} = \Gamma_i \tag{1}$$

$$\frac{\partial \alpha_i v_i}{\partial t} + \frac{\partial \alpha_i v_i v_i}{\partial x} = S_i, \tag{2}$$

where Γ_i, S_i denote source terms for volume flux and momentum transfer between the fields. In a typical continuum model, a pressure gradient is included where the pressure is a function of the sound velocity and density of the field.

Further simplification can be obtained by considering the model as a hyperbolic relaxation system where the source terms, accounting for the interactions between the phases and with exogenous forcing terms, drive the various fields asymptotically towards equilibrium at a finite rate. Imposing immediate equilibrium on such processes enables two dynamic equations to be combined to one and consequently allows for simpler models at the possible cost of a reduction in model fidelity (Flåtten and Lund, 2011). In this case we will assume impose immediate equilibrium on the pressure dynamics of all fields, which is equivalent to assuming the phases to be incompressible, essentially making the pressure gradient a non-local exogenous parameter that enters in the source term. The resulting reduction in fidelity is arguably negligible as the pressure dynamics operate on a much faster time-scale than that of the cuttings transport. Hence, we effectively obtain simpler and more tractable model with modest or negligible cost in model fidelity.

With these assumptions, we can obtain the quasi-linear form by expanding (2):

$$\frac{\partial \alpha_i}{\partial t}v_i + \frac{\partial v_i}{\partial t}\alpha_i + \frac{\partial \alpha_i v_i}{\partial x}v_i + \frac{\partial v_i}{\partial x}\alpha_i v_i = S_i, \tag{3}$$

and inserting (1) into (3), which yields the form

$$\frac{\partial}{\partial t}\begin{bmatrix}\alpha_i \\ v_i\end{bmatrix} + \begin{bmatrix} v_i & \alpha_i \\ 0 & v_i\end{bmatrix}\frac{\partial}{\partial x}\begin{bmatrix}\alpha_i \\ v_i\end{bmatrix} = \begin{bmatrix}\Gamma_i \\ \frac{S_i - v_i\Gamma_i}{\alpha_i}\end{bmatrix}, \tag{4}$$

where the transport matrix, characterizing the system (1) and (2), has the double eigenvalue v_i, corresponding to the velocity of the characteristic. Hence, we see that by removing the equation of state by assuming all densities to be constant (in both time and space), one of the equations of the system (1) and (2) becomes superfluous in the sense of conserving the information propagation properties of the system (due to the repeating eigenvalue) and can be removed to simplify the system. Following the formalism of relaxation processes, we will write (1) and (2) as simply

$$\frac{\partial \alpha_i}{\partial t} + \frac{\partial \alpha_i v_i}{\partial x} = \Gamma_i, \tag{5}$$

where the pressure field typically is contained as a gradient within the source term and can be recovered from the relaxed formulation of (2) from

$$S_i = \frac{\partial \alpha_i v_i v_i}{\partial x}. \tag{6}$$

Consequently, we have argued that for cases where the fast distributed pressure waves are not of critical importance (Aarsnes et al., 2016a), and a constant density is assumed (as is often the case in liquid-solid flow), the momentum balance can be assumed static and the relations of continuity for each field is a sufficient representation of the model. A similar approach has for instance been taken by Girolami et al. (2016), who concluded that the hydrodynamic time scale of the fluid flow is by a factor of order 10^6 smaller than the time scale on which evolution of the sediment bed takes place. Hence, from the solids bed point of view, the time rate of change of the fluid equations becomes instantaneous and the time-dependent terms in the equations may be disregarded. The role of the fluid momentum equation is thus reduced to a closure law relating bulk flow properties such as the superficial liquid velocity to shear stress acting on the bed.

2.1. General relations of continuity

We consider in the following a transient, averaged, three layer model of liquid-solids flow in a conduit, as schematically depicted in the top part of Fig. 1. The three layer model postulation is due to Doron and Barnea (1993, 1996) and Doron et al. (1997), which is a steady-state model. These three layers are typically referred to as the homogeneous layer, a moving bed layer, and a stationary bed layer.

Each layer consists of a combination of two components: liquid and solids. This yields a total of six fields for the model. For each field we denote the volume fraction $\alpha_{i,j}$ and velocity $v_{i,j}$, where $i \in \{h, m, b\}$ denote the homogeneous, moving bed and stationary bed layer respectively, while $j \in [s, l]$ denote the component as solid or liquid. The equations of continuity can be written

$$\frac{\partial \alpha_{i,j}}{\partial t} + \frac{\partial \alpha_{i,j} v_{i,j}}{\partial x} = \sum_k \Gamma_j^{k,i}, \tag{7}$$

where $\Gamma_j^{k,i}$ denotes the source term for transfer of component j from layer k to layer i. Written out

$$\frac{\partial \alpha_{h,s}}{\partial t} + \frac{\partial \alpha_{h,s} v_{h,s}}{\partial x} = \Gamma_s^{m,h} \tag{8}$$

$$\frac{\partial \alpha_{h,l}}{\partial t} + \frac{\partial \alpha_{h,l} v_{h,l}}{\partial x} = \Gamma_l^{m,h} + \Gamma_l^{b,h} \tag{9}$$

$$\frac{\partial \alpha_{m,s}}{\partial t} + \frac{\partial \alpha_{m,s} v_{m,s}}{\partial x} = \Gamma_s^{b,m} - \Gamma_s^{m,h} \tag{10}$$

$$\frac{\partial \alpha_{m,l}}{\partial t} + \frac{\partial \alpha_{m,l} v_{m,l}}{\partial x} = \Gamma_l^{b,m} - \Gamma_l^{m,h} \tag{11}$$

$$\frac{\partial \alpha_{b,s}}{\partial t} + \frac{\partial \alpha_{b,s} v_{b,s}}{\partial x} = -\Gamma_s^{b,m} \tag{12}$$

$$\frac{\partial \alpha_{b,l}}{\partial t} + \frac{\partial \alpha_{b,l} v_{b,l}}{\partial x} = -\Gamma_l^{b,m} - \Gamma_l^{b,h}. \tag{13}$$

Following Doron and Barnea (1993), we assume a constant packing density and homogeneous velocity of the layers b, m. By ‘packing density’ we mean the solid volume fraction of the stationary (typically 0.63 for close random packing of spheres) and moving bed layers (typically between 0.55 and 0.625 for loose random packing of spheres), where the solid particles are in stationary contact or rolling and sliding against each other, respectively. Hence, denoting the packing density C_i, where $i \in \{b, m\}$, we write $\alpha_i = \alpha_{i,s} + \alpha_{i,l}$, such that $\alpha_{i,s} = C_i\alpha_i$. Further, we assume $v_{i,l} = v_{i,s} = v_i$ for $i \in \{b, m\}$. We note that

$$\alpha_{b,l} = 1 - \alpha_m - \alpha_h - \alpha_{b,s}, \tag{14}$$

and, writing $\Gamma^{k,i} \equiv \Gamma_l^{k,i} + \Gamma_s^{k,i}$, we have

$$C_m\Gamma^{m,h} = -\Gamma_s^{h,m}. \tag{15}$$

When $C_b \neq C_m$, by noting that

$$\Gamma_s^{b,m} = -\Gamma_s^{m,b} \Rightarrow C_b\Gamma^{b,m} = -C_m\Gamma^{m,b}, \tag{16}$$

we get an exchange term between layer b and h:

$$\Gamma_l^{b,h} = \Gamma^{b,m}\left(1 - \frac{C_b}{C_m}\right), \tag{17}$$

These relations allows us to represent the volume fraction of the six fields by the three continuity equations

$$\frac{\partial \alpha_{h,s}}{\partial t} + \frac{\partial \alpha_{h,s} v_{h,s}}{\partial x} = -C_m\Gamma^{h,m} \tag{18}$$

$$\frac{\partial \alpha_m}{\partial t} + \frac{\partial \alpha_m v_m}{\partial x} = \Gamma^{h,m} - \Gamma^{m,b} \tag{19}$$

$$\frac{\partial \alpha_b}{\partial t} + \frac{\partial \alpha_b v_b}{\partial x} = \Gamma^{m,b}. \tag{20}$$

An equivalent formulation is

$$\frac{\partial \alpha_{h,s}}{\partial t} + \frac{\partial \alpha_{h,s} v_{h,s}}{\partial x} = -\Gamma_s^{h,m} \tag{21}$$

$$\frac{\partial \alpha_{m,s}}{\partial t} + \frac{\partial \alpha_{m,s} v_m}{\partial x} = \Gamma_s^{h,m} - \Gamma_s^{m,b} \tag{22}$$

$$\frac{\partial \alpha_{b,s}}{\partial t} + \frac{\partial \alpha_{b,s} v_b}{\partial x} = \Gamma_s^{m,b}, \tag{23}$$

where the layer area fractions are obtained from:

$$\alpha_m C_m = \alpha_{m,s} \tag{24}$$

$$\alpha_b C_b = \alpha_{b,s} \tag{25}$$

$$\alpha_h + \alpha_m + \alpha_b = 1. \tag{26}$$

Hence we have demonstrated that the continuity equations of the transient three layer model of solid-liquid flow can be represented as a third order Partial Differential Equation (PDE).

So far, no assumptions have been made on fluid rheology or inclination. However, depending on conditions, the m and/or b layers will not exist (e.g. in very steep and vertical sections), in which case these fields will be empty and the model can be simplified by removing them.

To complete the model for simulation, (21)–(23) must be combined with closure relations of the velocities v_b, v_m, $v_{h,\,s}$ and the source terms $\Gamma_s^{h,m}$, $\Gamma_s^{m,b}$, and finally, appropriate boundary conditions should be derived. The closure relations should be derived by combination of first principle considerations and empirical correlations derived from experiments. To comply with the requirements on simplicity and computational speed, it is the role of the closure relations to account for the presence of the drill pipe, and hence the existence of an annular flow field, as well as the role of drill pipe rotation and potential lateral movement.

For the purpose of illustrating how a complete simulation model is obtained, we will in the following sections of this paper choose a set of simple closure relations from the literature and implement the resulting model. We emphasize, however, that a formulation of the form (21)–(23) can accommodate a wide range of closure relations, and in effect enable turning a set of experimental results into a transient model.

To limit the complexity of the following derivation, and to make our illustration more clear, we limit the model to only two layers. Physically, this is valid depending on the flow patterns. For annular solid-liquid flows, higher superficial velocities, and in particular the presence of drill pipe rotation, enhance solid suspension such that the intermediate layer of rolling and sliding particles becomes very small, see e.g. Khatibi et al. (2018), and may be disregarded for the sake of added simplicity and computational speed.

3. Two layer model

In this section we derive the full two-layer model in the context of a wellbore being drilled, where the solids represent cuttings and the liquid represent the drilling mud.

In considering only two layers in the (21)–(23) formulation, we let the m layer be empty; $\alpha_m = 0$, and consequently set $\Gamma_s^{h,m} - \Gamma_s^{m,b} = 0$. Furthermore, we will assume the bed layer b to be stationary, i.e. $v_b = 0$, which is true for a close to horizontal section such that a potential sliding of the bed due to gravity does not occur, and thus obtain

$$\frac{\partial \alpha_{h,s}}{\partial t} + \frac{\partial \alpha_{h,s} v_{h,s}}{\partial x} = \Gamma_s^{b,h} \tag{27}$$

$$\frac{\partial \alpha_{b,s}}{\partial t} = -\Gamma_s^{b,h}, \tag{28}$$

where $x \in [0, L]$ and t are the space and time variables, with $x = 0$ denoting an upstream inlet and $x = L$ a downstream outlet of the considered flow domain, as depicted in Fig. 1. In addition, we have the closure relations

$$\alpha_b C_b = \alpha_{b,s} \tag{29}$$

$$\alpha_{h,l} + \alpha_{h,s} + \alpha_b = 1. \tag{30}$$

This system, (27) and (28), is a second order hyperbolic PDE with a zero eigenvalue associated with (28).

To complete this system, we further require the closure relations for the slip velocity of particles in suspension, $v_{h,\,s}$, and the erosion-deposition model $\Gamma_s^{b,h}$.

3.1. Boundary condition

Assuming a positive eigenvalue associated with (27), a boundary condition must be specified at the left ($x = 0$) boundary. If the mass-flux of cuttings at the boundary, W_c is known, the cuttings volume fraction can be found from $W_c = Q_{s,\mathrm{inj}} \rho_s = A \alpha_{h,s} \rho_s v_{h,s}$. Here $Q_{s,\,\mathrm{inj}}$ denotes the volumetric flowrate of solids at the boundary. For the case of $v_{h,l} = v_{h,s}$ (often used for horizontal pipes, see Section 3.2) we have

$$\alpha_{h,s}(x = 0) \equiv \alpha_{s,\mathrm{inj}} = \frac{Q_{s,\mathrm{inj}}}{Q_{s,\mathrm{inj}} + Q_{l,\mathrm{inj}}}, \tag{31}$$

where $Q_{s,\,\mathrm{inj}}$ and $Q_{l,\,\mathrm{inj}}$ are the solid and liquid volumetric flow rates, respectively. In a practical setting W_c, and thus $Q_{s,\,\mathrm{inj}}$, may be readily estimated from the drill bits dimension and rate of penetration (ROP) based on continuity.

3.2. Slip velocity

For transient cuttings transport models, the slip velocity of a cuttings particle, $v_{h,\,s}$, may be obtained by applying a local equilibrium assumption and hence taking the vector sum of the liquid velocity $v_{h,\,l}$ and the particles' terminal settling velocity V_S (Cayeux et al., 2014).

$$v_{h,s} = v_{h,l} + V_S, \tag{32}$$

where the particles' terminal settling velocity V_S may be expressed as

$$V_S = -\sqrt{\frac{4}{3}\frac{d_s g \sin\phi(x)}{C_d}\left(\frac{\rho_s}{\rho_l} - 1\right)}, \tag{33}$$

with g acceleration of gravity, $\phi(x)$ inclination with respect to horizontal, d_s diameter of cuttings particle, and C_d coefficient of drag. Note that the drag coefficient C_d is a function of the particle Reynolds number, which is a function of the fluids apparent viscosity and furthermore depends implicitly on $v_{h,\,s}$ via V_S. Further note that drilling fluids are typically shear-thinning and thus the apparent viscosity is a function of the shear rate. This is crucial in order to determine the settling velocity correct, because the shear rate of an individual particle is determined by contributions of both the shear of the background flow field at the particles location and the particle-induced shear based on the relative velocity (Busch and Johansen, 2018).

Forces considered in Eq. (32) are gravity, buoyancy, and drag as the usually dominating particle force. Forces not considered are the Basset and Virtual mass force as the rates of change of flow rates and hence velocities are rather small, i.e. we assume local equilibrium. The Saffman (1968, 1965) lift force (which incorporates the Magnus lift force as a second order correction) does not contribute as Eq. (32) only characterizes the x-component, i.e. the component in the direction of flow, and the lift force primarily acts normal to the flow direction for the 1D approach taken. Particle-particle interactions are neglected here as these are expected to only play a minor role in the homogeneous layer.

The liquid velocity is found from the continuity equation, and assuming an incompressible liquid, implying that $A\alpha_{h,l} v_{h,l} = Q_{\mathrm{inj}}$. I.e. we have from the total volumetric flow at the left boundary:

$$v_{h,l} = \frac{(Q_{l,\mathrm{inj}} + Q_{s,\mathrm{inj}})/A}{1 - \alpha_{h,s} - \frac{\alpha_{b,s}}{C_b}} \tag{34}$$

3.3. Erosion-deposition model

The source term $\Gamma_s^{b,h}$ required in Eqs. (27) and (28) is to be described by an adequate erosion-deposition model. As an example, we apply the erosion-deposition model proposed by Charru et al. (2004)

$$\Gamma_s^{b,h} = E - D, \tag{35}$$

where E, D denotes the erosion and deposition rate, respectively. These are given as

$$D = \frac{V_S d_s^2}{a} \alpha_{h,s}, \tag{36}$$

where V_S is the settling velocity given in (33), d_s is the particle diameter and a is a statistically determined constant which can be taken as 15 (Charru et al., 2004). The erosion rate is given as

$$E = \begin{cases} 0, & \alpha_b = 0 \text{ or } \theta < \theta_t \\ 18bV_S(\theta - \theta_t), & \alpha_b > 0 \text{ and } \theta \geq \theta_t \end{cases}, \tag{37}$$

with the non-dimensional Shields number

$$\theta = \frac{\mu\dot{\gamma}}{(\rho_s - \rho_l)d_s g\cos(\phi(x))}, \tag{38}$$

where $\dot{\gamma}$ is the shear rate, and may be taken as proportional to the intrinsically averaged fluid velocity, $v_{h,\,l}$; and μ is the fluid apparent viscosity.

The threshold for particle motion is given by the Shields curve $\theta_t = f(Re_p)$. However, because the relationship $\theta_t = f(Re_p)$ is implicit, an alternative formulation $\theta_t = f(d_*)$ is typically used, for instance $\theta_t = \frac{0.24}{d_*} + 0.055(1 - e^{-0.02d_*})$ (Soulsby, 1997), where d_* is a dimensionless particle diameter. According to Charru et al. (2004), the coefficient b may depend weakly both on the particle Reynolds number and on the number of moving particles. Since the Charru et al. (2004) formulation is purely based on the Stokes settling velocity this seems reasonable. However, in the modeling approach of Charru et al. (2004) it is taken as a constant and is used as a fitting parameter to experimental data.

Utilizing a particular erosion-deposition model may be considered as grey-box modeling, because the erosion-deposition model allows some insight to the dominating physics of the problem. However, if high-quality experimental data is available and/or not all modeling parameter values are known, it is beneficial to transform the utilized erosion-deposition model to a black-box model by introducing appropriately defined correlation parameters. This reduces the number of parameters needed to specify the closure relations and thus simplifies tuning the model. Assuming that the shear rate is proportional to the intrinsically averaged liquid velocity, $v_{h,\,l}$, the source term containing the erosion-deposition-model can be recast to:

$$D = \beta R\alpha_{h,s} \tag{39}$$

$$E = \begin{cases} 0, & \alpha_b = 0 \text{ or } \alpha_l^* < \alpha_{h,l} \\ \frac{\beta}{\alpha_{h,l}}\left(\alpha_l^* - \alpha_{h,l}\right), & \alpha_b > 0 \text{ and } \alpha_l^* \geq \alpha_{h,l}. \end{cases} \tag{40}$$

The correlation parameters β, α_l^*, R are given as:

$$\alpha_l^* = \frac{\mu D_H Q_{l,\text{inj}}/A}{(\rho_s - \rho_l)d_s g\cos\left(\phi(x)\right)\theta_t} \tag{41}$$

$$R = \frac{d_s^2}{a}\frac{1}{\theta_t 18b} \tag{42}$$

$$\beta = \theta_t V_S 18b, \tag{43}$$

where α_l^*, R are dimensionless and β has the unit of $[\frac{1}{\text{time}}]$. In defining the deposition and erosion rates as in (39) and (40), we have adopted the mathematical structure of Charru et al. (2004) in specifying these closure relations, but not necessarily the actual parameters. This allows for a more general framework for tuning the model to fit operating conditions and experimental data not directly covered by the work of Charru et al. (2004).

Eqs. (39) and (40) may alternatively be expressed in terms of the states by noting that $\alpha_b = \alpha_{b,s}/C_b$ and $\alpha_{h,s} = 1 - \alpha_b - \alpha_{h,l}$.

We point out that these parameters are dependent on local conditions, in particular α_l^* which is dependent on the exogenous liquid superficial velocity $Q_{l,\,\text{inj}}/A$. As an example, for higher superficial liquid velocities, the flow of the homogenous layer may become turbulent. In addition, for larger particle diameters, the assumption of Stokes flow is incorrect. The utilized closures (Charru et al., 2004) are based on the Stokes settling velocity V_S and the laminar bed shear stress $\mu\dot{\gamma}$ (see Eqs. (36) and (37)). Here, the molecular fluid viscosity μ may be a function of $\dot{\gamma}$ and the shear rate $\dot{\gamma}$ is based on the superficial liquid velocity and the annular geometry. For an adequate handling of turbulence, this formulation has to be improved by e.g. adding a turbulent viscosity to the molecular fluid viscosity using a simple mixing-length approach. However, wellbore flows are typically either laminar or transitional with bulk Reynolds number in the order of 10^2 to 10^3, which also applies to the experiments conducted by Sanchez et al. (1999), which we will later use to validate the model. Hence, we for now keep the laminar formulation knowing that for higher flow rates, low viscous fluids, and larger particle diameters an error might be present. The significance of the correlation parameters as given can be seen from the steady state relations developed in the following section.

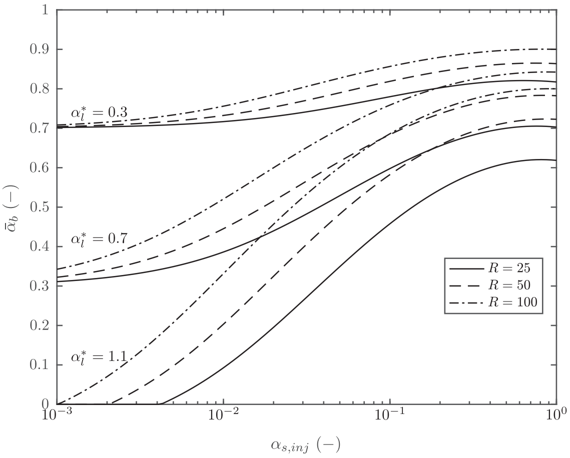

Fig. 2. Effect of correlation parameters R and α_l^* on the steady-state cuttings bed height $\bar{\alpha}_b$.

3.4. Steady state

Denote the steady-state with an overbar. We have, from (27) and (28)

$$\bar{\Gamma}_s^{b,h} = 0 \tag{44}$$

$$\frac{\partial\bar{\alpha}_{h,s}\bar{v}_{h,s}}{\partial x} = 0, \tag{45}$$

which entails

$$\bar{\alpha}_{h,s}\bar{v}_{h,s} = \frac{Q_{s,\text{inj}}}{A}, \tag{46}$$

and using $v_{h,s} = v_{h,l}$:

$$\bar{\alpha}_{h,s} = \frac{Q_{s,\text{inj}}\bar{\alpha}_h}{Q_{s,\text{inj}} + Q_{l,\text{inj}}}. \tag{47}$$

Now, by enforcing $E = D$ (which holds at steady state, see (44)) we obtain:

$$\frac{RQ_{s,\text{inj}}}{Q_{s,\text{inj}} + Q_{l,\text{inj}}}\bar{\alpha}_h + 1 = \frac{\alpha_l^*}{\bar{\alpha}_h}\frac{Q_{l,\text{inj}} + Q_{s,\text{inj}}}{Q_{l,\text{inj}}}, \tag{48}$$

which is a quadratic equation in the state $\bar{\alpha}_h$, i.e.,

$$\bar{\alpha}_h^2 R\frac{Q_{s,\text{inj}}Q_{l,\text{inj}}}{Q_{s,\text{inj}} + Q_{l,\text{inj}}} + \bar{\alpha}_h\frac{Q_{l,\text{inj}}}{Q_{l,\text{inj}} + Q_{s,\text{inj}}} - \alpha_l^* = 0, \tag{49}$$

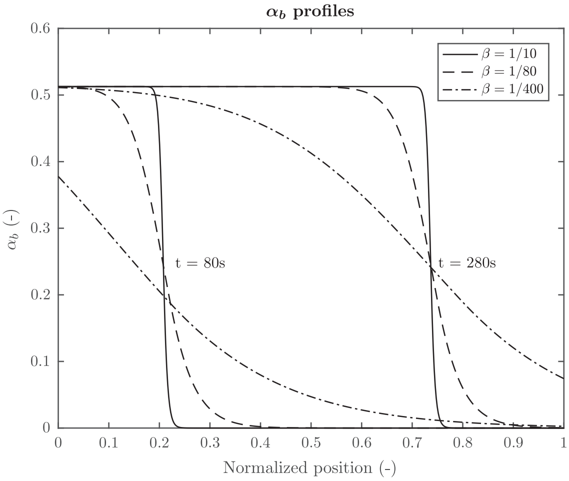

Fig. 3. Effect of changing β on the steepness of the propagating cuttings bed.

hence

$$\bar{\alpha}_h = \frac{Q_{s,\mathrm{inj}} + Q_{l,\mathrm{inj}}}{2RQ_{s,\mathrm{inj}}}\left(-1 + \sqrt{1 + \frac{4R\alpha_l^* Q_{s,\mathrm{inj}}}{Q_{l,\mathrm{inj}}}}\right) \tag{50}$$

and, finally,

$$\bar{\alpha}_b = 1 - \bar{\alpha}_h. \tag{51}$$

Note that using the approximation $\alpha_{s,\mathrm{inj}} \approx \frac{Q_{s,\mathrm{inj}}}{Q_{l,\mathrm{inj}}}$, (50) can be written approximately

$$\bar{\alpha}_h \approx \frac{\alpha_{s,\mathrm{inj}} + 1}{2R\alpha_{s,\mathrm{inj}}}\left(-1 + \sqrt{1 + 4R\alpha_l^* \alpha_{s,\mathrm{inj}}}\right). \tag{52}$$

Relation (52) is shown in Fig. 2. Hence, the steady state cuttings bed is determined by α_l^*, R while the rate of exchange between the cuttings bed and suspension, and consequently the steepness of a propagating cuttings bed, is determined by β as shown in Fig. 3.

3.5. Impact of coefficients

The qualitative effect of the correlation parameters can be summed up as follows.

- α_l^* gives the volume fraction of the liquid flow (essentially the effective cross sectional flow area of the injected liquid relative to the full cross sectional flow area A) at which the threshold Shields number θ_t is achieved. This corresponds to the steady-state liquid flow volume fraction, $\alpha_l^* = \alpha_{h,l}$, when zero solids are injected $Q_{s,\mathrm{inj}} = 0$.
- R determines the deposition rate relative to the erosion rate, and consequently how a non-zero solid injection rate $Q_{s,\mathrm{inj}} > 0$ affects the steady-state cuttings bed size $\bar{\alpha}_b$.
- β gives the transient rate of exchange between the cuttings in bed and cuttings in suspension.

4. Numerical implementation

The system of equations is discretized in space and time and the partial derivatives resolved with a first order upwind scheme. The discretization is done with the spatial grid size Δx, and temporal step size Δt. We denote the discretized states in parenthesis as $(\cdot)_l^k$ where l is used to denote the discretized position, and k the discretized time, e.g., for $\alpha_{b,l}$ we have

Table 1
Physical parameters of experiments.

Value	Symbol	Description
0.022 m^2	A	Wellbore model cross-sectional area
2.56–2.64 g/cm^3	ρ_s	Cuttings density
30.48 m	L	Test section length

$$(\alpha_{b,l})_l^k = \alpha_{b,l}(k\Delta t, l\Delta x). \tag{53}$$

The discretization in space can roughly be understood as a discretization into the computational control volumes depicted in Fig. 1, but this time with a non-zero axial length $\Delta x > 0$.

The first-order upwind discretized version of (27) and (28) can then be written as

$$(\alpha_{h,s})_l^{k+1} = (\alpha_{h,s})_l^k - \frac{\Delta t}{\Delta x}\left((v_{h,s}\alpha_{h,s})_l^k - (v_{h,s}\alpha_{h,s})_{l-1}^k\right) + \Delta t(\Gamma_s^{b,h})_l^k \tag{54}$$

$$(\alpha_{b,s})_l^{k+1} = (\alpha_{b,s})_l^k - \Delta t(\Gamma_s^{b,h})_l^k, \tag{55}$$

with

$$(\Gamma_s^{b,h})_l^k = (E)_l^k - (D)_l^k \tag{56}$$

$$(D)_l^k = \beta R(\alpha_{h,s})_l^k \tag{57}$$

$$(E)_l^k = \begin{cases} 0, & (\alpha_b)_l^k = 0 \text{ or } \alpha_l^* < (\alpha_{h,l})_l^k \\ \frac{\beta}{\alpha_{h,l}}\left(\alpha_l^* - (\alpha_{h,l})_l^k\right), & (\alpha_b)_l^k > 0 \text{ and } \alpha_l^* \geq (\alpha_{h,l})_l^k \end{cases} \tag{58}$$

$$(\alpha_{h,l})_l^k = 1 - (\alpha_b)_l^k - (\alpha_{h,s})_l^k, \tag{59}$$

where we are assuming $v_{h,s} > 0$.

The boundary condition, (31) is implemented as:

$$(\alpha_{h,s})_0^k = \alpha_{s,\mathrm{inj}}. \tag{60}$$

5. Simulation example

To evaluate the qualitative transient behavior of the model we compare it to the experiments performed by Sanchez et al. (1999). They conducted transient flow loop experiments, where the test section was an almost horizontal annulus with an inner pipe that could be rotated to replicate the conditions of a horizontal section of a wellbore being drilled. Our goal is to show that the presented approach yields an effective transient simulation model for appropriate closure relations, or with a reasonable tuning such as the one utilized in this study. To this end, we tune the correlation coefficients R, α_l^* to achieve the steady-state response from the experiments, and then modify β to match the transient response, to illustrate that the relative simple second order model given by (27) and (28) is sufficient to replicate the transient behavior of the transported cuttings. To be precise: by transient behavior we mean the behavior of the model when it is not at steady-state, i.e. when $\frac{\partial \alpha_{h,s}}{\partial t} \neq 0$ or $\frac{\partial \alpha_{b,s}}{\partial t} \neq 0$. Even though in most cases of slurry transport, solid velocities are not equal to averaged liquid velocity, for reasons of simplicity, and since not all relevant parameters required for modeling were disclosed by Sanchez et al. (1999), the solid velocity is set equal to the averaged liquid velocity $v_{h,s} = v_{h,l}$ for all the simulations.

The physical parameters of the experiments are summarized in Table 1, while Imperial to SI unit conversions is given in Table 3. Note that the liquid density used in the experiments was not provided, however, neither is it required as the tuning procedure employed matches the model output at steady-state to measurements from the experiment, and these outputs can be computed without needing the liquid density.

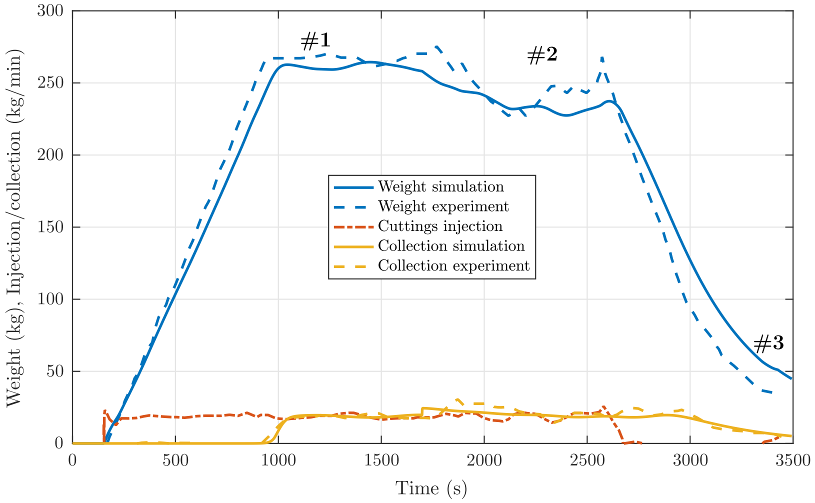

Fig. 4. Trend from experiment 1, with $\phi = 10^\circ$ inclination and 50 RPM pipe rotation starting from $t = 1700$.

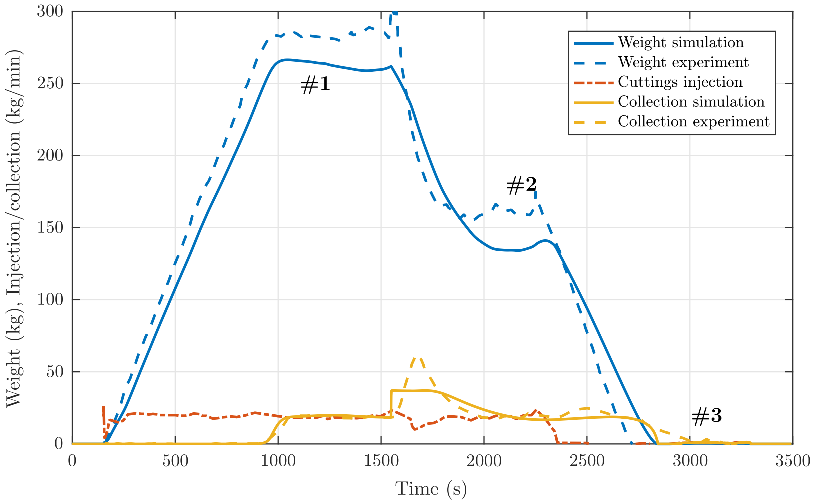

Fig. 5. Trend from experiment 2, with $\phi = 10^\circ$ inclination and 90 RPM pipe rotation starting from $t = 1550$.

5.1. Tuning the correlation coefficients

The measured output of the experiments of Sanchez et al. (1999) is the trend of the mass of the solids in the test section through the experiment. At steady state we have the following relation for the mass of solids in the test section

$$\frac{\text{Mass}}{LA\rho_s} = \bar{\alpha}_{b,s} + \bar{\alpha}_{h,s}, \tag{61}$$

and hence

$$\bar{\alpha}_h = \frac{1}{\frac{Q_{s,\text{inj}}}{Q_{s,\text{inj}}+Q_{l,\text{inj}}} - C_b}\left(\frac{\text{Mass}}{LA(\rho_s - \rho_l)} - C_b\right). \tag{62}$$

Then, using the steady state relation (48), we get

$$R = \frac{Q_{s,\text{inj}} + Q_{l,\text{inj}}}{\bar{\alpha}_h Q_{s,\text{inj}}}\left(\frac{\alpha_l^*}{\bar{\alpha}_h}\frac{Q_{l,\text{inj}} + Q_{s,\text{inj}}}{Q_{l,\text{inj}}} - 1\right) \tag{63}$$

or, equivalently,

$$\alpha_l^* = \frac{\bar{\alpha}_h Q_{l,\text{inj}}}{Q_{l,\text{inj}} + Q_{s,\text{inj}}}\left(\frac{RQ_{s,\text{inj}}}{Q_{s,\text{inj}} + Q_{l,\text{inj}}}\bar{\alpha}_h + 1\right). \tag{64}$$

The particular values used to find the numerical values of the correlation parameters determining the steady-state R, α_l^*, are summarized in Table 2.

5.2. Comments on comparison with experiment

The experimental results of Sanchez et al. (1999) and the simulation results are shown in Figs. 4–9. The steady states from these figures have been noted, summarized in Table 2, and then, using relations (62) and (63), the correlation coefficients R, α_l^* have been found such that the steady state of the simulation model yields a reasonable match to that of the experiment.

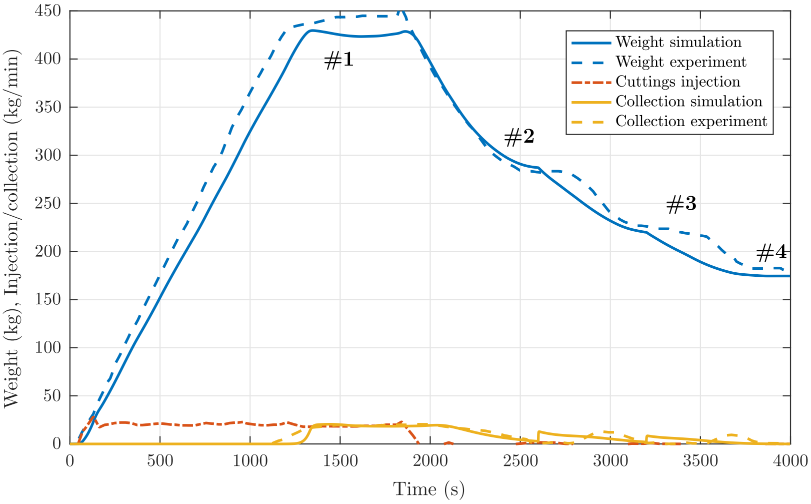

Fig. 6. Trend from experiment 3, with $\phi = 25^\circ$ inclination and 50 RPM pipe rotation starting from $t = 1550$, 50 RPM pipe rotation starting from $t = 2600$, 75 RPM pipe rotation starting from $t = 3200$.

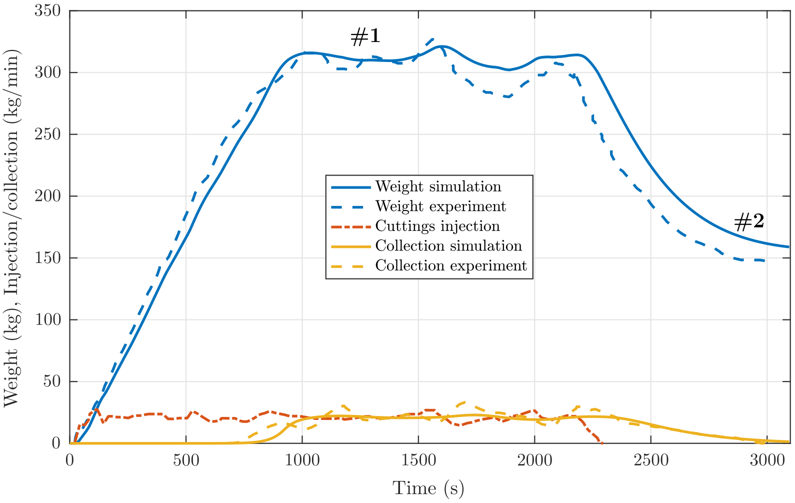

Fig. 7. Trend from experiment 4, with $\phi = 25^\circ$ inclination and 125 RPM pipe rotation.

Table 2
Non-dimensional parameter tuning values.

Ex.	Steady-state #	$Q_{s,\text{ inj}}/A$	$Q_{l,\text{ inj}}/A$	$\alpha_{s,\text{ inj}}$	Mass	$\tilde{\alpha}_b$	R	α_l^*	β
1	#1	0.0064 m/s	1.00 m/s	0.0063	270 kg	0.384	78	0.925	1/50
	#2	—“—	—“—	—“—	245 kg	0.349	—“—	0.980	—“—
	#3	0 m/s	—“—	0	36 kg	0.051	—“—	—“—	—“—
2	#1	0.0064 m/s	1.00 m/s	0.0063	281 kg	0.312	78	0.925	1/50
	#2	—“—	—“—	—“—	164 kg	0.176	—“—	1.152	—“—
	#3	0 m/s	—“—	0	0 kg	0.0	—“—	—“—	—“—
3	#1	0.007 m/s	0.85 m/s	0.0081	445 kg	0.500	90	0.679	1/50
	#2	0 m/s	—“—	0	281 kg	0.321	—“—	—“—	—“—
	#3	—“—	—“—	—“—	218 kg	0.248	54	0.752	—“—
	#4	—“—	—“—	—“—	181 kg	0.207	36	0.793	—“—
4	#1	0.0053 m/s	0.85 m/s	0.0062	295 kg	0.384	54	0.819	1/100
	#2	0 m/s	—“—	0	159 kg	0.349	—“—	—“—	—“—
5	#1	0.0067 m/s	0.85 m/s	0.0078	168 kg	0.179	29	0.969	1/30
	#2	0 m/s	—“—	0	27 kg	0.031	—“—	—“—	—“—
6	#1	0.0055 m/s	0.85 m/s	0.0064	182 kg	0.197	41	0.969	1/50
	#2	0 m/s	—“—	0	27 kg	0.031	—“—	—“—	—“—

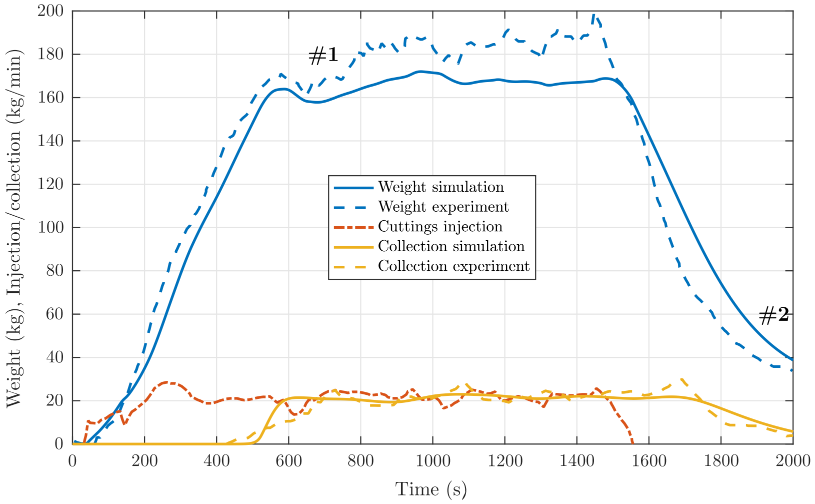

Fig. 8. Trend from experiment 5, with $\phi = 50^\circ$ inclination and no pipe rotation.

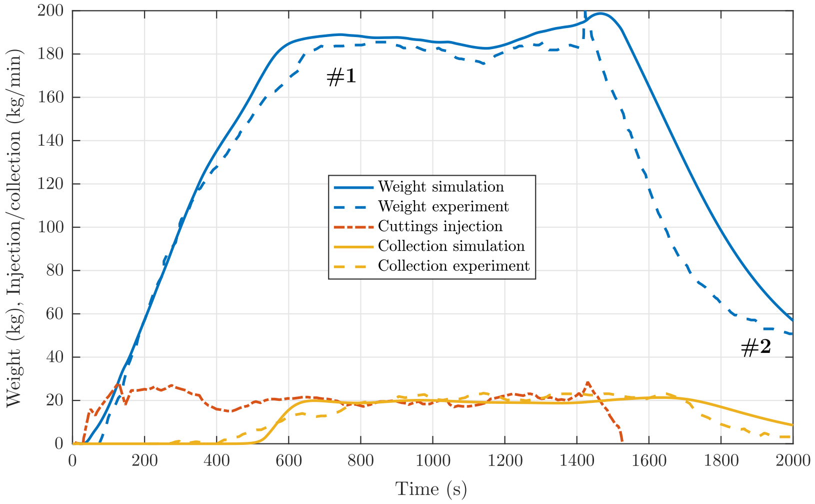

Fig. 9. Trend from experiment 6, with $\phi = 50^\circ$ inclination and 125 RPM pipe rotation.

Table 3
Imperial to SI unit conversions.

US or Imperial	SI units
1 pound (lb)	0.4536 (kg)
1 foot (ft)	0.3048 (m)
1 Gallon per minute (gpm)	6.309 $\times 10^{-5}$ (m^3/s)

For experiment 1, Fig. 4, we first find $\alpha_l^* = 0.980$ for 50 RPM rotation of the drill string from steady-state #3, which corresponds to $Q_{s,\text{inj}} = 0$. Hence we can compute $R = 78$ from steady-state #2, and then assuming R to be constant we find $\alpha_l^* = 0.925$ for the ”no rotation” case of steady-state #1. These same values are retained for experiment 2, shown in Fig. 5, where we find $\alpha_l^* = 1.152$ for 90 rpm from steady-state #3. In both these cases, we achieve a good fit in the transient behavior for these experiments with the pipe close to horizontal (note that the 80° specified in Sanchez et al. (1999) is given as angle from vertical, while we use ϕ to denote angle from horizontal).

For experiment 3, Fig. 6 the model fit is less good, although still reasonable. In particular, we note that when pipe rotation is increased there is a delay before cuttings leaves the test section. This could either be an artifact of the test procedure (about which information is somewhat limited), or it could be an actual effect of the specific solid-liquid flow occurring at 25° inclination not accurately captured by the present model.

For the remaining experiments: 4–6, shown in Figs. 7–9, α_l^* is found from steady-state #2 using the fact that $Q_{s,\text{inj}} = 0$, and then R is found from steady-state #1. Here we again see a very good transient fit for the model, even for the steeper inclinations of 50° used in experiment 5 and 6 (Figs. 8 and 9), where the simplifying assumption $v_{h,s} = v_{h,l}$ does not hold and, in addition, bed sliding may occur.

Overall, the model appears to capture the transient dynamics of solid transport in the experiments very well, even without having specified information on fluid rheology, pipe eccentricity, pipe rotation rates, or the annular cross-section. This indicates that the approach and the derivation of Section 2 are general and may be applied to scenarios where a transient model of solid transports is required and such specific information is lacking. In particular, the approach is expected to have applications in cuttings monitoring during drilling.

A more powerful model is obtained when the closure relations are specified directly in operating parameters (grey-box model, white-box model), instead of being tuned from data. However, this was not feasible in the present case as the necessary parameters were not provided by Sanchez et al. (1999). Obtaining experimental datasets is highly relevant for modeling activities; however, full disclosure of the related operating parameters is crucial (Busch et al., 2018).

6. Conclusions

The observations from the comparison with experiments in Section 5 lead us towards the conclusion that the simple, coupled, set of transport equations, namely Eqs. (27) and (28), derived from the continuity relations in Section 2, are in many cases sufficient to represent transient mass transport of solids in solid-liquid pipe and annular flow, when used with closure relations which gives accurate steady-state results. This conclusion is valuable in that such a simple dynamic representation of these phenomena makes model implementation and system analysis by simulation much simpler, as well as enabling model-based control and estimation design (Aarsnes et al., 2016b), which in turn can find application to optimize and monitor real-time processes where solid-liquid pipe and annular flow is encountered.

Acknowledgments

The work of the first author was financially supported by ConocoPhillips, AkerBP, Statoil, Wintershall and the RCN grant (203525/O30) DrillWell, by European Unions Seventh Framework Programme for research, technological development and demonstration under Marie Curie grant agreement no [608695], and the FRIPRO Mobility Grant Fellowship Programme (FRICON). The work of the second author was supported by the project Advanced Wellbore Transport Modeling (AdWell). Its sponsor, PETROMAKS 2/the Research Council of Norway (project 228391) and its partners Statoil, Neptune Energy Norge AS, IRIS, UiS, NTNU and SINTEF are gratefully acknowledged for funding and supporting this work.

References

Aarsnes, U.J.F., Ambrus, A., Di Meglio, F., Karimi Vajargah, A., van Oort, E., Aamo, O.M., 2016. A simplified two-Phase flow model using a quasi-equilibrium momentum balance. Int. J. Multiph. Flow 83 (July), 77–85. doi:10.1016/j.ijmultiphaseflow.2016.03.017.

Aarsnes, U.J.F., Flåtten, T., Aamo, O.M., 2016. Review of two-phase flow models for control and estimation. Annu. Rev. Control 42, 50–62. doi:10.1016/j.arcontrol.2016.06.001.

Busch, A., Islam, A., Martins, D.W., Iversen, F.P., Khatibi, M., Johansen, S.T., Time, R.W., Meese, E.A., 2018. Cuttings-transport modeling-Part 1: specification of benchmark parameters with a Norwegian-continental-shelf perspective. In: SPE Drilling & Completion. Society of Petroleum Engineers, Bergen, Norway, pp. 1–32. doi:10.2118/180007-PA.

Busch A., Johansen S.T. An Eulerian-Lagrangian CFD study of a particle settling in an orthogonal shear flow of a shear-thinning, mildly viscoelastic fluid, Journal of Non-Newtonian Rheology (02/2018), In Review.

Busch, A., Khatibi, M., Johansen, S.T., Time, R.W., 2017. A 2D sediment bed morphodynamics model for turbulent, non-Newtonian, particle-loaded flows. In: 12th Int. Conf. CFD Oil Gas, Metall. Process Ind., Trondheim, Norway.

Capecelatro, J., Desjardins, O., 2013. Eulerian-Lagrangian modeling of turbulent liquid-solid slurries in horizontal pipes. Int. J. Multiph. Flow 55, 64–79. doi:10.1016/j.ijmultiphaseflow.2013.04.006.

Cayeux, E., Leulseged, A., Kluge, R., Haga, J., 2016. Use of a transient cuttings transport model in the planning, monitoring and post analysis of complex drilling operations in the North Sea. In: IADC/SPE Drill. Conf. Exhib., Fort Worth doi:10.2118/178862-MS.

Cayeux, E., Mesagan, T., Tanripada, S., Zidan, M., Fjelde, K.K., 2014. Real-time evaluation of hole-cleaning conditions with a transient cuttings-transport model. SPE Drill. Complet. 29 (01), 05–21. doi:10.2118/163492-PA.

Charru, F., Mouilleron, H., Eiff, O., 2004. Erosion and deposition of particles on a bed sheared by a viscous flow. J. Fluid Mech. 519 (2004), 55–80. doi:10.1017/S0022112004001028.

Chien, S.-F., 1994. Settling velocity of irregularly shaped particles. SPE Drill. Complet. 9 (04), 281–289. doi:10.2118/26121-PA.

Doan, Q., Oguztoreli, M., Masuda, Y., Yonezawa, T., Kobayashi, A., Naganawa, S., Kamp, A., 2003. Modeling of transient cuttings transport in underbalanced drilling (UBD). SPE J. 8 (02), 160–170. doi:10.2118/85061-PA.

Doron, P., Barnea, D., 1993. A three-layer model for solid-liquid flow in horizontal pipes. Int. J. Multiph. Flow 19 (6), 1029–1043. doi:10.1016/0301-9322(93)90076-7.

Doron, P., Barnea, D., 1996. Flow pattern maps for solid-liquid flow in pipes. Int. J. Multiph. Flow 22 (2), 273–283. doi:10.1016/0301-9322(95)00071-2.

Doron, P., Simkhis, M., Barnea, D., 1997. Flow of solid-liquid mixtures in inclined pipes. Int. J. Multiph. flow 23 (2), 313–323.

Drew, D.A., 1983. Mathematical modeling of two-phase flow. Ann. Rev. Fluid Mech 15, 261–291.

Flåtten, T., Lund, H., 2011. Relaxation two-phase flow models and the subcharacteristic condition. Math. Model. Methods Appl. Sci. 21 (12), 2379–2407. doi:10.1142/S0218202511005775.

Florence, F., Iversen, F.P., 2010. Real-time models for drilling process automation: equations and applications. In: IADC/SPE Drill. Conf. Exhib.. Society of Petroleum Engineers doi:10.2118/128958-MS.

Girolami, L., Sherwood, J.D., Charru, F., 2016. Dynamics of a slowly-varying sand bed in a circular pipe. Int. J. Multiph. Flow 81, 113–129. doi:10.1016/j.ijmultiphaseflow.2016.02.007.

Kaushal, D., Thinglas, T., Tomita, Y., Kuchii, S., Tsukamoto, H., 2012. CFD modeling for pipeline flow of fine particles at high concentration. Int. J. Multiph. Flow 43, 85–100. doi:10.1016/j.ijmultiphaseflow.2012.03.005.

Khatibi, M., Time, R.W., Shaibu, R., 2018. Dynamical feature of particle dunes in Newtonian and shear-thinning flows: relevance to hole-cleaning in pipe and annulus. Int. J. Multiph. Flow 99 (October), 284–293. doi:10.1016/j.ijmultiphaseflow.2017.10.015.

Larsen, T., Pilehvari, A., Azar, J., 1997. Development of a new cuttings-transport model for high-angle Wellbores including horizontal wells. SPE Drill. Complet. 12 (June), 129–135. doi:10.2118/25872-PA.

Larsen, T.I.F., 1990. A Study of the Critical Fluid Velocity in Cuttings Transport for Inclined Wellbores. University of Tulsa Ph.D. thesis.

Li, J., Luft, B., 2014. Overview solids transport study and application in oil-gas industry-theoretical work. In: Int. Pet. Technol. Conf. International Petroleum Technology Conference doi:10.2523/IPTC-17832-MS.

Li, J., Walker, S., 2001. Sensitivity analysis of hole cleaning parameters in directional wells. SPE J. 6 (04), 356–363. doi:10.2118/74710-PA.

Martins, A., Santana, M., Gaspari, E., Campos, W., 1998. Evaluating the transport of solids generated by shale instabilities in ERW drilling. SPE Int. Conf. Horiz. Well Technol. (December) 254–259. doi:10.2118/50380-MS.

Naganawa, S., Sato, R., Ishikawa, M., 2017. Cuttings-transport simulation combined with large-scale-flow-loop experimental results and logging-while-drilling data for hole-cleaning evaluation in directional drilling. SPE Drill. Complet. 32 (03), 194–207. doi:10.2118/171740-PA.

Peker, S.M., Helvaci, S.S., 2008. Solid-Liquid Two Phase Flow, first ed. Elsevier, Boston. https://www.elsevier.com/books/solid-liquid-two-phase-flow/peker/978-0-444-52237-5.

Philip, Z., Sharma, M.M., Chenevert, M.E., 1998. The role of Taylor vortices in the transport of drill cuttings. In: SPE India Oil Gas Conf. Exhib. Society of Petroleum Engineers, pp. 7–9. doi:10.2118/39504-MS.

Pilehvari, A., Azar, J., Shirazi, S., 1999. State-of-the-art cuttings transport in horizontal wellbores. SPE Drill. Complet. 14 (03), 196–200. doi:10.2118/57716-PA.

Ramadan, A., Skalle, P., Saasen, A., 2005. Application of a three-layer modeling approach for solids transport in horizontal and inclined channels. Chem. Eng. Sci. 60 (10), 2557–2570. doi:10.1016/j.ces.2004.12.011.

Saffman, P.G., 1965. The lift on a small sphere in a slow shear flow. J. Fluid Mech. 22, 385—-400. doi:10.1017/S0022112065000824.

Saffman, P.G., 1968. The lift on a small sphere in a slow shear flow - corrigendum. J. Fluid Mech. 31 (3), 624. doi:10.1017/S0022112068999990.

Salazar-Mendoza, R., Espinosa-Paredes, G., 2009. A three-Region hydraulic model for solid-Liquid flow with a stationary bed in horizontal wellbores. Pet. Sci. Technol. 27 (10), 1033–1043. doi:10.1080/10916460802455905.

Sanchez, R.A., Azar, J.J., Bassal, A.A., Martins, A.L., 1999. Effect of drillpipe rotation on hole cleaning during directional-Well drilling. SPE J. 4 (02), 101–108. doi:10.2118/56406-PA.

Soulsby, R., 1997. Dynamics of marine sands: a manual for practical applications. Thomas Telford.

Tomren, P., Iyoho, A., Azar, J., 1986. Experimental study of cuttings transport in directional wells. SPE Drill. Eng. 1 (01), 43–56. doi:10.2118/12123-PA.

Wang, Z., Zhai, Y., Hao, X., Guo, X., Sun, L., 2010. Numerical simulation on three layer dynamic cutting transport model and its application on extended reach drilling. In: IADC/SPE Asia Pacific Drill. Technol. Conf. Exhib. Society of Petroleum Engineers, pp. 1–10. doi:10.2118/134306-MS.

Zhang, F., Filippov, A., Jia, X., Lu, J., Khoriakov, V., 2016. Transient solid-liquid two-phase flow modelling and its application in real-time drilling simulations. In: BHR Gr. - 10th North Am. Conf. Multiph. Technol. 2016, pp. 17–32.

Conference paper 2 (XV)

On Pragmatism in industrial modeling - Part II: Workflows and associated data and metadata

Josip Zoric, Alexander Busch, Ernst A. Meese, Milad Khatibi, Rune Wiggo Time, Stein Tore Johansen, H. A. Rabenjafimanantsoa

Eleventh International Conference on CFD in the Minerals and Process Industries CSIRO.

Presented at: The 11th International Conference on CFD in the Minerals and Process Industries, Melbourne, Australia, 2015

URL: http://www.cfd.com.au/cfd_conf15/PDFs/032JOH.pdf.

Conference paper 3 (XVII)

Investigation of Suspended Particles Around an Obstacle in Vertical Pipe Flow: Comparison Study Experimental and Simulation

Milad Khatibi, Rune Wiggo Time, Alexander Busch, Stein Tore Johansen, Dwayne Werner Martins, Md. Aminul Islam, Fionn Iversen

In: ASME 2017 36th International Conference on Ocean, Offshore and Arctic Engineering, Volume 8: Polar and Arctic Sciences and Technology; Petroleum Technology.

Presented at: ASME 2017 36th International Conference on Ocean, Offshore and Arctic Engineering, Trondheim, Norway, 2017.

DOI: 10.1115/OMAE2017-62244.

Conference paper 4 (XIV)

Judging the Generalized Newtonian Fluid assumption for cuttings transport modelling by applying time scale comparisons

Alexander Busch, Stein Tore Johansen

In: The Transactions of the Nordic Rheology Society, Vol. 24., pp. , 2018.

Presented at: The 27th Nordic Rheology Conference, Trondheim, Norway, 2018.

Official URL: http://nordicrheologysociety.org/transactions/

Alternative URL: https://www.researchgate.net/publication/326625654_Judging_the_Generalized_Newtonian_Fluid_assumption_for_cuttings_transport_modelling_by_applying_time_scale_comparisons

---

Manuscript 2 (XIII)

Estimating the level of turbulence and dunes in wellbore flows by means of bulk flow quantities

Alexander Busch, Stein Tore Johansen

with contributions from Aminul Islamn and Dwayne Martins

AdWell project report.

Trondheim, 2018.

Estimating the level of turbulence and dunes in wellbore flows by means of bulk flow quantities

Alexander Busch[1,*], Stein Tore Johansen[1, 2]

[1] Norwegian University of Science and Technology (NTNU), Trondheim, Norway

[2] SINTEF Materials and Chemistry, Trondheim, Norway

*Corresponding author: alexander.busch@ntnu.no, alexander.busch@alumni.ntnu.no

Keywords: Drilling, Wellbore Flows, Turbulence, Dunes, non-Newtonian, GNF, shear-thinning, annular, pipe,.

Abstract

The flow in the annulus of a wellbore is typically assumed laminar while the flow in the drill pipe is assumed to be of turbulent nature. However, the prevailing flow regime is highly dependent on the drilling fluid and its rheological properties. For the numerical parameter space established by Busch et al. (2018) representing drilling on the Norwegian Continental Shelf, we perform a Reynolds-number based ball-park analysis to evaluate the degree of turbulence in the industrially-relevant parameter space. Specifically, we apply the Reynolds number concept of Metzner and Reed (1955) as well as the Bingham Reynolds number of Wilson and Thomas (2006) Reynolds number formulations.

The results show that, in general, drill pipe flows are fully turbulent for the case of plain water and transitional for non-Newtonian drilling fluids, regardless of the Reynolds number concept used. However, annular flows are at best transitional and mostly laminar, depending on the particular YP/PV combination.

The presence of a cuttings bed (here a relative height of 1/3 of the hydraulic diameter) does not heavily affect the order of magnitude of the estimated Reynolds numbers. Simple rotation of the rill pipe (no lateral motion) does not really affect the pure flow dynamics in the deeper, smaller wellbore sections either. Here, here the axial flow velocity is so large compared to the rotational component that the additional rotational velocity accounted for by a simple vector magnitude concept does not contribute significantly.

For the investigated parameter space, the low viscous fluids tend to generate larger vortex dunes and sinuous dunes whereas the more viscous fluids result in smaller dunes. The occurrence and type of dunes is generally dependent on bed height and superficial Reynolds number, as well as particle diameter and Archimedes number.

Contents

Nomenclature

Greek symbols

γ	Strain.
$\dot{\gamma}$	Shear rate, total shear measure.
Δ	Difference.
ϵ	Turbulent dissipation rate.
η	Apparent shear viscosity.
λ	Rheological time scale, parameter in Cross and Carreau model.
μ	Newtonian shear viscosity.
ω	Specific turbulent dissipation rate
ρ	Density.

Latin symbols

A	Surface area.
c	Coefficient.
d	Diameter.
$\mathbf{D}$	Rate of deformation tensor.
f	Functional.
g	Gravity.
K	Parameter in Power-law and Yield-power-law flow models, also known as Consistency Index.
l	Length.
m	Mass.
n	Parameter in Power-law (PL), also known as PL exponent.
p	Pressure.
Re	Reynolds number.
t	Time.
T	Transposed.
$\mathbf{T}$	Stress tensor.
$\mathbf{u}$	Fluid velocity.
U	Fluid bulk velocity.
v	Particle velocity.
V	Volume.
w	Width.

x	Spatial dimension.
y	Spatial dimension.
z	Spatial dimension.

Indices

0	Zero, $\dot{\gamma} \to 0$.
∞	Infinity, $\dot{\gamma} \to \infty$.
Ca	Carreau.
Cr	Cross.
f	Fluid.
PL	Power Law.
t	Turbulent.

Abbreviations

2D, 3D	Two-, Three dimensional in space.
CFD	Computational Fluid Dynamics.
FC	Flow Curve.
GNF	Generalized Newtonian Fluid.
PL	Power-Law.

1 Introduction

Dimensional numbers are a convenient way to categorize physical phenomena. For instance, turbulent pipe flow of a Newtonian fluid is typically considered laminar for Reynolds numbers < 2100 and turbulent otherwise.

When modeling such systems *a priori* knowledge of the magnitude of characteristic non-dimensional numbers are beneficial because it allows for choosing the correct modeling strategy. With respect to the aforementioned pipe flow problem, it is crucial to estimate the magnitude of the Reynolds number in order to decide on whether to employ turbulence modeling or not.

We are here concerned with multiphase wellbore flows which may be turbulent under certain circumstances. Furthermore, these flows may develop dunes in horizontal sections of the well. In recent works, we have compiled information on the magnitude of the dimensional parameters (e.g. the dimensions of the annulus, the type of fluid and the bulk flow rate) of wellbore flows prevalent on the Norwegian Continental Shelf (Busch et al., 2018) and subsequently performed a dimensional analysis of wellbore flows (Busch et al., 2019). Now, we utilize this information to estimate the magnitude of the Reynolds number, the Shields number, and a modified Archimedes number in order to quantify the degree of turbulence and the occurrence and type of dunes to expect in wellbore flows.

2 Materials and Methods

2.1 Model equations

This subsection contains all relevant equations which allow for the order-of-magnitude estimate of non-dimensional numbers such as the Reynolds number, the Shields number, and the Archimedes number.

Based on the volumetric bulk flow rate delivered by the pump (assuming zero volumetric losses throughout the wellbore), we define the bulk velocity in the x-direction (in multiphase flows known as the superficial velocity of one phase) as

$$U_x = \frac{Q}{A}, \tag{1}$$

where A is the cross-sectional area of an arbitrarily-chosen annular element of the wellbore and is given by

$$A = \frac{\pi}{4}\left(d_o{}^2 - d_i{}^2\right), \tag{2}$$

where d_o is the outer and d_i is the inner diameter, with d_i = 0 for the pipe case.

For an annular geometry, the wetted perimeter is given as

$$P = \pi\left(d_o + d_i\right), \tag{3}$$

which, in combination with the cross-sectional area defined in equation (2) is used to define the annular hydraulic diameter

$$d_h = \frac{4A}{P} = d_o - d_i \tag{4}$$

The rotation of the drill string is typically given in Revolutions per Minute

$$RPM = \frac{60}{2\pi}\omega \, , \tag{5}$$

where ω is the angular frequency, and the tangential velocity at the surface of the drill pipe due to the rotary motion is then given as

$$U_{tan} = \omega \frac{d_i}{2} \tag{6}$$

We are here concerned with pure shear-thinning fluids which obey a General Newtonian Fluid constitutive equation, i.e. possess no thixotropic or viscoelastic properties. The most simple formulation accounting for shear-thinning behavior is the Ostwald material function (Ostwald, 1925), also known as power law (PL), where the fluid viscosity

$$\eta_f\left(\dot{\gamma}\right) = K\dot{\gamma}^{n_{PL}-1} \tag{7}$$

is a power-law function of the shear rate $\dot{\gamma}$.

In case of a polymeric solution as often used in laboratory experiments, the fluid viscosity is often better expressed with the Cross (Cr) (Cross, 1965) material function

$$\eta_f\left(\dot{\gamma}\right) = \frac{\mu_0 - \mu_\infty}{1 + \left(\lambda_{Cr}\dot{\gamma}\right)^{1-n_{Cr}}} + \mu_\infty \, . \tag{8}$$

This represents the apparent viscosity data much better for a wider shear rate range because it accounts for Newtonian viscosities at both low and high shear rates. Here, μ_0 is the zero-shear viscosity, μ_∞ is the infinite-shear viscosity, λ_{Cr} is the Cross time constant and n_{Cr} is the Cross exponent.

A classical fluid model in petroleum drilling is the Bingham (1922) material function, which in its oilfield variant reads (API RP 13D, 2010)

$$\eta_{YP-PV} = \frac{\tau_{YP-PV}}{\dot{\gamma}} = \frac{YP}{\dot{\gamma}} + PV \, , \tag{9}$$

where YP is the Yield Point in SI units of [Pa] and PV is the Plastic Viscosity in SI units of [Pa·s].

The Norwegian Continental Shelf drilling fluid information established in Busch et al. (2018) is based on equation (9). Based on the Metzner and Reed (1955) local PL concept, API RP 13D (2010) allows the reformulation of equation (9) to the stencil of equation (7).

For the flow through the drill pipe (higher shear rate ranges in the order of 500 s^{-1}…1000 s^{-1}), the coefficients equation (7) are given as

$$n_P = 0.657\log 10\left(\frac{\tau_{YP-PV}\left(\dot{\gamma} = 1022\ \mathrm{s}^{-1}\right)}{\tau_{YP-PV}\left(\dot{\gamma} = 511\ \mathrm{s}^{-1}\right)}\right), \tag{10}$$

$$K_P = \frac{\tau_{YP-PV}\left(\dot{\gamma} = 511\ \mathrm{s}^{-1}\right)}{511^{n_P}}, \tag{11}$$

and for the annulus (lower shear rate ranges in the order of 10 s^{-1} …300 s^{-1})

$$n_P = 0.657\log 10\left(\frac{\tau_{YP-PV}\left(\dot{\gamma} = 170\ \mathrm{s}^{-1}\right)}{\tau_{YP-PV}\left(\dot{\gamma} = 5\ \mathrm{s}^{-1}\right)}\right), \tag{12}$$

$$K_P = \frac{\tau_{YP-PV}\left(\dot{\gamma} = 170\ \mathrm{s}^{-1}\right)}{170^{n_P}}, \tag{13}$$

The wall shear rate of a steady, laminar flow of a Newtonian fluid in a pipe is given by

$$\dot{\gamma}_P = \frac{8U}{d_h} \tag{14}$$

whereas in the cases of an annulus it is given by

$$\dot{\gamma}_A = \frac{12U}{d_h} \tag{15}$$

However, for shear-thinning fluids, a shear rate correction is required.

$$\dot{\gamma}_P = \left(\frac{3n_P + 1}{4n_P}\right)^{\frac{n_P}{n_P - 1}} \frac{8U}{d_h} \tag{16}$$

whereas in the cases of an annulus it is given by

$$\dot{\gamma}_A = \left(\frac{2n_A + 1}{3n_A}\right)^{\frac{n_A}{n_A - 1}} \frac{12U}{d_h} \tag{17}$$

The Generalized Reynolds number is then computed as

$$\mathrm{Re} = \frac{\rho U d_h}{\eta}. \tag{18}$$

For YP-PV fluids, one may also construct a Generalized Reynolds in the form of equation (18)number by exploiting equations (10) to (13). Alternatively, on may use the Bingham Reynolds number instead, where the denominator is the Bingham plastic viscosity instead of the apparent viscosity.

The Shields number is computed as

$$Sh = \frac{\eta\dot{\gamma}}{\left(\rho_s - \rho_f\right) g d_h}. \tag{19}$$

and the critical Shields number Sh_{cr} as the Shields number magnitude required for incipient motion is taken from Soulsby (1997).

The Archimedes number is computed as

$$Ar = \frac{\rho_f \left(\rho_s - \rho_f\right) g d_h^{\,3}}{\eta^2}. \tag{20}$$

2.2 Parameter values

This section provides numerical values for the main parameters (wellbore dimensions, drilling fluid bulk flow rate, drill pipe rotation rate) used in this study based on previous work (Busch et al., 2018).

Figure 1 depicts dimensions of typical drill pipe and annulus dimensions as well as the hydraulic diameter (white numbers) for several wellbore sections.

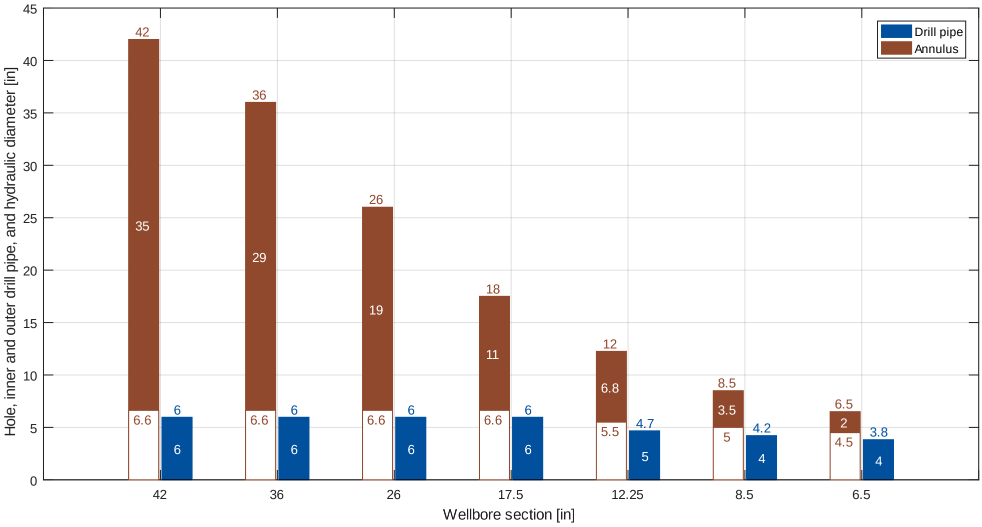

Figure 1: Hole, drill pipe and hydraulic diameter vs. hole sections.

In order to define a typical flow rate range, upper and lower flow rate limits were established based on industry input and field guidelines (Mims and Krepp, 2007) and are displayed in Figure 2. Note that the focus was on the lower sections and the flow rates for the 42” to 26” sections were chosen arbitrarily.

In the same manner, drill string rotation rates were established as shown in Figure 3.

Finally, based on the findings of Busch et al. (2018) who established parameter ranges for the Norwegian Continental Shelf, the range of drilling fluids covered in this study was determined by equally subdividing the established YP and PV ranges of Busch et al. (2018) into particular numerical values, as provided in Table 1. While the YP-PV model coefficients were straightforwardly defined based on the results obtained by Busch et al. (2018), the PL coefficients were computed based on equations (10) to (13).

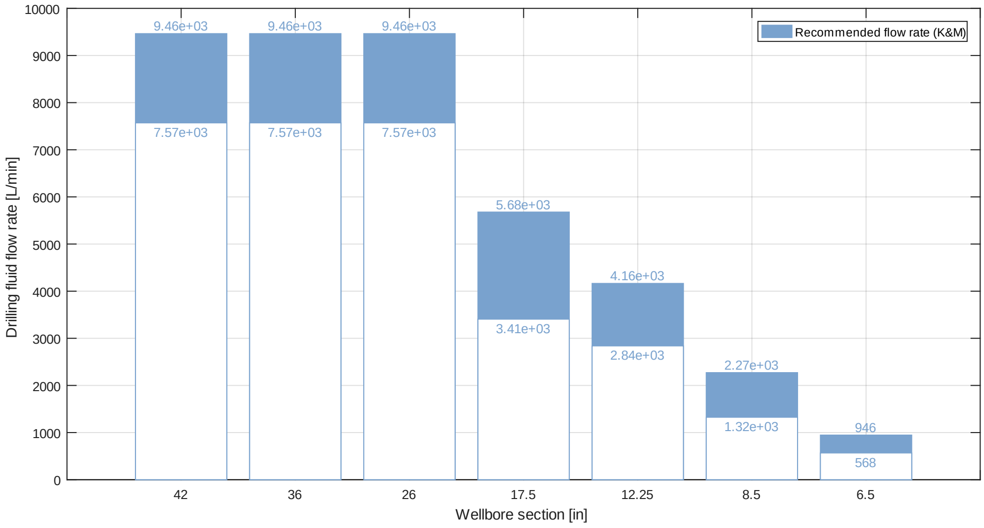

Figure 2: Upper and lower volumetric bulk flow rate vs. hole sections.

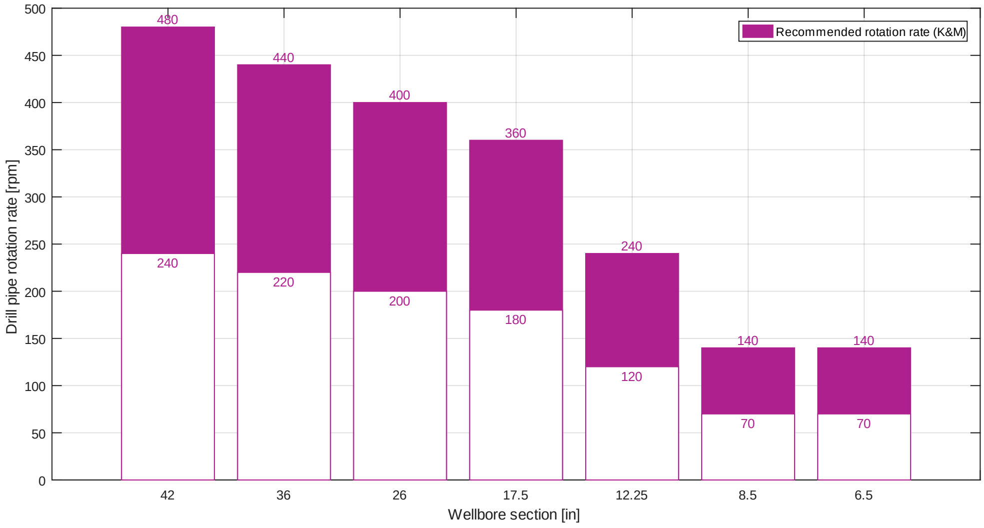

Figure 3: Upper and lower drill pipe rotation rates vs. hole sections.

The numerical model coefficients summarized in Table 1 along with their respective material functions constitute particular flow curves. Figure 4 to Figure 7 provide the respective flow curves for the drilling fluids investigated in this study based on the coefficients depicted in Table 1 and for the different shear rate ranges (pipe and annulus).

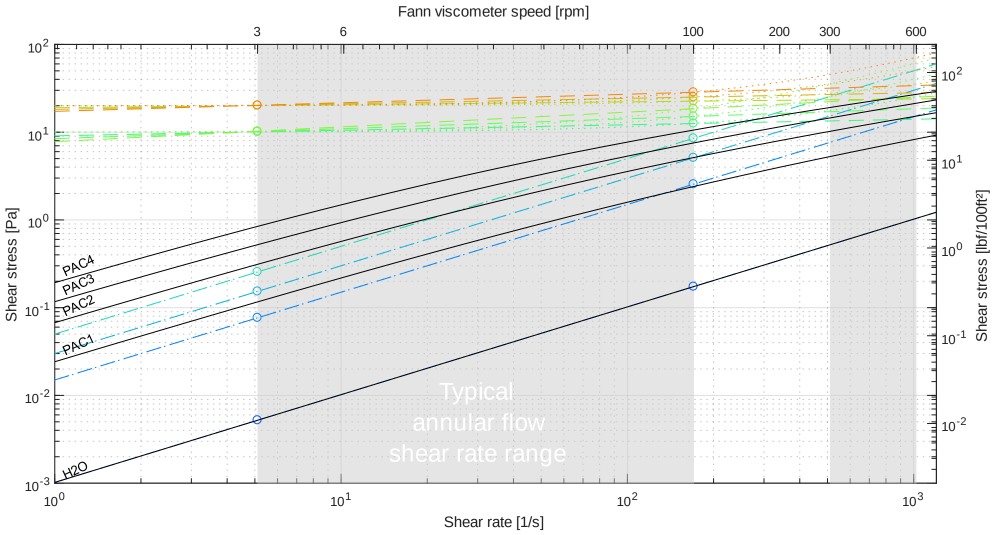

Figure 4: Drilling fluids flow curve for annular flow shear rate range: Shear stress vs. shear rate.

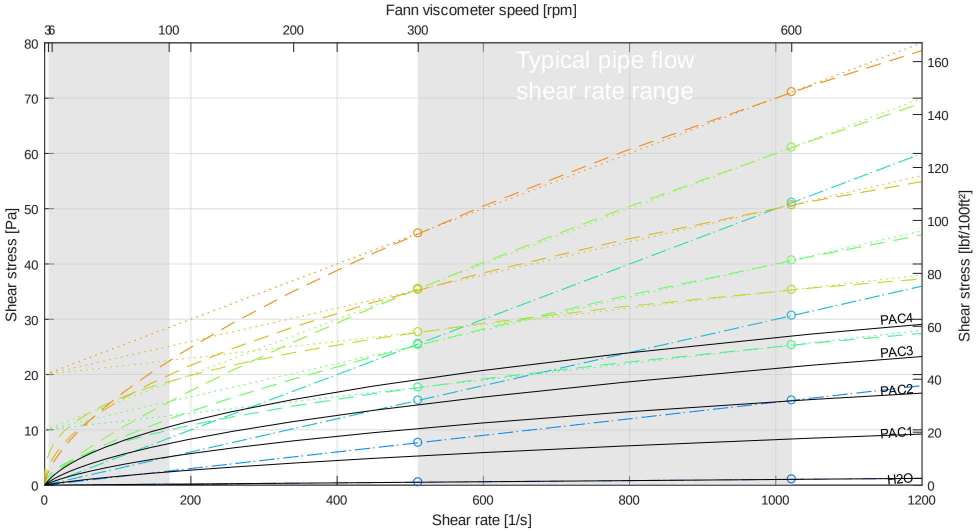

Figure 5: Drilling fluids flow curve for pipe flow shear rate range: Shear stress vs. shear rate.

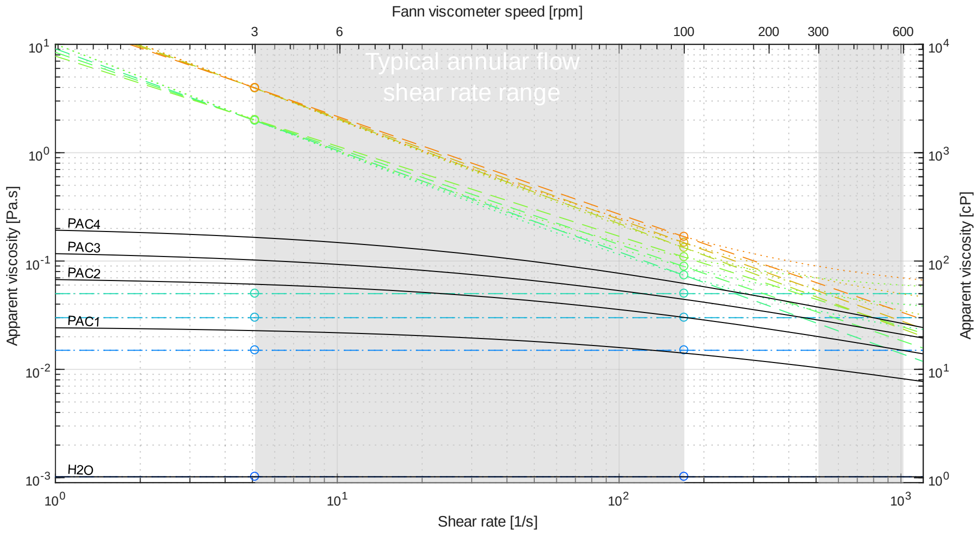

Figure 6: Drilling fluids flow curve for annular flow shear rate range: Apparent viscosity vs. shear rate.

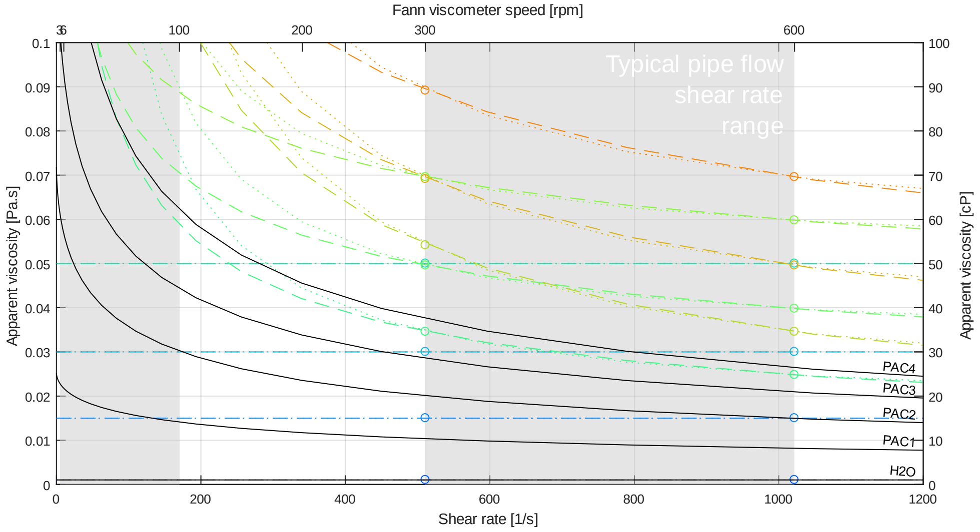

Figure 7: Drilling fluids flow curve for annular flow shear rate range: Apparent viscosity vs. shear rate.

Fluid	Dotted lines		Dashed lines			
	Oilfield YP-PV model coefficients based on Busch et al. (2018)		Local PL model coefficients for pipe flow shear rate range based on equations (10) to (11).		Local PL model coefficients for annular flow shear rate range based on equations (12) to (13).	
	YP [Pa]	**PV [Pa·s]**	**n_P [-]**	**K_P [Pa·s^n]**	**n_A [-]**	**K_A [Pa·s^n]**
1	0	0.001	1	0.001	1	0.001
2	0	0.015	1	0.015	1	0.015
3	0	0.03	1	0.03	1	0.03
4	0	0.05	1	0.05	1	0.05
5	10	0.015	0.52	0.69	0.063	9.1
6	10	0.03	0.68	0.36	0.11	8.4
7	10	0.05	0.78	0.27	0.17	7.8
8	20	0.015	0.35	3.1	0.033	19
9	20	0.03	0.52	1.4	0.063	18
10	20	0.05	0.64	0.83	0.098	17

Table 1: Drilling fluids and model coefficients investigated in this study. Legend for Figure 4 to Figure 7.

3 Results

3.1 Dimensional quantities

Figure 8 depicts bulk velocity magnitudes for both the drill pipe and annular configurations of Figure 1 for the respective bulk flow rates depicted in Figure 2 and the drill pipe rotation rates given in Figure 3. The latter are converted to tangential velocities and added to the streamwise velocities and the velocity magnitude is then given as

$$U = \sqrt{U_x^{\ 2} + U_{rot}^{\ 2}} \tag{21}$$

Here, U_{rot} is the bulk average of the rotational velocity field and is given by $U_{rot} = \frac{1}{2} U_{tan}$.

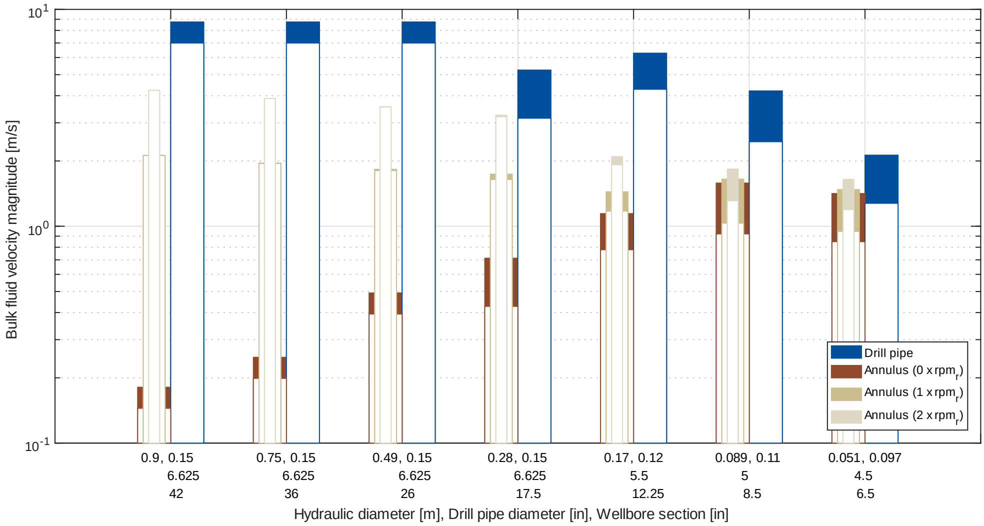

Figure 8: Bulk velocities.

The Newtonian wall shear rates are displayed in Figure 9.

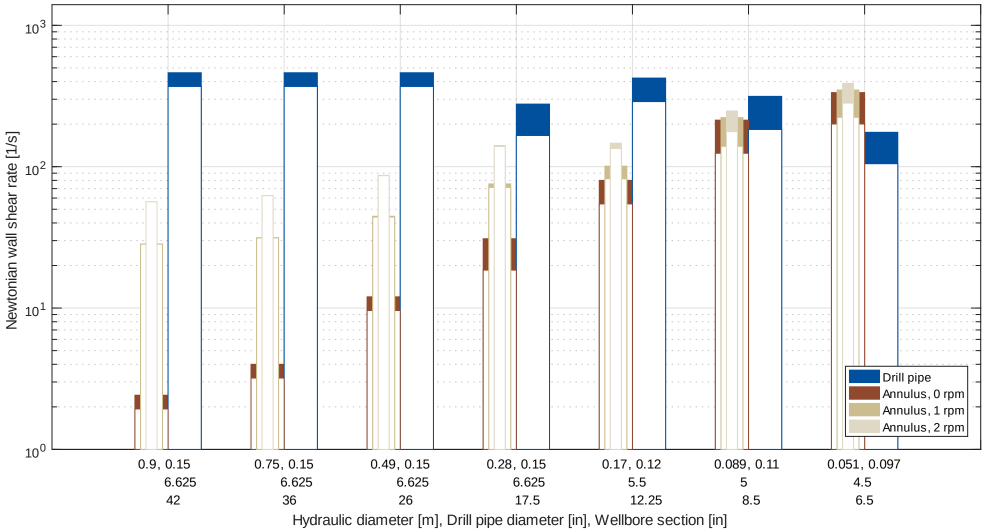

Figure 9: Newtonian wall shear rates.

The PL-based wall shear rates are displayed in Figure 10.

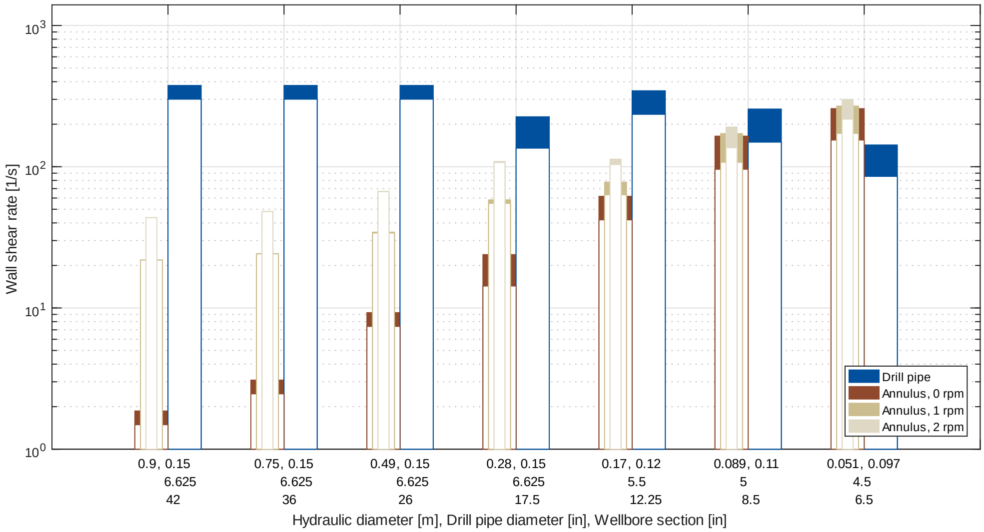

Figure 10: PL wall shear rates.

The YP-PV-based wall shear rates are displayed in Figure 11.

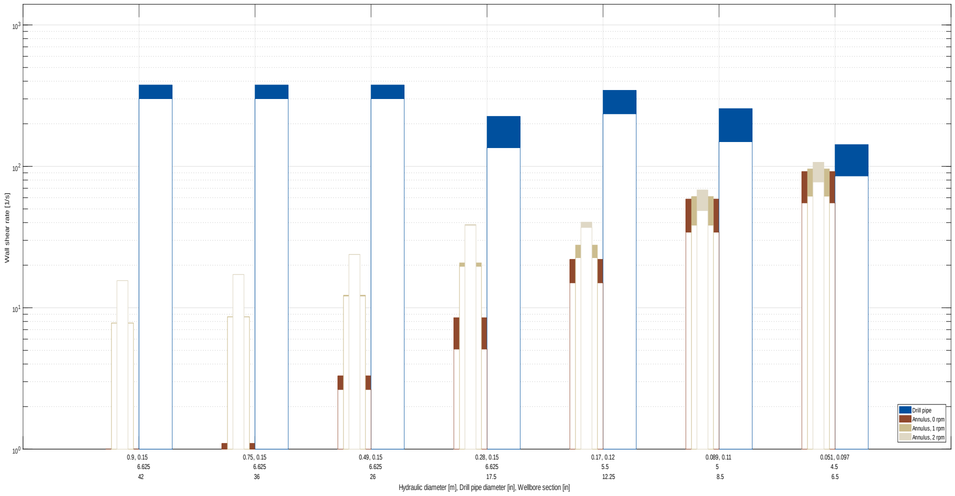

Figure 11: YP-PV wall shear rates.

Figure 12 and Figure 13 provide the apparent viscosity levels for PL and YP-PV fluid behavior, respectively.

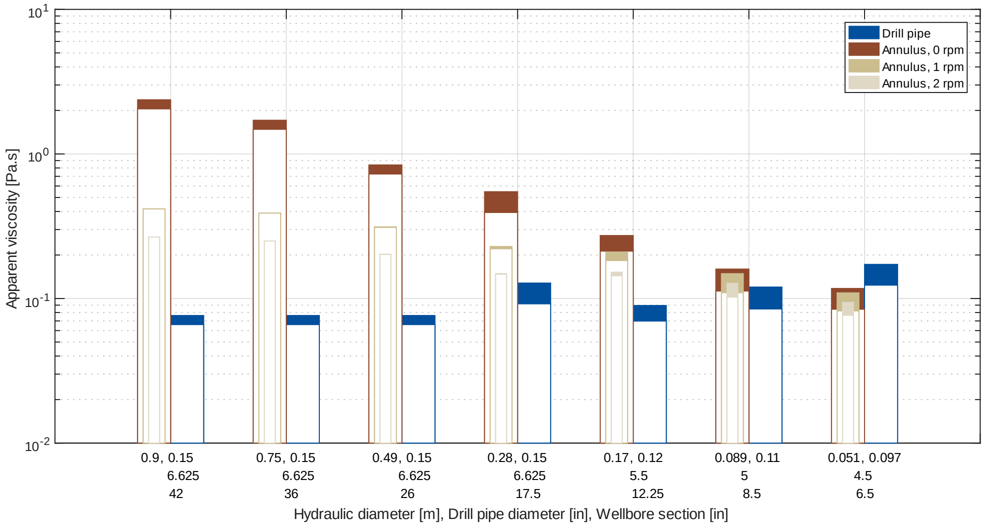

Figure 12: PL apparent viscosities.

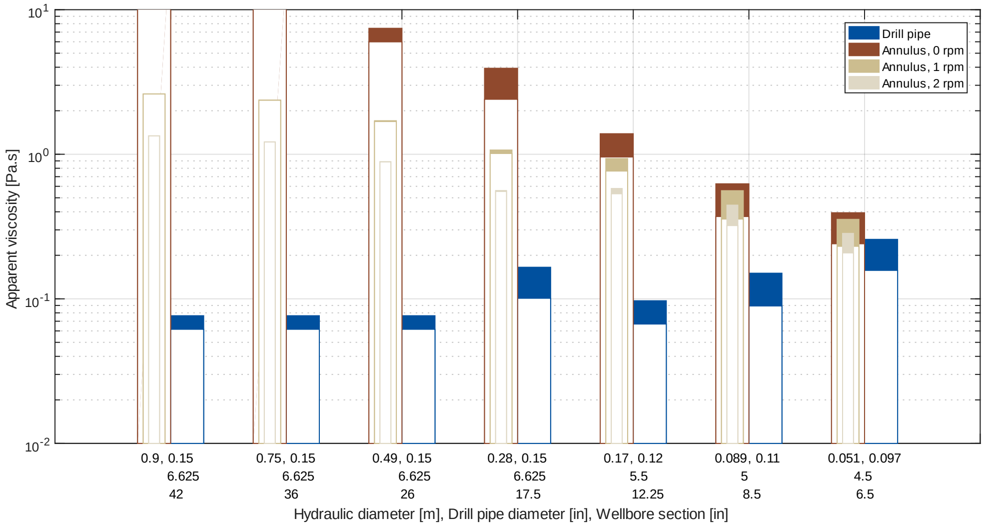

Figure 13: YP-PV apparent viscosities

3.2 Non-dimensional quantities

Figure 14 depicts the Generalized Reynolds number for the case of PL fluid behavior for all cases investigated, while Figure 15 highlights the particular example of fluid 8 (see Table 1 for fluid details).

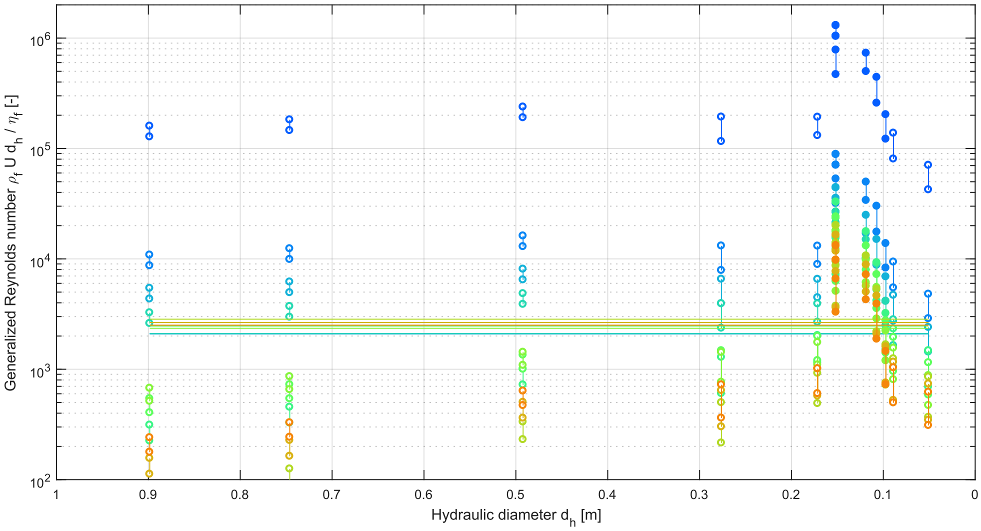

Figure 14: Generalized Reynolds number range for PL fluid behavior. Filled points denote pipe geometry, unfilled points denote annulus geometry. Horizontal solid lines represent the n_{PL}-dependent critical Reynolds number limit for transition to turbulent flow. For information on fluids see Table 1.

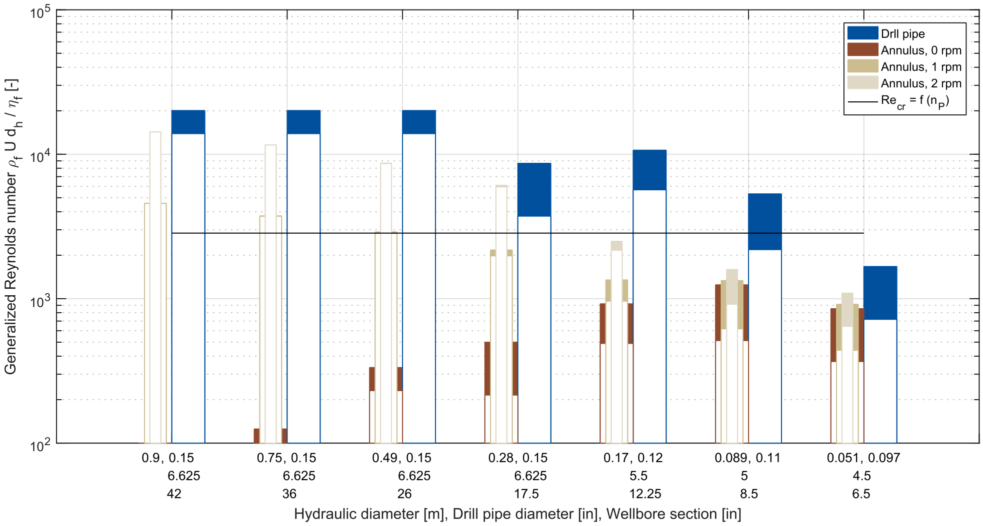

Figure 15: Generalized Reynolds number range for PL fluid behavior and the example of fluid 8 (see Table 1 for fluid details). Dashed and solid lines represent the n-dependent critical Reynolds number limit for transition to turbulent flow.

Figure 16 depicts the Generalized Reynolds number for the case of YP-PV fluid behavior for all cases investigated, while Figure 17 highlights the particular example of fluid 8 (see Table 1 for fluid details).

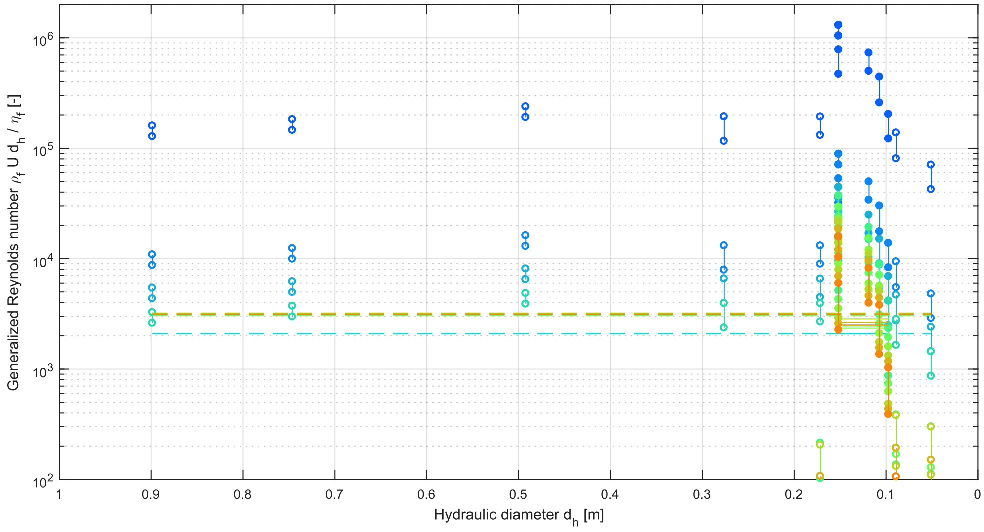

Figure 16: Generalized Reynolds number range for YP-PV fluid behavior. Filled points denote pipe geometry, unfilled points denote annulus geometry. Dashed lines represent the n-dependent critical Reynolds number limit for transition to turbulent flow. For information on fluids see Table 1.

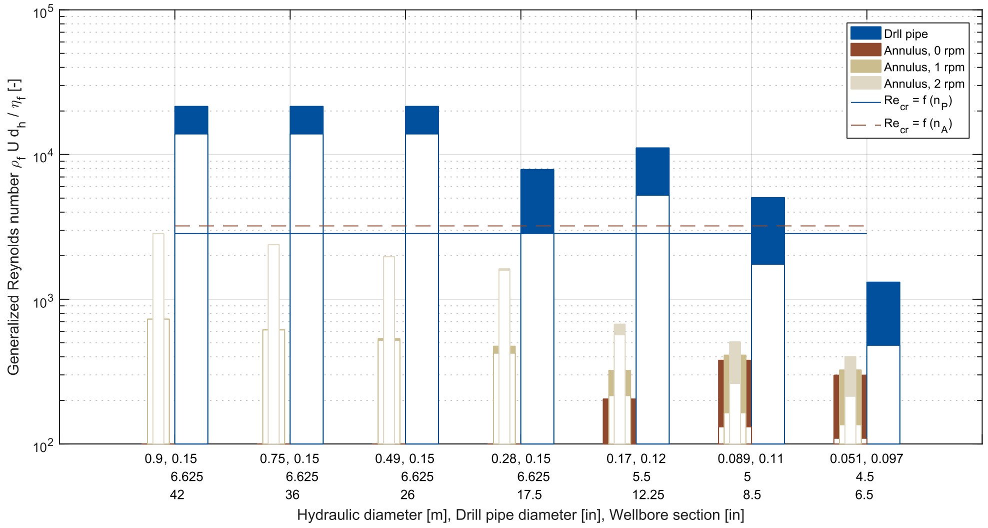

Figure 17: Generalized Reynolds number range for YP-PV fluid behavior and the example of fluid 8 (see Table 1 for fluid details). Dashed and solid lines represent the n-dependent critical Reynolds number limit for transition to turbulent flow.

Figure 18 depicts the Bingham Reynolds number for the case of YP-PV fluid behavior for all cases investigated, while Figure 19 highlights the particular example of fluid 8 (see Table 1 for fluid details).

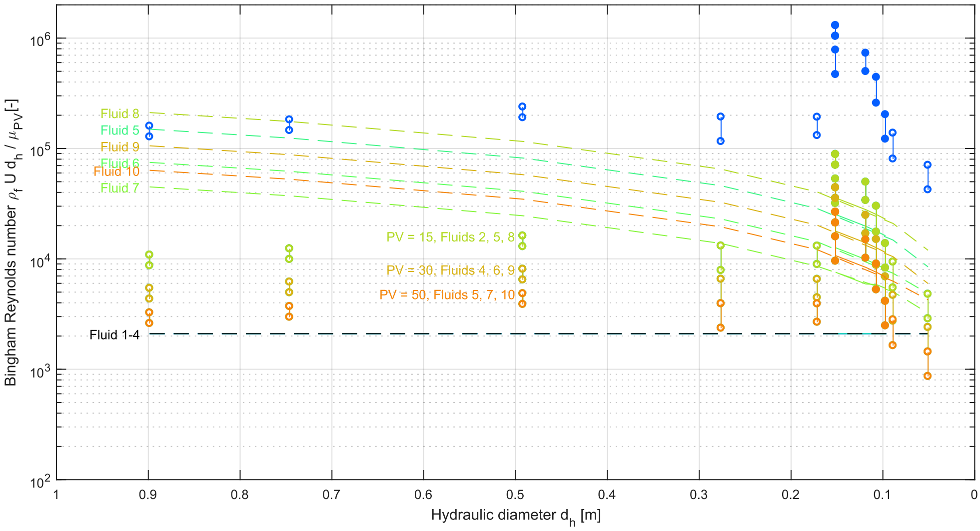

Figure 18: Bingham Reynolds number range for YP-PV fluid behavior. Filled points denote pipe geometry, unfilled points denote annulus geometry. Dashed lines represent the Bi-dependent critical Reynolds number limit for transition to turbulent flow. For information on fluids see Table 1.

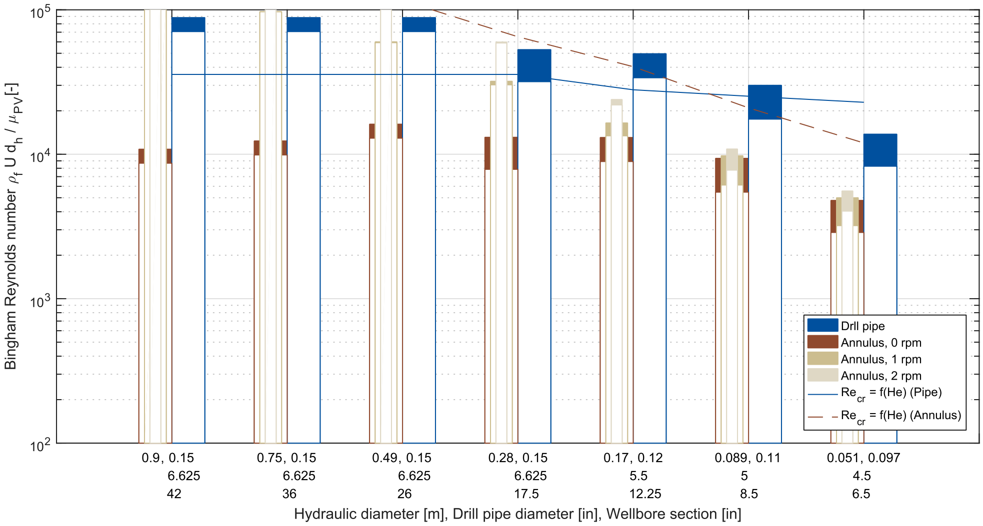

Figure 19: Bingham Reynolds number range for YP-PV fluid behavior and the example of fluid 8 (see Table 1 for fluid details). Dashed and solid lines represent the Bi-dependent critical Reynolds number limit for transition to turbulent flow.

Figure 20 depicts the Shields number Sh normalized with the critical Shields number Sh_{Cr} for the case of PL fluid behavior and a particle diameter of d_p = 1 mm for all cases investigated, while Figure 21 highlights the particular example of fluid 8 (see Table 1 for fluid details).

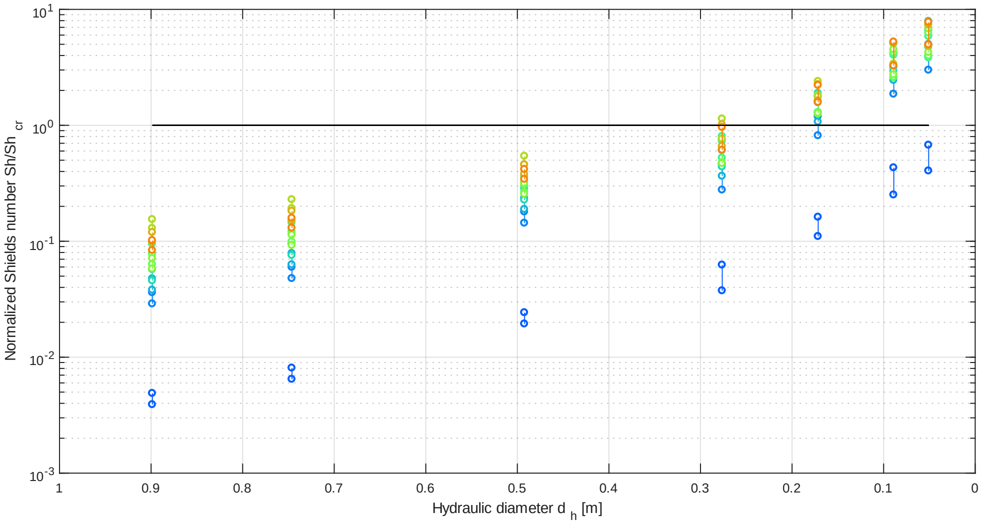

Figure 20: Normalized Shields number range for PL fluid behavior. The solid line represents incipient motion. For information on fluids see Table 1.

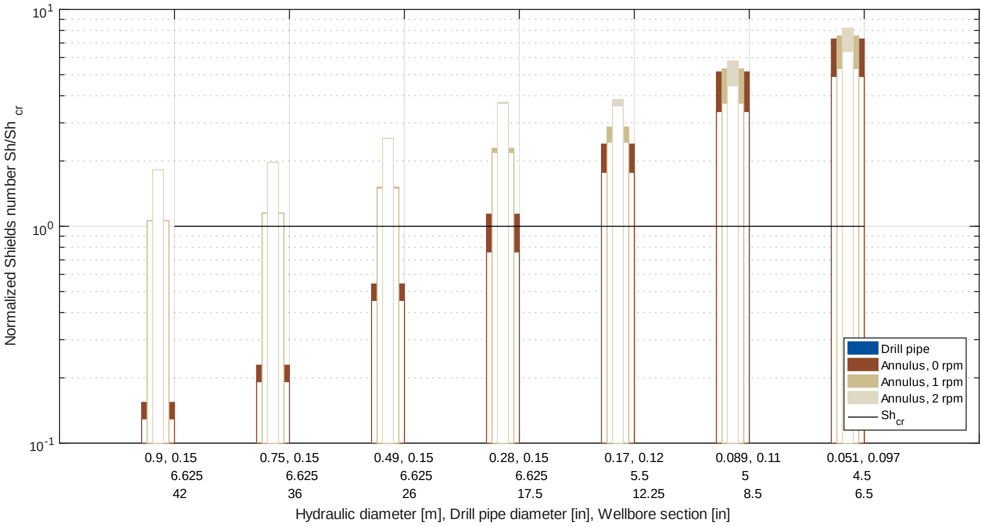

Figure 21: Normalized Shields number range for PL fluid behavior and the example of fluid 8 (see Table 1 for fluid details). The solid line represents incipient motion.

Figure 22 depicts the normalized Shields number for the case of YP-PV fluid behavior for all cases investigated, while Figure 23 highlights the particular example of fluid 8 (see Table 1 for fluid details).

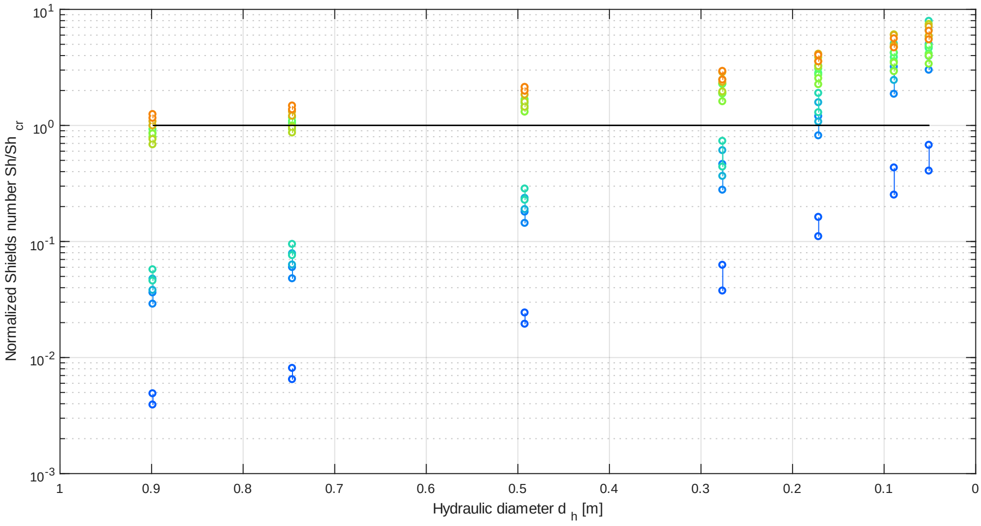

Figure 22: Normalized Shields number range for YP-PV fluid behavior. Filled points denote pipe geometry, unfilled points denote annulus geometry. The solid line represents incipient motion. For information on fluids see Table 1.

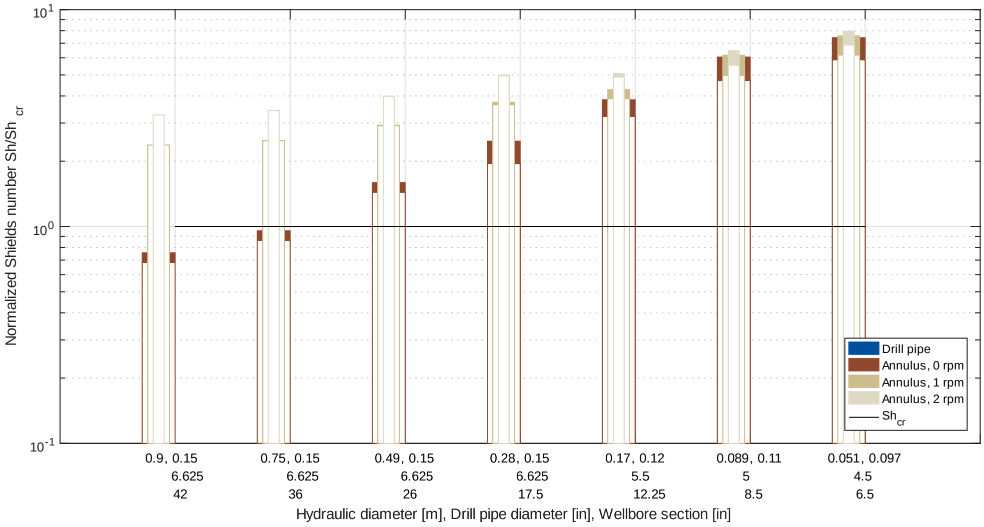

Figure 23: Normalized Shields number range for YP-PV fluid behavior and the example of fluid 8 (see Table 1 for fluid details). The solid line represents incipient motion.

3.3 The effect of cuttings bed height and particle diameter

So far, the cuttings bed height has been assumed equal to zero or almost zero. In this section, the effect of different cuttings bed heights (25 ,50 ,75% of d_o) are investigated as well as the influence of the particle diameter (d_p = 0.1, 1 10 mm). The computational scheme is the same as before, with the exception of the x-sectional area A, which is now reduced due to the cuttings bed presence and is being computed based on geometrical formulas (Cayeux et al., 2014). Consequently, the bulk velocity increases and a recalculation of the hydraulic diameter is required, too.

Assuming PL fluid behavior, Figure 24 shows the normalized Shields number vs. the Reynolds number.

Assuming PL fluid behavior, Figure 25 shows the Reynolds number vs. a modified Archimedes number (Ouriemi et al., 2010, 2009) superimposed on the dune flow pattern maps of Ouriemi et al. (2010, 2009). The dashed line represents incipient motion, the solid line represents a lower Reynolds number limit required for dune generation.

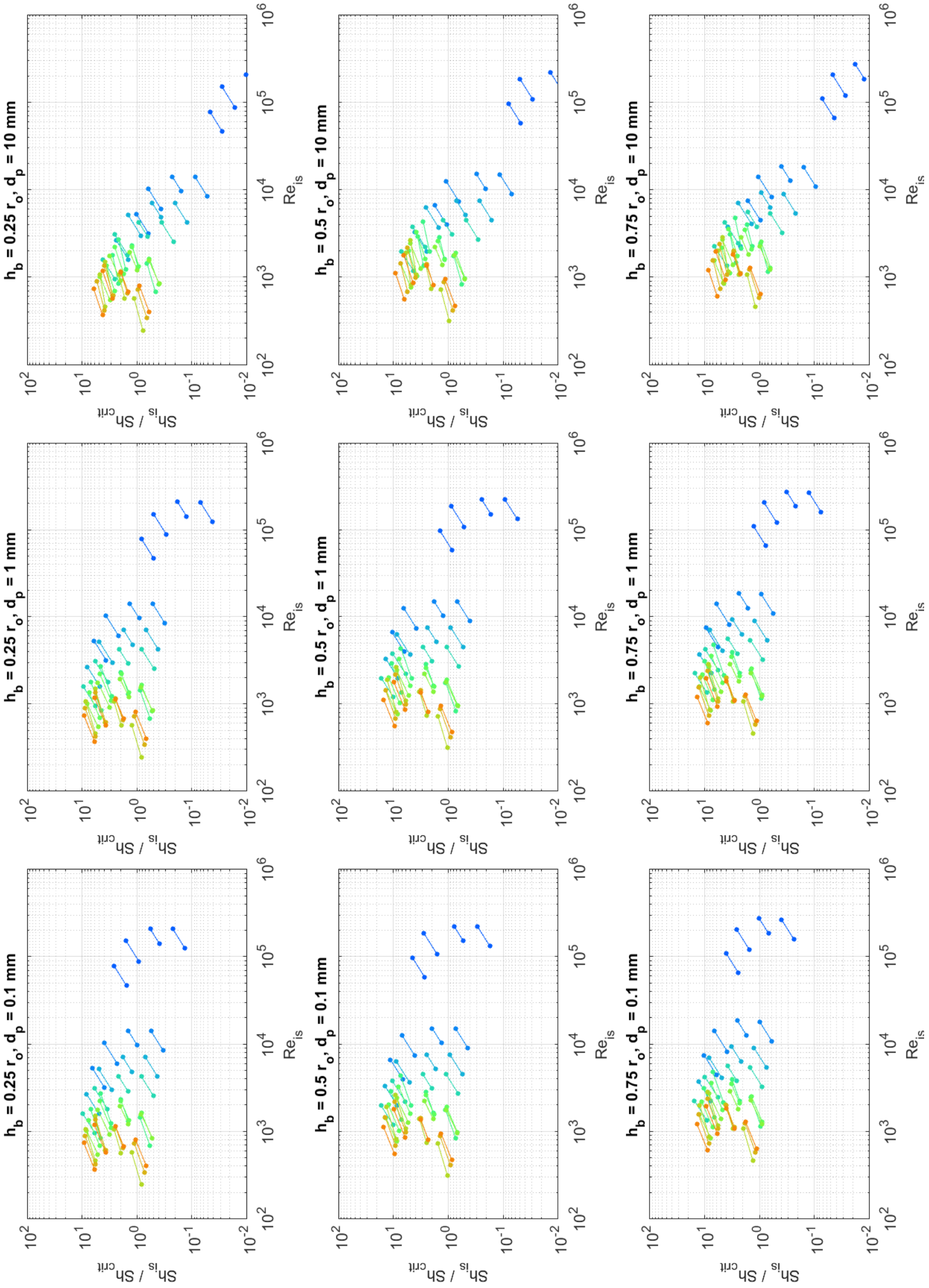

Figure 24: Normalized Shields number range for PL fluid behavior for different particle diameters and cuttings bed heights. For information on fluids see Table 1. The solid line represents incipient motion.

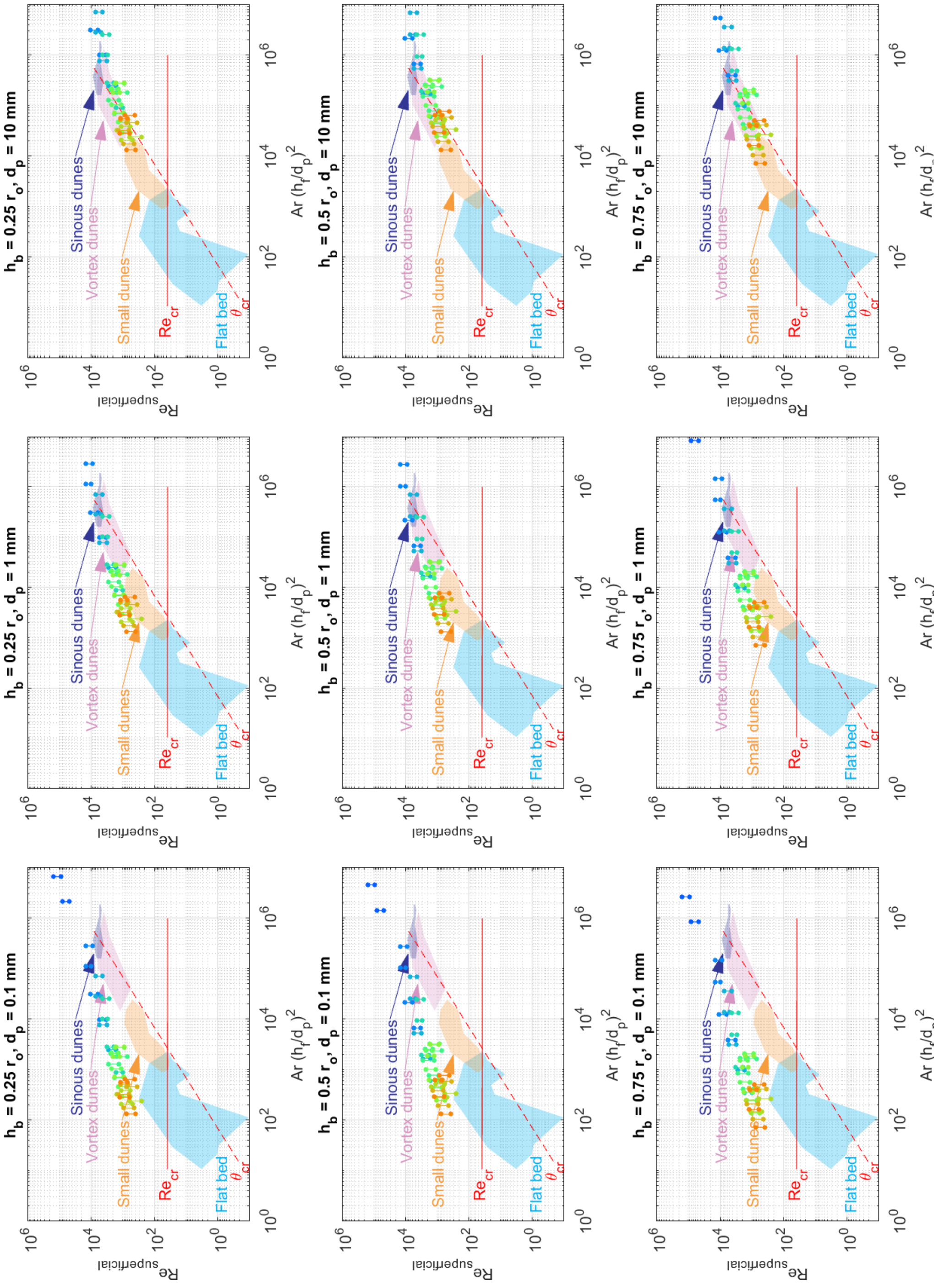

Figure 25: Reynolds number vs. modified Archimedes number for PL fluid behavior superimposed on dune flow pattern maps (Ouriemi et al., 2010, 2009). For information on fluids see Table 1.

4 Discussion

The results show that drill pipe flows are fully turbulent for the case of plain water and transitional for non-Newtonian drilling fluids. This is independent of the Reynolds number concept used.

Annular flows are at best transitional and mostly laminar. The flow state is highly dependable on the particular fluid and its rheological properties, here the YP/PV combination.

For CFD, this imposes a challenge if the flow is transitional because classical RANS models are not very accurate in the transitional regime. An error quantification of typically employed turbulence models (mainly the k-ϵ and k-ω family of models) applied to flow is required.

The presence of a cuttings bed, which here was simply assumed to have a relative height of 1/3 of the hydraulic diameter, does not heavily affect the order of magnitude of the estimated Reynolds numbers. The values are increasing slightly, but the general picture does not change.

Simple rotation of the drill pipe (that is no lateral motion, only rotation around its own axis) does not really affect the pure flow dynamics in the deeper, smaller wellbore sections. Here, the axial flow velocity is so large compared to the rotational component that the additional rotational velocity accounted for by a simple vector magnitude concept does not contribute significantly. However, the picture may change completely if lateral motion of the drill pipe is considered because of the immense additional flow disturbances generated.

For the investigated parameter space, the low viscous fluids tend to generate larger vortex dunes and sinuous dunes whereas the more viscous fluids result in smaller dunes. The occurrence and type of dunes is generally dependent on bed height and superficial Reynolds number, as well as particle diameter and Archimedes number. A flow model accounting for dunes is thus of interest.

Scaling is typically done based on the concept of Metzner and Reed (1955) and the also here employed Metzner and Reed (1955) Reynolds number, which may, however, fail in the turbulent regime (Björkman, 2008; Duffy, 2004). However, as may be seen in Table 2, this is based on the bulk velocity which is in the Metzner and Reed (1955) concept is established on the grounds of a laminar velocity profile. Alternatively, one may establish a wall viscosity on the pressure gradient. For the laminar flow regime, these two approaches should lead to identical results. However, for the transitional/turbulent flow regime, the Metzner and Reed (1955) concept is not accurate, and the pressure gradient approach seems more suitable for scaling purposes.

5 Conclusions

Based on the ballpark figures established, the following may be preliminarily concluded:

- Annular wellbore flows are transitional, if not laminar. The error of conventionally employed turbulence models needs to be investigated.
- Simple pipe rotation does not heavily affect the state of turbulence. However, lateral pipe motion may do so.

- Dunes are to be expected in annular wellbore flows. Hence, a modeling approach capable of handling dunes should be pursued.
- The classical Metzner and Reed (1955) Reynolds number is to be reconsidered when used for the turbulent flow regime.

Acknowledgements

The project Advanced Wellbore transport Modeling (AdWell) with its sponsor, PETROMAKS 2/the Research Council of Norway (project 228391) and its partners Equinor, Neptune Energy Norge AS, IRIS/NORCE, UiS, NTNU and SINTEF are gratefully acknowledged for funding and supporting this work. In addition, we are grateful for the computational resources provided at NTNU by UNINETT Sigma2 AS.

References

API RP 13D, 2010. Rheology and Hydraulics of Oil-Well Drilling Fluids. American Petroleum Institute (API), Washington, D. C.

Bingham, E.C., 1922. Fluidity and plasticity. McGraw-Hill Book Company, Inc.

Björkman, U., 2008. Reflections over Metzner's method. Annual Transactions of the Nordic Rheology Society 16.

Blasius, H., 1912. Das Aehnlichkeitsgesetz bei Reibungsvorgängen. Zeitschrift des Vereines deutscher Ingenieure 19, 639.

Busch, A., Islam, A., Martins, D., Iversen, F.P., Khatibi, M., Johansen, S.T., Time, R.W., Meese, E.A., 2018. Cuttings Transport Modeling - Part 1: Specification of Benchmark Parameters with a Norwegian Continental Shelf Perspective. SPE Drilling & Completion 33. https://doi.org/10.2118/180007-PA

Busch, A., Werner, B., Johansen, S.T., 2019. Cuttings Transport Modeling - Part 2: Dimensional Analysis and Scaling. progress, to be submitted to SPE Drilling & Completion.

Cayeux, E., Mesagan, T., Tanripada, S., Zidan, M., Fjelde, K.K., 2014. Real-Time Evaluation of Hole-Cleaning Conditions With a Transient Cuttings-Transport Model. SPE Drilling & Completion 29, 05–21. https://doi.org/10.2118/163492-PA

Chhabra, R.P., Richardson, J.F., 2011. Non-Newtonian flow and applied rheology: engineering applications. Butterworth-Heinemann.

Cross, M.M., 1965. Rheology of non-Newtonian fluids: a new flow equation for pseudoplastic systems. Journal of Colloid Science 20, 417–437. https://doi.org/10.1016/0095-8522(65)90022-X

Delplace, F., Leuliet, J.C., 1995. Generalized Reynolds number for the flow of power law fluids in cylindrical ducts of arbitrary cross-section. The Chemical Engineering Journal and the Biochemical Engineering Journal 56, 33–37. https://doi.org/10.1016/0923-0467(94)02849-6

Dodge, D.W., Metzner, A.B., 1959. Turbulent flow of non-newtonian systems. AIChE Journal 5, 189–204. https://doi.org/10.1002/aic.690050214

Duffy, G.G., 2004. Misapplication of the Metzner-Reed Non-Newtonian Correlation Method. Chemical Engineering Communications 191, 182–188. https://doi.org/10.1080/00986440490261836

Haaland, S.E., 1983. Simple and Explicit Formulas for the Friction Factor in Turbulent Pipe Flow. Journal of Fluids Engineering 105, 89–90. https://doi.org/10.1115/1.3240948

Irvine, T.F., 1988. A Generalized Blasius Equation for Power Law Fluids. Chemical Engineering Communications 65, 39–47. https://doi.org/10.1080/00986448808940242

Kozicki, W., Chou, C.H., Tiu, C., 1966. Non-Newtonian flow in ducts of arbitrary cross-sectional shape. Chemical Engineering Science 21, 665–679.

Metzner, A.B., Reed, J.C., 1955. Flow of non-newtonian fluids-correlation of the laminar, transition, and turbulent-flow regions. AIChE Journal 1, 434–440. https://doi.org/10.1002/aic.690010409

Mims, M., Krepp, T., 2007. Drilling Design and Implementation For Extended Reach and Complex Wells, 3rd ed. K&M Technologies Group, LLC.

Mooney, M., 1931. Explicit Formulas for Slip and Fluidity. Journal of Rheology 2, 210–222. http://dx.doi.org/10.1122/1.2116364

Morrison, F.A., 2013. Data Correlation for Friction Factor in Smooth Pipes.

Ostwald, W., 1925. Über die Geschwindigkeitsfunktion der Viskosität disperser Systeme. Colloid & Polymer Science 36, 99–117.

Ouriemi, M., Aussillous, P., Guazzelli, éLisabeth, 2009. Sediment dynamics. Part 2. Dune formation in pipe flow. Journal of Fluid Mechanics 636, 321. https://doi.org/10.1017/S0022112009007927

Ouriemi, M., Chauchat, J., Aussillous, P., Médale, M., Guazzelli, E., 2010. Sediment transport and dunes in pipe flow. Presented at the 7th International Conference on Multiphase Flow, pp. 1–6.

Rabinowitsch, B., 1929. Über die Viskosität und Elastizität von Solen. Z. Phys. Chem. A 145, 1–26.

Singh, J., Rudman, M., Blackburn, H.M., Chryss, A., Pullum, L., Graham, L.J.W., 2016. The importance of rheology characterization in predicting turbulent pipe flow of generalized Newtonian fluids. Journal of Non-Newtonian Fluid Mechanics 232, 11–21. https://doi.org/10.1016/j.jnnfm.2016.03.013

Soulsby, R., 1997. 6. Threshold of motion, in: Dynamics of Marine Sands. Thomas Telford Publishing, pp. 97–110.

Wilson, K.C., Thomas, A.D., 2006. Analytic Model of Laminar-Turbulent Transition for Bingham Plastics. The Canadian Journal of Chemical ldots 84. https://doi.org/10.1002/cjce.5450840502

Appendix A Definitions

Mass flow is converted to volume flow rate

$$Q = \frac{\dot{m}}{\rho} \tag{A1}$$

Bulk velocity in x-direction

$$U = \frac{Q}{A} \tag{A2}$$

The cross-sectional area

$$A = \frac{\pi}{4}\left(d_o{}^2 - d_i{}^2\right) \tag{A3}$$

where d_o is the outer and d_i is the inner diameter of an annulus, with d_i=0 for the pipe case.

The wetted perimeter

$$P = \pi\left(d_o + d_i\right) \tag{A4}$$

The hydraulic diameter

$$d_h = \frac{4A}{P} = d_o - d_i \tag{A5}$$

The pressure gradient is the pressure force per volume

$$\frac{\Delta p}{\Delta x} = \frac{\Delta p A}{A \Delta x} = \frac{F_p}{V} \tag{A6}$$

The shear stress at the wall (= mean wall shear stress)

$$\tau_w = \frac{\Delta p}{\Delta x}\frac{d_h}{4} \tag{A7}$$

The friction velocity

$$u_\tau = \sqrt{\frac{\tau_w}{\rho}} \tag{A8}$$

The Fanning friction factor

$$f = \frac{\tau_w}{\frac{1}{2}\rho U^2} \tag{A9}$$

Dimensionless wall distance y^+, also known as the local Reynolds number

$$y^+ = \left(R - r\right)\frac{\rho u_\tau}{\eta_w} \tag{A10}$$

where the factor $\delta = \eta_w/(\rho u_\tau)$ is the viscous layer.

Dimensionless velocity u^+

$$u^+ = \frac{u}{u_\tau} \tag{A11}$$

Dimensionless shear rate $\dot{\gamma}^+$

$$\dot{\gamma}^+ = \dot{\gamma}\frac{\eta_w}{\rho u_\tau{}^2} \tag{A12}$$

Revolutions per Minute (RPM)

$$RPM = \frac{60}{2\pi}\omega \tag{A13}$$

where the angular frequency ω is given by

$$\omega = \frac{U}{r} \tag{A14}$$

Typically, U and r are defined as $U = u(r = d_i/2)$ and $r = d_i/2$. However, in accordance with the bulk velocity used in the Reynolds number a better definition might be $U = U_r = u(r = d_i/2 + (d_o/2 - d_i/2)/2$ and $r = d_i/2$.

Appendix B Inner scaling

Mass conservation implies

$$\dot{m} = \rho\left(UA\right) = \int_A \rho\, u(r)\, dA \tag{B1}$$

where r is the radial coordinate with r = 0 at the center of the conduit.

Isolated for the superficial velocity U, this yields

$$U = \frac{\int_A \rho\, u(r)\, dA}{\rho\, A} = \frac{\int_0^R \rho\, u(r)\, 2\pi r\, dr}{\rho\, \pi R^2} = \frac{2}{R^2}\int_0^R \rho\, u(r)\, r\, dr \tag{B2}$$

where a pipe geometry is assumed.

Using the definitions (A10) and (A11), where R and r are nondimensionalized in the same manner as $y = R - r$, and after some manipulation, one obtains

$$U^+ = \frac{2}{\left(R^+\right)^2}\int_0^{R^+} u^+ y^+\, dy^+ \tag{B3}$$

Appendix C Outer scaling

C.1 Friction factor

With the concept of the hydraulic diameter $d_h = 4A/S$ as the ratio of x-sectional area A and wetted perimeter S, the wall shear stress may be developed from a force balance of pressure and viscous ("frictional") forces to

$$\tau_w = \frac{\Delta p d_h}{4\Delta x} \tag{C1}$$

The same result is obtained if one rearranges the laminar flow equation of a Newtonian fluid to

$$\frac{\Delta p d_h}{4\Delta x} = \mu \frac{8U}{d_h} \tag{C2}$$

where $8U/d_h$ is the Newtonian wall shear rate and $\Delta p d_h/4\Delta L$ is the wall shear stress.

Non-dimensionalising with a dynamic pressure yields the Fanning friction factor

$$f = \frac{\frac{\Delta p d_h}{4\Delta x}}{\rho \frac{U^2}{2}} \tag{C3}$$

which may also be obtained by manipulating equation (C2) to yield

$$f = \frac{16}{\mathrm{Re}} \tag{C4}$$

which is equivalent with (C3) and highlights the friction factor being a ratio of viscous and momentum stresses.

The Reynolds number in (C4) is defined as

$$\mathrm{Re} = \frac{\rho U D}{\mu} \tag{C5}$$

where μ is a Newtonian viscosity or an apparent viscosity of a GNF fluid.

C.1.1 Friction factor correlations for single phase, Newtonian flows

Morrison (Morrison, 2013) (laminar & turbulent, smooth walls)

$$f = \frac{16}{\mathrm{Re}} + \frac{0.0076\left(\frac{3170}{\mathrm{Re}}\right)^{0.165}}{1+\left(\frac{3170}{\mathrm{Re}}\right)^{7}} \tag{C6}$$

Haaland (Haaland, 1983) (turbulent, rough walls, s = roughness)

$$f = \frac{1}{4\left(-1.8\log_{10}\left(\left(\frac{s}{3.7d_h}\right)^{1.11} + \frac{6.9}{\mathrm{Re}}\right)\right)^2} \tag{C7}$$

Blasius (Blasius, 1912) (turbulent, smooth walls)

$$f = \frac{0.316\,\mathrm{Re}^{-0.25}}{4} \tag{C8}$$

C.1.2 Friction factor correlations for single phase, GNF fluid flows

Dodge-Metzner (Dodge and Metzner, 1959)

$$\frac{1}{\sqrt{f}} = \frac{4}{n^{0.75}}\log\left(\mathrm{Re}\ f^{\left(1-\frac{n}{2}\right)}\right) - \frac{0.4}{n^{1.2}} \tag{C9}$$

Irvine (Irvine, 1988)

$$f = \left(\frac{2^{(n+4)}}{7^{7n}}\left(\frac{4n}{3n+1}\right)^{3n^2}\mathrm{Re}^{-1}\right)^{\left(\frac{1}{3n+1}\right)} \tag{C10}$$

C.2 Generalized Reynolds number

Using the Re definition as given in equation C4 but with the viscosity at the wall $\eta_w(\dot{\gamma}_w)$ instead yields the generalized Reynolds number. Computing the correct viscosity η_w is, however, not straightforward because one must know the shear rate at the wall. For a PL fluid, the shear rate may be computed according to the Reynolds number concept of Metzner and Reed (1955).

However, two computational approaches are available summarized in Table 2: The one of Metzner and Reed (1955), which is based on the bulk velocity (or flow rate) and the shear-stress at the wall definition, which is based on the pressure gradient.

	Based on pressure gradient	**Based on bulk velocity (or flow rate)**
1	$\frac{\Delta p}{\Delta x}$	U
2	$\tau_w = \frac{\Delta p d_h}{\Delta x 4}$	
3	$\eta_w = \frac{\tau_w}{\dot{\gamma}_w}$	$\eta_w = K\dot{\gamma}_w^{\ n-1}$
4	$\dot{\gamma}_w = \left(\frac{\tau_w}{K}\right)^{\frac{1}{n}}$	$\dot{\gamma}_w = \frac{8U}{d_h}\left(\frac{3n+1}{4n}\right)^{\frac{n}{n-1}}$

5	$\eta_w = \left(\frac{\Delta p d_h}{\Delta x 4}\right)^{\left(1-\frac{1}{n}\right)} K^{\frac{1}{n}}$	$\eta_w = K\left(\frac{8U}{d_h}\right)^{n-1}\left(\frac{3n+1}{4n}\right)^{n}$

Table 2: Two computational approaches to estimate the Reynolds number for the case of pipe flow.

C.3 Generalized Reynolds number for PL fluid

C.3.1 Pipes

Based on a rheology-independent expression for the shear-rate at the wall of a fluid developed by (Rabinowitsch, 1929) and (Mooney, 1931), Metzner and Reed (1955) defined a **generalized Reynolds number for non-Newtonian fluids**

$$\mathrm{Re}_G = \frac{\rho U^{2-n'} D^{n'}}{K' 8^{n'-1}} \tag{C11}$$

with the denominator, termed “effective viscosity” by (Chhabra and Richardson, 2011, p. 127) and “generalized viscosity coefficient” by (Metzner and Reed, 1955),

$$\eta = K' 8^{n'-1}\,, \tag{C12}$$

the dimensionless exponent n defined as a derivative representing the slope of a logarithmic plot of the shear stress at the wall $d_h \Delta p / 4 \Delta p x$ (of a pipe) vs. the corresponding Newtonian shear rate $8U/d_h$

$$n' = \frac{d\left[\ln\left(\frac{d_h \Delta p}{4\Delta x}\right)\right]}{d\left[\ln\left(\frac{8U}{d_h}\right)\right]}\,, \tag{C13}$$

termed flow-behavior index and describing the degree of non-Newtonian behavior of the fluid, and the dimensionless coefficient K

$$K' = \frac{\frac{d_h \Delta p}{4\Delta x}}{\left(\frac{8U}{d_h}\right)^{n'}} \tag{C14}$$

termed fluid consistency index and describing the consistency, i.e. the degree of the apparent viscosity, of the fluid.

Equation (C11) is valid for all time-independent, purely viscous material functions if n and K are evaluated on small enough increments in an $d_h \Delta p / 4 \Delta x$ vs. $8U/d_h$ plot, as they in general are not necessarily constants.

However, in the case of power-law (pl) fluids as defined by (Ostwald, 1925)

$$\tau = K\dot{\gamma}^{n} \quad \leftrightarrow \quad \eta_{app} = \frac{\tau}{\dot{\gamma}} = K\dot{\gamma}^{n-1} \tag{C15}$$

n and K are in fact constants and may be related to the PL coefficients n and K as follows

$$n' = n$$
$$K' = K\left(\frac{3n+1}{4n}\right)^n \tag{C16}$$

yielding a Reynolds number Re_{pl} for power–law fluids

$$\mathrm{Re}_{pl} = \frac{\rho U^{2-n} D^n}{K\left(\frac{3n+1}{4n}\right)^n 8^{n-1}} \tag{C17}$$

which, after some manipulation[1], may be related to the Newtonian Reynolds number, equation (C5), as follows

$$\mathrm{Re}_{pl} = \frac{\mathrm{Re}}{\frac{3n+1}{4n}} \tag{C18}$$

C.3.2 Concentric annuli

Following (Kozicki et al., 1966) and (Delplace and Leuliet, 1995), two amendments need to be undertaken in order to obtain a consistent Reynolds number for concentric annuli

As with Newtonian fluids, the diameter needs to be replaced by an equivalent diameter, e.g. the hydraulic diameter:

$$d_h = \frac{4A}{S} = d_o - d_i \tag{C19}$$

A redefinition of the shear rate and corresponding generalized Re number is required to account for geometrical effects. (Kozicki et al., 1966) provided a generalized Re number based on two geometric factors a and b and (Delplace and Leuliet, 1995) introduced a functional β = b/a, generalized the friction factor $f\ =\ 48/\ \beta/Re_G$ and replaced the factor 8^{n-1} in equation (C17) with $(24/\beta)^{n-1}$.

The generalized Re number Re_G for a power-law fluid in a non-circular duct is obtained as

$$\mathrm{Re}_{pl-a} = \frac{\rho U^{2-n} {D_h}^n}{\left(\frac{24}{\beta}\right)^{n-1} K\left(\frac{1+n\beta}{n+n\beta}\right)^n} \tag{C20}$$

Considering a concentric annulus, two limiting cases can be distinguished. For

- Di → 0 (↔ Circular pipe of diameter D with Dh = D, β = 3 ↔ a = ¼ & b = ¾) equation (C20) reduces to equation (C17).
- Di →1 (↔narrow slot of hydraulic diameter Dh = Do-Di, β = 2 ↔ a = ½ & b = 1) equation (C20) yields

---

[1] Inserting the non-Newtonian shear rate at the wall into the PL apparent viscosity equation, and again inserting into the Newtonian Reynolds number, namely equation (C5), and rearranging/simplifying.

$$\mathrm{Re}_{pl-ns} = \frac{\rho U^{2-n} D_h^{\ n}}{12^{n-1} K \left(\frac{2n+1}{3n} \right)^n} \tag{C21}$$

	Newtonian, e.g. H2O	Non-Newtonian, e.g. PAC
Pipe	β = 3 n = 1 K = 0.00102	β = 3 n = f(Rheology) K = f(Rheology)
Annulus	β = 2 n = 1 K = 0.00102	β = 2 n = f(Rheology) K = f(Rheology)

Table 3: Overview of flow cases.

	Newtonian, e.g. H2O	Non-Newtonian, e.g. PAC
Pipe	$f_{n-p} = \frac{16}{\mathrm{Re}_{n-p}}$ $\mathrm{Re}_{n-p} = \frac{\rho U D}{\mu}$	$f_{nn-p} = \frac{16}{\mathrm{Re}_{nn-p}}$ $\mathrm{Re}_{nn-p} = \frac{\rho U^{2-n} D^n}{8^{n-1} K \left(\frac{3n+1}{4n} \right)^n}$
Annulus	$f_{n-a} = \frac{24}{\mathrm{Re}_{n-a}}$ $\mathrm{Re}_{n-a} = \frac{\rho U D_h}{\mu}$	$f_{nn-a} = \frac{24}{\mathrm{Re}_{nn-a}}$ $\mathrm{Re}_{nn-a} = \frac{\rho U^{2-n} D_h^{\ n}}{12^{n-1} K \left(\frac{2n+1}{3n} \right)^n}$

Table 4: Overview of friction factor and Reynolds number definitions.

C.3.3 Eccentric annuli

C.4 PL scaling based on Reynolds similarity

Based on Reynolds similarity $\mathrm{Re}_1 = \mathrm{Re}_2$, for a for a Newtonian fluid

$$\frac{\rho_2 U_2 d_{h2}}{\mu_2} = \frac{\rho_1 U_1 d_{h1}}{\mu_1} \tag{C22}$$

Rearranging

$$\mu_2 = \mu_1 \frac{\rho_2 U_2 d_{h2}}{\rho_1 U_1 d_{h1}} \tag{C23}$$

For the pipe DNS simulations, d_h=1m and ρ=1kg/m³. Assuming water (ρ=998.2kg/m³, μ=0.001002Pa·s) and d_h=0.045 (Singh et al., 2016) yields

$$\mu_2 = 0.001002 \frac{1 U_2\, 1}{998.2 U_1\, 0.045} = 2.23 \cdot 10^{-5} \tag{C24}$$

For a PL fluid, regardless of starting out with the Metzner-Reed Reynolds number or with a Generalized Reynolds number with an apparent viscosity based on a shear rate estimate of the order U/d, one obtains

$$K_2 = K_1 \frac{\rho_2 {U_2}^{2-n} {d_{h2}}^n}{\rho_1 {U_1}^{2-n} {d_{h1}}^n} \tag{C25}$$

where $n = n_1 = n_2$ because identical shear-thinning behavior is required.

However, if a Generalized Reynolds number with an apparent viscosity based on the wall shear stress is used instead, one obtains

$$K_2 = K_1 \left(\frac{\rho_2 U_2 d_{h2}}{\rho_1 U_1 d_{h1}} \right)^n \left(\frac{\tau_1}{\tau_2} \right)^{n-1} \tag{C26}$$

Appendix D Estimates

D.1 Bulk velocity U for given pressure gradient dp/dx

Turbulent flow regime, use Blasius (Blasius, 1912) friction factor correlation, i.e. equation (C8), with definition of friction factor, namely equation (C3)

$$\frac{0.316\,\mathrm{Re}^{-0.25}}{4} = \frac{\dfrac{\Delta p d_h}{4\Delta x}}{\rho\dfrac{U^2}{2}} \tag{D1}$$

Apply definition of Re and raise to fourth power, isolate U

$$U = \sqrt[7]{\frac{16\left(\dfrac{\Delta p}{\Delta x}\right)^4 d_h{}^5}{0.316^4\rho^3\eta}} \tag{D2}$$

D.2 First layer cell height

Rearrange definition of dimensionless wall distance y^+ and insert definition of friction velocity u_τ and rearranged Fanning friction factor f

$$\Delta_1 y = y^+\frac{\eta}{\rho u_\tau} = y^+\frac{\eta}{\rho U\sqrt{\dfrac{f}{2}}} \tag{D3}$$

Manuscript 2 (XI)

Conversion of engineering oil field rheological model parameters to SI model parameters

Alexander Busch

Personal memo.

Trondheim, 2015.

Conversion of engineering oil field rheological model parameters to SI model parameters

Alexander Busch[1],*

[1] Norwegian University of Science and Technology (NTNU), Trondheim, Norway

*Corresponding author: alexander.busch@ntnu.no, alexander.busch@alumni.ntnu.no

Keywords: Drilling, Wellbore Flows, non-Newtonian, GNF, shear-thinning, annular, pipe, rheoological models.

Abstract

This manuscript provides information on how to convert Fann viscometer data to shear stress and shear rate in SI units. Furthermore, the semi-empirical formulas of the current API standard are briefly explained and the relationships between the different material functions are provided.

Memo 2015-12-16

Contents

Nomenclature

Greek symbols

$\dot{\gamma}$	Shear rate, total shear measure.
η	Apparent shear viscosity.
μ	Newtonian shear viscosity.
θ	Fann viscometer dial reading.

Latin symbols

f	Functional.
K	Parameter in Power-law and Yield Power Law, also known as Consistency Index.
n	Parameter in Power-law and Yield Power Law, also known as PL exponent.

Indices

0	Zero, $\dot{\gamma} \to 0$.
∞	Infinity, $\dot{\gamma} \to \infty$.
f	Fluid.
FV	Fann Viscometer.
P	Plastic.
PL	Power Law.
y	Yield.

Abbreviations

DR	Dial Reading.
FC	Flow Curve.
PL	Power Law.
PV	Plastic Viscosity.
RS	Rotor speed.
YP	Yield Point.
YPL	Yield Power Law.

In case of a Newtonian drilling fluid such as e.g. pure water, the rheological model is based on the assumption that the shear stress τ is a linear function of the shear rate $\dot{\gamma}$ determined by the constant viscosity μ, i.e.

$$\tau = \mu\dot{\gamma} \tag{1}$$

For the case of drilling fluids, the viscosity may be non-constant. It varies with temperature and is also typically a function of the shear rate $\dot{\gamma}$ and may be experimentally determined by means of viscometry.

In the petroleum industry, the Fann viscometer is usually employed which allows for measuring the shear stress caused by a given shear rate (Tomlin, 2016). The applied rotor speed and the respective dial reading may be directly converted to shear stress and shear rate as shown in Table 1.

Fann reading	**Geometry factors f**	**Oilfield units**	**Unit conversion factors**	**SI units**
Dial reading $DR[°]$	$\xrightarrow{\cdot 1.066}$	Shear stress $\tau_{Of}\left[lb_f/100\ ft^2\right]$	$\xrightarrow{\cdot 0.4788026}$	Shear stress $\tau[Pa]$
Rotor speed $RS[rpm]$	$\xrightarrow{\cdot 1.703}$	Shear rate $\dot{\gamma}_{Of}\left[s^{-1}\right]$	$\xrightarrow{\cdot 1}$	Shear rate $\dot{\gamma}\left[s^{-1}\right]$

Table 1: Unit conversion factors for Fann viscometer readings.

Moreover, due to its geometric design, for the classical Bingham material function (Bingham, 1922)

$$\tau = \tau_Y + \mu_P\dot{\gamma} \tag{2}$$

where τ_Y is a yield stress and μ_P is the constant plastic viscosity, the Fann viscometer allows for direct determination of the model constants.

1 Obtaining model coefficients from Fann viscometer data

Rewriting equation (2) to suit the Fann viscometer design yields (API RP 13D, 2010; ISO/TC 67, SC 3, 2008)

$$DR = YP + \frac{PV}{600-300}RS \tag{3}$$

where DR is the Fann viscometer's Dial Readings at Rotor Speeds (RS) of 600 rpm and 300 rpm, YP is the oilfield Yield Point, and PV the oilfield Plastic Viscosity. The model constants YP and PV are obtained from the Fann viscometer readings as follows (API RP 13D, 2010; ISO/TC 67, SC 3, 2008):

$$PV\,[cP] = DR(RS = 600) - DR(RS = 300) \tag{4}$$

$$YP\left[lb_f\ /100\,ft^2\right] = 1.066\big(DR(300) - PV\big) \tag{5}$$

Often the YP is incorrectly reported in units of $lb_f/100ft^2$ without application of the geometrical correction factor 1.066. However, the error is relatively small.

Applying the unit conversion factors given in Table 1 to equation (3) yields

$$\tau\left[Pa\right] = 0.511 \cdot YP + \frac{PV}{1000} \cdot \dot{\gamma} \tag{6}$$

i.e. the coefficients of equation (2) are $\tau_y = 0.511 \cdot YP$ and $\mu_P = PV/1000$, when expressed based on the oilfield definitions (4) and (5).

The Power Law (PL) material function (Ostwald, 1929, 1925) describes shear-thinning (or-shear-thickening) behavior by making equation (1) non-linear via the modification of the shear rate $\dot{\gamma}$ with a flow exponent (or index) n [-].

$$\tau = K\dot{\gamma}^n \tag{7}$$

where K [Pa·s^n] is the consistency index.

Again, equation (7) may alternatively be based on Fann viscometer readings, hence

$$DR = K_{FV} RS^{n_{FV}} \tag{8}$$

and the model coefficients may be determined from Fann viscometer measurements (API RP 13D, 2010; ISO/TC 67, SC 3, 2008):

$$n_{FV}\left[-\right] = 3.32\log_{10}\frac{2PV + YP}{PV + YP} = 3.32\log_{10}\frac{\theta_{600}}{\theta_{300}} \tag{9}$$

$$K_{FV}\left[{}^\circ \cdot s^n\right] = \frac{PV + YP}{300^n} = \frac{\theta_{300}}{300^n} \tag{10}$$

which corresponds to a local PL approximation (Metzner and Reed, 1955) of the higher shear rate range representative for flow in the drill pipe, i.e. the Fann viscometer readings $DR = 300 \leftrightarrow \dot{\gamma} = 511$ and $DR = 600 \leftrightarrow \dot{\gamma} = 1022$.

Alternatively, equations (9) and (10) may be based on the lower shear rate range representative for flow in the wellbore annulus, i.e. the Fann viscometer readings $DR = 3 \leftrightarrow \dot{\gamma} = 5.1$ and $DR = 100 \leftrightarrow \dot{\gamma} = 170.3$.

Applying the unit conversion factors given in Table 1 to equations (9) and (10) yields

$$n\left[-\right] = 3.32\log_{10}\frac{\tau\left(\dot{\gamma} = 1022\right)}{\tau\left(511\right)} \tag{11}$$

$$K\left[Pa \cdot s^n\right] = \frac{\tau\left(\dot{\gamma} = 511\right)}{511^n} \tag{12}$$

as the SI coefficients for equation (7).

The very same approach amy be used for the Yield Power Law (YPL) (Herschel and Bulkley, 1926)

$$\tau = f_\theta\left(\tau_y + K\dot{\gamma}^n\right), \tag{13}$$

which is one of the two current standard oilfield models acc. to (API RP 13D, 2010). Here, $f_\theta$is a geometry factor[1] and n, K and τ_y are model coefficients to be determined from Fann viscometer measurements as follows:

- Fluid flow index

$$n\left[-\right] = 3.32\log_{10}\frac{\theta_{600}-\tau_y}{\theta_{300}-\tau_y} \tag{14}$$

- Fluid consistency index

$$K\left[lb_f \cdot s^n / 100\ ft^2\right] = \frac{\theta_{300}-\tau_y}{300^n} \tag{15}$$

- Yield stress

$$\tau_y\left[lb_f / 100\ ft^2\right] = 2\theta_3 - \theta_6 \tag{16}$$

Note that equation (13) requires the use of equations (14), (15) and (16) and returns $\tau\left[lb_f/100\ ft^2\ \right]$.

Alternatively, more advanced rheometric test data may be used to establish values for the model coefficients. In this case, a fit function of the form of the original YPL model formulation (Herschel and Bulkley, 1926), i.e. equation (13) with $f_\theta = 1$, would be to obtain n, K, and τ by data regression.

2 Obtaining PL and YPL coefficients from PV and YP values

The definitions of the PL model coefficients of the (API RP 13D, 2010), as given in equations (14) and (15) with $\tau_y = 0$ and therefore $\theta(0) = 0$, are based on the very same dial readings as PV and YP, as given in equations (4) and (5). Thus, n and K may be directly obtained from PV and YP data, see also (API RP 13D, 2010, p. 28). This is only possible within the frame of the (API RP 13D, 2010) model definitions, i.e. the assumptions that

$$\tau_{Bingham}\left(\dot{\gamma} = 511\right) = \tau_{PL}\left(\dot{\gamma} = 511\right) \quad \& \quad \tau_{Bingham}\left(\dot{\gamma} = 1022\right) = \tau_{PL}\left(\dot{\gamma} = 1022\right) \tag{17}$$

and thus, both models retain the same stress for the shear rates $\dot{\gamma}$ = 511 s^{-1} and $\dot{\gamma}$ = 1022 s^{-1}.

However, in general and as noted above, model coefficients are obtained via curve fits and data regression and no direct relationship between the Bingham and Power-Law/Herschel-Bulkley model coefficients may be exploited.

---

[1] The geometry factor f_θ is a consequence of the model formulation as a function of the Fann viscometer dial readings and is not part of the general model formulations as given by (Herschel and Bulkley, 1926).

The same concept of model coefficient conversion may be in principle applied to the YPL, however, here one degree of freedom and, thus uncertainty, is introduced through the yield stress τ_y , which, as it is clear from its definition in equation (16), is not related to the shear rates $\dot{\gamma}$ = 511 s^{-1} and $\dot{\gamma}$ = 1022 s^{-1}.

Relating equations (14) and (15) with (4) and (5) yields

- Fluid flow index

$$n\left[-\right] = 3.32\log_{10}\frac{2PV + YP - \tau_y}{PV + YP - \tau_y} \tag{18}$$

- Fluid consistency index

$$K\left[lb_f \cdot s^n \big/ 100\ ft^2\right] = \frac{PV + YP - \tau_y}{511^n} \tag{19}$$

The choice of τ_y is in principle arbitrary and only limited by the special cases for which the YPL, namely equation (13), collapses to one of the simpler models, i.e. equations (1), (3), or (7).

- Newtonian behavior $YP = 0 \ \leftrightarrow \ \tau_y = 0$ & $n = 1$
- Non-Newtonian, PL-like behavior $\tau_y = 0$
- Non-Newtonian, Bingham-like behavior $\tau_y = YP$ & $K = PV/511$

3 Calculation example

Fann data				Model shear stress			
Rotor speed [rpm]	**Shear rate [s^{-1}]**	**Dial reading [°]**	**Shear stress [Pa]**	**Bingham [Pa]**	**PL [Pa]**	**YPL w/ τ_y based on data [Pa]**	**YPL w/ τ_y chosen arbitrarily [Pa]**
0	0			4.02	0.00	0.86	2.55
3	5.109	2.35	1.20	4.04	0.69	1.32	2.70
6	10.218	3.00	1.53	4.08	0.98	1.54	2.80
100	170.3	8.54	4.36	4.96	3.96	4.11	4.48
200	340.6	10.79	5.51	5.91	5.59	5.64	5.75
300	510.9	13.41	6.85	6.85	6.85	6.85	6.85
600	1021.8	18.95	9.67	9.67	9.67	9.67	9.67
	1200	19.95	10.18	10.66	10.48	10.50	10.55
	1500			12.32	11.71	11.77	11.97
	2000			15.08	13.51	13.67	14.16

PV or K	5.53	0.60074435	0.36256036	0.08937086
n		0.4980509	0.55745393	0.7288015
YP or τ_y	7.88		1.68855535	5

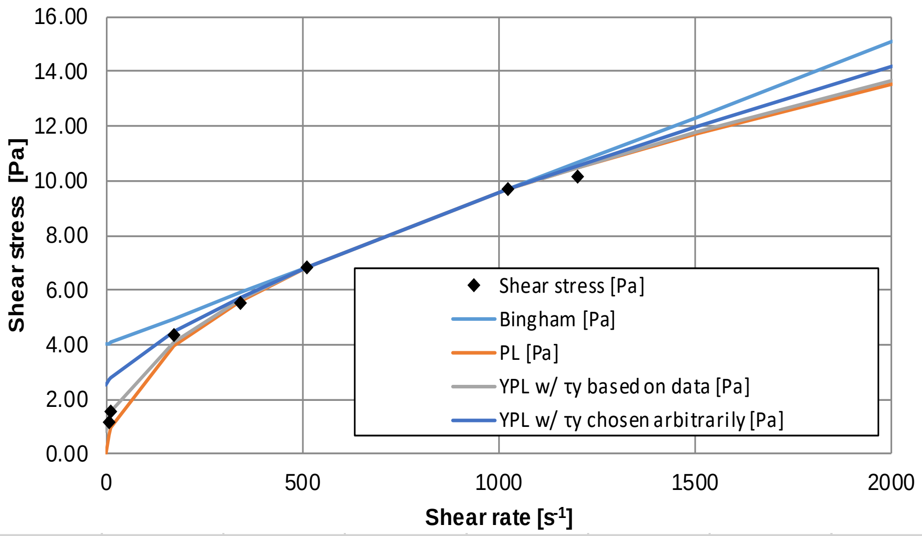

4 Summary

	YP/PL	PL	YPL
Pipe (High shear rate range)	$PV = \theta_{600} - \theta_{300}$ $YP = \theta_{300} - PV$	$n = 3.32 \log_{10} \frac{\theta_{600}}{\theta_{300}}$ $K = \frac{\theta_{300}}{511^n}$	$n = 3.32 \log_{10} \frac{\theta_{600} - \tau_y}{\theta_{300} - \tau_y}$ $K = \frac{\theta_{300} - \tau_y}{300^n}$ $\tau_y = 2\theta_3 - \theta_6$
Annulus (Low shear rate range)		$n = 0.657 \log_{10} \frac{\theta_{100}}{\theta_3}$ $K = \frac{\theta_{100}}{170.3^n}$	$n = 0.657 \log_{10} \frac{\theta_{100} - \tau_y}{\theta_3 - \tau_y}$ $K = \frac{\theta_{100} - \tau_y}{170.3^n}$ $\tau_y = 2\theta_3 - \theta_6$

References

API RP 13D, 2010. Rheology and Hydraulics of Oil-Well Drilling Fluids. American Petroleum Institute (API), Washington, D. C.

Bingham, E.C., 1922. Fluidity and plasticity. McGraw-Hill Book Company, Inc.

Herschel, W., Bulkley, R., 1926. Konsistenzmessungen von Gummi-Benzollösungen. Kolloid-Zeitschrift 39, pp 291-300. https://doi.org/10.1007/BF01432034

ISO/TC 67, SC 3, 2008. ISO 10414-1 : 2008 - Petroleum and natural gas industries - Field testing of drilling fluids - Part 1 - Water-based fluids.pdf. International Organization for Standardization (ISO).

Metzner, A.B., Reed, J.C., 1955. Flow of non-newtonian fluids-correlation of the laminar, transition, and turbulent-flow regions. AIChE Journal 1, 434–440. https://doi.org/10.1002/aic.690010409

Ostwald, W., 1929. Über die rechnerische Darstellung des Strukturgebietes der Viskosität. Colloid & Polymer Science 47, 176–187.

Ostwald, W., 1925. Über die Geschwindigkeitsfunktion der Viskosität disperser Systeme. Colloid & Polymer Science 36, 99–117.

Tomlin, M., 2016. Model 35 Viscometer Instruction Manual.

A.3. Other works

The reports listed below were generated in several DION projects conducted concurrently to this PhD project.

[XVIII] Elli Verhulst, Alexander Busch, and Kam Sripada. *Report Survey Post-Doctoral Researchers at NTNU*. Trondheim: The Interest Organization for PhDs, Post-Docs, and Temporary Scientific Employees at NTNU (DION), 2016, p. 15. URL: http://org.ntnu.no/dion/wp-content/uploads/2017/05/DION-postdoc-survey-results_Final-report_without-attachments.pdf.

[XIX] Alexander Busch, Kam Sripada, and Elli Verhulst. *PhD Budget Regulations at NTNU*. Trondheim: The Interest Organization for PhDs, Post-Docs, and Temporary Scientific Employees at NTNU (DION), 2016, p. 22. URL: http://org.ntnu.no/dion/wp-content/uploads/2017/04/DION-Report_PhD-Budget_160413_AB.pdf.

[XX] Alexander Busch, Kam Sripada, and Elli Verhulst. *PhD Duty Work Regulations at NTNU*. Trondheim: The Interest Organization for PhDs, Post-Docs, and Temporary Scientific Employees at NTNU (DION), 2016, p. 20. URL: http://org.ntnu.no/dion/wp-content/uploads/2017/04/DION-Report_PhD-DutyWork_160413_AB.pdf.

[XXI] Alexander Busch, Mathias Hauan Arbo, Sam A. Kasimba, and Kam Sripada. *PhD Working Conditions at NTNU with a Special Focus on PhD Candidates with Kids*. Trondheim: The Interest Organization for PhDs, Post-Docs, and Temporary Scientific Employees at NTNU (DION), 2017, p. 47. URL: http://org.ntnu.no/dion/wp-content/uploads/2017/05/DION-Report_PhD-WorkCond_PhD_with_kids.pdf.

B

User Defined Functions (UDF)

In this appendix, all UDF source codes relevant for the main part of this thesis are provided. Please note that XXX.

B.1. Dune2D - UDF code of paper (VI)

This appendix contains the UDF source code *Dune2D* of the conference paper *A 2D sediment bed morphodynamics model for turbulent, non-Newtonian, particle-loaded flows* [VI].

UDFs/dune2d.c

```c

/* Dune2D */

/* Fluent */
#include "udf.h"
#include "unsteady.h"
#include "mem.h"
#include "dynamesh_tools.h"
#include "sg.h"

/* Zone Identifiers */
#define BC_movingbed_ID (8) /* ID of MovingBed boundary */

/* Operating point */
#define FluidBulkVel (0.81) /* Fluid bulk velocity */
#define InitialBedHeight (0.005) /* Initial bed height */

/* Case geometry */
#define ChannelHeight (0.04) /* inlet height - TODO compute from mesh and make dynamic for inflow profile */
#define A_Pipe (M_PI*ChannelHeight*ChannelHeight/4.0) /* Pipe cross-sectional area */
#define Q_f (FluidBulkVel*A_Pipe) /* Volumetric fluid flow rate */
#define delta_z (1.0) /* z-spacing - Unit length as 2D */

/* Physical constants */
#define gravity (9.81) /* gravitational acceleration */

/* Fluid properties */
#define rho_f (1000.0) /* density water */
#define sigma_t (0.9) /* turbulent Prandt-Schmidt number */

/* Solid properties */
#define d_s (0.0012 ) /* particle diameter */
#define k_s (2.5*d_s) /* sediment roughness height */
#define rho_s (2500.0) /* solid density */
#define phi (30.0 * M_PI / 180.0) /* Angle of repose */
#define alpha_s_bed (0.55) /* Solids fraction in bed load layer */
```

```c
#define alpha_f_bed (1-alpha_s_bed) /* Fluids fraction in bed load layer, "Bed porosity", "Void fraction" */
#define s (rho_s/rho_f) /* Relative density */

/* Bed load model */
#define GravitationalStress (rho_f * (s - 1.0) * gravity * d_s) /* Denominator of Shields number */
#define C_q_0 (12.0 / ( 1.0 - alpha_f_bed)) /* Nominator is 12 in Tron, why? */
#define C_grad_h (1.5)

/* UDM enumerators */
enum UDMnames { WSS, BLTR, ECT, EST, SMF, SSRC, FSRC, NBH, DHDX, MBWF, SSV, N_REQ_UDM };
/*     Description
WSS    Wall shear stress on "moving bed"
BLTR   Bed load transport rate
ECT    Exner convective term
EST    Exner source term
SMF    Net solid volumetric flux from "moving bed" wall into wall-adjacent grid cell
SSRC   Solid mass source in wall-adjacent grid cell
FSRC   Fluid mass source in wall-adjacent grid cell
NBH    New bed height
DHDX   Geometrical gradient of "moving bed" face
MBWF   Cell flag <--> Cell is moving bed wall-adjacent
SSV    Settling velocity of solids in "moving bed" wall-adjacent grid cell
*/


/* Global variables */
real delta_x; /* x-spacing */
real U;  /* Current fluid bulk velocity */

/* Function declaration */
real CompFaceGradient(face_t, Thread *);
real CompDeltaX(face_t, Thread *);
real CompSetVel(real, real, real);
void UpdateUDM(enum UDMnames, face_t, Thread *, real);
void WriteUDMtoTextFile(real, Thread *);
real CompShearStress_mag(face_t, Thread *);
real CompBedLoadTranRate(real, real, face_t, Thread *);
real CompDepositionRate(face_t, Thread *);
real CompEntrainmentRate(face_t, Thread *);




/* ****************************************************************************************** */
/* Various functions */
/* ****************************************************************************************** */

/* Compute face gradient dh/dx for current face */
real CompFaceGradient(face_t face, Thread *mix_face_thread)
{
  real x_node[2], y_node[2], dx, dy, dhdx;
  int n;
  Node *node_p;

  /* Get x- and y-coordinates of face nodes */
  f_node_loop(face, mix_face_thread, n)
  {
    node_p = F_NODE(face, mix_face_thread, n);
    x_node[n] = NODE_X(node_p); /* x-coordinates of nodes */
    y_node[n] = NODE_Y(node_p); /* y-coordinates of nodes */
  }

  /* Compute dx and dy based on which node comes first in array */
  if (x_node[0] < x_node[1])
  {
    dx = x_node[1] - x_node[0];
    dy = y_node[1] - y_node[0];
  }
  else
  {
    dx = x_node[0] - x_node[1];
    dy = y_node[0] - y_node[1];
  }

```

```c

  dhdx = (y_node[1] - y_node[0]) / (x_node[1] - x_node[0]);
  dhdx = (y_node[0] - y_node[1]) / (x_node[0] - x_node[1]);


  /* Compute gradient */
  dhdx = dy / dx;

  /* ?????????????????????????????????????????????????????????????????????? */

  /* TODO Check if by using the following macros the face gradient is obtained more conveniently */
  real A[ND_ND];    /* area normal vector, boundary face area normals always point out of the domain */
  real ds;      /* distance between the cell centroid and the face centroid */
  real es[ND_ND];   /* unit normal vector in the direction from centroid of cell c0 to the face centroid */
  real A_by_es;   /* Projected area */
  real dr0[ND_ND];  /* value vector that connects the centroid of cell c0 to the face centroid */

  /* Fluid and solid wall face threads */
  Thread *flu_face_thread = THREAD_SUB_THREAD(mix_face_thread, 0);
  Thread *sol_face_thread = THREAD_SUB_THREAD(mix_face_thread, 1);


  /* Mixture thread values */
  BOUNDARY_FACE_GEOMETRY(face, mix_face_thread, A, ds, es, A_by_es, dr0);

  /* Fluid thread values */
  BOUNDARY_FACE_GEOMETRY(face, flu_face_thread, A, ds, es, A_by_es, dr0);

  /* Solid thread values */
  BOUNDARY_FACE_GEOMETRY(face, sol_face_thread, A, ds, es, A_by_es, dr0);

  /* ?????????????????????????????????????????????????????????????????????? */


  return dhdx;
}


/* Compute delta x for current face */
real CompDeltaX(face_t face, Thread *mix_face_thread)
{
  real x_node[ND_ND], dx;
  int n;
  Node   *node_p;

  /* Loop all face nodes and get node coordinates */
  f_node_loop(face, mix_face_thread, n)
  {
    node_p = F_NODE(face, mix_face_thread, n);
    x_node[n] = NODE_X(node_p); /* Get x-coordinates of nodes */
  }

  /* Compute delta_x */
  dx = fabs(x_node[1] - x_node[0]);

  return dx;
}


/* Re-compute solids settling velocity */
real CompSetVel(real v_set, real mu_eff, real gamma_dot_global)
{
  real Re_p, c_D, gamma_dot_eff, mu_eff2;

  /* Effective strain rate */
  /* gamma_dot_eff = sqrt(pow(gamma_dot_global, 2.0) + pow(2.0*v_set / d_s, 2.0)); */

  /* Effective viscosity based on effective strain rate */
  /* mu_eff2 = (0.0026 - 0.001) / (1.0 + pow(0.008*gamma_dot_eff, 0.37)) + 0.001; */

  /* Particle Reynolds number */
  /* Re_p = rho_f*v_set*d_s / mu_eff2; */

```

```
  /* Particle Reynolds number */
  Re_p = rho_f*v_set*d_s / mu_eff;

  /* Coefficient of drag (Schiller-Naumann) */
  c_D = (24.0 / Re_p)*(1.0 + 0.15*pow(Re_p, 0.687));

  /* Settling velocity */
  v_set = sqrt(4.0*d_s*gravity*(s - 1.0) / (3.0*c_D));

  return v_set;
}


/* Update F_UDMI and C_UDMI for current Enumerator value from current face */
void UpdateUDM(enum UDMnames Enumerator, face_t face, Thread *mix_face_thread, real new_value)
{
  /* Wall adjacent mixture cell index */
  cell_t mix_c0 = F_C0(face, mix_face_thread);

  /* Wall adjacent mixture cell Thread */
  Thread *mix_ct0 = THREAD_T0(mix_face_thread);

  /* Save to face UDM */
  F_UDMI(face, mix_face_thread, Enumerator) = new_value;

  /* Save to cell UDM */
  C_UDMI(mix_c0, mix_ct0, Enumerator) = new_value;
}


/* Write all UDM values to text file*/
void WriteUDMtoTextFile(real flow_time, Thread *mix_face_thread)
{
  /* Local variables */
  FILE *fp;
  face_t face;
  real face_pos[ND_ND];
  char *line = "------------------------------------------------------------"
    "------------------------------------------------------------"
    "------------------------------------------------------------"
    "------------------------------------------------------------"
    "------------------------------------------------------------"
    "\n";
  char *heading = "Time\t\t"
    "Face#\t"
    "x_face\t\t"
    "y_face = h_b\t"
    "tau_w\t\t"
    "q_b\t\t"
    "Convective\t"
    "Source\t\t"
    "E + D\t\t"
    "mass_src_s\t"
    "mass_src_f\t"
    "h_b_n\t \t"
    "DHDX\t\t"
    "vel_set_s \n";
  char *definitions = "%f\t"
    "%u\t"
    "%f\t"
    "%f\t"
    "%f\t"
    "%f\t"
    "%f\t"
    "%f\t"
    "%f\t"
    "%f\t"
    "%f\t"
    "%f\t"
    "%f\t"
    "%f\t"
    "\n";
  char filename[100];
  sprintf(filename, "./udm-values/UDM_values_t=%f.txt", flow_time);

```

```
  fp = fopen(filename, "a");
  fprintf(fp, line);
  fprintf(fp, "t = %f\n", flow_time);
  fprintf(fp, line);
  fprintf(fp, heading);
  fprintf(fp, line);

  begin_f_loop(face, mix_face_thread)
  {
    /* Get face coordinates of current face = Initial face positions */
    F_CENTROID(face_pos, face, mix_face_thread);

    fprintf(fp, definitions, \
      flow_time, \
      face, \
      face_pos[0], \
      face_pos[1], \
      F_UDMI(face, mix_face_thread, WSS), \
      F_UDMI(face, mix_face_thread, BLTR), \
      F_UDMI(face, mix_face_thread, ECT), \
      F_UDMI(face, mix_face_thread, EST), \
      F_UDMI(face, mix_face_thread, SMF), \
      F_UDMI(face, mix_face_thread, SSRC), \
      F_UDMI(face, mix_face_thread, FSRC), \
      F_UDMI(face, mix_face_thread, NBH), \
      F_UDMI(face, mix_face_thread, DHDX), \
      F_UDMI(face, mix_face_thread, SSV));
  }
  end_f_loop(face, mix_face_thread)

    fprintf(fp, "\n");
  fprintf(fp, "\n");
  fprintf(fp, "\n");
  fclose(fp);
}



/* ************************************************************************************** */
/* Boundary and initial conditions */
/* ************************************************************************************** */

/* Parabolic velocity profile at inlet */
DEFINE_PROFILE(parabolic_velocity_profile, phase_face_thread, position)
{

  /* This UDF defines a custom velocity profile for the inlet boundary zone and is hooked to  the appropriate velocity phase in Fluent in the relevant boundary condition dialog box.
  Appropriate phase variables will be passed to the function by the solver at run time. See UDF manual page 299 */

  /* Get mixture domain */
  Domain *mix_domain = Get_Domain(1);

  /* Get mixture face thread of "moving bed" */
  Thread *mix_face_thread = Lookup_Thread(mix_domain, BC_movingbed_ID);

  /* Local variables  */
  real  face_pos[ND_ND]; /* Face position vector */
  Node  *node_p;
  face_t  face = 298; /* First face */
  real  x_face, y_face, x_node, y_node; /* Face and node x- & y-coordinates */
  real  u, h, H, A_Bed, h_bed_inlet;

  real  current_time = CURRENT_TIME;
  int n;

  /* Get current bed height at inlet  */
  F_CENTROID(face_pos, face, mix_face_thread); /* Get face coordinates of first cell */
  x_face = face_pos[0]; /* Get x-component of current face */

  f_node_loop(face, mix_face_thread, n)
  {
    node_p = F_NODE(face, mix_face_thread, n);
    x_node = NODE_X(node_p); /* x-coordinate of node */
```

```
    y_node = NODE_Y(node_p); /* y-coordinate of node */

    /* Node is upstream <--> inlet node */
    if (x_node < x_face) { h_bed_inlet = y_node; }
  }

  H = ChannelHeight;
  h = h_bed_inlet;

  /* Current cross-sectional area of bed based on pipe cross-sectional area */
  A_Bed = (pow((H / 2.0), 2.0)*acos(1.0 - 2.0*h / H) - (H / 2.0 - h_bed_inlet)*pow((H*h - h*h), 0.5));

  /* Current fluid bulk velocity based on existing cross-sectional flow area */
  U = Q_f / (A_Pipe - A_Bed);

  /* Loop all boundary faces and compute corresponding x-velocity */
  begin_f_loop(face, phase_face_thread)
  {
    /* Get face coordinates */
    F_CENTROID(face_pos, face, phase_face_thread);
    y_face = face_pos[1]; /* Get y-component of current face */

    /* x-velocity in current cell */
    u = 2.0*U - 2.0*U / pow(((h - H) / 2.0), 2.0)*pow((y_face - (h + (H - h) / 2.0)), 2.0);

    /* Assign to current face */
    F_PROFILE(face, phase_face_thread, position) = u;
  }
  end_f_loop(face, phase_face_thread)

}

/* Solid mass source term for "moving bed"-adjacent grid cell */
DEFINE_SOURCE(sol_mass_SRC, cell, sol_cell_thread, dS, eqn)
{
  /* This macro will loop through all cells of the domain and will get passed the pointer to the cell thread of the solid phase as it is hooked to the solid mass transport equation? */

  /* Solid phase cell thread --> Mixture cell Thread */
  Thread *mix_cell_thread = THREAD_SUPER_THREAD(sol_cell_thread);

  real source;

  /* Check if the current cell is "moving bed"-adjacent */
  if (C_UDMI(cell, mix_cell_thread, MBWF) == 1.0)
  {
    /* Compute solid mass source with units [kg/m3/s] */
    source = C_UDMI(cell, mix_cell_thread, SMF)*rho_s*delta_x*delta_z / C_VOLUME(cell, mix_cell_thread); /* Solids fraction in bed load layer times total source */

    /* Update cell UDM */
    C_UDMI(cell, mix_cell_thread, SSRC) = source;
  }
  else
  {
    /* Cell is not "moving bed"-adjacent <--> Source term is zero */
    source = 0.0;
    dS[eqn] = 0.0;
  }
  return source;
}

/* Fluid mass source term for "moving bed"-adjacent grid cell */
DEFINE_SOURCE(flu_mass_SRC, cell, flu_cell_thread, dS, eqn)
{
  /* This macro will loop through all cells of the domain and will get passed the pointer to the cell thread of the fluid phase as it is hooked to the fluid mass transport equation? */

  /* Fluid phase cell thread --> Mixture cell Thread */
  Thread *mix_cell_thread = THREAD_SUPER_THREAD(flu_cell_thread);

  real source;

  /* Check if the current cell is "moving bed"-adjacent */
```

```c
  if (C_UDMI(cell, mix_cell_thread, MBWF) == 1.0)
  {
    /* Compute fluid mass source with units [kg/m3/s] */
    source = alpha_f_bed / alpha_s_bed*C_UDMI(cell, mix_cell_thread, SMF)*rho_f*delta_x*delta_z / C_VOLUME(cell, mix_cell_thread);

    /* Update cell UDM */
    C_UDMI(cell, mix_cell_thread, FSRC) = source;
  }

  else
  {
    /* Cell is not "moving bed"-adjacent <--> Source term is zero */
    source = 0.0;
    dS[eqn] = 0.0;
  }
  return source;
}

/* Initialisation */
DEFINE_INIT(initialisation, mix_domain)
{
  /* DEFINE_INIT always refers to the mixture domain.
  So far, only the UDMs are initialized, this should be phase-independent, therefore a loop in the mixture domain should be sufficent. */


  /* Mixture face thread of "moving bed" wall */
  Thread *mix_face_thread = Lookup_Thread(mix_domain, BC_movingbed_ID);

  /* Fluid and solid wall face threads */
  Thread *flu_face_thread = THREAD_SUB_THREAD(mix_face_thread, 0);
  Thread *sol_face_thread = THREAD_SUB_THREAD(mix_face_thread, 1);

  /* Local variables */
  cell_t cell, mix_c0;
  face_t face;
  Node   *node_p;
  Thread *mix_cell_thread, *mix_ct0;

  real face_pos[ND_ND], x_node[2], mu_eff, v_set;
  real flow_time = CURRENT_TIME;

  /* Check if sufficient amopunt of UDMs are available */
  if (N_UDM < N_REQ_UDM)
  {
    Message("Number of UDM's : %d\n", N_UDM);
    Message("Number of used UDM's : %d\n", N_REQ_UDM);
    Error("ERROR : Number of UDM's too small");
  }

  /* Loop over all cell threads in the mixture domain */
  thread_loop_c(mix_cell_thread, mix_domain)
  {
    /* Loop over all cells in current cell thread and sets UDMs to zero */
    begin_c_loop_all(cell, mix_cell_thread)
    {
      /* Loop through enumerations of UDMs */
      for (int i = WSS; i<N_REQ_UDM; i++)
      {
        C_UDMI(cell, mix_cell_thread, i) = 0.0;
      }
    }
    end_c_loop_all(cell, mix_cell_thread)
  }

  /* Loop over all faces of "moving bed" wall */
  begin_f_loop(face, mix_face_thread)
  {
    /* Get face coordinates of current face = Initial face positions */
    F_CENTROID(face_pos, face, mix_face_thread);

    /* Loop through enumerations of UDMs */
    for (int i = WSS; i < N_REQ_UDM; i++)
    {
```

```
      if (i == NBH)
      {
        F_UDMI(face, mix_face_thread, i) = face_pos[1];
      }
      else if (i == SSV)
      {
        F_UDMI(face, mix_face_thread, i) = v_set;
      }
      else if (i == MBWF)
      {
        F_UDMI(face, mix_face_thread, i) = 1.0;
      }
      else
      {
        F_UDMI(face, mix_face_thread, i) = 0.0;
      }
    }

    /* Wall adjacent mixture cell index & Thread */
    mix_c0 = F_C0(face, mix_face_thread); /* Get cell of current face */
    mix_ct0 = THREAD_T0(mix_face_thread); /* Get cell thread of current face thread*/

    /* Wall adjacent fluid cell index & Thread */
    cell_t flu_c0 = F_C0(face, flu_face_thread);
    Thread *flu_ct0 = THREAD_T0(flu_face_thread);

    /* Effective viscosity in wall-adjacent grid cell */
    mu_eff = C_MU_EFF(flu_c0, flu_ct0);

    /* Compute Stokes settling velocity */
    v_set = pow(d_s, 2.0)*(rho_s - rho_f)*gravity / (18.0*mu_eff);

    /* Set wall-adjacent cell UDMs */
    C_UDMI(mix_c0, mix_ct0, NBH) = face_pos[1]; /* bed height = face y-component */
    C_UDMI(mix_c0, mix_ct0, MBWF) = 1.0; /* Set flag <--> This cell is a "moving bed"-adjacent cell */
    C_UDMI(mix_c0, mix_ct0, SSV) = v_set; /* Stokes settling velocity */

    /* Compute mesh delta_x from first face */
    if (face == 298) { delta_x = CompDeltaX(face, mix_face_thread); }
  }
  end_f_loop(face, mix_face_thread)

    /* Write current values of all UDMs to text file */
    WriteUDMtoTextFile(flow_time, mix_face_thread);
}

/* Rename UDMs */
DEFINE_ON_DEMAND(rename_UDMs)
{
  Set_User_Memory_Name(0, "UDM0: Shear stress acting on bed");
  Set_User_Memory_Name(1, "UDM1: Bed load transport rate");
  Set_User_Memory_Name(2, "UDM2: Exner convective term");
  Set_User_Memory_Name(3, "UDM3: Exner source term");
  Set_User_Memory_Name(4, "UDM4: Net solid volumetric flux from bed load layer into wall-adjacent grid cell");
  Set_User_Memory_Name(5, "UDM5: Solid mass source in wall-adjacent grid cell");
  Set_User_Memory_Name(6, "UDM6: Fluid mass source in wall-adjacent grid cell");
  Set_User_Memory_Name(7, "UDM7: Bed height");
  Set_User_Memory_Name(8, "UDM8: Geometrical gradient of bed");
  Set_User_Memory_Name(9, "UDM9: Cell flag <--> Cell is moving bed wall-adjacent");
  Set_User_Memory_Name(10, "UDM10: Settling velocity of solids in bed load layer wall-adjacent grid cell");
}

/* ************************************************************************************** */
/* Exner equation */
/* ************************************************************************************** */

/* Compute shear stress for current face */
real CompShearStress_mag(face_t face, Thread *flu_face_thread)
{
  real ShearForce_mag, ShearStress_mag, area;
  real FC[ND_ND], A[ND_ND];

```

```c
  /* Get face area vector */
  F_AREA(A, face, flu_face_thread);

  /* Get face center position */
  F_CENTROID(FC, face, flu_face_thread);

  /* Get face area */
  area = NV_MAG(A);

  /* Compute shear force magnitude */
  ShearForce_mag = NV_MAG(F_STORAGE_R_N3V(face, flu_face_thread, SV_WALL_SHEAR));

  /* Compute shear stress magnitude based on face area */
  ShearStress_mag = ShearForce_mag / area;

  return ShearStress_mag;
}

/* Compute volumetric bed load transport rate for current face */
real CompBedLoadTranRate(real teta, real teta_cr, face_t face, Thread *mix_face_thread)
{
  cell_t flu_c0;
  Thread *flu_ct0;
  real q_x0, q_x, u_x;

  /* Get x-component of fluid velocity of wall-adjacent grid cell */
  Thread *flu_face_thread = THREAD_SUB_THREAD(mix_face_thread, 0);
  flu_c0 = F_C0(face, flu_face_thread);
  flu_ct0 = THREAD_T0(flu_face_thread);
  u_x = C_U(flu_c0, flu_ct0);

  /* Bed load transport rate for horizontal bed */
  q_x0 = C_q_0 * sqrt(gravity * (s - 1.0) * pow(d_s, 3.0) * teta) * (teta - teta_cr);

  /* Bed load transport rate for inclined bed*/
  q_x = q_x0 * (u_x / fabs(u_x) - C_grad_h * F_UDMI(face, mix_face_thread, DHDX)); /* TODO: What happens if dhdx is larger than 2/3? */

  return q_x;
}

/* Compute volumetric bed load transport rate incl. all variables for upstream face */
real CompBedLoadTranRate_us(face_t face_us, Thread *mix_face_thread)
{
  /* Fluid and solid wall face threads */
  Thread *flu_face_thread = THREAD_SUB_THREAD(mix_face_thread, 0);
  Thread *sol_face_thread = THREAD_SUB_THREAD(mix_face_thread, 1);

  /* Wall adjacent fluid cell index & Thread */
  cell_t flu_c0 = F_C0(face_us, flu_face_thread);
  Thread *flu_ct0 = THREAD_T0(flu_face_thread);

  /* Local variables */
  real face_pos[ND_ND];
  real dhdx, beta, ShearStress_mag, teta, angle, mu_eff, dstar, teta_cr0, teta_cr, q_x_us;
  real y_face, current_bed_height;

  /* Geometrical gradient of current face */
  dhdx = CompFaceGradient(face_us, mix_face_thread);

  /* Bed slope */
  beta = atan(dhdx);

  /* Wall shear stress magnitude acting on current (sloped) face */
  ShearStress_mag = CompShearStress_mag(face_us, flu_face_thread);

  /* Dimensionless Shields number for sloped face */
  teta = ShearStress_mag / GravitationalStress;

  /* Effective viscosity in wall-adjacent grid cell */
  mu_eff = C_MU_EFF(flu_c0, flu_ct0);

  /* Dimensionless particle diameter */
  dstar = d_s*pow((s - 1.0)*gravity / pow(mu_eff / rho_f, 2.0), 0.3333333333333);

```

```c
  /* Critical Shields number for horizontal bed */
  teta_cr0 = (0.24 / dstar) + 0.055 * (1.0 - exp(-0.02 * dstar));

  /* Critical Shields number with slope correction for inclined bed */
  angle = phi + beta;
  if (angle < 0.0) angle = 0.0; /* Limitation concept taken from Tron - TODO: Check with Export */
  if (angle > 0.5*M_PI) angle = 0.5 * M_PI; /* Limitation concept taken from Tron - TODO: Check with Export */
  teta_cr = teta_cr0 * sin(angle) / sin(phi);

  /* Get current bed height - TODO check approach from UDM vs from face*/
  F_CENTROID(face_pos, face_us, mix_face_thread); /* Get face coordinate of upstream cell */
  y_face = face_pos[1]; /* Get y-component of upstream face from face coordinate*/
  current_bed_height = F_UDMI(face_us, mix_face_thread, NBH); /* Get y-component of upstream face from UDM */

  /* Bed load transport rate per unit bed width of current face */
  /* Bed load transport only occurs */
  /* - if the bed shear stress is above the critical shear stress <--> teta > teta_c */
  /* - and if a bed exists <--> current_bed_height > 0 */
  if ((teta > teta_cr) && (current_bed_height > 0.0))
  {
    q_x_us = CompBedLoadTranRate(teta, teta_cr, face_us, mix_face_thread);
  }
  else
  {
    q_x_us = 0.0;
  }

  return q_x_us;
}

/* Compute deposition flux for current face */
real CompDepositionRate(face_t face, Thread *mix_face_thread)
{
  /* Fluid and solid wall face threads */
  Thread *flu_face_thread = THREAD_SUB_THREAD(mix_face_thread, 0);
  Thread *sol_face_thread = THREAD_SUB_THREAD(mix_face_thread, 1);

  /* Wall adjacent mixture cell index & Thread */
  cell_t mix_c0 = F_C0(face, mix_face_thread);
  Thread *mix_ct0 = THREAD_T0(mix_face_thread);

  /* Wall adjacent fluid cell index & Thread */
  cell_t flu_c0 = F_C0(face, flu_face_thread);
  Thread *flu_ct0 = THREAD_T0(flu_face_thread);

  /* Wall adjacent solid cell index & Thread */
  cell_t sol_c0 = F_C0(face, sol_face_thread);
  Thread *sol_ct0 = THREAD_T0(sol_face_thread);

  /* Get flow current time */
  real current_time = CURRENT_TIME;

  /* Get required cell values */
  real V = C_V(sol_c0, sol_ct0); /* Solid v-velocity, TODO compare with v_set */
  real alpha_f = C_VOF(flu_c0, flu_ct0); /* Fluid volume fraction */
  real alpha_s = C_VOF(sol_c0, sol_ct0); /* Solid volume fraction */
  real mu_eff = C_MU_EFF(flu_c0, flu_ct0); /* Effective viscosity */
  real gamma_dot = C_STRAIN_RATE_MAG(flu_c0, flu_ct0); /* Strain rate magnitude of background fluid */

  /* Local variables */
  real v_set, v_set_iter, Re_p, n, D;
  real delta_v_set = 1.0;

  /* Solids settling velocity guess from previous time step */
  v_set = C_UDMI(mix_c0, mix_ct0, SSV);

  /* Iteratively compute solids settling velocity */
  while (fabs(delta_v_set) > 0.01)
  {
    /* Re-compute solids settling velocity */
    v_set_iter = CompSetVel(v_set, mu_eff, gamma_dot);

```

```
    /* Difference of original and recomputed settling velocity */
    delta_v_set = v_set - v_set_iter;

    /* Overwrite settling velocity with re-computed settling velocity */
    v_set = v_set_iter;
  }

  /* Save current solids settling velocity to UDMs for next time step */
  UpdateUDM(SSV, face, mix_face_thread, v_set);

  /* Particle Reynolds number */
  Re_p = rho_f*v_set*d_s / mu_eff;

  /* Hindered settling exponent n of Zaki & Richardson */
  n = (0.27*pow(Re_p, 0.9) + 5.1) / (0.1*pow(Re_p, 0.9) + 1.0);

  /* Deposition rate incl. hindered settling */
  D = -alpha_s*(pow(alpha_f, n)*v_set);

  return D;
}

/* Compute entrainment flux for current face */
real CompEntrainmentRate(face_t face, Thread *mix_face_thread)
{
  /* Fluid and solid wall face threads */
  Thread *flu_face_thread = THREAD_SUB_THREAD(mix_face_thread, 0);
  Thread *sol_face_thread = THREAD_SUB_THREAD(mix_face_thread, 1);

  /* Wall adjacent mixture cell index & Thread */
  cell_t mix_c0 = F_C0(face, mix_face_thread);
  Thread *mix_ct0 = THREAD_T0(mix_face_thread);

  /* Wall adjacent fluid cell index & Thread */
  cell_t flu_c0 = F_C0(face, flu_face_thread);
  Thread *flu_ct0 = THREAD_T0(flu_face_thread);

  /* Wall adjacent solid cell index & Thread */
  cell_t sol_c0 = F_C0(face, sol_face_thread);
  Thread *sol_ct0 = THREAD_T0(sol_face_thread);

  /* Local variables */
  real mu_lam, mu_turb, mu_eff, d_eff, d_turb;
  real x_cell[ND_ND], face_pos[ND_ND];
  real y1, y2, dalphady, E;

  /* Get required cell values */
  mu_lam = C_MU_L(flu_c0, flu_ct0); /* Laminar viscosity */
  if (rp_turb)
  {
    mu_turb = C_MU_T(flu_c0, flu_ct0); /* Turbulent viscosity */
    mu_eff = C_MU_EFF(flu_c0, flu_ct0); /* Effective viscosity */
  }
  real alpha_s = C_VOF(sol_c0, sol_ct0); /* Solid volume fraction */

  /* Get solid volume fraction gradient - TODO Why does it not work? */
  if (NULL != THREAD_STORAGE(sol_ct0, SV_VOF_G)) /* Checks if gradient exists, does not in first
      iteration */
  {
    dalphady = C_VOF_G(sol_c0, sol_ct0)[1]; /* Get solid volume fraction gradient at cell center */
  }
  else
  {
    dalphady = 0.0;
  }

  /* Laminar diffusivity */
  d_eff = mu_lam;

  if (rp_turb)
  {
    d_turb = mu_turb / sigma_t; /* Turbulent diffusivity */
    d_eff += d_turb;
  }

```

```
  /* Compute solid fraction gradient, from wall-adjacent grid cell center to" moving bed" */
  y1 = F_UDMI(face, mix_face_thread, NBH); /* Get y-component of face coordinate from UDMI */
  F_CENTROID(face_pos, face, mix_face_thread); /* Get face coordinates */
  y1 = face_pos[1]; /* Get y-component of face coordinate from Face */
  C_CENTROID(x_cell, mix_c0, mix_ct0); /* Get cell center coordinates */
  y2 = x_cell[1]; /* Get y-component of cell coordinate from Face */
  dalphady = (alpha_s - alpha_s_bed) / (y2 - y1); /* Compute solid volume fraction gradient */

  /* Entrainment rate */
  E = -d_turb*dalphady / rho_s;

  return E;
}

/* Solve Exner equation with first-order upwind scheme */
DEFINE_EXECUTE_AT_END(solve_exner)
{
  /* Mixture domain and Thread */
  Domain *mix_domain = Get_Domain(1);
  Thread *mix_face_thread = Lookup_Thread(mix_domain, BC_movingbed_ID);

  /* Fluid and solid wall face threads */
  Thread *flu_face_thread = THREAD_SUB_THREAD(mix_face_thread, 0);
  Thread *sol_face_thread = THREAD_SUB_THREAD(mix_face_thread, 1);

  face_t face, face_us;

  real flow_time = CURRENT_TIME;
  real delta_t = CURRENT_TIMESTEP;
  real face_pos[ND_ND], A[ND_ND];
  real cellvolume, facearea;

  real dhdx, alpha, beta, teta, angle, mu_eff, dstar, teta_cr0, teta_cr;
  real tau_wall, ShearStress_mag, ShearStress_x, q_x, q_x_us, q_x_down, current_bed_height, new_bed_height, delta_h;
  real D, E, convectiveterm, sourceterm;

  /* NOTE: Fluent does not access the faces in the movingbed face loop in the correct order due to an odd face numbering concept.
  Check numbering with script "Ini_CheckCellNumbering_Standard.c" ,
  then implement and test correct stepwise treatment in "Ini_CheckCellNumbering_Stepwise.c".
  Current face IDs
  ----------------------------------------------
  |     |     |     |     |     |     |     |
  | 298 |  0  |  1  | ... | 296 | 297 | 299 |
  |     |     |     |     |     |     |     |
  ----------------------------------------------
  */

  /* Compute new bed height */
  begin_f_loop(face, mix_face_thread) /* Loop all faces of" moving bed" wall */
  {
    /* Wall adjacent mixture cell index & Thread */
    cell_t mix_c0 = F_C0(face, mix_face_thread);
    Thread *mix_ct0 = THREAD_T0(mix_face_thread);

    /* Wall adjacent fluid cell index & Thread */
    cell_t flu_c0 = F_C0(face, flu_face_thread);
    Thread *flu_ct0 = THREAD_T0(flu_face_thread);

    /* Wall adjacent solid cell index & Thread */
    cell_t sol_c0 = F_C0(face, sol_face_thread);
    Thread *sol_ct0 = THREAD_T0(sol_face_thread);


    /* Geometrical gradient of current face */
    dhdx = CompFaceGradient(face, mix_face_thread);

    /* Bed slope */
    beta = atan(dhdx);

    /* Wall shear stress magnitude acting on current (sloped) face */
    ShearStress_mag = CompShearStress_mag(face, flu_face_thread);

    /* Save Wall shear stress magnitude to UDMs */
```

```
  UpdateUDM(WSS, face, mix_face_thread, ShearStress_mag);

  /* Dimensionless Shields number for sloped face */
  teta = ShearStress_mag / GravitationalStress;

  /* Effective viscosity in wall-adjacent grid cell */
  mu_eff = C_MU_EFF(flu_c0, flu_ct0);

  /* Dimensionless particle diameter */
  dstar = d_s*pow((s - 1.0)*gravity / pow(mu_eff / rho_f, 2.0), 0.3333333333333);

  /* Critical Shields number for horizontal bed */
  teta_cr0 = (0.24 / dstar) + 0.055 * (1.0 - exp(-0.02 * dstar));

  /* Critical Shields number with slope correction for inclined bed */
  angle = phi + beta;
  if (angle < 0.0) angle = 0.0; /* Limitation concept taken from Tron - TODO: Check with Export */
  if (angle > 0.5*M_PI) angle = 0.5 * M_PI; /* Limitation concept taken from Tron - TODO: Check with Export */
  teta_cr = teta_cr0 * sin(angle) / sin(phi);

  /* Get current bed height - TODO check approach from UDM vs from face*/
  F_CENTROID(face_pos, face, mix_face_thread); /* Get face coordinates of current cell */
  current_bed_height = face_pos[1]; /* Get y-component of current face from face coordinate*/
  current_bed_height = F_UDMI(face, mix_face_thread, NBH); /* Get y-component of current face from UDM */

  /* Entrainment rate */
  /* Entrainment does not occur */
  /* - if the critical shields number is not exceeded <--> teta <= teta_c */
  /* - or if the sediment bed is not existing  <--> current_bed_height <= 0.0 */
  if ((teta <= teta_cr) || (current_bed_height <= 0.0))
  {
    E = 0.0;
  }
  else
  {
    E = CompEntrainmentRate(face, mix_face_thread);
  }

  /* Deposition rate */
  D = CompDepositionRate(face, mix_face_thread);

  /* Save net volumetric solid flux to UDMs */
  UpdateUDM(SMF, face, mix_face_thread, E + D);

  /* EXNER sourceterm */
  sourceterm = delta_t / alpha_s_bed * (E + D);

  /* Save Exner sourceterm to UDMs */
  UpdateUDM(EST, face, mix_face_thread, sourceterm);




  /* ???????????????????????????????????????????????????????????????????????? */

  /* ToDo - Test face area and volume values */
  cellvolume = C_VOLUME(mix_c0, mix_ct0);
  F_AREA(A, face, mix_face_thread);
  facearea = NV_MAG(A);

  /* ???????????????????????????????????????????????????????????????????????? */

  /* Bed load transport rate per unit bed width of current face */
  /* Bed load transport only occurs */
  /* - if the bed shear stress is above the critical shear stress <--> teta > teta_c */
  /* - and if a bed exists <--> current_bed_height > 0 */
  if ((teta > teta_cr) && (current_bed_height > 0.0))
  {
    q_x = CompBedLoadTranRate(teta, teta_cr, face, mix_face_thread);
  }
  else
  {
```

```c
      q_x = 0.0;
    }

    /* Save bed load transport rate to UDMs*/
    UpdateUDM(BLTR, face, mix_face_thread, q_x);


    /* Bed load transport rate  of upstream face */
    /* The upstream face depends on the direction of the bed load transport rate. */

    /* Check different face cases and determine upstream bed load transport rate */
    if (face == 0) /* Second face */
    {
      if (q_x > 0.0)
      {
        /* Positive fluid velocity direction --> face 298 */
        face_us = 298;
      }
      else
      {
        /* Negative fluid velocity direction --> face 298 */
        face_us = 1;
      }
      q_x_us = CompBedLoadTranRate_us(face_us, mix_face_thread);
    }
    else if (face == 298) /* First face */
    {
      if (q_x > 0.0)
      {
        /* Positive fluid velocity direction --> Ghost face */

        /* BC-Alternative 1: Upstream transport rate = current transport rate */
        q_x_us = q_x;

        /* BC-Alternative 2: Upstream transport rate = 0 */
        q_x_us = 0.0;

        /* BC-Alternative 3: Relate to wall shear stress of inlet velocity profile */
        /* current_bed_height = F_UDMI(face, mix_face_thread, NBH); */
        /* delta_h = ChannelHeight - current_bed_height; */
        /* tau_wall = mu_eff*8.0*FluidBulkVel / delta_h; */
        /* ... */
      }
      else
      {
        /* Negative fluid velocity direction --> face 0 */
        q_x_us = CompBedLoadTranRate_us(0, mix_face_thread);
      }
    }
    else if (face == 297) /* Third-last face */
    {
      if (q_x > 0.0)
      {
        /* Positive fluid velocity direction --> face 296 */
        face_us = face - 1;
      }
      else
      {
        /* Negative fluid velocity direction --> face 299 */
        face_us = face + 2;
      }
      q_x_us = CompBedLoadTranRate_us(face_us, mix_face_thread);
    }
    else if (face == 299) /* Last face */
    {
      if (q_x > 0.0)
      {
        /* Positive fluid velocity direction --> Ghost face */
        q_x_us = q_x;
      }
      else
      {
        /* Negative fluid velocity direction --> face 297 */
        q_x_us = CompBedLoadTranRate_us(297, mix_face_thread);
      }
```

```
    }
    else /* All other faces */
    {
      if (q_x > 0.0)
      {
        /* Positive fluid velocity direction --> face 296 */
        face_us = face - 1;
      }
      else
      {
        /* Negative fluid velocity direction --> face 299 */
        face_us = face + 1;
      }
      q_x_us = CompBedLoadTranRate_us(face_us, mix_face_thread);
    }

    /* Delta x of current face */
    delta_x = CompDeltaX(face, mix_face_thread);

    /* EXNER convective term */
    convectiveterm = delta_t / alpha_s_bed / delta_x*(q_x - q_x_us);

    /* Save convective term to UDMs*/
    UpdateUDM(ECT, face, mix_face_thread, convectiveterm);

    /* Compute new y-position of current face */
    new_bed_height = current_bed_height - convectiveterm - sourceterm;

    /* Save new y-position of current face to UDM */
    if (new_bed_height > 0.0)
    {
      UpdateUDM(NBH, face, mix_face_thread, new_bed_height);
    }
    else
    {
      UpdateUDM(NBH, face, mix_face_thread, 0.0);
    }
  }
  end_f_loop(face, mix_face_thread)

    /* Write current values of all UDMs to text file */
    WriteUDMtoTextFile(flow_time, mix_face_thread);
}



/* ********************************************************************************************* */
/* Update deformable boundary nodes */
/* ? Compute node from face values of field variables http://www.eureka.im/280.html */
/* https://www.cfd-online.com/Forums/fluent-udf/173970-node-data-usage-udf.html */
/* ********************************************************************************************* */
DEFINE_GRID_MOTION(update_node_positions, domain, dt, time, dtime)
{
  /* Mixture domain and thread */
  Thread *mix_face_thread = DT_THREAD((Dynamic_Thread *)dt);

  /* Local variables */
  face_t face, face_ds, face_us, face_min_gradient, face_max_peak;
  cell_t mix_c0;
  Thread *mix_ct0;
  Node   *node_p;
  real x_face, y_face_new, y_face_new_us, y_face_new_ds, dhdx; /* Face coordinates */
  real delta_x_node, x_node, y_node, x_node_us, x_node_ds, y_node_us_new, y_node_ds_new, dy, y_n_new; /* Node coordinates */
  real flow_time = CURRENT_TIME;
  real face_pos[ND_ND];
  int ReposeViolation = 0;
  int n;

  /* Local variables for searching faces */
  real y_face_new_pre, dhdx_pre;
  real y_face_new_max = 0.0;
  real dhdx_min = 0.0;


```

```

  /∗ ∗∗∗∗∗∗∗∗∗∗∗∗∗∗∗∗∗∗∗∗∗∗∗∗∗∗∗∗∗∗∗∗∗∗∗∗∗∗∗∗∗∗∗∗∗∗∗∗∗∗∗∗∗∗∗∗∗∗∗∗ ∗/
  /∗ Loop all faces ∗/
  /∗ Determine new node y−positions from face position −−> N_UDMI ∗/
  /∗ Determine face gradients, check face angle vs. angle of repose and set violation flag ∗/
  /∗ ∗∗∗∗∗∗∗∗∗∗∗∗∗∗∗∗∗∗∗∗∗∗∗∗∗∗∗∗∗∗∗∗∗∗∗∗∗∗∗∗∗∗∗∗∗∗∗∗∗∗∗∗∗∗∗∗∗∗∗∗ ∗/

  /∗ Modify first face and first node − Face ID 298 ∗/
  face = 298; /∗ Set face index of first face ∗/
  face_ds = 0; /∗ Set face index of downstream face ∗/

  /∗ Current first face x−coordinate ∗/
  F_CENTROID(face_pos, face, mix_face_thread); /∗ Get face coordinates ∗/
  x_face = face_pos[0]; /∗ Get x−component of first face ∗/

  /∗ New first and downstream face y−coordinates ∗/
  y_face_new = F_UDMI(face, mix_face_thread, NBH); /∗ Get new y−coordinate of first face ∗/
  y_face_new_ds = F_UDMI(face_ds, mix_face_thread, NBH); /∗ Get new y−coordinate of downstream face ∗/

  /∗ Loop the faces two nodes and compute new node y−positions ∗/
  f_node_loop(face, mix_face_thread, n)
  {
    node_p = F_NODE(face, mix_face_thread, n);
    x_node = NODE_X(node_p); /∗ x−coordinate of node ∗/
    y_node = NODE_Y(node_p); /∗ y−coordinate of node ∗/

    /∗ Check if node is downstream or upstream of face x−position and average accordingly. ∗/
    if (x_node < x_face) /∗ Node is upstream ∗/
    {
      /∗ Compute new node position based on current face and downstream face y−position ∗/
      y_node_us_new = y_face_new − 0.5∗(y_face_new_ds − y_face_new);

      /∗ Save new node position to N_UDMI ∗/
      N_UDMI(node_p, 0) = y_node_us_new;

      /∗ Save upstream node x−coordinate ∗/
      x_node_us = x_node;
    }
    else /∗ Node is downstream ∗/
    {
      /∗ Compute new node position based on current face and downstream face y−position ∗/
      y_node_ds_new = y_face_new + 0.5∗(y_face_new_ds − y_face_new);

      /∗ Save new node position to N_UDMI ∗/
      N_UDMI(node_p, 0) = y_node_ds_new;

      /∗ Save downstream node y−coordinate ∗/
      x_node_ds = x_node;
    }
  }

  /∗ Compute gradient of first face ∗/
  dhdx = (y_node_ds_new − y_node_us_new) / (x_node_ds − x_node_us);

  /∗ Set flag if angle of repose is violated ∗/
  if (fabs(atan(dhdx))>phi) { ReposeViolation = 1; }

  /∗ Loop all boundary faces and all corresponding nodes − This faceloop will only modify downsstream nodes as the upstream node is already modified ∗/
  begin_f_loop(face, mix_face_thread)
  {
    if (face == 298)
    {
      /∗ First face, do nothing as this has been modified already ∗/
    }
    else
    {
      /∗ Current face x−coordinate ∗/
      F_CENTROID(face_pos, face, mix_face_thread); /∗ Get face coordinates ∗/
      x_face = face_pos[0]; /∗ Get x−component of current face ∗/

      /∗ New current and downstream face x−coordinates ∗/
      y_face_new = F_UDMI(face, mix_face_thread, NBH); /∗ Get new y−coordinate of current face ∗/

```

```
      /* New y-component of downstream face */
      if (face == 297)
      {
        face_ds = face + 2; /* Second last face --> Downstream face 299 */
      }
      else if (face == 299) /* Last face */
      {
        face_ds = face; /* Last face --> Downstream Ghost face */
      }
      else /* All other faces */
      {
        face_ds = face + 1;
      }

      /* Get new y-coordinate of downstream face */
      y_face_new_ds = F_UDMI(face_ds, mix_face_thread, NBH);

      /* Loop the faces two nodes and compute new node y-positions */
      f_node_loop(face, mix_face_thread, n)
      {
        node_p = F_NODE(face, mix_face_thread, n);
        x_node = NODE_X(node_p); /* x-coordinate of node */
        y_node = NODE_Y(node_p); /* y-coordinate of node */

        /* Check if node is downstream or upstream of face x-position and average accordingly. */
        if (x_node < x_face) /* Node is upstream */
        {
          /* Node has been modified in previous loop, get node position from UDM */
          y_node_us_new = N_UDMI(node_p, 0);

          /* Save upstream node x-coordinate */
          x_node_us = x_node;
        }
        else /* Node is downstream */
        {
          /* Compute new node position based on current face and downstream face y-position */
          y_node_ds_new = y_face_new + 0.5*(y_face_new_ds - y_face_new);

          /* Save new node position to N_UDMI */
          N_UDMI(node_p, 0) = y_node_ds_new;

          /* Save downstream node y-coordinate */
          x_node_ds = x_node;
        }
      }

      /* Compute gradient */
      delta_x_node = x_node_ds - x_node_us;
      dhdx = (y_node_ds_new - y_node_us_new) / delta_x_node;

      /* Compute gradient of first face */
      dhdx = (y_node_ds_new - y_node_us_new) / (x_node_ds - x_node_us);

      /* Set flag if angle of repose is violated */
      if (fabs(atan(dhdx))>phi) { ReposeViolation = 1; }


      /* !!!!!!!!!!!!!!!!!!!!!!!!!!!!!!!!!!!!!!!!!!!!!!!!! */

      /* TEST - Search for largest negative gradient */
      if (dhdx < dhdx_min)
      {
        dhdx_min = dhdx;
        face_min_gradient = face;
      }
      dhdx_pre = dhdx;

      /* TEST - Search for highest peak */
      if (y_face_new > y_face_new_max)
      {
        y_face_new_max = y_face_new;
        face_max_peak = face;
      }
      y_face_new_pre = y_face_new;

```

```c
      /* !!!!!!!!!!!!!!!!!!!!!!!!!!!!!!!!!!!!!!!!!!!!!!!!!! */
    }
  }
  end_f_loop(face, mix_face_thread)


    /* ************************************************************ */
    /* Loop while ReposeViolation == TRUE */
    /* Set ReposeViolation == FALSE */
    /* Loop all faces */
    /* Determine face gradients  --> F_UDMI */
    /* Check if angle of repose is violated at current cell */
    /* Check if angle of repose is larer or smaller than zero */
    /* Compute required delta_y to satisfy angle of repose */
    /* Modify nodes accordingly --> N_UDMI */
    /* Set ReposeViolation == TRUE */
    /* ************************************************************ */


    while (ReposeViolation == 1)
    {
      /* Reset repose violation flag */
      ReposeViolation = 0;

      /* Loop all" moving bed" faces */
      begin_f_loop(face, mix_face_thread)
      {
        /* Current face x-coordinate */
        F_CENTROID(face_pos, face, mix_face_thread); /* Get face coordinates */
        x_face = face_pos[0]; /* Get x-component of current face */

        /* Loop the faces two nodes and get all new node coordinates */
        f_node_loop(face, mix_face_thread, n)
        {
          node_p = F_NODE(face, mix_face_thread, n);
          x_node = NODE_X(node_p); /* x-coordinate of node */
          y_node = NODE_Y(node_p); /* y-coordinate of node */

          /* Check if node is downstream or upstream of face x-position */
          if (x_node < x_face) /* Node is upstream */
          {
            /* Get node position from UDM */
            y_node_us_new = N_UDMI(node_p, 0);

            /* Save upstream node x-coordinate */
            x_node_us = x_node;
          }
          else /* Node is downstream */
          {
            /* Get node position from UDM */
            y_node_ds_new = N_UDMI(node_p, 0);

            /* Save upstream node x-coordinate */
            x_node_ds = x_node;
          }
        }

        /* Compute gradient */
        delta_x_node = x_node_ds - x_node_us;
        dhdx = (y_node_ds_new - y_node_us_new) / delta_x_node;

        /* Check for violation of angle of repose of current face */
        if (fabs(atan(dhdx)) > phi + 0.0001)
        {
          /* Set violation flag */
          ReposeViolation = 1;

          /* Compute required dy of nodes such that angle of repose is met */
          dy = delta_x_node / 2.0 * (fabs(dhdx) - tan(phi));

          /* Check for uphill or downhill slope */
          if (atan(dhdx) > 0.0) /* Slope is positive, i.e. uphill */
          {
            f_node_loop(face, mix_face_thread, n)
            {
```

```
            node_p = F_NODE(face, mix_face_thread, n);
            x_node = NODE_X(node_p); /* x-coordinate of node */

            /* Get new node y-coordinate from UDM */
            y_n_new = N_UDMI(node_p, 0);

            if (x_node < x_face) /* Node is upstream */
            {
              N_UDMI(node_p, 0) = y_n_new + dy;
            }
            else /* Node is downstream */
            {
              N_UDMI(node_p, 0) = y_n_new - dy;
            }
          }
        }
        else /* Slope is negative, i.e. downhill */
        {
          f_node_loop(face, mix_face_thread, n)
          {
            node_p = F_NODE(face, mix_face_thread, n);
            x_node = NODE_X(node_p); /* x-coordinate of node */

            y_n_new = N_UDMI(node_p, 0);

            if (x_node < x_face) /* Node is upstream */
            {
              N_UDMI(node_p, 0) = y_n_new - dy;
            }
            else /* Node is downstream */
            {
              N_UDMI(node_p, 0) = y_n_new + dy;
            }
          }
        }
      }
    }
    end_f_loop(face, mix_face_thread)
  }


/* ********************************************************** */
/* Modify mesh */
/* ********************************************************** */

/* Set deforming flag on adjacent cell zone --> cells adjacent to the deforming wall will also be deformed, in order to avoid skewness. */
SET_DEFORMING_THREAD_FLAG(mix_face_thread->t0);

/* Loop all boundary faces and all corresponding nodes, get new node y-coordinates from UDM and update mesh */
begin_f_loop(face, mix_face_thread)
{
  f_node_loop(face, mix_face_thread, n)
  {
    /* Get current node */
    node_p = F_NODE(face, mix_face_thread, n);

    /* Get new node y-position from N_UDMI */
    y_n_new = N_UDMI(node_p, 0);

    /* Assign new node y-coordinate to node */
    /* - if the new node y-position is not below the bottom channel wall <--> y_n_new  >= 0.0 */
    /* - if the new node y-position is not above the top channel wall <--> y_n_new  < ChannelHeight */
    /* - if the current node has not been updated previously */
    if (y_n_new >= 0.0 && y_n_new  < ChannelHeight && NODE_POS_NEED_UPDATE(node_p))
    {
      /* Set flag to indicate that the current node's position has been updated, so that it will not be updated during a future pass through the loop */
      NODE_POS_UPDATED(node_p);

      /* Overwrite the current nodes y-coordinate with the new y-coordinate */
      NODE_Y(node_p) = y_n_new;
    }
```

```
    }
    Update_Face_Metrics(face, mix_face_thread);

    /* Get updated face position */
    F_CENTROID(face_pos, face, mix_face_thread); /* Get face coordinates of current cell */

    /* Update all "new bed height" UDMs */
    UpdateUDM(NBH, face, mix_face_thread, face_pos[1]);

    /* Geometrical gradient of updated face */
    dhdx = CompFaceGradient(face, mix_face_thread);

    /* Save updated gradient to UDMs */
    UpdateUDM(DHDX, face, mix_face_thread, dhdx);
  }
  end_f_loop(face, mix_face_thread)
}
```

B.2. ParticleShear2D - UDF code of paper (II)

This appendix contains the UDF source code *Shear2D* of the journal paper *An Eulerian-Lagrangian CFD study of a particle settling in an orthogonal GNF shear flow* [II].

UDFs/ParticleShear2D.h

```
/* Particle Trajectory header file */




/*****************************************************************************************
Include
*****************************************************************************************/

#include <string.h>
#include <stdio.h>

#include "udf.h"
#include "unsteady.h"
#include "mem.h"
#include "sg.h"



/*****************************************************************************************
Definitions
*****************************************************************************************/

/* Case geometry */
#define h (RP_Get_Real("h_channel")) /* Inlet height [m] */
#define h_0 (0) /* Initial bed height [m] */

/* Physical constants */
#define gravity (9.81) /* gravitational acceleration */

/* Fluid properties */
#define u_bulk (RP_Get_Real("u_bulk")) /* Bulk velocity [m/s] */
#define eta_h2o (0.001002) /* Dynamic (shear) viscosity of water */
#define rho_f (1000.0) /* density water */

/* Rheological properties of the fluid (Cross model) */
/* #define lambda (RP_Get_Real("pac_cross_lambda")); */
/* #define n (RP_Get_Real("pac_cross_n")); */
/* #define mu_0 (RP_Get_Real("pac_cross_mu0")); */
/* #define mu_inf (eta_h2o); */

```

```
/* Solid properties */
#define d_s (0.0003) /* particle diameter */
#define rho_s (2650.0) /* solid density */
#define s (rho_s/rho_f) /* Relative density */



/**************************************************************************************************
Forward declarations
**************************************************************************************************/

/* struct PowerLaw;
struct FourParameterModel;
*/


/**************************************************************************************************
Structures
**************************************************************************************************/

struct PowerLaw {
  real K, n;
};

struct FourParameterModel {
    real lambda, n, mu_0, mu_inf;
};

/*Declares a PowerLaw structure
typedef struct PowerLaw Struct_PowerLaw;
typedef struct PowerLaw Struct_Carreau;
*/

/**************************************************************************************************
Functions
**************************************************************************************************/
/*
Cross2PL(real, real, real, real, real);
Carreau2PL(struct FourParameterModel, real);
*/

extern struct PowerLaw Cross2PL(real lambda, real n, real mu_0, real mu_inf, real SR);
extern struct PowerLaw Carreau2PL(struct FourParameterModel Carreau, real SR);

extern real ViscosityCross(struct FourParameterModel Cross, real SR);
extern real ViscosityCarreau(struct FourParameterModel Carreau, real SR);
```

UDFs/velocity_profiles.c

```
/**************************************************************************************************
UDF for specifying a steady-state velocity profile at 2D channel inlet
Fluent R17.2 UDF manual, 8.1.3. (page 496)
**************************************************************************************************/
/* Additional info
Parabolic velocity profile

Dimensional version adjusts for potentially changing sediment bed with height h_bottom

Requires
#include "udf.h"
*/

#include "ParticleShear2D.h"


/* Parabolic velocity profile

Dimensional version adjusts for potentially changing sediment bed with height h_bottom

Requires
#include "udf.h"
*/
DEFINE_PROFILE(par_vel_pro, thread, position)
```

```
{
  real x[ND_ND]; /* Position vector */
  real y, u1, u2;
  face_t f;
  real m = 1.0/7.0;
  real uTmax = (m+1.0)*(m+2.0)*u_bulk/2.0;


  /* Loop all inlet faces */
  begin_f_loop(f, thread)
  {
    /* Get vector x to current face center  */
    F_CENTROID(x, f, thread);

    if (rp_turb)  /* Turbulent velocity profile */
    {
      if (x[1] < h_0)
      {
        u1 = 0.0;
      }
      else if (x[1] < (h_0+(h-h_0)/2.0))
      {
        u1 = uTmax*pow(2.0*((x[1]-h_0)/(h-h_0)),m);
      }
      else
      {
        u1 = uTmax*pow(2.0*(1.0 -(x[1]-h_0)/(h-h_0)),m);
      }
    }
    else /* Laminar velocity profile */
    {

      /* Non-dimensional y coordinate and velocity u = f(x2) */
      y = 2.0*(x[1] - 0.5*h) / h;
      u1 = 3.0/2.0*u_bulk*(1.0 - y*y);

      /* Dimensional y coordinate and velocity u = f(x2) */
      y = x[1];
      u2 = 2.0*u_bulk-2.0*u_bulk/pow(((h_0-h)/2.0),2.0)*pow((y-(h_0 +(h- h_0)/2.0)),2.0);
    }

    /* Assign velocity */
    F_PROFILE(f, thread, position) = u1;
  }
  end_f_loop(f, thread)
}


/* Experimental velocity profile

Based on polynomials fitted toe xperimental data

Requires
#include "udf.h"
*/
DEFINE_PROFILE(exp_vel_pro, thread, position)
{
  real x[ND_ND]; /* Position vector */
  real y, u;
  real factor = 1.0;
  face_t f;
  real p1, p2, p3, p4, p5, p6;

  /* Determine coefficients of polynomial based on current fluid */
  int fluid = RP_Get_Integer("fluid");
  if (fluid == 1) /* H2O */
  {
    p1 = -5.699e+08;
    p2 = -4.222e+07 ;
    p3 = -1.055e+06;
    p4 = -1.161e+04;
    p5 = -57.62;
    p6 = 0.01091;
  }
  else if (fluid == 2) /* PAC2 */
```

```
  {
    p1 = 0.0;
    p2 = 0.0;
    p3 = 0.0;
    p4 = -780.4;
    p5 = -16.33;
    p6 = 0.002025;
  }
  else /* PAC4 */
  {
    p1 = 0.0;
    p2 = 0.0;
    p3 = 0.0;
    p4 = -1202.0;
    p5 = -24.86;
    p6 = 0.02218;

    /* Scale 0.085 velocity profile to 0.048 */
    if (u_bulk == 0.048)
    {
      factor = 0.048/0.085;
    }
    else
    {
      factor = 1.0;
    }

  }

  /* Loop all inlet faces */
  begin_f_loop(f, thread)
  {
    /* Get vector x to current face center  */
    F_CENTROID(x, f, thread);

    y = x[1]-h;

    u = factor * (p1*pow(y,5.0) + p2*pow(y,4.0) + p3*pow(y,3.0) + p4*pow(y,2.0) + p5*pow(y,1.0) + p6);

    /* Assign velocity */
    F_PROFILE(f, thread, position) = u;
  }
  end_f_loop(f, thread)
}
```

UDFs/utilities.c

```
#include "ParticleShear2D.h"



/* Compute PL coefficients from Cross model for current shear rate */
struct PowerLaw Cross2PL(real lambda, real n, real mu_0, real mu_inf, real SR)
{
  struct PowerLaw PL;

    PL.K = (pow(SR,n*(mu_inf*pow(lambda,2.0*n)*pow(SR,2.0*n) \
    +2.0*mu_0*pow(lambda,n)*pow(SR,n)+mu_0)/(mu_inf*pow(lambda,2.0*n) \
    *pow(SR,2.0*n)+pow(SR,n)*(mu_0+mu_inf)*pow(lambda,n)+mu_0)) \
    *mu_inf*pow(lambda,n) \
    + pow(SR,pow(lambda,n)*pow(SR,n)*n*(mu_0-mu_inf) \
    /(mu_inf*pow(lambda,2.0*n)*pow(SR,2.0*n)+pow(SR,n) \
    *(mu_0+mu_inf)*pow(lambda,n)+mu_0))*mu_0) \
    /(1.0+pow(lambda,n)*pow(SR,n));

    PL.n = (mu_inf*pow(lambda,2.0*n)*pow(SR,2.0*n)-((-n-1.0) \
    *mu_inf+mu_0*(n-1.0))*pow(SR,n)*pow(lambda,n)+mu_0) \
    /(mu_inf*pow(lambda,2.0*n)*pow(SR,2.0*n)+pow(SR,n) \
    *(mu_0+mu_inf)*pow(lambda,n)+mu_0);

  return PL;
}
```

```c


/* Compute PL coefficients from Carreau model for current shear rate */
struct PowerLaw Carreau2PL(struct FourParameterModel Carreau, real SR)
{
  struct PowerLaw PL;

  /* PL coefficients based on current shear rate */
  if (SR < (1.0/Carreau.lambda)) /* Newtonian zero-shear viscosity region */
  {
    PL.K = Carreau.mu_0;
    PL.n = 1.0;
  }
  else /* Shear-thinning region */
  {
    PL.K = Carreau.mu_0*pow(Carreau.lambda,(Carreau.n-1.0));
    PL.n = Carreau.n;
  }

  return PL;
}


/* Compute viscosity from Cross model for current shear rate */
real ViscosityCross(struct FourParameterModel Cross, real SR)
{
  real eta = Cross.mu_inf+(Cross.mu_0-Cross.mu_inf)/(1.0+pow(Cross.lambda*SR, Cross.n));

  return eta;
}


/* Compute viscosity from Carreau model for current shear rate */
real ViscosityCarreau(struct FourParameterModel Carreau, real SR)
{
  real eta = Carreau.mu_inf+(Carreau.mu_0-Carreau.mu_inf)*pow(1.0+pow(Carreau.lambda*SR, 2.0), (Carreau.n-1.0)/2.0);

  return eta;
}
```

UDFs/rheology.c

```c
/*****************************************************************************************
UDF for Cross rheology model
*****************************************************************************************/
/* Additional info
This rheology model differs from the Cross model of fluent as follows:
 - It features a high-shear-rate Newtonian viscosity mu_inf, which is equal to the solvent, here H2O.
 - It has the exponent = n_Cr, the Fluent version has the exponent = 1 - n_Cr

Requires
#include "udf.h"
*/

#include "ParticleShear2D.h"




DEFINE_PROPERTY(rheology_cross,c,t)
{
  real SR, eta;

  /* Rheological properties of the fluid */
  struct FourParameterModel Cross;
  Cross.lambda = RP_Get_Real("cross/lambda");
  Cross.n = RP_Get_Real("cross/n");
  Cross.mu_0 = RP_Get_Real("cross/mu_0");
  Cross.mu_inf = RP_Get_Real("cross/mu_inf");

  SR = C_STRAIN_RATE_MAG(c, t);
```

```c

  eta = ViscosityCross(Cross, SR);

  return eta;
}
```

UDFs/drag_force.c

```c
/**************************************************************************************************
UDF for computing DPM particle drag force for shear-thinning fluids

in the form required by Fluent: (18 Cd Re/24)
- where in general both c_D and Re are functions of a viscosity that varies with shear rate
- and the effective shear rate as seen by the particle is computed as the vector sum of Fluents
  shear rate and a shear rate induced by the particles relative velocity.

Two DPM drag macros DEFINE_DPM_DRAG are provided:
- DEFINE_DPM_DRAG(drag_force_st,Re,p) for shear-thinning fluids as described above and based on
  drag laws as defined in section "Functions" below.
- DEFINE_DPM_DRAG(drag_force_n,Re,p) for Newtonian fluids based on Schiller & Naumann (1933)


See Fluent R17.2 UDF manual, 2.5.3. (page 183)
**************************************************************************************************/
/* Additional info
DEFINE_DPM_DRAG is used to specify the drag between particles and fluid as a dimensionless group:
  (18 Cd Re/24)
  as it appears in the drag force per unit particle mass (eq. (2.19), page 183).

Drag coefficient of Fluent ("Spherical drag law") based on
  R. Clift, J. R. Grace and M. E. Weber "Bubbles, Drops, and Particles" (1978).

Requires
  #include "udf.h"
*/


#include "ParticleShear2D.h"



/**************************************************************************************************
Functions (Various drag laws)
**************************************************************************************************/
/* Additional info

*/
/* Coefficient of drag - Schiller-Naumann (1933) */
real c_D_SchillerNaumann(real Re)
{
  real c_D;
  if (Re > 1000.0)
  {
    c_D = 0.44;
  }
  else
  {
    c_D = (24.0 / Re)*(1.0 + 0.15*pow(Re, 0.687));
  }
  return (c_D);
}


/* Viscoelastic correction of drag_force, Acharya (1976)
- corrects Acharya drag law for viscoelastic effects
- uses particle Reynolds number based on  v_r / d_p */
real c_D_correction_Acharya(struct FourParameterModel Carreau, struct PowerLaw PL, real Re, real SR, real c_D)
{
  /* Time scale lambda */
  real lambda;
  int fluid = RP_Get_Integer("fluid");
  if (fluid == 1) /* H2O */
```

```
  {
    lambda = 0.0;
  }
  else if (fluid == 2) /* PAC2 */
  {
    /* Carreau time constant */
    lambda = Carreau.lambda;
  }
  else /* PAC4 */
  {
    /* PAC4 K_FNSC and n_FNSC from Busch et al. (2017) */
    real lambda = pow(0.084 / 2.0 / PL.K, 1.0 / (0.964 - PL.n));

    /* Carreau time constant */
    lambda = Carreau.lambda;
  }

  /* Weissenberg number */
  real Wi = lambda * SR;

  /* Correction of drag coefficent */
  c_D = c_D*(1 - 0.18* pow(Re*Wi, 0.19));

  return (c_D);
}


/* Coefficient of drag - Acharya (1976)
  - determines large Re drag coefficient based on PL model
  - the functions determines PL coefficients from the Carreau model for a given shear rate */
real c_D_Acharya(struct FourParameterModel Carreau, real v_r, real d_p, real Re, real SR)
{
  real f1, f2, f3;
  real c_D;
  struct PowerLaw PL;
  PL  = Carreau2PL(Carreau, SR);

  /* Drag law coefficients */
  f1 = pow(3.0,(3.0*PL.n-3.0)/2.0) \
    * (33.0*pow(PL.n,5.0)-64.0*pow(PL.n,4.0)-11.0*pow(PL.n,3.0)+97.0*pow(PL.n,2.0)+16.0*PL.n) \
    / (4.0*pow(PL.n,2.0)*(PL.n+1.0)*(PL.n+2.0)*(2.0*PL.n+1.0));
  f2 = 10.5*PL.n - 3.5;
  f3 = 0.32*PL.n + 0.13;

  /* Drag law coefficient correction of Kawase and Ulbrecht (1981) */
  f1 = pow(3.0,(3.0*PL.n-3.0)/2.0) \
    * (-22.0*pow(PL.n,2.0)+29.0*PL.n+2.0) \
    / (PL.n*(PL.n+2.0)*(2.0*PL.n+1.0));

  /* Drag law coefficient correction of Kawase and Moo-Young (1986) */
  f1 = pow(3.0,(3.0*PL.n-3.0)/2.0) \
    * (-7.0*pow(PL.n,2.0)+4.0*PL.n+26.0) \
    / (5.0*(PL.n+2.0));

  /* Particle Reynolds number */
  Re  = rho_f*pow(v_r,(2.0-PL.n))*pow(d_p,PL.n)/PL.K;

  /* Drag coefficient */
  if (Re < 1.0)
  {
    c_D = 24.0/Re*f1;
  }
  else
  {
    c_D = 24.0/Re*f1 + f2/(pow(Re,f3));
  }

  /* Viscoelastic correction of drag_force */
  c_D = c_D_correction_Acharya(Carreau, PL, Re, SR, c_D);

  return (c_D);
}


/* Coefficient of drag - Chhabra & Uhlherr (1980)
```

```
  - corrects Schiller & Naumann drag coefficient for nN effects based on Carreau model
  - uses Newtonian zero-shear viscosity based particle Reynolds number */
real c_D_ChhabraUhlherr(struct FourParameterModel Carreau, real Re0, real SR)
{
  /* Carreau number */
  real Ca = Carreau.lambda * SR; /* SR_p; */

  /* Schiller-Naumann coefficient of drag */
  real c_D = c_D_SchillerNaumann(Re0);

  /* nN Schiller-Naumann correction factor */
  real correction = 1.0 + 0.65*(Carreau.n-1.0)*pow(Ca,0.2);

  /* nN corrected Schiller-Naumann coefficient of drag */
  return (c_D*correction);
}


/* Coefficient of drag - Fluents spherical drag law
  - suggested valid range 20 < Re < 260
  - code is taken from https://www.cfd-online.com/Forums/fluent-udf/100432-how-add-velocity-dpm.html
  - is also available as macro in Fluent "drag_force = SphereDragCoeff(Re);"
  - "drag_force = SphereDragCoeff(p->Re);" makes use of Reynolds number provided to DPM drag law */
real c_D_Fluent_spherical(real Re)
{
  real drag_force;
  /* Code snippet from CFD online */
  if (Re < 0.01)
  {
    drag_force=18.0;
  }
  else if (Re < 20.0)
  {
    real w = log10(Re);
    drag_force = 18.0 + 2.367*pow(Re,0.82-0.05*w) ;
  }
  else
  {
    drag_force = 18.0 + 3.483*pow(Re,0.6305) ;
  }

  /* Fluent macro */
  drag_force = SphereDragCoeff(Re);

  /* Coefficient of drag */
  real c_D = 24.0*drag_force/18.0/Re;
  return (c_D);
}



/*************************************************************************************************
UDF particle drag force for non-Newtonian liquids based on several nN drag law models
*************************************************************************************************/
/* Additional info
Computational procedure:
1. Relative particle velocity and magnitude of relative particle velocity
2. Effective (Newtonian) shear rate as seen by the particle
3. True viscosity as seen by the particle based on Cross or Carreau constitutive equation
4. Reynolds number, either using efffective viscosity from 3. or depending on drag law
5. Drag law, one of the above defined functions
6. Return (18 Cd Re/24) to Fluent solver
*/
DEFINE_DPM_DRAG(drag_force_st,Re,p)
{
  /* Tracked_Particle *p cell index of the cell that the particle is currently in */
  cell_t c_p = P_CELL(p);

  /* Tracked particle *p pointer to the thread the particle currently is in */
  Thread *t_p = P_CELL_THREAD(p);

  /* Tracked particle position vector */
  real x[ND_ND];

```

```
/* Particle diameter */
real d_p = P_DIAM(p);

/* Fluid density */
real rho_l = C_R(c_p,t_p);

/* Velocity and shear rate vectors */
real u[ND_ND], v[ND_ND], v_r[ND_ND], a[ND_ND], e_m[ND_ND], e_p[ND_ND], SR_vector[ND_ND];

/* Looping variable and spatial dimensions */
int i, idim = ND_ND;

/* Models to be used */
int model_SR = RP_Get_Integer("model/sr");
int model_SR_p = RP_Get_Integer("model/sr_p");
char *model_R = RP_Get_String("model/rheology");
char *model_c_D = RP_Get_String("model/drag");

/* Rheological properties of the fluid */
struct FourParameterModel Cross;
Cross.lambda = RP_Get_Real("cross/lambda");
Cross.n = RP_Get_Real("cross/n");
Cross.mu_0 = RP_Get_Real("cross/mu_0");
Cross.mu_inf = RP_Get_Real("cross/mu_inf");
struct FourParameterModel Carreau;
Carreau.lambda = RP_Get_Real("carreau/lambda");
Carreau.n = RP_Get_Real("carreau/n");
Carreau.mu_0 = RP_Get_Real("carreau/mu_0");
Carreau.mu_inf = RP_Get_Real("carreau/mu_inf");

/* Shear rates & viscosity */
real SR, SR_p, SR_f = C_STRAIN_RATE_MAG(c_p, t_p);
real eta, eta_Fluent, Re_Fluent, Re0;

/* Drag law */
real w, c_D, c_D_Fluent, drag_force;



/*
    ————————————————————————————————————————————————————————————————————————
      */
/* Relative velocity and magnitude of relative velocity */
/*
    ————————————————————————————————————————————————————————————————————————
      */

/* Fluid velocity components of background shear flow */
u[0] = C_U(c_p,t_p);
u[1] = C_V(c_p,t_p);
#if RP_3D
u[2] = C_W(c_p,t_p);
#endif

/* Loop all spatial dimensions */
for (i=0; i < idim; i++)
{
  /* Particle position components */
  x[i] = P_POS(p)[i];
  real x1 = x[0];
  real x2 = x[1];

  /* Particle velocity components */
  v[i] = P_VEL(p)[i];

  /* Particle relative velocity components */
  v_r[i] = u[i]-v[i];
}

/* Velocity magnitudes */
real u_mag = NV_MAG(u);
real v_r_mag = NV_MAG(v_r);


/*
```

```
------------------------------------------------------------------------ */
/* Effective (Newtonian) shear rate as seen by the particle */
/* ------------------------------------------------------------------------ */

/* Particle relative-velocity induced  shear rate */
if (model_SR_p == 1) /* e.g. Acharya (1976) */
{
  SR_p = v_r_mag/d_p;
}
else if (model_SR_p == 2) /* e.g. Chhabra & Uhlherr (1980) */
{
  SR_p = v_r_mag/(d_p/2.0);
}
else if (model_SR_p == 3) /* Renaud et al. (2004) */
{
  SR_p = v_r_mag/(d_p/sqrt(6.0));
}
else if (model_SR_p == 4) /* tbd */
{}
else /*  */
{

}

/* Total shear based on current shear rate model */
if (model_SR == 1) /* STJ, Literature */
{
  SR = pow( pow(SR_f,2.0) + pow(SR_p,2.0), 0.5);
}
else if (model_SR == 2) /* Addition of shear rate vectors */
{
  NV_VS_VS(SR_vector, =, u, *, SR_f/u_mag, +, v_r, *, SR_p/v_r_mag);
  SR = NV_MAG(SR_vector );
}
else if (model_SR == 3) /* Substraction of shear rate vectors */
{
  NV_VS_VS(SR_vector, =, u, *, SR_f/u_mag, -, v_r, *, SR_p/v_r_mag);
  SR = NV_MAG(SR_vector );
}
else if (model_SR == 4) /*  */
{
  for (i = 0; i < idim; i++)
  {
    /* Unit vector components of fluid velocity directions */
    e_m[i] = u[i] / u_mag;

    /* Unit vector components of particle relative velocity directions */
    e_p[i] = v_r[i] / v_r_mag;
  }

  #if RP_2D
  real factor = abs(e_m[0]*e_p[1]-e_m[1]*e_p[0]);
  #endif

  #if RP_3D
  NV_CROSS(a,e_m,e_p);
  real factor = NV_MAG(a);
  #endif
  SR = pow(pow(SR_f, 2.0) + pow(factor*SR_p, 2.0), 0.5);
}
else /*  */
{

}


/* ------------------------------------------------------------------------ */
/* True viscosity as seen by the particle */
/* ------------------------------------------------------------------------
```

```
      */

  int fluid = RP_Get_Integer("fluid");

  /* Viscosity as determined by Fluent */
  eta_Fluent = C_MU_L(c_p, t_p);

  if (fluid == 1) /* H2O */
  {
    eta = eta_Fluent;
  }
  else /* Shear-thinning case, evaluate effective viscosity with computed total shear rate */
  {
    if (strcmp("Cross",model_R) == 0) /* Rheological model: CROSS */
    {
      eta = ViscosityCross(Cross, SR);
    }
    else if (strcmp("Carreau",model_R) == 0) /* Rheological model: CARREAU */
    {
      eta = ViscosityCarreau(Carreau, SR);
    }
    else /*  */
    {

    }
  }

  /* Turbulent viscosity */
  /* if (rp_turb)
  {

  }
  */


  /* ------------------------------------------------------------------------------------------- */
  /* Reynolds number */
  /* ------------------------------------------------------------------------------------------- */

  /* Fluent default particle Reynolds number based on Fluent macro */
  Re_Fluent = RE_NUMBER(rho_l,v_r_mag,d_p,eta_Fluent);

  /* Fluent default particle Reynolds number based on effective viscosity, should be identical to previous */
  Re_Fluent = rho_l*v_r_mag*d_p / eta_Fluent;

  /* True particle Reynolds number based on true effective viscosity, should be identical to previous */
  Re = rho_l*v_r_mag*d_p / eta;

  /* True particle Reynolds number based on Fluent macro */
  Re = RE_NUMBER(rho_l, v_r_mag, d_p, eta);

  if (strcmp("CU",model_c_D) == 0)
  {
    /* Particle Reynolds number based on Carreau zero-shear viscosity as required for Chhabra & Uhlherr (1980) drag law */
    Re0 = rho_l*v_r_mag*d_p / Carreau.mu_0;
  }

  /* ------------------------------------------------------------------------------------------- */
  /* Drag law */
  /* ------------------------------------------------------------------------------------------- */

  if (strcmp("FS",model_c_D) == 0) /* Fluents spherical drag law */
  {
    c_D_Fluent = c_D_Fluent_spherical(Re_Fluent);
```

```
    c_D = c_D_Fluent_spherical(Re);
  }
  else if (strcmp("SN",model_c_D) == 0) /* Schiller & Naumann (1935) */
  {
    c_D_Fluent = c_D_SchillerNaumann(Re_Fluent);
    c_D = c_D_SchillerNaumann(Re);
  }
  else if (strcmp("A",model_c_D) == 0) /* Acharya (1976) and correction for viscoelastic effects */
  {
    c_D_Fluent = c_D_Acharya(Carreau, v_r_mag, d_p, Re, SR_f);
    c_D = c_D_Acharya(Carreau, v_r_mag, d_p, Re, SR);
  }
  else if (strcmp("CU",model_c_D) == 0) /* Chhabra & Uhlherr (1980) */
  {
    c_D_Fluent = c_D_ChhabraUhlherr(Carreau, Re0, SR_f);
    c_D = c_D_ChhabraUhlherr(Carreau, Re0, SR);
  }
  else /*  */
  {
  }

  /* Drag force as required by Fluent including potential non-Newtonian viscosity correction (first term)*/
  drag_force = eta/eta_Fluent * 18.0*c_D*Re/24.0;

  /* -------------------------------------------------------------------------------------------- */
  /* Output in TUI */
  /* -------------------------------------------------------------------------------------------- */

  Message0("\n particle_drag_coefficient.c \
  \t x %f \
  \t y %f \
  \t SR_f %f \
  \t SR_p %f \
  \t SR %f \
  \t eta_F %f \
  \t eta %f \
  \t Re_Fluent %f \
  \t Re %f \
  \t c_D_Fluent %f \
  \t c_D %f \
  \
  \t \n", x[0], x[1], SR_f, SR_p, SR, eta_Fluent, eta, Re_Fluent, Re, c_D_Fluent, c_D);

  return (drag_force);
}


/*******************************************************************************************
UDF particle drag force for Newtonian fluids based on Schiller & Naumann (1933)
*******************************************************************************************/

DEFINE_DPM_DRAG(drag_force_n,Re,p)
{

  /* Schiller & Naumann (1935) */
  real c_D;
  if (Re > 1000.0)
  {
    c_D = 0.44;
  }
  else
  {
    c_D = (24.0 / Re)*(1.0 + 0.15*pow(Re, 0.687));
  }

  /* Drag force as required by Fluent including potential non-Newtonian viscosity correction (first term)*/
  real drag_force = 18.0*c_D*Re/24.0;

  return (drag_force);
```

```
}
```

B.3. Orbit3D - UDF code of paper (VIII)

This appendix contains the UDF source code *ParticleShear2D* of the journal paper *Cuttings transport: On the coupled effect of drillpipe rotation and lateral motion* [VIII].

UDFs/Orbit3D.c

```
/*****************************************************************************************
UDF for computing mid-point velocities of orbital moving drill string


*****************************************************************************************/

#include "udf.h"
#include "math.h"
#include "dynamesh_tools.h"



/* Global definition of parameters */
real y_0, A_y, A_z, f_y, f_z ;

DEFINE_ADJUST(pass_scheme,d)
{
#if !RP_NODE
  /* Parameters for position of drill string center */
  real y_0 = RP_Get_Real("geo/e")*(RP_Get_Real("geo/d_o")-RP_Get_Real("geo/d_i"))/2.0; /* Dimensional eccentricity = dimensional offset in y-direction */
  real A_y = RP_Get_Real("a/y");  /* Position amplitude y-direction */
  real A_z = RP_Get_Real("a/z");  /* Position amplitude z-direction */
  real f_y = RP_Get_Real("rpm_whirl")/60.0; /* Angular frequency y-direction */
  real f_z = RP_Get_Real("rpm_whirl")/60.0; /* Angular frequency z-direction */
#endif

#if PARALLEL
  host_to_node_real_1(y_0);
  host_to_node_real_1(A_y);
  host_to_node_real_1(A_z);
  host_to_node_real_1(f_y);
  host_to_node_real_1(f_z);
#endif

}



DEFINE_CG_MOTION(drillpipe_motion, dt, vel, omega, time, dtime)
{

  /* Reset velocities */
  NV_S (vel, =, 0.0);

  #if !PARALLEL
  /* Parameters for position of drill string center */
  real y_0 = RP_Get_Real("geo/e")*(RP_Get_Real("geo/d_o")-RP_Get_Real("geo/d_i"))/2.0; /* Dimensional eccentricity = dimensional offset in y-direction */
  real A_y = RP_Get_Real("a/y");  /* Position amplitude y-direction */
  real A_z = RP_Get_Real("a/z");  /* Position amplitude z-direction */
  real f_y = RP_Get_Real("rpm_whirl")/60.0; /* Angular frequency y-direction */
  real f_z = RP_Get_Real("rpm_whirl")/60.0; /* Angular frequency z-direction */
  #endif

  /* Velocities of drill string center */
```

```
  /* First time derivatives of y(t) = (y_0 + A_y) − A_y*cos(2.0*M_PI*f_y*time) and z(t) = A_z*cos(2.0*M_PI*f_z*time) */
  vel[1]=A_y*(2.0*M_PI*f_y)*sin(2.0*M_PI*f_y*time);
  vel[2]=A_z*(2.0*M_PI*f_z)*cos(2.0*M_PI*f_z*time);

}
```